



TECHNICAL REPORT RDMR-AF-14-02

ROTORWASH OPERATIONAL FOOTPRINT MODELING

John R. Preston

U.S. Army RDECOM Forward Element Command-Atlantic and
Aviation and Missile Research, Development, and Engineering Center
86-88 Blenheim Crescent
Ruislip, Middlesex HA4 7HB
United Kingdom

And

**Steven Troutman, Ernie Keen, Mark Silva,
and Natalie Whitman**
Naval Air Systems Command
Patuxent River, MD 20670

And

Mark Calvert, Mike Cardamone, and Marvin Moulton
Aviation Engineering Directorate
Aviation and Missile Research, Development, and Engineering Center
Redstone Arsenal, AL 35898

And

Samuel W. Ferguson
EMA
800 Muirfield Drive
Mansfield, TX 76063

July 2014

Distribution Statement A: Approved for public release; distribution is unlimited.

DISCLAIMER: Reference herein to any specific commercial, private or public products, process, or service by trade name, trademark, manufacturer, or otherwise, does not constitute or imply its endorsement, recommendation, or favoring by the United States Government. The views and opinions expressed herein are strictly those of the authors and do not represent or reflect those of the United States Government.



DESTRUCTION NOTICE

**FOR CLASSIFIED DOCUMENTS, FOLLOW THE PROCEDURES IN
DoD 5200.22-M, INDUSTRIAL SECURITY MANUAL, SECTION II-19
OR DoD 5200.1-R, INFORMATION SECURITY PROGRAM REGULATION,
CHAPTER IX. FOR UNCLASSIFIED, LIMITED DOCUMENTS, DESTROY
BY ANY METHOD THAT WILL PREVENT DISCLOSURE OF CONTENTS
OR RECONSTRUCTION OF THE DOCUMENT.**

DISCLAIMER

**THE FINDINGS IN THIS REPORT ARE NOT TO BE CONSTRUED
AS AN OFFICIAL DEPARTMENT OF THE ARMY POSITION
UNLESS SO DESIGNATED BY OTHER AUTHORIZED DOCUMENTS.**

TRADE NAMES

**USE OF TRADE NAMES OR MANUFACTURERS IN THIS REPORT
DOES NOT CONSTITUTE AN OFFICIAL ENDORSEMENT OR
APPROVAL OF THE USE OF SUCH COMMERCIAL HARDWARE
OR SOFTWARE.**

REPORT DOCUMENTATION PAGE			Form Approved OMB No. 074-0188
Public reporting burden for this collection of information is estimated to average 1 hour per response, including the time for reviewing instructions, searching existing data sources, gathering and maintaining the data needed, and completing and reviewing this collection of information. Send comments regarding this burden estimate or any other aspect of this collection of information, including suggestions for reducing this burden to Washington Headquarters Services, Directorate for Information Operations and Reports, 1215 Jefferson Davis Highway, Suite 1204, Arlington, VA 22202-4302, and to the Office of Management and Budget, Paperwork Reduction Project (0704-0188), Washington, DC 20503			
1. AGENCY USE ONLY	2. REPORT DATE July 2014	3. REPORT TYPE AND DATES COVERED Final	
4. TITLE AND SUBTITLE Rotorwash Operational Footprint Modeling		5. FUNDING NUMBERS	
6. AUTHOR(S) John R. Preston, Steven Troutman, Ernie Keen, Mark Silva, Natalie Whitman, Mark Calvert, Mike Cardamone, Marvin Moulton, and Samuel W. Ferguson			
7. PERFORMING ORGANIZATION NAME(S) AND ADDRESS(ES) Commander, U.S. Army Research, Development, and Engineering Command ATTN: RDMR-AF Redstone Arsenal, AL 35898-5000		8. PERFORMING ORGANIZATION REPORT NUMBER TR-RDMR-AF-14-02	
9. SPONSORING / MONITORING AGENCY NAME(S) AND ADDRESS(ES)		10. SPONSORING / MONITORING AGENCY REPORT NUMBER	
11. SUPPLEMENTARY NOTES			
12a. DISTRIBUTION / AVAILABILITY STATEMENT Approved for public release; distribution is unlimited.		12b. DISTRIBUTION CODE A	
13. ABSTRACT (Maximum 200 Words) Wind or “rotorwash” generated by rotors, ducts, or jets effect the operational suitability and utility of future Vertical Takeoff and Landing (VTOL) aircraft. As the aircraft’s physical size, weight, and disk loading increases beyond the range of current systems, the risk increases that rotorwash operational impact(s) may compromise an aircraft’s ability to satisfy the Warfighter’s needs. Early definition of anticipated rotorwash conditions will permit an assessment of operational suitability and determine whether specific design changes are warranted and/or if acceptable operational tactics, techniques, and procedures can be established.			
This report documents the assessment process, environmental limits, rotorwash modeling, and output display supporting the rotorwash operational footprint model. These elements graphically combine to display the rotorwash operational impact assessment on the ground environment as contour plots or “footprints.” The tools developed are for the single main rotor helicopter, tandem helicopter, and tiltrotor configurations, but they can be extended to encompass additional configurations. The rotorwash operational footprint displays the effect of winds generated by rotor thrust on the surrounding environment. These footprints can be used to evaluate compliance with aircraft performance specifications, verify safe separation distances, or inform design trade studies.			
14. SUBJECT TERMS Rotorwash, Downwash, Outwash, Assessment Process, Environmental Limits, Modeling, Display Operational Footprint			15. NUMBER OF PAGES 404
			16. PRICE CODE
17. SECURITY CLASSIFICATION OF REPORT UNCLASSIFIED	18. SECURITY CLASSIFICATION OF THIS PAGE UNCLASSIFIED	19. SECURITY CLASSIFICATION OF ABSTRACT UNCLASSIFIED	20. LIMITATION OF ABSTRACT SAR

Appendix Authors and Contributing Personnel

A: Rotorwash Scenarios	John Preston, U.S. Army Ernie Keen, U.S. Navy
B: Description of Representative Rotorcraft	Sam Ferguson, EMA John Preston, U.S. Army
C: Personnel Rotorwash Hazards	Sam Ferguson, EMA
D: Ground Structure Related Hazards	Sam Ferguson, EMA
E: Hazards Involving Impact Damage and Materials	Sam Ferguson, EMA
F: Rotorwash Generated Projectile and Debris Hazards	Sam Ferguson, EMA
G: Airport/Heliport Environment	Sam Ferguson, EMA
H: Collection of Field Experience	Natalie Whitman, U.S. Navy
I: Effect of Rotorwash on Trees and Plants	Sam Ferguson, EMA
J: Conceptual Level Model FORTRAN Code	Sam Ferguson, EMA
K: Correlation of Rotorwash Conceptual Level Model to Test Data	Sam Ferguson, EMA
L: Rotorwash High-Fidelity Modeling	Mike Cardamone, U.S. Army Mark Calvert, U.S. Army Marvin Moulton, U.S. Army Mark Silva, U.S. Navy
M: Rotorwash High-Fidelity Tool Correlation and Extension to Test Data	Mike Cardamone, U.S. Army Mark Calvert, U.S. Army Marvin Moulton, U.S. Army John Preston, U.S. Army Mark Silva, U.S. Navy
N: Effect of Wind-Over-Deck and Deck Edge on Rotorwash	Sam Ferguson, EMA
O: Conceptual Based Model Comparisons and Trends	John Preston, U.S. Army Sam Ferguson, EMA
P: Rotorwash Footprint Generation Process	Kenneth Smith, U.S. Navy
Q: Rotorwash Hazard Analysis Reference List	Sam Ferguson, EMA John Preston, U.S. Army Sam Ferguson, EMA
R: Comments on References Providing New Information or Insight to the Rotorwash Hazard Analysis Problem	

Executive Summary

Wind or “rotorwash” generated by rotors, ducts, or jets effect the operational suitability and utility of future Vertical Takeoff and Landing (VTOL) aircraft. As the aircraft’s physical size, weight, and disk loading increases beyond the range of current systems, the risk increases that rotorwash operational impact(s) may compromise an aircraft’s ability to satisfy the Warfighter’s needs. Early definition of anticipated rotorwash conditions will permit an assessment of operational suitability and determine whether specific design changes are warranted and/or if acceptable operational tactics, techniques, and procedures can be established.

This report documents the assessment process, environmental limits, rotorwash modeling, and output display supporting the rotorwash operational footprint model. These elements graphically combine to display the rotorwash operational impact assessment on the ground environment as contour plots or “footprints.” The tools developed are for the single main rotor helicopter, tandem helicopter, and tilt rotor configurations, but they can be extended to encompass additional configurations. The rotorwash operational footprint displays the effect of winds generated by rotor thrust on the surrounding environment. These footprints can be used to evaluate compliance with aircraft performance specifications, verify safe separation distances, or inform design trade studies.

The assessment process uses “scenarios” to describe the bounding conditions within the operational space. Each scenario contains a description of the aircraft flight state and environmental conditions. Together, the scenarios bound the evaluation of the operational space for a wider range of envisioned missions.

The surrounding environment is quantified by limits associated with rotorwash velocity, force and energy on personnel, structures, and materials. Military personnel limits are associated with the strength capabilities required to overcome rotorwash generated drag forces and tolerance to physical injury due to flying projectiles. Structural limits are associated with the magnitude of wind velocity (dynamic pressure based) required to damage surrounding buildings, shelters, and tents. Material limits are referenced to property damage caused by flying projectiles. An additional advisory limit is provided based on dynamic pressure magnitude for an airport or heliport and for landscaping.

Prediction of the wind velocity in the rotorwash flow field utilizes a momentum based conceptual model that is empirically tuned using flight test data. This model is implemented in the computer program, Rotorwash Footprint (RoWFoot). The report documents an unsuccessful attempt to utilize a high-fidelity tool to extend verification of RoWFoot beyond the range of existing flight test data. RoWFoot should be verified beyond the range of existing flight test data using a physics-based model. In the absence of this verification, the confidence in the tuned momentum-theory model is reduced where it extrapolates outside the bounds of correlated flight test data.

Velocity and drag force footprints were generated using RoWFoot results for each operational scenario. Velocity based outwash footprints display the maximum magnitude of wind velocity in the outwash. Force based outwash footprints utilize the PAXman

anthropometric model to determine the drag force on personnel for a given height-velocity profile. Both types of outwash footprints display relevant environmental limits as contour lines on a topographical plot. These footprints allow for “visualization” of the ability of a VTOL aircraft to safely conduct Warfighter missions as influenced by rotorwash effects. Future military VTOL aircraft must have a rotorwash footprint that enables mission requirements to be safely accomplished. Key factors that have the ability to significantly influence the aircraft design or operational envelope are:

- Ground personnel capability limits during external load operations
- Shipboard equipment limits
- Landing zone separation required during single or multiple aircraft operation

The influences of these key factors are captured as a suggested performance specification for future military VTOL aircraft. The text of this specification is—

Rotorwash shall permit operations up to operational capability limits without endangering, damaging, or exceeding physical capabilities of personnel, equipment, or structures.

Specifically, the rotorwash shall allow safe operation during:

- Ground and air taxi maneuvers
- Operations from an unprepared landing zone with internal and external loads
- Shipboard operations with internal and external loads during air operations
- Airborne operations including hoist, fast rope, air-to-air refuel, and air drop

This report documents the rotorwash operational footprint modeling with the associated assessment process, environmental limits, rotorwash modeling, and output display to verify compliance with the first two of the four bullet points of the suggested performance specification. The third bullet requires shipboard equipment limits to be specified. The report provides a limited amount of operational insight to the fourth bullet point.

Future work is recommended to strengthen the rotorwash operational footprint modeling capability expressed in this report. The highest priority efforts are:

- Extension of boundaries of flight test data using high-fidelity modeling
- Development of a LIDAR type sensor for acquisition of future rotorwash data
- Acquisition of test data to support refinement of the personnel stability ratio
- Acquisition of test and analytic modeling data for the effect of rotor spacing on rotorwash

Table of Contents

Table of Contents	1
1.0 Introduction	3
1.1 Purpose.....	4
1.2 Background.....	4
1.3 Approach to Modeling Environment.....	4
2.0 Operational Evaluation Process.....	6
2.1 Operational Evaluation Conditions	6
2.2 Description of Representative Rotorcraft	7
3.0 Operational Environment Characterization	9
3.1 Personnel Related Hazards.....	10
3.1.1 Personnel Overturning Forces and Moments	10
3.1.2 Personnel Biophysical Injury	12
3.2 Ground Structure Related Hazards	12
3.2.1 Permanent Structures	12
3.2.2 Wind Loading on Military Shelters and Tents	13
3.2.3 Wind Loading on Light Structures and Civilian Tents.....	13
3.3 Hazards Involving Impact Damage and Materials	13
3.3.1 Glass	13
3.3.2 Sheet Metal	14
3.3.3 Composite Panels	14
3.4 Rotorwash Generated Projectile and Debris Hazards.....	14
3.5 Airport/Heliport Environment	15
3.6 Landscaping.....	15
4.0 Rotorwash Modeling Methodologies.....	16
4.1 Reference Test Data	16
4.1.1 Flight Test Data	16
4.1.2 High-Fidelity Tool Modeling Data	16
4.2 Rotorwash Conceptual Level Momentum-Based Model	17
4.3 Rotorwash High-Fidelity Modeling	18
4.4 Shipboard Effects on Rotorwash	18
4.4.1 Effect of Wind-Over-Deck	18
4.4.2 Effect of Shipboard Deck Edges.....	19
4.5 Personnel Stability Limit Ratio	19
4.6 Conceptual Model Trends.....	19
5.0 Footprint of Large Rotorcraft on Operational Environment.....	21
5.1 Ground Taxi.....	24
5.2 Hovering Taxi.....	26
5.3 Landing Zone Operations with Internal Payload	28
5.4 Landing Zone Operations with External Payload	30
5.5 Shipboard Operations with Internal Payload	32
5.6 Shipboard Operations with External Payload	34
5.7 Low Altitude Fly-Over.....	36
5.8 Airborne Operations—Hover	36
5.9 Airborne Operations—Low Speed	36

6.0 Conclusions.....	37
7.0 Recommendations.....	38
7.1 Techniques to Mitigate Rotorwash Operational Effect.....	38
7.2 Operational Evaluation.....	39
7.3 Operational Environment Characterization.....	39
7.4 Rotorwash Modeling Methodologies.....	40
7.5 Footprint of Large Rotorcraft on Operational Environment.....	41
7.6 Flight Test Data Collection	41
8.0 References	43
Appendix A: Rotorwash Scenarios.....	44
Appendix B: Description of Representative Rotorcraft.....	50
Appendix C: Personnel Rotorwash Hazards	52
Appendix D: Ground Structure Related Hazards	72
Appendix E: Hazards Involving Impact Damage and Materials	78
Appendix F: Rotorwash Generated Projectile and Debris Hazards	105
Appendix G: Airport/Heliport Environment	120
Appendix H: Collection of Field Experience.....	123
Appendix I: Effect of Rotorwash on Trees and Plants.....	124
Appendix J: Conceptual Level Model FORTRAN Code	151
Appendix K: Correlation of Rotorwash Conceptual Level Model to Test Data.....	214
Appendix L: Rotorwash High-Fidelity Modeling.....	265
Appendix M: Rotorwash High-Fidelity Tool Correlation and Extension to Test Data.....	267
Appendix N: Shipboard Effects on Rotorwash	302
Appendix O: Conceptual Based Model Comparisons and Trends.....	307
Appendix P: Rotorwash Footprint Generation Process	331
Appendix Q: Rotorwash Hazard Analysis Reference List.....	338
Appendix R: Comments on References Providing New Information or Insight to the Rotorwash Hazard Analysis Problem.....	364

Annex—Limited Distribution Data

Associated with this report is an Annex containing flight test data used in correlation of the predictive models. At the time of publication, these data remain Distribution Statement B, with distribution limited to U.S. Government Agencies (Administrative or Operational Use). Other requests for this document shall be referred to the U.S. Army Research, Development, and Engineering Command, Aviation and Missile Research, Development, and Engineering Center, ATTN: RDMR-AF. MS-219-3, NASA Ames Research Center, Moffett Field, CA 94035-1000.

Contents of the Limited Distribution Annex (Distribution Statement B) include:

1. Appendix H: Results of Collection of Field Experience
2. Appendix K: Rotorwash Conceptual Level Model Correlation to UH-60, V-22, and CH-47 Flight Test Data
3. Appendix M: Rotorwash High-Fidelity Tool Correlation to V-22 Flight Test Data

1.0 Introduction

Utilization of Vertical Takeoff and Landing (VTOL) aircraft may be limited by their impact on the surrounding environment. The wake produced by a thrust-generating rotor can have nuisance to hazardous level effects on ground personnel, structures, and equipment as well as negatively affect airborne operations.

Rotorwash is defined as the overall velocity flow field produced by a rotor or other thrust generating device. Regions within the rotorwash include “downwash,” “transition,” and “outwash.” Downwash is the vertical component of the rotorwash flow field under the rotor(s). In the transition region, the downwash contacts the ground plane, turns, and becomes outwash. Outwash is the horizontal component of the rotorwash flow field outside of the area under the rotor(s). Figure 1-1 graphically displays the rotorwash under both a hovering single- and twin-rotor aircraft.

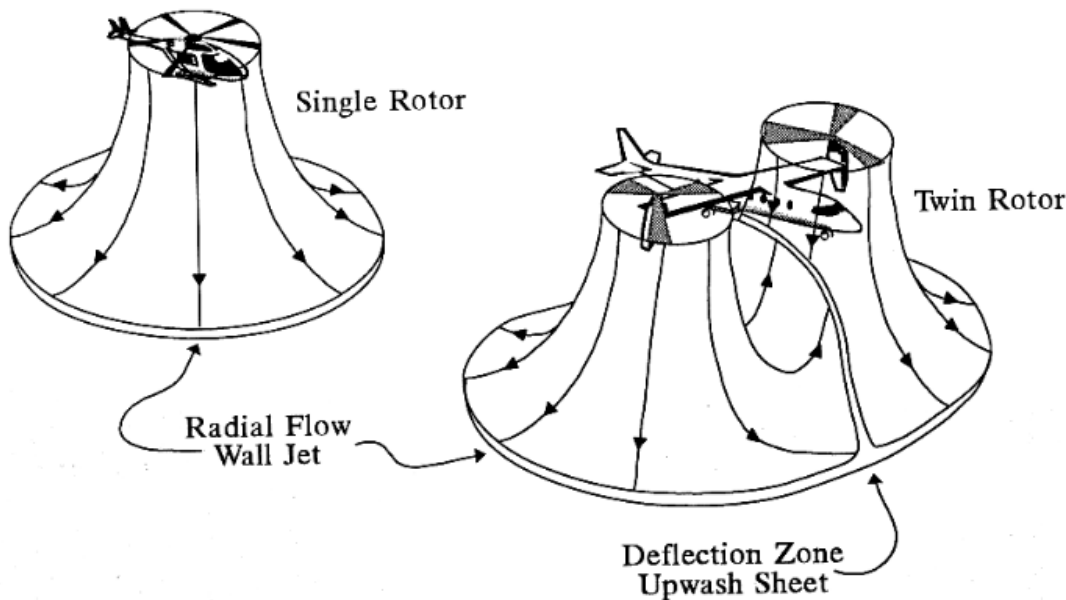


Figure 1-1 Rotorwash Flow Fields of Single- and Twin-Rotor Configurations Operating in Close Proximity to Ground (Reference 1)

The downwash primarily impacts operations directly under the aircraft such as airborne operations. Outwash primarily impacts the ground area surrounding the aircraft. Impact of the outwash on the surrounding environment can be represented as an operational footprint. This footprint defines the landing zone clearance needs, such as separation from structures, unprotected people, other aircraft, and shipboard equipment, as well as displaying the ability of ground personnel to approach and depart the aircraft.

1.1 Purpose

Quantification of the outwash impact supports the development of future aircraft requirements and specifications. This quantification methodology and the associated limits can be depicted as a footprint that the aircraft will have on its operational environment. Prediction and display of the outwash footprint on the ground environment allows visualization of the potential impact that current and future aircraft may have on military operations.

This report documents a methodology used to evaluate future concepts for their outwash footprint and is an evolution of previously used methodologies. The documentation includes evaluation conditions, environmental limitations, modeling methods, and a footprint display method. These methods and limits can be used to support future aircraft development.

A conceptual analysis tool predicts the rotorwash velocity flow field. When used in conjunction with appropriate environmental limits, post-processing allows generation of an outwash footprint to produce topographical-like plots of the VTOL operational impact on the ground environment. This ground environment includes personnel, structures, landscaping, and equipment.

1.2 Background

During the Joint Heavy Lift (JHL) Concept Development Activity (CDA), there were concerns that large VTOL aircraft would limit operations in the ground environment. Past experiences with tilt wing, fan-in-wing, and jet lift aircraft documented issues with the wake eroding ground surfaces and prohibiting operations under the aircraft. Experiences with larger Department of Defense (DoD) rotorcraft, including the CH-53 and V-22, suggested increasing rotor size and loading could prevent future platforms from being used in some operational environments.

This study was initiated to determine the performance-based operational limits related to rotorwash of VTOL aircraft. Results are intended to influence future VTOL rotorwash performance-based requirements.

An analysis and modeling capability for prediction of the outwash operational footprint was developed to support this study. This capability enables evaluation of the rotorwash operational impact of both current and future VTOL aircraft.

1.3 Approach to Modeling Environment

The developed modeling approach combines rotorwash flow field analysis with environmental limits. This facilitates production of operational footprints for hovering VTOL aircraft. These operational footprints appear as topographical-like plots that are

used to visualize the effect the aircraft will have on the ground environment. These plots represent the rotorwash flow field in terms of the impact (limits) on the surrounding environment. These plots also define the distance from the aircraft required for safe operations.

The modeling approach leverages and extends previous efforts in analyzing and modeling the rotorwash flow field. This approach uses a combination of conceptual level modeling and high-fidelity modeling. Modern computer systems and data visualization have enabled refinement beyond the previous state of the art for rotorwash prediction and analysis. High-fidelity modeling is slower, more expensive to execute, and requires a more complete geometric description of the aircraft than conceptual level modeling, but it has the potential to capture the flow field qualities outside the scope of the test data. After correlation to test data, the high-fidelity modeling was used to provide an extended set of values for correlation of the conceptual modeling. This extension included quantitative sets for height above ground, disk loading, and azimuth angle around the aircraft. Unfortunately, discrepancies within the high-fidelity modeling results did not allow the conceptual level modeling to be confidently extrapolated outside the boundaries of the available quality flight test data (as based on an extensive data correlation effort presented in this report). In the absence of this verification, the conceptual level modeling cannot be confidently extrapolated outside the scope of quality flight test data.

Human performance and environmental limits were derived from literature search results and Naval Air Systems Command (NAVAIR) performance testing of military personnel. The literature search produced limits associated with personnel, terrain, structures, landscaping, and equipment. Human performance testing increased the scope and sample size of known personnel limits associated with outwash environments.

2.0 Operational Evaluation Process

This section defines the evaluation cases and associated parameters to the rotorwash operational model. The evaluation cases describe the assessments to be completed. Within each evaluation case, the aircraft and its operational environment are defined by sets of parameters that serve as modeling inputs. Values for these inputs define the aircraft and the operational limits associated with the rotorwash in the surrounding environment. These limits are then used in conjunction with the flow velocity modeling to generate an operational impact footprint for an evaluation case.

2.1 Operational Evaluation Conditions

Assessment of the rotorwash operational impact is performed by a set of evaluation cases. These cases are represented as scenarios. In each scenario, the rotorwash interacts with the external environment including personnel, terrain, structures, and equipment. The operational cases and associated scenarios were constructed to support JHL CDA but can be applied to future acquisition efforts.

In each scenario, a set of conditions defines the aircraft's rotorwash interaction with the external environment. Each interaction contains qualities and characteristics that affect the resultant size of the outwash footprint. Scenarios describe the interaction to link physical limits for personnel or objects in the ground environment to analytical prediction of wind velocity profiles generated within the rotorwash flow field. Nine scenarios were derived to represent the evaluation conditions. These scenarios are documented in [Appendix A](#). During the JHL CDA, these scenarios were refined with Warfighter experience and expected future concept capability needs. The rotorwash evaluation scenarios are:

1. Ground Taxi
2. Hovering Taxi
3. Landing Zone Operations with Internal Payload
4. Landing Zone Operations with External Payload
5. Shipboard Operations with Internal Payload
6. Shipboard Operations with External Payload
7. Low Altitude Flyover
8. Airborne Operations—Hover
9. Airborne Operations—Low Speed

Each scenario contains a description of the operational task, flight state of the aircraft, environmental conditions, and the location of personnel. The expected contribution of the results to the overall operational rotorwash footprint is also defined.

A component of each scenario defines an operational task that is affected by rotorwash. This operational task definition is further expanded to identify the primary operational concern that requires the scenario to be evaluated.

The flight state of the aircraft encompasses the weight and operational characteristics that produce the highest flow velocity (including periodic effects) in the rotorwash region for an evaluation case. By using the maximum flow conditions in the analyses, these scenarios represent the corner points in the evaluation space for rotorwash interactions with the outside environment. This allows a limited number of total cases while capturing the impact to the Warfighter.

Scenario environmental conditions describe the ground state under the aircraft. Ground conditions can vary significantly from an unprepared site with sand, rocks, and/or dirt to the partial ground-plane of a shipboard deck with metal plating and deck movement. Other factors that will influence personnel limits such as the variation in surface roughness that affects the mobility of ground personnel in dry and wet conditions must also be identified.

The location of personnel within each evaluation case documents the presence of ground personnel in the vicinity of the aircraft. For some cases, such as taxi operations, ground personnel are not required in close proximity to the aircraft. The associated outwash footprint becomes a safe clearance area around the aircraft in this scenario. For external payload operations, the ground crew will need to be able to operate directly under the aircraft with the ability to safely enter/exit the hookup area. During this time, the external load rests on the ground and does not contribute to the lift required by the rotor(s).

The potential operational impact section describes the operational activities that may be affected by the rotorwash. This provides rationale behind the scenario case and may influence or enable potential workarounds or mitigation for future platforms.

2.2 Description of Representative Rotorcraft

For purposes of predicting the rotorwash flow field, a rotorcraft can be modeled by its geometry, engineering parameters, and flight state. During conceptual level modeling, the rotorcraft can be characterized by simple geometry, as depicted by the dimensions labeled in Figure 2-1 for a notional tilt rotor. High-fidelity modeling requires more detailed rotorcraft geometry. Once the rotorcraft geometry is defined, the flight state is defined for each of the evaluation cases defined in [Section 2.1](#). In conceptual level modeling, simple engineering parameters are used to generate the rotorwash predictions and link the geometry with the flight state. Although the present modeling development and representation is focused toward single main rotor helicopters, tandem helicopters, and tilt rotors, the methodology can be extended to other configurations. Details of the representative aircraft can be found in [Appendix B](#). Engineering judgment should be applied for conceptual level modeling extrapolated outside of correlating data.

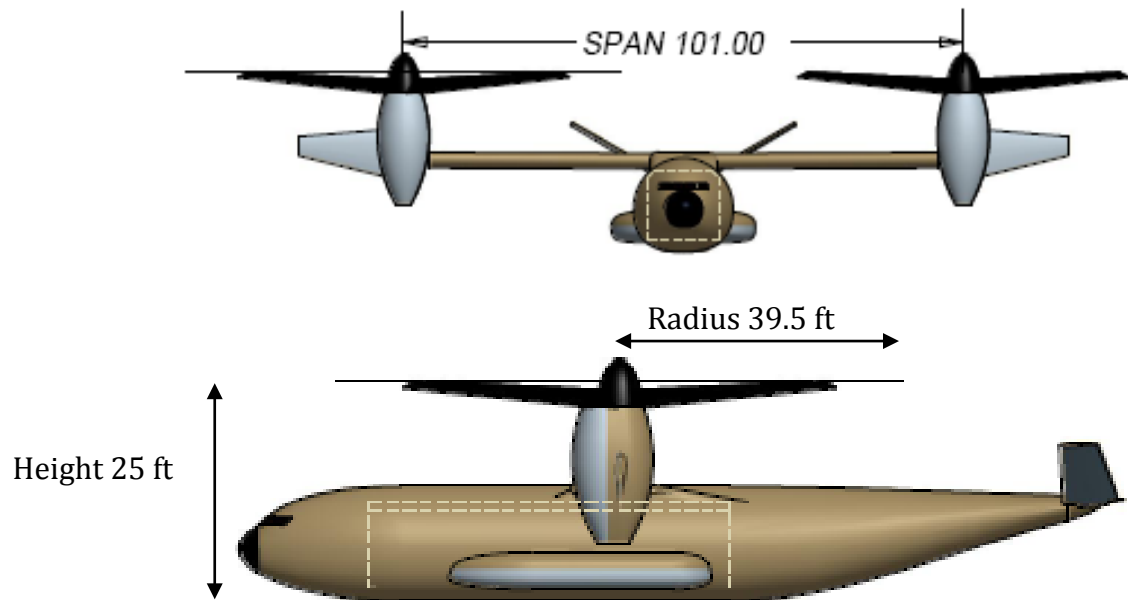


Figure 2-1 Conceptual Level Geometry for Notional Tilt Rotor Model

3.0 Operational Environment Characterization

The goal of this section is to define the primary hazards that predominate in the rotorwash environment and quantify threshold values that should not be exceeded for safety or economic related reasons. A summary list of these hazards, as determined from previous research, is presented in Table 3-1. A description of each hazard associated threshold values is also listed and supporting data are documented in Appendixes [C](#), [D](#), [E](#), and [G](#). Each threshold value is referenced to a “peak” or “mean” condition. The peak condition relates to the highest velocity or force generated by wind gusts. The mean conditions relate to the average wind encountered.

Table 3-1 “Not-To-Exceed Threshold” Outwash Related Hazards

Personnel			
Overturning Force and Moment			
Military			
Caution Zone	Mean	>80 lbs force (wrt PAXman Model)	
Caution Zone	Peak	87-115 lbs force (wrt PAXman Model)	
Hazard Zone	Mean	>87 lbs force (wrt PAXman Model)	
Hazard Zone	Peak	≥ 115 lbs force (wrt PAXman Model)	
Civilian (general population)			
Caution Zone	Peak	33.6-44.7* mph wind velocity	$q = 2.88 - 5.12 \text{ lb/ft}^2$
Hazard Zone	Peak	> 44.7* mph wind velocity	$q > 5.12 \text{ lb/ft}^2$
Biophysical Injury			
Unprotected (eye)		102 ft-lb/ ft^2 particle energy /area	
Protected (incapacitate)		58 ft-lb particle energy	
Structures			
Permanent Structures			
Wind Loading	Mean	62.5* mph wind velocity	$q = 10.0 \text{ lb/ft}^2$
Asphalt Shingles	Peak	60* mph wind velocity	$q = 9.21 \text{ lb/ft}^2$
Military Shelters	Mean	55* mph wind velocity	$q = 7.74 \text{ lb/ft}^2$
Military Shelters	Peak	65* mph wind velocity	$q = 10.81 \text{ lb/ft}^2$
Light Structures/Civilian Tents	Peak	35* mph wind velocity	$q = 3.13 \text{ lb/ft}^2$
Materials Damage by Gravel**			
Glass Damage (annealed glass)		17 mph particle velocity	
Sheet Metal Damage (military)		47.2 mph particle velocity for 0.02-inch depth dent	
Airport/Heliport Environment	Peak	40.3* mph wind velocity	$q = 4.15 \text{ lb/ft}^2$
Landscaping	Peak	39* mph wind velocity	$q = 3.89 \text{ lb/ft}^2$
*Wind Velocity Based on Sea Level Standard Atmospheric Conditions. Dynamic pressure ($q = 0.5 * \text{Air Density} * \text{Wind Velocity}^2$) should be utilized to determine appropriate wind velocity limit at other atmospheric conditions. **Representative gravel is $\frac{3}{4}$ inch with weight of 0.012125 lb (5.5 grams)			

Recommended limits presented in this section are supported by additional data documented in the attached appendixes. These recommended thresholds are based on available data at this point in time. Should additional information or research become available, these recommendations should be updated.

3.1 Personnel Related Hazards

Personnel related hazards in the rotorwash environment can be classified into one of two main categories. The first category involves human performance limitations while functioning within the rotorwash velocity flow field. For example, “Are the wind forces so great that personnel will be blown over?” The second category involves physical injury as the result of being struck by a projectile or piece of flying debris that is blown by the rotorwash flow field. These categories and the associated limits are described further in [Appendix C](#).

3.1.1 Personnel Overturning Forces and Moments

The personnel overturning force and moment hazard applies to ground personnel in close proximity to rotorcraft. This hazard can be subdivided into military and civilian related limits. Differences between these categories arise from assumptions on the physical condition and training associated with military personnel functioning in the rotorwash environment. Civilians in close proximity to rotorcraft will have larger differences in age, physical condition, and experience background that require more conservative limitations on acceptable levels of rotorwash velocity.

3.1.1.1 Military Related Requirements

The development of military personnel overturning force and moment requirements has evolved over time as the result of several ground and flight test experiments. Two major tests with results from three references established personnel limits with respect to overturning forces and moments associated with the CH-53E (Reference 2). A re-examination of these limits (Reference 3) and an extension of the original experiment to a larger sample size was conducted during JHL Concept Development activities (Reference 4). The specific limits, as taken directly from Reference 3, are:

1. The Caution zone begins when peak wind force as calculated using the PAXman human body representation equals 87 lbs. The Caution zone continues until the wind force equals 115 lbs (moving to a hazard zone), or when peak force drops back below 87 lbs.
2. The Hazard zone begins when peak wind force as calculated using the PAXman human body representation equals 115 lbs. The Hazard zone continues until the peak force drops back below 115 lbs.
3. Although unlikely, in any case where the average force exceeds 80 lbs regardless of peak force, there shall be a Caution zone designation.

4. Although unlikely, in any case where the average force exceeds 87 lbs regardless of peak force, there shall be a Hazard zone.
5. Two Hazard/Caution zone maps are required, one for zero ambient wind condition and one for 20-knot headwind ambient wind condition.

In order for ground crew operations to be safe, the non-hazardous zone must be wide enough in order for the crew to have a path of safe entry into the downwash and under the aircraft. A rule of thumb would require at least a 45-degree entrance/exit path (vertex of the angle located at the center of the aircraft downwash pattern).

The PAXman model was developed for military personnel as a reference area for wind drag calculations. It is based on the projection of a 6-foot tall person crouched over and leaning, as he would appear while immersed in the outwash. Reference 5 documents the detailed geometry of the PAXman model and the analysis methodology used to calculate drag. Figure 3-1 and Table 3-2 are taken directly from Reference 5 and document the PAXman area distribution as a 9th order polynomial (half of body width).

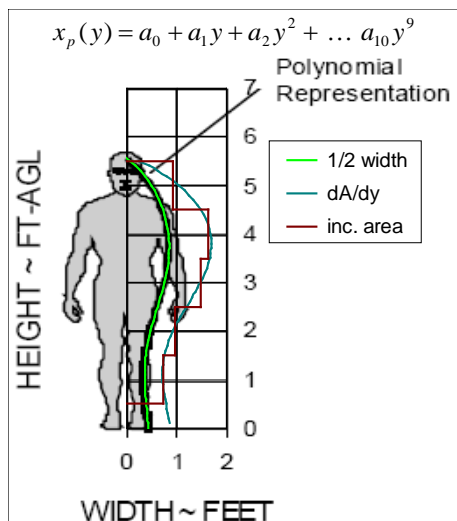


Figure 3-1 PAXman Area Distribution
(Reference 5)

a0	4.30939E-01
a1	-4.63972E-02
a2	-1.39649E-01
a3	1.37545E-01
a4	-2.48764E-02
a5	-5.49253E-04
a6	2.21653E-04
a7	-4.18444E-05
a8	1.45194E-05
a9	-7.80009E-08
a10	-1.89822E-07

Table 3-2 Polynomial Coefficients
(Reference 5)

3.1.1.2 Civilian Related Requirements

Civilian related requirements for wind exposure and overturning force are distinctly different than those for military personnel. Factors such as weight, size, age, health, protective clothing, and task (i.e. holding umbrella or pushing stroller) have important effects on wind velocity threshold limits. The wind engineering community has studied this subject for numerous reasons over the last 40 years. No references were identified that connect any of this research directly to rotorwash applications. However, for civilian rotorwash scenarios, this research provides excellent background and guideline information. The outwash peak velocity approximates the gusty wind conditions for the derived limits. Based on the information collected in [Appendix C](#), the equivalent Caution

zone is 33.6 – 44.7 mph and the Hazard zone is any peak velocity > 44.7 mph at sea level standard conditions. At other atmospheric conditions, the resultant dynamic pressure should be utilized to derive the appropriate velocity limits.

3.1.2 Personnel Biophysical Injury

Personnel “biophysical injury” in the context of this report is defined as “any injury that is the result of being struck by a projectile or debris that is propelled through the air by the rotorwash flow field.” Two major areas of concern have been identified: “What projectile velocities are required to penetrate or severely bruise human skin?” and “What projectile velocities are required to damage the unprotected human eye?” For unprotected personnel, the limiting factor is damage to the eye. The limiting factor for protected personnel is impact by airborne debris. Protective equipment includes eye, skin, and hearing protection. Clothing insulation may also be required for heat loss (i.e. wind chill).

Small objects propelled by rotorwash will produce progressive amounts of eye damage from corneal abrasion, hyphema (bruising), lens dislocation, retinal detachment, and globe (eyeball) rupture. Eye damage criteria apply to both unprotected civilian and military personnel. For this hazard, a conservative limit of 50% risk of corneal abrasion equates to 102 ft-lb/ft² as the limiting factor according to the reference information documented in [Appendix C](#), where ft-lb/ft² is object kinetic energy divided by its area of surface at impact.

Larger objects propelled by rotorwash can penetrate or severely bruise human skin. All velocities associated with these projectiles are related to their kinetic energy and not the rotorwash wind speed that generates the flying debris. Using documentation provided in [Appendix C](#), protected personnel are estimated to have a limit of 58 ft-lb of impact energy before becoming incapacitated due to impact by an airborne object or piece of debris.

3.2 Ground Structure Related Hazards

The wind velocities generated by a rotorwash flow field can damage or collapse structures. Three major categories of structures are considered: permanent structures, military shelters and tents, and light structures/civilian tents. Each category has different limitations as a function of wind speed at sea level standard conditions. At other atmospheric conditions, the resultant dynamic pressure should be utilized to derive the appropriate velocity limits. These categories and the associated limits are described further in [Appendix D](#).

3.2.1 Permanent Structures

Building codes in the United States (and most developed countries) have extensive wind loading requirements for single- and multi-story buildings, signs, and almost all other types of permanent structures. A separate limiting factor for building damage is the wind speed (when exceeded) that can result in damage to asphalt shingles. These two measures

become the defining metrics for rotorwash damage to permanent structures and were derived from the dataset documented in [Appendix D](#). These not-to-exceed metrics are 62.5 mph mean velocity for wind loading and 60 mph peak velocity for asphalt shingles.

3.2.2 Wind Loading on Military Shelters and Tents

Military shelters and tents are frequently cited in the literature and mishap databases as being involved in rotorwash mishaps. Literature survey results are presented in [Appendix D](#). From these results, the wind limits ranged from 40 mph to 100 mph. Based on the type and prevalence of types of structures, the researchers chose a 55 mph mean velocity limit and a 65 mph peak velocity limit for association with this category.

3.2.3 Wind Loading on Light Structures and Civilian Tents

For the purpose of this report, light construction is considered to be non-permitted, loosely constructed shelters. These shelters are ill-defined and are considered to have wind resistance characteristics similar to civilian tents. From the database survey results in [Appendix D](#), the peak wind velocity is 35 mph. This wind velocity is equated to the peak velocity in the outwash flow field.

3.3 Hazards Involving Impact Damage and Materials

Rotorwash related hazards involving debris and material impact often involve complex scenarios. For example, a rock ejected by the rotorwash flow field could shatter plate glass or break a vehicle windshield. The broken glass might also then become an airborne hazard to personnel. This section focuses on limitations associated with the initial impact of the material from rotorwash transported debris. These not-to-exceed limits are associated with several generally accepted damage concepts that are further associated with glass, metals, and composites, irrespective of how the debris impacts the material. Supporting documentation is presented in [Appendix E](#). This appendix also contains additional information on how debris becomes airborne and its associated kinetic energy potential. A $\frac{3}{4}$ -inch piece of gravel with mass of 5.5 grams (0.012125 lb) was chosen as the representative particle to measure impact from airborne debris.

3.3.1 Glass

This report focused on four main types of glass: 1) annealed (or “ordinary” glass), 2) heat-strengthened, 3) tempered, and 4) laminated glass. Most glass products are made from annealed glass, which is often referred to as “ordinary” glass. Different applications use different types of glass. A conservative not-to-exceed limit uses the lower part of a specified Mean Minimum Breakage Velocity (MMBV) range. This range is based on glass type, glass thickness, and standardized projectile or debris mass/energy/velocity combinations that could be present in windstorms or rotorwash flow fields. From the

information contained in [Appendix E](#), annealed glass from 0.2-0.4 inch thickness can withstand projectiles up to 5.5 grams with a MMBV of 17 mph or less (projectile velocity, not wind velocity). This represents the limit associated with glass used for general purposes.

3.3.2 Sheet Metal

In general, small particles or projectiles require substantially less energy to dent steel or aluminum sheet metal than to penetrate it. Components with sheet metal outer construction are frequently associated with other aircraft or vehicles. [Appendix E](#) provides significant detail on this subject. Debris damage to material coating (scratching of paint) is not considered as a limiting factor. Sheet metal material damage in civil applications is not expected to be a limiting condition for rotorwash environmental limitations due to the lower limit expressed in Section 3.3.1. For military aircraft operating in proximity to each other at unimproved landing sites, material damage limit(s) would facilitate determination of separation between aircraft. Using existing automotive research, a 0.02-inch depth dent was arbitrarily chosen by the authors as a limiting condition. Assuming kinetic energy equivalency with the automotive test, a $\frac{3}{4}$ -inch piece of gravel would have a velocity limit of 47.2 mph to produce the 0.02-inch dent.

3.3.3 Composite Panels

Properties of composites vary greatly with their application. In general, composites tend to be stiffer, less elastic in deformation, and have different properties from metals that define damage tolerance. [Appendix E](#) provides some detail on this subject. While damage to composite panels may occur from debris carried in the flow field, composite material damage is not expected to be a limiting condition for rotorwash environmental limitations for civilian applications due to the lower limit expressed in Section 3.3.1. For military applications, further research or application of existing research should be applied to determine acceptable damage levels and velocity limits associated with the representative $\frac{3}{4}$ -inch gravel.

3.4 Rotorwash Generated Projectile and Debris Hazards

It is well accepted and documented that rotorwash can quickly lift and accelerate sand, rocks, sticks, supplies, pieces of equipment, and debris to become hazardous projectiles. The probability that debris will become airborne depends on the type and configuration of the debris (and material properties) as well as the rotorwash flow field. The modeling of debris as projectiles can be broken into three phases: generation, trajectory, and impact. [Appendix E](#) documents a literature survey and presents potential solution methodologies to address each of these three phases of modeling. Accurate modeling of airborne debris is challenging due to the nature of the non-steady rotorwash velocity flow field, the wide variety of potential sources of debris, and the complex interaction of debris with the flow field.

For the purposes of this report, ¾-inch gravel with mass of 5.5 grams was chosen as the representative material for debris propelled by the rotorwash to determine the damage to the surrounding environment. This size of stone is representative of common construction material found on the ground and on rooftops and is also present in field settings where a foreign object debris sweep would have removed larger debris. The ¾-inch gravel is also large enough to do significant damage if it strikes personnel or other materials (glass) in a landing zone.

3.5 Airport/Heliport Environment

Research into the airport/heliport environment has not yielded significant quantifiable data (i.e. wind speeds) which can be used for detailed hazard analysis purposes. However, the available data have provided some insight as to recommended thresholds that should not be exceeded. These insights, documented in [Appendix G](#), are based on literature derived data based on various types of rotorwash related incidents, helicopter wind limitations, and lessons learned. Based on the information presented in [Appendix G](#), any rotorwash peak profile velocity above 40.3 mph has the potential to result in an airport/heliport incident of some type at sea level standard conditions. At other atmospheric conditions, the resultant dynamic pressure should be utilized to derive the appropriate velocity limits.

3.6 Landscaping

Rotorwash has been documented to damage surrounding plants and trees in numerous scenarios. However, a review of published rotorcraft related literature does not indicate any recommended velocity limits to avoid this damage. In contrast, research on windstorm damage does provide significant insight into the wind gust magnitudes that can damage plants and trees. This research is summarized in [Appendix I](#), along with documentation of recent rotorwash incidents and a proposed rotorwash wind velocity limit. The proposed rotorwash plant and tree limit (landscaping size) in the civil environment is 39 mph peak velocity at sea level standard conditions. At other atmospheric conditions, the equivalent dynamic pressure should be utilized to derive the appropriate velocity limit.

4.0 Rotorwash Modeling Methodologies

Rotorwash modeling methods, like most aerodynamics models, vary from simple conceptual models to highly complex Computational Fluid Dynamics (CFD) models. The rotorwash design goal of this project requires a model with rapid computational turnaround time that can be quickly adjusted for rotorcraft configuration differences, such as single main rotor, tandem, and tilt rotor configurations. These requirements inherently lead to the development of a simple modeling approach. The momentum-based modeling approach was chosen to achieve these goals. [Appendix J](#) contains a detailed description of the overall modeling effort and the resultant source code that has been developed as part of this project.

4.1 Reference Test Data

4.1.1 Flight Test Data

Flight test data of varying quality are available for calibration of both the conceptual level momentum-based modeling and high-fidelity modeling. [Appendix K](#) lists the relevant sources of available flight test data along with a summary of the data quality. Based on the available data, the models were primarily correlated to CH-53E (Reference 2), V-22 (Reference 6), and CH-47 (Reference 5) flight test data. These three sources represent the highest quality data for a range of flight conditions. Correlation of the conceptual level model was also conducted to lower quality flight test data for the XV-15 (Reference 7) and H-60 (Reference 8). Full-scale outwash data are often unrepeatable and subject to the variances inherent to flight testing.

It is important to note that a potential exists to dramatically improve the quantity and quality of acquired rotorwash flight test data. This improvement will depend on future investments in Laser Imaging, Detection, and Ranging (LIDAR) sensor technology.

[Appendix K](#) contains unpublished mean and peak velocity profile data from a V-22 hover test at a 20-foot wheel height. These data are compared to V-22 data from Reference 6 at similar test conditions. No effort was made to optimize the acquisition software for rotorwash data purposes, yet the correlation is extremely good. Use of this type of sensor would allow continuous profile measurements in the vertical axis. Adjustment for data acquisition at a different horizontal location would require only seconds. It is roughly estimated that use of this technology will allow for better quality data to be acquired in an order of magnitude less time than present tests require OR an order of magnitude more data in the same amount of time. The reader is referred to the discussion in [Appendix K](#) and the recommendations section for additional information.

4.1.2 High-Fidelity Tool Modeling Data

Current high-quality flight test data are limited in the range of disk loading, hover height, and location of velocity measurement sensors. It is hoped that these data sets can be

extended with some confidence by calibrating a high-fidelity tool's (and computationally expensive) methodology to generate an expanded range of data outside of the flight test data set. This extended data set should then be utilized to correlate a conceptual level model with increased confidence when extrapolating beyond the range of measured flight test conditions. However, at present, the very complex and unsteady flow field of a rotorcraft in-ground effect has only recently begun yielding to physics-based treatment. In absence of adequate analytical tools, full-scale flow field surveys remain the most viable means of characterizing the outwash flow field.

4.2 Rotorwash Conceptual Level Momentum-Based Model

The momentum-based rotorwash model presented in this report contains elements from previous efforts of the authors and others. The best components of these previous efforts are consolidated and extended using computer tools and high quality flight test data that did not exist at the time that the previous versions of the models were developed. A discussion of the momentum modeling, limitations, and validity range appears in [Appendix J](#). [Appendix J](#) also contains equation documentation and a source code listing of the Fortran 90 code implementation of the resultant conceptual level modeling method.

Correlation of the conceptual level model appears in [Appendix K](#) for the CH-53E, V-22, CH-47, XV-15, and H-60. From this correlation effort, effects of gross weight, rotor disk loading, ground effect, the number and position of the rotors, and the outwash distance from the center of the rotorcraft have been evaluated for the conceptual model. Examples of the conceptual model correlation appear as Figure 4-1. Test data points in the mean velocity profile are the average wind velocity over the time interval that data were taken. In the peak velocity profile, the data points are the highest magnitude recorded for each sensor over the time interval.

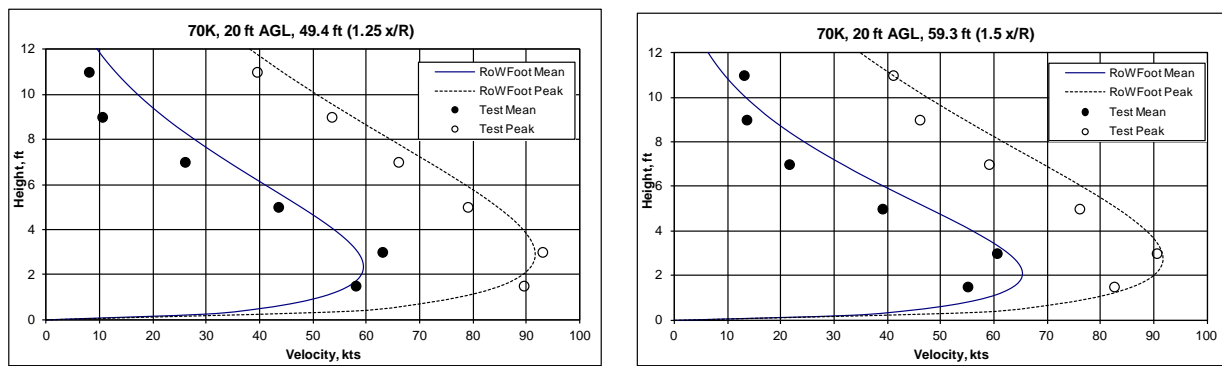


Figure 4-1 Correlation of Conceptual Model to CH-53E (Reference 9)

4.3 Rotorwash High-Fidelity Modeling

An attempt at high-fidelity modeling was conducted using the Comprehensive Hierarchical Aeromechanical Rotorcraft Model (CHARM) vortex model (Reference 10) to reproduce the land-based V-22 rotorwash downwash survey (Reference 6). A discussion of this modeling method is described with associated limits in [Appendix L](#). Correlation of the CHARM simulation to V-22 data appears in [Appendix M](#). From this correlation effort, effects of gross weight, rotor disk loading, ground effect, the number and position of the rotors, and the outwash distance from the center of the rotorcraft have been evaluated for use in conjunction with the conceptual model.

Review of the model correlation identified discrepancies with the CHARM modeling symmetry, gross weight to maximum velocity trend, and height above ground to maximum outwash velocity trends that indicate the modeling results contained in [Appendix M](#) are of limited utility in extension of the rotorwash flight test database. Further discussion of these discrepancies is contained in [Appendix M](#).

Results from using the CHARM vortex model for extrapolation beyond the available flight test data are retained in [Appendix K](#). Although these results are not usable to provide confidence of conceptual level model extrapolation beyond the region bounded by flight test data, the results and methodology are retained to display lessons learned and facilitate further work in this effort.

4.4 Shipboard Effects on Rotorwash

Personnel near or underneath rotorcraft (i.e. sling load operations) during shipboard operations have a very limited area to work and ships typically launch/recover aircraft into the wind. Also, the effect of a rotor being partially over the deck edge (i.e. V-22) has significant effects on the development of the rotorwash flow field below the aircraft when compared to operation over land. This section summarizes results presented in [Appendix N](#) for Wind-Over-Deck (WOD) and Deck Edge (DE) effects. Development or refinement of the associated conceptual level model is hampered by the lack of test data. The rotorwash operational footprints displayed in Sections [5.5](#) and [5.6](#) do not include shipboard effects for WOD and DE.

4.4.1 Effect of Wind-Over-Deck

V-22 test data that document rotorwash effects from the WOD shipboard environment or the ambient wind at a land location are very limited in quantity. However, these data provide a limited understanding of what can be expected for a typical tilt rotor WOD launch condition. The peak upwind profile velocities were substantially less at 0- and 20-knot WOD conditions when compared to the 0-knot condition on land. The peak downwind profile velocities averaged 10-knots more at the 20-knot WOD condition when compared to both the land and shipboard 0-knot conditions. This evidence agrees with operational experience with shipboard operations in [Appendix H](#). [Appendix N](#) contains a simple

derived mathematical model currently for wind speeds < 10 knots and provides reference to a ground vortex model for wind speeds above 10 knots.

4.4.2 Effect of Shipboard Deck Edges

When a hovering rotorcraft has a portion of one of its rotors over the DE, the rotorwash flow field will be affected due to associated loss of mass flow “dumped” overboard and not appearing on the flight deck. Limited test data indicate that the rotorwash flow field for the V-22 resembles those of single rotor helicopter velocity profiles on land when one of the rotors is exposed ~50% over the edge of the flight deck.

4.5 Personnel Stability Limit Ratio

The drag force on personnel is determined using the wind speed and shape of the representative person. For modeling purposes, a standard “PAXman” net frontal area distribution is used to represent the outline of a person in the outwash. Personnel maximum drag force uses this area with the peak velocity profile. As noted in [Section 4.2](#), the peak velocity profile is a “worst-case” compilation of maximum recorded wind speed magnitudes over a time interval and thus may over predict the associated peak drag force. To account for this over prediction and the effect of the non-steady rotorwash flow, the peak predicted drag force is connected to the personnel capability limits in [Section 3.1.1.1](#) with a personnel stability limit ratio of 0.8 for helicopter and tandem configurations and 1.0 for tilt rotors. This ratio is the actual peak drag force on personnel divided by the predicted peak drag force on personnel. Derivation of this ratio is contained in [Appendix O](#).

4.6 Conceptual Model Trends

At equivalent rotor conditions, outwash wind velocity profiles are dependent on the type of rotorcraft configuration. [Appendix O](#) documents these comparisons between configurations. The separation distance of multiple rotors changes the magnitude and distribution of the mass flow. For the radial outwash at the same thrust per rotor, the helicopter, tandem, and tilt rotor have similar mean velocity profiles. Within the peak velocity profile, the helicopter and tandem velocity profiles are similar, while the tilt rotor’s is smaller in magnitude. For centerline outwash, the tandem velocity magnitude (lateral axis) is higher than the tilt rotor (longitudinal axis). These differences are supported by flight test data. Explanation of the differences arises from the distribution of the air mass flow within the rotorwash and is presented in more detail in [Appendix O](#). [Appendix O](#) also contains engineering trends for the velocity profile and force on PAXman due to changes in the thrust per rotor, rotor radius, and height above ground for the helicopter, tandem, and tilt rotor. Figure 4-2 (extracted from [Appendix O](#)) describes the Rotorwash Footprint (RoWFoot) model sensitivity of a tilt rotor to changes in thrust/rotor and height above ground to force on PAXman. Flight conditions that are extrapolated outside the bounds of test data for disk loading or rotor height above ground are indicated in the legend along with the magnitude of the exceedance.

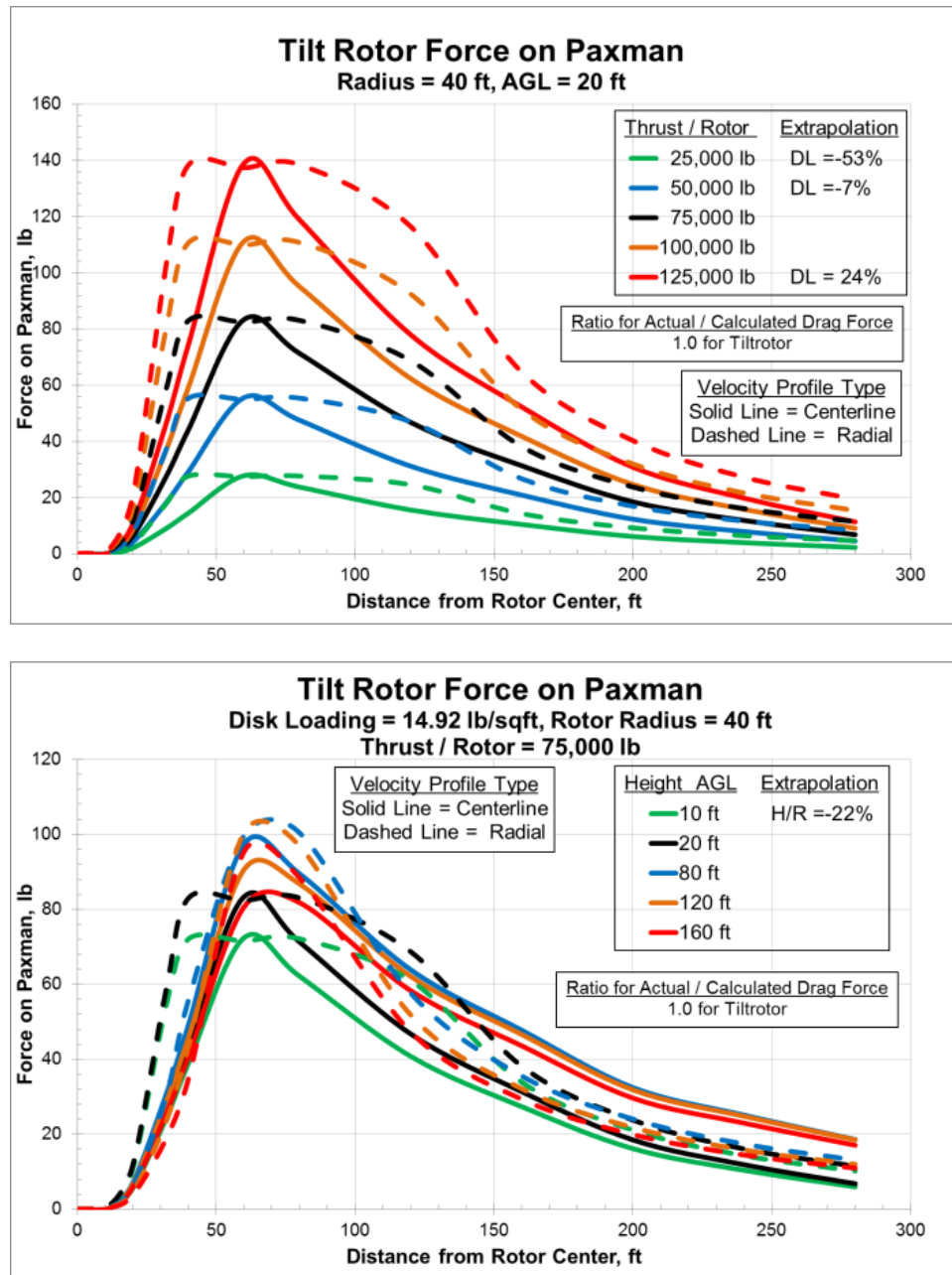


Figure 4-2 Tilt Rotor Operational Parameter Trends for Force on PAXman

5.0 Footprint of Large Rotorcraft on Operational Environment

Rotorwash footprints display the operational impact of the outwash around a hovering rotorcraft. These footprints are generated for the evaluation assessment conditions listed in [Appendix A](#). Contours within these footprints represent the constant values of velocity or force within the operational environment. The contours arise from post-processing of the rotorwash analytical modeling ([Section 4](#)) output at defined evaluation conditions. Environmental limits were previously defined in [Section 3](#). The rotorwash analytical modeling is the RoWFoot tool, as described in [Appendix J](#). This type of representation provides a visual display of the rotorwash impact on the ground environment.

Figure 5-1 presents an example CH-47 outwash personnel force footprint using experimentally measured velocity profile data. This technique is identical to the process used with RoWFoot generated velocity profile data in lieu of experiment data for creation of operational footprints.

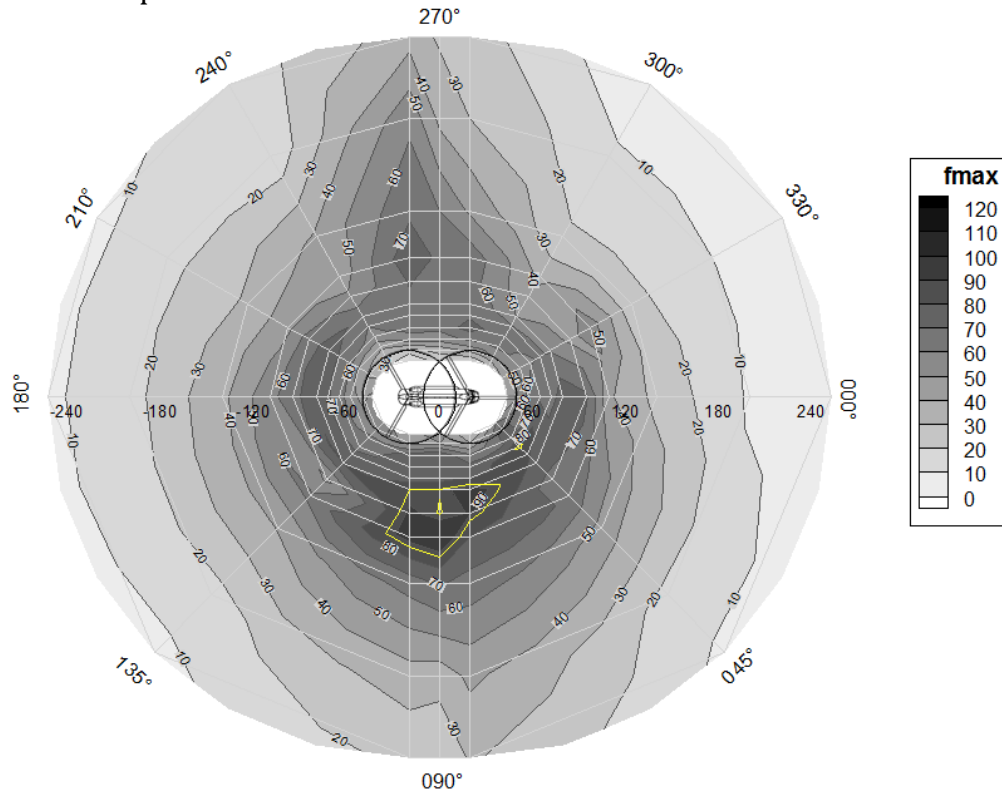


Figure 5-1 Outwash Survey Peak Forces Determined from Experimentally Testing a CH-47 at a 20 ft AGL Hover at 41,000 lbs (Reference 5)

As introduced in [Section 2.1](#) and detailed in [Appendix A](#), there are nine evaluation scenarios. Rotorwash footprints are presented for the first six of the nine scenarios using the notional tilt rotor described in [Section 2.2](#) and [Appendix B](#) (the last three scenarios are not presently capable of being modeled). Rotorwash footprints are produced using the outwash wind velocities or forces of the first six evaluation scenarios. [Appendix P](#) describes the methods used to generate the graphical display. The remaining three

scenarios are evaluated via similarity to field experience with DoD rotorcraft as presented in [Appendix H](#).

Results from the field experience survey contained in [Appendix H](#) provide valuable insight into the real-world application that the rotorwash footprint analysis analytically captures. [Appendix I](#) documents damage to trees and plants from V-22 rotorwash during three separate public events. This highlights the lessons learned concerning additional environmental considerations of rotorwash impact when operating in a civilian area.

Rotorwash operational footprints using the JHL CDA operational evaluation scenarios ([Section 2.1](#) and [Appendix A](#)) for the notional tilt rotor ([Section 2.2](#) and [Appendix B](#)) appear as Figures 5-2 through 5-13 in Sections [5.1](#) through [5.6](#). These footprints represent the typical operational conditions in the evaluation space of the rotorwash impact on the ground environment and are summarized in Table 5-1. The last column of Table 5-1 lists the reference numbers of Figures 5-2 through 5-13 for Velocity and Force plots. Utilization of the evaluation space conditions highlights areas of concern to the Warfighter at historical operational conditions. Based on this information, the user can then apply mitigation techniques as needed to lower the rotorwash impact to acceptable conditions.

Operational Evaluation Scenario	Gross Weight lb	Hover Height ft	Thrust to Weight Ratio	Altitude & Temp ft/deg F	Figures for Rotorwash Footprints Vel, Force
Ground Taxi	30% Max GTOW	0	0.30	0/59	5.2, 5.3
Hovering Taxi	Max GTOW	10	1.09	0/59	5.4, 5.5
LZ Ops, Int Pay	Max GTOW	20	1.09	0/59	5.6, 5.7
LZ Ops, Ext Pay	Max GTOW – Ext Load	50	1.09	0/59	5.8, 5.9
Ship, Int Pay	Max GTOW	20	1.09	0/59	5.10, 5.11
Ship, Ext Pay	Max GTOW – Ext Load	50	1.09	0/59	5.12, 5.13

Table 5-1 Rotorwash Operational Evaluation Space Conditions

For the notional tilt rotor, the aircraft weight is based on the Maximum Gross Takeoff Weight (Max GTOW) of 141,605 lbs. This corresponds to a disk loading of 15.7 lb/ft², where the disk loading is in terms of thrust. During external load operations, the aircraft weight does not include the external load (indicating the load has not been picked up). The external load is assumed to be a MILVAN plus external load handling kit (45,275 lb = 44,800 lb + 475 lb). External load operations use an aircraft weight of 96,330 lb which corresponds to a disk loading of 10.7 lb/ft². For each operational evaluation scenario, there is an associated velocity and force footprint.

Hover heights are representative of typical heights above ground of the landing gear based on historical operations. As seen in Figure 4-2, changes to the hover height affect the outwash conditions in the ground environment. For the notional tilt rotor, the distance from the landing gear to the rotor is 25 feet.

Thrust-to-weight ratio is the amount of thrust produced by the rotor relative to the aircraft gross weight. The delta above unity is due to vertical drag, or download, produced by the rotor induced flow over the airframe. During flight, the download is assumed to be 9% for the notional tilt rotor.

The altitude and temperature will vary based on mission requirements. As the altitude and temperature increases, the aircraft may not have the capability to hover at its Max GTOW. For the scenario conditions shown in Figures 5-2 through 5-13, the altitude and temperature were fixed at sea level standard values to enable flight at the Max GTOW.

Velocity footprints display the highest magnitude values in the outwash peak velocity profile. Force footprints display the peak force on ground personnel using the PAXman model. Both the velocity and force footprints can be associated with data previously presented in Table 3-1 as operational limits. Table 5-2 contains the limits associated with the peak velocity, and Table 5-3 contains the limits associated with drag force on military personnel. These tables are referenced with the Rotorwash Velocity and Force Footprints in Figures 5-2 through 5-13.

<u>Hazard Consideration</u>	<u>Dyn Press (lb/ft²)</u>	<u>Sea Level Std. Wind Speed (mph)</u>
Civilian (General Population)		
Caution Zone	2.88 – 5.12	33.6-44.7
Hazard Zone	> 5.12	44.7
Asphalt Shingles	9.21	60
Military Structures	10.81	65
Light Structures / Civilian Tents	3.13	35
Airport/Heliport Environment	4.15	40.3

Table 5-2 Wind Velocity Limits for Ground Environment

	<u>Force, lbs</u>
Caution Zone	>80 (mean) or 87–115 (peak)
Hazard Zone	>87 (mean) or ≥ 115 (peak)

Table 5-3 Force Limits for Military Ground Personnel

Environmental conditions may lower the values expressed in Tables 5-2 and 5-3. In Table 5-2, civilian wind limits may be lower if combined with uneven terrain, slick surfaces, and/or poor visibility. Table 5-3 force limits will be reduced for uneven terrain, slick surfaces, and/or poor visibility as well as rolling ship decks. Slick surfaces include wet grass, mud, and wet ship decks. Poor visibility can occur from blowing water spray, rain, sand, snow, dust, and other airborne particles. Laboratory tests that quantified the civilian and military personnel wind and force limits were collected while test subjects had good footing and visibility.

5.1 Ground Taxi

This scenario simulates a rolling taxi for a rotorcraft in a semi-prepared location. The primary concern is the clearance area associated with personnel, equipment, and other aircraft in the ground environment. A semi-prepared location assumes a bearing surface where the aircraft wheels will not sink into the ground and the rotorcraft can taxi with thrust ≤ 0.3 weight. This corresponds to operational experience for rolling taxis in [Appendix H](#). Table 5-4 summarizes this scenario's operational conditions.

Gross Weight = 141,605 lb (Max GTOW)	Thrust/Weight = 0.30
Altitude/Temp = 0 ft/59 deg-F	Hover Height = 0 ft AGL

Table 5-4 Ground Taxi Operating Conditions

Using these operational conditions, the rotorwash operational footprint for velocity is presented in Figure 5-2 and force on personnel is presented in Figure 5-3. Using the wind limits in Table 5-2 and the force limits in Table 5-3, safe separation distances can be identified for personnel, equipment, and structures in the ground environment.

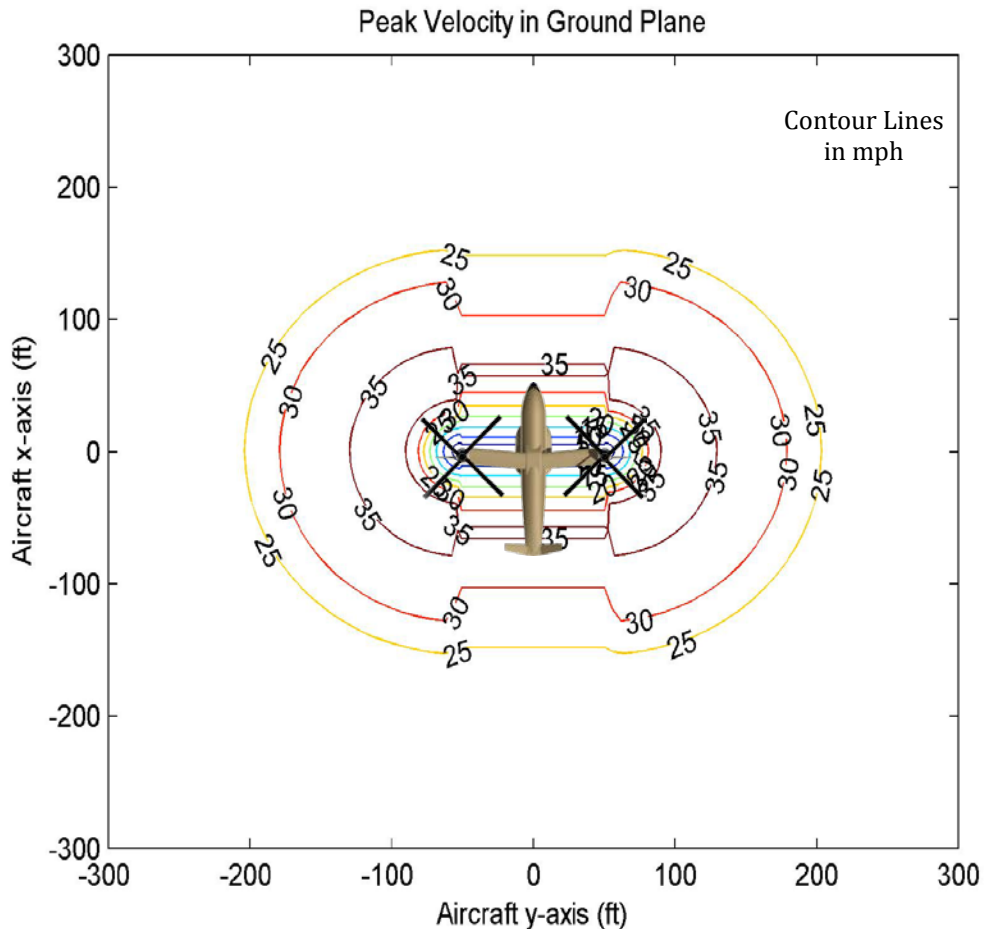


Figure 5-2 Peak Velocity Contour Plot

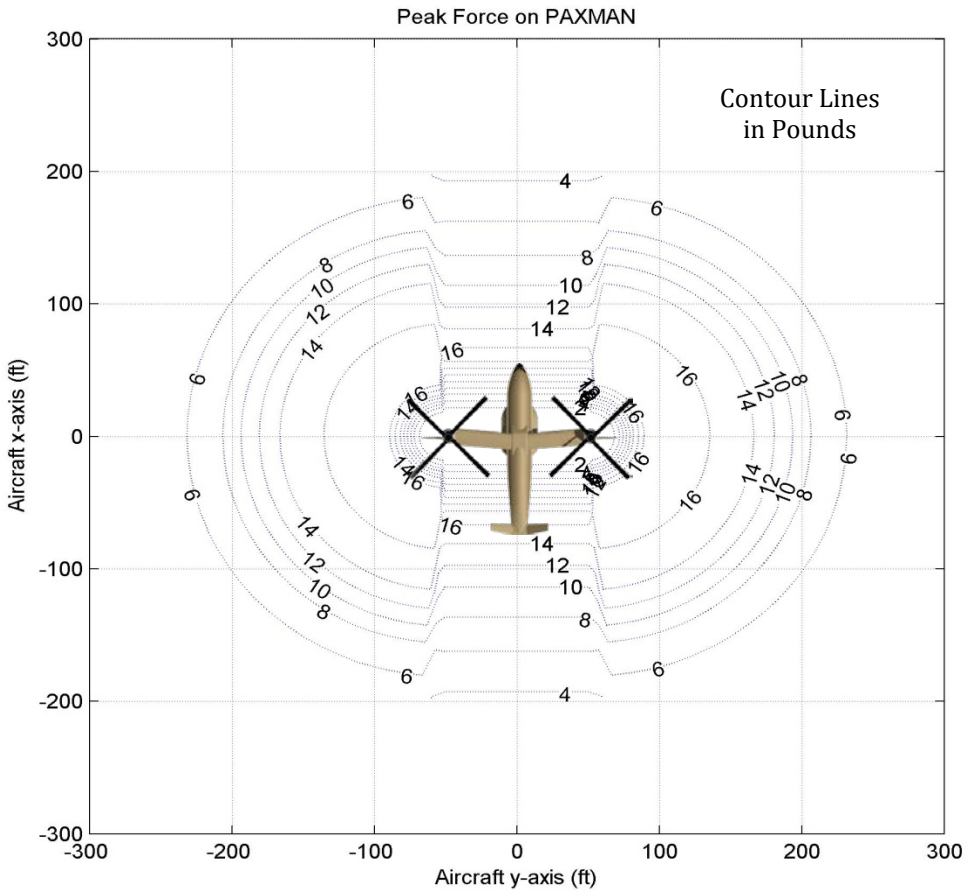


Figure 5-3 Personnel Force Contour Plot

This scenario does not require ground crew, equipment, or personnel to be in close proximity to the aircraft during the ground taxi. Ground control personnel in the vicinity are expected to be trained and protected military personnel. Operational needs such as the physical dimension of the landing zone size may result in closer separation than desired to military ground personnel, civilians, equipment, and structures.

Some of the rotorwash effects may be operationally mitigated by removal of personnel or equipment in the ground environment, modifying the state of the limiting condition (i.e. sheltering, bracing, protecting, etc.) or changing the operational condition of the aircraft from Table 5-4. The operating condition may necessitate a lower aircraft weight or reduction of the thrust required to ground taxi. The thrust used in the prediction assumes a thrust-to-weight ratio of 0.3. This value may be less for level and/or firm ground surfaces. Changing the direction of the thrust vector (e.g. tilting rotors forward on a tilt rotor) will also lessen the amount of thrust required but will also increase the outwash to the rear of the aircraft. Other mitigation techniques could include taxiing with one rotor over deck edge on a ship or using ambient wind conditions to divert some of the rotorwash toward a less sensitive direction.

5.2 Hovering Taxi

This scenario simulates a hovering taxi in ground effect. The primary concern is the clearance area associated with personnel, equipment, and other aircraft in the ground environment. The hover taxi assumes a slow transit at maximum takeoff gross weight where the rotorwash flow field is stable. During this maneuver, the download on the airframe is 9% and is represented with a thrust/weight ratio of 1.09. Table 5-5 summarizes this scenario's operational conditions.

Gross Weight = 141,605 lb (Max GTOW)
Altitude/Temp = 0 ft/59 deg-F

Thrust/Weight = 1.09
Hover Height = 10 ft AGL

Table 5-5 Hovering Taxi Operating Conditions

Using these operational conditions, the rotorwash operational footprint for velocity is presented in Figure 5-4 and force on personnel is presented in Figure 5-5. Using the wind limits in Table 5-2 and the force limits in Table 5-3, safe separation distances can be identified for personnel, equipment, and structures in the ground environment.

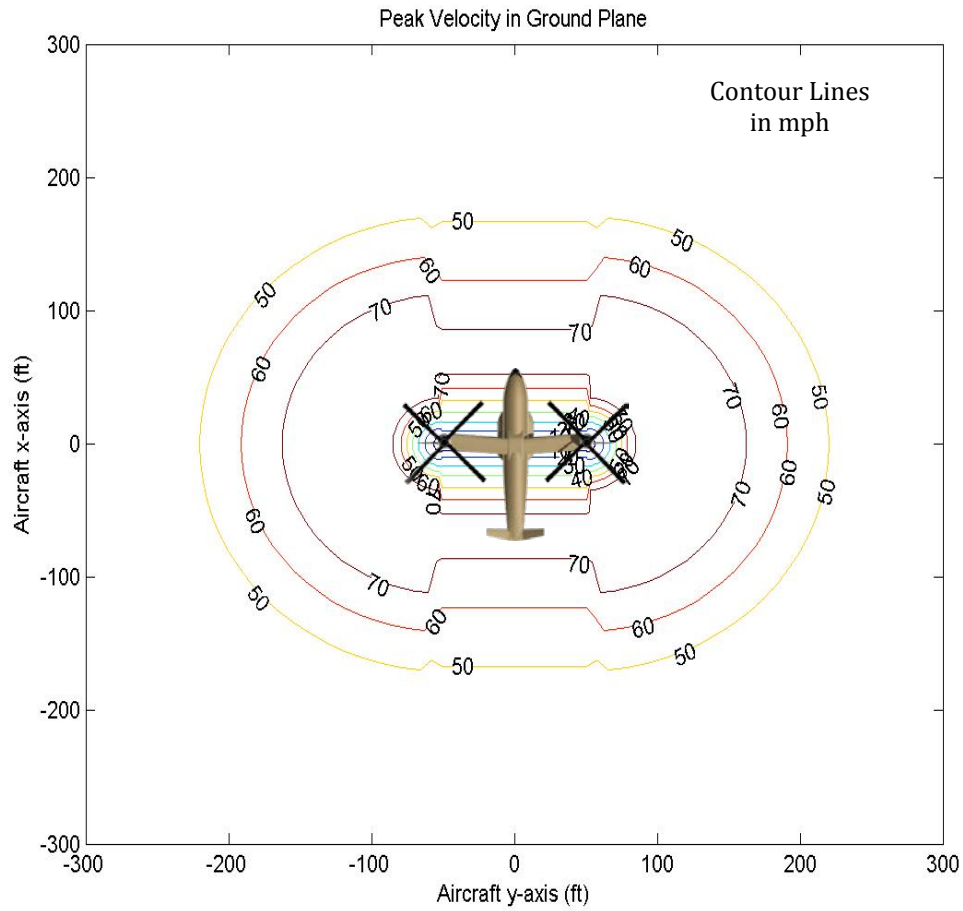


Figure 5-4 Peak Velocity Contour Plot

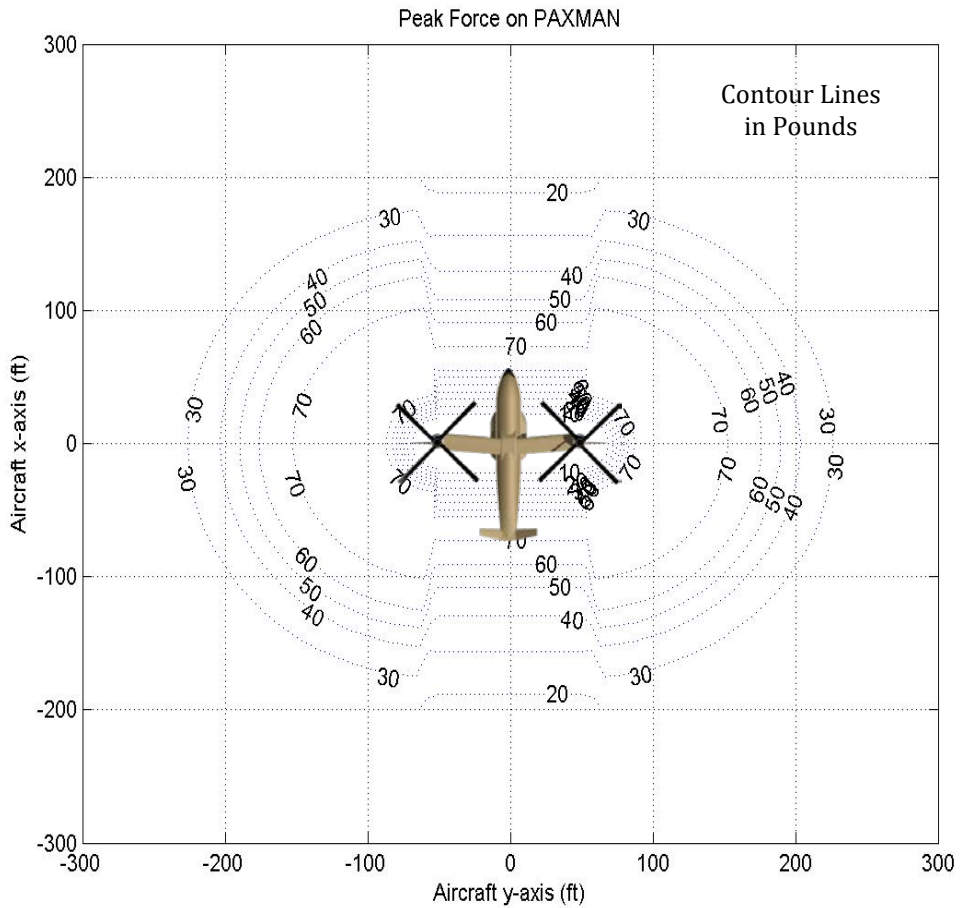


Figure 5-5 Personnel Force Contour Plot

This scenario does not require ground crew, equipment, or personnel to be in close proximity to the aircraft during the hover taxi. Ground control personnel in the vicinity are expected to be trained and protected military personnel. Operational needs such as the physical dimension of the landing zone size may result in closer separation than desired to military ground personnel, civilians, equipment, and structures.

Some of the rotorwash effects may be operationally mitigated by removal of personnel or equipment in the ground environment, modifying the state of the limiting condition (i.e. sheltering, bracing, protecting, etc.), or changing the operational condition of the aircraft from Table 5-5. The operating condition may necessitate a lower aircraft weight or elimination of the hover taxi with a ground taxi or vertical climb to altitude. The ground taxi would lower the rotor thrust and thus lower the magnitude of the outwash velocity. A vertical climb to altitude would negate the need to taxi beyond an area sensitive to the rotorwash. Another potential mitigation technique would use the ambient wind to divert some of the rotorwash toward a less sensitive direction.

5.3 Landing Zone Operations with Internal Payload

This scenario simulates hover over an unprepared or austere landing zone at a hover wheel height of 20 ft. The primary concern is the clearance area associated with personnel, equipment, and other aircraft in the ground environment. The rotorcraft is assumed holding a constant altitude at maximum takeoff gross weight where the rotorwash flow field is stable. During this maneuver, the download on the airframe is 9% and is represented with a thrust/weight ratio of 1.09. Table 5-6 summarizes this scenario's operational conditions.

Gross Weight = 141,605 lb (Max GTOW)
Altitude/Temp = 0 ft/59 deg-F

Thrust/Weight = 1.09
Hover Height = 20 ft AGL

Table 5-6 Landing Zone Operating with Internal Payload Conditions

Using these operational conditions, the rotorwash operational footprint for velocity is presented in Figure 5-6 and force on personnel is presented in Figure 5-7. Using the wind limits in Table 5-2 and the force limits in Table 5-3, safe separation distances can be identified for personnel, equipment, and structures in the ground environment.

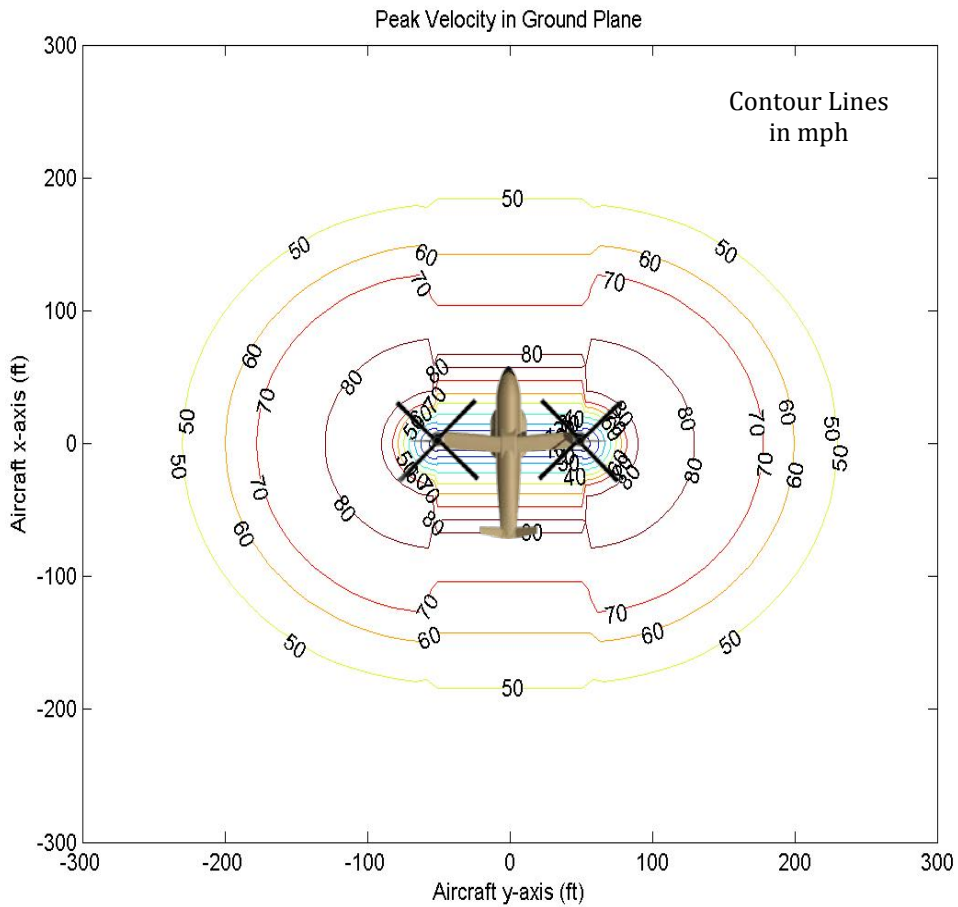


Figure 5-6 Peak Velocity Contour Plot

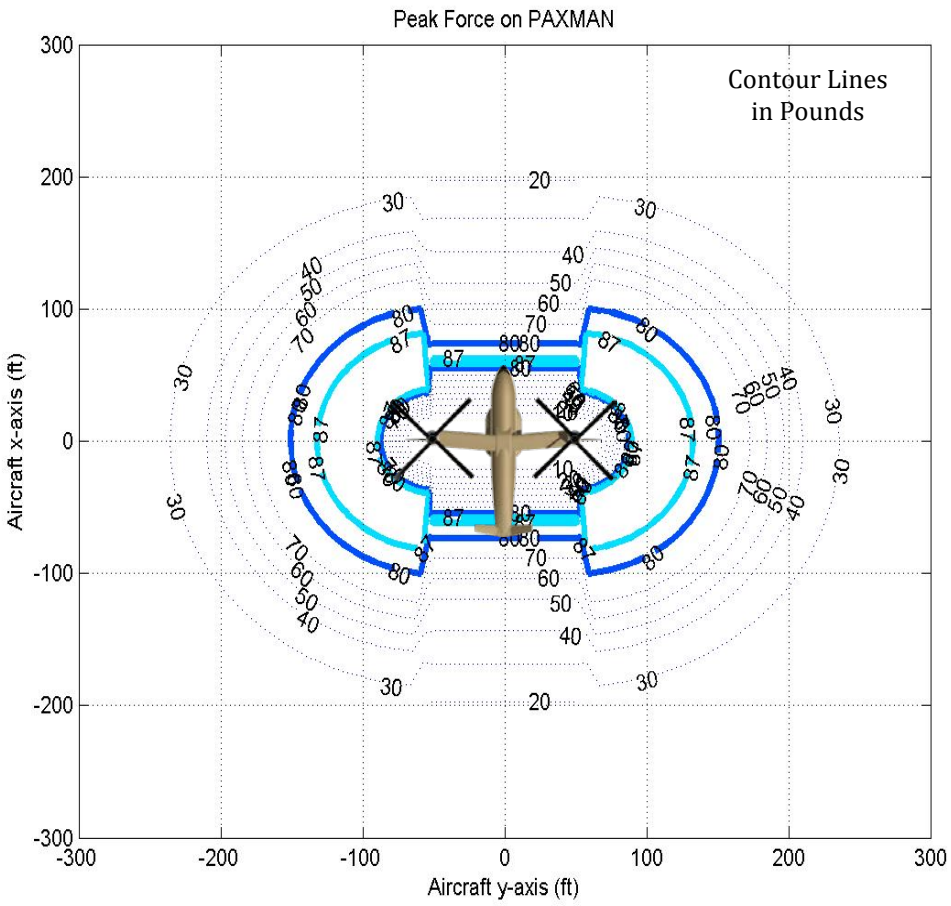


Figure 5-7 Personnel Force Contour Plot

This scenario does not require ground crew, equipment, or personnel to be in close proximity to the aircraft during the takeoff and landing. Number and type of people located in the ground environment will be mission dependent and may include civilians and/or military personnel. Ground control personnel in the vicinity are expected to be trained and protected military personnel. Operational needs such as the physical dimension of the landing zone size may result in closer separation than desired to military ground personnel, civilians, equipment, and structures.

Some of the rotorwash effects may be operationally mitigated by removal of personnel or equipment in the ground environment, modifying the state of the limiting condition (i.e. sheltering, bracing, protecting, etc.), or changing the operational condition of the aircraft from Table 5-6. The operating condition may necessitate a lower aircraft weight or conducting a ground taxi to approach desired location. Civilians located in the outwash flow field can be braced and shielded by protected military personnel to increase their allowable velocity limits. Ambient winds may be used to divert some of the rotorwash away from sensitive areas. The yaw angle of the tilt rotor (and tandem) can also be changed to orient the most benign outwash zone toward sensitive directions during takeoff and landing.

5.4 Landing Zone Operations with External Payload

This scenario simulates hover while hooking up an externally carried payload at a constant hover wheel height of 50 ft. The primary concern is the ability of the payload hookup crew to safely transit the rotorwash flow field. The aircraft weight is equal to the maximum take-off gross weight less the weight of the external load. During this maneuver, the download on the airframe is 9% and is represented with a thrust/weight ratio of 1.09. Table 5-7 summarizes this scenario's operational conditions.

Gross Weight = 96,330 lb (Max GTOW – Ext Load)
Altitude/Temp = 0 ft/59 deg-F

Thrust/Weight = 1.09
Hover Height = 50 ft AGL

Table 5-7 Landing Zone Operating with External Payload Conditions

Using these operational conditions, the rotorwash operational footprint for velocity is presented in Figure 5-8 and force on personnel is presented in Figure 5-9. Using the wind limits in Table 5-2, safe separation distances can be identified for personnel, equipment, and structures in the ground environment. Using the force limits in Table 5-3, the notional tilt rotor outwash does not exceed the capability of military personnel to safely transit the outwash depicted in Figure 5-9 from all azimuth angles.

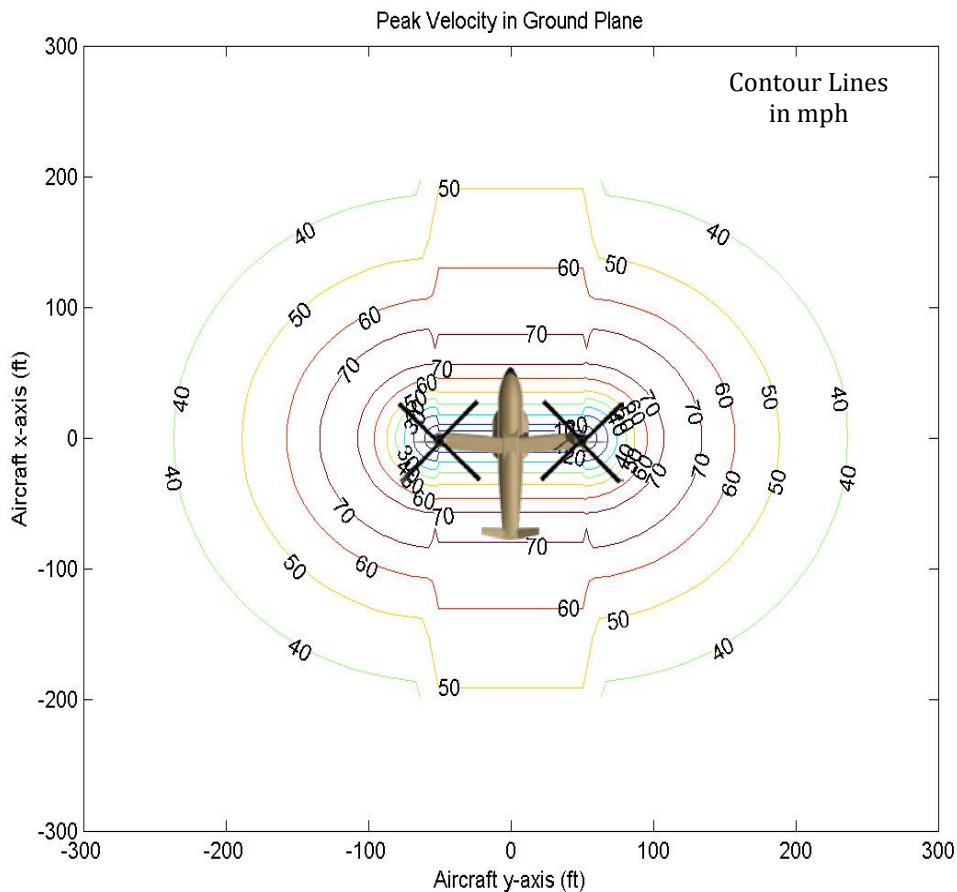


Figure 5-8 Peak Velocity Contour Plot

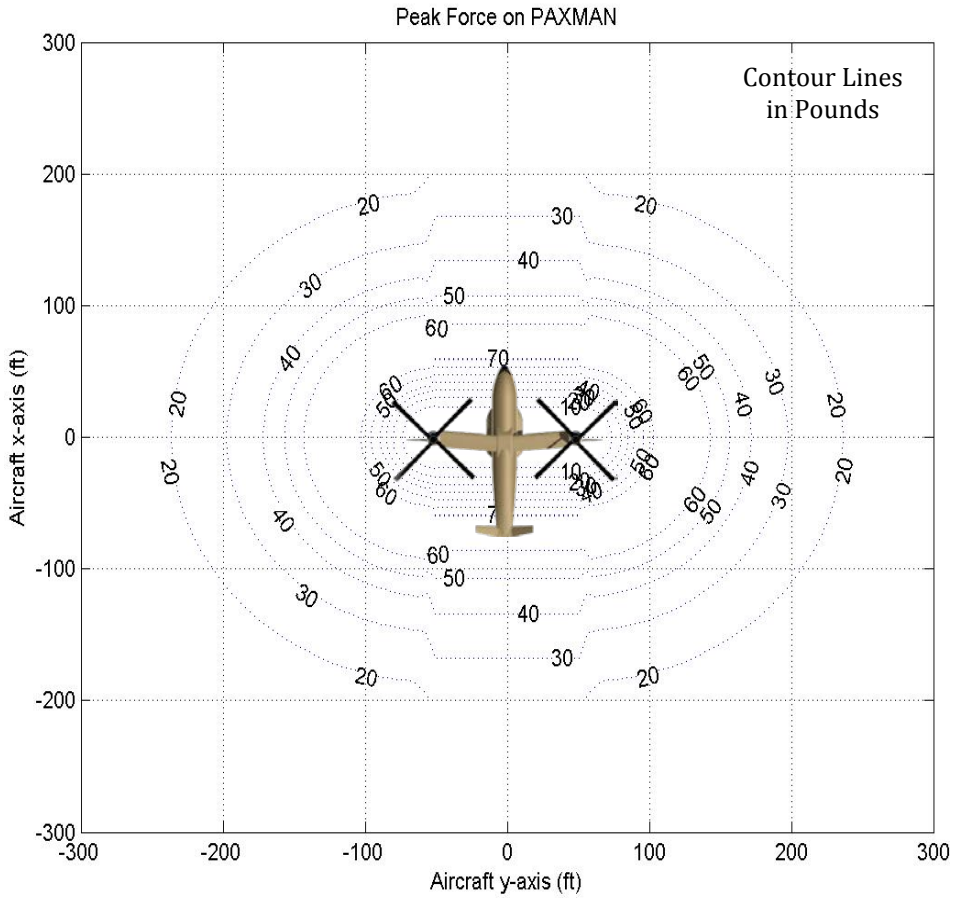


Figure 5-9 Personnel Force Contour Plot

This scenario requires ground crew to be in close proximity and able to transit the outwash flow field. The load is assumed to rest on the ground while personnel are under the aircraft and during transit. Ground personnel in the vicinity are expected to be trained and protected military personnel. After the load is lifted, the scenario would closely resemble the 5.3 scenario with the higher total aircraft weight.

Ground crew training in the outwash flow field may operationally mitigate some of the rotorwash effects. During approach and initial hover, the ground crew can be sheltered by the external load and/or the aircraft can do a vertical descent over the load. During hookup, the area directly below the aircraft does not experience the higher velocity and drag force encountered in other locations. Transit away from the load and reentry to correct a problem on hookup of the load are assumed to be the critical conditions. Potential mitigation strategies include having the ground crew remain a short distance from the load during pickup or move as a group during transit. If available, ambient winds may be used to divert some of the rotorwash away from the direction of transit.

5.5 Shipboard Operations with Internal Payload

This scenario simulates hover over a ship deck at a hover wheel height of 20 ft. The primary concern is the clearance area associated with personnel, equipment, and other aircraft in the shipboard environment. The rotorcraft is assumed holding a constant altitude at maximum takeoff gross weight where the rotorwash flow field is stable. During this maneuver, the download on the airframe is 9% and is represented with a thrust/weight ratio of 1.09. Table 5-8 summarizes this scenario's operational conditions.

Gross Weight = 141,605 lb (Max GTOW)
Altitude/Temp = 0 ft/59 deg-F

Thrust/Weight = 1.09
Hover Height = 20 ft AGL

Table 5-8 Shipboard Operations with Internal Payload Conditions

Using these operational conditions, the rotorwash operational footprint for velocity is presented in Figure 5-10 and force on personnel is presented in Figure 5-11. Using the wind limits in Table 5-2 and the force limits in Table 5-3, safe separation distances can be identified for personnel, equipment, and other aircraft in the shipboard environment. Shipboard equipment limits should be added to fully represent the shipboard environment under consideration.

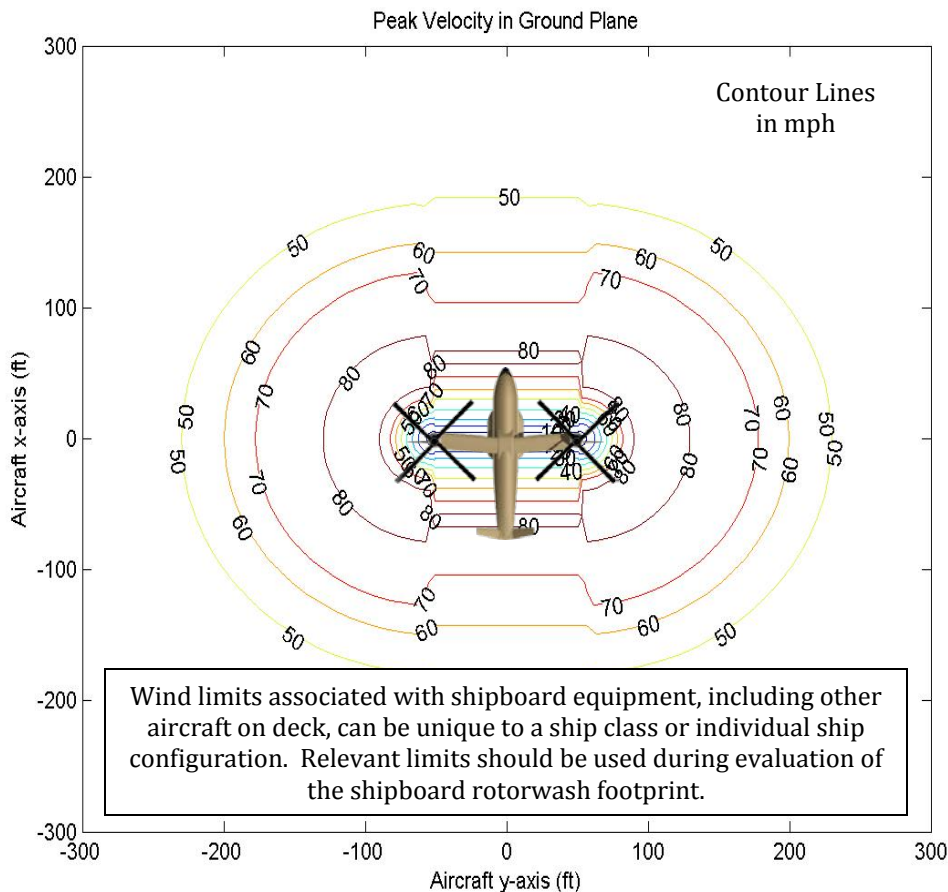


Figure 5-10 Peak Velocity Contour Plot

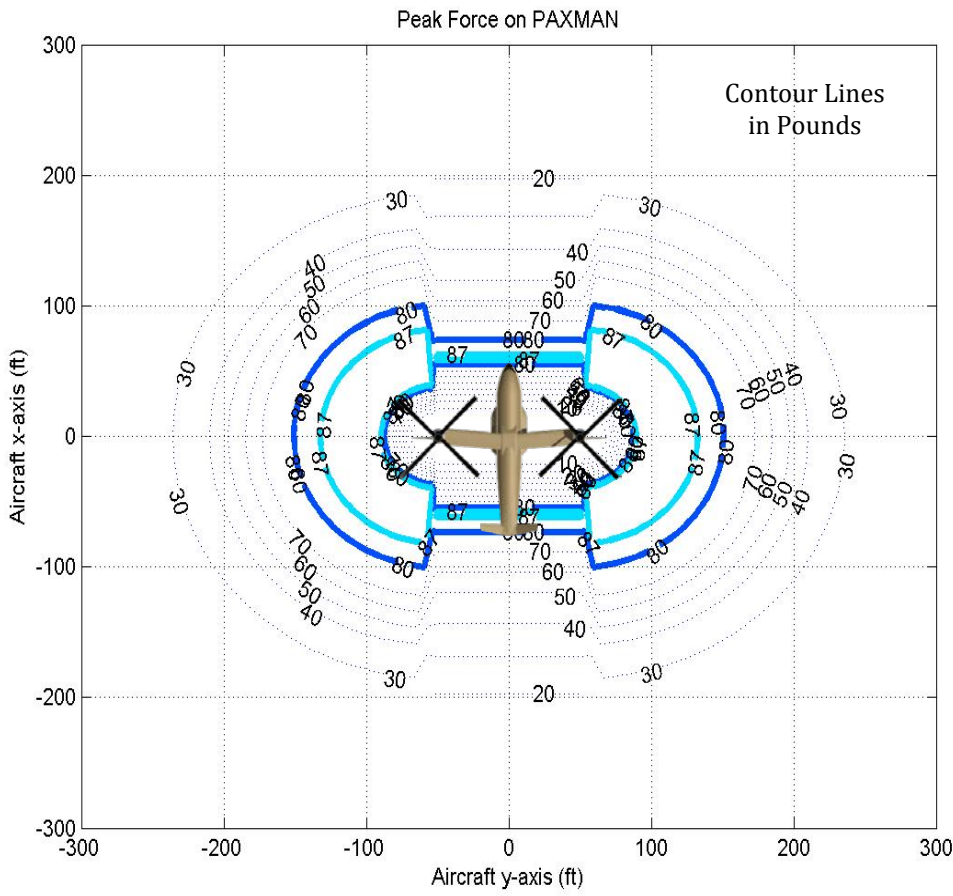


Figure 5-11 Personnel Force Contour Plot

This scenario may require ground crew to be in proximity to the aircraft during the takeoff and landing. Ground crew personnel in the vicinity are expected to be trained and protected military personnel. Operational limits such as the physical dimension of the flight deck size may result in closer separation than desired to military ground personnel, civilians, equipment, and structures. Location of the signal person should be considered in association with outwash footprints.

Some of the rotorwash effects may be operationally mitigated by removal of personnel or equipment in the ground environment, modifying the state of the limiting condition (i.e. sheltering, bracing, protecting, etc.), or changing the operational condition of the aircraft from Table 5-8. The operating condition may necessitate a lower aircraft weight or be towed / ground taxi to a more desired landing spot. For the tilt rotor, one of the rotors can be positioned over the deck edge to potentially lower centerline outwash effects. Wind over deck should be considered for locations where the outwash will be weaker (upwind) and stronger (downwind).

5.6 Shipboard Operations with External Payload

This scenario simulates hover while hooking up and placing an externally carried payload on a ship deck during a constant hover wheel height of 50 ft. The primary concern is the ability of the deck crew to safely transit the rotorwash flow field. The aircraft weight is equal to the maximum take-off gross weight less the weight of the external load. During this maneuver, the download on the airframe is 9% and is represented with a thrust/weight ratio of 1.09. Table 5-9 summarizes this scenario's operational conditions.

Gross Weight = 96,330 lb (Max GTOW – Ext Load)	Thrust/Weight = 1.09
Altitude/Temp = 0 ft/59 deg-F	Hover Height = 50 ft AGL

Table 5-9 Shipboard Operations with External Payload Conditions

Using these operational conditions, the rotorwash operational footprint for velocity is presented in Figure 5-12 and force on personnel is presented in Figure 5-13. Using the wind limits in Table 5-2, safe separation distances can be identified for personnel, equipment, and structures in the shipboard environment. Using the force limits in Table 5-3, the notional tilt rotor outwash does not exceed the capability of military personnel to safely transit the outwash depicted in Figure 5-13 from all azimuth angles.

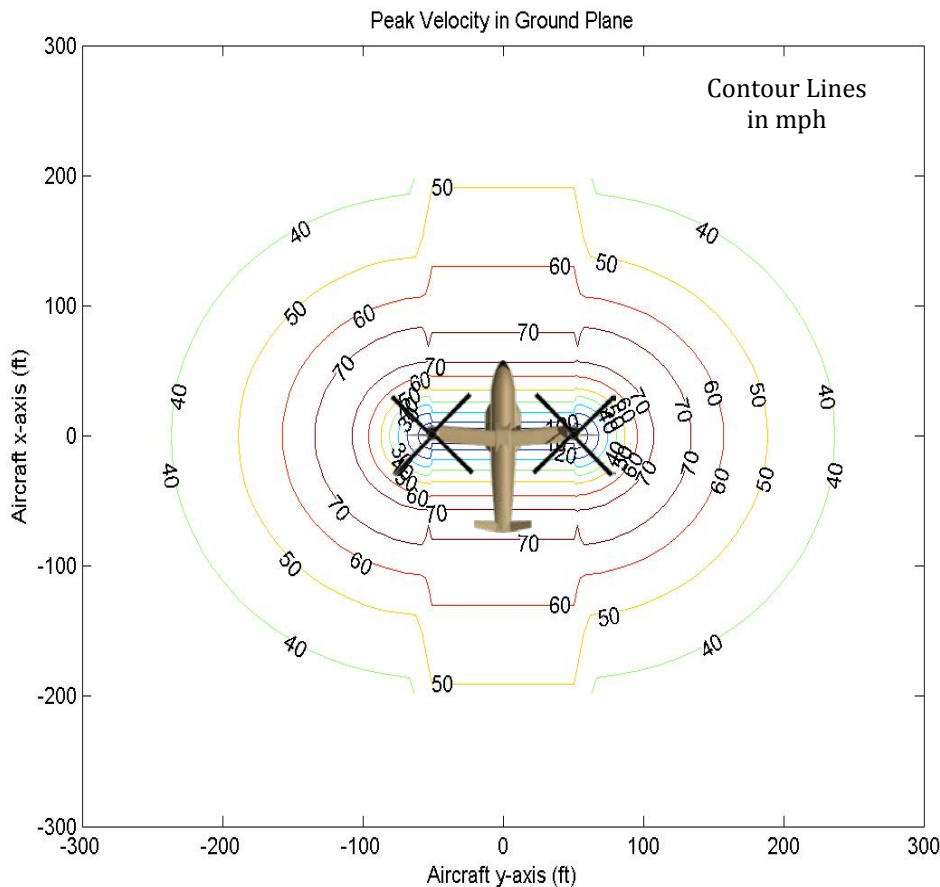


Figure 5-12 Peak Velocity Contour Plot

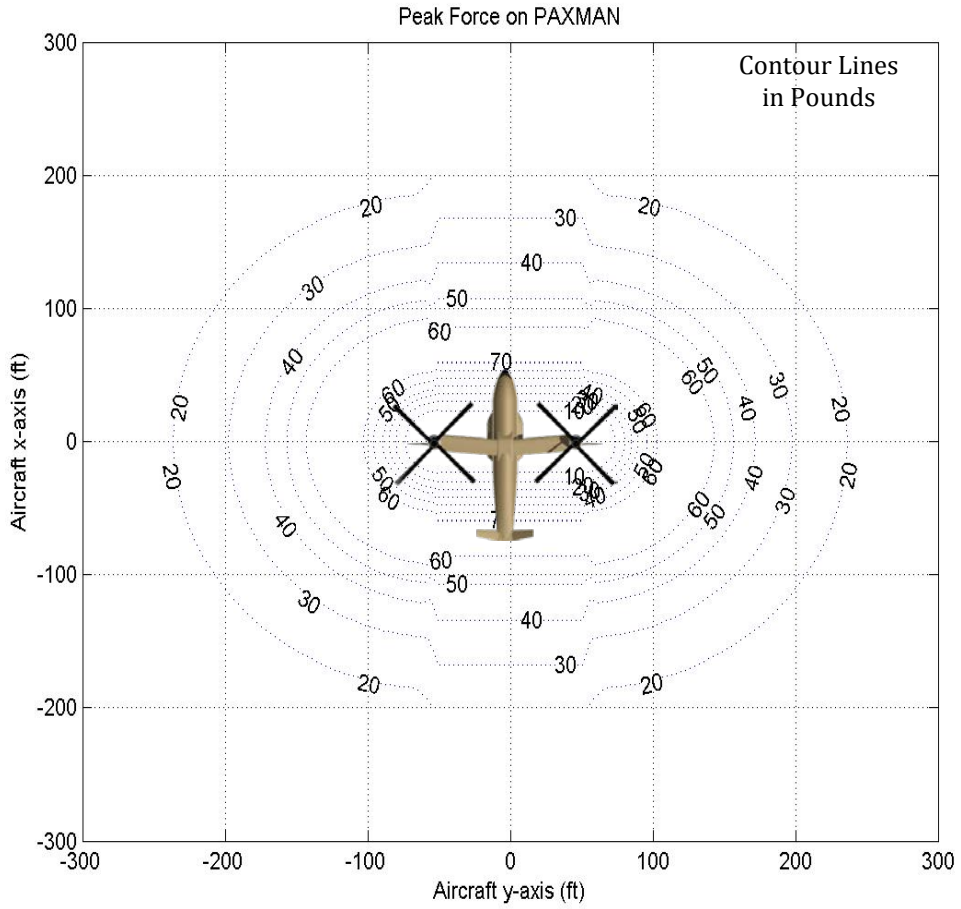


Figure 5-13 Personnel Force Contour Plot

This scenario requires the deck crew to be in close proximity and able to transit the outwash flow field. While personnel are under the aircraft and during transit, the load is assumed to rest on the ground. Ground personnel in the vicinity are expected to be trained and protected military personnel. After the load is lifted, the scenario would closely resemble the 5.5 scenario with the higher total aircraft weight.

Ground crew training in the outwash flow field may operationally mitigate some of the rotorwash effects. During approach and initial hover, the ground crew can be sheltered by the external load and/or the aircraft can do a vertical descent over the load. During hookup, the area directly below the aircraft does not experience the higher velocity and drag force encountered in other locations. Transit away from the load and reentry to correct a problem on hookup of the load is assumed to be the critical condition. Potential mitigation strategies include moving to safe havens located on the ship deck near the load and using guide lines to aid transit of the outwash flow field. If available, ambient winds may be used to divert some of the rotorwash away from the direction of transit.

5.7 Low Altitude Flyover

Operational experience indicates that rotorwash from a low altitude flyover with the rotorcraft in helicopter mode does not significantly impact the ground environment as long as the aircraft is approximately five rotor diameters above the ground. For this scenario's flight speeds and altitudes, the outwash component of the rotorwash does not have time to form or dissipates enough before reaching the ground and thus, the ground environment is not significantly affected.

5.8 Airborne Operations—Hover

Operational experience indicates that rotorwash from hovering does not significantly impact the ground environment as long as the aircraft is approximately five rotor diameters above the ground. For this scenario's altitude, the outwash component of the rotorwash dissipates enough before reaching the ground and thus the ground environment is not significantly affected.

At lower altitudes or with highly-loaded propellers, the rotorwash may affect airborne operations under the aircraft. Airborne operations will primarily affect personnel directly in the downwash flow field. Operational experience with fast roping from the V-22 in [Appendix H](#) indicated that ~1/3 of the rope length should be on the ground or weighted so that the rope will not whip around due to the rotorwash. Fast roping from the V-22 is conducted off the ramp and has also been tested from the side door. Both of the locations do not directly expose personnel on the fast rope to the rotor downwash.

A simulated hoist rescue (documented in Reference 11) describes a HH-53B (35,000 lb with 72.25 ft rotor diameter) operating at 125 ft AGL and 150 ft AGL. During the simulated hoist, the HH-53B broke off tree branches up to 2" in diameter and bent 5-6" diameter pine trees from a pretest height of ~40 ft tall to an arch ~25 ft tall. Later in a simulated hoist rescue under the same operational conditions, the XC-142 (31,825 lb with 4 x 15.625 ft rotor diameter) bent the same trees to an arch ~10 ft tall.

5.9 Airborne Operations—Low Speed

Operational experience indicates that rotorwash from airborne operations at low speeds does not significantly impact the ground environment as long as the aircraft is approximately five rotor diameters above the ground but could impact other aircraft in the immediate vicinity. At these altitudes, the outwash component of the rotorwash will dissipate before reaching the ground and thus the ground environment is not significantly affected. If the concern is the rotorwash impact on other aircraft, safe separation distances must be maintained in both the horizontal and vertical planes, as defined in standard military practices for tilt rotor aircraft.

6.0 Conclusions

This report presents an approach to determine the operational footprint produced by rotorwash on the surrounding environment. This approach incorporates processes, limits, modeling, and display to graphically depict the rotorwash operational footprint for current and future VTOL aircraft. This depiction allows “visualization” of the impact of the outwash on the surrounding environment and the recommended separation distances required for personnel, structures, equipment, other aircraft, and landscaping for safe operation.

The goals were to support development and evaluation of a rotorwash related performance specification with key specification elements, quantification of environmental limits, and development of the associated tools and analysis methodology.

The suggested specification for future military VTOL aircraft is: Rotorwash shall permit operations up to operational capability limits without endangering, damaging, or exceeding physical capabilities of personnel, equipment, or structures. Specifically, the rotorwash shall allow safe operation during:

- Ground and air taxi maneuvers
- Operations from an unprepared landing zone with internal and external loads
- Shipboard operations with internal and external loads during air operations
- Airborne operations including hoist, fast rope, air-to-air refuel, and air drop

Rotorwash footprints for unprotected military, civilian population, structures, equipment, airport/heliport environment, and landscaping are not considered to be driving requirements for a military performance specification. Resultant footprints for these considerations graphically display the safe separation distances from the VTOL aircraft.

The military and civil environmental limits are established as based on a combination of testing and literature review. These limits include wind limits for civilians, equipment, and structures; force limits for military personnel; energy limits for biophysical injuries; and velocity limits for materials damage.

The tools developed are capable of modeling rotorwash for a single main rotor, tandem, or tilt rotor configuration at the conceptual level. Empirically derived modeling can be refined or extended to a wider range of configurations and validity ranges with additional data.

Results presented within this report include the process and tools to conduct the associated analyses. These include:

- Conceptual level rotorwash modeling tool—RoWFoot
- Quantified operational environment limiting conditions
- Graphic display of the rotorwash operational footprint
- Evaluation of the operational space with a notional tilt rotor
- Process to validate or refine RoWFoot based on high fidelity modeling
- Summarization of published rotorwash related references

7.0 Recommendations

The work presented in this report documents a rotorwash operational evaluation process, environmental characterization and limits, flow field modeling, footprint display, and identification of key rotorwash impacts for future DoD VTOL aircraft. The authors recommend additional efforts to extend and refine this work. This report also documents the completion of efforts to develop and document process, modeling, and results for the rotorwash operational footprint. The framework presented allows for improvements contained within an individual piece of the process or model to be realized in the visualization and accuracy of the overall results.

Each recommendation has been ranked as a Priority 1, 2, or 3 level with Priority 1 having the highest importance. Within each category, the recommendations are further prioritized in descending order. The recommendations and their associated prioritizations are as follows:

7.1 Techniques to Mitigate Rotorwash Operational Effect

Priority 2: Multiple techniques can be operationally employed to mitigate the effect of rotorwash in the ground environment. These techniques are used every day with helicopters and tilt rotors in the current DoD inventory. A primary utility of rotorwash footprint modeling is examination and early quantification of operational issues and to allow proactive mitigation of these issues with changes to the aircraft operation or ground environment. Resultant mitigation may decrease the operational capability of an aircraft. The Warfighter decision then becomes “How much is too much?” Follow-on efforts are recommended to collect current fleet operational workaround techniques and quantify the impact of these techniques. A non-exhaustive list of these techniques may include:

- Mitigation by change to aircraft operation:
 - Lower aircraft weight (reduces magnitude of rotorwash wind speed)
 - Increase aircraft hover height (reduces outwash force on ground personnel)
 - Restrict landing ground surface type (mitigates ground erosion impact)
 - Restrict aircraft hover time in landing zone
 - Hover with one rotor off ship deck edge for tilt rotors (reduce strength of centerline flow)
 - Utilize shipboard wind over deck to decrease rotorwash impact on upwind personnel
 - Define ground personnel approach routes (i.e. avoid high-velocity outwash areas)
 - Ground personnel only approach with aircraft at flat pitch
- Mitigation by change to ground environment:
 - Employ devices to block outwash (such as jet blast deflectors on ships)
 - Increase ground personnel capabilities (i.e. multi vs. single person approach)
 - Remove need to enter/exit rotorwash to hook-up external loads

7.2 Operational Evaluation

Priority 3: Conduct a survey of the rotorwash operational footprint for the single main rotor helicopter and the tandem helicopter similar to the tilt rotor results displayed in [Section 5](#). Additionally, a discussion of other potentially limiting rotorwash effects from other configurations (e.g. small Unmanned Air Vehicles (UAVs) and jet lift) would help identify additional modeling required in the rotorwash operational footprint (i.e. jet lift and other aircraft configurations with hot exhaust, the effect of temperature should be included within footprint evaluation for the operational environment).

7.3 Operational Environment Characterization

Priority 2: The proposed environmental limits are based on the best available information and research that has been identified. An independent review of these proposed limits should be conducted to determine if any additional critical research is known to be available that was not identified. Values of limits should be reviewed to determine if they accomplish desired goals or if they should be adjusted.

Priority 2: Link statically measured personnel physical limits (force) to actual capability in rotorwash. The peak velocity profile is based on single sensor recorded data and may over predict the perceived force of a gust on an individual.

Priority 2: Most of the hazards associated with personnel overturning, flying debris, eye injury, glass breakage, denting, etc., should be reviewed and standardized into handbook hazard analysis procedures. The civil engineering community has wisely accomplished this task with handbooks that explain building standards, how to calculate compliance, and the associated background reference material. This type of handbook approach was initiated with the "Rotorwash Analysis Handbook" publication (References 1 and 9). However, this document is clearly out of date considering the reference material that is now available. Some of the more important procedures, i.e. the "PAXman" model for calculating overturning force, could easily be developed into a standardized subroutine for use in computer programs to promote standardization. This effort could readily be conducted as a university thesis project.

Priority 2: Limited amounts of test data exist for correlation of erosion model results. Until appropriate test data are acquired to support modeling updates, continued efforts to improve prediction capabilities cannot be calibrated or verified. Future testing is required to acquire the data necessary for further erosion model development.

Priority 3: Several representative aircraft windshield transparencies, sheet metal panels, and composite panels should be tested for sensitivity to breakage and denting (these components could be acquired from wrecked aircraft or scrap yards). This effort could readily be conducted as a university thesis project. This approach would encourage government/university cooperation and could pay for itself by yielding improved standards that would save the government maintenance funds.

Priority 3: Similar small projects using a load cell would determine what level of force is required to overturn a light aircraft, force open a door to damage hinges, and cause several other common types of military and civilian airport incidents. These projects are ideal for university thesis projects and would encourage government/university cooperation.

7.4 Rotorwash Modeling Methodologies

Priority 1: A new effort should be made to conduct the high-fidelity modeling extension of flight test data outside of the current bounds of flight test data. [Appendix L](#) documents the previous attempt with the CHARM vortex model. [Appendix M](#) documents the correlation to test data. Figures K-62 to K-85 in [Appendix K](#) document the comparison to the RoWFoot conceptual level model. These results can then be used to extend the rotorwash database, as described in [Section 4.3](#). To aid implementation, the supporting Excel spreadsheets (for the generation of graphs and tables) are available for the recommended work (Distribution Statement B: Distribution authorized to U.S. Government Agencies only).

Development and refinement of the conceptual and higher-fidelity rotorwash modeling should continue. This task will require correlation to additional/emerging flight test data with subsequent refinement of the modeling capabilities. In the absence of high-quality flight test data, the conceptual model should continue to be correlated to higher-fidelity modeling results to decrease the risk imposed by extrapolation outside of the regions of available flight test data. The conceptual model should also be refined and expanded for additional single and tandem rotor configurations and high disk loading props as well as fans and jet lift propulsion aircraft.

Priority 1: Additional test and development is needed to refine the effect of modeling the spacing between rotors for the rotorwash environment. As represented in [Appendix O](#), the tandem rotor produces a higher centerline outwash than the helicopter and tilt rotor due to the overlap rotor region. Separation of the tilt rotor rotors produces a fountain effect from the ground surface upwards from under the aircraft. In the centerline region, this seems to spread the outwash vertical and reduce the overall outwash velocity by pushing the mass flow higher in the wall-jet region. The tilt rotor also exhibits a lower peak velocity profile in the radial outwash as compared to the helicopter and tandem. These effects are not well understood and need further investigation with a conceptual level model update.

Priority 2: Research should be conducted to link the “constant wind” debris trajectory research by Lin and others with the “oscillating flow field” typical of rotorwash. Once this link is made, it should be possible to use the civil engineering results for the trajectories of compact-, plate-, and rod-like debris for rotorwash applications. Accomplishment of this task would be a powerful addition to the rotorwash analysis toolbox. The research that would be required would involve detailed simulation of standardized debris in both types of flow fields to determine the factor (or table of factors) required to produce equal debris accelerations, velocities, and displacements as a function of time. A typical mean/peak velocity ratio would have to be defined as a standard, and the frequency would have to be

extracted from the rotorwash test reports (these time history data are already available for each data run of several of the V-22 tests at all anemometer heights).

Priority 3: Further development should be conducted to refine the function defining the velocity profile shape used during configuration level modeling. As additional high-fidelity tool modeling and model/flight test data are obtained, the representation of the outwash velocity profile can be updated using numerical “best-fit” techniques to shape the full set of non-dimensionalized data. This “best-fit” can then be used to update the function for profile height to wind velocity representation in the outwash within the configuration level model.

Priority 3: Research should be conducted to model the effect of sloped ground environment on the rotorwash flow field. Operational selection of a sloped landing zone or external load pick up area may allow mitigation of rotorwash impacts due to using the slope to vector outwash away from an area of concern.

7.5 Footprint of Large Rotorcraft on Operational Environment

Priority 3: In the subject area of debris impact damage, several standards that are applicable to rotorwash scenarios should be discussed, evaluated, reviewed, and established with detailed documentation as justification. This is a “lesson learned” from the civil engineering community. There are too many scenarios, types of debris, and different kinds of incidents that can occur to try to plan for everything. An example would be the creation of velocity/distance footprints that avoid hazards, i.e. the footprint that ensures a 5.5-gram piece of gravel (that is lifted into the outwash flow) will not break a vehicle windshield made of laminated glass. These standards must be carefully chosen if they are to be meaningful. They should also be standards that try to ensure that other types of incidents will be prevented. For example, meeting a gravel/windshield glass breakage standard could be defined such that when it is achieved several other standards are also met. This careful choice of standards will minimize the work involved in analysis efforts and maximize safety within the rotorwash footprint. In summary, the review process should be methodically planned and carefully made if meaningful standards are to be produced (as well as a minimum number of useful standards). Incidents, like the V-22 incident mentioned in the first paragraph of [Appendix F](#) do and will continue to occur. However, many incidents can be prevented.

7.6 Flight Test Data Collection

Priority 1: It is highly recommended that the DoD develops an advanced LIDAR type sensor (laser anemometer) for the acquisition of future rotorwash data. The present method of mounting anemometers at several heights on a pole and varying the distance of the pole from the rotorcraft is “antiquated” when considering modern sensor technology. This data acquisition technique acquires a very limited set of velocity data

at only several heights above the ground surface. LIDAR technology has the capability to measure a continuous velocity profile from ground level to a specified height within seconds. Then, the beam can be refocused at a different distance from the rotor and the process repeated.

Priority 1: It is recommended that the DoD acquire additional test data to support refinement of the personnel stability ratio derived in [Appendix O](#). The value for the helicopter is based on only 2 data points taken from the CH-53E flight tests in Reference 2. An equivalent ratio is assumed by similarity for the tandem based on the similarity to the helicopter outwash profiles and is weakly supported by engineering methodology. The tilt rotor personnel stability ratio is a conservative estimate with no traceability to specific test data.

Priority 2: Data reduction methodologies used in processing flight test results need to more accurately capture the rotorwash peak velocity. Improved post processing methodologies should be applied to future flight tests and could potentially be used to reprocess existing flight test results for the V-22, CH-53E, XV-15, and other high-quality test data. The issue is how to better represent the “true” peak velocity conditions in the outwash as opposed to independently recording the maximum wind velocity at each sensor location and then plotting that value as the peak velocity measured at that location (independent of time and statistical analysis). For example, during V-22 data reduction in Reference 6, the peak velocity is the maximum recorded for each sensor over a 5-second time interval out of the recorded 20 seconds of test data. Any “spike” in the velocity recorded during the 5-second interval by the ultrasonic anemometer would give an isolated, exaggerated value of the peak velocity. Using a different data reduction method over the entire 20-second record could reduce the influence of spikes that might exist in current published test results. An example of this methodology is the 98th percentile data reduction method utilized in Reference 5 for the CH-47 data.

8.0 References

1. Ferguson, S. W., "Rotorwash Analysis Handbook, Volume I – Development and Analysis," Federal Aviation Administration, Washington D.C., Technical Report DOT/FAA/RD-93/31,I, June 1994.
2. Harris, D. J., and Simpson, R. D., "CH-53E Helicopter Downwash Evaluation. Final Report," Naval Air Test Center Technical Report No. SY-89R-78, August 1, 1978.
3. "Human Limits In Rotor Craft Downwash/Outwash," NAWCAD/4.6.5.5/2008-003, Naval Air Warfare Center Aircraft Division, Patuxent River, MD, 18 April 2008.
4. "Human Stability in Downwash," NAWCAD/4.6.5.5/2009-014, Naval Air Warfare Center Aircraft Division, Patuxent River, MD, February 2010.
5. Silva, M. J., "CH-47D Tandem Rotor Outwash Survey," NAWCADPAX/EDR-2010/120, August 2010.
6. Lake, R. E., and Clark, W. J., "V-22 Rotor Downwash Survey," NAWCADPAX-98-88-RTTR, July 1998.
7. Harris, D. J., and Simpson, R. D., "Technical Evaluation of the Rotor Downwash Flow Field of the XV-15 Tilt Rotor Research Aircraft," Naval Air Test Center Technical Report No. SY-14R-83, July 1983.
8. Meyerhoff, C. L.; Lake R.; and Peters, Lt. D., "H-60 Helicopter Rotor Downwash Wind Velocity Evaluation," Naval Air Warfare Center Report SY-3R-94, February 1994.
9. Ferguson, S. W., "Rotorwash Analysis Handbook, Volume II – Appendixes," Federal Aviation Administration, Washington D.C., Technical Report DOT/FAA/RD-93/31,II, June 1994.
10. Wachspress, D.A.; Quackenbush, T.R.; and Boschitsch, A.H., "CHARM Version 3.0 User's Manual (Comprehensive Hierarchical Aeromechanics Rotorcraft Model)," CDI-TN-05-11, Continuum Dynamics, Inc., Ewing, NJ, March 2007.
11. Anon., "Comparative Downwash and Simulated Forest Rescue Tests of the HH-3E, HH-53B and the XC-142A Aircraft," Aeronautical Systems Division X68-15759, December 1967.

Appendix A: Rotorwash Scenarios

John Preston and Ernie Keen

This appendix contains scenarios requiring ground crew activities and airborne operations in the proximity of Joint Heavy Lift (JHL) aircraft operation. These scenarios are used to define the operational and technical issues and criteria for what impact varying levels of downwash/outwash have on the operability of JHL. Information presented here relates to the following specific task objectives:

- Establish military need and operational capabilities of personnel and equipment in outwash region
- Establish effects of downwash/outwash on operational takeoff and landing environments
- Establish effects of downwash on airborne operations with JHL aircraft

The purpose of this document is to provide scenarios in which downwash/outwash are of particular interest for JHL concepts. These scenarios are based on operational needs derived from operational experience and the expected performance specifications.

These scenarios are not intended to be exhaustive but should cover the range of operations encountered during the JHL Concept Development Activity (CDA). These scenarios represent the corner points in the evaluation space for rotorwash interactions with the outside environment. This allows a limited number of total cases while capturing the impact to the Warfighter.

Each scenario is listed below as well as where this situation would occur within the flight profiles. Each scenario also lists the possible location of personnel and equipment, flight state and weight condition of the aircraft, and a description and duration of personnel tasks. Some distinction is made between concepts that use internal vs. external cargo arrangements. The rotorwash evaluation scenarios are:

1. Ground Taxi
2. Hovering Taxi
3. Landing Zone Operations with Internal Payload
4. Landing Zone Operations with External Payload
5. Shipboard Operations with Internal Payload
6. Shipboard Operations with External Payload
7. Low Altitude Flyover
8. Airborne Operations—Hover
9. Airborne Operations—Low Speed

The first section of each scenario is a situation. The situation describes an operational task that is affected by rotorwash. This operational task definition is further expanded upon to identify the primary operational concern that requires the scenario to be evaluated.

The second section defines the flight state of the aircraft. This encompasses the weight and operational characteristics that will produce the highest flow velocity (including periodic effects) in the rotorwash region for the situation.

The next section defines environmental conditions. These conditions describe the ground state under the aircraft. Ground conditions can vary significantly from an unprepared site with sand, rocks, and/or dirt to a shipboard deck with metal plating and deck movement.

The next section describes the location of personnel. This documents the required presence of ground personnel in the vicinity of the aircraft. For some cases, such as taxi operations, ground personnel are not required in close proximity to the aircraft. The associated outwash footprint becomes a safe clearance area around the aircraft in this scenario. For external payload operations, the ground crew will need to be able to operate directly under the aircraft with an ability to safely enter/exit the hookup area.

The potential operational impact section describes the operational activities that may be affected by the rotorwash. This provides rationale behind the scenario case and may influence or enable potential workarounds or mitigation for future platforms.

Downwash/Outwash Scenarios:

(1) Ground Taxi

Situation: Semiprepared landing zone operations for rolling taxi. The primary concern in this scenario involves clearance requirements of personnel, equipment, and other aircraft during the taxi maneuver up the slope.

Flight State of Aircraft: The aircraft has rotor thrust equal to amount needed to taxi on sod. The aircraft weight will be at Maximum VTOL Gross Weight.

Environmental Conditions: Terrain type may be assumed from sod/grass to concrete. During soft soil or sand conditions the aircraft will utilize a hovering taxi.

Location of Personnel: This scenario *does not* require any ground crew to be in close proximity to the aircraft. Personnel/equipment located at the edge of LZ.

Potential Operational Impacts: Approximate personnel and light structure separation from aircraft limits are needed for entrained debris and wind damage effects. These limits could be much different than the geometric size needed to get the aircraft into and out of the LZ.

(2) Hovering Taxi

Situation: Unprepared or austere landing zone operations for a hover taxi. The primary concern in this scenario involves clearance requirements of personnel, equipment, and other aircraft during the taxi maneuver.

Flight State of Aircraft: The aircraft hovers in ground effect and proceeds up the slope. The aircraft weight will be at Maximum VTOL Gross Weight.

Environmental Conditions: Terrain type may be assumed to run the full spectrum from fine dust and sand to sod/grass.

Location of Personnel: This scenario *does not* require any ground crew to be in close proximity to the aircraft. Personnel/equipment located at the edge of LZ.

Potential Operational Impacts: Approximate separation limits of personnel and light structures from the aircraft for entrained debris and wind damage effects. These limits could be much different than the geometric size needed to get the aircraft into and out of the LZ.

(3) Landing Zone Operations with Internal Payload

Situation: Unprepared or austere landing zone operations for internally carried payload concepts. The primary concern in this scenario involves a loss of the pilot's visual cueing in landing and the possibility of debris being thrown beyond the limits of the immediate landing area.

Flight State of Aircraft: The aircraft may be assumed to have a minimal hover time of 1 minute before descent from a given AGL. The aircraft weight will be Maximum VTOL Gross Weight.

Environmental Conditions: Terrain type may be assumed to run the full spectrum from fine dust and sand to sod/grass.

Location of Personnel: This scenario *does not* require any ground crew to be in close proximity to the aircraft during hover or any movement through the outwash field. Personnel/equipment located at the edge of LZ.

Potential Operational Impacts: Options are needed for addressing the loss of pilot visual cueing in high-particle entrainment situations. Also, for different types of terrain, some approximate distance limits for distance between the aircraft and personnel and light structures are needed to keep them from being damaged by entrained debris. These limits could be much different than the geometric size needed to get the aircraft into and out of the LZ.

(4) Landing Zone Operations with External Payload

Situation: Unprepared or austere landing zone operations for externally carried payload concept. The primary concerns here are similar to Scenario 3, with the added considerations for crew debarkation through the outwash field.

Flight State of Aircraft: The aircraft may be assumed to have a minimal hover time of 1 minute before descent from a given AGL. The aircraft weight will be at Maximum VTOL Gross Weight minus weight of payload and external handling kit. (MVTOW – 45,275)

Environmental conditions: Terrain type may be assumed to run the full spectrum from fine dust and sand to sod/grass.

Location of personnel: Depending upon the method of crew debarkation, the crew will be traversing the outwash field. A signal person should be able to operate and move in front of the aircraft as needed during all flight conditions.

Potential Operational Impacts: Outwash force limits for stability of personnel near the aircraft. Operational limits should also address dust and debris effects on personnel working under the aircraft in the cargo hook-up regions.

(5) Shipboard Operations with Internal Payload

Situation: General shipboard operations with internal cargo. The primary concern in this scenario is the ability of personnel to maintain stability at a given distance from the aircraft.

Flight State of Aircraft: The worst case for this scenario is the initial hover. The aircraft weight will be at Maximum VTOL Gross Weight.

Environmental conditions: The environment can be assumed to be free of dust and debris, and ship motion is limited to flight operational levels.

Location of personnel: Personnel will not be required to be close/under the aircraft or to traverse the outwash field. However, in the space-limited shipboard environment, personnel may still be subjected to large destabilizing forces. A ground signal person should be able to operate and move in front of the aircraft as needed during all flight conditions.

Potential Operational Impacts: Outwash force limits are needed for stability of personnel near the aircraft in hover.

(6) Shipboard Operations with External Payload

Situation: Shipboard operations with external cargo. The primary concern in this scenario is the ability to work in the destabilizing environment under the aircraft.

Flight State of Aircraft: The worst-case scenario for the MILVAN mission would occur during initial load hook-up. While personnel would be well clear of the aircraft when the

load is lifted, the initial hook-up would still occur at the Maximum VTOL Gross Weight minus nominal payload and external handling kit. (MVTOW – MILVAN)

Environmental conditions: The environment can be assumed to be free of dust and debris, and ship motion for external operations is limited to acceptable levels.

Location of personnel: Personnel will be required to enter and leave the outwash field. Personnel under the aircraft at cargo hookup areas can work and traverse the outwash field during the course of external cargo hook-up. Per the Navy response to the JHL CDA Q&A question, the duration of this task varies but should align with current operational experience.

Potential Operational Impacts: Outwash force limits are needed for stability/effectiveness of personnel near the aircraft in hover.

(7) Low Altitude Flyover

Situation: Low altitude, low speed flyover of JHL aircraft. The primary concern in this scenario is effects on aircraft, ground equipment, and debris from erosion.

Flight State of Aircraft: The worst case for this scenario is low altitude approach of 5 rotor diameters height above ground with aircraft in helicopter mode. The aircraft weight will be at Maximum VTOL Gross Weight.

Environmental conditions: Terrain type may be assumed to run the full spectrum from fine dust and sand to sod/grass.

Location of personnel: This scenario *does not* require any ground crew to be in close proximity to the aircraft.

Potential Operational Impacts: Approximate personnel and light structure separation from aircraft limits are needed for entrained debris and wind damage effects. These limits could be much different than the geometric size needed to get the aircraft into and out of the LZ.

(8) Airborne Operations - Hover

Situation: Low altitude, hovering JHL aircraft. The primary concern in this scenario is downwash on airborne operations under the aircraft such as hoist and fast rope operations.

Flight State of Aircraft: The worst case for this scenario is low altitude hover of 20 ft height above ground. The aircraft weight will be maximum 4k/95 Hover Gross Weight.

Environmental conditions: Terrain type may be assumed to run the full spectrum from fine dust and sand to sod/grass.

Location of personnel: This scenario requires ground crew to be directly under the aircraft during the operation.

Potential Operational Impacts: Project impact of downwash and turbulence from hovering on airborne operations. Workarounds such as hover height, reduced aircraft weight, or location of the operation (door, cargo ramp ...) may have an impact on severity of the downwash on the activity. Force or velocity limits for certain airborne tasks may necessitate workarounds. Attaching a weight to the end of the hoist line or fast rope has been used to alleviate the problem of the rope whipping around under the aircraft.

(9) Airborne Operations—Low Speed

Situation: Moderate speed flight conditions for JHL aircraft. The primary concern in this scenario is downwash on airborne operations under and behind the aircraft such as air-to-air refueling and air drop operations.

Flight State of Aircraft: The worst case for this scenario is 120 ± 5 knots cruise speed. The aircraft weight will be 2.5g Operational Weight

Environmental conditions: Level flight conditions

Location of personnel: This scenario does not require any ground crew near the aircraft during the operation.

Potential Operational Impacts: Project impact of downwash and turbulence during level flight on airborne operations. Wake from rotors or aircraft may necessitate workarounds such as change to flight speed, reduced aircraft weight, or characteristics of the operation (fuel probe location, length of jump line...). Force or velocity limits for certain airborne tasks may necessitate workarounds.

Appendix B: Description of Representative Rotorcraft

Sam Ferguson and John Preston

Conceptual level modeling of the rotorwash flow field utilizes simple aircraft geometry parameters. These parameters relate to the number, size, location and operating state of the thruster(s). For rotorcraft, these include the number of rotors, number of blades per rotor, rotor tip speed, rotor radius, height above the bottom of the aircraft, and separation between the rotors (if needed) number of blades. Table B-1 provides example geometric inputs for an example large helicopter (CH-53E) and a notional large tilt rotor. Figure B-1 provides a graphic depiction of the geometry associated with the conceptual level input set for the notional large tilt rotor.

Table B-1 Example Conceptual Level Aircraft Geometry

	<u>CH-53E Helicopter</u>	<u>Notional Large Tilt rotor</u>
Number of Rotors	1	2
Number of Blades/Rotor	7	4
Rotor Tip Speed, ft/sec	700	700
Rotor Radius, ft	39.5	39.5
Distance From Gear to Rotor, ft	17	25
Separation Between Rotor Centers, ft	0	101

Engineering parameters refining conceptual level modeling includes the ratio of thrust-to-weight for each rotor. This factor accounts for the drag generated by the downwash as it blows across the fuselage and/or wing under the rotor. Table B-2 provides example engineering inputs for large helicopter and tilt rotor configurations.

Table B-2 Example Engineering Parameters

	<u>CH-53E Helicopter</u>	<u>Notional Large Tilt rotor</u>
Thrust/Weight	1.05	1.09

The aircraft flight state defines the aircraft operational parameters for the evaluation case under consideration. The rotorcraft geometry and engineering parameters will not vary case to case. The aircraft weight, height above ground, and air density are included as part of the flight state and will vary according to analysis requirements. Table B-3 provides example flight state values for the CH-53E and the notional large tilt rotor. This flight state corresponds to [Appendix A](#), Scenario 3 for flight state of aircraft at Maximum VTOL Gross Weight, 20 ft hover height and Sea Level Standard Day conditions.

Table B-3 Example Operational Engineering Parameters

	<u>CH-53E Helicopter</u>	<u>Notional Large Tilt Rotor</u>
Aircraft Weight, lb	73,500	141,605
Height Above Ground, ft	20	20
Air Density, slug/ft ³	0.002378	0.002378

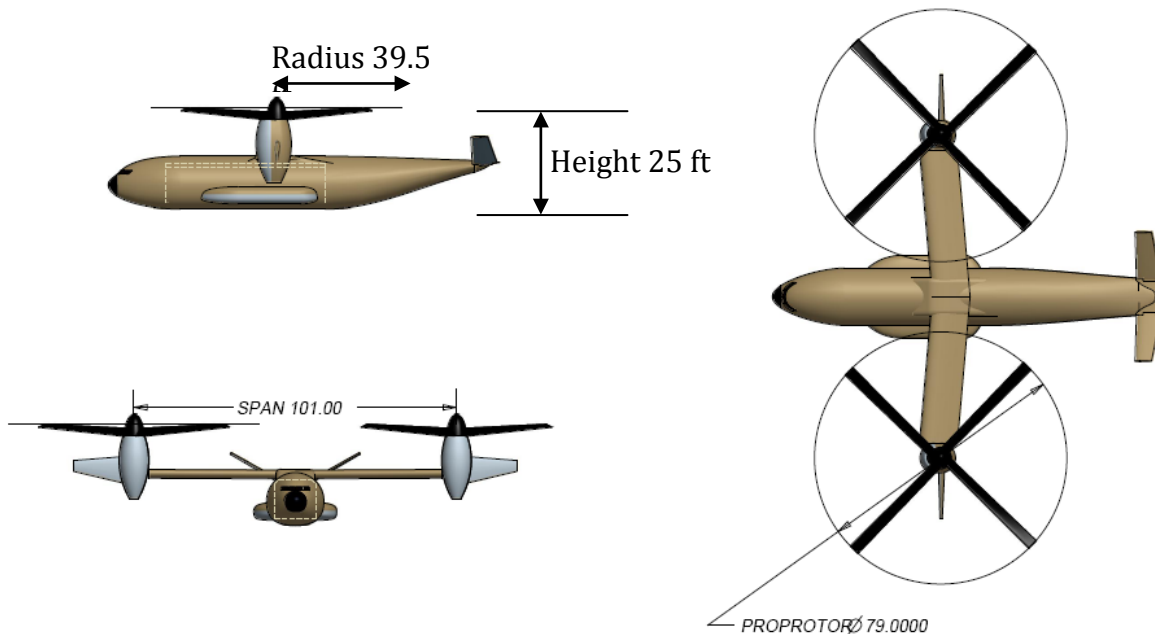


Figure B-1 Example Conceptual Level Inputs—Visual Geometry

Weight will vary depending on the mission need and capability of the aircraft. For example, the atmospheric flight condition can limit the hover weight and design constraints such as structural limits or maximum fuel load may limit the hover weight achievable.

Appendix C: Personnel Rotorwash Hazards

Sam Ferguson

In the development of any type of rotorwash related separation criteria, the most important hazards to consider are those that directly involve the safety and general welfare of people. Almost all personnel related hazards in the rotorwash environment fit into one of two categories. The first category involves human performance limitations for functioning in or being blown over by the high dynamic pressure (or wind velocities) of the rotorwash flow field. The second category involves physical injury as the result of being struck by a projectile or piece of flying debris that is blown through the rotorwash flow field. Obviously, all personnel injuries are the priority for avoidance if at all possible. Training and protective clothing can minimize injury and maximize functionality if work must be performed near rotorcraft. Otherwise, total avoidance of the high dynamic pressure regions of the rotorwash flow field are recommended for unprotected and untrained personnel.

Conclusions of this appendix are summarized in Table C-1. This table represents the limiting conditions associated with personnel in the vicinity of the aircraft. Limits associated with these conditions are displayed in a range of units and represented in terms of force, energy, velocity, and dynamic pressure. Underlined data are the limiting condition derived from research presented later within this appendix.

	Mean Force	Peak Force	Dyn Press	Peak Wind Velocity				Particle Energy/area		Object Energy
	lb	lb	lb/ft ²	ft/s	kts	mph	m/s	J/m ²	ft-lb/ft ²	ft-lb
OVERTURNING FORCES & MOMENTS										
Military										
Caution Limit	<u>80</u>	<u>87</u>								
Hazard Limit	<u>87</u>	<u>115</u>								
Civilian (General)										
Caution Limit			2.88	49.2	29.2	33.6	<u>15</u>			
Hazard Limit			5.12	65.6	38.9	44.7	<u>20</u>			
BIOPHYSICAL INJURY										
Unprotected (eye)								<u>1487</u>	102	
Protected (incapacitate)										<u>58</u>

Table C-1 Rotorwash Personnel Limits

Utilization of dynamic pressure in lieu of wind velocity removes variations due to changes in the air density. For conservatism, wind velocity limits are converted to dynamic pressure limits using Sea Level Standard (SLS) air density. At atmosphere conditions other than SLS, velocity limits can be calculated using the limit dynamic pressure and the evaluation case air density.

Personnel Overturning Forces and Moments

The personnel overturning force and moment hazard has been researched by the DoD for ground crew working in close proximity to rotorcraft. Most of this research has focused on quantifying requirements and developing procedures with the use of protective gear. Also, this research has largely been based upon the assumption that military personnel working in a rotorcraft downwash environment will be adults, in good health, and will receive at least some special training for working in this environment. Very little research, if any, has been conducted to define what can be considered comfortable and uncomfortable to a person that is working while fully immersed in a rotorwash flow field. Understandably, none of this research has also examined the civilian side of the problem. Much of this research is detailed and summarized in the discussion presented in Section 5.1 of Reference C-1 (with some limited civilian application updates as presented in Reference C-2, pages 85 – 143). These previously discussed data will only be summarized in this section for the purposes of defining not-to-exceed threshold guidelines for military personnel working in the rotorwash flow field.

It was originally stated in Reference C-1 that, “Minimal work has been conducted to quantify what is unpleasant, uncomfortable, or dangerous to the untrained and therefore unsuspecting human (adult or child) that is suddenly either partially or fully immersed in a rotorwash flow field. Even less quantitative data exists to answer questions about what might happen to a person that is standing in or passing through such an environment while wearing a hat, or carrying a purse or briefcase, or “towing” a startled and scared child.” In 1994, this statement was true and yet false to some degree. During this study, with the aid of Internet databases, research was identified for unprotected civilians in high or gusty winds. The wind engineering community has conducted this research for application in urban environments. While these data are not directly related to rotorwash applications, they nevertheless provide excellent guidelines for unprotected personnel, especially the young and the elderly. These data also support or improve previously made assumptions about civilians in a rotorcraft environment that were discussed in Reference C-1. The sources associated with this research and the results will be discussed in the civilian related requirements section.

Military Related Requirements

The development of military personnel overturning force and moment requirements has evolved over time as the result of several ground and flight test experiments. As stated previously, a detailed summary of this literature is documented in Section 5.1 of Reference C-1. The first practical requirements were first documented in Reference C-3 as part of the evaluation of the CH-53E rotorwash characteristics. The supporting laboratory experiment to this flight test evaluation utilized four test subjects to evaluate the range of forces that could be tolerated as a function of body weight. These results are presented in Figure C-1.

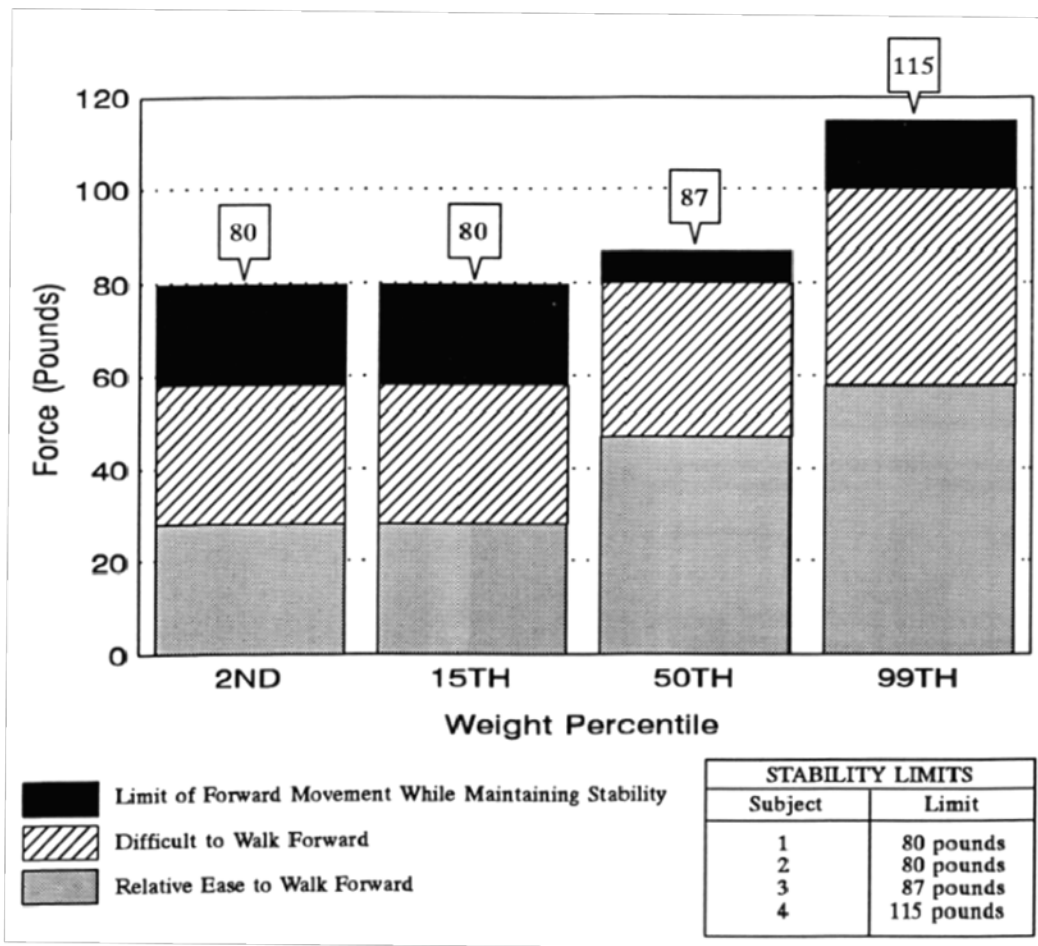


Figure C-1 Overturning Force Limits Defined by Harris and Simpson (Reference C-3)

It is important to note that these forces, applied through a body harness at 3 feet to the test subject's height, were not dynamically applied like an oscillatory rotorwash profile. However, the use of these force limits over time, as documented in this figure by the solid black ranges, has generally found these limits to be quite useful and not out of line with the results from subsequent tests.

The link between the laboratory force limit data presented in Figure C-1 and forces measured from flight test data (as calculated from the integration of measured velocity profiles) have been accomplished using the "PAXman" model. This analytical representation of a man working in a rotorwash environment was developed for the CH-53E rotorwash test. However, the model was not formally documented until References C-1 and C-4 were published. Additional experiments to link the laboratory force with comments from personnel immersed in rotorwash have been conducted. One of these tests involved the Bell XV-15 tilt rotor (Reference C-5). Three people (one from the CH-53E rotorwash test) walked through the critical regions of the rotorwash flow field while the XV-15 was hovering overhead and provided commentary as to their ability to traverse the

regions. These regions, Region I through IV, are graphically indicated in Figure C-2. Forces calculated from measured rotorwash velocity profiles are also indicated on the figure. The recorded comments, when linked to the forces derived from the PAXman model using the measured velocity profiles, compare favorably with the laboratory limits defined during the CH-53E experiment. The details of this evaluation are available from References C-1 and C-5.

In May 2007, Air Force research personnel published results from an experiment to determine rotorwash limits for trained para-rescue personnel with protective clothing in close proximity to a rotorcraft. This experiment, documented in Reference C-6, was also conducted in a laboratory environment. The resulting proposed limit is 65 kts. It is important to note that this limit, like the previous CH-53E laboratory experiment, did not take into account an oscillating flow field scenario.

In 2008, O'Connor reviewed available force limit data from the literature and NAVAIR testing results and proposed preliminary force limits for use with JHL in reference C-7. This review recommended that force limits should be defined around the rotorcraft in a zonal context for an ambient wind condition and a 20-kt headwind condition (shipboard condition). A "Caution Zone" would be defined whenever the PAXman average force calculation exceeds 80 lbs or the peak force calculation exceeds 87 lbs. A "Hazard Zone" would similarly be defined when the PAXman average force calculation exceeds 87 lbs or peak force calculation exceeds 115 lbs. This proposal introduces the "rotorwash footprint concept" discussed in this report. Additional requirements with this proposal require that personnel be a minimum weight of 133 lbs, with protective gear, grip shoes, etc. as outlined in the reference.

In January 2010, NAVAIR published new human stability test results in reference C-8. This test repeated the personnel force limit tests previously conducted in reference 4 with a larger number and wider range of test subjects. Data collected with the larger sample size increased the confidence that recommended human stability limits were understood for the full range of military personnel. Twenty-two subjects participated in the tests. The test subjects included both male and female Soldiers with a wide range of age, height, weight, and BMI. Results from these tests support previously defined caution and hazard zones. Specifically, reference C-8 states "...a caution zone can be represented by equivalent downwash forces of 80-87 lbs and a hazard zone can be represented by equivalent forces of 87-115 lbs. No crewmen should attempt to enter an area that shows possible wind speeds equating to 115 lbs or above." These results confirm the previous limits in Reference C-7 by specifying a downwash force range in the caution and hazard zones where the lower values are based on the mean force and the upper values are based on the peak force.

Shipboard conditions were compared to land-based in Reference C-9. In this report, the V-22 was surveyed on an LHA during 0 to 20-knot Wind Over Deck (WOD) conditions. These flow field forces and hazard levels were compared to land-based CH-53E results in Reference C-3. Shipboard operations with one of the V-22 rotors located off the flight deck exhibited flow field forces (shape of velocity profile) similar to a single rotor. When using landing spots in the center of the flight deck, the flow field forces were consistent with

land-based results. Increasing magnitudes of WOD influenced the rotorwash by decreasing the outwash velocity and flow field forces in upwind of the aircraft and increasing outwash velocity and flow field forces downwind. Figure C-3 from Reference C-9 depicts a recommended V-22 downwash shipboard safe operating zone diagram. The safety zone is based on 0- to 20-kt WOD condition range and $\geq 75^{\text{th}}$ weight percentile stability limits. Additionally, Reference C-9 states, “Additional caution should apply when WOD is greater than 20 kts, at areas around the superstructure, or when inexperienced personnel or those of smaller stature are working around the aircraft.”

The personnel overturning “not-to-exceed” threshold criteria from each of these military laboratory experiments and flight test projects are summarized in Table C-2 for quick reference (along with civilian criteria to be discussed in the next section).

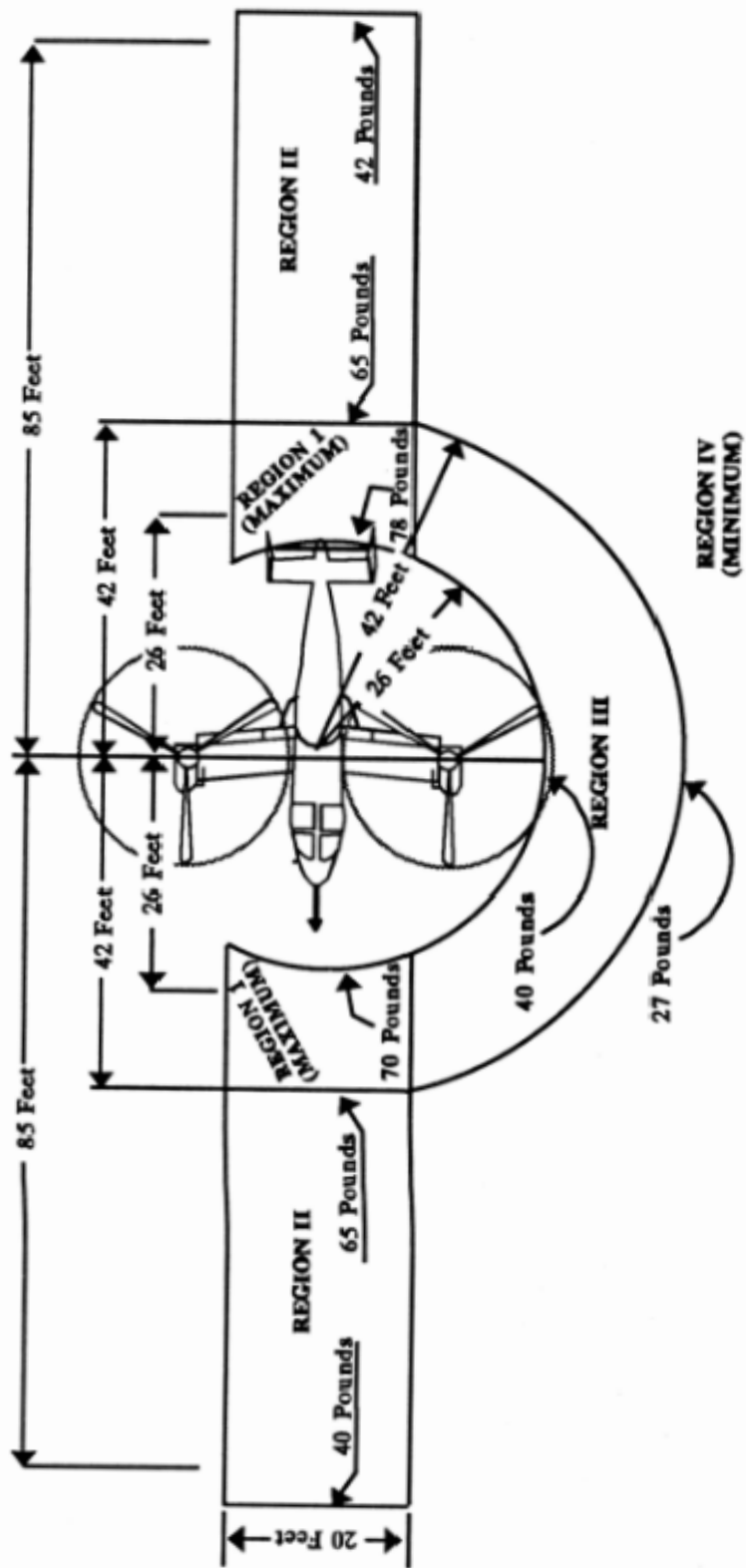


Figure C-2 XV-15 Overturning Force Limits (Reference C-1)

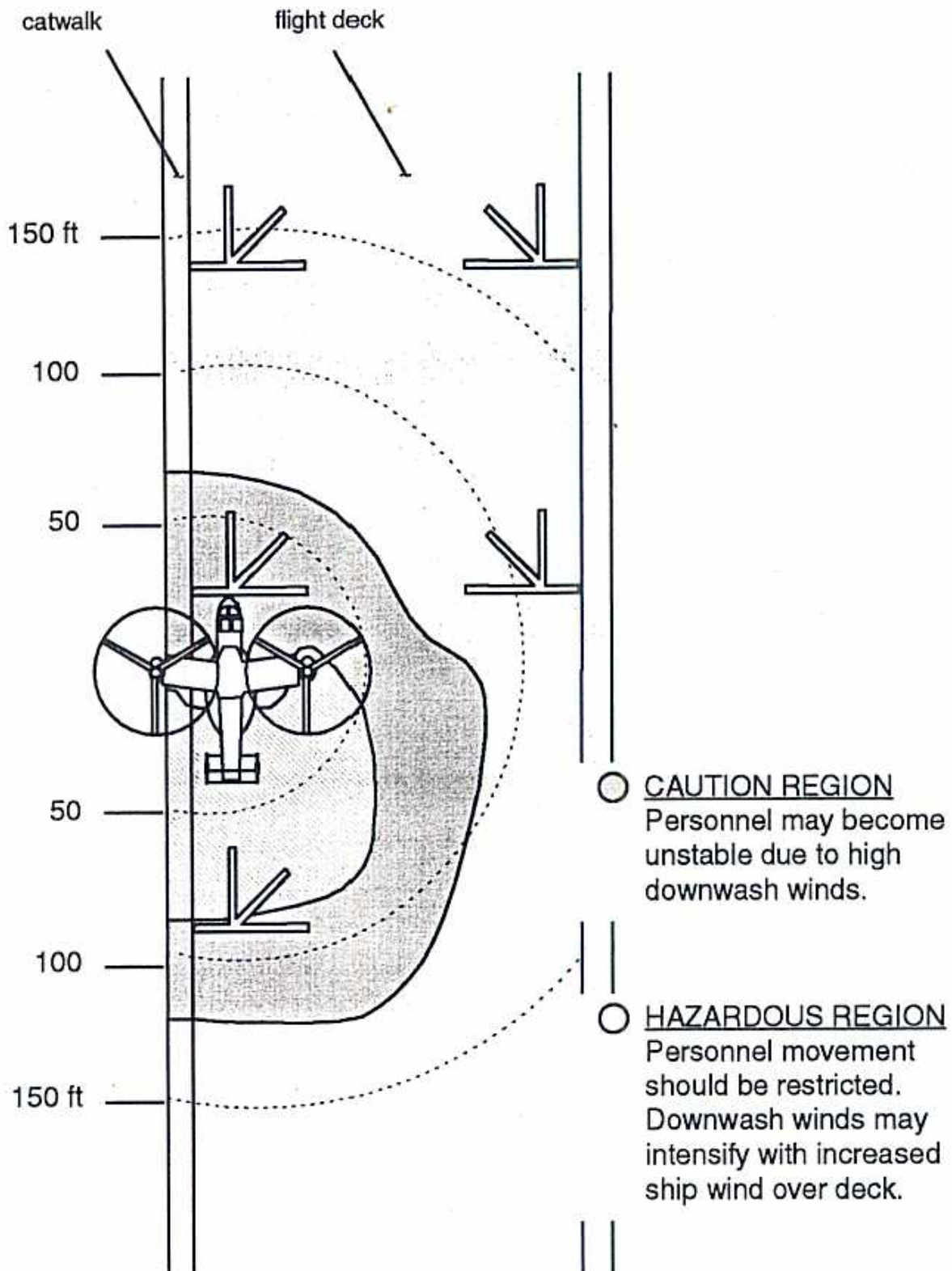


Figure C-3 V-22 Shipboard Downwash Hazard Regions (Reference C-9)

Table C-2 Personnel Overturning Not-To-Exceed Threshold Criteria

Hazard	Recommended Threshold Criteria	Reference
Overturning Force – Military	<p>Caution, Hazard, and No Entry zones based on equivalent downwash forces (at peak wind conditions) :</p> <ol style="list-style-type: none"> 1. Caution Zone - 80 – 87 lbs 2. Hazard Zone – 87-115 lbs 3. No Entry Zone – Greater than 115 lbs <p>Proposal assumes people of minimum weight, protective gear, grip shoes, etc.</p>	C-8
Overturning Force – Military	<p><u>Preliminary</u> proposal is to define a Caution and Hazard zone around rotorcraft:</p> <ol style="list-style-type: none"> 1. Caution Zone - PAXman average force calculation exceeds 80 lbs or peak force calculation exceeds 87 lbs. 2. Hazard Zone - PAXman average force calculation exceeds 87 lbs or peak force calculation exceeds 115 lbs. <p>Proposal assumes people of minimum weight, protective gear, grip shoes, etc.</p>	C-7
Overturning Force – Military and Civilian	<p>Force limits as based on PAXman projected model:</p> <ol style="list-style-type: none"> I. Trained and protected ramp personnel frequently working in a rotorcraft downwash environment, limit = 80 lb II. Untrained and unprotected personnel rarely or never exposed to the rotorcraft downwash environment, limit = 40 lb III. Untrained and unprotected children likely to be walking without assistance from an adult in the rotorcraft downwash environment, limit = 30 lb 	C-1
Wind Limit – Trained Military Para-rescue Personnel	<p>Limit for trained para-rescue personnel with protective clothing in close proximity to a rotorcraft.</p> <p>65 kts (74.8 mph)</p>	C-6
Wind Limit – Civilians	<p>Series of three wind experiments involving pedestrians of all sizes, ages, and sexes (not protected military personnel). Proposed limits are defined where u = instantaneous wind speed averaged over 3 seconds. Limits are:</p> <p>$u > 15 \text{ m/s}$ (33.6 mph), very serious (peak forces: 13 - 20 lb depending on test subject)</p> <p>$u > 20 \text{ m/s}$ (44.7 mph), dangerous (peak forces: 22 - 34 lb depending on test subject).</p>	C-10, C-11

	Comparison data for PAXman size person exist (data confirm projected area and drag coefficient used by PAXman). It should be noted that the wind tunnel data only involved young men/women from 4.9 to 5.9 ft tall and 85 to 140 lbs. This is the lower range for force calculations to apply (conservative criteria).	
Wind Limit – Civilians	<p>Research is for unprotected civilians. Research done at lower wind velocities. Results include effects on older people (> 50 years old). Gusty winds above 8.5 m/s were shown to have a quantifiable effect on stability (13 to 15 m/s normally considered threshold for this effect). Final criteria for safety of walking are:</p> <p>Steady uniform wind, $u < 20\text{-}30 \text{ m/s}$ ($20 \text{ m/s} = 44.7 \text{ mph}$)</p> <p>Non-uniform winds (except elderly), $u < 13\text{-}20 \text{ m/s}$</p> <p>Gusty winds, $u^* < 20 \text{ m/s}$ (where u^* is not the instantaneous peak, see reference for definition)</p>	C-12
Wind Limit – Civilians	Reviews of pedestrian wind acceptability criteria from 1975 through late 1980s. Isyumov and Davenport (1975) indicate a mean wind speed of > 34 mph is “dangerous”. Lawson and Penwarden (1975) state a mean wind speed above 13.85 m/s (31 mph) or a peak > 23.7 m/s (53 mph) is “unacceptable”. Melbourne (1978) states a peak > 23.0 m/s (51.4 mph) is “unacceptable”.	C-13
Sudden Gust Limit – Civilians	50% of test subjects displaced by a sudden 11-12 m/s (24.6 mph) gust, 100% displaced by 15 m/s gust (33.6 mph) or a sudden delta of approximately 13.5 lb (female) and 19.3 lb (male) overturning force.	C-14, C-15
Wind Limit – Civilians	<p>The Design Guide for Wind states: “Although there is an obviously subjective element to a person's "comfort", and there are slight divergences of opinion amongst researchers, there is a remarkably close agreement on the general effects of winds upon people. These may be summarized as:</p> <p>10 m/s - limit for comfort when standing/sitting for lengthy periods in an open space</p> <p>15 m/s - limit of comfort acceptability for walking</p> <p>18 m/s - threshold of danger for walking</p> <p>23 m/s - completely unsuitable for walking”</p>	C-16
Wind Limit – Civilians	Table C-4 for wind effects	C-17

PAXman Method For Calculating Outwash Forces (Reference C-18)

The following three pages of this section describing the PAXman model are copied directly from Reference C-18.

Personnel immersed in the outwash flow field experience an aerodynamic drag force which is a function of the individual's size, posture, air density, and the horizontal velocity distribution with respect to height. This drag force can be calculated mathematically given the following equation:

$$D = C_D \int_0^H \frac{1}{2} \rho u_y^2 dA_y dy$$

Where

- D = drag force (lb)
- C_D = drag coefficient (dimensionless) = 1
- H = projected subject height, (ft)
- ρ = air density (slugs/ft³)
- u_y = outwash velocity distribution (ft/sec)
- dA_y = body frontal area distribution (ft²/ft)
- dy = incremental distance in the y (height) direction (ft)

The area distribution most often used in the above expression, commonly referred to as the "PAXman" model, is that of a representative 6 foot tall subject leaning 20 degrees into the wind, resulting in a projected height above ground of 5.5 feet. The PAXman area distribution is typically expressed as a 9th order polynomial describing the projected body half-width as a function of height, $x_p(y)$, as shown in Figure C-4. Table C-3 provides the body profile polynomial coefficients. The resulting area distribution, $dA(y) = 2x_p(y)$, is shown in Figure C-4.

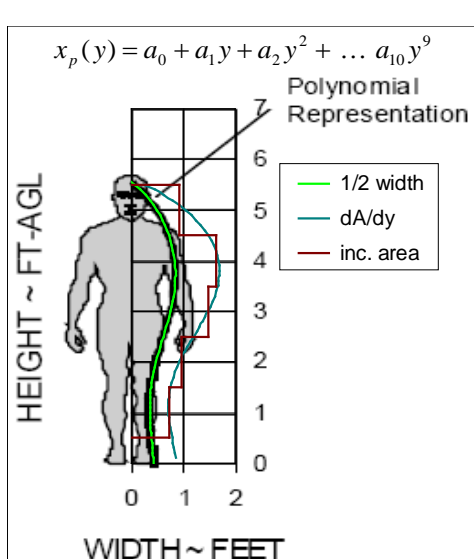


Figure C-4 PAXman Area Distribution
(Reference C-18)

a0	4.30939E-01
a1	-4.63972E-02
a2	-1.39649E-01
a3	1.37545E-01
a4	-2.48764E-02
a5	-5.49253E-04
a6	2.21653E-04
a7	-4.18444E-05
a8	1.45194E-05
a9	-7.80009E-08
a10	-1.89822E-07

Table C-3 Polynomial Coefficients
(Reference C-18)

In past implementations, a cubic spline of user selected resolution, Δy , would be fitted to the discrete measured outwash velocity values making up the velocity-height profile, with a zero point added to represent the no-slip condition at the ground as shown in Figure C-5.

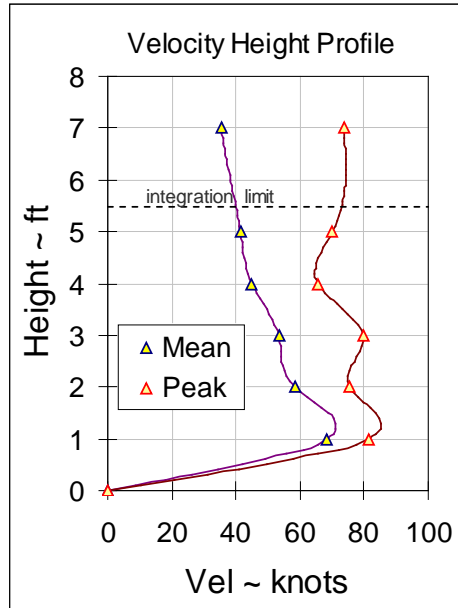


Figure C-5
Typical Outwash Velocity Profile
(reference C-18)

Evaluating the body half-width polynomial expressions at heights from 0 to $H = 5.5$ feet at the same resolution as the cubic spline fit allows the net PAXman outwash force to be expressed as

$$F_{PAXman} = C_D \sum_{i=0}^N \frac{1}{2} \rho u_i^2 \cdot 2x_{p_i} \cdot \Delta y$$

Where

- Δy = incremental height distance (ft)
- N = total number of height increments, $H/\Delta y$
- C_D = drag coefficient (dimensionless) = 1
- ρ = air density (slugs/ft³)
- u_i = outwash velocity cubic spline fit evaluated at $y = i \cdot \Delta y$, (ft/sec)
- x_{p_i} = body half-width polynomial evaluated at $y = i \cdot \Delta y$, (ft)

PAXman force can be computed for each time step that outwash data was recorded, yielding, in effect, an outwash force time history. This unsteady data can then be post-processed to provide more meaningful and realistic statistical metrics for outwash force than the previous approach of computing mean and peak forces from the mean and (composite, not instantaneous) peak outwash velocity profiles.

Civilian Related Requirements

Civilian related requirements for wind exposure and overturning force are distinctly different than those for military personnel. Factors such as weight, size, age, health, protective clothing, and task (i.e. holding umbrella or pushing stroller) all have important effects on wind velocity threshold limits. The wind engineering community has studied this subject for numerous reasons over the last 40 years. No references were found that connect this research directly to rotorwash applications. However, for civilian rotorwash scenarios, this research provides excellent background and guideline information. References within this section refer to wind velocity as the limiting parameter. For conservatism, this wind velocity is assumed at sea level standard conditions. In rotorwash applications, the resultant dynamic pressure at sea level standard conditions should be used to derive the equivalent limit wind velocity for application at other atmospheric conditions.

The following discussion is a summary of the reference material that has been identified during this study. A further very brief description of this material is summarized as not-to-exceed threshold information in Table C-2.

Murikami (References C-10 and C-11) documents three excellent experiments (one wind tunnel and two outdoors) involving pedestrians as affected by winds of a range of airspeeds and turbulence levels. The test subjects are people of all size, weight, sex, and age combinations (not protected military personnel). Extensive documentation is provided, including wind tunnel drag measurements for both men and women from several positions relative to the wind. The results are also compared with prior experiments. The result of these experiments is the development of criteria for evaluating wind effects on pedestrians where u = the instantaneous wind speed averaged over 3 seconds.

$u < 5 \text{ m/s}$	no effect
$5 < u < 10 \text{ m/s}$	some effect
$10 < u < 15 \text{ m/s}$	serious effect
$15 < u < 20 \text{ m/s}$	very serious (peak force: 13-20 lb depending on test subject)
$u > 20 \text{ m/s}$	dangerous (peak force: 22-34 lb depending on test subject)

It should be noted that the wind tunnel force balance data (experiment 1) only involved young men/women from 4.9 to 5.9 ft tall and 85 to 140 lbs. This is the lower weight range for using the data with applied force criteria (conservative criteria). Also, some data carrying umbrellas as well as wind azimuth effects on test subjects are provided. In summary, these references are quite detailed with photos and graphs of results. While there is overlap in data, a review of both documents is required to obtain the most complete understanding of the experiments.

Hunt (Reference C-12) documents a series of very interesting wind tunnel experiments for unprotected civilian personnel as affected by winds in a wide range of settings. Unfortunately, most of the data are below the threshold for rotorcraft applications. The test subjects are generally people of all size, weight, sex, and age combinations. Extensive documentation is provided, including wind tunnel force measurements. Novel use of

mechanisms is demonstrated to measure personnel force (as exerted by feet) and generate gust conditions for test purposes. The results are also compared with prior experiments. One of the several interesting results is the development of criteria for defining safety of walking. This condition is as follows:

Steady uniform wind, $u < 20\text{-}30 \text{ m/s}$
Non-uniform winds (except for elderly), $u < 13\text{-}20 \text{ m/s}$
Gusty winds, $u^* < 20 \text{ m/s}$ (where u^* is not the instantaneous peak, see reference for definition)

Results for elderly people (> 50 years old) indicate that gusty winds above 8.5 m/s clearly have a quantifiable effect on stability (13 to 15 m/s is normally considered the threshold for this effect). It should be noted that the majority of the test subjects appear to be people on the lower range of weight and height distributions as compared to the general population today (and especially with respect to the military population).

Ratliff and Peterka (Reference C-13) review and compare pedestrian wind acceptability criteria from 1975 through the late 1980s. These comparisons include the work of Isyumov and Davenport (1975) that indicates a mean wind speed of $> 34 \text{ mph}$ is "dangerous." Lawson and Penwarden (1975) state a mean wind speed above 13.85 m/s (31 mph) or a peak $> 23.7 \text{ m/s}$ (53 mph) is "unacceptable." Melbourne (1978) states a peak $> 23.0 \text{ m/s}$ (51.4 mph) is "unacceptable." Hunt indicates acceptability (with conditions) for wind speeds $< 20\text{-}30 \text{ m/s}$ (44.7-67.1 mph) for steady wind, $< 20 \text{ m/s}$ (44.7 mph) for non-uniform or gusty wind (gusty defined by equation, not instantaneous or peak wind speed).

Jordan (References C-14 and C-15) documents a very recent series of wind tunnel experiments and analytical calculations undertaken to evaluate the response of an individual to a sudden change in wind speed. The wind tunnel testing subjected 31 people (male/female = 19/12, age 18-50 years, average mass male/female = 118/160 lbs) to step changes in wind speed of up to 20 m/s as applied in approximately 0.2 seconds. These test subjects were unprotected civilian personnel. Loss of balance (to a gust) was demonstrated to be a function of orientation to the wind and test subject weight. Loss of balance does not mean a fall occurs but that the body must compensate by moving the legs so as not to fall. Being pushed backwards in a pivot over the heel is less stable than a forward pivot on the toes. Whereas sideways is the least stable, it is compensated for by a lower drag coefficient. The developed analytical model for predicting unbalance is shown to correlate relatively well with the test data. This model is developed to simulate a starting wind speed condition with a gust of varying frequency. Also, a reference list is provided of reported limiting values of acceleration for human stability. The 50th percentile child is shown to be particularly sensitive to sudden changes in wind velocity by the analytical model. Some general results are:

- 1) 50% of test subjects are displaced by a sudden 11-12 m/s (24.6 mph) gust
- 2) 100% of test subjects are displaced by 15 m/s gust (33.6 mph) or a sudden delta of approximately 13.5 lb (female) and 19.3 lb (male) overturning force

Reference C-15, the Ph.D. thesis, is the most complete presentation of results.

The Wellington, New Zealand city "Design Guide for Wind" (Reference C-16) states "Although there is an obviously subjective element to a person's "comfort", and there are slight divergences of opinion amongst researchers, there is a remarkably close agreement on the general effects of winds upon people. These may be summarized as:

- 10 m/s - generally the limit for comfort when standing or sitting for lengthy periods in open space
- 15 m/s - generally the limit of acceptability for comfort whilst walking
- 18 m/s - threshold of danger level
- 23 m/s - completely unsuitable for walking."

No detailed background or source for these criteria is provided. Additionally, the document does provide sketches on how to mitigate undesirable wind conditions within urban environments.

Lastly, Simiu and Scanlan, in a 1978 textbook (Reference C-17) present the following table for general use. The data in this table approximate the results from the previously discussed sources.

Table C-4 Wind Effects Summary Defined by Simiu and Scanlan (Reference C-17)

Generally a wind speed (V) above 5 m/s is considered as uncomfortable wind speed. However, wind speed above 10 m/s definitely causes unpleasantness and a speed above 20 m/s is dangerous.

<u>Description of Wind</u>	<u>Speed (m/s)</u>	<u>Description of Wind Effects</u>
Calm	< 0.4	No noticeable wind.
Light airs	0.4 – 1.5	No noticeable wind.
Light breeze	1.6 – 3.3	Wind felt on face.
Gentle breeze	3.4 – 5.4	Wind extends light flag, hair is disturbed, clothing flaps.
Moderate breeze	5.5 – 7.9	Wind raises dust, dry soil and loose paper. Hair disarranged.
Fresh breeze	8.0 – 10.7	Force of wind felt on body. Drifting snow becomes airborne. Limit of agreeable wind on land.
Strong breeze	10.8 – 13.8	Umbrellas used with difficulty. Hair blown straight. Difficulty to walk steadily. Wind noise on ears unpleasant. Windborne snow above head height, (blizzard).

Moderate gale	13.9 – 17.1	Inconvenience felt when walking
Fresh gale	17.2 – 20.7	Generally impedes progress. Great difficulty with balance in gusts.
Strong gale	20.8 – 24.4	People blown over by gusts.

Personnel Biophysical Injury

Personnel “biophysical injury” in the context of this report is defined as “any injury that is the result of being struck by a projectile or debris that is propelled through the air by the rotorwash flow field.” This definition does not include muscle strains, tissue damage, or broken bones that are the result of overturning forces and moments, as discussed in the previous section. In further breaking down the above definition, two major areas of concern have been identified. One concern involves an answer to the question, “What projectile velocities are required to penetrate or severely bruise human skin?” The second and more applicable concern is, “What projectile velocities are required to damage the unprotected human eye?”

The question of what projectile velocities are required to severely bruise human skin could not be answered for this report. First, the definition of an “acceptable bruise” was not found in the available literature and no data on the bruising or skin from projectiles or debris were identified. The answer to the question of what projectile velocities are required to penetrate human skin is also not easy to answer. Hueske (Reference C-19) best sums up the problem when he states, “the minimum velocity required for a projectile to perforate human skin largely depends on projectile shape and mass, and varies between about 200 and 300 ft/sec.” The parameters of projectile shape and mass clearly introduce physics that do not support a simple answer. Evans (Reference C-20) offers a slightly more conservative answer by stating that the minimum velocity is between 125 and 230 ft/sec. Bellamy (Reference C-21) simply states that the minimum velocity is 262 ft/sec. While other forensic medicine texts might offer additional data, the answer is clearly that a range of velocities exists as a function of projectile shape and mass. Fortunately, for rotorwash applications, these projectile velocities are relatively high and are therefore not a strong consideration in determining limitations on personnel. It will be shown in later sections that other hazards are more limiting when defining safe separation distances for personnel from rotorcraft.

Schane (Reference C-22) defines a different type of projectile impact threshold by stating that “localized impact of projectiles on humans having energies in excess of 58 ft-lb is incapacitating.” The details of the types of projectiles and locations of body impact associated with this threshold are not provided. However, two simple ballistic type examples can be calculated to gain some insight. If, for example, a baseball (5 oz = 0.3125 lbm) is fully stopped from a constant velocity impact of 109.28 ft/sec (74.5 mph), then the energy (E) that is absorbed by the body is 58 ft-lb. The calculation would be as follows:

$$\text{Kinetic Energy} = E = 0.5 m V^2$$

$$58 \text{ ft-lb} = 0.5 * (0.3125 \text{ lbm} / 32.174 \text{ lbmslug}) * (109.28 \text{ ft/sec})^2$$

A more practical example would be an empty wooden pallet. Assuming a weight of 50 lb, to achieve the 58-ft-lb impact energy level the pallet would need to be traveling at < 9 ft/s, well below the outwash velocity rear a hovering rotorcraft.

$$58 \text{ ft-lb} = 0.5 * (50 \text{ lbm} / 32.174 \text{ lbmslug}) * (8.64 \text{ ft/sec})^2$$

By comparison, a 357 Magnum revolver firing a 180 grain slug at 1020 ft/sec (muzzle velocity) has the impact energy of 415.8 ft-lb (if, by completely stopping the bullet, the energy is fully absorbed by the body).

$$415.8 \text{ ft-lb} = 0.5 * (180 \text{ g} / 7000 \text{ g/lbm} / 32.174 \text{ lbmslug}) * (1020 \text{ ft/sec})^2$$

However, in this case, it is quite possible that the bullet might retain much of this energy and completely pass through the body. In summary, 58 ft-lb is an energy level worth avoiding!

Fortunately, it is much easier to answer the question of what projectile velocities are required to damage the unprotected human eye. Threshold criteria associated with this question are considered very important for the rotorwash environment. Excellent research (References C-23 and C-24) has been conducted in recent years to define the damage potential of small projectiles that strike the human eye. Detailed data are provided in the cited references that define the probability curves for corneal abrasion, hyphema (bruising), lens dislocation, retinal detachment, and globe (eyeball) rupture. These probability curves are quantified as a function of normalized impact energy (projectile energy as distributed over the projected impact area). For rotorwash applications, the data associated with corneal abrasion and hyphema (bruising) are considered the limiting conditions. Any injury more serious than either of these two conditions will probably result in permanent eye damage. Values associated with these conditions are:

$$50\% \text{ risk of corneal abrasion} = 1,487 \text{ J/m}^2$$

$$50\% \text{ risk of hyphema (bruising)} = 12,756 \text{ J/m}^2$$

It should be noted that 1 Joule (J) = 1 kg-m²/sec² = 0.7376 ft-lb. An example of the projected impact area for a spherical projectile would be simply pi (π) times the radius squared. Additional documentation on this research was still in preparation at the time of the writing of this report. However, Dr. Kennedy has stated that the values for corneal abrasion and hyphema should remain essentially unchanged.

The document previously cited by Schane (Reference C-22) also contains some limited data for eye injury as based on tests conducted with rabbits at least 50 years ago (Figure C-6). These data are also documented in detail in reference C-1. However, considering the age of these data and the lack of detail documented with the results, these data should be

considered of limited value in defining threshold criteria when compared with the excellent data from recent research.

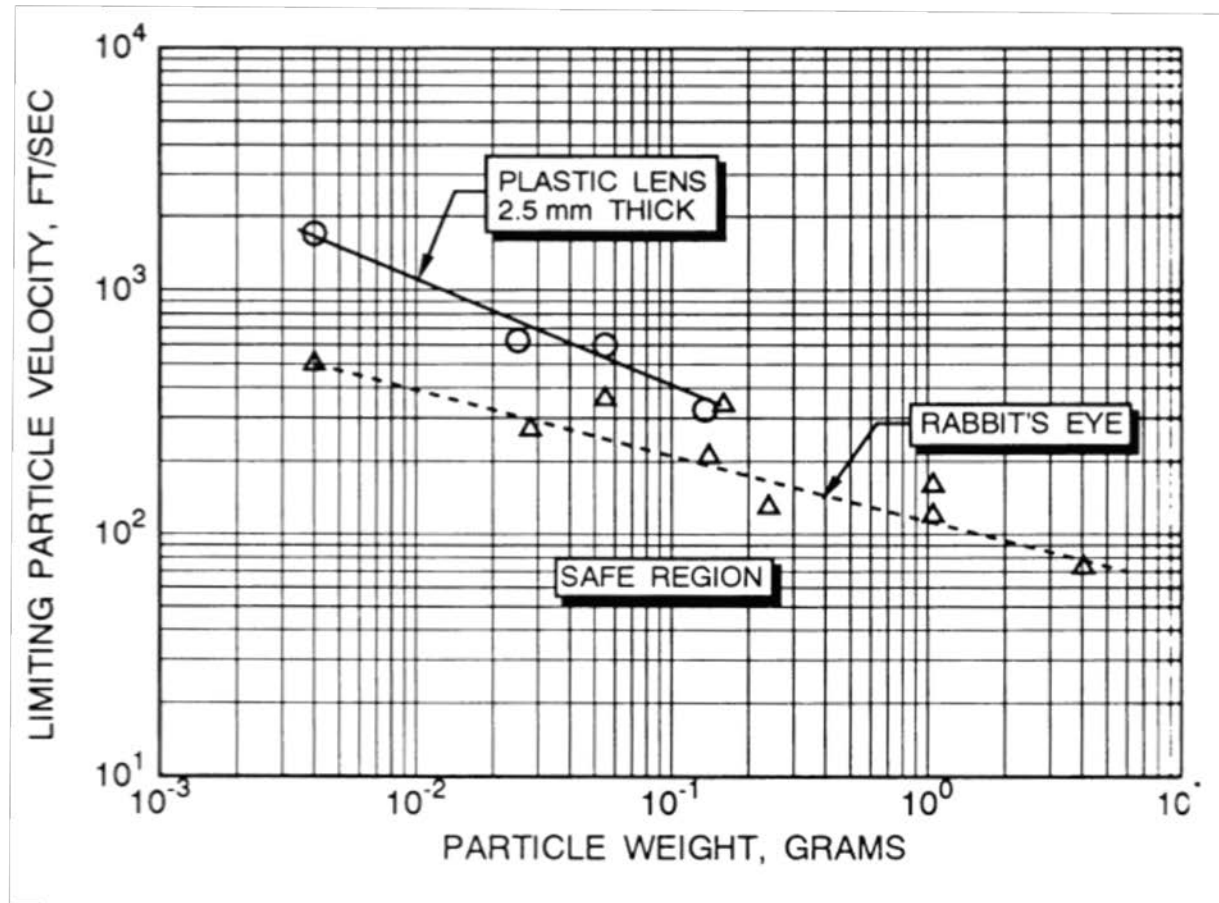


Figure C-6 Maximum Particle Velocity and Weight Limits for Eye Protection
(Reference C-22)

A summary of the research documented in this section is presented in Table C-5 for easy reference. It must be emphasized that all velocities associated with these hazards are still air projectile velocities, and rotorwash wind velocities are not relevant. It must also be emphasized that small projectiles are transported through rotorwash flow fields at only a fraction of the instantaneous air velocity in the flow field. Otherwise, the lift and drag forces would not sustain the projectiles for continued air transport. Much more will be discussed about the aerodynamics of projectile trajectories in the rotorwash generated projectile and debris hazards section.

Table C-5 Personnel Biophysical Injury Not-To-Exceed Threshold Criteria

Hazard	Recommended Threshold Criteria	Reference
Projectile penetration of human skin (dependent on shape and mass)	200 – 300 ft/sec 136 – 205 mph 61.0 – 91.4 m/s	C-19
Projectile penetration of human skin (dependent on shape and mass)	125 – 230 ft/sec 85 – 157 mph 38.1 – 70.1 m/s	C-20
Projectile penetration of human skin	262 ft/sec 179 mph 80 m/s	C-21
Incapacitating impact energy	58 ft-lb	C-22
Eye injury	1,487 J/m ² (50% risk of corneal abrasion) 12,756 J/m ² (50% risk of hyphema)	C-23, C-24

References

- C-1. Ferguson, S. W., "Rotorwash Analysis Handbook, Volume I – Development and Analysis," Federal Aviation Administration, Washington D.C., Technical Report DOT/FAA/RD-93/31,I, June 1994.
- C-2. Smith, R. D., "Heliport/Vertiport Design Deliberations, 1997-2000," DOT/FAA/ND-00/1, May 2001.
- C-3. Harris, D. J., and Simpson, R. D., "CH-53E Helicopter Downwash Evaluation. Final Report," Naval Air Test Center Technical Report No. SY-89R-78, August 1, 1978.
- C-4. Lake, R. E., and Clark, W. J., "V-22 Rotor Downwash Survey," NAWCADPAX-98-88-RTTR, July 1998.
- C-5. Harris, D. J., and Simpson, R. D., "Technical Evaluation of the Rotor Downwash Flow Field of the XV-15 Tilt Rotor Research Aircraft," Naval Air Test Center Technical Report No. SY-14R-83, July 1983.
- C-6. Wright, N. L., and Plaga, J. A., "Assessment of Human Performance in a Simulated Rotorcraft Downwash Environment," AFRL-HE-WP-TR-2007-0064, May 2007.
- C-7. O'Connor, R., "Human Limits in Rotor Craft Downwash/Outwash," NAWCAD/4.6.5.5/2008-003, April 18, 2008.
- C-8. "Human Stability in Downwash," Report No: NAWCAD/4.6.5.5/2009-014, Naval Air Warfare Center Aircraft Division, Patuxent River, MD, February 2010.

- C-9. Lake, R. E., "Shipboard V-22 Rotor Downwash Survey," NAWCADPAX-99-87-RTT, September 1999.
- C-10. Murakami, S., and Deguchi, K., "New Criteria for Wind Effects on Pedestrians," Journal of Wind Engineering and Industrial Aerodynamics, Vol. 7, 1981.
- C-11. Murakami; Uehara, S., K.; and Deguchi, K., "Wind Tunnel Modeling Applied to Pedestrian Comfort," 5th International Conference on wind Engineering, Ft. Collins, CO, Paper No. III-6, 1979.
- C-12. Hunt, J. C. R.; Poulton, E. C.; and Mumford , J. C., "The Effects of Wind on People: New Criteria Based on Wind Tunnel Experiments," Building and Environment, Vol. 11, 1976.
- C-13. Ratcliff, M.A., and Peterka, J. A., "Comparison of Pedestrian Wind Acceptability Criteria," Journal of Wind Engineering and Industrial Aerodynamics, Vol. 36, 1990.
- C-14. Jordan, S. C.; Johnson T.; Sterling M.; and Baker, C. J., "Evaluating and Modeling the Response of an Individual to a Sudden Change in Wind Speed," Building and Environment, Vol. 43, 2008.
- C-15. Jordan, S. C., "An Investigation of the Slipstreams and Wakes of Trains and the Associated Effects on Trackside People and Objects," PH. D. Dissertation in Civil Engineering, University of Birmingham, January 2008.
- C-16. Anon, "Design Guide for Wind," Wellington City District Plan (New Zealand), July 2000.
- C-17. Simiu, E., and Scanlan, R.H., Wind Effects on Structures - An Introduction to Wind Engineering, John Wiley & Sons, New York, 1978.
- C-18. Silva, M. J., "CH-47D Tandem Rotor Outwash Survey," NAWCADPAX/EDR-2010/120, August 2010.
- C-19. Hueske, E. (MD), "Practical Analysis and Reconstruction of Shooting Incidents," CRC Press, November 2005.
- C-20. Evans, M. B. (MD), "Gunshot Wound Ballistics," Baylor College of Medicine, February 2004.
- C-21. Bellamy, R. F. (MD), and Zajtchuk, R. (MD), "Textbook of Military Medicine," Section on Conventional Warfare Ballistic, Blast, and Burn Injuries, Chapter 4 - The Physics and Biophysics of Wound Ballistics," Borden Institute (Office of the Surgeon General, Department of the Army), pp 111. 1990.
- C-22. Schane, W. P., "Effects of Downwash Upon Man," U.S. Army Aeromedical Research Unit Report No. 68-3, November 1967.

C-23. Kennedy, E.; Manoogian, S.; and Duma, S., "Development of Parametric Eye Injury Criteria," USAARL Contract Report No. CR-2008-05, July 2008.

C-24. Duma, S. M.; Ng, T. P.; Kennedy, E. A.; Stitzel, J. D.; Herring, I. P.; and Kuhn, F., "Determination of Significant Parameters for Eye Injury Risk from Projectiles," The Journal of Trauma Injury, Infection, and Critical Care, October 2005.

Appendix D: Ground Structure Related Hazards

Sam Ferguson

The wind velocities generated by a rotorwash flow field can damage or collapse structures. Three major categories of structures (permanent structures, military shelters and tents, light structures and civilian tents) define the major categories in this appendix. Each has different limitations due to winds present in the rotorwash. For conservatism, this wind velocity is assumed at sea level standard conditions. In rotorwash applications, the resultant dynamic pressure at sea level standard conditions should be used to derive the equivalent limit wind velocity for application at other atmospheric conditions.

Conclusions of this appendix are summarized in Table D-1. This table represents the limiting conditions associated with structures in the vicinity of the aircraft. Limits associated with these conditions are displayed in a range of units and represented in terms of wind velocity and dynamic pressure. Underlined data are the limiting condition derived from research presented later within this appendix.

	Dynamic Pressure	Peak Wind Velocity			
	lb/ft ²	ft/s	kts	mph	m/s
Permanent Structures					
Asphalt Shingles	9.21	88.0	52.1	<u>60.0</u>	26.8
Military Shelters					
Peak Limit	10.81	95.3	56.5	<u>65.0</u>	29.1
Light Structures / Civilian Tents	3.13	51.3	30.4	<u>35.0</u>	15.6
		Dynamic Pressure	Mean Wind Velocity		
		lb/ft ²	ft/s	kts	mph
Permanent Structures					
Wind Loading	<u>10.0</u>	91.7	54.3	62.5	27.9
Military Shelters					
Mean Limit	7.74	80.7	47.8	<u>55.0</u>	24.6

Table D-1 Rotorwash Structure Limits

Utilization of dynamic pressure in lieu of wind velocity removes variations due to changes in the air density. For conservatism, wind velocity limits are converted to dynamic pressure limits using Sea Level Standard (SLS) air density. At atmosphere conditions other than SLS, velocity limits can be calculated using the limit dynamic pressure and the evaluation case air density.

Permanent Structures

An extensive review was conducted for this report to better understand how permanent structure building code requirements interact with rotorwash as a potential hazard. Initially, it was believed that building codes would be more than adequate to protect against most wind loadings generated by rotorwash. Generally, this statement has been

found to be correct. In many parts of the United States, the requirements for hurricane and high gusty wind conditions are quite extensive. Of course, these requirements should not be assumed to apply in many developing countries or zones where conflict is in progress. The American Society of Civil Engineers (ASCE) is an excellent resource for constantly updated building code documents. The documents generated by this organization explain the building codes, how to use and apply them, the historical reasons for certain requirements, and even provide example calculations for the practicing engineer. ASTM International (originally the "American Society for Testing and Materials" when formed over 100 years ago) is also an excellent resource for standardization documents. As an example, the design, classification, and testing requirements for asphalt shingles are controlled through regularly updated ASTM International standards. Documents from these two organizations will be referenced frequently in this appendix and in the reference lists for Appendixes [E](#) and [F](#).

Wind Loading on Permanent Structures

Building codes for the United States (and most developed countries) have extensive wind loading requirements for single- and multi-story buildings, signs, and almost all other types of permanent structures. The interaction of these codes and rotorwash as a potential hazard became a task of defining the minimum building code requirements that might apply in the rotorwash environment.

ASCE Standard ASCE/SEI 7-05 (Reference D-1) provides minimum load requirements for the design of buildings and other structures that are subject to building code requirements. Chapter 6 – Wind Loads provides detailed requirements for wind loads using three accepted methods. These three methods are: Method 1 – Simplified Procedure as specified in Section 6.4, Method 2 – Analytical Procedure as specified in Section 6.5, and Method 3 – Wind Tunnel Procedure, as specified in Section 6.6. While many of these procedural requirements are not applicable to issues involving rotorwash, the wind loads specified in Sections 6.1.4.1 and 6.2.4.2 are applicable. These sections specify the absolute minimum allowed loads for any design situation. Section 6.1.4.1 applies to the Main Wind-Force Resisting System (MWFRS). The MWFRS is defined as “the assemblage of structural elements assigned to provide support and stability for the overall structure.” Section 6.1.4.2 applies to components and cladding, defined as “elements of the building envelope that do not qualify as part of the MWFRS.” In both of these sections, the minimum wind load “shall not be less than 10 lb/ft² (0.48 kN/m²) multiplied by the area of the building or structure projected onto a vertical plane normal to the assumed wind direction.” It should be noted that structures, as defined by sections in the standard, could be street signs, light poles, and other odd shaped fixed objects. Therefore, for rotorwash applications, it should be assumed that 10 lb/ft² (0.48 kN/m²) should be considered a key threshold condition that should not be exceeded in avoiding hazardous situations involving buildings and structures.

In a separate telephone discussion with Dr. J. A. Peterka, one of the people involved in helping to develop the series of ASCE wind standards over the years, he notes that this minimum load condition is not based solely on winds, but it is considered as a minimum from several different historical perspectives (i.e. people pressing on a surface and age of

structure). The reason for this discussion resulted from the calculation of the dynamic pressure (not necessarily the load since load is equal to the pressure times an area) that results from using the minimum wind speeds required for use in Methods 1 and 2 (from Figure 6-1 Basic Wind Speed in the standard). The minimum wind speeds are 85 mph in the three west coast states (California, Oregon, and Washington) and 90 mph on the interior of the rest of the United States (coastal regions have special requirements). These wind speeds are defined as 3-second gust wind speeds in miles per hour at 33 feet above ground (in the boundary layer the wind speed would be reduced). The strict calculation of dynamic pressure (q) using air velocity (V) in ft/sec ($q = 0.5 \times \text{air density} \times V^2$) for 90 mph (132 ft/sec) is 20.71 lb/ft². However, the formula used in the standard is based on units of mph as the input. Therefore, the 7-05 formula "dynamic pressure" at 90 mph is 9.63 lb/ft² as multiplied by additional coefficients that exist in the equation that also correct for the "units problem." Values for these coefficients are obtained from tables in the standard. These dynamic pressures, as defined at 33 feet, are considerably higher than the 10 lb/ft² minimum. Therefore, the question arises as to how this standard of 10 lb/ft² (0.48 kN/m²) should be applied for rotorwash related hazards, i.e. to signs or small fixed structures that can be totally engulfed by rotorwash. The air velocity associated with a strict calculation of dynamic pressure for 10 lb/ft² is 62.5 mph (or 91.2 ft/sec or 54.3 kts). More will be discussed about this issue after the next several paragraphs.

The design wind requirements for asphalt shingles are detailed in Standards ASTM D3161 and ASTM D7158 (References D-2 and D-3). Wind speed requirements are as follows:

**ASTM D3161-09 - Standard Test Method for Wind-Resistance
of Asphalt Shingles (Fan-Induced Method)**

- Class A: 60 mph (97 km/h)
- Class D: 90 mph (145 km/h)
- Class F: 110 mph (177 km/h)

**ASTM D7158-08d - Standard Test Method for Wind-Resistance
of Asphalt Shingles (Uplift Force/Uplift Resistance Method)**

- Class D: 90 mph (145 km/h)
- Class G: 120 mph (193 km/h)
- Class H: 150 mph (242 km/h)

ASTM D3161-09 is based upon a controlled test at a design wind speed for up to 2 hours or to failure. ASTM D7158-08d is based upon a wind resistance calculation procedure using a 3-sec gust speed and validated with extensive wind tunnel and full-scale testing. These ASTM standards take into account strict quality controls for setup of the test. However, from a rotorwash hazard perspective, these tests do not take into account the effects of roof weathering, age, or incorrect installation. For this study, tile-roofing standards were not investigated and more will be discussed in a later section about commercial ballast (gravel) roofing.

As can be easily observed in the ASTM Standard requirements, only one class of asphalt shingles is rated below 90 mph during standards testing. Therefore, one could say that the standard is generally more stringent than the 62.5 mph associated with a strict dynamic pressure calculation of 10 lb/ft². However, the effects of roof weathering, age, or incorrect installation would lower the effective speed below 90 mph in an actual rotorwash scenario. Unfortunately, no data exist to estimate a practical value for the reduction in wind speed that might be expected.

As another perspective, older guidelines for defining threshold rotorwash generated pressure loads on structures are provided in Reference D-4. The data discussed in this document were obtained from several sources, including a FAA funded study (Reference D- 5). However, problems were identified with some of the data that were utilized in the study. The final conclusion was that only a few large rotorcraft could generate the 15 to 20 lb/ft² minimum that was above the requirements in the building codes at that time. Also, an extensive operator survey discussed in the FAA study supported the conclusion that rotorcraft had minimal impact on permanent structures other than blowing about roof gravel. It should also be noted that wind tunnel data, discussed in Reference D-4 for the Dallas Vertiport prior to its construction and discussions with Dr. J. A. Peterka at that time, provided additional perspective. Dr. Peterka noted that 2-dimensional predictions of peak pressure loads tend to over predict 3-dimensional measurements, as based on CPP wind tunnel testing, by approximately 15 percent. Other analytical 2D to 3D prediction methods usually indicate similar type results.

Wind Loading on Military Shelters and Tents

Military shelters and tents are frequently cited in the literature and mishap databases as being involved in rotorwash mishaps. In this project, the group responsible for portable shelter development at the U.S. Army Research, Development and Engineering Command (RDECOM) was contacted for support. Also, literature on the family of shelters presently in the military inventory was reviewed. A summary of these data is tabulated in Table D-2.

The performance specification for the Modular General Purpose Tent System (MGPTS) that was released on June 29, 2001 (Paragraph 3.3.5, Page 5) is considered the accepted requirement for wind loading at present (Reference D-6). For this family of shelters, the design wind loading is 55 mph for 30 minutes with gusts to 65 mph for 10 sec. Most other shelter designs, as listed in the table, generally meet or exceed this standard.

Wind Loading on Light Structures and Civilian Tents

An estimated tent/light structure not-to-exceed threshold value was also proposed in Reference 3.1-1 following the analysis of several mishap reports. These mishaps mostly involved civilian incidents in scenarios where little detailed information was available, and the tents were not prepared for high wind conditions involving rotorwash. The estimated peak wind threshold value from this analysis was 30+ kts (approximately 35 mph). It is interesting to note that the design wind limit is 40 to 50 mph for the 2 -4 man family of small tents in Table D-2. This controlled specification value is only slightly greater than the

proposed threshold value of 30+ kts that involves reported mishaps in an uncontrolled field environment.

Table D-2 Military Shelter and Tent Not-To-Exceed Threshold Criteria

Hazard	Recommended Threshold Criteria	Reference
Modular General Purpose Tent System (MGPTS)	55 mph (30 min), 65 mph (10 sec)	Performance Specification - Modular General Purpose Tent System (MGPTS), June 29, 2001 (Paragraph 3.3.5, Page 5)
Medium Airbeam Shelter (MASTER) lwh (ft) = 52x40x16	64 mph	RDECOM Brochure, REV 04-01-06 OPSEC 06-135
Family of Small Tents: 2-man 3-man 4-man	40 mph 50 mph 50 mph	RDECOM Brochure, REV 05-04-05 OPSEC 02-017
Small Tactical Airbeam Tent (STAT-Model 24) lwh (ft) = 24x22x11 (STAT-Model 32) lwh (ft) = 32x22x11	65 mph	RDECOM Brochure, REV 04-01-06 OPSEC 06-135
Army: General Purpose Shelters Small Shelters Air Force: Expeditionary Medical Support Medium Shelter System (MSS)	55 mph (steady), 65 mph (gust) 50 mph (steady), 65 mph (gust) 100 mph 100 mph	US Army NSRDEC, Commanders' Smartbook Equipment Catalog, February 2007 OPSEC 05-60 (pages 14-15, 33-34)
Tent, Frame-Type, Expandable Tent, Extendable, Modular, Personnel Air Force Small Shelter (Alaska) Alaska AMEDD Medical Shelter Family of Airbeam Temper Tents Air Force Medium Shelter System (MSS) Air Force Rapid Deployment Bare Base Shelter Advanced Solar Cover (ASC) Types 1,2	55 mph 55 mph 100 mph 100 mph 55 mph 100 mph 70 mph (steady), 100 mph (gust) 45 mph	US Army NSRDEC, Guide for Tactical Training Bases, Shelters Handbook, 26 October 2007, Distribution A (2008), REV 10-20-08 OPSEC 08-215

Summary of Ground Structure Related Hazards

It is probably fair to assume that structurally most permanent ground structures will not be susceptible to rotorwash damage. This assumption is based upon the requirements detailed in the building codes of most developed countries. It is also generally supported by rotorwash related incident reports. Rotorwash related damage is much more likely to be associated with the component parts of structures like low height architectural walls, asphalt shingles, window glass, sheet metal, and composite exterior materials. Detailed research on these component materials will be documented in [Appendix E](#) (along with

their likelihood of becoming dangerous flying debris in [Appendix F](#)). Light temporary structures like military shelters and tents are much more susceptible to rotorwash. Table D-3 presents proposed rotorwash not-to-exceed threshold values for ground structures as based on the data presented in this report. It is acknowledged that the application of the 10 lb/ft² (0.48 kN/m²) load standard on the projected surface areas of permanent structures presents some issues as based on the supporting documentation. However, if the 10 lb/ft² value is based upon the value of 62.5 mph (91.2 ft/sec or 54.3 kts), then the threshold value should be conservative. This standard will better account for situations involving age to structures, components like low height architectural walls, and structures in locations where building codes are not rigidly followed. In many instances, this standard will probably still not be the identified limiting rotorwash related threshold anyway. Asphalt shingles and components like glass will in most cases be more limiting.

Table D-3 Ground Structure Not-To-Exceed Threshold Criteria

Hazard	Recommended Threshold Criteria	Reference
Minimum structural loading on a permanent structure	10 lb/ft ² (applied to projected area) 0.48 kN/m ²	D-1
Asphalt shingles	60 – 90 mph	D-2, D-3
Military shelter	55 mph (30 min), 65 mph (10 sec)	D-6
Light structures/tents	30+ kts (peak wind velocity)	D-4

References

- D-1. "Minimum Design Loads for Buildings and Other Structures," American Society of Civil Engineers (ASCE) Press, ASCE Standard ASCE/SEI 7-05, Copyright 2006.
- D-2. "Standard Test Method for Wind-Resistance of Asphalt Shingles (Fan-Induced Method)," ASTM Standard D3161-09, January 2009.
- D-3. "Standard Test Method for Wind-Resistance of Asphalt Shingles (Uplift Force/Uplift Resistance Method)," ASTM Standard D7158-08d, September 2008.
- D-4. Ferguson, S. W., "Rotorwash Analysis Handbook, Volume I – Development and Analysis," Federal Aviation Administration, Washington D.C., Technical Report DOT/FAA/RD-93/31,I, June 1994.
- D-5. Schwartz, C. W.; Witczak, M. W.; and Leahy, R. B., "Structural Design Guidelines for Heliports," DOT/FAA/PM-84/23, October 1984.
- D-6. Anon, "Performance Specification - Modular General Purpose Tent System (MGPTS)," U.S. Army Research, Development and Engineering Command (RDECOM), June 29, 2001.

Appendix E: Hazards Involving Impact Damage and Materials

Sam Ferguson

Rotorwash related hazards involving debris and material impact usually involve complex scenarios. For example, a rock ejected by the rotorwash flow field could shatter plate glass or break a vehicle windshield. The broken glass, itself property damage, might also then become an airborne hazard to personnel. This subject could easily justify a report or a book by itself. Therefore, it is desirable to understand some of the properties of materials to determine whether they just become property loss issues like cracked glass or plastic, scratched paint, or more dangerous problems like airborne missiles.

In this report, the subject is discussed in several different ways. This appendix will attempt to associate several generally accepted damage concepts with some not-to-exceed values that are associated with glass, metals, and composites, irrespective of how the debris impacts the material. The much more serious issue of how flying debris are transported through the air to become missiles that can seriously injure personnel and severely damage property will be discussed in [Appendix F](#). In general, the impact resistance (or lack of it) of modern materials will be discussed only to define threshold velocities for which damage "could occur." Any effort to document the details of even the major combinations of material type, thickness, number of laminations, hardening process, type of installation, and numerous additional factors is beyond the scope of this appendix. Awareness of the potential for damage by a large rotorcraft is the primary focus and intent.

Glass

Glass is truly a product of marvel. It has incredible properties for many applications and comes in many forms. In the context of this study though, glass can be a serious hazard to personnel as well as a property and liability problem depending on its application and how it becomes damaged. However, before the issue of glass breakage and its relationship to rotorwash hazard analysis can be discussed, several basics about the different types of glass need to be reviewed.

Types of Glass

Glass is used in an incredible number of applications and comes in many different sizes, shapes, and chemical compositions. In this report, the discussion will focus on four main types of glass. These four types are: 1) annealed (or "ordinary" glass), 2) heat-strengthened, 3) tempered, and 4) laminated glass. Flat glass is produced by flowing and slowly cooling a molten silica-based mix under very carefully controlled conditions. This "annealing" procedure removes undesirable stresses from the glass so that it can be used to make useful products. Most glass products are made from annealed glass, which is often referred to as "ordinary" glass. If annealed glass is heated to a temperature near its softening point and forced to cool rapidly under additional carefully controlled conditions, then this glass becomes heat-treated glass. This type of glass has its outer surfaces in compression and its center in tension. The heat treat process can be customized to produce other more desirable forms of glass with induced stresses that result in additional

strength, resistance to thermal stress, and improved impact resistance. In general, the other physical properties of the glass remain unchanged.

Heat-treated glasses are usually classified as either heat strengthened or fully tempered. Federal specification DD-G-1403B defines heat strengthened glass as having a surface compression of between 3,500 and 10,000 psi or an edge compression of between 5,500 and 9,700 psi. Fully tempered glass, the next step up in quality, must have a surface compression of at least 10,000 psi or an edge compression of at least 9,700 psi. As a very general rule, fully tempered glass can be expected to be approximately four times stronger than annealed or ordinary glass. It can also be expected to stop small projectiles at up to twice the velocity of annealed or ordinary glass. Thermal resistance can be expected to be up to 200 – 300 deg-F greater in range than what would cause annealed glass to crack. Therefore, in applications involving safety issues, fully tempered glass would be the first choice.

However, for many safety related applications, fully tempered glass is simply “not good enough.” The next step up in safety is laminated glass. Laminated glass is typically used in high-rise and commercial buildings, aircraft windshields, and especially in automobile windshield applications. The design approach is to take two or more layers of tempered glass and bind them together with a polymer interlayer, typically polyvinyl butyric, or PVB (depending on the application). The number of layers and the thicknesses are a function of design requirements and application.

Glass Breakage

Glass breaks, in most cases, because some type of impact occurs and the energy in the impacting projectile exceeds the strength characteristics of the glass. As all of us have experienced, annealed glass tends to break into dangerous irregular shaped shards of all sizes. Conversely, fully tempered glass (sometimes called safety glass) breaks into many extremely small non-lacerative particles. Unfortunately, as we shall soon discuss, the projectile or debris mass/energy/velocity combinations that produce the Mean Minimum Breakage Velocity (MMBV) required to crack or break the various types of glass are easily attained in windstorms or rotorwash flow fields.

On August 18, 1983, Hurricane Alicia struck downtown Houston, Texas. Researchers were allowed into downtown Houston the following day to help survey the damage and eventually develop a “lessons learned” report (Reference E-1). Several key lessons were learned that are applicable to rotorwash analysis: 1) high winds produce impact damage from many types of windborne projectiles and missiles, i.e. roof gravel size stones, sheet material, lumber, debris, and failed parts of secondary structures located on exteriors and roofs of structures (lights, signs, antennas); 2) secondary aerodynamic flows like shed roof corner vortices can significantly aid in helping to inject projectiles into the flow field; and 3) roof gravel size stones (1/4 to 1/2 inch) can easily be lifted into the wind stream at lower than expected velocities (< 50 mph) and break all common types and thicknesses of glass, i.e. ¾-inch thick tempered glass can be broken at a MMBV of 54.6 fps (37.2 mph) by average size roof gravel.

As a general rule, it can be expected that roof gravel size stones will be accelerated by high gusty winds to projectile velocities of one-half or more of the wind value. Minor (Reference E-2) showed that gravel with masses of 0.61 and 5.55 grams could be sustained as windborne projectiles at wind velocities as low as 52 mph (84 km/h) and 74 mph (119 km/h), respectively. The details of projectile dynamics that are associated with the various different types of projectiles will be presented in later sections. References E-2 through E-7 and the references in [Appendix F](#) all document additional detailed information on wind-produced damage as based on more than 30 years of continuous research.

Single Pane Glass Breakage

Several researchers, using various sizes of projectiles, have studied the MMBV that is required to break single panes of annealed, heat strengthened, and tempered glass. A brief summary of these projectile sizes (for both steel and stone) is provided for reference in Table E-1. Minor, Beason, and Harris provide the best single summary of collected results in Table 3 of Reference E-6. These three researchers published much of the publicly available data for these types of single pane glass. However, References E-1 through E-5 and E-7 have to be reviewed to compile a more complete list. For use with rotorwash investigations, these data have been consolidated in Figures E-1 and E-2 (some of the data that do not provide trend information have not been graphed). All of these data are for impact by spherical steel projectiles and for glass that is not under an applied pressure load (i.e. a constant wind impacting the glass).

Table E-1 Projectile Size Characteristics

Weight, grams (g)	Diameter, mm	Diameter, inches
Steel (0.00785 g/mm ³):		
0.61	5.29	0.208
0.7	5.54	0.218
2	7.87	0.310
5	10.67	0.420
5.55	11.05	0.435
8.4	12.69	0.500
28.2	19.00	0.748
Stone (0.0026 g/mm ³):		
0.61	7.65	0.301
0.7	8.01	0.315
2	11.37	0.448
5	15.43	0.607
5.55	15.97	0.629
8.4	18.34	0.722
28.2	27.46	1.081

1 gram = 0.0022 lb

The effect of glass thickness on the MMBV is summarized in Figure E-1 for impact by a 5.5-gram (0.0122 lb) projectile. This steel ball size is accepted in the literature as an acceptable substitute for roof gravel (which is considered much harder to use for repeatability in an experimental setting). It is interesting to observe that for thin single pane glass, the temper process significantly improves impact resistance to a 5.5-gram projectile. However, as glass approaches a thickness of 0.75 inches, the impact resistance becomes approximately equal with that of annealed glass. At this thickness, tempered glass may even have slightly reduced impact resistance. No detailed discussion was available from the available references as to why the MMBV values converge. However, glass is mentioned in several of the references as having non-linear characteristics that affect how cracks initiate and how energy is absorbed. Clearly, by design, the temper process significantly affects the outer layer stress characteristics when compared with annealed glass. Heat strengthened glass, for the limited data available, appears to have impact resistance approximately equal to annealed glass.

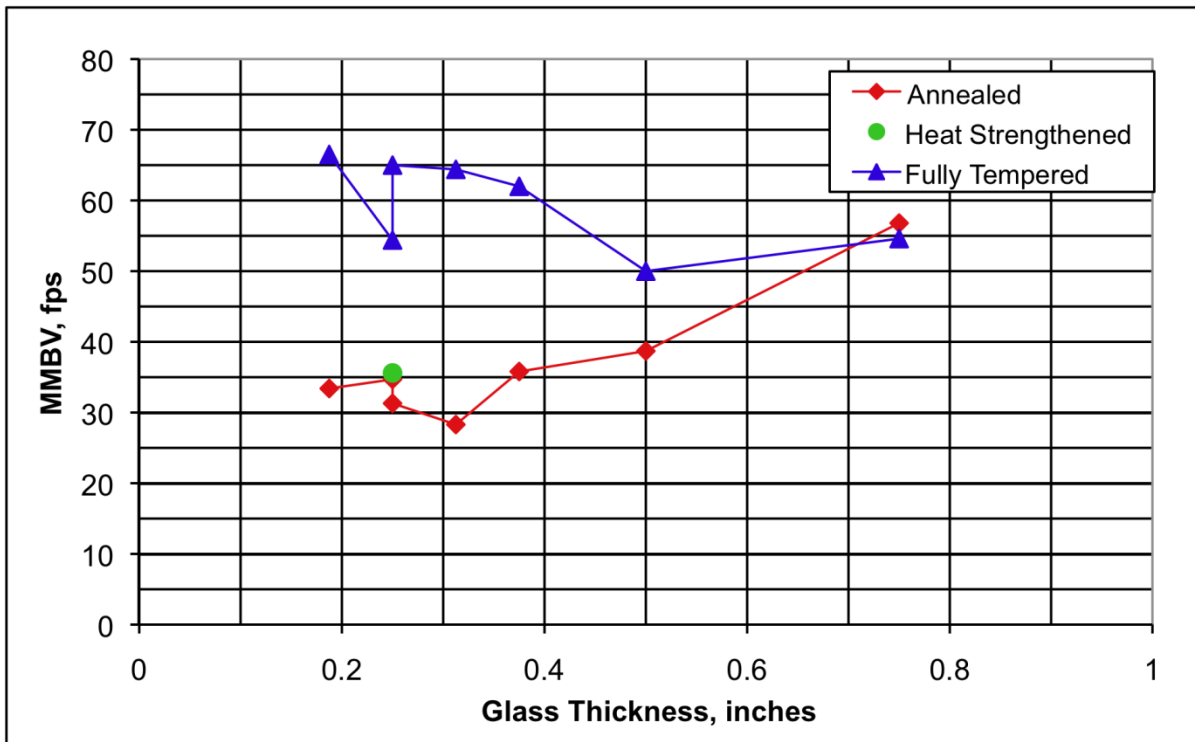


Figure E-1 The Effect of Glass Thickness on Projectile (5.5 g) Impact Resistance

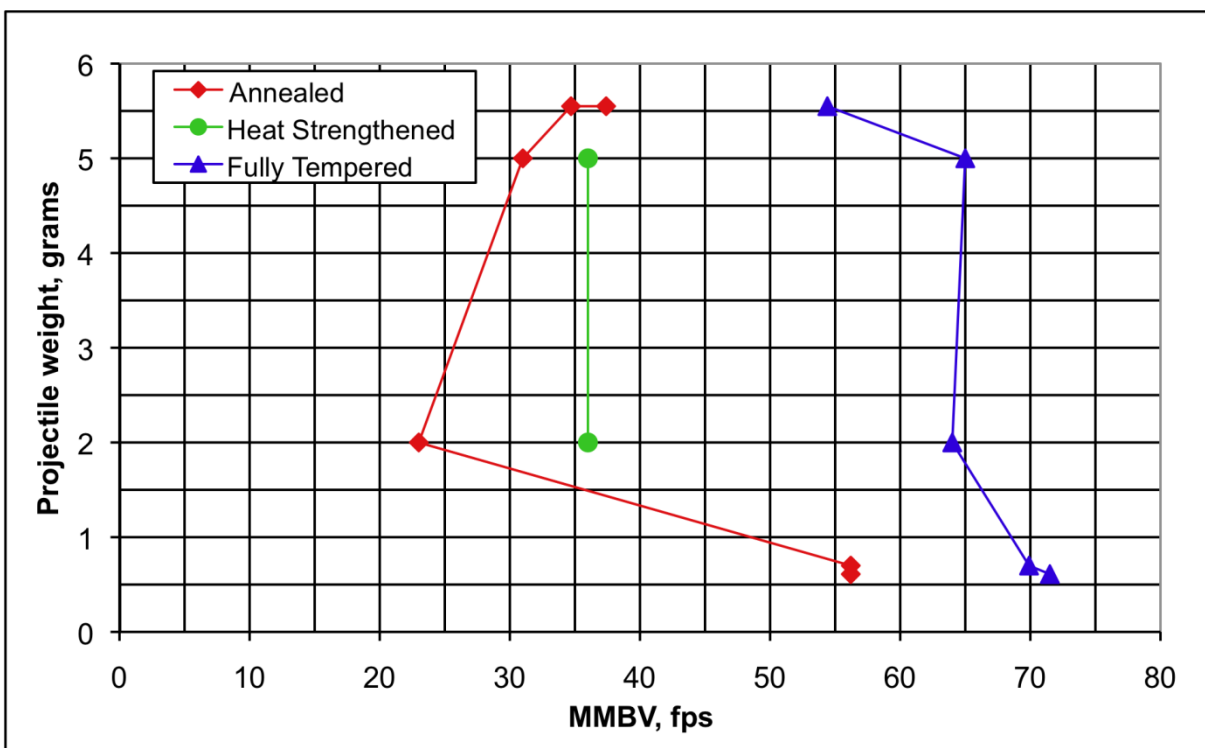


Figure E-2 The Effect of Projectile Size on Impact Resistance (0.25-inch Glass)

The effect of projectile size on the MMBV of 0.25-inch thick glass is summarized in Figure E-2. Projectiles of 0.61, 0.7, 2.0, 5.0, 5.5 grams are mentioned in the literature. Results for the 2.0-gram data, documented in Reference E-3, do not appear to trend appropriately when compared with data for the other two projectile sizes. Attempts to determine the original source of these data were unsuccessful, as the referenced source only discusses results for a 5.5-gram projectile. Therefore, the 2.0-gram data are considered suspect, possibly a typographical error(s) exist. If the 2.0-gram data are discarded, the results indicate that as projectile size increases, the impact resistance decreases by 15 to 20 fps from 0.7 to 5.5 grams. It should be noted that the energy levels for the MMBV are not the same for the 0.7- and 5.5-gram impacts. The slower impacts have more kinetic impact energy, but the projected impact area is also larger (the diameter of the steel ball increases from 5.4 to 11 mm). Also, depending on the rebound energy of the steel balls, the amount of energy absorbed by the glass due to the experimental design could be significantly different.

Saxe, in Reference E-8, comments on the size effects of the impacting steel ball projectile in his laminated glass experiment as he varied size in increments of 7.9 mm (5/16 in), 12.7 mm (1/2 in), and 19.1 mm (3/4 in). The corresponding increases in kinetic energy he used were 2,134, 2,646, and 3,610 g·m²/s², respectively. His observation was that the increase in size or mass led to more deflection of the glass in its fixture and more absorption of the ball's total energy, thereby posing more of a hazard than just the kinetic energy increase alone. Beason, in Reference E-7, also presents data for glass in a preloaded condition, i.e. with a constant wind pressure applied. These results show that a preload on the surface of the glass can slightly improve impact resistance. Therefore, one must conclude that non-linear effects associated with experimental design can become important factors when reviewing, comparing, or extrapolating test data for MMBV.

Residential glass (annealed) has also been tested for impact resistance to "large missile" 2x4 foot lumber and pieces of roofing shingle material. These results are presented in Reference E-9. The annealed glass tested included various aspect ratios (2x2 and 2x4 ft panels) of 3/32- and 5/32-inch thick glass. The impact speed to determine fragility was accomplished by two methods. One method involved use of a pendulum and the second used an air cannon. The 2x4 ft missile used in the test was a 3-foot long Southern Yellow Pine weighting 4.6 pounds. The shingle "missile" was a 0.46-pound piece of three-tab GAF composition roof shingle.

Results from these tests are presented in Figure E-3 based on momentum ($P = mv$, lb-sec) and kinetic energy ($E = 0.5mv^2$, ft-lb). These same data are tabulated in Table E-2 in units of both momentum and energy. These results indicate a steep slope for the momentum that is required to break 100% of the test specimens of both thicknesses of glass. There was also little difference in fragility between the two thicknesses impacted by the 2x4 missile (during the tests, all the glass specimens shattered except one). With the shingle missiles, the momentum required to break the glass was less, but there was more variability required to break 100% of the test specimens. It was also reported that post-failure analysis indicated that the glass showed more signs of perforation. This indicates a different loading per unit surface area upon impact for the two types of missiles.

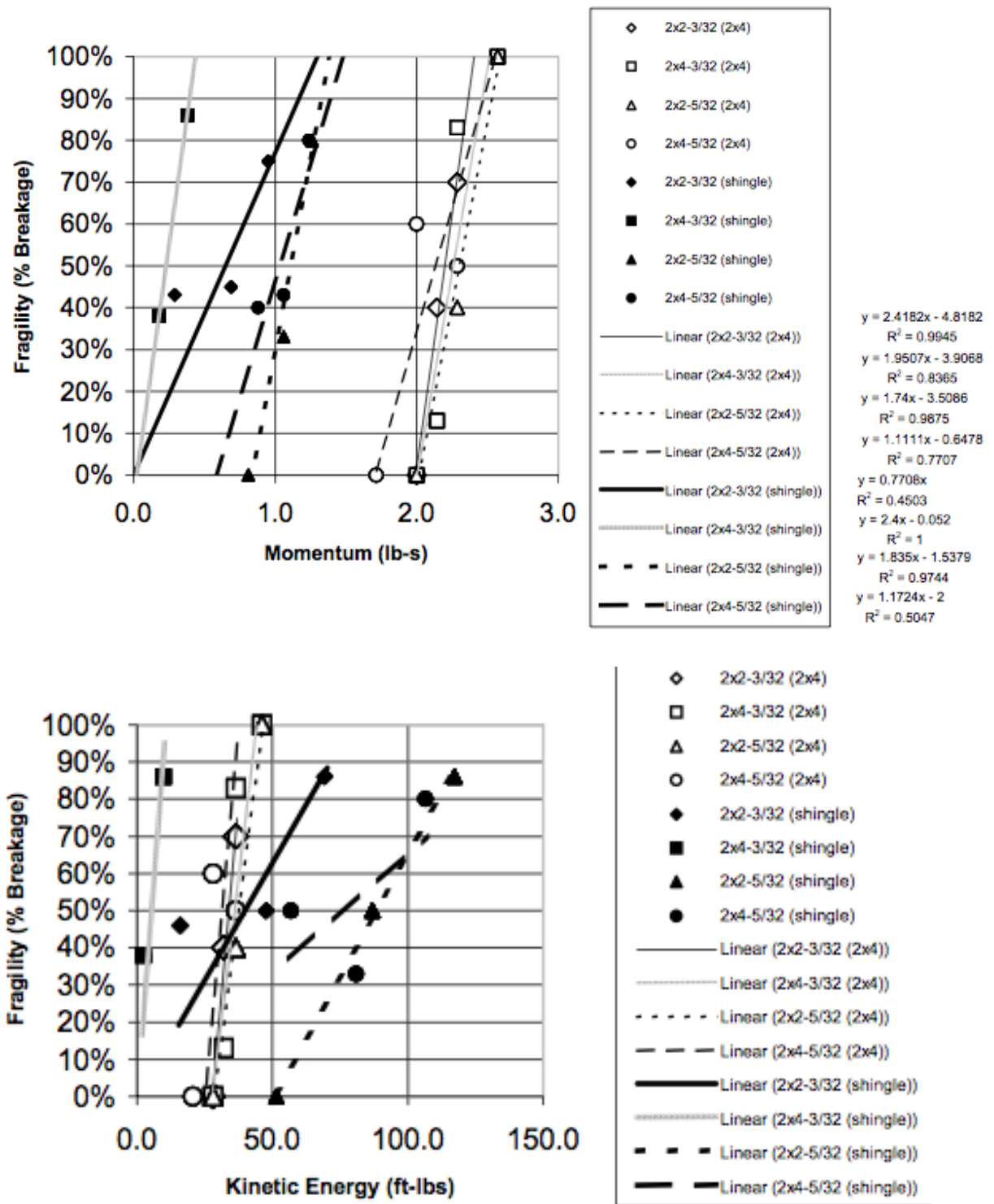


Figure E-3 Fragility of Annealed Glass to Large 2x4 and Shingle Missiles (Reference E-9)

TABLE 4
SUMMARY OF 2X4 MISSILE FRAGILITY DATA

SPECIMEN	SAMPLE SIZE	WEIGHT	SPEED (ft/s)	MOMENTUM (lb-s)	ENERGY (ft-lbs)	PERCENT BREAKAGE (FRAGILITY)*		
						n=1	n<=3	n<=5
2X2-3/32	5	4.6	14	2.0	28.0	0%	0%	0%
	5	4.6	15	2.1	32.1	40%	60%	80%
	10	4.6	16	2.3	36.6	70%	90%	100%
2X4-3/32	5	4.6	14	2.0	28.0	0%	0%	0%
	8	4.6	15	2.1	32.1	13%	38%	38%
	6	4.6	16	2.3	36.1	83%	100%	100%
	5	4.6	18	2.6	46.3	100%	100%	100%
2X2-5/32	6	4.6	14	2.0	28.0	0%	33%	50%
	5	4.6	16	2.3	36.6	40%	60%	80%
	5	4.6	18	2.6	46.3	100%	100%	100%
2X4-5/32	5	4.6	12	1.7	20.6	0%	0%	0%
	5	4.6	14	2.0	28.0	60%	60%	60%
	6	4.6	16	2.3	36.6	50%	100%	100%

*Percent breakage is a cumulative value based on total sample size within each glass size – missile speed category.

Note: 60% value for 2x4-5/32 and n=1 may be classified as 40% since the group contained the only sample that cracked (across bottom) rather than completely shattered (i.e., 'destroyed').

TABLE 5
**SUMMARY OF SHINGLE MISSILE FRAGILITY DATA
BASED ON MOMENTUM (SINGLE IMPACT ONLY)**

SPECIMEN	SAMPLE SIZE	BINS OF MOMENTUM (lb-s)	AVERAGE MOMENTUM (lb-s)	% BREAKAGE (FRAGILITY)
2X2-3/32	7	0.22-0.52	0.29	43%
	11	0.53-0.82	0.69	45%
	12	0.83-1.11	0.95	75%
2X4-3/32*	8	0.14-0.23	0.18	38%
	7	0.33-0.41	0.38	86%
2X2-5/32	4	0.72-0.94	0.81	0%
	6	0.95-1.16	1.06	33%
	10	1.17-1.38	1.26	80%
2X4-5/32	5	0.85-0.99	0.88	40%
	7	1.00-1.14	1.06	43%
	5	1.15-1.28	1.24	80%

*Middle bin not included due to small sample size of one in bin.

Table E-2 Fragility of Annealed Glass to Large 2x4 and Shingle Missiles (Reference E-9)

TABLE 6
SUMMARY OF SHINGLE MISSILE FRAGILITY DATA
BASED ON ENERGY (SINGLE IMPACT ONLY)

SPECIMEN	SAMPLE SIZE	BINS OF ENERGY (ft-lbs)	AVERAGE ENERGY (ft-lbs)	% BREAKAGE (FRAGILITY)
2X2-3/32	13	3.5-31.3	15.8	46%
	10	31.4-59.1	47.8	50%
	7	59.2-86.9	69.4	86%
2X4-3/32*	8	1.2-4.5	2.3	38%
	7	7.7-11.0	9.8	86%
2X2-5/32	5	36.1-69.3	51.4	0%
	8	69.4-102.5	86.9	50%
	7	102.6-135.8	117.3	86%
2X4-5/32	6	52.0-71.9	56.9	50%
	6	72.0-91.9	80.9	33%
	5	92.0-111.9	106.6	80%

*Middle bin not included due to small sample size of one in bin.

Table E-2 Fragility of Annealed Glass to Large 2x4 and Shingle Missiles (Reference E-9)
[Concluded]

It is important to note that Bole (reference E-10) cautions about using kinetic energy (ft-lb) as a comparative measure of what is required to break glass. His experiment investigated impact resistance of several types of glass to constant kinetic energy impact while varying missile (2x4 lumber) mass and velocity. The conclusion is that varying momentum (with a constant energy) results in different impact resistance results. These results do not directly impact rotorwash related hazard analyses as discussed in this report, but the concept must be kept in mind for future extension of results presented in this report. Kennedy noted a similar type of caution in his discussion about normalized impact energy being critical for defining eye injuries ([Appendix C](#)).

Laminated Glass Breakage

Laminated glass units consisting of at least two soda lime glass plies adhered by a polymer interlayer (polyvinyl butyryl or PVB) are commonly used for architectural, aviation, and automotive glazing. PVB is the industry standard polymeric interlayer because of its excellent adhesive and optical qualities. When subjected to severe dynamic blast pressure or missile impacts, even if these laminated glass structures break, the fragments of the broken glass plies still adhere to the interlayer. This feature dramatically reduces the possibility of bodily injury and property damage due to glass fragments. Another important characteristic is that the outer glass ply, when impacted by a projectile like a stone or roof gravel, can be fractured while the inner glass ply remains undamaged. A study of damage caused during Hurricane Alicia, which struck Houston, TX in August 1983, confirmed that the occurrence of widespread window breakage was caused by windborne

debris impact (Reference E-1). This type of hazard should also be expected to be a serious problem when landing a large rotorcraft near vehicles or commercial structures at semi-prepared landing sites.

If a projectile or windborne missile strikes laminated glass with just enough energy to initiate a failure, then the tensile forces in the surface will cause cracks. In the case of a small round projectile, the crack might be circular and its diameter greater than the diameter of the projectile. As the energy of the projectile increases, compressive stresses begin to play a larger part in producing damage to the surface as crushing is initiated at the impact site. The damaged area will increase in size and eventually lead to the formation of a Hertz cone in the outer glass ply. If the impact velocity of a given windborne missile is sufficiently high, fracture will occur in both the outer and inner glass plies of a laminated glass unit. An enlightening discussion of the fracture of glass and its dependency on the loading rate of the impact is presented in Reference E-11 for the interested reader.

In Reference E-12, the probability of impact site damage is investigated to the outer ply of laminated glass that is subjected to low velocity projectile impact. Instead of just measuring the minimum velocity required to damage the outer layer, a series of controlled impact tests were conducted to establish the Probability of Damage (P_d) at various impact velocities. A compressed air cannon was used to propel a 2 g steel ball of 7.94-mm diameter normal to the outer glass ply with a cannon-to-glass distance of 25 mm. This distance insured that the velocity loss between the cannon muzzle and the impact site was negligible.

Results from this experiment are presented in Figures E-4 and E-5. The laminated glass unit in Figure E-4 is composed of two 4.81-mm glass layers sandwiching a PVB inter-layer of 1.52 mm. Results indicate that the 50% and 100% lines of probability for damage of this thicker test specimen are at 6.75 m/s and 13.5 m/s, respectively. The unit in Figure E-5 is composed of two 4.78-mm glass layers sandwiching a PVB inter-layer of 0.76 mm. The same probabilities of damage are 5.5 m/s and 10.0 m/s, respectively. It must be emphasized that these damage probabilities are for the outside layer of glass and do not suggest inner layer damage or failure of the laminated glass unit as a whole. Minimal velocities for the initiation of damage to the inner layer are provided in later references for informational purposes. For this study, it is believed that failure of the outer glass layer is the critical issue from both a functionality and liability perspective. Therefore, the definition of a footprint should have the goal of defining the distance at which projectiles will no longer have enough energy to induce the outer layer glass failure.

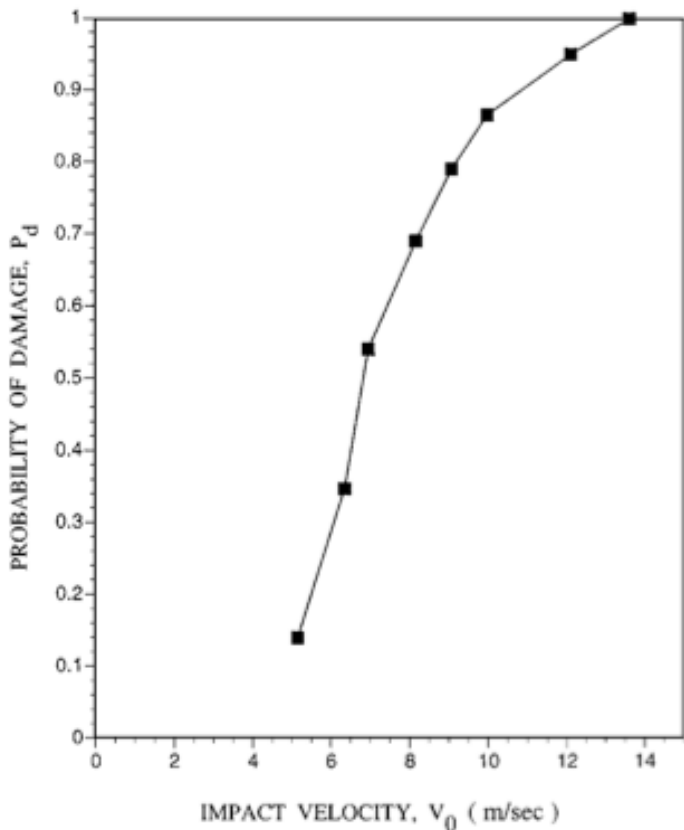


Figure E-4 Damage Probability Velocities for a Laminated Glass Unit ($h_{\text{PVB}} = 1.52 \text{ mm}$)
(Reference E-12)

The effect of varying the thickness of individual glass layers on the outer layer impact resistance of a range of laminated glass constructions (similar to that which might be used in vehicle or aircraft “safety glass” windshields) is examined in Reference E-13 (an excellence reference that even traces the history of research on the topic of glass impact resistance back to 1881). Granite chippings (gravel), similar to those used in traditional road construction, were used as projectiles and accelerated to velocities in excess of 20 m/s at impact. Tests were conducted at both normal and 45-degree angles relative to the surface of the outer glass laminate and the critical velocity for damage initiation is well documented. It must be emphasized that the key damage criterion in this study is “the initialization” of damage to the outer layer of glass. In no case is the outer glass ply penetrated by the projectile, the PVB interlayer damaged, or the inner glass ply damaged. Other references in this section will be presented and discussed that are applicable to this higher level of impact damage.

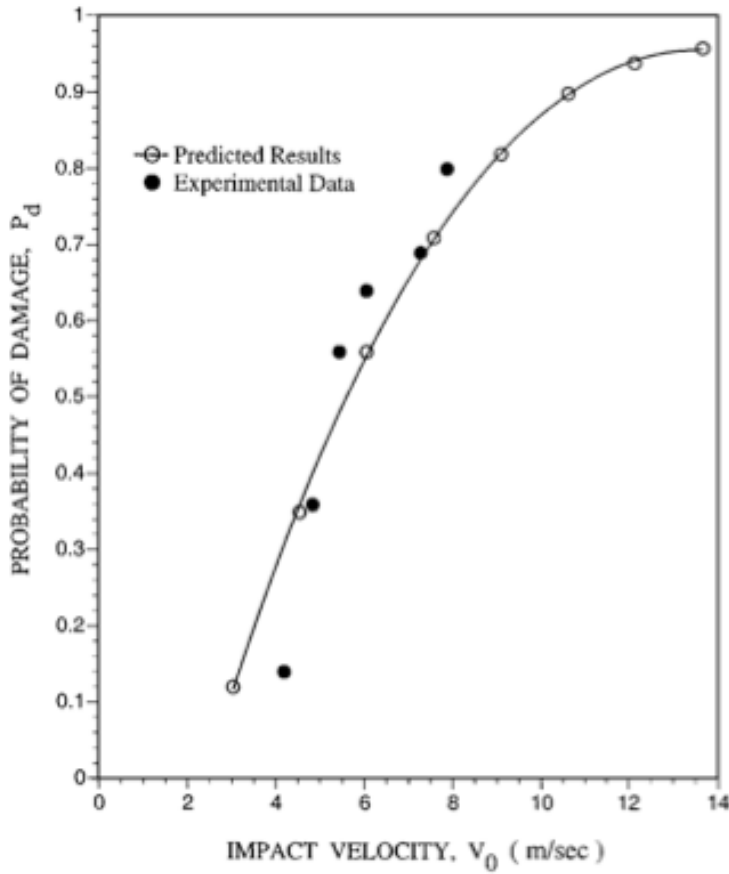


Figure E-5 Damage Probability Velocities for a Laminated Glass Unit ($h_{\text{PVB}} = 0.76 \text{ mm}$)
(Reference E-12)

The results of this low velocity experiment indicate that the thickness of the outer glass ply is the primary parameter in determining the critical velocity for damage initiation, whereas the inner thickness has a secondary influence on the velocity threshold. Table E-3 and Figure E-6 document these results. The thinnest outer/inner laminate construction (0.7 mm/0.7 mm) sustains surface damage as low as 4.0 m/s (8.98 mph). The thickest laminate (2.5 mm/1.1 mm) resists damage up to 10.6 m/s (23.7 mph). The 45-degree off-axis impact testing indicates that it is the normal component of the impact velocity that determines the damage threshold. Figure E-7 documents the “apparent” increase in impact resistance. This “apparent” increase is shown to be negated when the normal component of velocity is calculated and plotted in Figure E-8. A detailed optical inspection of the failed laminates highlighted the changes in the fracture mode from flexure-induced star cracking to top surface cone cracking as the overall laminate thickness was increased, as indicated in Figure E-9.

Application of these results for a rotorwash damage study becomes a little more complicated because laminated glass is used in many different thicknesses and shapes for many different applications. Also, damage at the critical velocities as indicated by this research are generally cosmetic in nature. The damage impairs a clear view through the

glass and incurs a liability for a damaged windshield or window. These critical velocities do not incur a liability for property on the protected side of the laminated glass structure since penetration by the projectile is not an issue and laminated glass is designed to not shatter into dangerous smaller pieces of glass.

Table E-3 Summary of the Critical Velocities for Laminates Examined (Reference E-13)

Laminate Construction	V_{CRIT} (m/s)
0.7 / 0.7	4.0
1.1 / 1.1	5.0
1.1 / 1.6	5.0
1.1 / 2.1	5.0
1.1 / 2.5	5.0
1.6 / 1.1	7.3
1.6 / 1.6	7.3
1.6 / 2.1	7.8
2.1 / 1.1	7.3
2.1 / 1.6	8.4
2.1 / 2.1	9.5
2.5 / 1.1	10.6

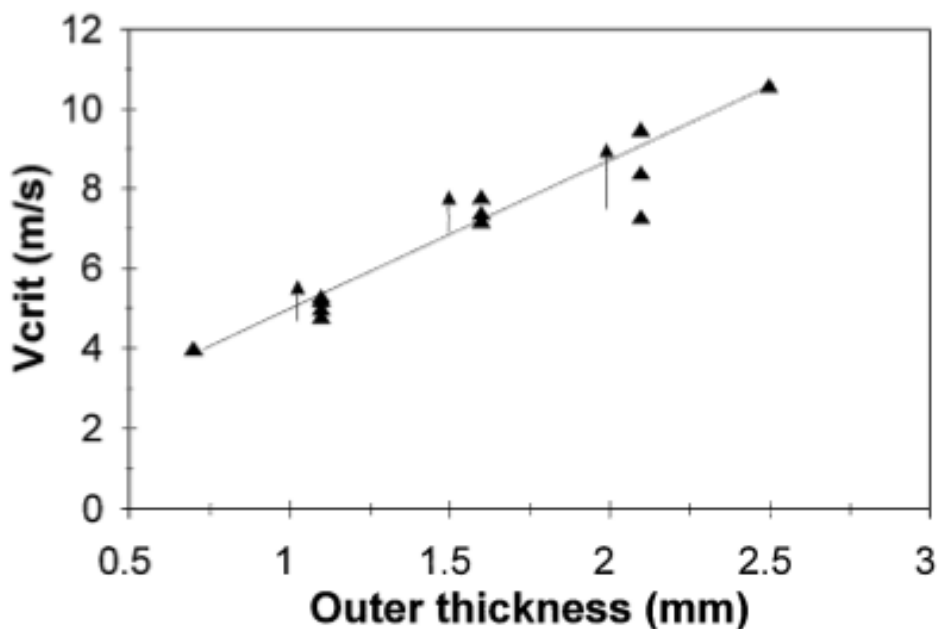


Figure E-6 Variation of Critical Velocity with Outer Thickness for 12 Laminates
(Reference E-13)

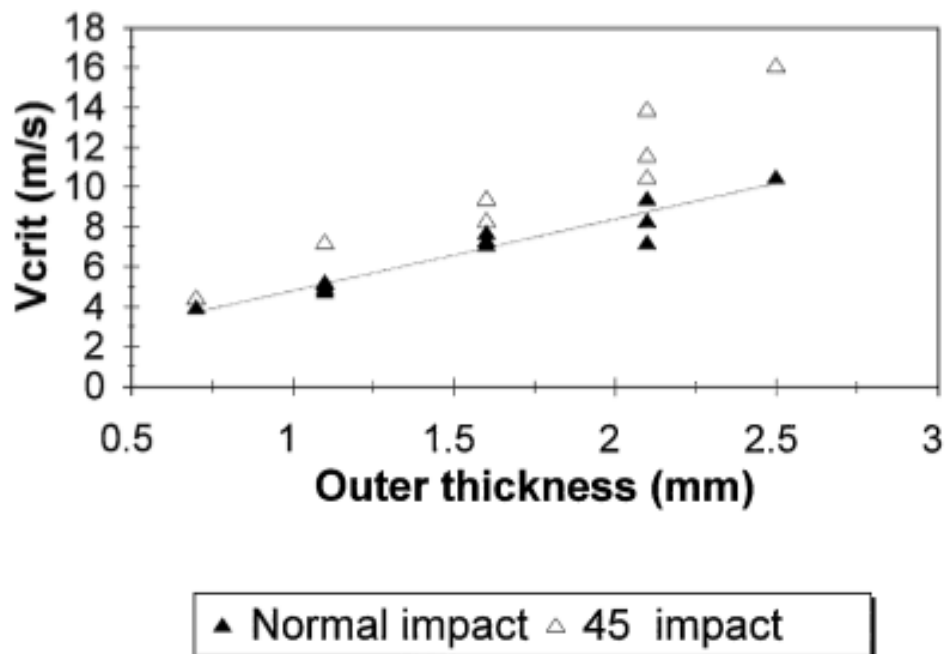


Figure E-7 Effect of Thickness and Impact Angle on Critical Velocity (Reference E-13)

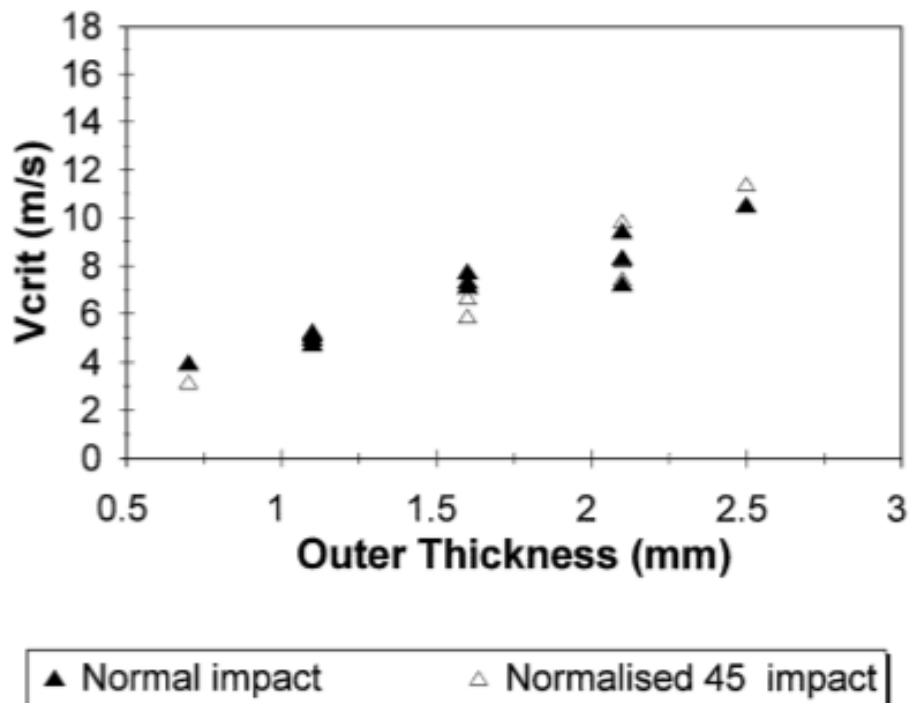


Figure E-8 Effect of Thickness and Normalized Impact Angle on Critical Velocity (Reference E-13)

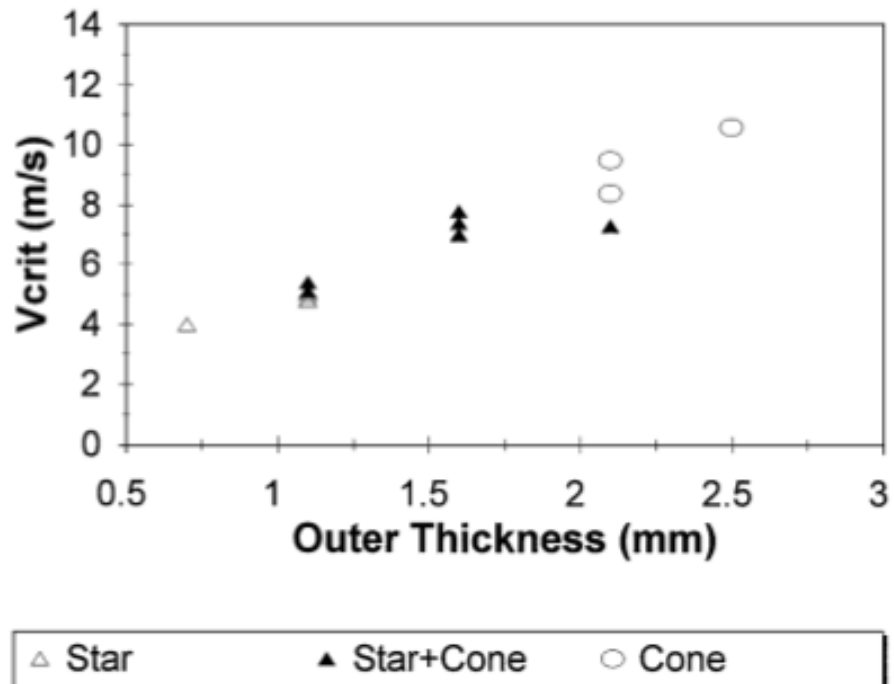


Figure E-9 Summary of Failure Modes Observed in 12 Laminates (Reference E-13)

Table E-4 Heat Strengthened (HS) Laminated Glass Impact Results (Reference E-14)

Specimen #	MMDT Velocity ft/sec (m/s)	MMBT Velocity ft/sec (m/s)
1-1	37.5 (11.43)	
1-2	29.0 (8.84)	
1-3	28.4 (8.66)	
3-1	28.9 (8.81)	45.8 (13.96)
3-2	22.1 (6.74)	53.3 (16.25)
3-3	22.5 (6.86)	
5-1	19.3 (5.88)	
5-2	19.8 (6.04)	
7-1	32.5 (9.91)	52.4 (15.97)
7-2	21.7 (6.61)	
7-3	26.1 (7.96)	54.2 (16.52)

MMDT – Mean Minimum Damage Threshold velocity

MMBT – Mean Minimum Breakage Threshold velocity

Heat strengthened (HS) laminated architectural glass specimens are tested in Reference E-14 for outer ply impact resistance to a steel ball the size of 2.03 gm. The interlayer thickness/type is varied in specimens 1 through 9. Two glass plies of 5 mm (3/16 inch) each are used. Breakage criteria are defined as: 1) DT—the minimum missile impact velocity that produces a surface fracture that can be visually detected at arm's length in good light and 2) BT—the minimum missile impact velocity that causes a glass ply to fracture through its entire thickness. The average DT value for the glass specimens with a PVB interlayer is 26.2 fps (8.0 m/s) and the mean BT value is 51.4 fps (15.7 m/s), a factor of approximately 2. Detailed results from the test are presented in Table E-4. These data are certainly applicable for rotorwash related applications when heat-strengthened glass is of interest.

Data on the potential for damage to the inner layers of laminated architectural glass are presented in References E-8, E-15, and E-16. Annealed (AN), heat-strengthened, and fully tempered glass specimens are all tested. The applicability of these data to rotorwash related scenarios is certainly limited because damage to the inner layer means that the outer layer has been "sacrificed" to stop a projectile. Rotorwash not-to-exceed criteria need to be formulated to protect the outer layer. Collectively, the three references evaluate the impact resistance of the inner layers for steel balls weighing 2.0, 8.4, and 28.2 grams. Results are provided in a cumulative breakage probability format as a function of the impact velocity on the outer layer. An example of this format is presented in Figure E-4. Overall, this documentation is excellent and thorough.

Glass Summarized

The experimental data summarized in the previous sections provides guidance as to what range of projectile velocities are excessive for the various types of glass. It is not possible to specify a single Mean Minimum Breakage Velocity (MMBV) for all types of glass in all circumstances. The MMBV depends on the type of glass, thickness and projectile characteristics. A reasonable glass breakage limit is based on commonly used glass type and thickness. The particle size should be commonly available in a wide variety of environments and able to be transported by the rotorwash. For rotorwash evaluation purposes, the derived not-to-exceed limit uses annealed glass with a 0.2-0.4 inch thickness. This glass can withstand projectiles up to 5.5 grams with a MMBV of 25 fps particle velocity. Discussion of particles of this weight class is contained in [Appendix F](#).

It is critical to note, just because peak rotorwash velocities may be a certain value, this does not mean that a stone like projectile will remain airborne at close to the same velocity. This portion of the problem will be further discussed in [Appendix F](#).

Sheet Metal

In general, it takes a substantial energy level for small particles or projectiles to penetrate steel or aluminum sheet metal. A simple method to estimate penetration velocities of sheet metal by small projectiles is documented in Reference E-17 (and repeated with example calculations in Reference E-18). The most likely rotorwash application of this methodology would be if a particle or projectile is blown into the path of another piece of moving or

rotating structural sheet metal so that this energy of motion is added to the projectile velocity. Anyone interested in additional details for this method is advised to consult the listed references, engineering material science texts, or investigate the many material properties sites on the Internet. Sources such as SAE International, the International Journal of Impact Engineering, and journals by the various societies devoted to the development of specific types of materials are highly recommended. Also, the American Society for Testing and Materials (ASTM) is an excellent data source for structural materials.

The more likely problem associated with sheet metal products is the problem of dynamic denting (composites will be discussed in a later section). In this scenario, rotorwash would blow a projectile (i.e. a stone) or a piece of debris at a certain energy level (due to its velocity or kinetic energy) to impact a sheet material structure. Also, a hailstone impact typifies dynamic denting. Literature references indicate that the two groups most interested in this problem have been the automobile industry (as based on a long list of reasons) and the roofing industry (as based on hail damage). A wide range of sheet metal products have been tested using both quasi-static and dynamic dent testing methods to determine their sensitivity to denting. In the case of dynamic denting, the phenomena are more localized, with more focus of the material deformation in the impact region. The dynamic dent depth is the resulting permanent deformation. As one would expect, every type of sheet material has different stress-strain and elastic properties, so the definition of a not-to-exceed threshold criteria for denting (or even chipping of paint) requires detailed knowledge of the material, its material properties, its thickness, and its manufacturing process (i.e. baking or hardening treatments applied).

Unfortunately, there is no magic not-to-exceed threshold value for energy level or force that can be utilized to define an unacceptable dent in the generalized context of rotorwash hazard analysis. However, guidelines do exist if the type of material can be generally specified. One standard by the American Iron and Steel Institute defines a minimum dent resistance of 9.7 J and a stiffness that should exceed 45 N/mm for automobile panels. Probably the most common standard is a dent depth of 0.1 mm. The history of this standard is well presented from a historical perspective by Hodgins (Reference E-19).

Two simplified methods that quantify dent resistance to a depth of 0.1 mm have been utilized by industry over the years. DiCello and George (Reference E-20) proposed a method based on applied work or energy. This method utilizes the following equation to empirically relate applied denting energy ($W_{0.1}$) for a 0.1 mm dent to other common (and measurable) material properties.

$$W_{0.1} = K \sigma_y^2 t^4 / S$$

The equation is a function of the sheet or panel yield strength (σ_y), thickness (t), and stiffness (S) at the location of the dent. For the specific material of interest, a constant (K) is required to relate the other parameters. One key issue with the application of this equation (or other methods) for rotorwash scenarios is the issue of stiffness. If the sheet material can absorb projectile energy elastically (like a trampoline), the plastic work that

forms the dent will be reduced and the rebound energy of the projectile will be observed to be greater.

The second approach, presented by Yutori (Reference E-21), relates the critical load to produce a permanent 0.1 mm dent in the following way:

$$P_{0.1} = K \sigma_y t^n$$

In this equation, critical load ($P_{0.1}$) is a function of panel yield strength (σ_y) and thickness (t). A constant (K) for the specific material and geometry is required, and the exponent (n), based on experimental data, varies between 2.3 and 2.4 in value (or 2.0 to 2.4, Reference E-22). While this equation is useful for comparing the relative dent resistances of similar types of materials with different strength levels, care must be used when comparing materials of differing strengthening mechanisms.

Both of these simplified methods depend on empirical data and are best utilized for parameter variation studies about the baseline data. Both of these methods also have limitations and cautions associated with their use. Thomas (Reference E-23) and Hodgins (Reference E-19) both provide good explanations of the background to these limitations and cautions. Thomas also discusses extensions of these theories that were subsequently developed. Dynamic dent data for a mild strength (IF), medium strength (IFR), and two bake hardened steels (BH) of several gauges are presented in Reference E-24. The authors discuss the limitations of these methods and how the hardening process of steel and the impact velocity of the test method affect use of these two methods.

Additional sources of experimental data that can be used to estimate dynamic denting characteristics can be found from several sources. Thomas (Reference E-23 or E-25) provides data for AA6111 and AA5754 aluminum alloy sheet products. Tests were performed using both a quasi-static loading procedure and a drop test procedure with a 25.4-mm diameter steel ball. The quasi-static data were used to produce residual dent data as a function of peak applied load. These data are presented in Figure E-10 for the AA6111 alloy. The dynamic test data were used to produce residual dent data as a function of impact velocity. These data are presented in Figure E-11 for the same alloy. From these data and the material characteristics as documented in the report, it would be possible to calculate the impact energy. These data could also be used to baseline either of the two simplified methods mentioned previously for purposes of estimating parameter variations.

Burley, Niemeier, and Koch (Reference E-26) published data in 1976 for aluminum sheet (2036-T4, 5182-0, and 5056-H111) and steel (1010-CQ) used in automobile panels. Their data, presented as the ratio of dent depth to sheet thickness as a function of impact velocity, are presented in Figure E-12. They termed the Y-axis intercept of the linear data, where denting should initiate, as the threshold velocity. Using this intercept value and the slope allowed prediction of dent depth from impacts varying from 20 to 60 mph. The minimum and maximum gauge of the panels tested varied from 0.027 to 0.040 inches, respectively. The projectile used to make the dent with the use of an air cannon was a one-inch diameter aluminum ball.

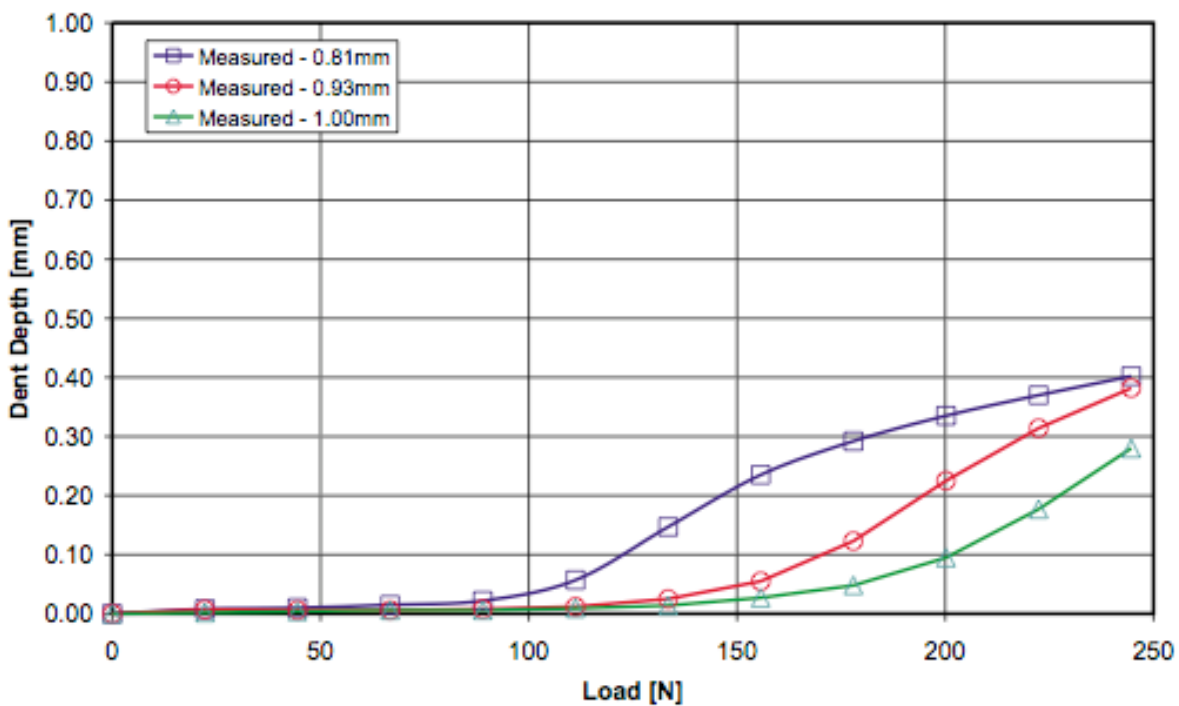


Figure E-10 Measured Residual Dent Depths for 0.81-, 0.93-, and 1.00-mm Thick AA6111 Panels Versus Peak Applied Load at Center Position (Reference E-23 or E-25)

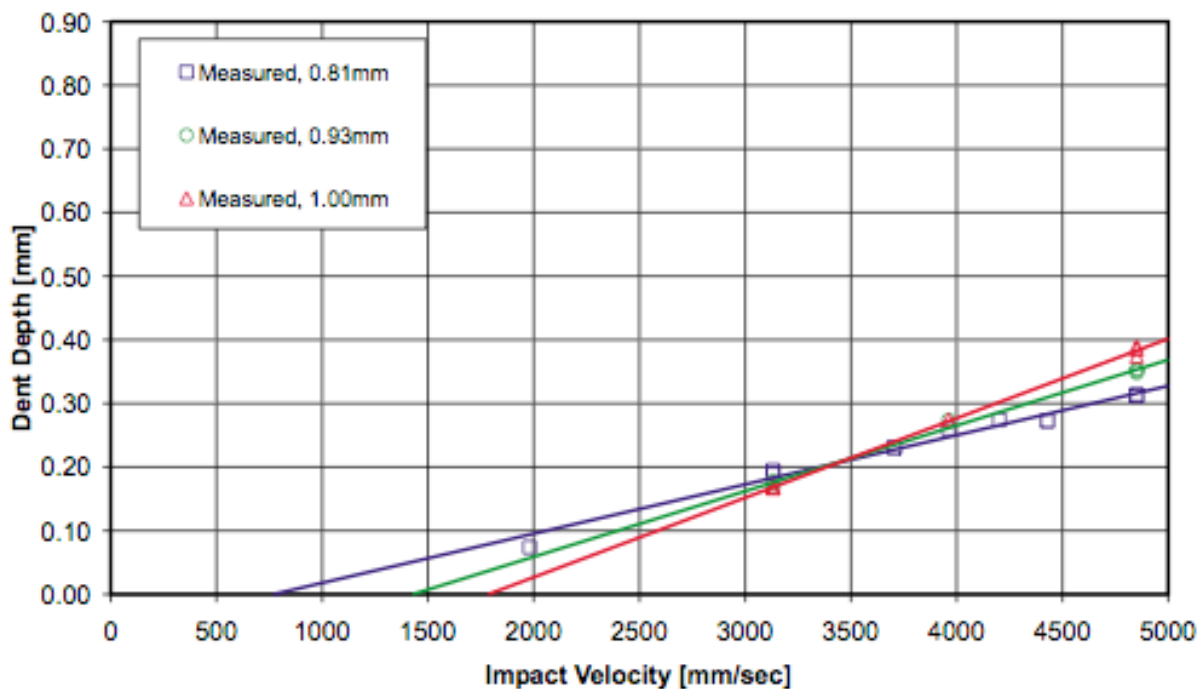


Figure E-11 Measured Residual Dent Depths for 0.81-, 0.93-, and 1.00-mm Thick AA6111 Panels Versus Impact Velocity at Center Position (Reference E-23 or E-25)

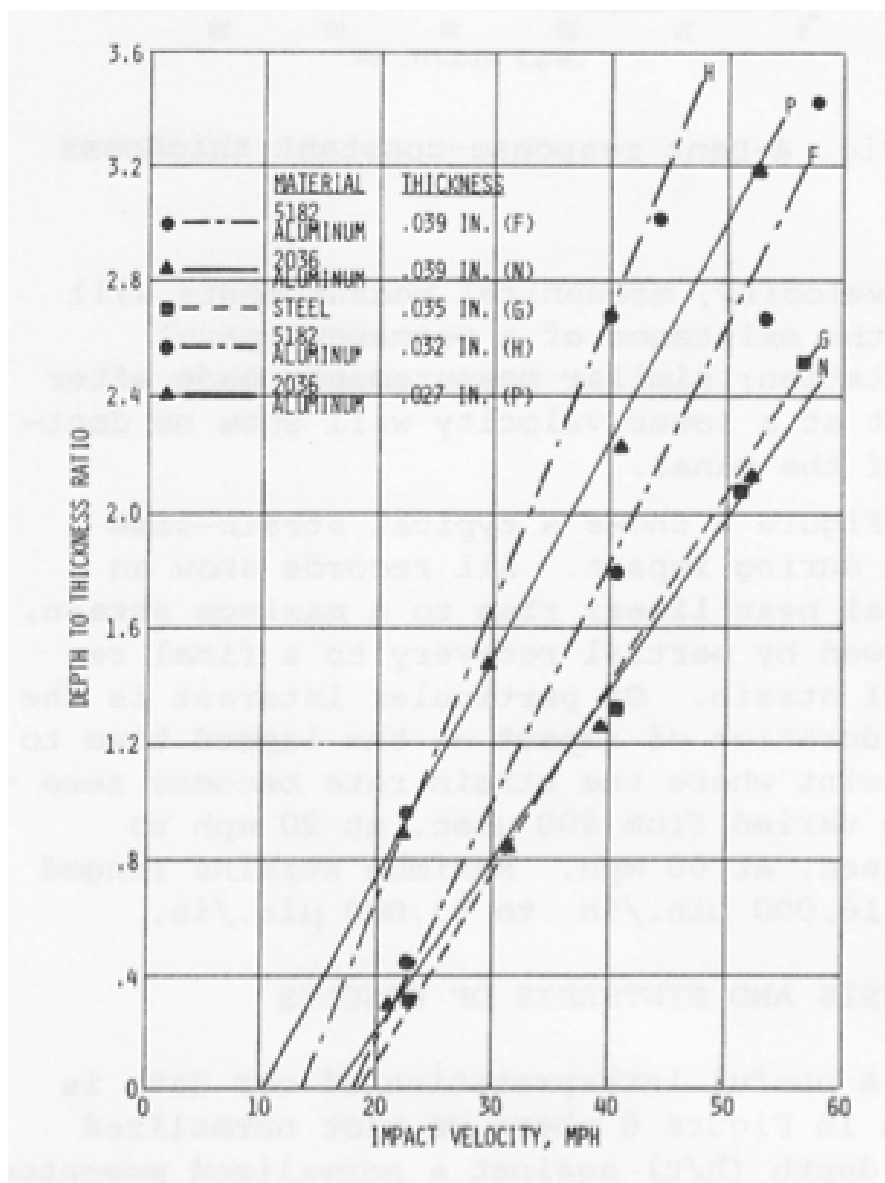


Figure E-12 Dynamic Dent Depths for Aluminum and Steel Panels (Reference E-26)

Burley and Niemeier expanded upon their original work with tests on actual automotive roof, fender, and door units in Reference E-27. Both aluminum and steel components were used in these tests. The minimum and maximum gauge of these panels varied from 0.0317 (doors) to 0.040 (roof) inches, respectively. These data are presented as dent depth versus impact velocity for each material and component type. The impact velocity range was still 20 to 60 mph for most components, and the projectile was the same one-inch diameter aluminum ball.

Burley and Niemeier's best rotorwash applicable results are probably presented in Reference E-28. This paper publishes dynamic dent data for the effects of real and

simulated hail on four steel and four aluminum production automobile hoods (model year 1977). These data are presented in the form of dent depth versus impact velocity as summarized in Figure E-13. As can be seen, a depth of 0.1 mm (0.004 inches) begins at impact velocities of as low as 15 to 20 mph for a one-inch aluminum ball indentor (or a 1.5-inch diameter hailstone). A correlation between hail of 1.25 and 1.5 inches in diameter and a one-inch aluminum ball indentor is also established for reference purposes. This correlation is based on laboratory and actual field data collected from a hailstorm that damaged a 1977 model automobile with a hood like the one used in the laboratory testing. These data are excellent for rotorwash hazard analysis purposes, especially since the correlation is verified between the indentors of varying density (or size).

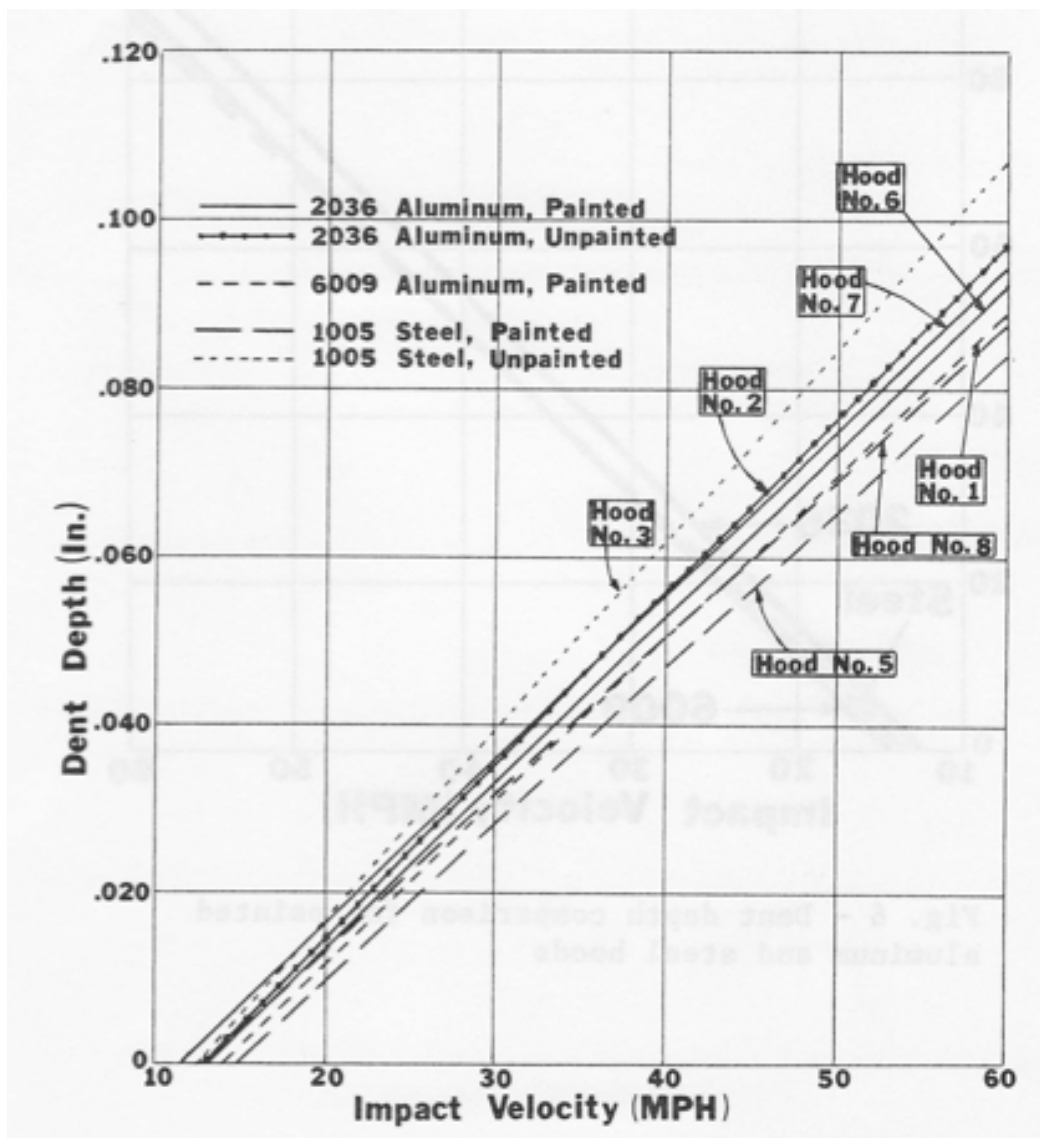


Figure E-13 Dent Depth Versus Impact Velocity for Seven Automobile Hoods
(Reference E-26)

Reference E-26 test results were applied to rotorwash hazard analysis by equating the kinetic energy from the one-inch aluminum ball indentor to a representative $\frac{3}{4}$ -inch piece of gravel. Mass of the 1" spherical aluminum ball is calculated as 0.001587 slugs. For an arbitrarily chosen 0.02-inch dent in Figure E-13, the kinetic energy of the aluminum ball traveling at 23 mph equates to the $\frac{3}{4}$ -inch gravel traveling at 47.2 mph (mass of 5.5 grams or 0.000377 slugs). Use of automotive (car hood) data toward rotorcraft (aircraft skin) assumes the sheet metal properties are the same between applications. Further research is required to confirm the equivalent kinetic energy relation for different size, density, and shape particles as well as sheet metal properties for the aircraft skin when applied to test data applied from other sources such as the automotive industry.

Additional sources of dynamic denting data can be identified for AA5754 and AA6061-T6 aluminum in Reference E-29. Data on DQSK, DP600, BH210, and BH 280 steel sheet (from U.S. Steel Corporation) can be obtained from Reference E-30. Data on AKDQ, BH, and Rephos steels of differing thicknesses are provided in Reference E-31 as well as curve fit coefficients for the equations of the two previously mentioned simplified methods. Data on AKDQ, 210B, 220B, Isotropic, and Rephos automobile panel steels of differing thicknesses (German and North American sourced) are provided in Reference E-32 as well as data to curve fit the coefficients of the equations of the two simplified methods. Extensive data on a wide range of steels are presented as part of Section 10 in Reference E-33 and Section 8 of Reference 3.3-33. These last two references can be downloaded from the Internet (see reference list for the Internet address) and are quite large documents. Supporting files with the raw data in Excel format are available with reference E-34. Lastly, data on the dent resistance of AZ31 magnesium alloy sheets are provided in Reference E-35.

Additional references related to hailstone impact damage of aircraft components are presented in References E-36 and E-37. The second reference is interesting in itself as it traces the 1952 perspective of everything known about hail as far back as 1784. With additional correlation work using data from several of the more recent laboratory experiments discussed in this section, different methods to estimate dent depth due to impact are contained within both of references.

Composite Panels

Just as with sheet metal, there is no magic not-to-exceed threshold value of energy level or force for acceptable composite damage. Composites tend to be stiffer, less elastic in deformation, and have different properties from metals that define damage tolerance. In this section, several examples of critical velocities or energies that produce damage in composite materials are provided. This discussion is by no means extensive or intended to be anything more than an example for awareness purposes. Anyone interested in the details of this problem will have to become familiar with the vocabulary of composites, consult engineering material science texts and material literature, and investigate the many material properties sites on the Internet. Sources such as the International Journal of Impact Engineering and journals by the various societies devoted to the development of specific types of materials are highly recommended. Also, the American Society of Civil Engineers (ASCE) and American Society for Testing and Materials (ASTM) are excellent data sources for structural materials.

Reference E-38 was chosen as an example for discussion in this section because it provides impact damage documentation for “modern/advanced lightweight composite panel materials” that are presently used (or planned for use) in air/marine/road/rail vehicles. This reference in itself is not unique. However, it provides an excellent example of the type of impact damage that could be expected from flying debris. Therefore, the limiting impact velocity data provided in the document are representative and for awareness purposes. Specimens of Sheet Moulding Compound (SMT) and Glass Mat Thermoplastic (GMT) were impact tested by 5-kg projectiles (by drop test) at 4.4 m/s (9.8 mph), or from a height of 1.0 meter. Specimens of honeycomb sandwich panel (with different skin/core materials) were impact tested by 1.55-kg projectiles at velocities from 1.98 m/s (4.43 mph) to 4.4 m/s (9.8 mph) or from a height of 0.2 to 1.0 meters (in 0.2-meter increments). Damage, as summarized in Figure E-14, is documented in detail and varies depending on the velocity at impact and the specific type of material. However, for almost all test conditions, at least a small amount of damage was measurable.

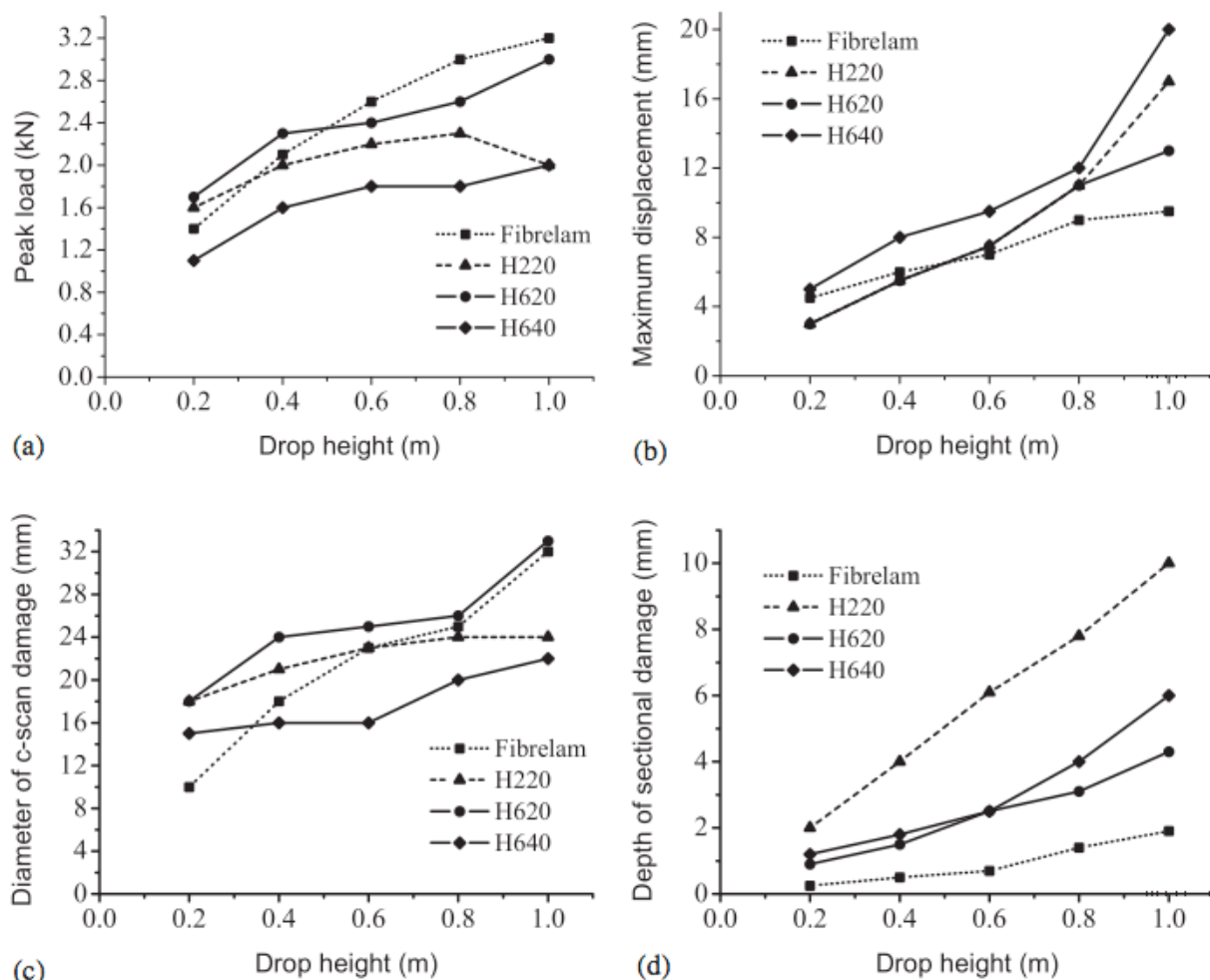


Figure E-14 Composite Panel Damage Summary for 1.55- and 5-kg Projectiles
(Reference E-38)

While the exact formulations of the materials tested might not necessarily be widely in use at this time, they must be considered representative of materials that will be encountered in present and future military and non-military structures and vehicles (i.e. while providing aid to a disaster recovery effort where debris would be expected). From a mass/velocity combination, these data certainly represent examples of possible damage since substantial research is documented in this report that confirms flying debris in the 1.55- to 5-kg range can be produced by a large rotorcraft (both analytically as well as based on experiment and accident reports). Also, even though damage might be minimal in some cases, for damage associated with private property a liability may still exist.

References

- E-1. Beason, W. L.; Meyers, G. E.; and James, R. W., "Hurricane Related Window Glass Damage in Houston," Journal of Structural Engineering, Vol. 110, December 1984, pp. 2843-2857.
- E-2. Minor, J. E., "Analysis of the window damaging mechanism in windstorms", PhD dissertation, Dept. of Civil Engineering, Texas Tech Univ., Lubbock, Tex, 1974.
- E-3. Minor, J. E., "Lessons Learned from Failures of the Building Envelope in Windstorms," Journal of Architectural Engineering, Vol. 11, March 2005, pp. 10-13.
- E-4. Minor, J. E., "Performance of Roofing Systems in Wind Storms," NRCA/NBS Proceedings of the Symposium on Roofing Technology, Paper 17, September 1977.
- E-5. Minor, J. E., "Windborne Debris and the Building Envelope," Journal of Wind Engineering and Industrial Aerodynamics, Vol. 53, 1994, pp. 207-227.
- E-6. Minor, J. E.; Beason, W. L.; and Harris, P. L., "Designing for Windborne Missiles in Urban Areas," Journal of Structural Division, Vol. 104, November 1978, pp. 1749-1780.
- E-7. Beason, W. L., "Breakage Characteristics of 1/4 Inch Tempered Glass Subjected to Small Missile Impact," Final Report to Institute for Disaster Research, Texas Tech University, October 1975.
- E-8. Saxe, T. J.; Behr, R. A.; Minor, J. E.; Kremer, P. A.; and Dharani, L. R., "Effects of Missile Size and Glass Type on Impact Resistance of "Sacrificial Ply" Laminated Glass," Journal of Architectural Engineering, Vol. 8, March 2002, pp. 24-39.
- E-9. Anon, "Wind-Borne Debris, Impact Resistance of Residential Glazing," NAHB Research Center, January 2002.
- E-10. Bole, S., "Investigation of the Mechanics of Windborne Missile Impact on Window Glass," Master Thesis in Civil Engineering, Texas Tech University, December 1999.

- E-11. Persson, J.; Breder, K.; and Rowcliffe, D. J., "Loading Rate Effects During Indentation and Impact on Glass with Small Spheres," *Journal of Materials Science*, Vol. 28, 1993, pp. 6484-6489.
- E-12. Ji, F. S.; Dharani, L. R.; and Behr, R. A., "Damage Probability in Laminated Glass Subjected to Low Velocity Small Missile Impacts," *Journal of Materials Science*, Vol. 33, 1998, pp. 4775-4782.
- E-13. Grant, P. V.; Cantwell, W. J.; McKenzie, H.; and Corkhill, P., "The Damage Threshold of Laminated Glass Structures," *International Journal of Impact Engineering*, Vol. 21, 1998, pp. 737-746.
- E-14. Pantelides, C. P.; Horst, A. D.; and Minor, J. E., "Postbreakage Behavior of Heat Strengthened Laminated Glass Under Wind Effects," *Journal of Structural Engineering*, Vol. 119, February 1993, pp. 454-467.
- E-15. Kaiser, N. D.; Behr, R. A.; Minor, J. E.; Dharani, L. R.; Ji, F.; and Kremer, P. A., "Impact Resistance of Laminated Glass Using "Sacrificial Ply" Design Concept," *Journal of Architectural Engineering*, Vol. 6, March 2000, pp. 24-34.
- E-16. Dharani, L. R.; Ji, F.; Behr, R. A.; Minor, J. E.; and Kremer, P. A., "Breakage Prediction of Laminated Glass Using the "Sacrificial Ply" Design Concept," *Journal of Architectural Engineering*, Vol. 10, December 2004, pp. 126-135.
- E-17. George, M. M., "Downwash Impingement Design Criteria for VTOL Aircraft," TREC Report 64-48, U.S. Army Transportation Research Command, Fort Eustis, VA, August 1964.
- E-18. Ferguson, S. W., "Rotorwash Analysis Handbook, Volume I – Development and Analysis," Federal Aviation Administration, Washington D.C., Technical Report DOT/FAA/RD-93/31,I, June 1994.
- E-19. Hodgins, B., "The Numerical Prediction of the Dent Resistance of Medium Scale Aluminum Structural Panel Assemblies," M.S. Dissertation in Mechanical Engineering, University of Waterloo (Canada), 2001.
- E-20. DiCello, J. A., and George, R.A., "Design Criteria For The Dent Resistance Of Auto Body Panels," SAE International, Paper 740081, 1974.
- E-21. Yutori, Y.; Nomura, S.; Kokubo, I.; and Ishigaki, H., "Studies On The Static Dent Resistance," Proceedings of the 11th IDDRG, Memoires Scientifiques Revue Metallurgie, Volume 77(4), pp. 561-569, April 1980.
- E-22. Anon, "Advanced Vehicles Concepts, Technical Transfer Dispatch #6, ULSAB-AVC Body Structure Materials," ULSAB-AVC Consortium, May 2001. (refer to "<http://www.autosteel.org/Content/NavigationMenu2/Automotive/TechnicalInformation/default.htm>")

- E-23. Thomas, D., "The Numerical Prediction of Panel Dent Resistance Incorporating Panel Forming Strains," M.S. Dissertation in Mechanical Engineering, University of Waterloo (Canada), 2001.
- E-24. Shi, M. F.; Brindza, J. A.; Michel, P. F.; Bucklin, P.; Belanger, J. P.; and Prencipe, J. M., "Static and Dynamic Dent Resistance Performance of Automotive Steel Body Panels," SAE International, Paper 970158, 1997.
- E-25. Thomas, D; Hodgins, B.; Worswick, M.; Finn, M. J.; and Gong, K., "Static and Dynamic Denting of Paint Baked AA6111 Panels: Comparison of Finite Element Predictions and Experiments," SAE International, Paper 2001-01-3047, 2001.
- E-26. Burley, C. E.; Niemeier, B. A.; and Koch, G. P., "Dynamic Denting of Autobody Panels," Society of Automotive Engineers, SAE Paper 760165, February 1976.
- E-27. Burley, C. E., and Niemeier, B. A., "Denting Properties of Aluminum Autobody Components," Society of Automotive Engineers, SAE Paper 770199, February 1977.
- E-28. Niemeier, B. A., and Burley, C. E., "Hailstone Response of Body Panels – Real and Simulated," Society of Automotive Engineers, SAE Paper 780398, February 1978.
- E-29. Wang, Y., and Mallick, P. K., "Dynamic Denting Study of Aluminum Alloys," SAE International, Paper 2004-01-0183, 2004.
- E-30. Shih, H. C., and Horvath, C. D., "Effects of Material Bending and Hardening on Dynamic Dent Resistance," SAE International, Paper 2005-01-0832, 2005.
- E-31. Shi, M. F.; Meuleman, D. J.; Alaniz, C. L.; and Zurdosky, S. J., "An Evaluation of the Dynamic Dent Resistance of Automotive Steels," SAE International, Paper 910287, 1991.
- E32. McCormick, M. A.; Fekete, J. R.; Meuleman, D. J.; and Shi, M. F., "Effect of Steel Strengthening Mechanisms on Dent Resistance of Automotive Body Panels," SAE International, Paper 980960, 1998.
- E33. Anon, "Ultralight Steel Auto Closures – Engineering Report," Porsche Engineering Services, April 2000. (refer to "<http://www.autosteel.org/Content/NavigationMenu2/Automotive/TechnicalInformation/default.htm>")
- E-34. Sadagopan, S., and Urban, D., "Formability Characterization of a New Generation of High Strength Steels," American Iron and Steel Institute, Report TRP 0012, March 2003. (refer to "<http://www.autosteel.org/Content/NavigationMenu2/Automotive/TechnicalInformation/default.htm>")
- E-35. Yukutake, E.; Kaneko, Sugamata, J.; M.; and Kubota, M., "Dent Resistance of AZ31 Magnesium Alloy Sheets," Journal of Japan Institute of Light Metals, Vol. 56, No. 5, pp. 277-282., 2006.

E-36. Thomson, R. G., and Hayduk, R. J., "An Analytical Evaluation of the Denting of Airplane Surfaces by Hail," NASA TN D-5363, August 1969.

E-37. Souter, R. K., and Emerson, J. B., "Summary of Available Hail Literature and the Effect of Hail on Aircraft in Flight," NACA TN 2734, September 1952.

E-38 Dear, J. P.; Lee, H.; and Brown, S. A., "Impact Damage Processes in Composite Sheet and Sandwich Honeycomb Materials," International Journal of Impact Engineering, Vol. 32, 2005, pp. 130-154.

Appendix F: Rotorwash Generated Projectile and Debris Hazards

Sam Ferguson

It is well accepted and documented that rotorwash can quickly lift and accelerate sand, rocks, supplies, pieces of equipment, and debris to hazardous velocities as dangerous projectiles or missiles. The operational survey conducted for this project ([Appendix H](#)) contains the following statement from a V-22 pilot: *"The pilot is responsible to check environmental conditions prior to landing, and will most likely not land at a location where he believes there would be a problem. Sometimes those conditions cannot be speculated, for instance, there was a test here at PAX where a load was placed on a 2x4 and then attached to the aircraft using an 8-foot pendent. Once raised, the 2x4 turned into a projectile, severely injuring a person on the ground."* These types of unfortunate incidents with rotorcraft are all too common because of the almost infinite number of scenarios that are possible when operating close to the ground. Even if people are not injured, damage to equipment, vehicles, or structures may also occur.

As stated by several people, including Lin (Reference F-1), the projectile or debris problem may be simply summarized as one of "generation, trajectory, and impact." In the civil engineering literature, significant work has been conducted in the last 15 years on these three components of the problem. The impetus of these efforts has been to reduce the injury and property damage that results from hurricanes, typhoons, and tornadoes. Building codes around the world have already implemented changes as a result of this ongoing research. However, early in this effort, the researchers realized that the problem would have to be simplified to develop useful criteria and standards because of the infinite number of sizes, masses, and types of projectiles and debris that could be propelled by high winds.

Significant research work was conducted from the 1970s through the 1990s on various types of projectiles and missiles, like gravel and 2x4 lumber. However, the paper by Wills, Lee, and Wyatt in 2002 (Reference F-2) is credited as one of the first to begin to formally simplify the debris impact problem. This paper geometrically defines projectiles and debris, for the purposes of developing standards and conducting testing, as compact-like, plate-like, and rod-like. To further define these types, compact-like would include rocks, roof gravel, hailstones, or other solid or hollow cubes or spheres. Plate-like objects would include sheet-like building material like 4- ft by 8-ft plywood panels, roof tiles, and shingles. Rod-like materials would include various shapes and sizes of lumber, tree branches, plastic piping, and sheet metal ducting. This classification system has since led to more focused and useful research, most of which is directly applicable to rotorwash hazard analysis applications.

The next several sections in this appendix will primarily focus discussion using the two classification concepts presented in the proceeding paragraphs. It should be noted for the record that little organized rotorwash hazard analysis research related to the "generation, trajectory, and impact" of projectiles or debris has been identified in the literature.

Generation of Rotorwash Related Particle and Debris Hazards

In their paper, Wills, Lee, and Wyatt (Reference F-2) noted that when they decided to investigate the “production and delivery of wind-borne debris” in typhoon prone areas, they found little evidence of attempts to systematically model the problem. Tachikawa had conducted research, considered excellent by most peers, on the trajectories of simple shaped bodies in uniform flows. However, much of this work was in Japanese. As a result of the lack of modeling data, a flight model was developed. Wind tunnel tests were then conducted to validate the predictions of the model for initial flight speeds.

The details of the Wills, Lee, and Wyatt model should to be reviewed in detail before use, but it can be summarized for the three classes of projectile/debris types as follows:

$$\begin{aligned} U^2 &= (2)(\rho_m/\rho_a)(I/CF)(l)(g) && \text{(compact-like objects)} \\ U^2 &= (2)(\rho_m/\rho_a)(I/CF)(t)(g) && \text{(plate-like objects)} \\ U^2 &= (\pi/2)(\rho_m/\rho_a)(I/CF)(d)(g) && \text{(rod-like objects)} \end{aligned}$$

In these equations, the common parameters are U = wind speed, ρ_m = material density, ρ_a = air density, I = friction coefficient (the ratio of the restraining force to the object weight), CF = generalized force coefficient, and g = gravity constant. The length dimensions are l = the common dimension that approximately describes the compact or cube object to obtain volume (l^3), t = thickness, or d = equivalent diameter. The friction coefficient is $<$ or $= 1$ when an object is freely resting and > 1 when the object has some restraint other than the force of gravity. Using these equations, when the wind speed value of U is exceeded for the proper inputs, the projectile or debris becomes airborne. Then, the projectile or debris will accelerate to a speed “ u ” which is sustained by the projectile or debris aerodynamics for the wind speed U . This fraction, sometimes referred to as J , will be discussed in later paragraphs.

To validate this modeling approach, the authors conducted two wind tunnel tests in 1999. Tests were conducted on a range of 18 different compact-like objects of different material densities and sizes to simulate 3-dimensional affects. Likewise, 20 different types of plate-like objects were tested. Due to tunnel safety concerns, no rod like objects were tested.

Graphs of the results of the measured initial flight speeds for these two sets of data are presented as Figures F-1 and F-2. The experimental data are depicted as data points. The lines represent the calculated values of initial flight speed from the equations presented earlier in this section. As can be easily seen, both groups of objects show an encouraging consistency in linear relationships with initial flight speed where the slope of the line is the dimensionless parameter $(I/CF)^{0.5}$. The implied values of (I/CF) are 2.3 and 1.3 for the compact-like and plate-like objects, respectively. For additional discussion about the appropriateness of the values of I and CF required to generate these slopes, the reader is referred to Reference F-2.

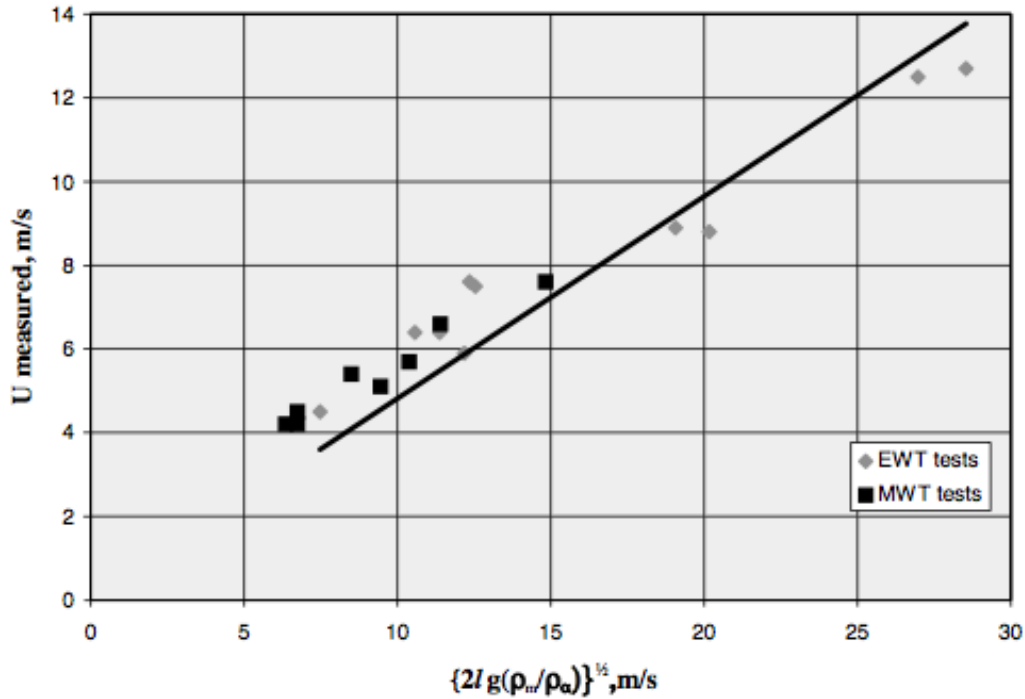


Figure F-1 Initial Flight Speeds for Compact-Like Objects (Reference F-2)

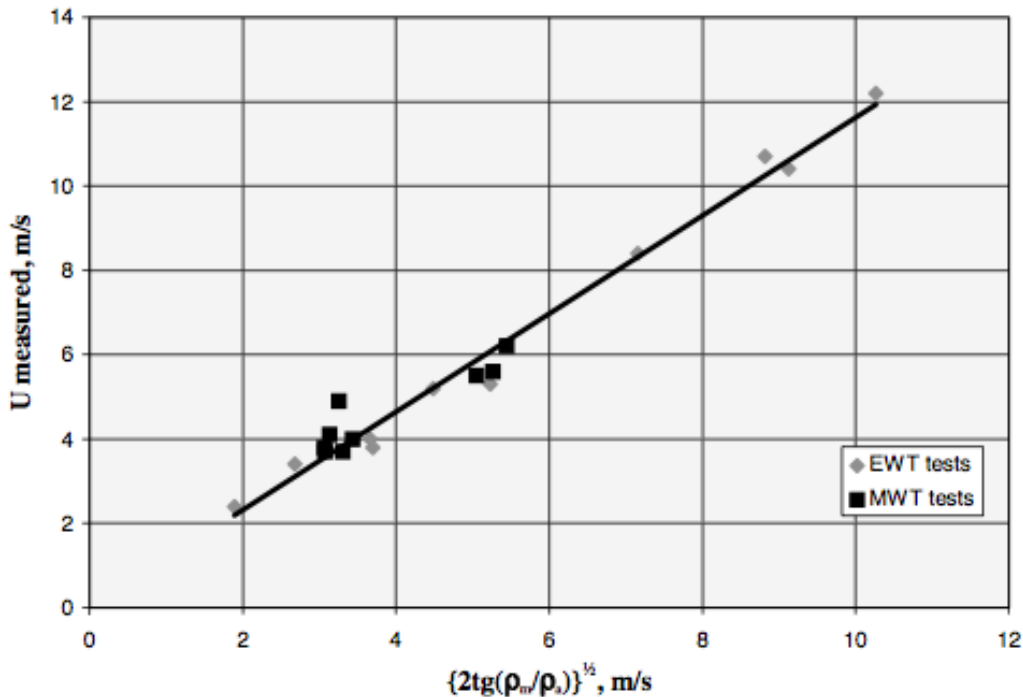


Figure F-2 Initial Flight Speeds for Plate-Like Objects (Reference F-2)

In the wind tunnel tests used to obtain these initial flight speed results, the objects were all released from a 1-meter high platform in the wind tunnel. As would be expected, the compact-like objects immediately blew down the wind tunnel and struck the floor. This result is what the simple equation of motion due to gravity would predict. As part of the tests, the friction coefficient was also increased so that test objects could be restrained to higher release speeds than those measured when freely resting on the launch platform. These test conditions allowed for measurement of the acceleration of the objects relative to the higher (yet constant) tunnel speed. The average value of J , the fraction of wind speed that the object reached before impact, was 0.36 for compact-like objects with a standard deviation of 0.11.

So that these results are not mistakenly extrapolated, several items should be noted. First of all, the wind speed in the tunnel was always a constant value during the period of flight of each object (approximately 0.45 sec). The flow was also horizontal in the tunnel. This meant that no upward vector of the flow could "lift" the compact-like objects in opposition to the gravity force and prolong flight time. In a rotorwash flow field, the release conditions could be expected to be different. The flow field could have an upward vector of velocity as a compact-like object entered the flow field and the wind velocity could increase up to some height above ground in the boundary layer as well as be oscillatory and turbulent.

Results from the analysis of plate-like objects are more complicated. Depending on an object's initial angle-of-attack at release, the trajectory can widely vary as the object departs its launch position. However, the details of this subject will be discussed in the next section. For the test conditions in Reference F-2, it was noted that the average value of J for the sheets reached 0.64 with a standard deviation of 0.11.

As confirmation of the results by Wills, Lee, and Wyatt; Wang (Reference F-3 or F-4) conducted wind tunnel tests on sheet debris in the Texas Tech University wind tunnel. The goals of the research project were to 1) examine flight initiation wind speeds for sheet debris under different restraining forces and 2) examine sheet debris flight behavior after takeoff. In both experiments, an electromagnet was used to vary restraining force from a free or zero restraint condition up to the desired test restraint value.

Wang also expanded on the concept of Wills, Lee, and Wyatt that lighter density particles and sheets can be more dangerous than heavy particles and sheets. Quite simply, if a large wood sheet becomes airborne, it can accelerate to obtain significant momentum or energy before impact. A similar size metal sheet may not become airborne as easily and therefore could present less of an overall hazard. This characteristic is represented by the fact that the initial flight speed for sheets is such that $u \propto (\rho_{mt})^{0.5}$ or the mass times the sheet thickness. The sheet size and mass per unit area play a less critical role.

Wang's results are quite interesting. Early in his experiments, he tried to confirm the results of Wills, Lee, and Wyatt. However, he was not successful even though he freely mounted test specimens in the middle of the wind tunnel. These results are shown in Figure F-3. Wang's sheet value of (I/CF) was 7.02, not the expected value of 1.3.

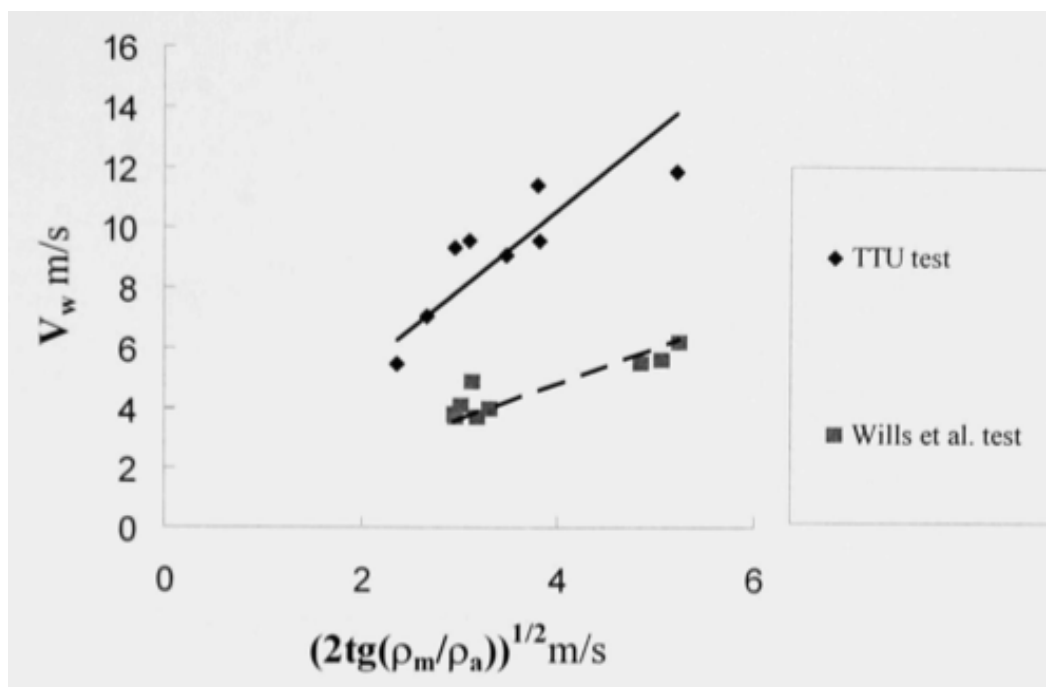


Figure F-3 Wang's Initial Flight Speeds for Plate-Like Objects (Reference F-3)

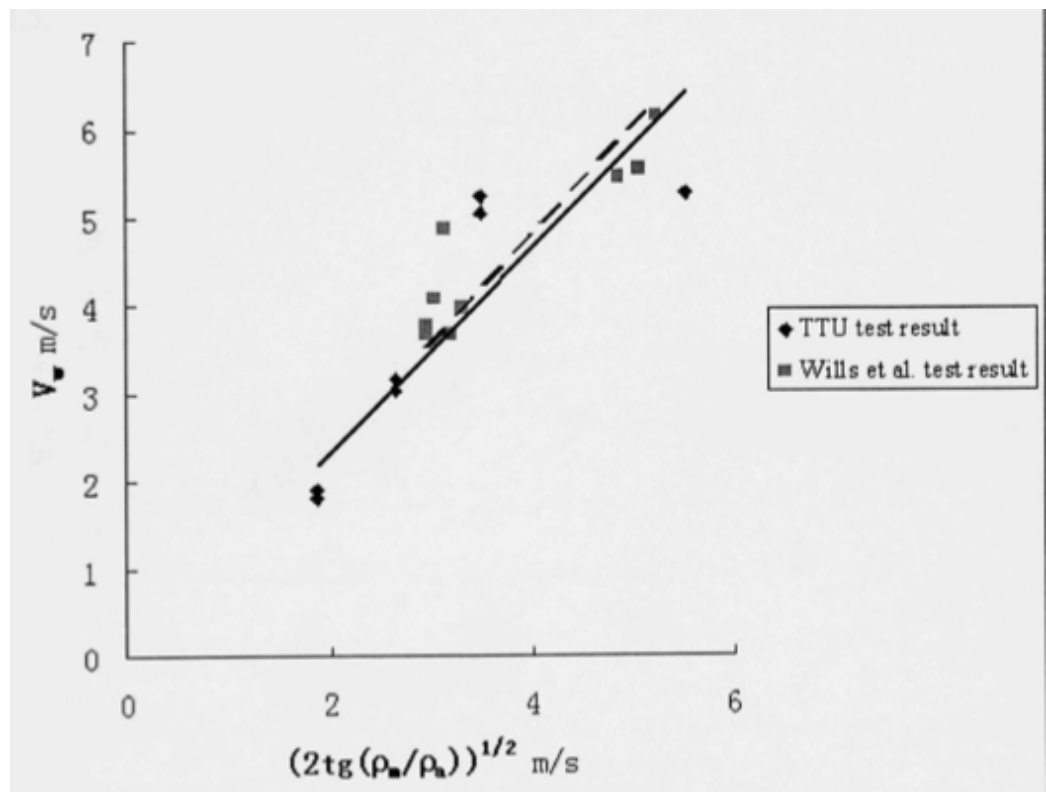


Figure F-4 Wang's Alternative Mounting Results for Plate-Like Objects (Reference F-3)

After a review of the data, Wang determined the results could be the effect of the friction coefficient (I). As a result, the mounting system was then changed to provide a very slight gap (< 3 mm) between the sheet and the mounting surface in the center of the tunnel. Results from the second experimental mounting configuration, presented in Figure F-4, almost exactly matched the results of Wills, Lee, and Wyatt. The details of this experimental process can be followed in Reference F-3. The important lesson to be learned for rotorwash applications is that slight adjustments in the friction coefficient of a projectile or debris can significantly affect the initial flight speed that causes the projectile or debris to become airborne.

Two additional important results are quantified through Wang's experiments. The first result is that the average value of J (Wang calls this α), the fraction of wind speed that the object reaches during flight, varies as a function of thickness or mass increase. This result is presented in Figure F-5. It is interesting to note that the result from Wills, Lee, and Wyatt does not fit on the graph where it might be expected. Wang discusses possible reasons for this in his discussion. The more important result is that plate-like objects can be expected to accelerate to between 0.5 and 0.8 times the wind speed that is propelling them before impact. The second result is that Wang's variation of restraining force had minimal, if any, effect on the average value of J prior to impact. The only significant affect was on the initial speed for the object to become airborne.

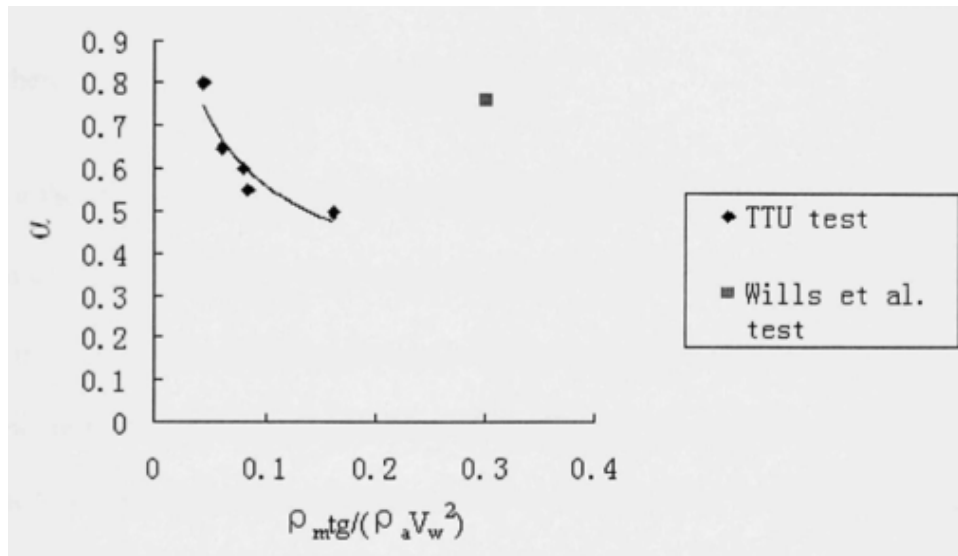


Figure F-5 Wang's Maximum Relative Speed for Plate-Like Objects (Reference F-3)

Masters and Gurley document further confirmation of the soundness of the Wills, Lee, and Wyatt methodology with respect to gravel or stone in Reference F-5. They present an analysis of the wind gust speeds required to propel roof ballast gravel off buildings. In their report, they compare the predicted results from Reference F-5 to predictions using the method of Kind and Wardlaw, Reference F-6. The critical gust wind speed predicted for 0.63-inch diameter roof gravel to be blown off a building is 57 mph and 59 mph for the two methods, respectively. Other gravel versus critical speed combinations are tabulated in Table F-1.

Table F-1 Threshold of Flight for Various Gravel Sizes (Reference F-5)

Sieve Size		Threshold of Flight	
in	mm	m/s	mph
0.093	2.36	9.8	22
0.187	4.75	13.9	31
0.374	9.50	19.7	44
0.492	12.50	22.6	51
0.630	16.00	25.6	57
0.748	19.00	27.8	62
0.984	25.00	31.9	71

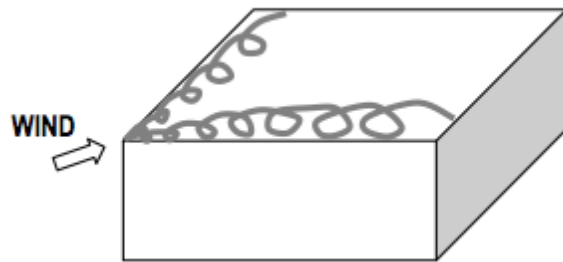


Figure F-6 Winds Traveling Over a Corner Parapet of a Building (Reference F-5)

The Masters and Gurley report documents an excellent simplified process through which initial conditions associated with gravel can be evaluated to predict the critical gust speed for flight off a flat surface. It is important to note that the methods employed in References F-5 and F-6 take into account the possibility that roof edge vortices may have an impact on the critical gust speed. Figure F-6 provides a conceptual sketch of a roof vortex system. Roof vortices add turbulence to a flow field and reduce the straight-line critical gust speed required to lift and propel gravel. Kind and Gurley demonstrated that 0.75-inch roof gravel will begin to move about on a surface (or scour) at as low as 47 mph and lift off at as low as 62 mph. While the roof edge system may not be a factor in most rotorwash scenarios, it is certainly possible that other devices, equipment, or obstructions within a particular scenario could produce a similar flow interaction with surface stones (the rotorwash flow field itself is vortex driven by nature). Therefore, these results do have application worthy of note during rotorwash analysis efforts. Additional references on gravel and roof vortex interactions are provided in References F-7 through F-10.

Trajectories of Rotorwash Related Particle and Debris Hazards

As mentioned earlier, Lin stated that the projectile or debris problem could be simply summarized as one of “generation, trajectory, and impact.” Unfortunately, this is where “simple” abruptly ends because trajectory solutions are both deterministic and probabilistic problems. To precisely predict the flying behavior of just several projectile or debris types (of the almost infinite number of types) is a complex task requiring sophisticated computer modeling of projectile/debris aerodynamics AND a statistically appropriate number of runs to simulate varying initial conditions and turbulence in the flow.

While this task is technologically possible, it is not generally a practical solution to solving the trajectory problem because of the time and resources required. Even if the engineer gets past the decision of what projectile or debris type is the appropriate one to model for his application, another issue becomes significant. This issue involves the fidelity of the solution. Some types of projectiles or debris can be modeled as 1-, 2-, 3-, or even 6 Degrees-Of-Freedom (DOF) trajectory problems depending on the level of accuracy that is required.

In summary, the problems mentioned in the previous two paragraphs are what have driven the requirement toward solutions involving “standards” in the civil engineering world. This process is still ongoing; however, tests (and formalized standards) using nine-pound 2x4 ft sections of lumber and 5.5-gram steel balls as generalized impact projectiles are examples of the effort to simplify and obtain practical solutions. Another practical and simplifying aid to solution of the trajectory problem is the generally agreed upon principle that most “real-world” trajectory flight times are of only one- to three-second duration. After this length of time, something is impacted and this something is usually the ground (References F-1 and F-11). This principle intuitively makes a lot of sense for most rotorwash applications since the velocity of rotorwash rapidly decays with distance from the rotorcraft. Use of this principle shortens the period of time that the trajectory problem needs to be solved before the most likely impact energy or momentum values are built up in the projectile or debris. Ultimately, calculation of these values is the desired outcome of most types of analyses (Reference F-12). The actual prediction of the flight path itself is often not a critical requirement except in special cases. Even then, it often becomes a probabilistic problem because of varying initial conditions and unknowns that must be approximated or assumed.

Using the previously discussion as background, the issue becomes one of “What approach is best taken for rotorwash hazard analysis applications?” If we specify a requirement to define a type of projectile or debris and its exact trajectory needs to be computed, then several options exist. Wills et al., Wang, and Masters (References F-2, F-3, and F-5) utilize some very simple methods for quick trajectory calculations. The methods presented in References F-1, F-11, and F-13 through F-17 all introduce variations of 3-DOF trajectory solutions. Within these references, approximately three different variations in the computational approach are proposed that non-dimensionalize the equations of motion. Through the non-dimensional process, the authors demonstrate how to better enable research goals and correlate results with the limited available data from wind tunnel and

field tests. Most of the documented 3-DOF methods also discuss simplifications that can be made to obtain quick trajectory estimates. Richards et al., in Reference F-18 discuss excellent work for the full 6-DOF solution of plates and rods. He also provides excellent new wind tunnel data on aerodynamic force coefficients for plates and rods and discussion on unsteady flow effects. In summary, all of these references present well-explained approaches and most demonstrate correlation with test results. As a whole, they provide an excellent “reference library” for the trajectory problem.

If, on the other hand, we specify a requirement to define a generic standard for a type of projectile or debris and its likely impact velocity, energy, or momentum needs to be computed, then a different solution approach can be utilized. These alternative methods still provide trajectory results, but the results are more probabilistic in the way they are calculated based upon the methods (and test data) used in their development. Baker provides a discussion of how he proposes accomplishing this task in Section 4.2 of Reference F-11. He develops simple equations for both compact-like and plate-like objects that relate non-dimensional horizontal distance, horizontal velocity, and time. For example, it can be shown for short flight times of compact-like objects that:

$$\bar{u} = \sqrt{2 C_D \bar{x}}$$

For plate-like objects, a similar equation can be shown that takes into account initial conditions of clockwise or counterclockwise rotation of the plate.

$$\bar{u} = (1 \pm 0.51 \Omega) \left(1 - e^{(-1.2 \bar{x}^{0.5})} \right)$$

The weakness of Bakers proposed method, as he presents it, is a lack of development and correlation with wind tunnel and full-scale test data. However, the methodology would appear sound as based on the work that will be discussed next.

Beginning in 2003, the team of Lin, Holmes, and Letchford published a comprehensive series of papers (and a thesis) on the aerodynamic behavior and trajectories of compact-, plate-, and rod-like objects. In summary these documents are:

Type	Year	Reference
compact-like	2003	F-14
compact-, plate-, rod-like	2005	F-13
plate-like	2005	F-15
plate-like	2005	F-16
compact-, rod-like	2007	F-1

In the first paper, Holmes discusses the horizontal/vertical trajectories of spheres for the effects of including/neglecting vertical air resistance and turbulence. He also provides example case results for 8-mm stone and 80-mm wooden spheres. Holmes conclusions are that vertical drag resistance can be a significant effect in some cases as it increases flight

times and horizontal velocity and displacement. The effect of turbulence is to introduce variability into flight trajectories. However, the mean trajectories averaged over a number of samples are similar to those obtained with no turbulence.

In 2005, Lin published a thesis (Reference F-13) that investigated the aerodynamics of flying debris through simulating debris trajectories. However, the most important thing that she accomplished was to link an extensive set of wind tunnel and full-scale debris tests for 3D (compact-like), 2D (plate-like), and 1D (rod-like) debris with her simulated results. The wind tunnel data were obtained using the Texas Tech University wind tunnel, and the full-scale data were obtained through the use of a C-130 as a “wind generator.” Three categories of parameters affecting debris trajectories were investigated: wind field, debris properties, and debris initial support. It was determined that although many parameters influence debris trajectory in the vertical direction, the Tachikawa parameter, K , governs the horizontal trajectory of debris. This parameter is a non-dimension factor that relates the ratio of aerodynamic force to gravity force.

$$K = \rho_a U^2 A / 2 m g$$

In this equation, ρ_a = air density, U = wind speed, A = reference area, m = mass, and g = gravity constant.

For rotorwash applications, the link with the Tachikawa parameter is an important piece of information. This is because most rotorwash projectile/debris problems are horizontal not vertical in nature. Vertical trajectory issues become much more critical when projectiles/debris are blown off tall buildings and remain airborne for longer periods of time.

Using this information, Lin, Holmes, and Letchford were able to non-dimensionalize all of the experimental data (these data are well presented in the thesis) and augment it with some simulation data to collapse the trajectory data. This process is well-documented in the thesis for the plate-like debris and slightly updated in the two papers from 2005 (References F-15 and F-16). The same process is documented for compact-like and rod-like debris in the 2007 paper (Reference F-1).

The non-dimensional trajectory results for plate-like debris are presented in Figure F-7. In the top part of the figure, the data indicate that for the observed debris trajectory the velocity (u) can be approximated by an exponential function relationship using horizontal displacement ($K\bar{x}$) as the independent parameter.

$$\bar{u} = 1 - e^{-\sqrt{2} C_p K \bar{x}}$$

The best-fit parameter for the plate-like debris is a $C_p = 0.911$ with a standard deviation of $\sigma = 0.0814$.

Likewise, horizontal displacement ($K\bar{x}$) can be approximated using a polynomial function with time ($K\bar{t}$) as the independent parameter. This relationship is:

$$K\bar{x} \approx 0.4555(K\bar{t})^2 - 0.148(K\bar{t})^3 + 0.024(K\bar{t})^4 - 0.0014(K\bar{t})^5$$

The standard deviation for this relationship is $\sigma = 0.1341$.

With these relationships established, a powerful analysis tool becomes available. Suppose that a researcher is interested in the trajectory of a roof tile that is 300 x 300 x 15 mm and weighs 3.1 kg. These relationships allow construction of a family of trajectories that can be used to define the velocity (or impact energy) as a function of horizontal displacement, as shown in Figure F-8. Lin also notes in this figure that a numerically calculated trajectory of a detailed plate model falls with the family of trajectories for one standard deviation. Additional examples of the practical use of these relationships are provided in Section 3.5 of Reference F-13.

Additional equations defining the trajectory families for cubes, spheres, rods placed perpendicular to the wind, and rods placed parallel to the wind are defined in References F-13, F-15, and F-1.

In standing back and reviewing these empirical relationships from a rotorwash hazard analysis perspective, several issues become apparent. One of these issues involves the wind assumption in these relationships. As noted in the references, the relationships are based on the assumption of a constant wind. However, rotorwash is an oscillatory flow field that decreases in velocity with increasing distance from the aircraft. Fortunately, this difference in the flow field characteristics should make the empirical relationships conservative. However, a second issue arises in deciding the initial value of wind to use, the peak profile velocity, the mean profile velocity, or some value in between. Also, at what distance from the aircraft should the projectile or debris be inserted into the flow field? Obviously, a distance that represents the start of the wall jet (or even closer like the V-22 incident) should be the worst case location since this is the location of the highest rotorwash velocity.

Lin, Holmes, and Letchford discuss the effect of gusts in Reference F-16. Since full-scale debris flight times usually last only a couple of seconds, they show that the average 2-3 gust speed is appropriate to use for wind velocity when calculating impact velocities. An assumption similar to this would probably be appropriate for rotorwash applications. However, this question would best be answered through additional research comparing numerically calculated 3-DOF constant wind trajectories to rotorwash generated trajectories for sample cases of each type of projectile or debris. Representative rotorwash magnitude/frequency data exist in several test reports to conduct this task. The results of this effort could then be used to define an analysis procedure for using the presented empirical relationships with a rotorwash flow field's quasi-static oscillatory/decay characteristics. Using this procedure, horizontal impact criteria for trajectory flight times of 2 to 3 seconds maximum flight time could be evaluated without having to actually conduct time intensive numerical studies of debris in the time domain using actual rotorwash flow field models.

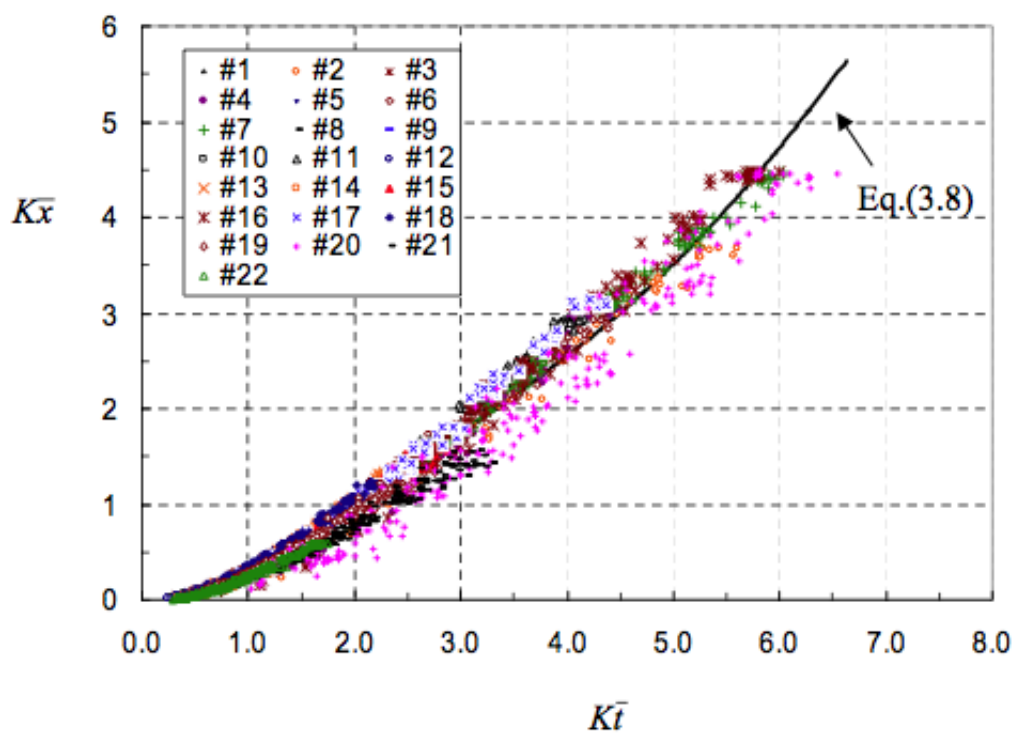
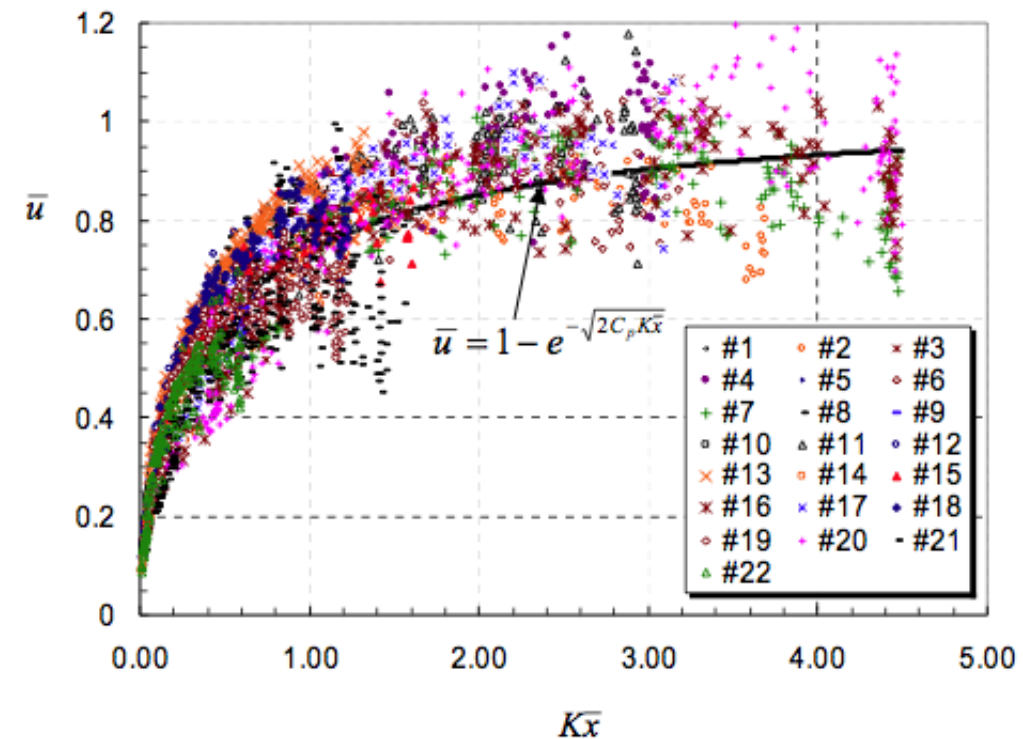


Figure F-7 Horizontal Trajectory of 2D (Plate) Debris ($C_p = 0.911$)
(Reference F-13)

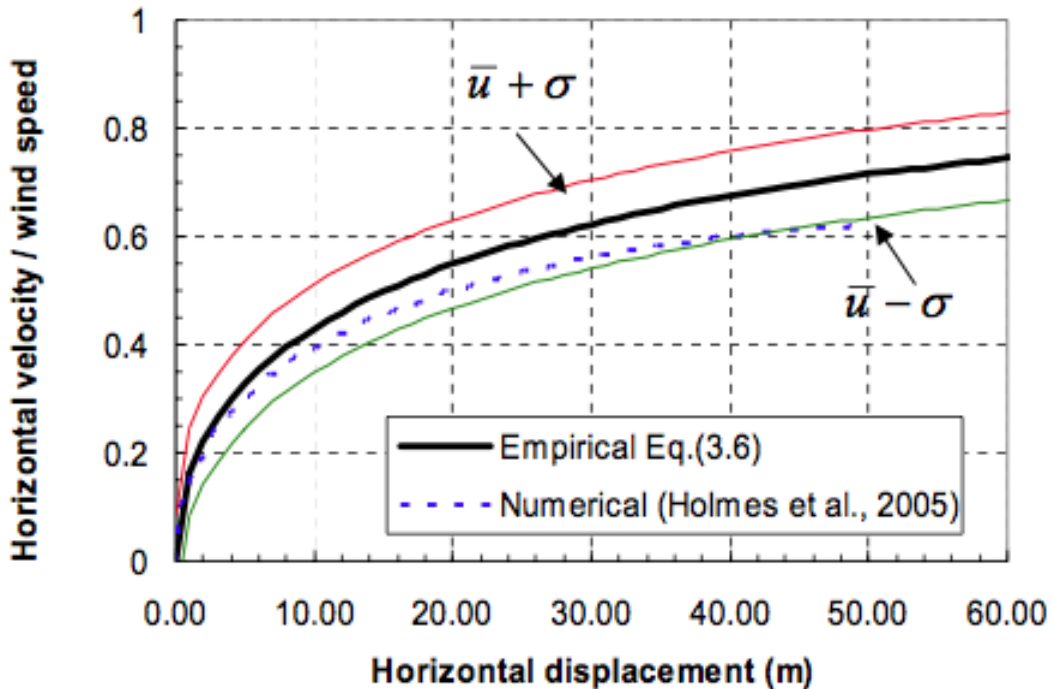


Figure F-8 Trajectory of a Concrete Tile (300 x 300 x 15mm, 3.1 kg, $\alpha_0 = 0^0$)
 (Reference F-13)

Another issue for rotorwash hazard analysis applications is how to decide what are representative projectiles or debris for rotorwash environments when setting standards. One option is to use the same objects as the civil engineering community, i.e. a nine-pound 2x4-foot section of lumber or 5.5-gram piece of gravel. This subject also deserves additional research to better ensure that useful criteria are set for rotorwash hazard analysis applications.

Impact of Rotorwash Related Particle and Debris Hazards

The ultimate goal of the process of investigating rotorwash generated projectiles and debris is to determine representative impact velocities and the associated energy/momentum values. Once these values are known, the connection can be made to the acceptability of the effects on human tissue (eye), window glass, metal or composite material denting, etc. Some of these types of links were attempted using limited available information in Reference F-12. However, based on the research presented in the previous sections, many more links can now be attempted with better quality results.

Summary for Rotorwash Related Particle and Debris Hazards

In this appendix, we have considered Lin's concept of the projectile or debris problem, simply summarized as one of "generation, trajectory, and impact." References have been

identified to begin a systematic attack of the problem as related to the application of rotorwash hazard analysis. Also, problems linking this referenced research to rotorwash hazard analysis have been identified. However, additional research is required to apply "constant wind" civil engineering derived results to the different characteristics of the rotorwash flow field. This can be accomplished. However, until further work is conducted, a table of not-to-exceed threshold velocities for a wide range of projectiles for the compact-like, rod-like and plate-like debris cannot be constructed in a meaningful and verifiable way. Once the additional research is completed, a link can be made from the trajectory problem to the impact problem to determine acceptability and ultimately define separation criteria. Also, acceptable standardized projectiles and debris need to be defined for rotorwash applications. This was a critical step in the civil engineering field to making much of their work useful for defining standards. This same problem exists for the rotorwash hazard analysis application.

Rotorwash can cause a wide range of debris to become airborne. This range includes particles as small as a grain of sand and larger than wooden pallets. A single common "standard" type and size particle can simplify the hazard evaluation for rotorwash generated debris. A $\frac{3}{4}$ -inch gravel was chosen as the representative material for debris propelled by the rotorwash in terms of damage to the surrounding environment. This size of stone is representative of common construction material found on the ground and on rooftops. It is also present in field settings where a foreign object debris sweep would have removed larger debris. The $\frac{3}{4}$ -inch size of gravel is also large enough to do significant damage if it strikes personnel or other materials (glass) in a landing zone.

References

- F-1. Lin, N.; Holmes, J. D.; and Letchford, C. W., "Trajectories of Wind-Borne Debris in Horizontal Winds and Applications to Impact Testing," Journal of Structural Engineering, ASCE, Vol. 133, February 2007, pp. 274-282.
- F-2. Wills, J. A. B.; Lee, B. E.; and Wyatt, T. A., "A Model of Wind-Borne Debris Damage," Journal of Wind Engineering and Industrial Aerodynamics, Vol. 90, 2002, pp. 555-565.
- F-3. Wang, K., "Flying Debris Behavior," Master Thesis in Civil Engineering, Texas Tech University, May 2004.
- F-4. Wang, K. Y., and Letchford, C. W., "Flying Debris Behavior," Proceedings of the Eleventh International Conference on Wind Engineering, Lubbock, Texas, June 2-5, 2003, pp. 1663-1678.
- F-5. Masters, F., and Gurley, K., "Performance of Embedded Gravel Roof Systems in Extreme Wind Loading," Department of Civil and Coastal Engineering, University of Florida, March 18, 2008.
- F-6. Kind, R. J., and Wardlaw, R. L., "Design of Rooftops Against Gravel Blow-off," NRC No. 15544, National Aeronautical Establishment, National Research Council of Canada, Ottawa, Canada, 1976.

F-7. Lin, J. X.; Montpellier, P. R.; Tillman, C. W.; and Riker, W. I., "Aerodynamic Devices for Mitigation of Wind Damage Risk," 4th International Conference on Advances in Wind and Structures (AWAS '08), Jeju, Korea, May 2008.

F-8. Wu, F., "Full-Scale Study of Conical Vortices and Their Effects Near Roof Corners," PH. D. Dissertation in Civil Engineering, Texas Tech University, 2000.

F-9. Zhao, Z., "Wind Flow Characteristics and Their Effects on Low-Rise Buildings," PH. D. Dissertation in Civil Engineering, Texas Tech University, December 1997.

F-10. Zhu, H., "C-130 Testings on Low-Rise Buildings," PH. D. Dissertation in Civil Engineering, Texas Tech University, May 2006.

F-11. Baker, C. J., "The Debris Flight Equations," Journal of Wind Engineering and Industrial Aerodynamics, Vol. 95, 2007, pp. 329-353.

F-12. Ferguson, S. W., "Rotorwash Analysis Handbook, Volume I – Development and Analysis," Federal Aviation Administration, Washington D.C., Technical Report DOT/FAA/RD-93/31,I, June 1994.

F-13. Lin, N., "Simulation of Windborne Debris Trajectories," Master Thesis in Civil Engineering, Texas Tech University, August 2005.

F-14. Holmes, J. D., "Trajectories of Spheres in Strong Winds with Application to Windborne Debris," Journal of Wind Engineering and Industrial Aerodynamics, Vol. 92, 2004, pp. 9-22.

F-15. Lin, N.; Letchford, C. W.; and Holmes, J. D., "Investigations of Plate-Type Windborne Debris – Part I: Experiments in Wind Tunnel and Full Scale," Journal of Wind Engineering and Industrial Aerodynamics, Vol. 94, 2006, pp. 51-76.

F-16. Holmes, J. D.; Letchford, C. W.; and Lin, N., "Investigations of Plate-Type Windborne Debris – Part II: Computed Trajectories," Journal of Wind Engineering and Industrial Aerodynamics, Vol. 94, 2006, pp. 21-39.

F-17. Kordi, B., and Kopp, G. A., "Evaluation of the Quasi-Steady Theory Applied to Windborne Flat Plates in Uniform Flow," Journal of Engineering Mechanics, ASCE, Vol. 135, July 2009, pp. 657-668.

F-18. Richards, P. J.; Williams, N.; Laing, B.; McCarty, M.; and Pond, M., "Numerical Calculation of the Three-Dimensional Motion of Wind-Borne Debris," Journal of Wind Engineering and Industrial Aerodynamics, Vol. 96, 2008, pp. 2188-2202.

F-19. Simiu, E., and Cordes, M. R., "Tornado-Borne Missile Speed Probabilities," Journal of Structural Engineering, ASCE, Vol. 109, January 1983, pp. 154-168.

Appendix G: Airport/Heliport Environment

Sam Ferguson

The number of different airport/heliport scenarios that have a potential for rotorwash related incidents is virtually unlimited. This fact is quickly realized when military and FAA incident/accident reports are reviewed. Unfortunately, it is very rare that these reports contain quantifiable data, i.e. wind speeds, which can subsequently be used for hazard analysis purposes. However, persistence in collecting data has provided some insight as to recommended thresholds that should not be exceeded. For conservatism, this threshold wind velocity is assumed at sea level standard conditions. In rotorwash applications, the resultant dynamic pressure should be used to derive the equivalent limit wind velocity for application at other atmospheric conditions. Utilization of dynamic pressure in lieu of wind velocity removes variations due to changes in the air density. At atmosphere conditions other than sea level standard, velocity limits can be calculated using the limit dynamic pressure and the evaluation case air density.

Analysis of Airport/Heliport Incidents

The only known public domain analysis of various types of rotorwash related incidents is contained in Reference G-1. The analysis presented in this reference was driven by the availability of data for analysis and not by any methodical process. Details of this analysis will not be reproduced in this appendix. However, a summary of the rotorwash peak velocity threshold values, that when exceeded, lead to airport/heliport incidents are as presented in Table G-1. The general conclusion from this analysis effort was that any rotorwash peak profile velocity above 30 knots (34.5 mph) has the potential to result in an airport/heliport incident of some type. Using sea level standard atmospheric conditions, this wind velocity would equate to a dynamic pressure of 3.05 lb/ft².

Additional helicopter wind limitations data were identified during this study in the tie-down procedures section of References G-2 and G-3. These CH-53E (7-blade rotor) and H-60 (4-blade) NATOPS manuals document a 60-knot limit for rotors when not restrained. Manuals originally referenced in Reference G-1 for the 2-blade OH-58C, UH-1D, and AH-1S and the 3-blade CH-47C and H-46 all indicate limits varying between 30 and 45 knots. Collectively, these results indicate that 2-blade rotors present the most critical scenario condition for potential high wind and rotorwash mishaps.

Table G-1 Airport/Heliport Not-To-Exceed Threshold Criteria

Hazard	Recommended Threshold Criteria	Reference
Damage to open aircraft doors/cowls	30 – 40 kts (peak wind velocity) 34.5 – 46 mph 15.4 – 20.6 m/s	G-1
Damage to rotor blades and boom strikes	30 – 37 kts (peak wind velocity) 34.5 – 42.6 mph 15.4 – 19.0 m/s	G-1
Damage to light structures	30+ kts (peak wind velocity) 34.5+ mph 15.4+ m/s	G-1

Damage to vehicles/motorcycles	30 – 40 kts (peak wind velocity) 34.5 – 46 mph 15.4 – 20.6 m/s	G-1
Overturn empty oil drum	43 – 47 kts (peak wind velocity) 49.5 – 54.1 mph 22.1 – 24.2 m/s	G-1
Overturn unrestrained light aircraft (Piper Cub)	35 kts (peak wind velocity) 40.3 mph 18.0 m/s	G-1

Airport Wind Damage—Lessons Learned

On June 17, 1985, a severe storm struck the Regional Airport at Columbia, Missouri. This storm struck at midnight and passed directly through the National Weather Service Station that was equipped with sophisticated weather instruments. During the one-minute period of time containing the maximum gust of the storm, the average wind speed was 50 mph (43.5 kts, 22 m/s) and the largest several second gust peaked at 96 mph (83 kts, 43 m/s), a ratio of 1.92. The results were heavy damage to 24 lightweight aircraft parked outdoors, a hanger, most parked cars, and to other airport facilities. Details and additional references are contained in Reference G-4.

The damage in this incident was certainly not rotorwash related. However, the magnitudes and gust ratio of the wind speeds are certainly representative of the rotorwash field of a large rotorcraft. Therefore, lessons learned from this incident are valuable. Of the 24 aircraft damaged or destroyed, approximately 50% were high wing and 50% were low wing configurations. Many of these aircraft were turned upside down. Most of these aircraft were determined to have had complete failure of their tie-down systems. Two modes of failure were involved: 1) failure of the rope and 2) failure of the connector ring on the aircraft. Samples of the broken ropes, mostly nylon and polypropylene, were collected and laboratory tested. Of the tested ropes, none were able to exceed 40% of the load capability of a new rope of the same material. The processes of aging and weathering (especially due to UV light) had clearly weakened these materials. Subsequent trips to the airport over the next several months documented that the average tie-down procedures used were very lax and often improper to restrain an aircraft.

The survey of vehicle damage in the terminal parking lot indicated that almost all of the vehicles on the north side had lost a windshield or window(s) or both. Paint was also damaged and dents were found in panels. Small gravel was strewn about and was the most obvious source of glass and structural damage (gravel was also found inside vehicles). Safety glass had in many cases been broken and then collapsed and pushed inside the vehicle by the wind dynamic pressure. A survey of the airport layout revealed that the gravel came from a small gravel road to the southwest of the parking lot. Along the line of the wind the gravel had caused substantial damage, including the breaking of windows in the National Weather Service building. Vehicles and structures, such as the terminal building, that were not along the path of the wind from the road did not sustain damage. Additional damage documented at the airport was the result of more random events involving flying debris and structural failure, such as a hanger door.

In the final analysis, if the equipment (ropes and tie-down rings) had met standards and if proper procedures and techniques had been used, then aircraft damage would have been substantially less. If the road and parking lot had been located in the proper location and designed with appropriate materials, then car damage would have been minimal. Other mitigations could likewise have reduced property damage. To avoid rotorwash related damage scenarios, these lessons emphasize that safety factors should be appropriate to consider the effects of weathered and worn equipment, lax procedures, improper techniques, and the unexpected. Standards based solely on damage tolerance test results of equipment when it is new and in a laboratory environment should not be expected to remain valid over extended periods of time in real world scenarios.

References

- G-1. Ferguson, S. W., "Rotorwash Analysis Handbook, Volume I – Development and Analysis," Federal Aviation Administration, Washington D.C., Technical Report DOT/FAA/RD-93/31,I, June 1994.
- G-2. NATOPS Flight Manual Navy Model CH-53E Helicopters, A1-H53BE-NFM-000, 15 August 2002, Naval Air Systems Command.
- G-3. NATOPS Flight Manual Navy Model MH-60S Aircraft, A1-H60SA-NFM-000, 15 March 2005, Naval Air Systems Command.
- G-4. Liu, H., and Nateghi, F., "Wind Damage to Airport: Lessons Learned," Journal of Aerospace Engineering, Vol. 1, April 1988, pp. 105-116.

Appendix H: Collection of Field Experience

Natalie Whitman

This appendix summarizes results of the effort to collect rotorwash field experience. The scope of this collection included:

1. This information includes both airborne and ground operations with field techniques and operational workarounds required to mitigate the outwash effects.
2. Airborne operations pertain to the aerial environment such as air-to-air refueling, air drops, fast roping and recovery by hoist.
3. Ground operations pertain to the surface environment under and around the aircraft.
 - a. Some of the factors that may affect the severity of the ground environment are ground erosion, terrain, ambient wind, footing on ground surface and personnel training and experience
 - b. Some of the factors that may affect the impact of the ground environment are size of the takeoff and landing area and locations of fixed equipment, equipment/supplies and ground personnel.

A questionnaire was formulated that focused on CH-47, CH-53, and V-22 platforms. It was passed out to approximately 15 people ranging from department heads to fleet pilots. Since it was difficult to reach current CH-47 pilots, CH-46 pilots were consulted. The questionnaire also served as a guide during interviews that were conducted. Responses from participants, test results, and NATOPS guidance were combined. A general answer was formulated per platform.

At the time of publication, the results of this effort are not publicly releasable. This appendix in its entirety is contained in a limited distribution annex to this report.

Appendix I: Effect of Rotorwash on Trees and Plants

Sam Ferguson

As far as can be determined from the available literature, no organization or individual researcher has ever formally investigated and documented any information about the effects of rotorwash on trees and plants. However, extensive research has been conducted relative to high wind damage, i.e. hurricanes, on trees in regions such as South Florida. This appendix will attempt to initiate a contribution to the study of rotorwash related effects on trees and plants by first documenting some of the available storm related information. The appendix will propose rotorwash velocity limits and then conclude with documentation from three recent V-22 tilt rotor experiences that add some insight to this subject.

Probably the best general guideline that relates wind velocity to its effect on trees and plants is the “modern” Beaufort scale. Several versions of this scale with slightly varying wording and graphic cartoons have been identified in the literature (References I-1 through I-4). The Beaufort scale is “credited” to Francis Beaufort of the British Royal Navy as the first to devise a scale of wind force. A page from his private log on 13 January 1806 documents his work (Reference I-5). While Beaufort may get credit for organizing his thoughts for water applications and documenting his work, similar scales are now known to have existed from at least a century before Beaufort. By 1780, a “land effects” version of a wind scale involving trees was published by the Palatine Meteorological Society of Mannheim (the world’s first meteorological society). By 1906, a revised Beaufort scale had begun to appear in the literature adding wind’s land effects to the original sea effects. For the reader that is interested in this history, quite interesting text and graphics can be enjoyed with Reference I-5 (as obtained online from the “Met Office” in the U.K.).

Since several versions of the “modern” Beaufort scale were found in the literature with slightly different wording; a “land only” version of the scale has been edited from these sources to create a version for “rotorwash” application. This version, referencing several different units of wind velocity, is presented as Table I-1. This scale can best be described as functionally elegant in that the wording is simple yet concise in providing general guidelines with respect to trees and plants. Several additional comments from the scale that apply to personnel have been added for additional reference.

The Beaufort number that begins to result in tree and plant damage is a value of “8.” This wind velocity range is 17.2 – 20.7 m/s (34 - 40 kts). The observations note that the wind breaks twigs and small branches and that the ground becomes littered with broken vegetation. From a personnel perspective, walking is considered to be difficult. At the other extreme, substantial forest destruction is easily verified in the literature at a Beaufort value of “11” (References I-6 through I-9). Reference I-6 notes that peak winds of < 35 m/s (68 kts) resulted in devastating forest tree loss in Sweden in January 2005. However, for scientific integrity, it must be noted that these winds were not peak gusty winds of short duration like rotorwash. These trees were also exposed to their full vertical extent, significantly above that obtained with a rotorwash profile. References I-7 through I-9 document the damage details and statistics for a substantial number of tree species on the

U.S. Gulf Coast for ten hurricanes with sustained winds ranging from 80 to 165 mph. The corresponding urban forest loss, in percent (%), varied from 11 to 38 % (Figure I-1).

Table I-1 Modern Beaufort Scale for Rotorwash Application

Beaufort Number	Wind Velocity			Observations
	m/s	kts	mph	
1	0.3 - 1.5	1 - 2	1 - 3	Wind barely moves tree leaves.
2	1.6 - 3.4	3 - 6	4 - 7	Leaves rustle and small twigs move.
3	3.4 - 5.4	7 - 10	8 - 12	Leaves and small twigs in constant motion. Wind blows up dry leaves from the ground.
4	5.5 - 7.9	11 - 15	13 - 17	Wind moves small branches.
5	8.0 - 10.7	16 - 20	18 - 24	Large branches and small trees in leaf begin to sway.
6	10.8 - 13.8	21 - 26	25 - 30	Large branches in continuous motion. [Umbrellas difficult to control]
7	13.9 - 17.1	27 - 33	31 - 38	Whole trees in motion. [Becoming difficult to walk]
8	17.2 - 20.7	34 - 40	39 - 46	Wind breaks twigs and small branches. [Walking is difficult]
9	20.8 - 24.4	41 - 47	47 - 54	Ground is littered with many small twigs and broken branches. [Construction/temporary signs and barricades blown over. 40 - 72 mph is F0 tornado on Fujita Tornado Scale]
10	24.5 - 28.4	48 - 55	55 - 63	Small trees may be blown over and uprooted (and broken). Saplings bent and deformed.
11	28.5 - 32.6	56 - 63	64 - 72	Widespread damage to vegetation. Larger trees blown over and uprooted.
12	≥ 32.7	≥ 64	≥ 73	Severe and extensive damage. Trees uprooted. [> 73 mph is Category 1 hurricane on Saffir-Simpson Hurricane Scale, F1 tornado on Fujita Tornado Scale]

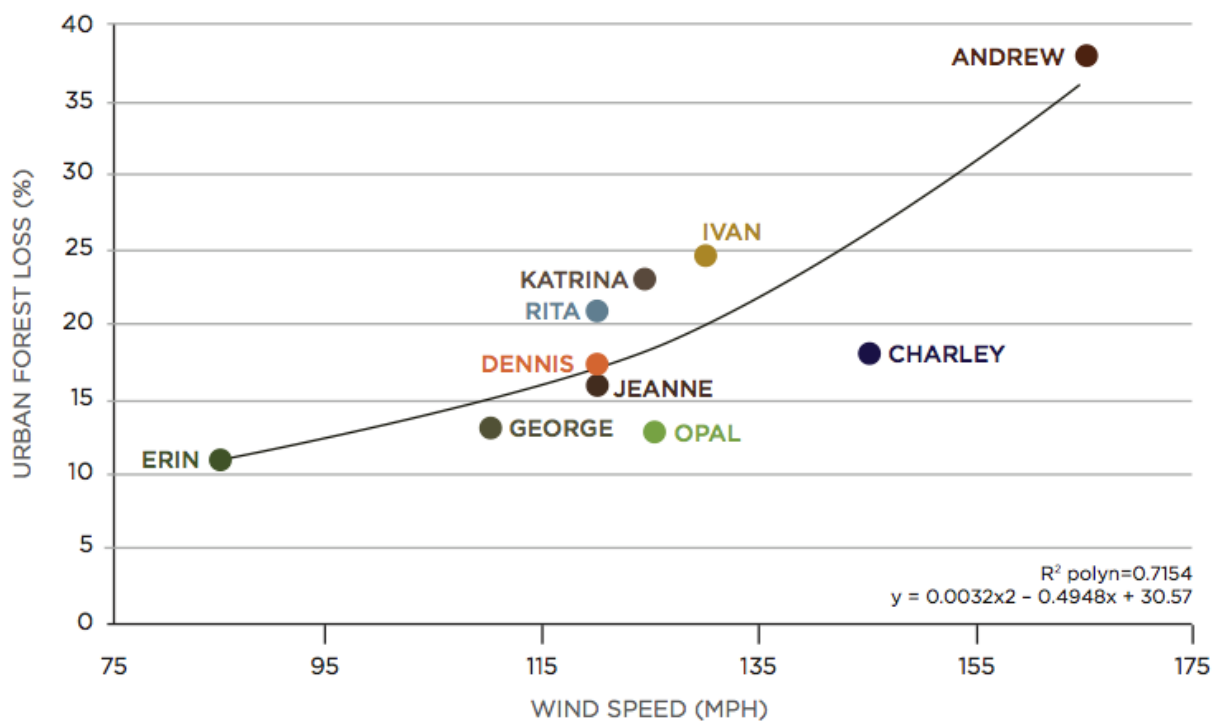


Figure I-1 Urban Forest Loss as a Function of Wind Speed in Ten Hurricanes (Ref. I-6)

Analyzing the mechanics of tree (or plant) dynamics and predicting damage is not a simple task. The literature documents finite element models for trees, simulation models for tree

and forest dynamics as well as documentation of tree overturning force, bending moment, and damping ratio tests (References I-10 through I-12). It would appear that more than just helicopter engineers are interested in dynamics simulation.

Factors that affect tree and plant damage are both intuitive and non-intuitive to the rotorcraft engineer. Figure I-2 provides a free-body diagram of the basics or more intuitive factors that would be expected.

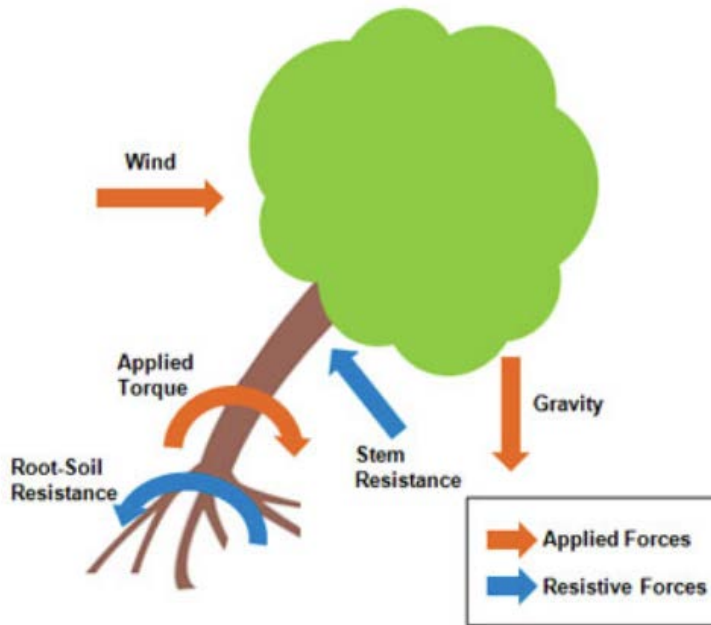


Figure I-2 Forces and Factors Acting on a Tree in High Winds (Reference I-6)

However, the non-intuitive factors for trees and plants are just as critical to determining their vulnerability to damage. A tree or plant's susceptibility to wind damage is affected by a complex relationship between wind, climate, individual tree/plant and stand characteristics, soil and site conditions, and mitigation and management practices of those responsible for tree/plant growth. These factors are summarized in Figure I-3.

Tree/plant/site characteristics that affect the ability to resist wind include:

- Height—taller generally more vulnerable
- Age—older generally more vulnerable
- Slenderness Ratio—broader are less vulnerable
- Species—root structures, height/diameter ratio (lower is better), density of branches/leaves, trunk/crown characteristics, wood density (higher is better)
- Soil—type, moisture level, bedrock depth, temperature (frozen topsoil better)
- Stand—density, thinning, open gaps, shape perimeter
- Terrain—slope, elevation, nearby barriers
- Climate—trees adapt based on average wind speeds

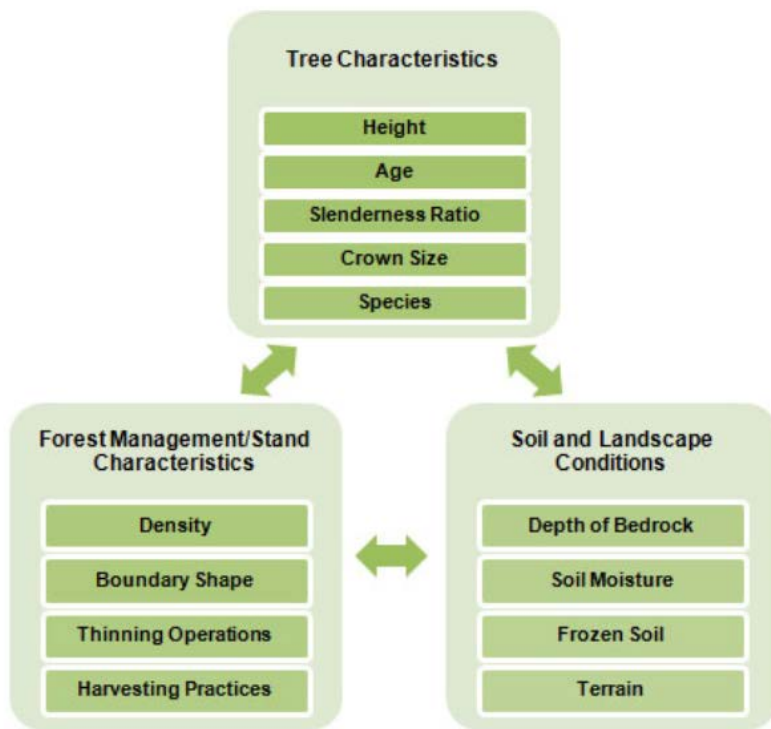


Figure I-3 Vulnerability Complexity for Tree Damage in Winds (Reference I-6)

Examples of critical wind speeds over the duration of 1 hour that significantly damage fully immersed Norway Spruce, Scots Pine, and Birch are provided in Figure I-4. Unfortunately, no known link exists between these data and smaller sizes of these trees for much shorter durations of time.

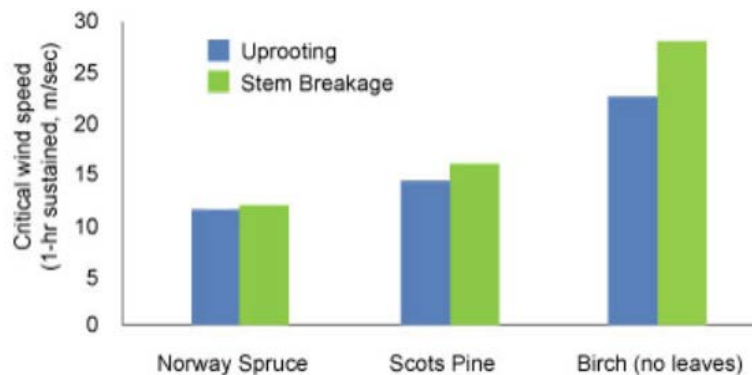


Figure I-4 Critical Wind Speeds for Three Types of Trees (Reference I-6)

A study of tropical tree damage from storms (Reference I-13) documents additional data as based on peak gust speed data. For 81 species identified in these regions at 18 sites, at gust

velocities < 16.6 m/s (32.4 kts) there was minimal damage. Beginning at 16.6 m/s the damage increased rapidly with gusts up to 36.1 m/s (70 kts). At speeds higher than 36.1 m/s, the damage was severe enough that little additional damage could be measured. Statistical results are also provided in this reference for the interested reader. It is important to note that these results compare very well with the general results presented in Table I-1.

As stated in the opening paragraph, no known studies have been made that evaluate the effect of rotorcraft on trees and plants. Therefore, other than the proposed "Modern Beaufort Scale for Rotorwash Application" (Table I-1), any definitive and quantitative criteria involving rotorcraft that could be proposed simply don't have a solid technical basis for adoption at this time. However, there are lessons that can be learned from the literature for rotorwash application. Reference I-9 provides an excellent summary of lessons learned from storms. The relevant points that will be applicable to the subsequent V-22 case studies are as follows:

1. As trees age, they encounter root, stem, and branch decay. Usually, those responsible do not regularly trim dead and weak branches from the canopy. When storm winds are encountered, the research clearly documents that larger trees (40 to 79 inches in diameter) lose a significantly greater percentage of their branches when compared to small trees (less than 8 inches in diameter). Unfortunately, the loss of branches from large trees also significantly increases the risk of collateral damage when the failure occurs. Reference I-7 notes the statistic that 20% of trees and branches that fall damage property. Of those trees and branches that do fall, 74% damage major property (house, power lines, screened enclosures, automobiles, and so on) and 26% damage minor property (fences, sheds, sidewalks). Research verifies that when trees are properly pruned, they are much more likely to survive high winds with much less damage. Reference I-14 provides excellent information on how a tree should be trimmed for encountering high winds.
2. A strong supporting root system with adequate rooting space is the most critical factor to the ability of trees to withstand high winds. Therefore, when trees and plants are planted in close proximity to sidewalks, curbs, buildings, parking lots, driveways, and other urban structures, they are prone to stem or overturning damage due to restricted root development.
3. Leaf loss in high winds does not mean that a tree is dead, just that photosynthesis is stopped (temporarily). This result can be a good strategy by a tree or plant species to reduce drag on the limbs and reduce long-term damage.

The relevance of these factors will become more instructive in the three V-22 tilt rotor case studies that are presented in the following sections in chronological order. It is important to note that the V-22 is not necessarily any more likely to cause tree or plant damage than another high disk loading rotorcraft, i.e. the CH-53E. It is simply the result of data availability that causes the three case studies to be V-22 related.

Based on the available research, the proposed rotorwash landscape limit in a civil environment is 39 mph peak velocity at sea level standard conditions. This value is the lower value in the Beaufort Number 8 condition listed in Table I-1 for the proposed modern Beaufort scale for rotorwash application. Observations for this condition are "Wind breaks twigs and small branches. [Walking becomes difficult]." The value of 39 mph (17.2 m/s) corresponds well to results contained in Reference I-13 that document storm damage to tropical trees increased rapidly for wind gust velocities > 16.6 m/s. For gust velocities < 16.6 m/s there was minimal damage reported.

V-22 Case Study #1—Frankfort, KY - September 29, 2009

While few factual details are documented about this incident in the press, it occurred as the result of an “urban training” exercise in Frankfort, KY on the evening of September 29, 2009. According to Reference I-15, “Neighbors say the aircraft was flying right over their rooftops and caused tree limbs to come crashing down, lawn furniture to be thrown several feet, and playsets to be tipped over.” Available documented details relative to the incident should be available from the files of the 24th Marine expeditionary unit (a Captain Robert Shuford is reported to have investigated and apologized for the unfortunate aspects of the training exercise). In lieu of the documentation, it is clearly indicated that the over flight of a V-22 in an approach to a confined area will produce downwash of a strength to dislodge old branches from trees. While no injuries were reported, it is possible that they could have occurred had people been present in certain locations. More detail will be discussed on the quantitative numbers associated with this downwash in V-22 Case Study #2.

V-22 Case Study #2—Clove Lakes Park Preserve, Staten Island, NY - May 31, 2010

During Memorial Day “Fleet Week” demonstrations on May 31, 2010, a V-22 made a landing in the Clove Lakes Park Preserve, Staten Island, NY. The landing approach was probably very similar to that discussed in the previous case study. However, this time when the trees were over flown, approximately 10 people were injured and the incident was well documented by the press on video. References I-16 through I-19 provide “representative” press reports. Unfortunately, no credit can be provided to the many video sources due to the length of time since the incident. However, many of the video sources are still accessible on the Internet.

The incident occurred at approximately 9:10 a.m. As the V-22 flew over several older and mature trees, the downwash broke off numerous branches, both large and small. Reference I-19 reports one person as stating, “Branches just came down. They were all over the park. ... It was really scary.” The reporter also notes that, “one tree lost all its branches on one side.” A different observer noted, “It looked like two tornadoes, the trees were bending and then branches broke.” Fire Department Chief Dan O’Gara reported approximately 10 heavy limbs on the ground. Other rotorcraft (i.e. a CH-46 and AH-1W) preceded the V-22 in the landing sequence. It must be noted that these aircraft “could” have weakened the branches of the trees that the V-22 subsequently broke. However, there is no way this possible contributing factor can be verified.

Video from the incident indicates that at the time the V-22 passed over the trees, it was probably less than one wing-span (50 ft) from the top of the tree canopy. The V-22 was traveling forward at a very slow airspeed with a slight rate of descent. Nothing is known about the ambient wind. If it is assumed that the downwash approximates the momentum calculation of induced velocity near the tree canopy, then for 45,000 pounds gross weight (troops were onboard for a deployment demonstration), the induced velocity should be approximately 110 to 120 ft/sec (65 to 71 kts). Based on the proposed modern Beaufort scale for rotorwash application (Table 1), this would be a Beaufort Number 11.



Figure I-5A Overhead View of Approach—Limbs in Center Have Just Broken



Figure I-5B Front View Past Trees Prior to Landing



Figure I-5C Landing with CH-46 in Background



Figure I-6A Broken Branches and Severely Damaged Tree Stems



Figure I-6B Broken and Severed Branches



Figure I-6C Broken Limb



Figure I-6D Broken Branches on Ground



Figure I-7 Red Garbage Can Airborne

This Beaufort value would result in the expectation of large branch damage, particularly for mature trees that are not regularly pruned. This result is exactly what is indicated in the photos from the various video sources (Figures I-5 and I-6). It is also very interesting to note that a garbage can is airborne in Figure I-7 as an extremely dangerous piece of flying debris.

Fortunately, according to Lauren Schulz of the U.S. Marines, all of the injuries were minor (to spectators), with seven people transported to Richmond University Medical Center and the rest receiving treatment on the scene. All injured were released by the end of the same day. Ms. Schultz also states, “as is standard with military public displays, medical and fire personnel were already on the ground and prepared to deal with the accident.” The event was continued as planned, and the crowd could be seen touring the aircraft once it was on the ground safely.

Two conclusions from this incident (and Case Study #1) are:

1. The previously discussed storm research that documents issues associated with aging trees and their vulnerability to high winds clearly applies to rotorcraft situations and cannot be ignored.
2. Using the V-22 or any other higher disk loading rotorcraft in a disaster or an urban area is going to present operational problems unless careful attention is directed to learning from these mishaps. These mishaps are classic examples of “teachable moments.”



Figure I-8A Vertical Landing on Sand Soil



Figure I-8B Sand and Debris Blown Inside MIT Window

In ending this case study, one additional comment was made in the press that revealed additional interesting results. This comment was by Vickie Karp, a Parks spokeswoman. She stated that the V-22 had been displayed in Boston and Maryland for similar events without any problems. Information was uncovered for one Boston event where the V-22 was landed at MIT's large intermural field (Reference I-21). Clearly trees are not a problem, but it is curious why the pilot decided to land in the center of the field where sand was clearly exposed. He could have just as easily made a choice to land on the grass (Figure I-8). The student taking the video from his office or dorm room window makes the comment on the video, "Ha Ha, I should have closed my windows." While the details of this decision are unknown, at first glance this would appear to be a case where the wise and "fly neighborly" decision was not made.

V-22 Case Study #3—AHS 2011 Annual Forum, Virginia Beach, VA - May 4-5, 2011

This case study focuses on the recent public display of the V-22 at the American Helicopter Society's (AHS) 2011 Annual Forum at the Virginia Beach, VA convention center. Todd Hodges and John Davis (who both attended the Forum) coordinated and provided the majority of the source information presented in this case study. Many of the photos and video were provided by the staff of the Virginia Beach Convention Center (Cassandra B. Murdough and Katie Glaser). The effort of each of these contributors is most appreciated.

The V-22 arrived at Virginia Beach Convention Center extremely early (6:50 a.m.) on the morning of May 4, 2011. It departed early the next morning. The work to prepare a safe Landing Zone (LZ) to display the aircraft was initiated several days prior in the adjacent parking area. Figure I-9 provides a general layout of the parking area and notes several items that will be discussed in subsequent paragraphs. The primary "modification" to the LZ was the removal of six light poles to clear an approach to the 146-ft by 116-ft touchdown area. The light pole locations are indicated by the placement of the red stars in Figure I-9. Figure I-10 provides an expanded overhead view of the area around the convention center for additional reference (LZ marked by the red box).

The aircraft and atmospheric positions at the time of the landing and takeoff were reported by several sources. Unfortunately, the reported winds at the approximate time of landing in the parking area are conflicting. However, the convention center LZ location could have easily experienced wind blockage at touchdown that resulted in lower observed winds than were reported at nearby airports that were clear of trees and buildings. A brief summary is as follows:

- Pilot (Major Samuel Schoolfield, USMC) reported that the winds were calm during landing and a 5-kts tailwind was observed during takeoff. The estimated gross weights were 41,000 pounds for landing and 42,000 pounds for takeoff.
- Winds at 7:00 a.m. were reported as 210 degrees at 9 kts at Oceana NAS (2.5 miles away) and 220 degrees at 10 kts (12.5 miles away) at Norfolk Airport.



Figure I-9 V-22 Landing Zone at Virginia Beach Convention Center

The V-22 approach and landing were captured on video from several angles by both private and press cameras. Figure I-11A provides photos of the V-22 at the moment it reached a high hover over the touchdown point (> 100 ft at 57 seconds on video clock). Figure I-11B indicates touchdown after a slow vertical descent at 1:32 seconds. This was followed by main landing gear strut compression (power lever to idle power) at 1:37 seconds. Figure I-11C documents the final shutdown position.

The first task in the analysis of rotorwash effects on the trees and plants in the LZ area began with a review of the videos and photos to obtain the exact touchdown points for the nose and main gear. This task was easily accomplished using the numerous available photos and the residual heat marks left by the engine exhaust on the asphalt surface. Detailed position measurements were made in late June 2011 in the parking lot to document the position and survey the health of the adjacent trees and plants. The measured target positions were the left-side tire locations on the nose and left main gear due to the photo information. Examples of the available photos are presented in Figure I-12. The accuracy of tire location is estimated to be within less than one foot for documentation purposes. The measurement between the targets, 26.05 ft, was verified to be < 0.2 ft from the expected dimension based on a V-22 lines drawing.

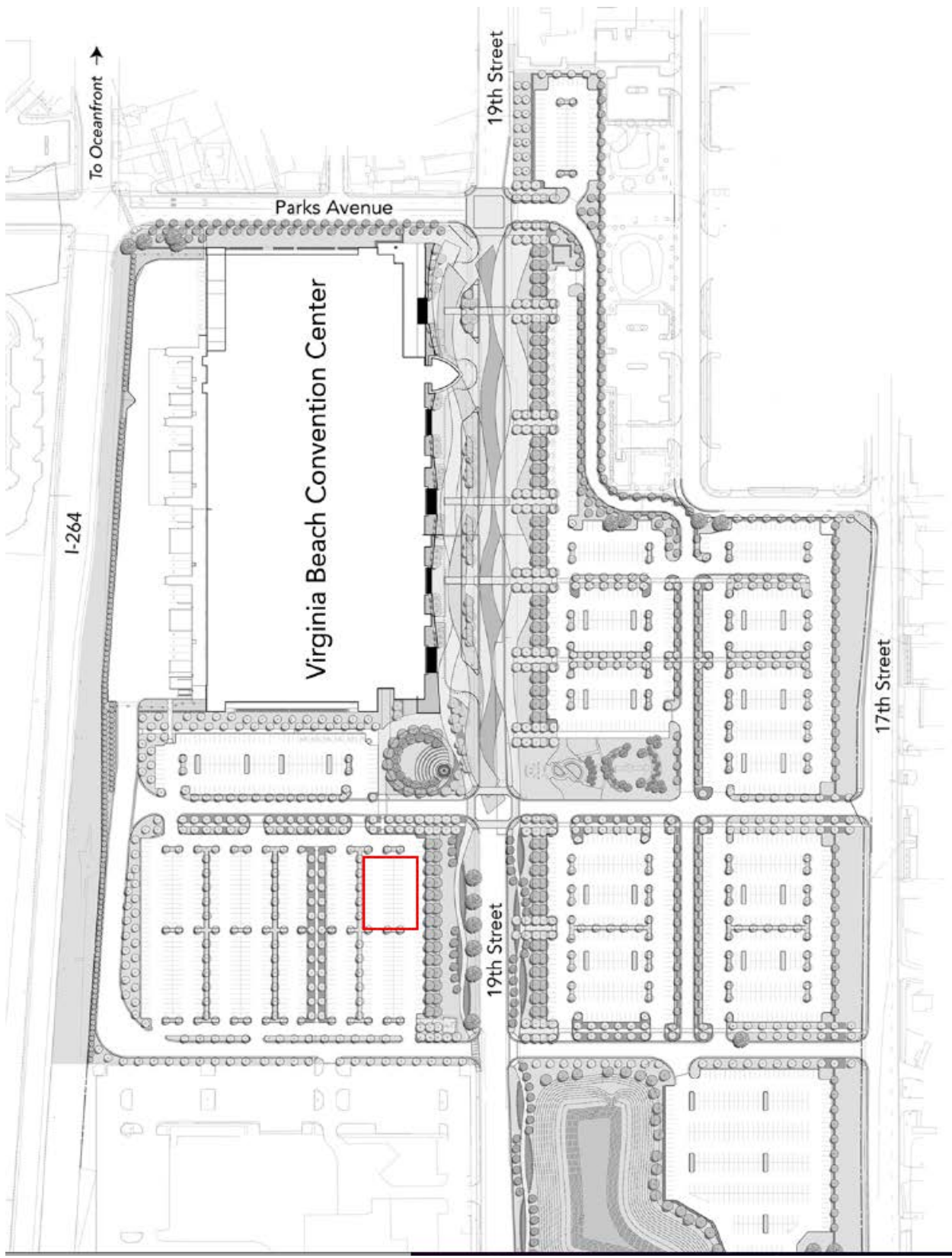


Figure I-10 Expanded View of the Virginia Beach Convention Center



Figure I-11A V-22 High Hover Position at 57 Seconds

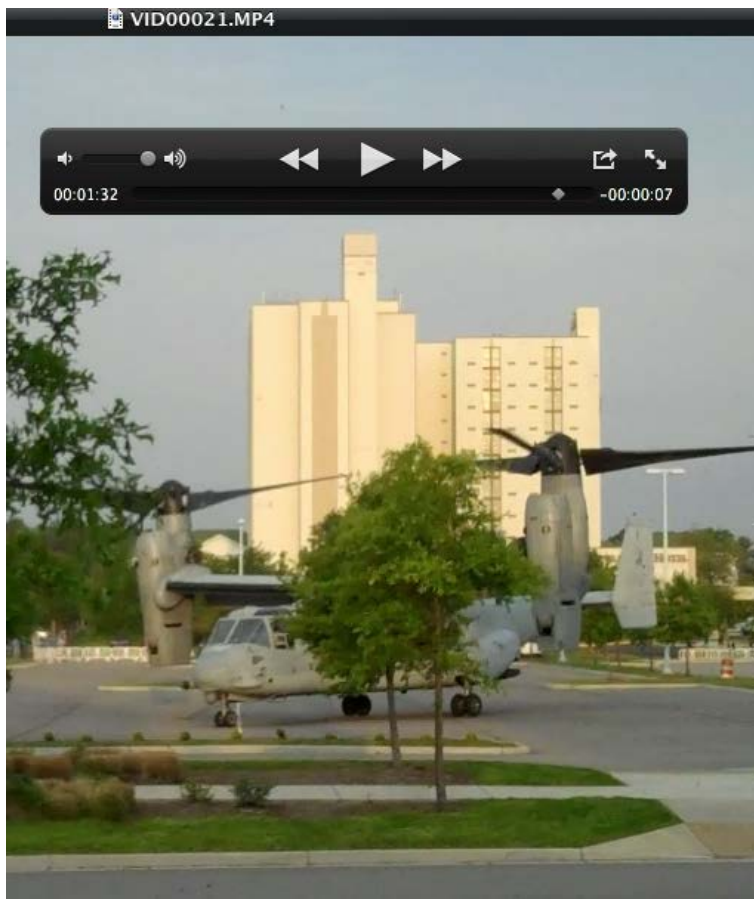


Figure I-11B V-22 Touchdown Position at 1:32 Seconds



Figure I-11C V-22 Final Position at Shutdown, > 1:37 Seconds



Figure I-12 Examples of Landing Gear Location Photos

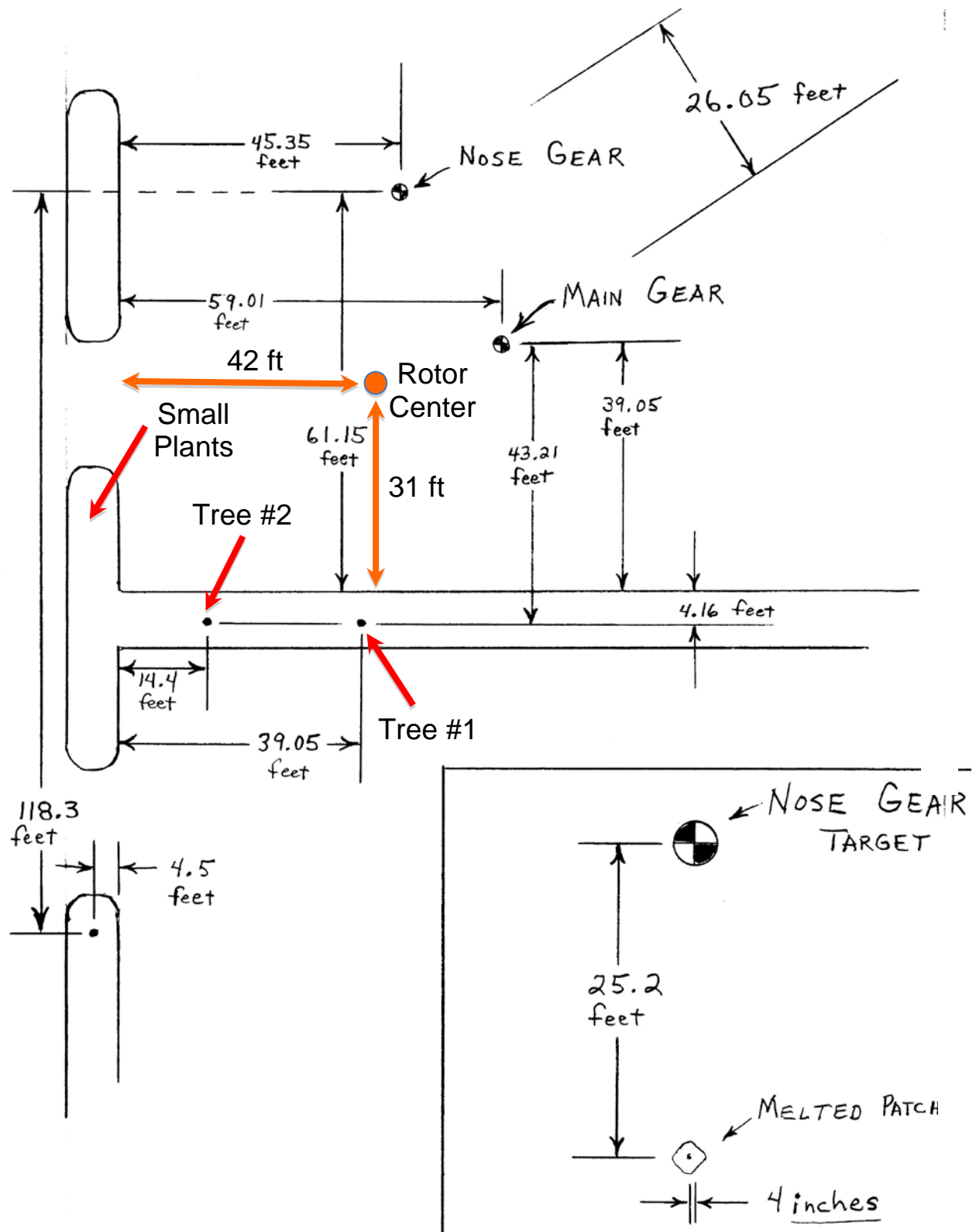


Figure I-13 Sketch of Key LZ Dimensions (Courtesy Todd Hodges)

Using the measured tire location data, the center of the left-hand rotor was located using lines data. Each of the important dimensions that are required for the rotorwash analysis is documented in Figure I-13.

Now that the background information has been presented, it is possible to analyze the rotorwash effects on the trees and plants. Four major topics will be covered as follows:

1. Rotorwash impact on trees
2. Rotorwash impact on flowering plants
3. Unexpected impacts
4. Lessons learned

The primary reason that this study was considered worthwhile was the result of the accidental discovery of video showing the V-22 rotorwash impact on the trees noted as Trees #1 and #2 in Figures I-9 and I-13. Tree #1 can also be seen in the highlighted background of Figure I-11C with rotors turning and at rest in Figure I-14. The video was being broadcast as part of the weekly podcast of "This Week @ NASA" on May 6, 2011 (reference I-22). Two frames from this video are shown in Figure I-15. In the frame noted as Figure I-15A, Tree #1 cannot be seen on the horizon because the upper portion of the tree is almost horizontal to the ground. In Figure I-15B, the rotor thrust has been reduced following touchdown and the tree is returning to the vertical. If the video is watched in its entirety, Trees #1 and #2 take an incredible beating for between 1 to 2 minutes.



Figure I-14 Tree #1—No Wind



Figure I-15A Tree #1 Blown Almost Horizontal in Low Hover



Figure I-15B Tree #1 Returning to Vertical after Touchdown

After watching this video, the question immediately arose, "I wonder what the long term effects of this rotorwash are on these trees and the other plants in the immediate vicinity of the landing?" Using the geometry information in Figure I-13, it is possible to determine the approximate distance and azimuth to several of the critically positioned trees and plants. These distances are based upon the touchdown position/azimuth of the V-22 and assume the descent from 100 ft was totally vertical. These data are approximately as follows. Note, as a reference, straight out the LH wing from the aircraft center through the LH rotor hub is 270 degrees:

Tree / Plant (Figure I-13)	Distance From LH Rotor, Ft	Azimuth From LH Rotor, Deg	Distance From A/C Center, Ft	Azimuth From A/C Center, Deg
Tree #1 (Willow Oak) 16 ft tall, 10.1 in circumference @ 2 ft	36	231	55	247
Tree #2 (Willow Oak) 14 ft tall, 10.5 in circumference @ 2 ft	45	263	68	266
Small Plants (Nandina Domestica or Fireplant)	48 - 52	292 - 297	70 - 74	285 - 288

With the distances and azimuths identified, it is possible to use the conceptual level model (RoWFoot) described in Appendix J to calculate the mean and peak rotorwash velocities present at the location of the plants. At a gross weight of 42,000 lb and a wheel height of 20 ft, the rotorwash profiles at 36-, 45-, and 50-foot distances from rotor center are presented in Figures I-16, I-17, and I-18 for Tree #1, Tree #2, and the Small Plants respectively.

Tree #1, as listed in the table, is located at 55 ft at 247 degrees from the center of the V-22. This corresponds to 36 ft at 231 degrees azimuth from the V-22 port rotor. As shown in the photo in Figure I-14, most of the limbs are located above 5 feet (photo taken in June after the AHS Annual Forum). Therefore, using Figure I-16, the highly oscillatory rotorwash velocity impinging upon the majority of the tree should vary from a mean of approximately 10 kts to a peak of as high as +45 kts in the 5- to 7-foot height range. Based on correlation studies, it is believed that the conceptual model slightly underpredicts the peak velocity at these heights close to the rotor. It is important to note that rotorwash has a destabilizing effect on a tree. This means that as a tree is blown more horizontal (Figure I-15A), more of the tree is repositioned into the higher velocity part of the rotorwash profile so that the tree is bent over even further. This range of velocity puts Tree #1 into a Beaufort number range of between 9 and 10 (Table I-1). This Beaufort number range is near the critical area for a tree. However, this willow oak apparently survived without any apparent damage. This good fortune is probably a result of the following known facts:

1. Willow oaks are strong trees and recommended for hurricane areas (Ref. I-7, I-9)
2. Tree #1 is young, healthy, has small flexible limbs, and is not dry
3. Tree #1 is cared for on a scheduled basis and is pruned

4. Exposure time to the rotorwash was short in duration

Tree #2 is located at 68 ft at 266 degrees from the center of the V-22 with corresponding location relative to the port rotor of 45 ft at 263 degrees azimuth. A similar analysis, using Figure I-17, for this willow oak indicates that the rotorwash velocities are similar in magnitude from a mean of approximately 10 kts to a peak of as high as +45 kts in the 5- to 7-foot height range. This range of velocity also puts Tree #2 into a Beaufort Number range of between 9 and 10. This Beaufort number range is still near if not in the critical range for most trees. However, like Tree #1, this willow oak also appears to have survived without any apparent long-term damage.

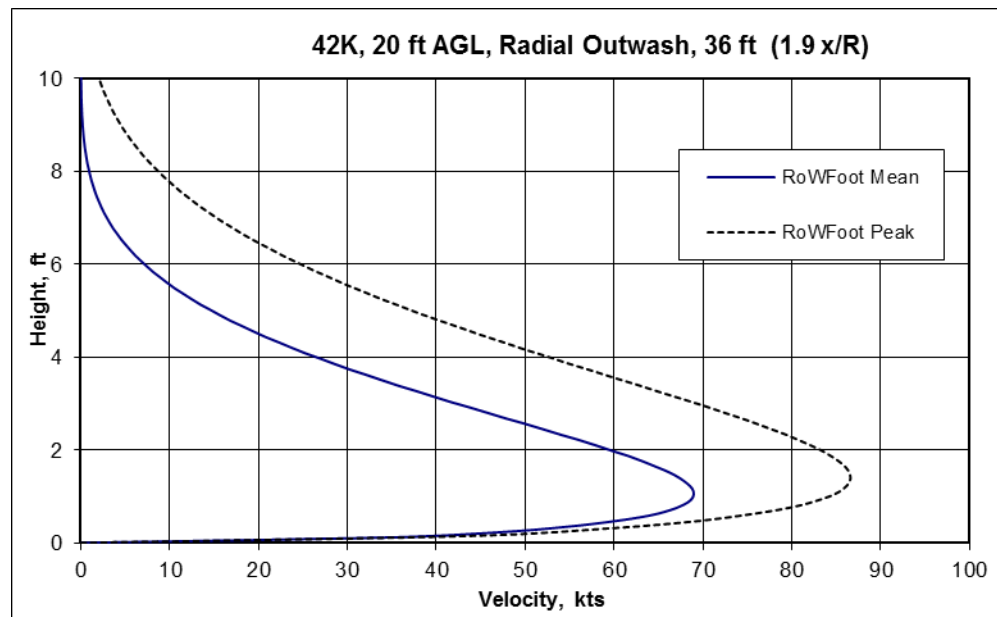


Figure I-16 V-22 Mean/Peak Velocities at Tree #1

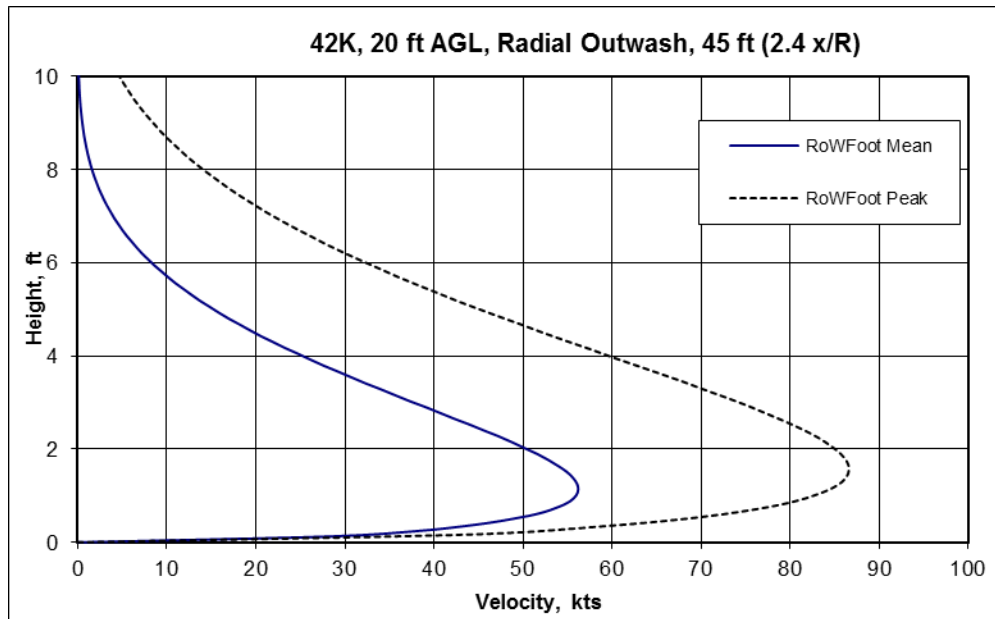


Figure I-17 V-22 Mean/Peak Velocities at Tree #2

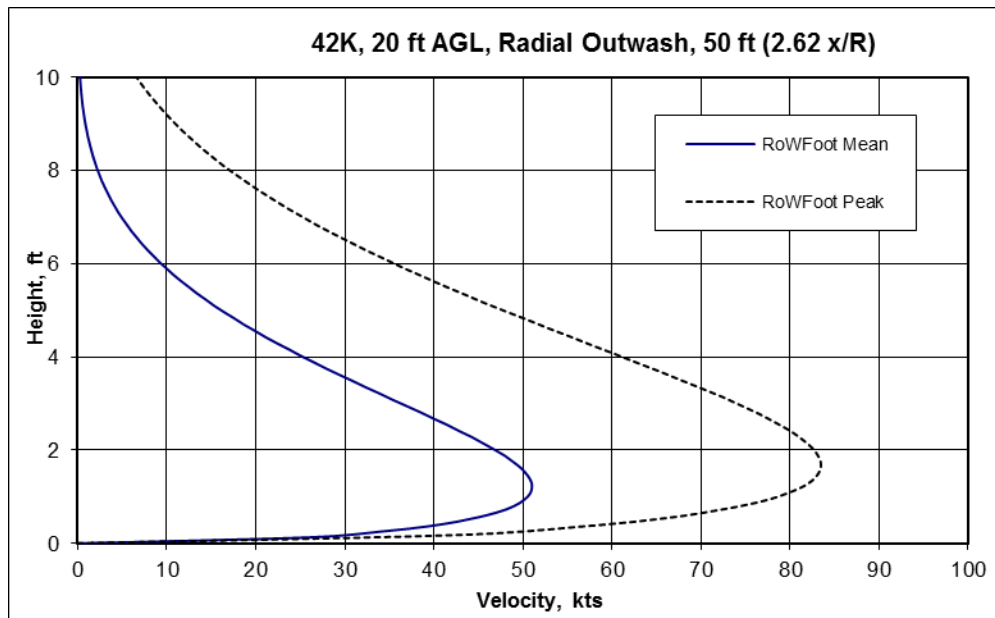


Figure I-18 V-22 Mean/Peak Velocities at the Small Plants



Figure I-19 Tree #1, Tree #2, and Fireplants in Late June 2011

The rotorwash effect on the small *Nandina Domestica* (or Fireplant) plants shown in the photos also appears to be minimal. The gardening staff indicated that none of the plants died after the V-22 event and their health in late June was judged to be equal to other plants in similar settings around the convention center (see plants in foreground of Figure I-19). However, the plants were very young and small at the time of the event (based on the video information) and have had time to grow significantly. Their minimal height at the time of the event probably located them within the boundary layer of the rotorwash profile. Based on the location of the plants (approximately 70 to 74 ft at 285 to 288 degrees from aircraft center), if they had been a little taller they could have experienced peak rotorwash velocities in the range of +80 kts (see Figure I-18). This would equate to a Beaufort Number 12, a Cat 1 or greater hurricane. Therefore, the survival of these plants with minimal damage could be explained as the result of "lucky" timing and the short exposure time.

Takeoff exposure time, as based on the video, was much shorter as the V-22 lifted off and proceeded to make a rapid vertical climb. Therefore, it is concluded that the exposure of the trees and plants was minimal upon departure.

One significant, yet unexpected impact of the V-22 landing was the quantity of debris blown on the spectators and video personnel. More specifically, after departure over 40 cubic yards of garden mulch had to be replaced in the flowerbeds around the LZ. This problem was clearly visible in all of the videos and can be clearly observed in Figure I-11A when blown up in size. Fortunately, the mulch was extremely low in density and its impact on personnel did not result in any injuries. However, a risk existed in that someone could have fallen in trying to avoid the debris or had the debris enter an eye. The results could then have been much more serious (eye injuries are discussed in detail in [Appendix C](#) of this report). Also, some risk existed for engine FOD. However, rotorcraft are designed for landing on unprepared surfaces where similar FOD matter would be expected to exist. In summary, this unexpected consequence is another factor that should be considered in future large rotorcraft demonstration events.

Conclusions

Several conclusions that can be made from Case Study #3 (and the other two case studies to a lesser extent) are as follows:

1. The event was well planned by the AHS and the VBCC personnel. The LZ was carefully surveyed and obstructions (light poles) were removed. Except for the risk presented by the mulch debris to personnel or as engine FOD, no significant problems or plant damage occurred.
2. The analysis of the two willow oak trees further verifies expectations based on the storm literature. Young, healthy and well-maintained trees and plants can generally be expected to withstand most rotorwash scenarios without significant damage. However, this observation does not mean that if the trees had been a different species or if several of the factors discussed earlier in this appendix were different that the exact same positive outcome would have occurred. This warning is very clear from the storm literature. For example, had the trees been older, less healthy, and poorly pruned, then Case Study #2's unfortunate results could have been repeated at this site.
3. While very simple in format, the proposed "Modern Beaufort Scale for Rotorwash Application" (Table I-1) appears to survive this initial test of its usefulness as a predictive guideline for rotorwash interactions with trees and plants. Considering the expense required to obtain more quantitative data for criteria development, this scale may be the best available tool for the foreseeable future.
4. Like always, the unexpected impacts are what cause problems and incidents. In this case study, it could have been the debris if the density of the mulch had been higher. In Case Study #2, the large old trees were assumed strong because they had been there a long time. Also, a survey of the site did not identify the garbage barrel hazard. Therefore, the strongest conclusion resulting from this review is that vigilance must never stop in trying to "expect the unexpected" with the demonstration of rotorcraft in close proximity to people.

References

- I-1. Anon, "Beaufort Scale," Wikipedia, 2011 [http://en.wikipedia.org/wiki/Beaufort_scale].
- I-2. Anon, "Estimating Wind Speeds with Visual Cues," National Weather Service Portland [<http://weather.gov/portland>].
- I-3. Anon, "The Beaufort Scale," Howtoons, 2006 [<http://www.howtoons.com/wp-content/uploads/2009/05/beaufortscale.png>].
- I-4. Cullen, S., "Trees and Wind: Wind Scales and Speeds," Journal of Arboriculture, September 2002.
- I-5. Anon, "Beaufort," National Meteorological Library and Archive (Met Office), United Kingdom, 2010 [http://www.metoffice.gov.uk/media/pdf/4/4/Fact_Sheet_No._6_-Beaufort_Scale.pdf].
- I-6. Kafali, C., "Gone With the Wind: Modeling Forest Risk in Europe," Air Worldwide, February 2011 [<http://www.air-worldwide.com>].
- I-7. Duryea, M. L.; Kampf, E.; and Littell, R. C., "Hurricanes and the Urban Forest: I. Effects on Southeastern United States Coastal Plain Tree Species," Arboriculture & Urban Forestry, March 2007.
- I-8. Duryea, M. L.; Kampf, E.; Littell, R. C.; and Rodriguez-Pedraza, C. D., "Hurricanes and the Urban Forest: II. Effects on Tropical and Subtropical Tree Species," Arboriculture & Urban Forestry, March 2007.
- I-9. Duryea, M., and Kampf, E., "Wind and Trees: Lessons Learned from Hurricanes," University of Florida IFAS Extension, Publication No. FOR 118, February 2011 [<http://hort.ifas.ufl.edu/treesandhurricanes/>].
- I-10. Bruchert, F., and Gardiner, B., "The Effect of Wind Exposure on the Tree Aerial Architecture and Biomechanics of Sitka Spruce," American Journal of Botany, 2006.
- I-11. Gardiner, B.; Byrne, K.; Hale, S.; Kamimura, K.; Mitchell, S.; Peltola, H.; and Ruel, J., "A Review of Mechanistic Modeling of Wind Damage Risk to Forests," Forestry, 2008.
- I-12. Kane, B., and Clouston, P., "Tree Pulling Tests of Large Shade Trees in the Genus Acer," Arboriculture & Urban Forestry, March 2008.
- I-13. Francis, J. K., and Gillespie, A., "Relating Gust Speed to Tree Damage in Hurricane Hugo, 1989," Journal of Arboriculture, November 1993.

I-14. Broschat T. K., and Burch, D., "How to Minimize Wind Damage in the South Florida Landscape," University of Florida IFAS Extension, Publication No. ENH64, August 2010 [<http://edis.ifas.ufl.edu>].

I-15. Kennedy M., "Marine Aircraft Causes Damage in Neighborhood," WKYT 27, Lexington, KY, September 29, 2009 [<http://www.wkyt.com/news/headlines/62770327.html#>].

I-16. Karoliszyn H.; Yaniv, O.; and Nelson, K., "Marine Corps Osprey Helicopter Landing Injures Ten in Staten Island Park During Memorial Day Event," NY daily News, May 31, 2010 [http://www.nydailynews.com/ny_local/2010/05/31/2010-05-31_marine_corps_osprey_helicopter_landing_injures_eight_in_staten_island_park.html].

I-17. Hooper C., "Osprey Downdraft: MV-22 Wounds 10 at NYC Fleet Week," Next Navy, May 31, 2010 [<http://nextnavy.com/osprey-downdraft-mv-22-wounds-10-at-nyc-fleet-week/>].

I-18. Solomon J., "Wind Blast from Aircraft Downs Limbs at Ceremony, 10 Injured," CNN, May 31, 2010 [http://articles.cnn.com/2010-05-31/us/new.york.fleetweek.accident_1_tilt-rotor-aircraft-marines-coast-guard-team?s=PM:US].

I-19. Peltz J., "Osprey Mishap Injures 10 at NYC Park," Marine Corps Times, June 1, 2010 [http://www.marinecorpstimes.com/news/2010/06/ap_osprey_mishap_nyc_060110/].

I-20. Anon, "Military Fly-Over Injures 10 on Staten Island," NY1 News, May 31, 2010 [http://statenisland.ny1.com/content/top_stories/119548/military-fly-over-injures-10-on-staten-island].

I-21. Mills C., "Looked Out My Window and What Did I See," MIT Admissions Blog, May 3, 2010 [http://mitadmissions.org/blogs/entry/looked_outside_my_window_and_w].

I-22. Anon, This Week @ NASA Podcast, May 6, 2011 [http://www.nasa.gov/multimedia/podcasting/TWAN_05_06_11.html].

I-23. Lake, R. E., and Clark, W. J., "V-22 Rotor Downwash Survey," NAWCADPAX-98-88-RT, July 1998.

Appendix J: Conceptual Level Model FORTRAN Code

Sam Ferguson

Rotorwash modeling methods, like most aerodynamics models, vary from simple conceptual models to the highly complex Computational Fluid Dynamics (CFD) models. A viable conceptual level rotorwash model requires rapid computational turnaround time with the ability to quickly adjust for rotorcraft configuration differences, i.e. single main rotor, tandem, and tilt rotor configurations. These requirements inherently lead to the development of a simple modeling approach. The modeling approach that best meets these requirements is described as the momentum-based aerodynamic approach as empirically tuned to correlate with a database of test data for difference rotorcraft configurations.

Historical Perspective on Momentum-Based Rotorwash Modeling

Momentum-based models for helicopter rotor aerodynamics have a long history and are described in all rotorcraft aerodynamic textbooks. Gessow and Myers authored one of the classic texts on this subject in 1952 (Reference J-1). In 1968, George, Kisielowski, and Douglas (Reference J-2) further developed this modeling approach for helicopter rotorwash applications. Previously, Glauert (Reference J-3) and others had developed simple models for “hovering” jets that impinged upon and expanded across the ground plane.

In 1986, Ferguson and Kocurek (Reference J-4) expanded on the work of George et al., and further developed the rotorwash model for single main rotor, tandem, and tilt rotor configurations. This model was updated (Reference J-5) in 1994 and an extensive correlation of model results with almost all available flight test data (CH-53E, XV-15, V-22, CL-84, and H-60) was documented for the first time. At the same time that this work was being conducted, Velkoff and Preston were developing a similar momentum-based rotorwash model in parallel. This model and some of their predicted results are presented in References J-7 and J-8.

In 1993, Miller and Wilson (Reference J-9) produced some excellent experimental data for single and twin high-pressure jets impinging on a ground plane. Their paper also developed some good scaling approaches for modeling their test data. Liu, McVeigh, Rajagopalan (Reference J-10) further developed a version of George’s original model in 2001 to include a method for developing a 360-degree rotorwash footprint around a V-22. They presented limited correlation of this approach with the V-22 flight test data documented by Lake in Reference J-11. In summary, these references generally summarize the state-of-the-art for momentum-based modeling approaches at the start of the project that is documented by this report.

Capabilities and Limitations of Momentum-Based Models

As noted previously, the conceptual level rotorwash model requires rapid computational turnaround time that can be quickly adjusted for rotorcraft configuration differences, i.e. single main rotor, tandem, and tilt rotor configurations. The momentum-based modeling approach is the only practical way to achieve these goals. However, it is important to

highlight some of the limitations of this approach. The original references by Glauert, George, et. al., and others and the more recent reference by Miller and Wilson all assume a model based primarily on a “jet” of air that impinges on the ground surface and spreads out radially across the ground. This is shown graphically in Figure J-1.

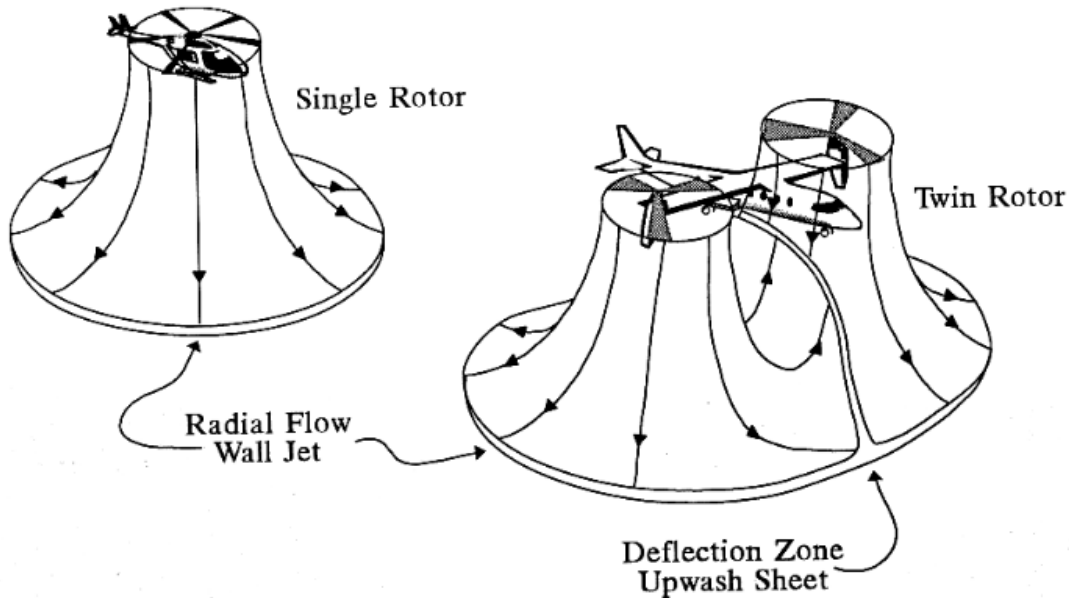


Figure J-1 Rotorwash Flow Fields of Single- and Twin-Rotor Configurations Operating in Close Proximity to Ground

The “jet” model in these references is a continuous mass flow device. As a result, it is easy in laboratory experiments to measure the boundaries of the flow field and apply the principles of conservation of mass and momentum to the modeled flow field. Using these basic fundamentals of physics, the radial decay rates of the flow and the wall-jet profiles can be scaled and modeled. This modeling approach is well detailed in References J-2 through J-8 since these rotorcraft models use most of these same “jet” modeling approaches.

However, in the case of rotorcraft, there are additional features in the development of the rotorwash flow field that complicate modeling when using the “jet” model assumptions. The basics of physics still apply to the rotorcraft’s “open rotor,” but the measurement and scaling of test data to obtain aerodynamic coefficients for this form of momentum model are considerably more complex. This complexity leads to empirical adjustments and additions because of the simplicity inherent in the basic “jet” momentum model. These modeling adjustments and additions are utilized to compensate for the “open rotor” model differences. A list of critical differences between the “jet” and “open rotor” configurations is provided in Table J-1. These differences are not listed to discourage use of momentum-based modeling methods. Instead, they are listed to highlight the increased level of complexity required to use a momentum-based model to obtain acceptable correlation with flight test data.

Table J-1 Momentum Modeling Differences Between “Jets” and “Open Rotors”

“Jet” Model Features	“Open Rotor” Model Features
“Jet” flow velocity out the nozzle is uniform across the exit and continuous.	“Open Rotor” flow velocity through a rotor is non-uniform radially outward and pulses with rotor blade passage.
The wake does not accelerate and contract downstream.	The wake accelerates and contracts in diameter downstream of the rotor.
The flow is continuous as it turns 90 degrees at the ground and expands in a radial path outward.	The flow is highly oscillatory, contains vorticity, and has a swirl component as it turns 90 degrees at the ground and expands outward in a radial path.
Generally, there is conservation of mass in the wall-jet profile with the radial expansion process.	Mass flow is “lost” from the wall-jet radial expansion process near the ground due to recirculation back through the center of the rotor and back toward the rotor about the tips of the rotor above the wall jet.
During the outward expansion of the flow field from the start of the wall jet (highest velocities), the flow is non-oscillatory.	The flow field is highly oscillatory prior to the start of the wall jet and throughout the expansion process. This results in the min-mean-peak profile definitions that are involved with the measurement and analysis efforts.
“Jet” configurations typically have only fuselage configuration effects that complicate the modeled flow field with single- or twin-jet configurations.	Rotorcraft configuration effects that distort the wall-jet flow field include tail rotors, engine exhausts, number of rotors, and the fuselage—usually in non-symmetrical patterns.

Reference Test Data

All of the known sources of full-scale rotorwash test data for helicopter and tilt rotor configurations through 1994 are listed in detail in Table 1 of Reference J-5. This table lists the type of aircraft, the reference, and a review of the quality of the data and any known problems with the data. The major types of aircraft listed in this table for which the data are considered of high quality are the CH-53E helicopter, the XV-15 tilt rotor, and the CL-84 tiltwing. Very limited sources of data for the V-22 and H-60 are also listed in the table.

Since 1994, extensive additional rotorwash testing has been conducted by NAVAIR for the V-22 (References J-11 [land] and J-12 [ship]), the H-60 (Reference J-13) and CH-47 (Reference J-14). The hovering V-22 data are quite extensive and considered excellent. Also, V-22 data were acquired for the FAA at different power settings on the ground and during low speed flight maneuvers in Reference J-15. The H-60 data are generally good; however, at the 10- and 30-ft wheel heights the average winds reached at least 4 to 6 knots

during testing. This magnitude of wind clearly affected the quality of the data to an unknown extent by reducing the velocities in the wall-jet profiles (wind was blowing against the outwash flow). Data at 50- and 150-ft wheel heights, when the winds were 0 to 3 knots, correlate better with model predictions.

Finally, Hewitt (Reference J-16) used acoustic anemometers to acquire data for several Agusta-Westland helicopters (EH-101, Apache, AW-109, Lynx, and Schweizer 269C) for her Master's Thesis. However, as she notes in the thesis, wind was a problem with these tests since she was forced to acquire data on an "as available basis." All of the additional known references for test data are listed in [Appendix R](#) under the first heading, "DOWNWASH /OUTWASH FLOW FIELD DATA – FULL-SCALE ROTORCRAFT."

Conceptual Level Momentum-Based Model

One of the primary steps in the development of the conceptual level model was the review of literature and the evaluation of available momentum-based modeling options. The goal was to develop a prototype model capable of predicting a 360-degree rotorwash footprint around a single- or twin-rotor configuration rotorcraft. This task was accomplished in several steps, and the resulting model is presented at the end of this appendix in a FORTRAN code format.

The general approach to the development of this conceptual model was to first prototype components and test with Excel. Subsequent to this step, the FORTRAN computer code was developed and verified with the Excel model. This multi-step design process can generally be quantified as follows:

1. The models developed by Velkoff and Preston (Reference J-6 through J-8), Ferguson (Reference J-5), and others were reviewed as to their respective strengths and weaknesses.
2. Choices were selectively made to incorporate the best aspects of these models into an initial version of the prototype conceptual model.
3. Flight test data from the CH-53E, V-22, H-60, XV-15, and CH-47 were normalized into graphical formats to test the prediction capabilities of component parts of the conceptual model, i.e. the single- and twin-rotor velocity profile decay rates as a function of distance from the center of the rotor and the shape of the mean/peak velocity profiles. The majority of this task was completed using Excel models for quick turnaround time, the graphic evaluation of results, and documentation purposes.
4. Improvements were incorporated into the Excel-based component parts of the conceptual model and tested. When major improvements were completed, the conceptual model was coded in FORTRAN, tested against the Excel component parts, and evaluated with respect to the available flight test database (also in Excel).

5. This cycle of prototyping, testing, coding, and testing was completed first for the single-rotor helicopter configuration, then the non-interaction plane of the twin-rotor (tilt rotor and tandem) configuration (90- and 270-degree azimuths for tilt rotor and 0- and 180-degree azimuths for tandem), the interaction plane of the twin-rotor configuration (0- and 180-degree azimuths for tilt rotor, and 90- and 270-degree azimuths for tandem), and finally the key gaps in the 360-degree azimuth between the non-interaction and interaction planes. This completed the full 360-degree footprint modeling capability.
6. The final version of the conceptual FORTRAN model was completed and is documented for reference in the report.

When the development of the equations for the prototype conceptual model (end of the previous Step 2) was initially completed in the early 1990s, much of the now available flight test data were not then available or had not been extensively evaluated with any momentum based models. Therefore, ideas for improvements to the initial version of the prototype conceptual model were first based upon the normalized flight test data. Some insight into model structure was also provided by the work of Miller and Wilson (Reference J-9). Also, each improvement was developed while consciously keeping in mind the differences between a “jet” and an “open rotor” configuration, as listed in Table J-1. Improvements associated with modeling outwash between the cardinal azimuths for the twin-rotor configuration were made based upon the concepts first proposed by Liu, McVeigh, and Rajagopalan in Reference J-10. However, in the final version of the model, a simplified approach was found to be satisfactory.

As would be expected from the text in the previous paragraphs, the final version of the prototype conceptual model is a hybrid. It is foundationally based on the original work conducted through the early 1990’s by several authors. It is also foundationally based on a modified “jet” momentum theory. However, due to known weaknesses of these earlier models, as based upon correlation with flight test data, the models have been empirically modified to improve correlation for the “open rotor” configuration. As a result, both the mean and peak velocity profile characteristics, as a function of distance from the rotor, can now be estimated a full 360-degrees around the azimuth.

Empirical Tuning of Momentum-Based Model

One question is often never asked about engineering models in reports and papers. If it is asked, it is often poorly answered or talked about in vague generalities. This question is “How do you know your model works?” This question is a fundamental question and deserves a straight answer. People that use an engineering model are taking a risk with the calculated results and risk management of these results is a legitimate concern! Even though the answer to this question may be different depending on the perspective of author versus the user, this question has been asked by the authors of this conceptual level model and an attempt to provide a clear answer will be provided in the following paragraphs.

RoWFoot uses a mathematical framework based on historical momentum models with empirically derived coefficients and exponents within the equations. Correlation of RoWFoot to flight test data is fundamental to quantitatively trying to determine the model's validity when it is used. Therefore, the developers have made a sincere attempt to not exclude any of the available flight test data from an extensive model correlation effort. This correlation effort is presented in [Appendix K](#) in Figures K-2 through K-61. In some areas, the correlation is excellent, and in others, it is less than what was desired. Future improvements to this model can be expected to add refinement to the model. However, the conceptual model that is presented is a starting point with documentation.

An additional factor that must also be discussed relates to a similar question: "How do you know that the flight test data used for correlation are good?" This is also a very valid question, one that is not always easy to answer. A good model correlated to bad data is also a poor model. The answer that will be provided for this model is summarized as follows:

1. Flight test data that were chosen for correlation were required to have used either an ion-beam or an acoustic velocity sensor. Justification for excluding data sources using mechanical sensors is provided in References J-5 and J-17.
2. Flight test data were not excluded or specifically used to tune the model at the expense of other similar data. Questions with respect to data precision do exist for some of the older test data during the test runs, i.e. to input data values such as ambient wind, air density, and gross weight (and sometimes no value is documented). It is believed that altitude and position of the sensor array is reasonably accurate since the rotorcraft were hovered in a fixed position and the sensor array was moved along a track on a cart. Therefore, correlation with the "flight test database" as a whole was the objective to minimize the unknown risks during the correlation effort. Generally, as a qualitative evaluation of the [Appendix K](#) data sources, the CH-47 data are the best documented, followed by the V-22 data. The CH-53E data are considered good but were processed many years ago with an analog process (all original paper records are not available). The XV-15 data (analog processing) and H-60 (digital processing) are limited in scope and winds were a factor during most of the H-60 test according to the authors of the report.
3. No matter what the perceived model correlation is, the authors believe that future correlation will improve the model and should be conducted if additional flight test data become available. Since extensive "quality" data exist for only one tilt rotor (two total), one tandem, and two single main rotor helicopters, there is still a potential for systematic error in the data used for correlation.
4. Even the best test data, when reduced to a non-dimensional format, do display unexplainable irregularities. An example of this problem for actual test data is presented in Figure J-2. The expected decay of the maximum velocity measured along a vertical profile, according to the physics of the problem, would be constantly decreasing with increasing distance from the rotor (x/R), i.e. the red line. Cases like

the solid blue and black lines deviate from the expected behavior and directly impact perceived correlation for a conceptual level model. For example, along the solid blue line the velocity at a distance of 4.0 is less than the velocity at a distance of 5.5 x/R. Along the dash black line, the velocities at distances of 6.8 and 9.2 are equal to or larger than the distance at 9.2 x/R. While explanations may exist for these irregularities due to winds, configuration, mass flow lost above the sensors, or data reduction errors to name a few, these irregularities nevertheless affect perceived correlation and any modeling required to account for these “features” (if explained) is beyond the capabilities of a conceptual model to differentiate.

The mathematical framework of the conceptual model is broken up into three regions within the rotorwash including the downwash, transition, and outwash regions. Judgment was employed to adjust the empirically derived coefficients and exponents to give the best correlation possible with the available test data. Poor correlation of the present model in some cases for distances underneath the rotor and at distances less than the start of the walljet ($x/R <$ approximately 1.5 to 1.7) is due to the modeling assumption that flow is horizontal. This assumption is not valid in close proximity to the rotor and model improvements can (and are planned) for this region.

Within the downwash region, the modeling uses functions to represent the magnitude of the velocity decay with rotor height above ground and disk loading. Within this region, the rotorwash mixes differently for a tandem rotor aircraft with overlapping rotors than it does for a tilt rotor with separated rotors or a single rotor helicopter. Within the transition region, the modeling uses the magnitude of the wake velocity from the downwash region and determines the initial characteristics of the walljet at the start of the outwash region. These characteristics include the magnitude of the maximum velocity, height of the velocity profile, and start location of the outwash region. A single rotor helicopter will not have the mixing of multi-rotor aircraft and thus different modeling characteristics.

Within the outwash region, the model uses the historical momentum theory framework for velocity decay, height growth, and the velocity profile. Limits are placed on the magnitude of the maximum profile velocity according as based on the maximum downwash velocity. Coefficients and exponents for the height growth and velocity decay are empirically derived and based on the available test data.

In summary, this modeling effort clearly confirmed the belief that the different rotorcraft configurations generate different flow interactions within the rotorwash structure. Helicopters, tandems, and tilt rotors clearly require different conceptual modeling coefficient adjustments due to the measured differences in flow mixing and interactions within the three discussed regions (as a function of azimuth around the rotorcraft). Mass flow differences from the different rotor configurations yield different velocity decay rates (also, in numerous cases, mass flow may have been escaping back toward the rotor above the maximum sensor height during the tests). These differences have to be modeled at the conceptual level using empirically derived coefficients and exponents through feedback from an iterative flight test correlation process.

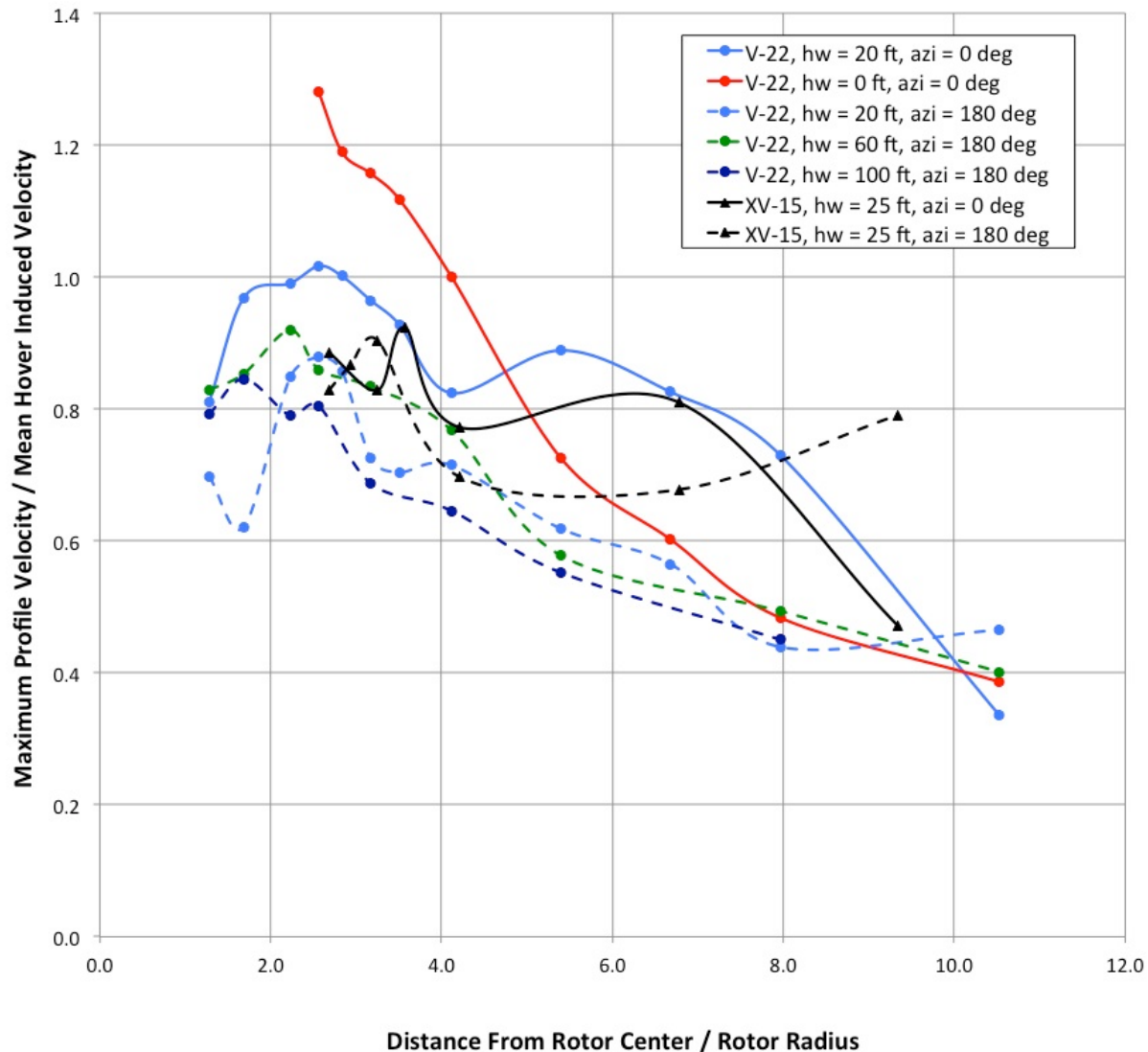


Figure J-2 Non-Dimensional Rotorwash Decay as a Function of Distance From Rotor

Range of Validity for the Conceptual Model

The conceptual modeling of the rotorwash flow field is based upon a common analytical model. Each configuration in the model (helicopter, tandem, and tilt rotor) is independently tuned using all known quality flight test data. The resultant confidence in the conceptual model's capability is highest within the bounds of these flight test data. Outside the range of the test data, the quality of the prediction has not been demonstrated. This section specifies the range of validity of the conceptual model based on the flight test data and presents an engineering discussion for the expected quality of the extrapolation outside of this range.

Good to excellent quality flight test data are available for two single main rotor helicopters (References J-13 and J-18), one tandem configuration (Reference J-14) and two tilt rotors (References J-4 and J-19). Aircraft descriptive data for the five rotorcraft are documented in Table J-2.

	H-60	CH-53E	CH-47	XV-15	V-22
Number of Rotors	1	1	2	2	2
Number of Blades/Rotor	4	7	3	3	3
Rotor Radius (R), ft	26.83	39.5	30.0	12.5	19.0
Distance From Gear to Rotor, ft	9.42	17	18.0	12.67	21.3
Separation Between Rotors, ft	0	0	39.2	32.2	46.6
Thrust/Weight	1.035	1.05	1.055	1.13	1.105

Table J-2 Rotorcraft Descriptive Data

For the rotorcraft in Table J-2, flight test data are available for variations in aircraft Gross Weight (GW) and wheel height Above Ground Level (AGL). Data were acquired at a range of distances along the ground and for the tandem and tilt rotors, at multiple azimuth angles. Data for the helicopters were acquired along a single azimuth angle.

When rotorcraft descriptive data, flight conditions, and distance from the rotor are non-dimensionalized, the range of available flight test data can be quantified. Thus, the validity range of the conceptual rotorwash model can be defined. Examples of Non-Dimensionalized (ND) parameters include the rotor height AGL / rotor Radius (R), the sensor array distance from the rotor/R, and the separation between rotors/R. The disk loading (rotor thrust/rotor area) is a fundamental dimensional parameter that drives the mean rotor induced velocity.

Graphs documenting the conceptual rotorwash model correlation with all of the available test data are presented in [Appendix K](#). As further test data become available, the conceptual model should be correlated and updated using these data. The user of this conceptual model should recognize that the analysis contained in RoWFoot is a starting point based on the best information available at this time. It is expected that the

conceptual model should evolve over time as the database of available flight test data grows in scope.

Model Limits Based on Rotorcraft Configuration

The range of test conditions for available flight test data and the associated non-dimensionalized parameters are defined in Tables J-3, J-4, and J-5 for the single main rotor helicopter, tandem, and tilt rotor configurations, respectively. The rotor radius (R) is the primary scaling parameter used to create non-dimensional parameters. Underlined values in Tables J-3, J-4, and J-5 represent the bounds of the model validity based on engineering review of the correlation graphs presented in [Appendix K](#). These boundaries are considered common for all similar rotorcraft configurations.

Single Main Rotor Helicopter Configuration

The presented boundaries are for the minimum and maximum test conditions for the two helicopters that were flight tested. After a review of the correlation graphs, the data directly under the rotor were observed to be poorly correlated and did not conform well to the conceptual level modeling approach being used. This result was expected because the flow field has a large vertical component very close to the rotor and modeling within this regime was not the highest priority. For this reason, a lower bound of 0.80 R was chosen as the non-dimensional rotor distance where correlation of the conceptual level model is considered acceptable.

	<u>H-60</u>		<u>CH-53E</u>	
Number of Rotors	1		1	
Number of Blades/Rotor	4		7	
Rotor Radius (R), ft	26.83		39.5	
Distance From Gear to Rotor, ft	9.42		17	
Separation Between Rotors, ft	0		0	
Thrust/Weight Ratio	1.035		1.05	
Range of Available Test Data	Minimum	Maximum	Minimum	Maximum
Aircraft Weight, lb	18,000	20,000	45,000	70,000
Rotor Thrust/Rotor Area, psf	<u>8.24</u>	9.15	9.46	<u>14.99</u>
Wheel Height Above Ground, ft	10	150	20	100
Rotor Height/R	<u>0.72</u>	<u>5.94</u>	0.94	2.96
Dist. from Rotor Center (RC), ft	13.5	81	31.6	177.8
Dist. from RC/R	0.50	3.02	<u>0.80</u>	<u>4.50</u>

Table J-3 Helicopter Descriptive Data with Test Condition Bounds

Tandem Helicopter Configuration

Only one tandem helicopter configuration was judged to provide quality flight test data. The presented boundaries in Table J-4 are for the CH-47 minimum and maximum test conditions. After a review of the correlation graphs, the boundaries of the test data were selected as the range of conceptual model validity. These boundaries appear as the underlined quantities in Table J-4. As with the single main rotor helicopter, the correlation with test data improves as the distance from the rotor increases.

The non-dimensional separation between the CH-47 rotors is 1.31 R. This value (< 2) indicates an overlap of the rotors that causes the flow from the front and rear rotor to combine in the overlap region. Centerline or Interaction Plane (IP) outwash at the 90- and 270-degree azimuth angles will contain flow where the two rotors combine from the overlap region. This results in an increased velocity magnitude in the downwash and after the flow transitions, in the outwash. For this reason, the non-dimensional separation distance between the rotors is included as a parameter of the conceptual model validity. Since there is only one data point, very limited extrapolation (e.g. 10%) is appropriate for this parameter. Data ranges and corresponding model validity boundaries are considered separately for the radial and centerline outwash cases.

CH-47			
Number of Rotors	2		
Number of Blades/Rotor	3		
Rotor Radius (R), ft	30		
Distance From Gear to Rotor, ft	18		
Separation Between Rotors, ft	39.2		
Separation Between Rotors, ND	<u>1.31</u>		
Thrust/Weight Ratio	1.055		
Range of Available Test Data	Minimum	Maximum	
Aircraft Weight, lb	33,000	50,000	
Rotor Thrust/Rotor Area, psf	<u>6.16</u>	<u>9.33</u>	
Wheel Height Above Ground, ft	20	100	
Rotor Height/R	<u>1.27</u>	<u>3.93</u>	
Range of Available Test Data	Radial	IP	Radial IP
Dist. from Rotor Center (RC), ft	24.0	24.0	232.5 232.5
Dist. from RC/R	<u>0.80</u>	<u>0.80</u>	<u>7.75</u> <u>7.75</u>

Table J-4 Tandem Descriptive Data with Test Condition Bounds

Tilt Rotor Configuration

The presented boundaries are for the minimum and maximum test conditions for the two tilt rotors that were flight tested. After a review of the correlation graphs, the boundaries of the test data were selected as the valid range of conceptual model validity. These boundaries appear as the underlined quantities in Table J-5. As with the single main rotor helicopters and the tandem helicopter, the correlation with test data improves as the distance from the rotor increases. For modeling validity consistency, a lower bound of 0.80 R was chosen as the non-dimensional rotor distance where correlation of the conceptual level model is considered acceptable.

The non-dimensional separation between the rotor centers ranges from 2.45 to 2.58 R. These values (> 2) indicate that there is no overlap of the rotors, and the flow from the port and starboard rotors do not combine in the downwash region. Centerline or Interaction Plane (IP) outwash at the 0- and 180-degree azimuth angles will contain flow were the two rotors combine during the transition from downwash to outwash. This results in a larger mass flow in the outwash but not an increase in velocity magnitude as seen in the rotor overlap region in the tandem helicopter. The shape of the centerline outwash will be affected by the rotor separation amount. For this reason, the non-dimensional separation distance between the rotors is included as a bounding limit of the conceptual model validity. Data ranges and corresponding model validity boundaries are considered separately for the radial and centerline outwash cases.

	XV-15		V-22	
Number of Rotors	2		2	
Number of Blades/Rotor	3		3	
Rotor Radius (R), ft	12.5		19.0	
Distance From Gear to Rotor, ft	12.67		21.3	
Separation Between Rotors, ft	32.2		46.6	
Separation Between Rotors, ND	<u>2.58</u>		<u>2.45</u>	
Thrust/Weight Ratio	1.13		1.105	
Range of Available Test Data	Minimum	Maximum	Minimum	Maximum
Aircraft Weight, lb	12,475	12,475	22,000	45,900
Rotor Thrust/Rotor Area, psf	14.36	14.36	<u>10.67</u>	<u>22.27</u>
Wheel Height Above Ground, ft	20	50	0	100
Rotor Height/R	2.61	5.01	<u>1.12</u>	<u>6.37</u>
Range of Available Test Data	Radial	IP	Radial	IP
Dist. from Rotor Center, ft	10	26.1	75	31.7
Dist. from RC/R	<u>0.80</u>	2.09	6.00	2.54
			Radial	IP
			15.1	19
			<u>0.79</u>	<u>1.00</u>
			133.1	156
			<u>6.99</u>	<u>8.19</u>

Table J-5 Tilt Rotor Descriptive Data with Test Condition Bounds

Extrapolation Outside of Conceptual Model Boundaries

The quality of conceptual level model extrapolation outside of the identified test boundaries will vary depending on which boundary is exceeded. The following engineering discussion summarizes expected trends when these boundaries are exceeded based on the non-dimensional height (rotor height/R), disk loading (rotor thrust/rotor area), and distance from the rotor center (distance/R).

In the downwash portion of the flow field, the rotor induced velocity decay and distribution are a function of the aircraft configuration, hover height, and disk loading. The geometry of the rotor layout, e.g. the separation or overlap, determines where and how the flow field mixes in the downwash, transition, and outwash regions. This representation is not well described or understood as based upon the first principles of physics. The decay of the downwash and the turning efficiency in the transition region defines the magnitude of the initial velocity and the flow height at the formation of the horizontal wall jet.

As described in [Appendix J](#), neither the rotor height nor the disk loading (as defined independently) were found to explain some of the changes observed in the flight test data. Therefore, the conceptual model uses a combined function for the effect of rotor height and disk loading on the calculation of initial wall jet characteristics. Due to the limited data available during development and tuning of the conceptual model, the confidence decreases as the degree of extrapolation increases. This is a conceptual level model characteristic that is highly recommended for future refinement.

Flight test data become poorly behaved as the distance to the rotor center decreases inside the formation of the wall jet. As this distance approaches the lower boundary, the correlation deteriorates. For extrapolation inside the lower validity boundary, the rotorwash is in a transition state from downwash to outwash and model extrapolation is expected to be poor in quality. For test data, at distances less than 0.8 R, the direction of the flow field has too large of a vertical velocity component for good correlation using the simple conceptual model.

Flight test data become well behaved and have a consistent decay trend as the distance from the center of the rotor increases, especially outside the formation of the wall jet. As this distance approaches the upper boundary, the correlation generally improves. As the distance increases outside of the flight test data range, the outwash is expected to gradually transition from rotorcraft configuration unique to be more generic. Extrapolation beyond the upper bound of the flight test data is expected to have slowly decreasing confidence in the modeling for the radial outwash and decreasing confidence in modeling for the centerline outwash.

In summary, the confidence levels for extrapolation of basic parameters beyond the test data boundaries identified in Tables J-3, J-4, and J-5 are expected to be:

- Disk Loading: Decreasing confidence with extrapolation
- Rotor Height: Decreasing confidence with extrapolation
- Disk Loading + Rotor Height: Rapidly decreasing confidence with extrapolation

- Distance from Rotor Center

Below Wall Jet Formation: Rapidly decreasing confidence with extrapolation

Beyond Wall Jet Formation:

Radial Outwash: Slowly decreasing confidence with extrapolation

Centerline Outwash: Decreasing confidence with extrapolation

Documentation of Equations for the Conceptual Level Rotorwash Model

The conceptual level modeling of the RoWFoot computer code is documented in this section. The intent of this documentation is to convey the analysis method in simple terms so that the RoWFoot analysis procedure can be understood and modified as additional test data become available or an extension to the existing test database is enabled through high-fidelity modeling. Computer variable names are used instead of symbols to provide a direct linkage to the RoWFoot source code. Reuse of some variables and internal logic structures are avoided because a 1:1 comparison with the code would make it harder for the reader to understand the conceptual model design. Many of the coefficients and exponents contained in the source code are empirically derived by correlation to flight test data. This documentation approach is not intended as a theory manual.

For additional detail and actual implementation, the interested reader is recommended to refer to the FORTAN listing provided in this appendix. Comments within the code provide guidelines as to some of the choices made during the correlation effort.

The rotorwash conceptual level modeling analysis is described in the Rotor Parameters, Downwash and Transition Region, and Outwash Region sections. This sequence corresponds to the rotorwash flow sequence as it progresses from generation at the rotor, descends vertically in the downwash, turns from vertical to horizontal in the transition region, and then exits horizontally as outwash. The arrangement of equations and logic flow within each section also follows the logical progression for the generation of rotorwash.

User Inputs

User inputs to the conceptual model are included in [Appendix B](#). However, a brief summary of these RoWFoot equation inputs and their associated definitions are listed below.

Conceptual Level Aircraft Geometry

NUMBER_ROTORS	Number of Rotors
NUMBER_BLADES	Number of Blades per Rotor
TIP_SPEED	Rotor Tip Speed, ft/sec
RADIUS	Rotor Radius, ft
GEAR_TO_ROTOR	Distance From Landing Gear to Rotor, ft
SEPARATION	Separation Between Rotor Centers, ft

Engineering Parameter

THRUST_TO_WEIGHT	Rotor(s) Thrust to Aircraft Weight Ratio
------------------	--

Operational Engineering Parameters

GROSS_WEIGHT	Aircraft Weight, lb
DENSITY_air	Air Density, slug/ft ³
AGL_GEAR	Wheel Height Above Ground, ft

Decision flags

MESHIN	Decision flag for centerline flow direction MESHIN = 0: Rotor tips rotating towards the airframe MESHIN = 1: Rotor tips rotating away from the airframe (MESHIN = 1 used in the Rotorwash Operational Footprint calculations)
--------	--

Sensor_Offset	Sensor offset distance from centerline of outwash (twin rotor cases) (Not used in the Rotorwash Operational Footprint calculations)
---------------	--

Rotor Parameters

Analysis at the rotor uses simple momentum based modeling. For these calculations, the rotor height (EXIT_HEIGHT), thrust per rotor (THRUST), coefficient of thrust (COEF_THRUST), disk loading (DISK_LOAD), and induced velocity (VEL_INDUCED) are determined as:

```
EXIT_HEIGHT = AGL_GEAR + GEAR_TO_ROTOR
COEF_THRUST = DISK_LOAD / DENSITY_air * TIP_SPEED**2
VEL_INDUCED = (COEF_INDUCED * DISK_LOAD / DENSITY_air)**0.5

COEF_INDUCED = 0.5
DISK_LOAD     = THRUST / (PIE * RADIUS**2)
THRUST        = THRUST_TO_WEIGHT * GROSS_WEIGHT / NUMBER_ROTORS
```

Downwash and Transition Regions

Analysis in these regions utilizes results obtained from the rotor parameters section and models rotorwash through to the outwash region. Within the downwash, the flow contracts until it reaches a maximum velocity (EQUIV_VEL). After this maximum velocity is reached, the flow begins to expand and slow. As the flow transitions from downwash to the start of outwash, it continues to expand. The number of rotors and their separation, disk loading, and height above ground all influence the velocity decay in the downwash and how the flow turns in the transition region. Output parameters from this section are the maximum velocity in the downwash prior to the transition region (WAKE_vel) and the starting conditions for the outwash at the beginning of the wall jet or outwash region. The parameters are the distance from the rotor center (RFLOW_init) and initial wall jet height (HFLOW_init).

```
EQUIV_VEL = Maximum magnitude of velocity in the rotor wake
WAKE_vel   = Magnitude of velocity in downwash prior to entry of transition region
HFLOW_init = height of wall jet velocity profile at start of outwash region
RFLOW_init = distance from rotor center to start of wall jet at start of outwash region
```

The maximum velocity in the rotor wake (EQUIV_VEL) is calculated based on momentum theory with a wake contraction ratio (DIAM_ratio = 0.78) and a ratio to quantify the effect of ground effect (GRD_EFF). Calculation of GRD_EFF uses the non-dimensional rotor height above the ground and the coefficient KG_coef = 0.9.

```

EQUIV_VEL = (1/DIAM_ratio**2) * VEL_INDUCED * GRD_EFF

GRD_EFF = 1.0 - KG_coef * EXP(-2.0 * EXIT_HEIGHT / RADIUS)

Where:    KG_coef = 0.9
          DIAM_ratio = 0.78

```

The variables WAKE_vel, HFLOW_init, and RFLOW_init are interrelated. The radius of the wake at the start of the transition region is RW. The solution process requires simultaneous solution of HFLOW_init, RFLOW_init, RW, WAKE_vel, and Z in the equations below. This is accomplished with an initial guess of Z = 3 which is then iterated until solution convergence (10 iterations used).

```

RW      = (1.0 + WAKE_decay * Z) * EQUIV_DIAM / 2.0
HFLOW_init = RW**2 / (2.9 * RFLOW_init)
RFLOW_init = 2.35 * (EQUIV_DIAM/2) * (VEL_INDUCED * GRD_EFF / WAKE_vel)**RFLOW_init_exp
WAKE_vel = EQUIV_VEL / (1 + WAKE_decay * Z)
Z        = (EXIT_HEIGHT + Z_FACTOR - 2.0 * HFLOW_init) / 2 * RADIUS

Where:    WAKE_decay      = 0.1696
          RFLOW_init_exp = 0.486

```

Supporting values in the equations above are the maximum wake contraction diameter (EQUIV_DIAM) and a distance of contraction until the maximum wake contraction is realized (Z_FACTOR).

```

EQUIV_DIAM = 2 * DIAM_ratio * RADIUS
Z_FACTOR   = (2 * PIE * RADIUS / NUMBER_BLADES) * (K1 + 3 * K2)

K1 = K1_coef * (COEF_THRUST / NUMBER_BLADES**0.5)**0.75
K2 = K2_coef * (COEF_THRUST / 2)**0.5

Where:    K1_coef = -2.3
          K2_coef = -1.41

```

As the downwash approaches the ground plane, it is turned in the transition region. In the conceptual level model, the analysis is separated into radial and centerline procedures. The term centerline describes the geometry with respect to a line perpendicular to and one-half way between multiple rotors, not the fuselage centerline. The single main rotor helicopter only has the radial case (or procedure). The tandem helicopter has centerline flow along its 90- and 270-degree azimuth angles. A tilt rotor has centerline flow along the 0- and 180-degree azimuth angles. The outwash flow field is dominated by the single rotor in the radial case (e.g. in front of a tandem helicopter). The rotorwash from two rotors interacts and combines prior to establishing a wall jet in the outwash region, thereby creating the centerline flow case.

Radial Case

The combined effect of rotor height and disk loading on rotor wake velocity (WAKE_vel) is represented as a single ratio. This ratio includes changes to the rotorwash velocity in both the downwash and transition regions. To correspond to fluctuations in the outwash as described in the following outwash section, this ratio is calculated for both a mean velocity ratio (hDL_func_MN) and a peak velocity ratio (hDL_func_PK). A single disk loading function (DL_func) is used for both the mean and the peak cases. Application of the mean velocity ratio (hDL_func_MN) and peak velocity ratio (hDL_func_PK) to the rotor wake velocity (WAKE_vel) yields the transition region maximum exit velocity for the mean (Wvel_Max_MN) and peak cases (Wvel_Max_PK).

Different equation coefficients were used in the rotor height function for the mean ($h_{over_R_func_MN}$) and the peak cases ($h_{over_R_func_PK}$). The coefficient and function limits were derived by empirically tuning the model using flight test data. Limiting bounds of the DL_func, $h_{over_R_func_MN}$ and $h_{over_R_func_PK}$ functions are shown to the right of the relevant equations.

```

Wvel_Max_MN = WAKE_vel * hDL_func_MN
Wvel_Max_PK = WAKE_vel * hDL_func_PK

hDL_func_MN = h_over_R_func_MN + DL_func
hDL_func_PK = h_over_R_func_PK + DL_func

Helicopter:      DL_func = -0.17 + 0.0016 * (DISK_LOAD**2)          0.0 ≤ DL_func ≤ 1.0
Tandem:          DL_func = -0.78 + 0.0057 * (DISK_LOAD**2)          0.0 ≤ DL_func ≤ 1.0
Tilt Rotor:       DL_func = -0.78 + 0.0057 * (DISK_LOAD**2)          0.0 ≤ DL_func ≤
1.0

```

Helicopter:	$h_{over_R_func_MN} = 0.86 + 1.1/(EXIT_HEIGHT/RADIUS)^{**3}$	$hDL_func_MN \leq 1.45$
Helicopter:	$h_{over_R_func_PK} = 1.75 + 1.1/(EXIT_HEIGHT/RADIUS)^{**3}$	$hDL_func_PK \leq 2.45$
Tandem:	$h_{over_R_func_MN} = 1.21 + 1.1/(EXIT_HEIGHT/RADIUS)^{**3}$	$hDL_func_MN \leq 1.48$
Tandem:	$h_{over_R_func_PK} = 2.05 + 1.1/(EXIT_HEIGHT/RADIUS)^{**3}$	$hDL_func_PK \leq 2.65$
Tilt Rotor:	$h_{over_R_func_MN} = 0.86 + 1.1/(EXIT_HEIGHT/RADIUS)^{**3}$	$hDL_func_MN \leq 1.60$
Tilt Rotor:	$h_{over_R_func_PK} = 1.75 + 1.1/(EXIT_HEIGHT/RADIUS)^{**3}$	$hDL_func_PK \leq 2.55$

Centerline Case

The effect of rotor height on the rotor wake velocity (WAKE_vel) is represented as the ratio $h_{over_R_func}$. This ratio includes changes to the rotorwash velocity in both the downwash and transition regions. To correspond to fluctuations in the outwash as described in the following outwash section, this ratio is calculated for both a mean velocity ratio ($h_{over_R_func_MN}$) and a peak velocity ratio ($h_{over_R_func_PK}$). In the centerline case, a disk loading function is not used. Difference equation coefficients were used in the rotor height function for the mean ($h_{over_R_func_MN}$) and the peak cases ($h_{over_R_func_PK}$). The coefficient and function limits were derived by empirically tuning the model using flight test data. Limiting bounds of the $h_{over_R_func}$ functions are shown to the right of the relevant equations.

Test data indicate that the outwash varies slightly between the port and starboard sides of a tandem helicopter and along the front and rear of a tilt rotor. This is perceived to be due to the rotational direction of the rotors and the imparted swirl of the rotor wake. Analysis modeling in the conceptual code included this effect by separately deriving imperial constants and bounding limits for both the rotor tips rotating toward (MESHIN = 0) and away (MESHIN = 1) from the fuselage. During generation of the Rotorwash Operational Footprints in the main section of the report, the analysis was conducted for rotors tips rotating away from the airframe (MESHIN = 1).

Rotors tips rotating towards the airframe (MESHIN = 0)

Tandem:	$h_{over_R_func_MN} = CST_Decay_MN - 0.0355*EX_HT_ov_RAD^{**2}$	$h_{over_R_func_MN} \leq 2.12$
Tandem:	$h_{over_R_func_PK} = CST_Decay_PK - 0.0352*EX_HT_ov_RAD^{**2}$	$h_{over_R_func_PK} \leq 2.65$

Where: $CST_Decay_MN = 2.10 + 0.1500 * Iplane_Offset$

```

CST_Decay_PK = 2.48 + 0.1200 * Iplane_Offset

Tilt Rotor: h_over_R_func_MN = CST_Decay_MN - 0.0175*EX_HT_ov_RAD**2
h_over_R_func_MN<1.72
Tilt Rotor: h_over_R_func_PK = CST_Decay_PK - 0.0155*EX_HT_ov_RAD**2
h_over_R_func_PK<2.10

```

Where: CST_Decay_MN = 1.70 - 0.0501 * abs(Iplane_Offset)
CST_Decay_PK = 2.05 - 0.0501 * abs(Iplane_Offset)

Rotors tips rotating away from the airframe (MESHIN = 1)

```

Tandem: h_over_R_func_MN = CST_Decay_MN - 0.0331*EX_HT_ov_RAD**2 h_over_R_func_MN<2.20
Tandem: h_over_R_func_PK = CST_Decay_PK - 0.0334*EX_HT_ov_RAD**2 h_over_R_func_PK<2.85

```

Where: CST_Decay_MN = 2.13 + 0.0700 * Iplane_Offset
CST_Decay_PK = 2.75 + 0.0800 * Iplane_Offset

```

Tilt Rotor: h_over_R_func_MN = CST_Decay_MN - 0.00359*EX_HT_ov_RAD**2
h_over_R_func_MN<1.45
Tilt Rotor: h_over_R_func_PK = CST_Decay_PK - 0.00500*EX_HT_ov_RAD**2
h_over_R_func_PK<2.00

```

Where: CST_Decay_MN = 1.41 + 0.0601 * Iplane_Offset
CST_Decay_PK = 1.90 + 0.0401 * Iplane_Offset

Where: -1 ≤ Iplane_Offset = Sensor_Offset / (SEPARATION / 2) ≤ 1

Sensor_Offset is the sensor offset distance from the outwash centerline.
Sensor_Offset was primarily used during correlation with flight test data and initial development of non-uniform centerline outwash flow field between the rotor centers. During the Rotorwash Operational Footprint generation, the value of Sensor_Offset was set to zero to remove the effect of centerline velocity variation between the rotors.

Outwash Region

Rotorwash conceptual level modeling in the outwash region uses the output from the downwash and transition regions to define the wall jet starting location (`XFLOW_init`), height, and velocity. Radial and centerline cases are calculated separately. In each case, both mean and peak conditions are calculated for the wall jet height and velocity. Constants in these equations are derived through empirical tuning of the equations using flight test data.

Radial Wall Jet Maximum Velocity

In each of the cases, the calculation of the horizontal outwash is broken into two sections: 1) Before Start of the Wall Jet, and 2) After the Start of the Wall Jet. The wall jet starting location (`XFLOW_init`) is the boundary between these sections. The horizontal distance from the rotor hub is specified by the non-dimensional distance from the rotor center (`RjXROT`). After calculation of the maximum velocity magnitude in the mean (`WFLOW_av_MN`) and peak (`WFLOW_av_PK`) wall jets, the result is evaluated to confirm that it does not exceed an upper limit that is applied to the flow velocity.

Before the Start of Wall Jet ($RjXROT < XFLOW_{init}$)

$$\begin{aligned} WFLOW_{av_MN} &= Wvel_Max_MN * (RjXROT/XFLOW_{init})^{**0.75} & WFLOW_{av_MN} &\leq WAKE_vel_LMT_MN \\ WFLOW_{av_PK} &= Wvel_Max_PK * (RjXROT/XFLOW_{init})^{**1.25} & WFLOW_{av_PK} &\leq WAKE_vel_LMT_PK \end{aligned}$$

After the Start of the Wall Jet ($RjXROT \geq XFLOW_{init}$)

$$\begin{aligned} WFLOW_{av_MN} &= Wvel_Max_MN * (XFLOW_{init}/RjXROT)^{**Exp_Cu_MN} & WFLOW_{av_MN} &\leq WAKE_vel_LMT_MN \\ WFLOW_{av_PK} &= Wvel_Max_PK * (XFLOW_{init}/RjXROT)^{**Exp_Cu_PK} & WFLOW_{av_PK} &\leq WAKE_vel_LMT_PK \end{aligned}$$

The velocity decay rate of the wall jet velocity is defined by the exponents `Exp_Cu_MN` and `Exp_Cu_PK`. These exponents and their associated upper limits are empirically tuned using flight test data.

$$\begin{aligned} \text{Helicopter: } Exp_Cu_MN &= 0.56 + Exp_GEF_func + EXP_DL_func & Exp_Cu_MN &\leq 0.75 \\ \text{Helicopter: } Exp_Cu_PK &= 0.60 + Exp_GEF_func + EXP_DL_func & Exp_Cu_PK &\leq 0.75 \end{aligned}$$

Tandem:	$Exp_Cu_MN = 0.73 + Exp_GEF_func + EXP_DL_func$	$Exp_Cu_MN \leq 0.95$
Tandem:	$Exp_Cu_PK = 0.70 + Exp_GEF_func + EXP_DL_func$	$Exp_Cu_PK \leq 0.95$
Tilt rotor:	$Exp_Cu_MN = 0.73 + Exp_GEF_func + EXP_DL_func$	$Exp_Cu_MN \leq 0.95$
Tilt rotor:	$Exp_Cu_PK = 0.70 + Exp_GEF_func + EXP_DL_func$	$Exp_Cu_PK \leq 0.95$
Where:	$Exp_GEF_func = (1/GRD_EFF^{**2}) - 1.0$	
	$Exp_DL_func = -0.065 + 0.00055 * (DISK_LOAD^{**2})$	

Limits for the radial case confirm that calculated values for WFLOW_av_MN and WFLOW_av_PK do not exceed an upper limit derived from a review of flight test data. Limits applied to h_ov_R_WJ_lmt_MN and h_ov_R_WJ_lmt_PK are also tuned using test data. The upper bound for the ratio is as follows:

WAKE_vel_LMT_MN = h_ov_R_WJ_lmt_MN * EQUIV_VEL
 WAKE_vel_LMT_PK = h_ov_R_WJ_lmt_PK * EQUIV_VEL

Helicopter:	$h_ov_R_WJ_lmt_MN = 0.8 + 0.7 / (\text{EXIT_HEIGHT/RADIUS})$	$h_ov_R_WJ_lmt_MN \leq 1.75$
Helicopter:	$h_ov_R_WJ_lmt_PK = 1.2 + 0.7 / (\text{EXIT_HEIGHT/RADIUS})$	$h_ov_R_WJ_lmt_PK \leq 2.25$
Tandem:	$h_ov_R_WJ_lmt_MN = 0.8 + 0.7 / (\text{EXIT_HEIGHT/RADIUS})$	$h_ov_R_WJ_lmt_MN \leq 1.75$
Tandem:	$h_ov_R_WJ_lmt_PK = 1.2 + 0.7 / (\text{EXIT_HEIGHT/RADIUS})$	$h_ov_R_WJ_lmt_PK \leq 2.25$

1.10	Tilt Rotor:	$h_ov_R_WJ_lmt_MN = 0.8 + 0.7 / (\text{EXIT_HEIGHT/RADIUS})$	$h_ov_R_WJ_lmt_MN \leq$
1.375	Tilt Rotor:	$h_ov_R_WJ_lmt_PK = 1.2 + 0.7 / (\text{EXIT_HEIGHT/RADIUS})$	$h_ov_R_WJ_lmt_PK \leq$

Centerline Wall Jet Maximum Velocity

In each of the cases, the calculation of the horizontal outwash is broken into two sections: 1) Before Start of the Wall Jet, and 2) After the Start of the Wall Jet. The wall jet starting location (XFLOW_init) is the boundary between these sections. The horizontal location from the rotor hub is specified by the non-dimensional distance from the rotor center ($RjXROT$). After calculation of the ratio for the maximum velocity magnitude in the mean (WFLOW_IP_MN) and peak (WFLOW_IP_PK) wall jets, the result is evaluated to confirm that it does not exceed an upper limit

that is applied to the flow velocity. For the centerline case, the distance from the rotor is with respect to the plane intersecting the rotors.

```
WFLOW_av_MN = WFLOW_max_MN = EQUIV_VEL * WFLOW_IP_MN  
WFLOW_av_PK = WFLOW_max_PK = EQUIV_VEL * WFLOW_IP_PK
```

Before the Start of Wall Jet ($RjXROT < XFLOW_{init}$)

```
WFLOW_IP_MN = WAKE_vel_LMT_MN * (RjXROT/XFLOW_{init})^{0.75}      WFLOW_IP_MN \leq WAKE_vel_LMT_MN  
WFLOW_IP_PK = WAKE_vel_LMT_PK * (RjXROT/XFLOW_{init})^{0.75}      WFLOW_IP_PK \leq WAKE_vel_LMT_PK
```

After the Start of the Wall Jet ($RjXROT \geq XFLOW_{init}$)

The velocity decay rate of the wall jet velocity is defined by the exponents Exp_IP_MN and Exp_IP_PK . These exponents and their associated upper limits are empirically tuned using flight test data.

```
WFLOW_IP_MN = h_over_R_func_MN - 0.30 * RjXROT^{Exp\_IP\_MN}      0.2 < WFLOW_IP_MN \leq WAKE_vel_LMT_MN  
WFLOW_IP_PK = h_over_R_func_PK - 0.30 * RjXROT^{Exp\_IP\_PK}      0.2 < WFLOW_IP_PK \leq WAKE_vel_LMT_PK
```

The values of $h_{over_R_func_MN}$ and $h_{over_R_func_PK}$ were calculated in the preceding section and represent the decay in the downwash wake velocity with height.

```
WFLOW_IP_MN = 0.2 * EXP(-0.2 + (h_over_R_func_MN-0.30*RjXROT^{Exp\_IP\_MN}))      WFLOW_IP_MN \leq 0.2  
WFLOW_IP_PK = 0.2 * EXP(-0.2 + (h_over_R_func_PK-0.30*RjXROT^{Exp\_IP\_PK}))      WFLOW_IP_PK \leq 0.2
```

The above equation updates the previous empirically derived function for extrapolation outside of existing test data boundaries ($WFLOW_IP_MN$ and $WFLOW_IP_PK < 0.2$) and produces an expected decay trend in the far field outwash.

Test data indicate that the outwash varies slightly between the port and starboard sides of a tandem helicopter and along the front and rear of a tilt rotor. This is perceived to be due to the rotational direction of the rotors and the imparted swirl of the rotor wake. Analysis modeling in the conceptual code includes this effect by separately deriving imperial constants and bounding limits for both of the conditions where the rotor tips rotate toward and away from the fuselage.

Rotors tips rotating towards the airframe (MESHIN = 0)

Tandem Configuration:

$$\begin{aligned} \text{Exp_IP_MN} &= 0.64420 + 0.0 * \text{abs(Iplane_Offset)} + 0.05764 / \text{EX_HT_ov_RAD}^{**2} \quad 0.60 \leq \text{Exp_IP_MN} \leq 0.72 \\ \text{Exp_IP_PK} &= 0.59376 + 0.0 * \text{abs(Iplane_Offset)} + 0.06064 / \text{EX_HT_ov_RAD}^{**2} \quad 0.55 \leq \text{Exp_IP_PK} \leq 0.68 \end{aligned}$$

Tilt Rotor Configuration:

$$\begin{aligned} \text{Exp_IP_MN} &= 0.51908 + 0.12 * \text{abs(Iplane_Offset)} + 0.1744 / \text{EX_HT_ov_RAD}^{**2} \quad 0.50 \leq \text{Exp_IP_MN} \leq 0.70 \\ \text{Exp_IP_PK} &= 0.55534 + 0.08 * \text{abs(Iplane_Offset)} + 0.1190 / \text{EX_HT_ov_RAD}^{**2} \quad 0.50 \leq \text{Exp_IP_PK} \leq 0.68 \end{aligned}$$

Where: $\text{EX_HT_ov_RAD} = \text{EXIT_HEIGHT} / \text{RADIUS}$
 $\text{Iplane_Offset} = [\text{Sensor_Offset} / (\text{SEPARATION} / 2)]$ $-1 \leq \text{Iplane_Offset} \leq 1$

Sensor_Offset is the sensor offset distance from the outwash centerline. Sensor_Offset was primarily used during correlation with flight test data and initial development of non-uniform centerline outwash flow field between the rotor centers. During the Rotorwash Operational Footprint generation, the value of Sensor_Offset was set to zero to remove the effect of centerline velocity variation between the rotors.

Rotors tips rotating away from the airframe (MESHIN = 1)

Tandem Configuration:

$$\begin{aligned} \text{Exp_IP_MN} &= 0.67690 + 0.0 * \text{Iplane_Offset} + 0.13524 / \text{EX_HT_ov_RAD}^{**2} \quad 0.60 \leq \text{Exp_IP_MN} \leq 0.80 \\ \text{Exp_IP_PK} &= 0.67946 + 0.0 * \text{Iplane_Offset} + 0.18386 / \text{EX_HT_ov_RAD}^{**2} \quad 0.68 \leq \text{Exp_IP_PK} \leq 0.82 \end{aligned}$$

Tilt Rotor Configuration:

$$\begin{aligned} \text{Exp_IP_MN} &= 0.53287 + 0.08 * \text{Iplane_Offset} + 0.1158 / \text{EX_HT_ov_RAD}^{**2} \quad 0.50 \leq \text{Exp_IP_MN} \leq 0.69 \\ \text{Exp_IP_PK} &= 0.57478 + 0.06 * \text{Iplane_Offset} + 0.1583 / \text{EX_HT_ov_RAD}^{**2} \quad 0.50 \leq \text{Exp_IP_PK} \leq 0.70 \end{aligned}$$

Where: $\text{EX_HT_ov_RAD} = \text{EXIT_HEIGHT} / \text{RADIUS}$

```
Iplane_Offset = [Sensor_Offset / (SEPARATION / 2)]      -1 ≤ Iplane_Offset ≤ 1
```

Sensor_Offset is the sensor offset distance from the outwash centerline. Sensor_Offset was primarily used during correlation with flight test data and initial development of non-uniform centerline outwash flow field between the rotor centers. During the Rotorwash Operational Footprint generation, the value of Sensor_Offset was set to zero to remove the effect of centerline velocity variation between the rotors.

Limits for the centerline case confirm that calculated ratios of maximum rotor wake velocity to outwash wall jet maximum velocity (WFLOW_IP_MN, WFLOW_IP_PK) do not exceed upper limits derived from the flight test data (WAKE_vel_LMT_MN, WAKE_vel_LMT_PK). These limits are based on the flight test data (Test_data_LMT_MN, Test_data_LMT_PK) and modeling of the outwash decay (WFLOW_Rj_ref_MN, WFLOW_Rj_ref_PK). The upper bounds for these ratios are as follows:

WAKE_vel_LMT_MN = minimum of WFLOW_Rj_ref_MN and Test_data_LMT_MN
WAKE_vel_LMT_PK = minimum of WFLOW_Rj_ref_PK and Test_data_LMT_PK

Where: WFLOW_Rj_ref_MN is the calculated mean velocity limit
 WFLOW_Rj_ref_PK is the calculated peak velocity limit

Test_data_LMT_MN is the flight test data derived mean velocity limit
Test_data_LMT_PK is the flight test data derived peak velocity limit

Calculated velocity limits in the outwash are determined for conditions at the start of the wall jet (RFLOW_init) using the previously determined height functions (h_over_R_func_MN, h_over_R_func_PK) and decay rates (EXP_IP_MN, EXP_IP_PK).

WFLOW_Rj_ref_MN = h_over_R_func_MN - 0.30 * RJ**EXP_IP_MN
WFLOW_Rj_ref_PK = h_over_R_func_PK - 0.30 * RJ**EXP_IP_PK

Where: RJ = RFLOW_init / (EQUIV_DIAM/2)
 h_over_R_func_MN, h_over_R_func_PK were previously defined
 EXP_IP_MN, EXP_IP_PK were previously defined

Flight test derived velocity limits are imposed for cases of: 1) Wheels on Ground (AGL_GEAR < 0.25) and 2) Hover (AGL \geq 0.25). As previously explained, these limited vary slightly between the port and starboard sides of a tandem helicopter and along the front and rear of a tilt rotor. The limiting values based on test data are further broken out into conditions of rotors tips rotating towards the airframe (MESHIN = 0) and away from the airframe (MESHIN = 1).

Wheels on Ground (AGL_GEAR < 0.25)

Tandem: Test_data_LMT_MN = 2.0
Tandem: Test_data_LMT_PK = 3.0

Tilt Rotor: Test_data_LMT_MN = 2.0
Tilt Rotor: Test_data_LMT_PK = 3.0

Rotors tips rotating towards the airframe (MESHIN=0) and Hover (AGL_GEAR \geq 0.25)

Tandem: Test_data_LMT_MN = 1.40
Tandem: Test_data_LMT_PK = 1.90

Tilt Rotor: Test_data_LMT_MN = 1.0
Tilt Rotor: Test_data_LMT_PK = 1.35

Rotors tips rotating away from the airframe (MESHIN=1) and Hover (AGL_GEAR \geq 0.25)

Tandem: Test_data_LMT_MN = 1.57
Tandem: Test_data_LMT_PK = 2.14

Tilt Rotor: Test_data_LMT_MN = 0.95
Tilt Rotor: Test_data_LMT_PK = 1.40

Wall Jet Maximum Height

As the distance from the rotor increases, the height of the outwash wall jet increases. As previously described, both mean and peak conditions are calculated for the wall jet height.

Calculation of the height uses functions of the distance (HFLOW_av_MN, HFLOW_av_PK) and ratios empirically derived from flight test data (CST_HFLOW_WALL_MN, CST_HFLOW_WALL_PK).

```
HFLOW_wall_MN = HFLOW_av_MN / CST_HFLOW_WALL_MN  
HFLOW_wall_PK = HFLOW_av_PK / CST_HFLOW_WALL_PK
```

The function based on distance from the rotor (HFLOW_av_MN, HFLOW_av_PK) has one component related to distance from the rotor center (hM_Decay_MN, hM_Decay_PK) and one to the starting location of the wall jet (HFLOW_ref_MN, HFLOW_ref_PK). The coefficients in both functions are empirically tuned using flight test data.

```
HFLOW_av_MN = (hM_Decay_MN + HFLOW_ref_MN)* 0.78 * RADIUS  
HFLOW_av_PK = (hM_Decay_PK + 0.0)* 0.78 * RADIUS
```

```
hM_Decay_MN = 1.265 - 3.085 / (RjXROT**0.5) + 2.304 / RjXROT  
hM_Decay_PK = 2.105 - 4.812 / (RjXROT**0.5) + 3.373 / RjXROT
```

```
RjXROT = XROTOR_dist / (Radius * 0.78)
```

```
HFLOW_ref_MN = HFLOW_init / (EQUIV_DIAM/2) - hM_Decay_MN  
HFLOW_ref_PK = HFLOW_init / (EQUIV_DIAM/2) - hM_Decay_PK
```

```
HFLOW_init = from start of the wall jet conditions  
EQUIV_DIAM = 2 * DIAM_ratio * RADIUS
```

```
hM_Decay_MN = 1.237 - 2.915 / Rj**0.5 + 2.075 / Rj  
hM_Decay_PK = 2.200 - 5.152 / Rj**0.5 + 3.592 / Rj
```

```
Rj = RFLOW_init / (EQUIV_DIAM / 2)
```

Radial Case

Radial outwash uses constant ratios empirically derived from flight test data to determine the height of the wall jet velocity profile. These ratios are as follows for the mean and peak outwash. In the radial case, the horizontal distance from the rotor hub is specified by the non-dimensional distance from the rotor center (RjXROT).

Helicopter:	CST_HFLOW_WALL_MN = 0.29
Tandem:	CST_HFLOW_WALL_MN = 0.20
Tilt Rotor:	CST_HFLOW_WALL_MN = 0.29
Helicopter:	CST_HFLOW_WALL_PK = 0.32
Tandem:	CST_HFLOW_WALL_PK = 0.30
Tilt Rotor:	CST_HFLOW_WALL_PK = 0.39

Centerline Case

For the centerline case, the distance from the rotor is with respect to the plane intersecting the rotors. Test data indicate the outwash varies slightly between the port and starboard sides of a tandem helicopter and along the front and rear of a tilt rotor. This is perceived to be due to the rotational direction of the rotors and the imparted swirl of the rotor wake. The conceptual code analysis includes this effect by separately deriving imperial constants and bounding the limits for conditions of the rotor tips rotating toward (MESHIN = 0) and away (MESHIN = 1) from the fuselage. During generation of the Rotorwash Operational Footprints in the main section of the report the analysis was conducted for Rotors tips rotating away from the airframe (MESHIN = 1).

Rotors tips rotating towards the airframe (MESHIN=0)

Tandem:	CST_HFLOW_WALL_MN = 0.15 + 0.00 * abs(Iplane_Offset)
Tilt Rotor:	CST_HFLOW_WALL_MN = 0.10 + 0.08 * abs(Iplane_Offset)
Tandem:	CST_HFLOW_WALL_PK = 0.19 + 0.00 * abs(Iplane_Offset)
Tilt Rotor:	CST_HFLOW_WALL_PK = 0.14 + 0.10 * abs(Iplane_Offset)

Rotors tips rotating away from the airframe (MESHIN=1)

Tandem:	CST_HFLOW_WALL_MN = 0.15 + 0.00 * abs(Iplane_Offset)
Tilt Rotor:	CST_HFLOW_WALL_MN = 0.10 + 0.07 * abs(Iplane_Offset)
Tandem:	CST_HFLOW_WALL_PK = 0.19 + 0.00 * abs(Iplane_Offset)
Tilt Rotor:	CST_HFLOW_WALL_PK = 0.12 + 0.06 * abs(Iplane_Offset)

Where: $-1 \leq I_{\text{plane_Offset}} = \text{Sensor_Offset} / (\text{SEPARATION} / 2) \leq 1$

Sensor_Offset is the sensor offset distance from the outwash centerline. Sensor_Offset was primarily used during correlation with flight test data and initial development of non-uniform centerline outwash flow field between the rotor centers. During the Rotorwash Operational Footprint generation, the value of Sensor_Offset was set to zero to remove the effect of centerline velocity variation between the rotors.

Wall Jet Velocity Profile

The outwash wall jet velocity profile combines a shape function with the maximum velocity (WFLOW_av_MN, WFLOW_av_PK) and maximum height (HFLOW_wall_MN, HFLOW_wall_PK) to predict the local horizontal velocity at any point in the outwash flow field.

$$\text{VEL_LOCAL} = \text{WFLOW_max} * (\text{PROFILE_ZDIST}^{**N}) * (1 - \text{PROFILE_ZDIST})^{**M} / [(\text{N}/(\text{N}+\text{M}))^{**N} + (1 - \text{N}/(\text{N}+\text{M}))^{**M}]$$

Maximum velocity magnitude is defined by WFLOW_max. The value of WFLOW_max is dependent on whether it is representative of the mean (WFLOW_av_MN) or peak (WFLOW_av_PK) outwash.

Mean Outwash Velocity Profile:

WFLOW_max = WFLOW_av_MN

Peak Outwash Velocity Profile:

WFLOW_max = WFLOW_av_PK

The vertical distance in the velocity profile height is ZDIST_object. This value is non-dimensionalized to the maximum height of the wall jet velocity profile (HFLOW_wall_MN, HFLOW_wall_PK).

$$\text{PROFILE_ZDIST} = \text{ZDIST_object} / \text{HFLOW_wall}$$

Mean Outwash Velocity Profile:

HFLOW_wall = HFLOW_wall_MN

Peak Outwash Velocity Profile:

HFLOW_wall = HFLOW_wall_PK

The shape of the wall jet velocity profile is described by a function using constants and exponents "M" and "N", and the non-dimensional height (PROFILE_ZDIST). As the non-dimensional height goes from 0 to 1, the resultant curve defines the calculated rotorwash outwash velocity

profile. Empirical tuning of the model with flight test data resulted in an update to coefficients used in the shape function of the velocity profile base on aircraft configuration type.

$$(\text{PROFILE_ZDIST}^{**N}) * (1 - \text{PROFILE_ZDIST})^{**M} / [(N/(N+M))^{**N} + (1 - N/(N+M))^{**M}]$$

All Cases, All Configurations: M = 5.0

Radial Outwash

Helicopter, Mean Outwash N = 0.5
Helicopter, Peak Outwash N = 0.4

Tandem, Mean Outwash N = 0.5
Tandem, Peak Outwash N = 0.5

Tilt Rotor, Mean Outwash N = 0.5
Tilt Rotor, Peak Outwash N = 0.5

Centerline Outwash

Tandem, Mean Outwash N = 0.22
Tandem, Peak Outwash N = 0.22

Tilt Rotor, Mean Outwash N = 0.25
Tilt Rotor, Peak Outwash N = 0.25

Summary

RoWFoot has a mathematical framework based on historical momentum-based models. It uses empirically derived coefficients and exponents from flight test data. It is capable of predicting outwash velocity profiles and resultant forces on ground personnel for helicopters, tandems, and tilt rotors. The RoWFoot modeling is highest within the bounds of the quality flight test data and reduces as the modeling analysis is extrapolated beyond this range.

References

- J-1. Gessow, A., and Myers, G. C., "Aerodynamics of the Helicopter," Ungar Publishing Co., 1952.
- J-2. George, M.; Kisielowski, E.; and Douglas, D. S., "Investigation of the Downwash Environment Generated by V/STOL Aircraft Operating in Ground Effect," USAAVLABS Technical Report 68-52, July 1968.
- J-3. Glauert, M. B., "The Wall Jet," Journal of Fluid Mechanics, Vol. 1, Part 6, December 1956, pp. 625-643.
- J-4. Ferguson, S. W., and Kocurek, J. D., "Analysis and Recommendation of Separation Requirements for Rotorcraft Operation at Heliports and Airports," Systems Technology, Inc., STI Report TR-1224-1, September 1986.
- J-5. Ferguson, S. W., "Rotorwash Analysis Handbook, Volume I – Development and Analysis," Federal Aviation Administration, Washington D.C., Technical Report DOT/FAA/RD-93/31,I, June 1994.
- J-6. Velkoff, Dr. H. R., "A Comparative Study of Downwash-Outflow Effects of Various VTOL Configurations as a Factor in the Design Selection Process," Advanced Systems Research and Analysis Office, U. S. Army Aviation and Troop Command, NASA Ames Research Center, January 1993.
- J-7. Velkoff, Dr. H. R., "A Comparative Study of Downwash-Outflow Effects of Various VTOL Configurations as a Factor in the Design Selection Process," Paper Presented at the 18th European Rotorcraft Forum, Avignon, France, September 15-18, 1992.
- J-8. Preston, J. R., "VTOL Downwash/Outwash Operational Effects Model," Paper Presented at the 50th Annual Forum of the American Helicopter Society, Washington D.C., May 11-13, 1994.
- J-9. Miller, P., and Wilson, M., "Wall Jets Created by Single and Twin High Pressure Jet Impingement," Aeronautical Journal, pp. 87-100, March 1993.

J-10. Liu, J.; McVeigh, M. A.; and Rajagopalan, Dr. G., "Single- and Dual-Rotor Flowfield and Outwash Predictions," American Helicopter Society Tilt Rotor/Runway Independent Aircraft Technology and Applications Specialists' Meeting, Arlington, Texas, March 2001.

J-11. Lake, R. E., and Clark, W. J., "V-22 Rotor Downwash Survey," NAWCADPAX-98-88-RTTR, July 1998.

J-12. Lake, R. E., "Shipboard V-22 Rotor Downwash Survey," NAWCADPAX-99-87-RTTR, September 1999.

J-13. Meyerhoff, C. L.; Lake, R.; and Peters, Lt. D., "H-60 Helicopter Rotor Downwash Wind Velocity Evaluation," Naval Air Warfare Center Report SY-3R-94, February 1994.

J-14. Silva, M. J., "CH-47D Tandem Rotor Outwash Survey," NAWCADPAX/EDR-2010/120, August 2010.

J-15. Smith, R. D., "Heliport/Vertiport Design Deliberations, 1997-2000," DOT/FAA/ND-00/1, May 2001.

J-16. Hewitt, J. J., "Downwash Measurement – A Standardized Test," Master's Thesis in Aerospace Engineering, University of Glasgow, May 2008.

J-17. Meyerhoff, C. L.; Lake, R. E.; and Gordge, D. N., "Rotorwash Wind Sensor Evaluation," DOT/FAA/RD-93/10, August 1993.

J-18. Harris, D. J., and Simpson, R. D., "CH-53E Helicopter Downwash Evaluation. Final Report," Naval Air Test Center Technical Report No. SY-89R-78, August 1, 1978.

J-19. Harris, D. J., and Simpson, R. D., "Technical Evaluation of the Rotor Downwash Flow Field of the XV-15 Tilt Rotor Research Aircraft," Naval Air Test Center Technical Report No. SY-14R-83, July 1983.

Listing of Conceptual Level Computer Source Code (FORTRAN)

```
PROGRAM ROWFOOT
C
C -----
C   "USE IFPORT" IS FOR MAC FORTRAN DATE/TIME
C -----
C
C xxx mac      USE IFPORT
C
C     INCLUDE 'DATE_____.CMN'
C     INCLUDE 'GENERAL_.CMN'
C
C     CALL GETDAT (IYEAR, IMONTH, IDAY)
C
C     CALL GETTIM (IHOUR, IMINUTE, ISECOND, I100TH)
C
C     CALL INPUTS
C
```

```

CALL CORRELATION_OUTPUT_DATA
C
CALL GRAPHIC_OUTPUT_DATA
C
CLOSE (UNIT = DOUTPUT)
C
END
C
-----
C END ROWFOOT
C -----
C
BLOCK DATA
C
*****
C THIS ROUTINE CONTAINS THE DEFAULT DATA FOR THE PROGRAM
C *****
C
INCLUDE 'GENERAL_.CMN'
INCLUDE 'LABELS_.CMN'
INCLUDE 'FLOW_____.CMN'
INCLUDE 'OBJECT_____.CMN'
INCLUDE 'FLTCOND_.CMN'

C
C -----
C DATA CONTROL
C -----
C
DATA      GOUTPT,      DOUTPUT,      INPT,      DEBUG_FLAG
1   /          4,           11,          12,      .FALSE. /
DATA      G2OUTPT,      VOUTPT
1   /          13,           11 /
C
C -----
C GENERAL INPUTS / CONSTANTS
C -----
C
DATA      PIE,      ECONST
1   /      3.1415926,    2.7182818 /
DATA      kts_fps,      mph_fps
1   /      1.6878097,    1.4666667 /

C
C -----
C AIRCRAFT
C -----
C
DATA      TITLE,      NUMBER_ROTORS,      TIP_SPEED
1   /      'DEFAULT',          2,           750 /
DATA      RADIUS,      NUMBER_BLADES,      THRUST_TO_WEIGHT
1   /          39.5,           4,           1.09 /
DATA      SEPARATION,      GROSS_WEIGHT,      GEAR_TO_ROTOR
1   /          91.0,        150000,           20.83 /
C
C -----
C WAKE AND WALL JET PARAMETERS
C -----
C
DATA      M_EXPONENT,      WAKE_decay,      RFLOW_init_exp
1   /          5.0,           0.1696,           0.486 /

C
C -----
C ACTUATOR PARAMETERS
C -----
C
DATA      COEF_INDUCED,      DIAM_ratio
1   /          0.5,           0.78 /
DATA      K1_coef,      K2_coef,      KG_coef
1   /          -2.3,          -1.41,           0.9 /
C
C -----
C OPERATING CONDITIONS
C -----

```

```

      DATA    DENSITY_air,      AGL_GEAR,   PURE_RADIAL_ANGLE
1     /      0.002378,           20.0,        20 /
C
      DATA    Sensor_Offset
1     /      0.0 /
C
C -----
C OBJECT DESCRIPTION
C -----
C
      DATA    DIST_number,    TYPE_OUTFLOW,      MESHIN
1     /          50,          'RADIAL',          0 /
      DATA    DIST_units,     OBJ_SHAPE,    PEAK_OR_MEAN
1     /      'NONDIM',      'PAXMAN',      'PEAK' /
      DATA    WindVelocity_kts / 0.0 /
      DATA    fPersonalStability / 0.8 /
      DATA    DIST_values
1     /  1.1, 1.2, 1.3, 1.4, 1.5, 1.6, 1.7, 1.8, 1.9, 2.0,
2     1.1, 1.2, 1.3, 1.4, 1.5, 1.6, 1.7, 1.8, 1.9, 2.0,
3     2.1, 2.2, 2.3, 2.4, 2.5, 2.6, 2.7, 2.8, 2.9, 3.0,
4     3.1, 3.2, 3.3, 3.4, 3.5, 3.6, 3.7, 3.8, 3.9, 4.0,
5     4.1, 4.2, 4.3, 4.4, 4.5, 4.6, 4.7, 4.8, 4.9, 5.0 /
      END
C
C -----
C END BLOCK DATA
C -----
C
      SUBROUTINE CORRELATION_OUTPUT_DATA
C ****
C THIS SUBROUTINE DETERMINES THE OUTWASH VELOCITY PROFILE FOR USER
C INPUT CASES AND OUTPUTS THE INFORMATION TO .CSV FILE FOR COMPARISON
C TO FLIGHT TEST DATA.
C ****
C
      INCLUDE 'DATE_____.CMN'
      INCLUDE 'GENERAL_.CMN'
C
      INTEGER K
      REAL    CALC_ANGLE
C
      CALC_ANGLE = 0
      K          = 0
C
      CALL ROTOR_WAKE
C
      CALL CALCULATE_PROFILE_DATA
C
      OPEN (UNIT=GOUTPT, STATUS='UNKNOWN',
1      FILE='C:\DATA\PROGRAMS\ROWFOOT\OUTPUT\PROFILES.CSV')
C xxx mac      1 FILE='ELITE_ROWF/PROFILES.CSV')
C
      CALL OUTPUT_PROFILE_DATA (CALC_ANGLE, K, GOUTPT)
C
      CLOSE (UNIT = GOUTPT)
C
      RETURN
      END
C
C --- END CORRELATION_OUTPUT_DATA
C
      SUBROUTINE INPUTS
C
C ****
C THIS SUBROUTINE READS THE DATA IN FROM THE INPUT FILE. THE INPUT
C FILE IS SET UP IN NAMELIST FORMAT WITH SEVERAL NAMELISTS. THE
C MAIN NAMELIST (CONFIG) IS CHOOSES THE CORRECT CONFIGURATION.
C THE SURROUNDING CONDITIONS ARE CONTAINED IN THE OTHER NAMELIST
C (ENVIRONMENT).
C ****
C
      INCLUDE 'GENERAL_.CMN'
      INCLUDE 'LABELS___.CMN'

```

```

INCLUDE 'FLOW_____.CMN'
INCLUDE 'OBJECT_____.CMN'
INCLUDE 'FLTCOND_____.CMN'

C
C -----
C NAMELISTS USED IN THIS SECTION
C
C /ENVIRONMENT/      OPERATING CONDITIONS AROUND AIRCRAFT
C /ROTORCRAFT/       GENERAL AIRCRAFT INPUT INFORMATION
C /WAKE_PARAMETER/   WAKE AND WALL JET FLOW PARAMETERS
C /ACTUATOR_OPEN/    PARAMETERS FOR OPEN ROTOR SYSTEM
C -----
C
C NAMELIST /OUTPUT_SET/
1 DENSITY_air, AGL_GEAR, Sensor_Offset, TYPE_OUTFLOW, MESHIN,
2 DIST_values, DIST_number, DIST_units, fPersonalStability,
3 DEBUG_FLAG, PURE_RADIAL_ANGLE, OBJ_SHAPE, PEAK_OR_MEAN,
4 WindVelocity_kts

C
C NAMELIST /ROTORCRAFT/
1 TITLE,           NUMBER_BLADES, TIP_SPEED,     THRUST_TO_WEIGHT,
2 SEPARATION,      GROSS_WEIGHT,  GEAR_TO_ROTORS,
3 NUMBER_ROTORS,   RADIUS

C
C NAMELIST /WAKE_PARAMETER/
1 WAKE_decay, RFLOW_init_exp, M_EXPONENT

C
C NAMELIST /ACTUATOR_OPEN/ COEF_INDUCED, DIAM_ratio,
1                 K1_coef,   K2_coef,     KG_coef

C
C -----
C OPEN INPUT FILE
C -----
C
C OPEN (UNIT=INPT, STATUS='OLD',
1 FILE='C:\DATA\PROGRAMS\ROWFOOT\INPUT\ROWFOOT.IN')
c xxx mac      1 FILE='ELITE_ROWFOOT/ROWFOOT.IN')

C
C -----
C READ IN CASE RUN DATA FOR SPECIFIED CONFIGURATION
C -----
C
C READ (INPT, OUTPUT_SET)

C
C -----
C READ IN CONFIGURATIONS PARAMETERS FOR REQUESTED CONCEPT
C -----
C
C READ (INPT, ROTORCRAFT)

C
C -----
C WAKE AND WALL JET FLOW PARAMETERS
C -----
C
C READ (INPT, WAKE_PARAMETER)

C
C READ (INPT, ACTUATOR_OPEN)

C
C OPEN (UNIT=DOUTPUT, STATUS='UNKNOWN',
1 FILE='C:\DATA\PROGRAMS\ROWFOOT\OUTPUT\DEBUG.OUT')
c xxx mac      1 FILE='ELITE_ROWFOOT/DEBUG.OUT')

C
C IF (NUMBER_ROTORS.EQ.1) THEN
  CONFIGURATION = 'SINGLE_ROTOR'
  TYPE_OUTFLOW = 'RADIAL'
ELSE IF (NUMBER_ROTORS.GT.1 .AND. (2*RADIUS).LT.SEPARATION) THEN
  CONFIGURATION = 'TILT_ROTOR'
ELSE IF (NUMBER_ROTORS.GT.1 .AND. (2*RADIUS).GE.SEPARATION) THEN
  CONFIGURATION = 'TANDEM_ROTOR'
END IF

C
C IF (DEBUG_FLAG) THEN
  WRITE (DOUTPUT, 100) CONFIGURATION, NUMBER_ROTORS,

```

```

1           RADIUS,           SEPARATION
100      FORMAT(1X, 'Subroutine Inputs', //,
1           '           CONFIGURATION = ', A12, //,
2           '           NUMBER_ROTORS = ', F4.1, //,
3           '           RADIUS = ', F8.2, ' ft ', //,
4           '           SEPARATION = ', F8.2, ' ft ', //)
      END IF
C
      RETURN
C
      END
C
C -----
C END INPUTS
C -----
C
SUBROUTINE ROTOR_WAKE
***** SUBROUTINE GIVES THE ROTOR WAKE OF A SPECIFIC CONFIGURATION.
C OPEN AND CLOSED ROTOR SYSTEMS ARE CONSIDERED. FINAL ROTOR WAKE
C VELOCITY AND REFERENCE WALL JET HEIGHT AND VELOCITY ARE DEFINED.
*****
C
INCLUDE 'GENERAL_.CMN'
INCLUDE 'FLOW_____.CMN'
INCLUDE 'LABELS_____.CMN'
INCLUDE 'FLTCOND_____.CMN'
INCLUDE 'OBJECT_____.CMN'
C
INTEGER I, J
REAL h_over_R_func_MN, hDL_func_MN, DL_func, K1,
3   h_over_R_func_PK, hDL_func_PK, Exp_DL_func, K2,
4   h_ov_R_WJ_lmt_MN, hM_Decay_MN, Exp_GEF_func, RW,
5   h_ov_R_WJ_lmt_PK, hM_Decay_PK, EX_HT_ov_RAD, Rj,
6   Wvel_Veq_fac_MN, hM_Offset_MN, Cu_ref_MN, Z,
7   Wvel_Veq_fac_PK, hM_Offset_PK, Cu_ref_PK, Z_FACTOR,
8   WFLOW_Rj_ref_MN, CST_Decay_MN, Iplane_Offset, GRD_EFF,
9   WFLOW_Rj_ref_PK, CST_Decay_PK, EXIT_HEIGHT, THRUST,
1   Test_data_LMT_MN, CST_EXP_IP_MN, VEL_INDUCED, EQUIV_DIAM,
2   Test_data_LMT_PK, CST_EXP_IP_PK, COEF_THRUST
C
C -----
C PRELIMINARY CALCULATIONS
C -----
C
EXIT_HEIGHT = AGL_GEAR + GEAR_TO_ROTOR
THRUST = THRUST_TO_WEIGHT * GROSS_WEIGHT / NUMBER_ROTORS
DISK_LOAD = THRUST / (PIE * RADIUS**2)
COEF_THRUST = DISK_LOAD /(DENSITY_air * TIP_SPEED**2)
C
C -----
C Iplane_Offset (Sensor_Offset must be less than 1/2 rotor separation)
C Sign convention: Looking outward from the aircraft between the rotors
C the offset is positive if the sensor line moves toward the left.
C Tiltrotor looking forward (0-deg), if the sensor line moves toward the
C left rotor it is positive. Tandem looking out left side of aircraft
C (270-deg), if the sensor line moves toward the aft rotor it is
C positive. Calculated Iplane_Offset is .GE. -1.0, .LE. 1.0 always.
C
C -----
C Iplane_Offset = Sensor_Offset / (SEPARATION / 2)
IF (Iplane_Offset .LT. -1.0) Iplane_Offset = -1.0
IF (Iplane_Offset .GT. 1.0) Iplane_Offset = 1.0
C
C -----
C CHECK DISTANCE FROM ROTOR AND CONVERT TO NONDIMENSIONAL VALUES
C IF THEY WEREN'T ENTERED AS NONDIMENSIONAL VALUES
C
C -----
C
IF (DIST_units .EQ. 'DIMEN') THEN
    DO 100, I = 1, DIST_number
        DIST_NONDIM(I) = DIST_values(I) / RADIUS
100    CONTINUE

```

```

ELSE IF (DIST_units .EQ. 'NONDIM') THEN
    DO 200, I = 1, DIST_number
        DIST_NONDIM(I) = DIST_values(I)
200    CONTINUE
ELSE
    WRITE(NOUTPT,*)'DIST_UNITS VALUE IS NOT VALID'
END IF
C
C -----
C OPEN ROTOR
C -----
C
K1          = K1_coef * (COEF_THRUST / NUMBER_BLADES**0.5)**0.75
K2          = K2_coef * (COEF_THRUST / 2)**0.5
Z_FACTOR    = (2 * PIE * RADIUS / NUMBER_BLADES) * (K1 + 3 * K2)
EQUIV_DIAM = 2 * DIAM_ratio * RADIUS
VEL_INDUCED = (COEF_INDUCED * DISK_LOAD / DENSITY_air)**0.5
GRD_EFF    = 1.0 - KG_coef * (EXP(-2.0 * (EXIT_HEIGHT / RADIUS)))
EQUIV_VEL   = (1 / DIAM_ratio**2) * VEL_INDUCED * GRD_EFF
C
C -----
C ITERATE TO FIND AIRCRAFT PARAMETERS RFLOW_init, HFLOW_init,
C XFLOW_init, WAKE_vel.  USE GUESS OF INITIAL VALUE FOR Z.
C -----
C
Z = 3.0
DO 10, J=1,10
    RW = (1. + WAKE_decay * Z) * EQUIV_DIAM / 2.0
    WAKE_vel = EQUIV_VEL / (1 + WAKE_decay * Z)
C
    RFLOW_init = 2.35 * (EQUIV_DIAM/2) *
1      (VEL_INDUCED * GRD_EFF / WAKE_vel)**RFLOW_init_exp
C
    HFLOW_init = RW**2 / (2.9 * RFLOW_init)
    Z = (EXIT_HEIGHT + Z_FACTOR - 2.0 * HFLOW_init) / (2 * RADIUS)
10  CONTINUE
C
C -----
C TANDEM ROTORS WITH OVERLAP
C -----
C
IF (CONFIGURATION .EQ. 'TANDEM_ROTOR') THEN
    h_over_R_func_MN = 1.21 + 1.1 / (EXIT_HEIGHT / RADIUS)**3
    h_over_R_func_PK = 2.05 + 1.1 / (EXIT_HEIGHT / RADIUS)**3
ELSE IF (CONFIGURATION .EQ. 'SINGLE_ROTOR' .OR.
1       CONFIGURATION .EQ. 'TILT_ROTOR') THEN
    h_over_R_func_MN = 0.86 + 1.1 / (EXIT_HEIGHT / RADIUS)**3
    h_over_R_func_PK = 1.75 + 1.1 / (EXIT_HEIGHT / RADIUS)**3
C
END IF
C
C -----
C DISK LOADING EFFECT COEFFICIENT (MEAN AND PEAK)
C -----
C
IF ((CONFIGURATION .EQ. 'TANDEM_ROTOR' .OR.
1       CONFIGURATION .EQ. 'TILT_ROTOR') .AND.
2       TYPE_OUTFLOW .EQ. 'RADIAL') THEN
    DL_func = -0.17 + 0.0016 * (DISK_LOAD**2)
ELSE
    DL_func = -0.78 + 0.0057 * (DISK_LOAD**2)
END IF
C
IF(DL_func .LT. 0.0) DL_func = 0.0
IF(DL_func .GT. 1.0) DL_func = 1.0
C
C -----
C COMBINED h/R AND DISK LOADING EFFECT (MEAN AND PEAK)
C -----
C
hDL_func_MN = h_over_R_func_MN + DL_func
hDL_func_PK = h_over_R_func_PK + DL_func
C

```

```

IF (CONFIGURATION .EQ. 'SINGLE_ROTOR') THEN
    IF(hDL_func_MN.GT.1.45) hDL_func_MN = 1.45
    IF(hDL_func_PK.GT.2.45) hDL_func_PK = 2.45
ELSE IF (CONFIGURATION .EQ. 'TILT_ROTOR') THEN
    IF(hDL_func_MN.GT.1.60) hDL_func_MN = 1.60
    IF(hDL_func_PK.GT.2.55) hDL_func_PK = 2.55
ELSE IF (CONFIGURATION .EQ. 'TANDEM_ROTOR') THEN
    IF(hDL_func_MN.GT.1.48) hDL_func_MN = 1.48
    IF(hDL_func_PK.GT.2.65) hDL_func_PK = 2.65
END IF
C
C -----
C CALCULATION OF EXPONENT IN THE VELOCITY DECAY (Cu) EQUATION
C -----
C
Exp_DL_func = -0.065 + 0.00055 * (DISK_LOAD**2)
Exp_GEF_func = (1/GRD_EFF**2) - 1.0
C
IF (CONFIGURATION .EQ. 'SINGLE_ROTOR') THEN

    Exp_Cu_MN = 0.56 + Exp_GEF_func + Exp_DL_func
    Exp_Cu_PK = 0.60 + Exp_GEF_func + Exp_DL_func
C
    Exp_Cu_MN = MIN(0.75, Exp_Cu_MN)
    Exp_Cu_PK = MIN(0.75, Exp_Cu_PK)

ELSE
C
    Exp_Cu_MN = 0.73 + Exp_GEF_func + Exp_DL_func
    Exp_Cu_PK = 0.70 + Exp_GEF_func + Exp_DL_func
C
    Exp_Cu_MN = MIN(0.95, Exp_Cu_MN)
    Exp_Cu_PK = MIN(0.95, Exp_Cu_PK)
C
END IF
C
C -----
C h/R LIMIT ACROSS START OF WALJET BOUNDARY (MEAN AND PEAK)
C -----
C
h_ov_R_WJ_lmt_MN = 0.8 + 0.7 / (EXIT_HEIGHT / RADIUS)
h_ov_R_WJ_lmt_PK = 1.2 + 0.7 / (EXIT_HEIGHT / RADIUS)
C
IF (CONFIGURATION .EQ. 'SINGLE_ROTOR') THEN
    Test_data_LMT_MN = 1.75
    Test_data_LMT_PK = 2.25
ELSE IF (CONFIGURATION .EQ. 'TILT_ROTOR') THEN
    Test_data_LMT_MN = 1.1
    Test_data_LMT_PK = 1.375
ELSE IF (CONFIGURATION .EQ. 'TANDEM_ROTOR') THEN
    Test_data_LMT_MN = 1.75
    Test_data_LMT_PK = 2.25
END IF
C
IF(h_ov_R_WJ_lmt_MN.GT.Test_data_LMT_MN) THEN
    h_ov_R_WJ_lmt_MN = Test_data_LMT_MN
ENDIF
C
IF(h_ov_R_WJ_lmt_PK.GT.Test_data_LMT_PK) THEN
    h_ov_R_WJ_lmt_PK = Test_data_LMT_PK
ENDIF
C
C -----
C WAKE_vel LIMIT IN SUBROUTINE NORMAL_PROFILE ACROSS
C TRANSITION OF START OF WALJET, FUNC OF h/R
C -----
C
WAKE_vel_LMT_MN = h_ov_R_WJ_lmt_MN * EQUIV_VEL
WAKE_vel_LMT_PK = h_ov_R_WJ_lmt_PK * EQUIV_VEL
C
C -----
C VELOCITY RATIO SCALING FACTOR AT START OF WALJET (MEAN AND PEAK)
C Informational Calculation, not used anywhere in code.

```

```

C -----
C
C Wvel_Veq_fac_MN = (WAKE_vel/EQUIV_VEL) * hDL_func_MN
C Wvel_Veq_fac_PK = (WAKE_vel/EQUIV_VEL) * hDL_func_PK
C
C -----
C MAX PROFILE VELOCITY AT START OF WALJET (MEAN AND PEAK)
C USED TO SET DECAY CONSTANTS AT WALJET (NOT LIMITED)
C Terms used below in Cu and SUBROUTINE NORMAL_PROFILE
C
C -----
C Wvel_Max_MN = WAKE_vel * hDL_func_MN
C Wvel_Max_PK = WAKE_vel * hDL_func_PK
C
C -----
C HALF-VELOCITY HEIGHT SCALING FACTOR AT START OF WALJET
C (hM_Decay_MN equation is used to decay calculated wallet
C value and decay is relative to calculated value. This
C is the reason for the offset. No peak value model exists.
C Therefore, the hM_Decay_PK offset is calculated, but not
C used when generating the profile later in the code.
C Height for the peak profile is used straight from the
C equation as generated from CH-53E flight test data.)
C
C -----
C Rj = RFLOW_init / (EQUIV_DIAM/2)
C
C hM_Decay_MN = 1.237 - 2.915/(Rj**0.5) + 2.075 / Rj
C hM_Decay_PK = 2.2 - 5.152/(Rj**0.5) + 3.592 / Rj
C
C hM_Offset_MN = (HFLOW_init / (EQUIV_DIAM/2)) - hM_Decay_MN
C hM_Offset_PK = (HFLOW_init / (EQUIV_DIAM/2)) - hM_Decay_PK
C
C -----
C FIND INITIAL WORST CASE LOCATION IN OUTFLOW
C RFLOW_init DIVIDED BY "EQUIV_DIAM/2", NOT "RADIUS"
C
C -----
C XFLOW_init = Rj
C
C -----
C REFERENCE CONDITIONS FOR GROWTH/DECAY OF TRADITIONAL WALL JET
C
C Cu_ref_MN = Wvel_Max_MN * (Rj**Exp_Cu_MN)
C Cu_ref_PK = Wvel_Max_PK * (Rj**Exp_Cu_PK)
C
C WFLOW_ref_MN = Cu_ref_MN
C WFLOW_ref_PK = Cu_ref_PK
C
C HFLOW_ref_MN = hM_Offset_MN
C HFLOW_ref_PK = hM_Offset_PK
C
C #####
C
C INTERACTION PLANE OF TWIN ROTOR CONFIGURATION
C
C -----
C DETERMINE INITIAL HEIGHT OF FLOW IN CENTERLINE CASE BY MASS FLOW
C CONSIDERATIONS. DERIVATION OF THIS METHOD IS INCLUDED IN AN
C ADDITION TO THE PAPER BY DR. VELKOFF.
C
C -----
C NEXT 4 NAMES SET TO -1.0 FOR DIAGNOSTIC PRINT IF .NE. 'CENTER'
C
C Exp_IP_MN = -1.0
C Exp_IP_PK = -1.0
C WFLOW_Rj_ref_MN = -1.0
C WFLOW_Rj_ref_PK = -1.0
C
C EX_HT_ov_RAD = EXIT_HEIGHT / RADIUS
C
C IF (TYPE_OUTFLOW .EQ. 'CENTER') THEN

```

```

C
C -----
C CALCULATION OF TWIN ROTOR h/R EFFECTS
C -----
C
C IF (CONFIGURATION .EQ. 'TILT_ROTOR') THEN
C
C -----
C TWIN ROTOR (TILTROTOR) WITHOUT BLADE TIP OVERLAP
C -----
C
C IF (MESHIN .EQ. 0) THEN
C
C -----
C ROTOR TIPS APPROACHING AIRFRAME (XV-15 0-DEG)
C -----
C
C h/R EFFECT COEFFICIENTS (MEAN AND PEAK)
C -----
C
C CST_Decay_MN = 1.70 - 0.0501 * (Iplane_Offset**2)**0.5
C CST_Decay_PK = 2.05 - 0.0501 * (Iplane_Offset**2)**0.5
C
h_over_R_func_MN = CST_Decay_MN - 0.0175 * (EX_HT_ov_RAD)**2
h_over_R_func_PK = CST_Decay_PK - 0.0155 * (EX_HT_ov_RAD)**2
C
h_over_R_func_MN = MIN(1.72, h_over_R_func_MN)
h_over_R_func_PK = MIN(2.10, h_over_R_func_PK)
C
Test_data_LMT_MN = 1.0
Test_data_LMT_PK = 1.35
C
C CST_HFLOW_WALL_MN = 0.10 + 0.08 * (Iplane_Offset**2)**0.5
C CST_HFLOW_WALL_PK = 0.14 + 0.10 * (Iplane_Offset**2)**0.5
C
ELSE
C
C -----
C ROTOR TIPS DEPARTING AIRFRAME (XV-15 180-DEG)
C -----
C
C CST_Decay_MN = 1.41 + 0.0601 * Iplane_Offset
C CST_Decay_PK = 1.90 + 0.0401 * Iplane_Offset
C
h_over_R_func_MN = CST_Decay_MN - 0.00359 *(EX_HT_ov_RAD)**2
h_over_R_func_PK = CST_Decay_PK - 0.00500 *(EX_HT_ov_RAD)**2
C
h_over_R_func_MN = MIN(1.45, h_over_R_func_MN)
h_over_R_func_PK = MIN(2.00, h_over_R_func_PK)
C
Test_data_LMT_MN = 0.95
Test_data_LMT_PK = 1.40
C
C CST_HFLOW_WALL_MN = 0.10 + 0.07 * (Iplane_Offset**2)**0.5
C CST_HFLOW_WALL_PK = 0.12 + 0.06 * (Iplane_Offset**2)**0.5
C
END IF
C
ELSE IF (CONFIGURATION .EQ. 'TANDEM_ROTOR') THEN
C
C -----
C TWIN ROTOR (TANDEM) WITH BLADE TIP OVERLAP
C -----
C
C IF (MESHIN .EQ. 0) THEN
C
C -----
C ROTOR TIPS APPROACHING AIRFRAME (CH-47 270-DEG)
C -----
C
C h/R EFFECT COEFFICIENTS (MEAN AND PEAK)
C -----

```

```

CST_Decay_MN = 2.10 + 0.15 * Iplane_Offset
CST_Decay_PK = 2.48 + 0.12 * Iplane_Offset
C
h_over_R_func_MN = CST_Decay_MN - 0.0355 * (EX_HT_ov_RAD)**2
h_over_R_func_PK = CST_Decay_PK - 0.0352 * (EX_HT_ov_RAD)**2
C
h_over_R_func_MN = MIN(2.12, h_over_R_func_MN)
h_over_R_func_PK = MIN(2.65, h_over_R_func_PK)
C
Test_data_LMT_MN = 1.40
Test_data_LMT_PK = 1.90
C
ELSE
C
-----  

C ROTOR TIPS DEPARTING AIRFRAME (CH-47 90-DEG)  

C -----  

C
CST_Decay_MN = 2.13 + 0.07 * Iplane_Offset
CST_Decay_PK = 2.75 + 0.08 * Iplane_Offset
C
h_over_R_func_MN = CST_Decay_MN - 0.0331 * (EX_HT_ov_RAD)**2
h_over_R_func_PK = CST_Decay_PK - 0.0334 * (EX_HT_ov_RAD)**2
C
h_over_R_func_MN = MIN(2.20, h_over_R_func_MN)
h_over_R_func_PK = MIN(2.85, h_over_R_func_PK)
C
Test_data_LMT_MN = 1.57
Test_data_LMT_PK = 2.14
C
END IF
C
CST_HFLOW_WALL_MN = 0.15 + 0.0 * (Iplane_Offset**2)**0.5
CST_HFLOW_WALL_PK = 0.19 + 0.0 * (Iplane_Offset**2)**0.5
C
END IF
C
-----  

C TWIN ROTOR DISK LOADING EFFECT COEFFICIENT (MEAN AND PEAK)  

C DEFAULT VALUE SET = 0 AT THIS TIME  

C -----  

C
DL_func = 0.0
C
-----  

C TWIN ROTOR COMBINED h/R AND DISK LOADING EFFECT (MEAN AND PEAK)  

C -----  

C
hDL_func_MN = h_over_R_func_MN + DL_func
hDL_func_PK = h_over_R_func_PK + DL_func
C
-----  

C CALCULATION OF EXPONENT IN THE VELOCITY DECAY (Cu) EQUATION  

C -----  

C
IF (CONFIGURATION .EQ. 'TILT_ROTOR') THEN
C
-----  

C TWIN ROTOR (TILTROTOR) WITHOUT BLADE TIP OVERLAP  

C -----  

C
IF (MESHIN .EQ. 0) THEN
C
-----  

C ROTOR TIPS APPROACHING AIRFRAME (XV-15 0-DEG)  

C -----  

C
h/R EFFECT COEFFICIENTS (MEAN AND PEAK)  

C -----  

C
CST_EXP_IP_MN = 0.51908 + 0.12 * (Iplane_Offset**2)**0.5
CST_EXP_IP_PK = 0.55534 + 0.08 * (Iplane_Offset**2)**0.5
C

```

```

Exp_IP_MN = CST_EXP_IP_MN + 0.1744 / (EX_HT_ov_RAD)**2
Exp_IP_PK = CST_EXP_IP_PK + 0.1190 / (EX_HT_ov_RAD)**2
C
Exp_IP_MN = MAX(0.5, MIN(0.70, Exp_IP_MN))
Exp_IP_PK = MAX(0.5, MIN(0.68, Exp_IP_PK))
C
ELSE
C
-----
C ROTOR TIPS DEPARTING AIRFRAME (XV-15 180-DEG)
-----
C
CST_EXP_IP_MN = 0.53287 + 0.08 * Iplane_Offset
CST_EXP_IP_PK = 0.57478 + 0.06 * Iplane_Offset
C
Exp_IP_MN = CST_EXP_IP_MN + 0.1158 / (EX_HT_ov_RAD)**2
Exp_IP_PK = CST_EXP_IP_PK + 0.1583 / (EX_HT_ov_RAD)**2
C
Exp_IP_MN = MAX(0.5, MIN(0.69, Exp_IP_MN))
Exp_IP_PK = MAX(0.5, MIN(0.70, Exp_IP_PK))
C
END IF
C
ELSE IF (CONFIGURATION .EQ. 'TANDEM_ROTOR') THEN
C
-----
C TWIN ROTOR (TANDEM) WITH BLADE TIP OVERLAP
-----
C
IF (MESHIN .EQ. 0) THEN
C
-----
C ROTOR TIPS APPROACHING AIRFRAME (CH-47 270-DEG)
-----
C
-----  
h/R EFFECT COEFFICIENTS (MEAN AND PEAK)
-----
C
CST_EXP_IP_MN = 0.64420 + 0.0 * Iplane_Offset
CST_EXP_IP_PK = 0.59376 + 0.0 * Iplane_Offset
C
Exp_IP_MN = CST_EXP_IP_MN + 0.05764 / (EX_HT_ov_RAD)**2
Exp_IP_PK = CST_EXP_IP_PK + 0.06064 / (EX_HT_ov_RAD)**2
C
Exp_IP_MN = MAX(0.60, MIN(0.72, Exp_IP_MN))
Exp_IP_PK = MAX(0.55, MIN(0.68, Exp_IP_PK))
C
ELSE
C
-----
C ROTOR TIPS DEPARTING AIRFRAME (CH-47 90-DEG)
-----
C
CST_EXP_IP_MN = 0.67690 + 0.0 * Iplane_Offset
CST_EXP_IP_PK = 0.67946 + 0.0 * Iplane_Offset
C
Exp_IP_MN = CST_EXP_IP_MN + 0.13524 / (EX_HT_ov_RAD)**2
Exp_IP_PK = CST_EXP_IP_PK + 0.18386 / (EX_HT_ov_RAD)**2
C
Exp_IP_MN = MAX(0.60, MIN(0.80, Exp_IP_MN))
Exp_IP_PK = MAX(0.68, MIN(0.82, Exp_IP_PK))
C
END IF
C
END IF
C
-----
C REFERENCE CONDITIONS FOR DECAY OF INTERACTION PLANE FLOW
C AT THE WALJET DISTANCE (BASED ON SINGLE ROTOR FLOW)
-----
C
CST1_MN = h_over_R_func_MN
CST1_PK = h_over_R_func_PK

```

```

CST2_MN = -0.30
CST2_PK = -0.30
C
WFLOW_Rj_ref_MN = CST1_MN + CST2_MN * (Rj**Exp_IP_MN)
WFLOW_Rj_ref_PK = CST1_PK + CST2_PK * (Rj**Exp_IP_PK)
C
C -----
C WAKE_vel LIMIT IN SUBROUTINE NORMAL_PROFILE FOR IPLANE
C -----
C
IF (AGL_GEAR .LT. 0.25) Test_data_LMT_MN = 2.0
IF (AGL_GEAR .LT. 0.25) Test_data_LMT_PK = 3.0
C
WAKE_vel_LMT_MN = MIN(WFLOW_Rj_ref_MN, Test_data_LMT_MN)
WAKE_vel_LMT_PK = MIN(WFLOW_Rj_ref_PK, Test_data_LMT_PK)
C
END IF
C
C -----
C DIAGNOSTIC PRINT
C -----
C
IF (DEBUG_FLAG) THEN
    WRITE (DOUTPUT, 800) THRUST, GROSS_WEIGHT,
1     AGL_GEAR, Iplane_Offset, SEPARATION,
2     Sensor_Offset, EXIT_HEIGHT, EX_HT_ov_RAD,
3     VEL_INDUCED, GRD_EFF, EQUIV_VEL, WAKE_vel,
4     RFLOW_init, RW, Z, Rj,
5     CST_Decay_MN, CST_Decay_PK,
6     CST_HFLOW_WALL_MN, CST_HFLOW_WALL_PK,
7     h_over_R_func_MN, h_over_R_func_PK,
8     Test_data_LMT_MN, Test_data_LMT_PK,
9     DL_func, hDL_func_MN, hDL_func_PK,
1     Exp_DL_func, Exp_GEF_func,
2     Exp_Cu_MN, Exp_Cu_PK,
3     h_ov_R_WJ_lmt_MN, h_ov_R_WJ_lmt_PK,
4     Wvel_Veq_fac_MN, Wvel_Veq_fac_PK,
5     WAKE_vel_LMT_MN, WAKE_vel_LMT_PK,
6     Wvel_Max_MN, Wvel_Max_PK,
7     hM_Decay_MN, hM_Offset_MN,
8     hM_Decay_PK, hM_Offset_PK, Cu_ref_MN, Cu_ref_PK,
9     XFLOW_init, HFLOW_init,
1     WFLOW_ref_MN, WFLOW_ref_PK,
2     HFLOW_ref_MN, HFLOW_ref_PK,
3     Exp_IP_MN, Exp_IP_PK,
4     WFLOW_Rj_ref_MN, WFLOW_Rj_ref_PK
C
800  FORMAT(1X, 'Subroutine ROTOR_WAKE', '/',
1      'THRUST = ',F8.0, ' lbs ',/,
2      'GROSS_WEIGHT = ',F8.0, ' lbs ',/,
3      'AGL_GEAR = ',F8.2, ' ft ',/,
4      'Iplane_Offset = ',F8.4, ' ND ',/,
5      'SEPARATION = ',F8.2, ' ft ',/,
6      'Sensor_Offset = ',F8.2, ' ft ',/,
7      'EXIT_HEIGHT = ',F8.2, ' ft ',/,
8      'EX_HT_ov_RAD = ',F8.4, ' ND ',/,
9      'VEL_INDUCED = ',F8.2, ' ft/s ',/,
1      'GRD_EFF = ',F8.4, ' ND ',/,
2      'EQUIV_VEL = ',F8.2, ' ft/s ',/,
3      'WAKE_vel = ',F8.2, ' ft/s ',/,
4      'RFLOW_init = ',F8.2, ' ft ',/,
5      'RW = ',F8.4, ' ND ',/,
6      'Z = ',F8.4, ' ft ',/,
7      'Rj = ',F8.4, ' ND ',/,
8      'CST_Decay_MN = ',F8.4, ' ND ',/,
9      'CST_Decay_PK = ',F8.4, ' ND ',/,
1      'CST_HFLOW_WALL_MN = ',F8.4, ' ND ',/,
2      'CST_HFLOW_WALL_PK = ',F8.4, ' ND ',/,
3      'h_over_R_func_MN = ',F8.4, ' ND ',/,
4      'h_over_R_func_PK = ',F8.4, ' ND ',/,
5      'Test_data_LMT_MN = ',F8.4, ' ND ',/,
6      'Test_data_LMT_PK = ',F8.4, ' ND ',/

```

```

7      '      DL_func = ',F8.4, ' ND ',/,,
8      '      hDL_func_MN = ',F8.4, ' ND ',/,,
9      '      hDL_func_PK = ',F8.4, ' ND ',/,,
1      '      Exp_DL_func = ',F8.4, ' ND ',/,,
2      '      Exp_GEF_func = ',F8.4, ' ND ',/,,
3      '      Exp_Cu_MN = ',F8.4, ' ND ',/,,
4      '      Exp_Cu_PK = ',F8.4, ' ND ',/,,
5      '      h_ov_R_WJ_lmt_MN = ',F8.4, ' ND ',/,,
6      '      h_ov_R_WJ_lmt_PK = ',F8.4, ' ND ',/,,
7      '      Wvel_Veq_fac_MN = ',F8.4, ' ND ',/,,
8      '      Wvel_Veq_fac_PK = ',F8.4, ' ND ',/,,
9      '      WAKE_vel_LMT_MN = ',F8.2, ' ft/s',//,
1      '      WAKE_vel_LMT_PK = ',F8.2, ' ft/s',//,
2      '      Wvel_Max_MN = ',F8.2, ' ft/s',//,
3      '      Wvel_Max_PK = ',F8.2, ' ft/s',//,
4      '      hM_Decay_MN = ',F8.4, ' ND ',/,,
5      '      hM_Offset_MN = ',F8.4, ' ND ',/,,
6      '      hM_Decay_PK = ',F8.4, ' ND ',/,,
7      '      hM_Offset_PK = ',F8.4, ' ND ',/,,
8      '      Cu_ref_MN = ',F8.4, ' ND ',/,,
9      '      Cu_ref_PK = ',F8.4, ' ND ',/,,
1      '      XFLOW_init = ',F8.4, ' ND ',/,,
2      '      HFLOW_init = ',F8.4, ' ft ',/,,
3      '      WFLOW_ref_MN = ',F8.2, ' ft/s',//,
4      '      WFLOW_ref_PK = ',F8.2, ' ft/s',//,
5      '      HFLOW_ref_MN = ',F8.4, ' ND ',/,,
6      '      HFLOW_ref_PK = ',F8.4, ' ND ',/,,
7      '      Exp_IP_MN = ',F8.4, ' ND ',/,,
8      '      Exp_IP_PK = ',F8.4, ' ND ',/,,
9      '      WFLOW_Rj_ref_MN = ',F8.4, ' ND ',/,,
1      '      WFLOW_Rj_ref_PK = ',F8.4, ' ND ',//)
1
END IF
C
RETURN
END
C
-----
C END ROTOR_WAKE
C -----
C
SUBROUTINE CALCULATE_PROFILE_DATA
*****
THIS ROUTINE PRINTS THE PROFILE GRAPHICS OUTPUT DATA TO THE
FILE 'PROFILES.CSV'. THE DATA IS COMMA DELIMITATED TO MAKE
IT IMPORTABLE TO SPREADSHEETS SOFTWARE.
*****
INCLUDE 'GENERAL_.CMN'
INCLUDE 'LABELS__.CMN'
INCLUDE 'PROFILES.CMN'
INCLUDE 'OBJECT__.CMN'
INCLUDE 'FLOW____.CMN'
INCLUDE 'FLTCOND_.CMN'
C
INTEGER I, J
CHARACTER*2 MNPK_PROFILE
C
DO 500, I=1, DIST_number
C
IF (DEBUG_FLAG) THEN
  WRITE (DOUTPUT, 800) I, DIST_NONDIM(I),
1           DIST_NONDIM(I)/0.78,
2           DIST_NONDIM(I)*RADIUS
800  FORMAT(//, 1X 'Case # ', I2, /
1           1X, 'Subroutine CALCULATE_PROFILE_DATA', //,
2           ' DIST_NONDIM = ', F8.2, ' ND ',
3           ' DIST_NONDIM/0.78 = ', F8.2, ' ND ',
4           ' Distance = ', F8.1, ' ft', //)
END IF
C
CALL NORMAL_PROFILE (DIST_NONDIM(I)*RADIUS)
C
-----
```

```

C      MEAN VELOCITY PROFILE DEFINITION
C -----
C
C      DO 100, J=1, 101
C
C      MNPK_PROFILE = 'MN'
C
C      PT_HEIGHT_MN(I,J) = (J-1) * HFLOW_wall_MN / 100.0
C      CALL VELOCITY_PROFILE(MNPK_PROFILE, PT_HEIGHT_MN(I,J))
C      PROFILE_VEL_MN(I,J) = VEL_LOCAL
C
C -----
C      PEAK VELOCITY PROFILE DEFINITION
C -----
C
C      MNPK_PROFILE = 'PK'
C
C      PT_HEIGHT_PK(I,J) = (J-1) * HFLOW_wall_PK / 100.0
C      CALL VELOCITY_PROFILE(MNPK_PROFILE, PT_HEIGHT_PK(I,J))
C      PROFILE_VEL_PK(I,J) = VEL_LOCAL
C
C      100     CONTINUE
C
C      500     CONTINUE
C      RETURN
C      END
C
C -----
C      END CALCULATE_PROFILE_DATA
C -----
C
C      SUBROUTINE NORMAL_PROFILE (XDIST_object)
C
C ****
C THIS ROUTINE DETERMINES THE FLOW VALUES A GIVEN DISTANCE
C FROM THE AIRCRAFT ROTOR BASED ON CONVENTIONAL METHODS
C ****
C
C      INCLUDE 'FLOW_____.CMN'
C      INCLUDE 'GENERAL__.CMN'
C      INCLUDE 'LABELS_____.CMN'
C      INCLUDE 'FLTCOND_____.CMN'
C
C      REAL    HFLOW_av_MN, hM_Decay_MN, WFLOW_max_MN_kts, XROTOR_dist,
C      1      HFLOW_av_PK, hM_Decay_PK, WFLOW_max_PK_kts, XDIST_object,
C      2      WFLOW_av_MN, WFLOW_IP_MN, WFLOW_IP_MN_Old, RjXROT,
C      3      WFLOW_av_PK, WFLOW_IP_PK, WFLOW_IP_PK_Old
C
C -----
C      SET DEFAULT FOR PRINT
C -----
C
C      WFLOW_IP_MN = -2.0
C      WFLOW_IP_PK = -2.0
C      WFLOW_IP_MN_Old = -2.0
C      WFLOW_IP_PK_Old = -2.0
C
C -----
C      FIND DISTANCE FROM ROTOR CENTER TO POINT IN OUTFLOW
C -----
C
C      XROTOR_dist = XDIST_object
C
C -----
C      FLOW CONDITIONS AT NONDIMENSIONAL DISTANCE FROM ROTOR CENTER
C -----
C
C      RjXROT = XROTOR_dist / (RADIUS*0.78)
C
C -----
C      RADIAL AXIS FLOW
C -----

```

```

IF (TYPE_OUTFLOW .EQ. 'RADIAL') THEN
    IF (RjXROT .GE. XFLOW_init) THEN
C
C
C-----+
C      FLOW IS OUTSIDE START OF WALJET
C-----+
C
        WFLOW_av_MN = WFLOW_ref_MN / RjXROT**Exp_Cu_MN
        WFLOW_av_PK = WFLOW_ref_PK / RjXROT**Exp_Cu_PK
C
    ELSE IF (RjXROT .LT. XFLOW_init) THEN
C
C
C-----+
C      FLOW IS INSIDE START OF WALJET
C-----+
C
        WFLOW_av_MN = Wvel_Max_MN * (RjXROT / XFLOW_init)**0.75
        WFLOW_av_PK = Wvel_Max_PK * (RjXROT / XFLOW_init)**1.25
    END IF
C
    IF (WFLOW_av_MN.GT.WAKE_vel_LMT_MN) WFLOW_av_MN=WAKE_vel_LMT_MN
    IF (WFLOW_av_PK.GT.WAKE_vel_LMT_PK) WFLOW_av_PK=WAKE_vel_LMT_PK
END IF
C
C-----+
C      INTERACTION PLANE FLOW
C-----+
C
IF (TYPE_OUTFLOW .EQ. 'CENTER') THEN
    IF (RjXROT .GE. XFLOW_init) THEN
C
C
C-----+
C      FLOW IS OUTSIDE START OF WALJET
C-----+
C
        WFLOW_IP_MN = CST1_MN + CST2_MN * (RjXROT**Exp_IP_MN)
        WFLOW_IP_PK = CST1_PK + CST2_PK * (RjXROT**Exp_IP_PK)
C
C-----+
C      VELOCITY RATIO IS ADJUSTED IN THE FAR FIELD TO AN
C      EXPONENTIAL WASHOUT IF THE RAIO IS =< 0.2
C-----+
C
        WFLOW_IP_MN_Old = 0.0
        WFLOW_IP_PK_Old = 0.0
C
        IF (WFLOW_IP_MN .LE. 0.2) THEN
            WFLOW_IP_MN_Old = WFLOW_IP_MN
            WFLOW_IP_MN = 0.2*EXP(-0.2 + WFLOW_IP_MN)
        ENDIF
C
        IF (WFLOW_IP_PK .LE. 0.2) THEN
            WFLOW_IP_PK_Old = WFLOW_IP_PK
            WFLOW_IP_PK = 0.2*EXP(-0.2 + WFLOW_IP_PK)
        ENDIF
C
    ELSE IF (RjXROT .LT. XFLOW_init) THEN
C
C
C-----+
C      FLOW IS INSIDE START OF WALJET
C-----+
C
        WFLOW_IP_MN = WAKE_vel_LMT_MN * (RjXROT / XFLOW_init)**0.75
        WFLOW_IP_PK = WAKE_vel_LMT_PK * (RjXROT / XFLOW_init)**0.75
C
        WFLOW_IP_MN_Old = 0.0
        WFLOW_IP_PK_Old = 0.0
C
    END IF
C
        IF (WFLOW_IP_MN.GT.WAKE_vel_LMT_MN) WFLOW_IP_MN=WAKE_vel_LMT_MN
        IF (WFLOW_IP_PK.GT.WAKE_vel_LMT_PK) WFLOW_IP_PK=WAKE_vel_LMT_PK
C

```

```

WFLOW_av_MN = EQUIV_VEL * WFLOW_IP_MN
WFLOW_av_PK = EQUIV_VEL * WFLOW_IP_PK
C
END IF
C
WFLOW_max_MN = WFLOW_av_MN
WFLOW_max_PK = WFLOW_av_PK
C
WFLOW_max_MN_kts = WFLOW_av_MN/kts_fps
WFLOW_max_PK_kts = WFLOW_av_PK/kts_fps
C
hM_Decay_MN    = 1.265 - 3.085/(RjXROT**0.5) + 2.304 / RjXROT
hM_Decay_PK    = 2.105 - 4.812/(RjXROT**0.5) + 3.373 / RjXROT
C
HFLOW_av_MN    = (hM_Decay_MN + HFLOW_ref_MN)*(RADIUS*0.78)
HFLOW_av_PK    = (hM_Decay_PK + 0.0)*(RADIUS*0.78)
C
-----
C PROFILE COEFFICIENTS HFLOW_wall AND N_Exponent
C BOTH DEPENDENT ON ROTORCRAFT CONFIGURATION
C EMPIRICALLY ADJUSTED FROM FLIGHT TEST DATA
C -----
C
IF (TYPE_OUTFLOW .EQ. 'RADIAL') THEN
C
    HFLOW_wall_MN = HFLOW_av_MN / 0.29
    HFLOW_wall_PK = HFLOW_av_PK / 0.32
C
    IF (CONFIGURATION .EQ. 'TANDEM_ROTOR') THEN
        HFLOW_wall_MN = HFLOW_av_MN / 0.20
        HFLOW_wall_PK = HFLOW_av_PK / 0.30
    ENDIF
C
    IF (CONFIGURATION .EQ. 'TILT_ROTOR') THEN
        HFLOW_wall_MN = HFLOW_av_MN / 0.29
        HFLOW_wall_PK = HFLOW_av_PK / 0.39
    ENDIF
C
    ELSE IF (TYPE_OUTFLOW .EQ. 'CENTER') THEN
C
C INTERACTION PLANE HEIGHT FUNCTION IS NOT ADJUSTED WHEN THE
C CORRESPONDING VELOCITY RATIO IS ADJUSTED IN THE FAR FIELD
C TO AN EXPONENTIAL WASHOUT (WFLOW_IP_MN =< 0.2)
C
        HFLOW_wall_MN = HFLOW_av_MN / CST_HFLOW_WALL_MN
        HFLOW_wall_PK = HFLOW_av_PK / CST_HFLOW_WALL_PK
    END IF
C
    IF (TYPE_OUTFLOW .EQ. 'RADIAL') THEN
C
        N_Exponent_MN = 0.5
        N_Exponent_PK = 0.5
C
        IF (CONFIGURATION .EQ. 'SINGLE_ROTOR') THEN
            N_Exponent_MN = 0.5
            N_Exponent_PK = 0.4
        ENDIF
C
        ELSE IF (TYPE_OUTFLOW .EQ. 'CENTER') THEN
            IF (CONFIGURATION .EQ. 'TANDEM_ROTOR') THEN
                N_Exponent_MN = 0.22
                N_Exponent_PK = 0.22
            ELSE
                N_Exponent_MN = 0.25
                N_Exponent_PK = 0.25
            ENDIF
        END IF
C
        -----
C DIAGNOSTIC PRINT
C -----
C
        IF (DEBUG_FLAG) THEN

```

```

      WRITE (DOUTPUT, 800) XROTOR_dist, RjXROT,
1           Exp_Cu_MN,   Exp_Cu_PK,
2           Wvel_Max_MN, Wvel_Max_PK,
3           WFLOW_ref_MN, WFLOW_ref_PK,
4           WFLOW_av_MN, WFLOW_av_PK,
5           WFLOW_max_MN_kts, WFLOW_max_PK_kts,
6           hM_Decay_MN, hM_Decay_PK,
7           HFLOW_ref_MN, HFLOW_ref_PK,
8           HFLOW_av_MN, HFLOW_av_PK,
9           HFLOW_wall_MN, HFLOW_wall_PK,
1           N_Exponent_MN, N_Exponent_PK,
2           WFLOW_IP_MN_Old, WFLOW_IP_PK_Old,
3           WFLOW_IP_MN, WFLOW_IP_PK

C
800    FORMAT(1X, 'Subroutine NORMAL_PROFILE', '/',
1           XROTOR_dist = ', F8.0, ' ft' ,/',
2           RjXROT = ', F8.4, ' ND' ,/',
3           Exp_Cu_MN = ', F8.4, ' ND' ,/',
4           Exp_Cu_PK = ', F8.4, ' ND' ,/',
5           Wvel_Max_MN = ', F8.2, ' ft/s' ,/',
6           Wvel_Max_PK = ', F8.2, ' ft/s' ,/',
7           WFLOW_ref_MN = ', F8.2, ' ft/s' ,/',
8           WFLOW_ref_PK = ', F8.2, ' ft/s' ,/',
9           WFLOW_av_MN = ', F8.2, ' ft/s' ,/',
1           WFLOW_av_PK = ', F8.2, ' ft/s' ,/',
2           WFLOW_max_MN_kts = ', F8.2, ' kt' ,/',
3           WFLOW_max_PK_kts = ', F8.2, ' kt' ,/',
4           hM_Decay_MN = ', F8.4, ' ND' ,/',
5           hM_Decay_PK = ', F8.4, ' ND' ,/',
6           HFLOW_ref_MN = ', F8.3, ' ND' ,/',
7           HFLOW_ref_PK = ', F8.3, ' ND' ,/',
8           HFLOW_av_MN = ', F8.3, ' ft' ,/',
9           HFLOW_av_PK = ', F8.3, ' ft' ,/',
1           HFLOW_wall_MN = ', F8.3, ' ft' ,/',
2           HFLOW_wall_PK = ', F8.3, ' ft' ,/',
3           N_Exponent_MN = ', F8.4, ' ND' ,/',
4           N_Exponent_PK = ', F8.4, ' ND' ,/',
5           WFLOW_IP_MN_Old = ', F8.4, ' ND' ,/',
6           WFLOW_IP_PK_Old = ', F8.4, ' ND' ,/',
7           WFLOW_IP_MN = ', F8.4, ' ND' ,/',
8           WFLOW_IP_PK = ', F8.4, ' ND' ,/)

C
END IF

C
RETURN
END

C
-----
C
END NORMAL_PROFILE
-----

C
SUBROUTINE VELOCITY_PROFILE (MNorPK_PROFILE, ZDIST_object)
C
*****
C THIS ROUTINE FINDS THE VELOCITY OF THE CENTROID OF THE
C OBJECT BASED ON THE SHAPE OF THE FLOW PROFILE AND LOCATION
C OF THE OBJECT
C ****
C
INCLUDE 'GENERAL_.CMN'
INCLUDE 'LABELS__.CMN'
INCLUDE 'FLOW____.CMN'
INCLUDE 'OBJECT__.CMN'
INCLUDE 'FLTCOND_.CMN'

C
REAL N_EXPONENT, ZDIST_object, WFLOW_max,
1     PROFILE_ZDIST, HFLOW_wall
CHARACTER*2 MNorPK_PROFILE

C
-----
C
VALUES SET ON "MNorPK_PROFILE" - MEAN OR PEAK
C
-----
```

```

IF (MNorPK_PROFILE .EQ. 'MN') THEN
    WFLOW_max = WFLOW_max_MN
    HFLOW_wall = HFLOW_wall_MN
    N_EXPONENT = N_Exponent_MN
ELSE IF (MNorPK_PROFILE .EQ. 'PK') THEN
    WFLOW_max = WFLOW_max_PK
    HFLOW_wall = HFLOW_wall_PK
    N_EXPONENT = N_Exponent_PK
ENDIF
C
HFLOW_rpeak = N_EXPONENT/(N_EXPONENT + M_EXPONENT)
C
C -----
C GET THE COEFFICIENT OF THE INTEGRAL FOR THE FORCE AND MOMENT
C CALCULATIONS
C -----
C
VELOCITY_coef = WFLOW_max / (HFLOW_rpeak**N_EXPONENT *
1      (1 - HFLOW_rpeak)**M_EXPONENT)
C
PROFILE_ZDIST = ZDIST_object / HFLOW_wall
C
C -----
C CHECK TO SEE IF POINT CONSIDERED IS OUTSIDE VELOCITY PROFILE,
C IF IT IS, THEN SET THE VELOCITY OF THE OUTFLOW TO ZERO
C -----
C
IF ((PROFILE_ZDIST .LT. 0.0) .OR. (PROFILE_ZDIST .GT. 1.0)) THEN
    VEL_LOCAL = 0
C
ELSE
    VEL_LOCAL = VELOCITY_coef *
1          (PROFILE_ZDIST**N_EXPONENT) *
2          (1 - PROFILE_ZDIST)**M_EXPONENT
    IF (VEL_LOCAL .LT. 0) VEL_LOCAL = 0
END IF
C
RETURN
C
C -----
C DIAGNOSTIC PRINT
C -----
C
IF (DEBUG_FLAG) THEN
    WRITE (DOUTPUT, 800) MNorPK_PROFILE,
1        VELOCITY_coef, WFLOW_max, HFLOW_wall,
2        HFLOW_rpeak, M_EXPONENT, N_EXPONENT,
3        PROFILE_ZDIST, VEL_LOCAL/kts_fps,
4        ZDIST_object
C
800    FORMAT(1X, 'Subroutine VELOCITY_PROFILE', '/',
1          ' MNorPK_PROFILE = ', A2,
2          ' VELOCITY_coef = ', F8.2, ' ND ',
3          ' WFLOW_max = ', F8.2, ' ND ',
4          ' HFLOW_wall = ', F8.3, ' ND ',
5          ' HFLOW_rpeak = ', F8.4, ' ND ',
6          ' M_EXPONENT = ', F8.4, ' ND ',
7          ' N_EXPONENT = ', F8.4, ' ND ',
8          ' PROFILE_ZDIST = ', F8.1, ' ft ',
9          ' VEL_LOCAL = ', F8.2, ' kts',
1          ' ZDIST_objectL = ', F8.3, ' ft', //)
    END IF
C
RETURN
C
END
C
C -----
C END VELOCITY_PROFILE
C -----
C
SUBROUTINE OUTPUT_PROFILE_DATA (CALC_ANGLE, K, GNOUTPT)
C ****

```

```

C THIS ROUTINE PRINTS THE PROFILE GRAPHICS OUTPUT DATA TO THE FILE
C 'PROFILES.CSV'. THE DATA IS COMMA DELIMITED TO MAKE IT
C IMPORTABLE TO SPREADSHEETS SOFTWARE.
C ****
C
INCLUDE 'PROFILES.CMN'
INCLUDE 'GENERAL_.CMN'
INCLUDE 'DATE_____.CMN'
INCLUDE 'FLTCOND_.CMN'
INCLUDE 'LABELS_____.CMN'
INCLUDE 'OBJECT_____.CMN'
INCLUDE 'FLOW_____.CMN'

C
REAL CALC_ANGLE
INTEGER I, K, GNOUTPT
CHARACTER*1 MER

C -----
C "MER" PROCESSING IS FOR MAC FORTRAN DATE/TIME
C

IF (IHOUR .GT. 12) THEN
    MER = 'P'
    IHOUR = IHOUR - 12
ELSE
    MER = 'A'
END IF

C
IF(K .EQ. 0) THEN
    WRITE(GNOUTPT,900) TITLE,      IMONTH, IDAY,
1                      IYEAR,     IHOUR,   IMINUTE,
2                      ISECOND,  I100TH, MER
C
    WRITE(GNOUTPT,910) GROSS_WEIGHT, AGL_GEAR, DENSITY_AIR,
1                      THRUST_TO_WEIGHT
    WRITE(GNOUTPT,920)
    WRITE(GNOUTPT,970) CALC_ANGLE
    IF (DIST_UNITS .EQ. 'DIMEN') THEN
        WRITE(GNOUTPT,940) DIST_values(1), DIST_values(2),
1                        DIST_values(3), DIST_values(4),
2                        DIST_values(5), DIST_values(6),
3                        DIST_values(7), DIST_values(8),
4                        DIST_values(9), DIST_values(10),
5                        DIST_values(11), DIST_values(12)
    ELSE
        WRITE(GNOUTPT,940) DIST_values(1)*RADIUS, DIST_values(2)*RADIUS,
1                        DIST_values(3)*RADIUS, DIST_values(4)*RADIUS,
2                        DIST_values(5)*RADIUS, DIST_values(6)*RADIUS,
3                        DIST_values(7)*RADIUS, DIST_values(8)*RADIUS,
4                        DIST_values(9)*RADIUS, DIST_values(10)*RADIUS,
4                        DIST_values(11)*RADIUS, DIST_values(12)*RADIUS
    END IF
END IF

IF(K .GT. 0) WRITE(GNOUTPT,970) CALC_ANGLE

C
IF (DIST_UNITS .EQ. 'DIMEN') THEN
    WRITE(GNOUTPT,950) DIST_values(1), DIST_values(1),
1                    DIST_values(2), DIST_values(2),
2                    DIST_values(3), DIST_values(3),
3                    DIST_values(4), DIST_values(4),
4                    DIST_values(5), DIST_values(5),
5                    DIST_values(6), DIST_values(6),
6                    DIST_values(7), DIST_values(7),
7                    DIST_values(8), DIST_values(8),
8                    DIST_values(9), DIST_values(9),
9                    DIST_values(10), DIST_values(10),
1                    DIST_values(11), DIST_values(11),
2                    DIST_values(12), DIST_values(12)
ELSE
    WRITE(GNOUTPT,955) DIST_values(1), DIST_values(1),
1                    DIST_values(2), DIST_values(2),
2                    DIST_values(3), DIST_values(3),

```

```

3           DIST_values(4),  DIST_values(4),
4           DIST_values(5),  DIST_values(5),
5           DIST_values(6),  DIST_values(6),
6           DIST_values(7),  DIST_values(7),
7           DIST_values(8),  DIST_values(8),
8           DIST_values(9),  DIST_values(9),
9           DIST_values(10), DIST_values(10),
1           DIST_values(11), DIST_values(11),
2           DIST_values(12), DIST_values(12)
END IF
C
DO 100, I=1, 101
  WRITE(GNOUTPT,960)
1   PT_HEIGHT_MN(1,I), PROFILE_VEL_MN(1,I)/kts_fps,
1   PT_HEIGHT_PK(1,I), PROFILE_VEL_PK(1,I)/kts_fps,
2   PT_HEIGHT_MN(2,I), PROFILE_VEL_MN(2,I)/kts_fps,
2   PT_HEIGHT_PK(2,I), PROFILE_VEL_PK(2,I)/kts_fps,
3   PT_HEIGHT_MN(3,I), PROFILE_VEL_MN(3,I)/kts_fps,
3   PT_HEIGHT_PK(3,I), PROFILE_VEL_PK(3,I)/kts_fps,
4   PT_HEIGHT_MN(4,I), PROFILE_VEL_MN(4,I)/kts_fps,
4   PT_HEIGHT_PK(4,I), PROFILE_VEL_PK(4,I)/kts_fps,
5   PT_HEIGHT_MN(5,I), PROFILE_VEL_MN(5,I)/kts_fps,
5   PT_HEIGHT_PK(5,I), PROFILE_VEL_PK(5,I)/kts_fps,
6   PT_HEIGHT_MN(6,I), PROFILE_VEL_MN(6,I)/kts_fps,
6   PT_HEIGHT_PK(6,I), PROFILE_VEL_PK(6,I)/kts_fps,
7   PT_HEIGHT_MN(7,I), PROFILE_VEL_MN(7,I)/kts_fps,
7   PT_HEIGHT_PK(7,I), PROFILE_VEL_PK(7,I)/kts_fps,
8   PT_HEIGHT_MN(8,I), PROFILE_VEL_MN(8,I)/kts_fps,
8   PT_HEIGHT_PK(8,I), PROFILE_VEL_PK(8,I)/kts_fps,
9   PT_HEIGHT_MN(9,I), PROFILE_VEL_MN(9,I)/kts_fps,
9   PT_HEIGHT_PK(9,I), PROFILE_VEL_PK(9,I)/kts_fps,
1   PT_HEIGHT_MN(10,I), PROFILE_VEL_MN(10,I)/kts_fps,
1   PT_HEIGHT_PK(10,I), PROFILE_VEL_PK(10,I)/kts_fps,
1   PT_HEIGHT_MN(11,I), PROFILE_VEL_MN(11,I)/kts_fps,
1   PT_HEIGHT_PK(11,I), PROFILE_VEL_PK(11,I)/kts_fps,
1   PT_HEIGHT_MN(12,I), PROFILE_VEL_MN(12,I)/kts_fps,
1   PT_HEIGHT_PK(12,I), PROFILE_VEL_PK(12,I)/kts_fps
100  CONTINUE
C
900  FORMAT('1', /, 1X, A80,'.....', I2, '/', I2.2, '/', I4.4,
1      ',', I2, ':', I2.2, ':', I2.2, '.', I2.2, ' ', A1, 'M')
C
910  FORMAT(1X, 'Plot Title:, EFFECTS Profile Output - ',
1      'GW: ', F8.0, ' lbs  ALG: ', F5.1, ' ft',
2      ' Air Density: ', F8.5, ' slug/ft^3  T/W: ', F8.3)
920  FORMAT(1X, 'X Axis: ,Velocity (kts), ', 'Y Axis: ,Height (ft)')
940  FORMAT(1X, 'Distance (ft):,, ', F8.2,' ', F8.2,
1      ', ', F8.2,' ', F8.2,' ', F8.2,
2      ', ', F8.2,' ', F8.2,' ', F8.2,
3      ', ', F8.2,' ', F8.2,/)
950  FORMAT(/,1X,' Height ,', F6.1, ' ft Mean,',,
1      ' Height ,', F6.1, ' ft Peak,',,
2      ' Height ,', F6.1, ' ft Mean,',,
2      ' Height ,', F6.1, ' ft Peak,',,
3      ' Height ,', F6.1, ' ft Mean,',,
3      ' Height ,', F6.1, ' ft Peak,',,
4      ' Height ,', F6.1, ' ft Mean,',,
4      ' Height ,', F6.1, ' ft Peak,',,
5      ' Height ,', F6.1, ' ft Mean,',,
5      ' Height ,', F6.1, ' ft Peak,',,
6      ' Height ,', F6.1, ' ft Mean,',,
6      ' Height ,', F6.1, ' ft Peak,',,
7      ' Height ,', F6.1, ' ft Mean,',,
7      ' Height ,', F6.1, ' ft Peak,',,
8      ' Height ,', F6.1, ' ft Mean,',,
8      ' Height ,', F6.1, ' ft Peak,',,
9      ' Height ,', F6.1, ' ft Mean,',,
9      ' Height ,', F6.1, ' ft Peak,',,
1      ' Height ,', F6.1, ' ft Mean,',,
1      ' Height ,', F6.1, ' ft Peak,',,
2      ' Height ,', F6.1, ' ft Mean,',,
2      ' Height ,', F6.1, ' ft Peak,',,
3      ' Height ,', F6.1, ' ft Mean,',,

```

```

3           ' Height ,', F6.1, ' ft Peak,/,)
C
955  FORMAT(1X,' Height ,', F6.2, ' x/R Mean,',
1     ' Height ,', F6.2, ' x/R Peak,',
2     ' Height ,', F6.2, ' x/R Mean,',
2     ' Height ,', F6.2, ' x/R Peak,',
3     ' Height ,', F6.2, ' x/R Mean,',
3     ' Height ,', F6.2, ' x/R Peak,',
4     ' Height ,', F6.2, ' x/R Mean,',
4     ' Height ,', F6.2, ' x/R Peak,',
5     ' Height ,', F6.2, ' x/R Mean,',
5     ' Height ,', F6.2, ' x/R Peak,',
6     ' Height ,', F6.2, ' x/R Mean,',
6     ' Height ,', F6.2, ' x/R Peak,',
7     ' Height ,', F6.2, ' x/R Mean,',
7     ' Height ,', F6.2, ' x/R Peak,',
8     ' Height ,', F6.2, ' x/R Mean,',
8     ' Height ,', F6.2, ' x/R Peak,',
9     ' Height ,', F6.2, ' x/R Mean,',
9     ' Height ,', F6.2, ' x/R Peak,',
1    ' Height ,', F6.2, ' x/R Mean,',
1    ' Height ,', F6.2, ' x/R Peak,',
2    ' Height ,', F6.2, ' x/R Mean,',
2    ' Height ,', F6.2, ' x/R Peak,',
3    ' Height ,', F6.2, ' x/R Mean,',
3    ' Height ,', F6.2, ' x/R Peak,/,)
C
960  FORMAT(2X, F7.2, ' ,', F6.2, ' ,', F7.2, ' ,', F6.2,
1     ' ,', F7.2, ' ,', F6.2, ' ,', F7.2, ' ,', F6.2,
2     ' ,', F7.2, ' ,', F6.2, ' ,', F7.2, ' ,', F6.2,
3     ' ,', F7.2, ' ,', F6.2, ' ,', F7.2, ' ,', F6.2,
4     ' ,', F7.2, ' ,', F6.2, ' ,', F7.2, ' ,', F6.2,
5     ' ,', F7.2, ' ,', F6.2, ' ,', F7.2, ' ,', F6.2,
6     ' ,', F7.2, ' ,', F6.2, ' ,', F7.2, ' ,', F6.2,
7     ' ,', F7.2, ' ,', F6.2, ' ,', F7.2, ' ,', F6.2,
8     ' ,', F7.2, ' ,', F6.2, ' ,', F7.2, ' ,', F6.2,
9     ' ,', F7.2, ' ,', F6.2, ' ,', F7.2, ' ,', F6.2,
1    ' ,', F7.2, ' ,', F6.2, ' ,', F7.2, ' ,', F6.2,
2    ' ,', F7.2, ' ,', F6.2, ' ,', F7.2, ' ,', F6.2)
970  FORMAT(1X,'Azimuth Angle:,,',F8.1,'Degrees from centerline',/)
C
      RETURN
      END
C
C --- END OUTPUT_PROFILE_DATA
C
      SUBROUTINE OUTPUT_MAX_PROFILE(PROFILE_VEL_MAX,
1                           ANGLE_STORE, DIST_TO_CENTER)
      REAL PROFILE_VEL_MAX(3,12)
      REAL ANGLE_STORE(*), DIST_TO_CENTER
C ****
C THIS ROUTINE PRINTS THE MAXIMUM VELOCITY DATA TO THE FILE MAX_V_PROFILES.CSV
C ****
C
      INCLUDE 'PROFILES.CMN'
      INCLUDE 'GENERAL_.CMN'
      INCLUDE 'DATE____.CMN'
      INCLUDE 'FLTCOND_.CMN'
      INCLUDE 'LABELS__.CMN'
      INCLUDE 'OBJECT__.CMN'
      INCLUDE 'FLOW____.CMN'
C
      REAL I
      CHARACTER*1 MER
C -----
C "MER" PROCESSING IS FOR MAC FORTRAN DATE/TIME
C
      IF (IHOUR.GT.12) THEN
         MER = 'P'
         IHOUR = IHOUR - 12
      ELSE
         MER = 'A'
      END IF

```

```

C
      WRITE(VOUTPT,900) TITLE,    IMONTH, IDAY,
1          IYEAR,     IHOUR,   IMINUTE,
2          ISECOND,  I100TH, MER
C
      WRITE(VOUTPT,910) GROSS_WEIGHT, AGL_GEAR, DENSITY_AIR,
1          THRUST_TO_WEIGHT, PEAK_OR_MEAN
      WRITE(VOUTPT,920)
      WRITE(VOUTPT,930)
      WRITE(VOUTPT,940) DIST_TO_CENTER, RADIUS
C
C      large IF statement to print peak/mean items
C
      IF (DIST_UNITS .EQ. 'DIMEN') THEN
C
        WRITE(VOUTPT,950) 'Dist (ft):',
1 DIST_values(1), DIST_values(2), DIST_values(3), DIST_values(4),
2 DIST_values(5), DIST_values(6), DIST_values(7), DIST_values(8),
3 DIST_values(9), DIST_values(10),DIST_values(11),DIST_values(12),
4 'Azimuth,,', 'Max Velocities:'
C
      ELSE
        WRITE(VOUTPT,960) 'Dist (ft):',
1 DIST_values(1) *RADIUS, DIST_values(2) *RADIUS,
2 DIST_values(3) *RADIUS, DIST_values(4) *RADIUS,
3 DIST_values(5) *RADIUS, DIST_values(6) *RADIUS,
4 DIST_values(7) *RADIUS, DIST_values(8) *RADIUS,
5 DIST_values(9) *RADIUS, DIST_values(10)*RADIUS,
6 DIST_values(11)*RADIUS, DIST_values(12)*RADIUS,
7 'Azimuth,,', 'Max Velocities (mph):'
C
      WRITE(VOUTPT,970)
1 DIST_values(1), DIST_values(2), DIST_values(3), DIST_values(4),
2 DIST_values(5), DIST_values(6), DIST_values(7), DIST_values(8),
3 DIST_values(9), DIST_values(10),DIST_values(11),DIST_values(12)
C
      END IF
C
      DO 100 I =1,3
        WRITE(VOUTPT,980)ANGLE_STORE(I),
1           PROFILE_VEL_MAX(I,1)/mph_fps,'',
2           PROFILE_VEL_MAX(I,2)/mph_fps,'',
3           PROFILE_VEL_MAX(I,3)/mph_fps,'',
4           PROFILE_VEL_MAX(I,4)/mph_fps,'',
5           PROFILE_VEL_MAX(I,5)/mph_fps,'',
6           PROFILE_VEL_MAX(I,6)/mph_fps,'',
7           PROFILE_VEL_MAX(I,7)/mph_fps,'',
8           PROFILE_VEL_MAX(I,8)/mph_fps,'',
9           PROFILE_VEL_MAX(I,9)/mph_fps,'',
1           PROFILE_VEL_MAX(I,10)/mph_fps,'',
2           PROFILE_VEL_MAX(I,11)/mph_fps,'',
3           PROFILE_VEL_MAX(I,12)/mph_fps,''
C
100  CONTINUE
C
900  FORMAT('1', /, 1X, A80,'.....', I2, '/', I2.2, '/', I4.4,
1      ',', I2, ':', I2.2, ':', I2.2, '.', I2.2, ' ', A1, 'M')
910  FORMAT(1X, 'Plot Title: EFFECTS Max Velocity Profile- ',
1      'GW: ', F8.0, ' lbs ALG: ', F5.1, ' ft',
2      ' Air Density: ', F8.5, ' slug/ft^3 T/W: ', F8.3,
3      ' Force Calculation: ',A)
920  FORMAT(1X, 'X Axis: ,Velocity (kts)')
930  FORMAT(1X, 'Y Axis: ,Angle (deg)', '/')
940  FORMAT(1x,'Distance from Rotor to Center:,,,',
1      F6.2,/Radius:,,,F6.2/)
950  FORMAT(1X,',',A,
1      F8.2, ',', F8.2, ',', F8.2, ',', F8.2, ',',
2      F8.2, ',', F8.2, ',', F8.2, ',', F8.2, ',',
3      F8.2, ',', F8.2, ',', F8.2, ',', F8.2, //, A,A,/)
960  FORMAT(1X,',',A,
1      F8.2, ',', F8.2, ',', F8.2, ',', F8.2, ',',
2      F8.2, ',', F8.2, ',', F8.2, ',', F8.2, ',',
3      F8.2, ',', F8.2, ',', F8.2, ',', F8.2, //, A,A)

```

```

970  FORMAT(1X,',,',
1   F6.2, 'x/R ', F6.2, 'x/R ', F6.2, 'x/R ', F6.2, 'x/R ',
2   F6.2, 'x/R ', F6.2, 'x/R ', F6.2, 'x/R ', F6.2, 'x/R ',
3   F6.2, 'x/R ', F6.2, 'x/R ', F6.2, 'x/R ', F6.2, 'x/R ')
980  FORMAT(F7.2, ',,', F7.2, A, F7.2, A, F7.2, A, F7.2, A, F7.2, A,
1   F7.2, A, F7.2, A, F7.2, A, F7.2, A, F7.2, A, F7.2, A)
C
      RETURN
END
C
C --- END OUTPUT_MAX_PROFILE
C
C
      SUBROUTINE OUTPUT_FORCES_MOMENTS(FORCE_STORAGE,
1           MOMENT_STORAGE, ANGLE_STORE)
      REAL FORCE_STORAGE(3,12), MOMENT_STORAGE(3,12), ANGLE_STORE(3)
C
C ****
C THIS ROUTINE PRINTS THE FORCE AND MOMENT DATA TO THE FILE MAX_V_PROFILES.CSV
C ****
C
INCLUDE 'PROFILES.CMN'
INCLUDE 'GENERAL_.CMN'
INCLUDE 'DATE_____.CMN'
INCLUDE 'FLTCOND_.CMN'
INCLUDE 'LABELS_____.CMN'
INCLUDE 'OBJECT_____.CMN'
INCLUDE 'FLOW_____.CMN'
C
REAL I
C
      WRITE(VOUTPT,900) OBJ_SHAPE
C
      IF (DIST_UNITS .EQ. 'DIMEN') THEN
         WRITE(VOUTPT,910)
1   DIST_values(1), DIST_values(2), DIST_values(3), DIST_values(4),
2   DIST_values(5), DIST_values(6), DIST_values(7), DIST_values(8),
3   DIST_values(9), DIST_values(10), DIST_values(11), DIST_values(12)
      ELSE
         WRITE(VOUTPT,920)
1   DIST_values(1), DIST_values(2), DIST_values(3), DIST_values(4),
2   DIST_values(5), DIST_values(6), DIST_values(7), DIST_values(8),
3   DIST_values(9), DIST_values(10), DIST_values(11), DIST_values(12)
      END IF
C
      IF (DIST_UNITS .EQ. 'NONDIM') THEN
         WRITE(VOUTPT,930) 'Dist (ft):',
1   DIST_values(1) *RADIUS, DIST_values(2) *RADIUS,
2   DIST_values(3) *RADIUS, DIST_values(4) *RADIUS,
3   DIST_values(5) *RADIUS, DIST_values(6) *RADIUS,
4   DIST_values(7) *RADIUS, DIST_values(8) *RADIUS,
5   DIST_values(9) *RADIUS, DIST_values(10)*RADIUS,
6   DIST_values(11)*RADIUS, DIST_values(12)*RADIUS, 'Azimuth'
      ELSE
         WRITE(VOUTPT,930) 'Dist (ft):',
1   DIST_values(1), DIST_values(2), DIST_values(3), DIST_values(4),
2   DIST_values(5), DIST_values(6), DIST_values(7), DIST_values(8),
3   DIST_values(9), DIST_values(10), DIST_values(11), DIST_values(12),
4   'Azimuth'
      END IF
C
      DO 100 I =1,3
         WRITE(VOUTPT,940) ANGLE_STORE(I),',Force (lbs) ->,',
1   FORCE_STORAGE(I,1), ' ', FORCE_STORAGE(I,2), ' ',
2   FORCE_STORAGE(I,3), ' ', FORCE_STORAGE(I,4), ' ',
3   FORCE_STORAGE(I,5), ' ', FORCE_STORAGE(I,6), ' ',
4   FORCE_STORAGE(I,7), ' ', FORCE_STORAGE(I,8), ' ',
5   FORCE_STORAGE(I,9), ' ', FORCE_STORAGE(I,10), ' ',
6   FORCE_STORAGE(I,11), ' ', FORCE_STORAGE(I,12), ' '
C
         WRITE(VOUTPT,950)
1   MOMENT_STORAGE(I,1), ' ', MOMENT_STORAGE(I,2), ' ',
2   MOMENT_STORAGE(I,3), ' ', MOMENT_STORAGE(I,4), ' '

```

```

3     MOMENT_STORAGE(I,5),   ',',      MOMENT_STORAGE(I,6),   ',',
4     MOMENT_STORAGE(I,7),   ',',      MOMENT_STORAGE(I,8),   ',',
5     MOMENT_STORAGE(I,9),   ',',      MOMENT_STORAGE(I,10),  ',',
6     MOMENT_STORAGE(I,11),  ',',      MOMENT_STORAGE(I,12),  ','
100    CONTINUE
C
C -----
C
900  FORMAT(//'Object Shape:,,A,/ )
910  FORMAT(1X,',,,
1   F7.1, ' ft Peak,', F7.1, ' ft Peak,', F7.1, ' ft Peak,', 
2   F7.1, ' ft Peak,', F7.1, ' ft Peak,', F7.1, ' ft Peak,', 
3   F7.1, ' ft Peak,', F7.1, ' ft Peak,', F7.1, ' ft Peak,', 
4   F7.1, ' ft Peak,', F7.1, ' ft Peak,', F7.1, ' ft Peak,')
920  FORMAT(1X,',,,
1   F8.2, ' x/R Peak,', F8.2, ' x/R Peak,', F8.2, ' x/R Peak,', 
2   F8.2, ' x/R Peak,', F8.2, ' x/R Peak,', F8.2, ' x/R Peak,', 
3   F8.2, ' x/R Peak,', F8.2, ' x/R Peak,', F8.2, ' x/R Peak,', 
4   F8.2, ' x/R Peak,', F8.2, ' x/R Peak,', F8.2, ' x/R Peak,')
C
930  FORMAT(6X,   ',',      A,   6X, F8.2,   ',',      F8.2,   ',',
1       F8.2,   ',',      F8.2,   ',',      F8.2,   ',',      F8.2,   ',',
7       F8.2,   ',',      F8.2,   ',',      F8.2,   ',',      F8.2,   /,A)
C
940  FORMAT(   F8.2, A, F8.2, A, F8.2, A, F8.2, A, F8.2, A, F8.2, A,
1 F8.2, A, F8.2, A, F8.2, A, F8.2, A, F8.2, A, F8.2, A)
C
950  FORMAT(',','Moment (ft-lbs) ->,',
1      F20.2, A, F20.2, A, F20.2, A, F20.2, A, F20.2, A,
2      F20.2, A, F20.2, A, F20.2, A, F20.2, A, F20.2, A)
C
      RETURN
      END
C
C --- END OUTPUT_FORCES_MOMENTS
C
      SUBROUTINE GRAPHIC_OUTPUT_DATA
C ****
C THIS SUBROUTINE CALLS THE WAKE CALCULATION ROUTINES FOR CENTER FLOW
C THEN RADIAL FLOW.  THEN IT COMBINES THE TWO FLOWS AND OUTPUTS THE
C DATA.
C ****
C
      INCLUDE 'DATE_____.CMN'
      INCLUDE 'GENERAL__.CMN'
      INCLUDE 'LABELS___.CMN'
      INCLUDE 'FLOW_____.CMN'
      INCLUDE 'OBJECT_____.CMN'
      INCLUDE 'FLTCOND__.CMN'
      INCLUDE 'PROFILES.CMN'
C
      INTEGER I, J
C
      REAL PT_HEIGHT_MN_CENTER(12,101)
      REAL PT_HEIGHT_PK_CENTER(12,101)
      REAL PROFILE_VEL_MN_CENTER(12,101)
      REAL PROFILE_VEL_PK_CENTER(12,101)
C
      REAL PT_HEIGHT_MN_RADIAL(12,101)
      REAL PT_HEIGHT_PK_RADIAL(12,101)
      REAL PROFILE_VEL_MN_RADIAL(12,101)
      REAL PROFILE_VEL_PK_RADIAL(12,101)
C
C Call the first time with center flow selected
C Unless there is only one rotor, then radial flow is the
C only thing that makes sense.
      IF (NUMBER_ROTORS.EQ.1) THEN
        TYPE_OUTFLOW ='RADIAL'
      ELSE
        TYPE_OUTFLOW ='CENTER'
      END IF
C
      CALL ROTOR_WAKE

```

```

C
      CALL CALCULATE_PROFILE_DATA

C      Create Second copy of centerline profile variables
DO 200, I = 1, 12
      DO 199, J = 1, 101
          PT_HEIGHT_MN_CENTER(I,J)      = PT_HEIGHT_MN(I,J)
          PT_HEIGHT_PK_CENTER(I,J)      = PT_HEIGHT_PK(I,J)
          PROFILE_VEL_MN_CENTER(I,J)    = PROFILE_VEL_MN(I,J)
          PROFILE_VEL_PK_CENTER(I,J)    = PROFILE_VEL_PK(I,J)
199      CONTINUE
200      CONTINUE
C
C      Call the second time with radial flow selected
      TYPE_OUTFLOW ='RADIAL'
C
      CALL ROTOR_WAKE
C
      CALL CALCULATE_PROFILE_DATA

C      Create Second copy of radial profile variables
DO 300, I = 1, 12
      DO 299, J = 1, 101
          PT_HEIGHT_MN_RADIAL(I,J)     = PT_HEIGHT_MN(I,J)
          PT_HEIGHT_PK_RADIAL(I,J)     = PT_HEIGHT_PK(I,J)
          PROFILE_VEL_MN_RADIAL(I,J)   = PROFILE_VEL_MN(I,J)
          PROFILE_VEL_PK_RADIAL(I,J)   = PROFILE_VEL_PK(I,J)
299      CONTINUE
300      CONTINUE
C
C      Combine radial and centerline flow
      CALL COMBINE_FLOWS(PT_HEIGHT_MN_CENTER, PROFILE_VEL_MN_CENTER,
1                      PT_HEIGHT_PK_CENTER, PROFILE_VEL_PK_CENTER,
2                      PT_HEIGHT_MN_RADIAL, PROFILE_VEL_MN_RADIAL,
3                      PT_HEIGHT_PK_RADIAL, PROFILE_VEL_PK_RADIAL)
C
      RETURN
      END
C
C --- END GRAPHIC_OUTPUT_DATA
C
      SUBROUTINE COMBINE_FLOWS
1      (PT_HEIGHT_MN_CENTER, PROFILE_VEL_MN_CENTER,
2      PT_HEIGHT_PK_CENTER, PROFILE_VEL_PK_CENTER,
4      PT_HEIGHT_MN_RADIAL, PROFILE_VEL_MN_RADIAL,
6      PT_HEIGHT_PK_RADIAL, PROFILE_VEL_PK_RADIAL)

C
      REAL PT_HEIGHT_MN_CENTER(12,101), PROFILE_VEL_MN_CENTER(12,101)
      REAL PT_HEIGHT_PK_CENTER(12,101), PROFILE_VEL_PK_CENTER(12,101)
      REAL PT_HEIGHT_MN_RADIAL(12,101), PROFILE_VEL_MN_RADIAL(12,101)
      REAL PT_HEIGHT_PK_RADIAL(12,101), PROFILE_VEL_PK_RADIAL(12,101)

C ****
C THIS SUBROUTINE COMBINES THE PROFILE DATA FROM THE CENTERLINE AND
C RADIAL FLOW RUNS.
C ****
C
      INCLUDE 'DATE_____.CMN'
      INCLUDE 'GENERAL__.CMN'
      INCLUDE 'LABELS___.CMN'
      INCLUDE 'FLOW_____.CMN'
      INCLUDE 'OBJECT___.CMN'
      INCLUDE 'FLTCOND___.CMN'
      INCLUDE 'PROFILES.CMN'

C
      INTEGER I, J, K
      INTEGER NUM_INTERP PTS
      REAL CALC_ANGLE,           HEIGHT_MAX(12),    PT_HEIGHT_MAX(3,12),
1      CENTER_WEIGHT,          AREA_TOTAL(12),
2      DIST_TO_CENTER,         VEL_MAX(12),      PROFILE_VEL_MAX(3,12),
3      FORCE_TOTAL(12),        FORCE_STORAGE(3,12),
4      RADIAL_WEIGHT,          MOMENT_TOTAL(12),  MOMENT_STORAGE(3,12),
5      ANGLE_STORE(3)

```

```

C
OPEN (UNIT=G2OUTPT, STATUS='UNKNOWN',
C xxx mac      1 FILE='ELITE_ROWF/Graph_PROFILES.CSV')
      1   FILE='C:\DATA\PROGRAMS\ROWFOOT\OUTPUT\Graph_PROFILES.CSV')
C
C   The number of radials interpolated between centerline and radial flow
C   This ends up being hardcoded because of array initialization, so it can't
C   be changed easily
NUM_INTERP PTS =1
C   Find the distance from the rotor-center to the center of the aircraft
IF (NUMBER_ROTORS .EQ. 1) THEN
    DIST_TO_CENTER = 0
ELSE
    DIST_TO_CENTER = SEPARATION/2.0
END IF
C
C   For centerline, radial, and all points in between:
DO 401, K = 0, (NUM_INTERP PTS+1)
    Set the angle at which we are calculating (deg)
    CALC_ANGLE = PURE_RADIAL_ANGLE*(K/(NUM_INTERP PTS+1.0))
C   These weights are for the weighted average of the velocities based on the
C   anle. (ex. full center flow means calc_anlg = 0 so center_weight =1 and
C   radial weight =0)
    CENTER_WEIGHT = (PURE_RADIAL_ANGLE-CALC_ANGLE)/PURE_RADIAL_ANGLE
    RADIAL_WEIGHT = 1-CENTER_WEIGHT
C   For each distance and height:
DO 400, I = 1, 12
    DO 399, J = 1, 101
        Average the peak velocities based on the weights above
        PROFILE_VEL_PK(I,J) =
1           (PROFILE_VEL_PK_RADIAL(I,J) * RADIAL_WEIGHT +
2           PROFILE_VEL_PK_CENTER(I,J) * CENTER_WEIGHT)
C   Average the mean velocities based on the weights above
        PROFILE_VEL_MN(I,J) =
1           (PROFILE_VEL_MN_RADIAL(I,J) * RADIAL_WEIGHT +
2           PROFILE_VEL_MN_CENTER(I,J) * CENTER_WEIGHT)
C   This explicitly assigns heights for pure center flows
C   and pure radial flows to avoid potential calculation errors
        IF (K .EQ. 0) THEN
            PT_HEIGHT_MN(I,J) = PT_HEIGHT_MN_CENTER(I,J)
            PT_HEIGHT_PK(I,J) = PT_HEIGHT_PK_CENTER(I,J)
        ELSE IF (K.EQ.(NUM_INTERP PTS+1)) THEN
            PT_HEIGHT_MN(I,J) = PT_HEIGHT_MN_RADIAL(I,J)
            PT_HEIGHT_PK(I,J) = PT_HEIGHT_PK_RADIAL(I,J)
C   The heights corresponding to interpolated velocities are also interpolated
        ELSE
            PT_HEIGHT_MN(I,J) =
1           (PT_HEIGHT_MN_RADIAL(I,J) * RADIAL_WEIGHT +
2           PT_HEIGHT_MN_CENTER(I,J) * CENTER_WEIGHT)
            PT_HEIGHT_PK(I,J) =
1           (PT_HEIGHT_PK_RADIAL(I,J) * RADIAL_WEIGHT +
2           PT_HEIGHT_PK_CENTER(I,J) * CENTER_WEIGHT)
        END IF
399     CONTINUE
400     CONTINUE
C   Find the maximum peak velocity at each distance on this radial
        CALL FIND_MAX_VEL(HEIGHT_MAX, VEL_MAX)
C
C   Store the max velocities and corresponding heights in a larger array
C   which holds these values for all radials
        DO 500, J = 1, 12
            PT_HEIGHT_MAX(K+1,J) = HEIGHT_MAX(J)
            PROFILE_VEL_MAX(K+1,J)= VEL_MAX(J)
500     CONTINUE
C
C   Store the radial angle in this array for output later
        ANGLE_STORE(K+1) = CALC_ANGLE
C
C   Output all the profile data for this radial
        CALL OUTPUT_PROFILE_DATA (CALC_ANGLE, K, G2OUTPT)
C
C   Calculate the forces and moments on an object along this radial
        CALL FORCES_MOMENTS(FORCE_TOTAL, MOMENT_TOTAL, AREA_TOTAL)

```

```

C      Store the forces and moments in a larger array which holds these
C      values for all radials and helps make outputting easier
      DO 600, J = 1, 12
         FORCE_STORAGE(K+1,J) = FORCE_TOTAL(J)
         MOMENT_STORAGE(K+1,J) = MOMENT_TOTAL(J)
600   CONTINUE
401   CONTINUE
C
      CLOSE (UNIT = G2OUTPT)
C
      OPEN (UNIT=VOUTPT, STATUS='UNKNOWN',
     1 FILE='C:\DATA\PROGRAMS\ROWFOOT\OUTPUT\2MAX_V_PROFILES.CSV')
C xxx MAC      1 FILE='ELITE_RUNS/2MAX_V_PROFILES.CSV')
C
C      Output the maximum velocity data
      CALL OUTPUT_MAX_PROFILE(PROFILE_VEL_MAX,
     1                      ANGLE_STORE,DIST_TO_CENTER)
C      Output the force and moment data to the same output file
      CALL OUTPUT_FORCES_MOMENTS(FORCE_STORAGE,MOMENT_STORAGE,
     1                           ANGLE_STORE)
      CLOSE (UNIT = VOUTPT)
C
      RETURN
      END
C
C --- END COMBINE_FLOWS
C
      SUBROUTINE FIND_MAX_VEL(HEIGHT_MAX, VEL_MAX)
      REAL HEIGHT_MAX(12), VEL_MAX(12)
C ****
C THIS SUBROUTINE FINDS THE MAXIMUM VELOCITY AND CORRESPONDING HEIGHT
C AT EACH DISTANCE FROM THE CENTER
C ****
C
      INCLUDE 'DATE_____.CMN'
      INCLUDE 'GENERAL__.CMN'
      INCLUDE 'LABELS_____.CMN'
      INCLUDE 'FLOW_____.CMN'
      INCLUDE 'OBJECT_____.CMN'
      INCLUDE 'FLTCOND_____.CMN'
      INCLUDE 'PROFILES.CMN'
C
      INTEGER I, J
C
      Initialize the max arrays to zero
      DO 500, J = 1, 12
         HEIGHT_MAX(J) = 0
         VEL_MAX(J)= 0
500   CONTINUE
C
      For each distance, go through all the heights and find the highest velocity
      DO 600, I = 1, 12
         DO 599, J = 1, 101
C
         added in the following nested "IF" statement to do mean - KWS
         IF (PEAK_OR_MEAN .EQ. 'PEAK') THEN
            IF (PROFILE_VEL_PK(I,J) .GT. VEL_MAX(I)) THEN
               HEIGHT_MAX(I) = PT_HEIGHT_PK(I,J)
               VEL_MAX(I) = PROFILE_VEL_PK(I,J)
            END IF
         ELSEIF (PEAK_OR_MEAN .EQ. 'MEAN') THEN
            IF (PROFILE_VEL_MN(I,J) .GT. VEL_MAX(I)) THEN
               HEIGHT_MAX(I) = PT_HEIGHT_MN(I,J)
               VEL_MAX(I) = PROFILE_VEL_MN(I,J)
            END IF
         END IF
599   CONTINUE
600   CONTINUE
      RETURN
      END
C --- END FIND_MAX_VEL
C

```

```

SUBROUTINE FORCES_MOMENTS(FORCE_TOTAL, MOMENT_TOTAL, AREA_TOTAL)
REAL FORCE_TOTAL(12), MOMENT_TOTAL(12), AREA_TOTAL(12)

C ****
C THIS SUBROUTINE FINDS THE FORCES AND MOMENTS ON THE SELECTED OBJECT BASED
C ON PEAK VELOCITIES AND THE DISTANCE OF THE OBJECT FROM THE ROTOR
C ****
C

INCLUDE 'DATE_____.CMN'
INCLUDE 'GENERAL__.CMN'
INCLUDE 'LABELS_____.CMN'
INCLUDE 'FLOW_____.CMN'
INCLUDE 'OBJECT_____.CMN'
INCLUDE 'FLTCOND_____.CMN'
INCLUDE 'PROFILES.CMN'

C
DOUBLE PRECISION AREA(100), WIDTH(101), DELTA_H
REAL FORCE_COMP(100), MOMENT_COMP(100)
DOUBLE PRECISION OBJ_TOP_INDEX, HEIGHT_OBJ, VEL_AT_TOP
INTEGER I, Itemp, J, Jtemp, K, W
REAL H, CD

REAL PROFILE_VEL(12,101), PT_HEIGHT(12,101)

C Use generic profile velocity and height (in place of redundant peak and mean calcs)
DO 130, Itemp = 1, 12
    DO 120, Jtemp = 1, 101
        IF (PEAK_OR_MEAN .EQ. 'PEAK') THEN
            PROFILE_VEL(Itemp, Jtemp) = PROFILE_VEL_PK(Itemp, Jtemp)
            PT_HEIGHT(Itemp, Jtemp) = PT_HEIGHT_PK(Itemp, Jtemp)
        ELSE IF (PEAK_OR_MEAN .EQ. 'MEAN') THEN
            PROFILE_VEL(Itemp, Jtemp) = PROFILE_VEL_MN(Itemp, Jtemp)
            PT_HEIGHT(Itemp, Jtemp) = PT_HEIGHT_MN(Itemp, Jtemp)
        END IF
120     CONTINUE
130     CONTINUE

C Calculate the width and Cd of the object in the flow at this height
C fPersonalStability is the human performance ratio for static test / flight test values
IF (OBJ_SHAPE .EQ. 'PAXMAN') THEN
    HEIGHT_OBJ = 5.5
    CD = 1
ELSE IF (OBJ_SHAPE .EQ. 'FLTPLT') THEN
    HEIGHT_OBJ = 10
    CD = 1
ELSE
    WRITE(NOUTPT,700) OBJ_SHAPE
700    FORMAT(1X, 'OBJ_SHAPE value = ', A6, 'is not valid.', //
1           'Value reset to PAXMAN', //)
    END IF

C Added in the very large if-then-else statement to handle peak/mean
C For each distance, at each height:
DO 170, I = 1, 12
    OBJ_TOP_INDEX = 101

C For each distance, at each height:
DO 140, W = 1, 101
    IF (PT_HEIGHT(I,W) .GT. HEIGHT_OBJ) THEN
        IF (W .LT. OBJ_TOP_INDEX) THEN
            OBJ_TOP_INDEX = W
        END IF
    END IF
140     CONTINUE

C
VEL_AT_TOP = PROFILE_VEL(I,OBJ_TOP_INDEX-1) +
1             (PROFILE_VEL(I,OBJ_TOP_INDEX-1)-
2              PROFILE_VEL(I,OBJ_TOP_INDEX))*(
3              (HEIGHT_OBJ - PT_HEIGHT(I,OBJ_TOP_INDEX-1))/(
4                  (PT_HEIGHT(I,OBJ_TOP_INDEX)-
5                  PT_HEIGHT(I,OBJ_TOP_INDEX-1)))
C
DO 150, J = 1, 101

```

```

C
C Temporarily use variable H to store height for convenience
C
    IF (J .EQ. OBJ_TOP_INDEX) THEN
        H = HEIGHT_OBJ
    ELSE
        H = PT_HEIGHT(I,J)
    END IF

C
C Calculate the width and Cd of the object in the flow at this height
    IF (OBJ_SHAPE .EQ. 'PAXMAN') THEN
        WIDTH(J) = 0.431 - 0.0464*H - .14*(H**2) + 0.138*(H**3) -
1            0.0249*(H**4) - 0.000549*(H**5) + 0.000222*(H**6) -
2            0.0000418*(H**7) + 0.0000145*(H**8) -
3            0.00000078*(H**9) -0.00000019*(H**10)

C
    ELSE IF (OBJ_SHAPE .EQ. 'FLTPLT') THEN
        WIDTH(J) = 5
    END IF

C
    IF (H .GT. HEIGHT_OBJ) THEN
        WIDTH(J) = 0
    END IF

C
C Calculate the area by multiplying the average width of the
C panel by the height of the panel by two, because the width is
C for half a man
    IF (J .GT. 1) THEN
        IF (J .EQ. OBJ_TOP_INDEX) THEN
            DELTA_H = HEIGHT_OBJ-PT_HEIGHT(I,J-1)
            AREA(J-1) = 2*(DELTA_H)*(WIDTH(J)+WIDTH(J-1))/2
        ELSE
            DELTA_H = PT_HEIGHT(I,J)-PT_HEIGHT(I,J-1)
            AREA(J-1) = 2*(DELTA_H)*(WIDTH(J)+WIDTH(J-1))/2
        END IF

C
        IF (J .GT. OBJ_TOP_INDEX) THEN
            AREA(J-1) = 0
        END IF

C
        Calculate the force (drag) on this panel
        IF (J .EQ. OBJ_TOP_INDEX) THEN
            FORCE_COMP(J-1) = 0.5*DENSITY_AIR*
1                ((VEL_AT_TOP+PROFILE_VEL(I,J-1))/2)**2*
2                AREA(J-1)*CD
        ELSE
            FORCE_COMP(J-1) = 0.5*DENSITY_AIR*
1                ((PROFILE_VEL(I,J)+PROFILE_VEL(I,J-1))/2)**2*
2                AREA(J-1)*CD
        END IF

C
        IF (PEAK_OR_MEAN .EQ. 'PEAK')
1            FORCE_COMP(J-1) = FORCE_COMP(J-1) * fPersonalStability

C
        Calculate the moment on this panel (force*avg_height)
        IF (J .EQ. OBJ_TOP_INDEX) THEN
            MOMENT_COMP(J-1) = FORCE_COMP(J-1)*
1                (HEIGHT_OBJ + PT_HEIGHT(I,J-1))/2
        ELSE
            MOMENT_COMP(J-1) = FORCE_COMP(J-1)*
1                (PT_HEIGHT(I,J)+PT_HEIGHT(I,J-1))/2
        END IF
    END IF

C
    150    CONTINUE

C
C Sum up all the force components to find the total drag on the object
C at this distance
    FORCE_TOTAL(I) = 0
    MOMENT_TOTAL(I) = 0
    AREA_TOTAL(I) = 0

C
C Now Force/Moment_Total(i) has the force on the object at each distance for
C this radial

```

```

C
      DO 160 K = 1, 100
          FORCE_TOTAL(I) = FORCE_TOTAL(I) + FORCE_COMP(K)
          MOMENT_TOTAL(I) = MOMENT_TOTAL(I) + MOMENT_COMP(K)
C      Sum up the areas to make sure they work as expected
          AREA_TOTAL(I) = AREA_TOTAL(I) + AREA(K)
160      CONTINUE
C
      IF (DEBUG_FLAG) THEN
          WRITE (DOUTPUT, 800) I, PEAK_OR_MEAN,
1             OBJ_SHAPE, HEIGHT_OBJ, CD,
2             OBJ_TOP_INDEX, VEL_AT_TOP, DENSITY_AIR,
3             fPersonalStability, I, FORCE_TOTAL(I), I,
4             MOMENT_TOTAL(I), I, AREA_TOTAL(I)
C
800      FORMAT(1X, 'Subroutine FORCES_MOMENTS', //,
1             ' Case Number = ', I2, '/',
1             ' PEAK_OR_MEAN = ', A4, '/',
2             ' OBJ_SHAPE = ', A6, '/',
3             ' HEIGHT_OBJ = ', F8.2, ' ft ', '/',
4             ' CD = ', F8.5, ' ND ', '/',
5             ' OBJ_TOP_INDEX = ', F8.4, ' ND ', '/',
6             ' VEL_AT_TOP = ', F8.4, ' ft/sec ', '/',
7             ' DENSITY_AIR = ', F8.6, ' slug/cuft ', '/',
8             ' fPersonalStability = ', F8.1, ' ND ', '/',
9             ' FORCE_TOTAL(', I2, ') = ', F8.2, ' lb', '/',
9             ' MOMENT_TOTAL(', I2, ') = ', F8.2, ' ftlb', '/',
9             ' AREA_TOTAL(', I2, ') = ', F8.2, ' lb', //)
      END IF
C
170      CONTINUE
C
      RETURN
      END
C --- END FORCES_MOMENTS

```

RowFoot Common Blocks

```

COMMON / DATE____ /
1      IMONTH, IDAY, IYEAR, IHOUR, IMINUTE, ISECOND, I100TH
C
      INTEGER*4
1      IMONTH, IDAY, IYEAR, IHOUR, IMINUTE, ISECOND, I100TH
C

-----
COMMON / FLOW____/
1      HFLOW_wall_MN, WFLOW_max_MN, CST1_MN, Exp_IP_MN,
2      HFLOW_wall_PK, WFLOW_max_PK, CST1_PK, Exp_IP_PK,
3      HFLOW_ref_MN, WFLOW_ref_MN, CST2_MN, Exp_Cu_MN,
4      HFLOW_ref_PK, WFLOW_ref_PK, CST2_PK, Exp_Cu_PK,
5      HFLOW_rpeak, WFLOW_ratio, KG_coef, CST_HFLOW_WALL_MN,
6      HFLOW_ratio, Wvel_Max_MN, K1_coef, CST_HFLOW_WALL_PK,
7      HFLOW_init, Wvel_Max_PK, K2_coef, WAKE_vel_LMT_MN,
8      RFLOW_init, VEL_LOCAL, WAKE_vel, WAKE_vel_LMT_PK,
9      XFLOW_init, VELOCITY_coef, WAKE_DECAY, RFLOW_INIT_EXP,
1      N_Exponent_MN, N_Exponent_PK, M_EXPONENT
C
      REAL
1      HFLOW_wall_MN, WFLOW_max_MN, CST1_MN, Exp_IP_MN,
2      HFLOW_wall_PK, WFLOW_max_PK, CST1_PK, Exp_IP_PK,
3      HFLOW_ref_MN, WFLOW_ref_MN, CST2_MN, Exp_Cu_MN,
4      HFLOW_ref_PK, WFLOW_ref_PK, CST2_PK, Exp_Cu_PK,
5      HFLOW_rpeak, WFLOW_ratio, KG_coef, CST_HFLOW_WALL_MN,
6      HFLOW_ratio, Wvel_Max_MN, K1_coef, CST_HFLOW_WALL_PK,
7      HFLOW_init, Wvel_Max_PK, K2_coef, WAKE_vel_LMT_MN,
8      RFLOW_init, VEL_LOCAL, WAKE_vel, WAKE_vel_LMT_PK,
9      XFLOW_init, VELOCITY_coef, WAKE_DECAY, RFLOW_INIT_EXP,
1      N_Exponent_MN, N_Exponent_PK, M_EXPONENT
C

-----
COMMON / FLTCOND_ /
1      NUMBER_BLADES, GEAR_TO_ROTOR, THRUST_TO_WEIGHT,
2      NUMBER_ROTORS, SEPARATION, PURE_RADIAL_ANGLE,
3      GROSS_WEIGHT, TIP_SPEED, COEF_INDUCED,
4      DISK_LOAD, DENSITY_AIR, Sensor_Offset,
5      AGL_GEAR, DIAM_RATIO, EQUIV_VEL,
6      RADIUS, MESHIN, WindVelocity_kts,
7      PEAK_OR_MEAN, TYPE_OUTFLOW, CONFIGURATION
C
      REAL
1      NUMBER_BLADES, GEAR_TO_ROTOR, THRUST_TO_WEIGHT,
2      NUMBER_ROTORS, SEPARATION, PURE_RADIAL_ANGLE,
3      GROSS_WEIGHT, TIP_SPEED, COEF_INDUCED,
4      DISK_LOAD, DENSITY_AIR, Sensor_Offset,
5      AGL_GEAR, DIAM_RATIO, EQUIV_VEL,
6      RADIUS, MESHIN, WindVelocity_kts
C
      CHARACTER*4 PEAK_OR_MEAN
      CHARACTER*10 TYPE_OUTFLOW
      CHARACTER*12 CONFIGURATION
-----

COMMON /GENERAL_/ kts_fps, mph_fps, PIE, ECONST, GCONST,
1      GOUTPT, NOUTPT, VOUTPT, INPT, DOUTPUT, G2OUTPT,
2      DEBUG_FLAG
C
      REAL          kts_fps, mph_fps, PIE, ECONST, GCONST
      INTEGER GOUTPT, NOUTPT, VOUTPT, INPT, DOUTPUT, G2OUTPT
      LOGICAL DEBUG_FLAG
-----
```

```

COMMON / LABELS__ /
1           TITLE,             FILE,
3           TYPE_OUTPUT,        CONFIG_NAME,      DIST_units
C
CHARACTER *5  TYPE_OUTPUT
CHARACTER *6  DIST_units
CHARACTER*11  CONFIG_NAME
CHARACTER*13  FILE
CHARACTER*80  TITLE
-----
COMMON / OBJECT__/
1           DIST_NONDIM,       DIST_number,
2           DIST_values,        fPersonalStability, OBJ_SHAPE
C
INTEGER    DIST_number
REAL       DIST_NONDIM, DIST_values, fPersonalStability
CHARACTER*6 OBJ_SHAPE
C
DIMENSION DIST_NONDIM(50), DIST_values(50)
-----
COMMON / PROFILES /  PT_HEIGHT_MN, PROFILE_VEL_MN,
1                   PT_HEIGHT_PK, PROFILE_VEL_PK
C
REAL PT_HEIGHT_MN(12,101), PROFILE_VEL_MN(12,101),
1       PT_HEIGHT_PK(12,101), PROFILE_VEL_PK(12,101)
-----
```

RoWFoot Input Data Set

```

&OUTPUT_SET
  DEBUG_FLAG = .TRUE.,      MESHIN          = 1,
  PEAK_OR_MEAN = 'PEAK'     TYPE_OUTFLOW     = 'RADIAL',
  DENSITY_AIR = 0.002378,   Sensor_Offset   = 0,
  AGL_GEAR    = 50.0,        PURE_RADIAL_ANGLE = 5,
  OBJ_SHAPE   = 'PAXMAN',    fPersonalStability = 0.8,
                           WindVelocity_kts = 0.0,
  DIST_NUMBER = 12,         DIST_UNITS       = 'NONDIM',
  DIST_VALUES =
    0.1, 0.3, 0.5, 0.8, 1.0, 1.5, 2.0, 3.0, 4.0, 5.0, 6.0, 7.0,
/
&ROTORCRAFT
  TITLE = 'Ground Taxi, Case 2',
  THRUST_TO_WEIGHT = 1.09,
  NUMBER_ROTORS = 2,          RADIUS          = 39.5,  SEPARATION    = 101,
  NUMBER_BLADES = 4,          TIP_SPEED       = 700,   GEAR_TO_ROTOR = 25,
  GROSS_WEIGHT  = 42482,
/
&WAKE_PARAMETER
  M_EXPONENT = 5.0,          RFLOW_INIT_EXP = 0.486,
  WAKE_DECAY = 0.1696,
/
&ACTUATOR_OPEN
  KG_COEF = 0.9,            COEF_INDUCED = 0.5,
  K1_COEF = -2.3,           DIAM_RATIO   = 0.78,
  K2_COEF = -1.41,
```

Appendix K: Correlation of Rotorwash Conceptual Level Model to Test Data

Sam Ferguson

This appendix contains correlation results of the conceptual level model (RoWFoot) described in [Appendix I](#) to flight test data. Model correlation includes the H-60, CH-53E, XV-15, V-22, and CH-47 test data contained in References K-1, K-2, K-3, K-4, and K-5 respectively. This correlation effort included variation of rotorcraft configuration, gross weight, rotor disk loading, and distance in development of the conceptual model.

For each aircraft, both the mean and peak velocity profile is displayed. During flight testing, a vertical array of sensors measured the magnitude of the horizontal velocity component of the outwash. The mean velocity profile is the time-averaged velocity measured over a defined time interval. The peak velocity profile is the maximum velocity measured for each sensor over the time interval. Neither the mean nor peak velocity profiles represents a “true” velocity profile as the rotorwash pulsates and gusts. The mean velocity profile is representative of the “average” wind profile, and the peak velocity profile represents a maximum gust wind condition.

In general, the outwash can be divided into two categories: radial and centerline (or interaction plane). Figure K-1 shows the radial and centerline (deflection zone) outwash. Radial outwash occurs where the horizontal rotorwash is dominated by a single rotor. Examples of radial outwash include the entire outwash for a single rotor helicopter and the sideward outwash from a tilt rotor (90 and 270 degrees from the aircraft nose). Centerline outwash occurs where the rotorwash from two rotors mix along the interaction plane. Examples include the forward and aft regions of the tilt rotor (0 and 180 degrees from the aircraft nose) and laterally for a tandem helicopter (90 and 270 degrees from the aircraft nose).

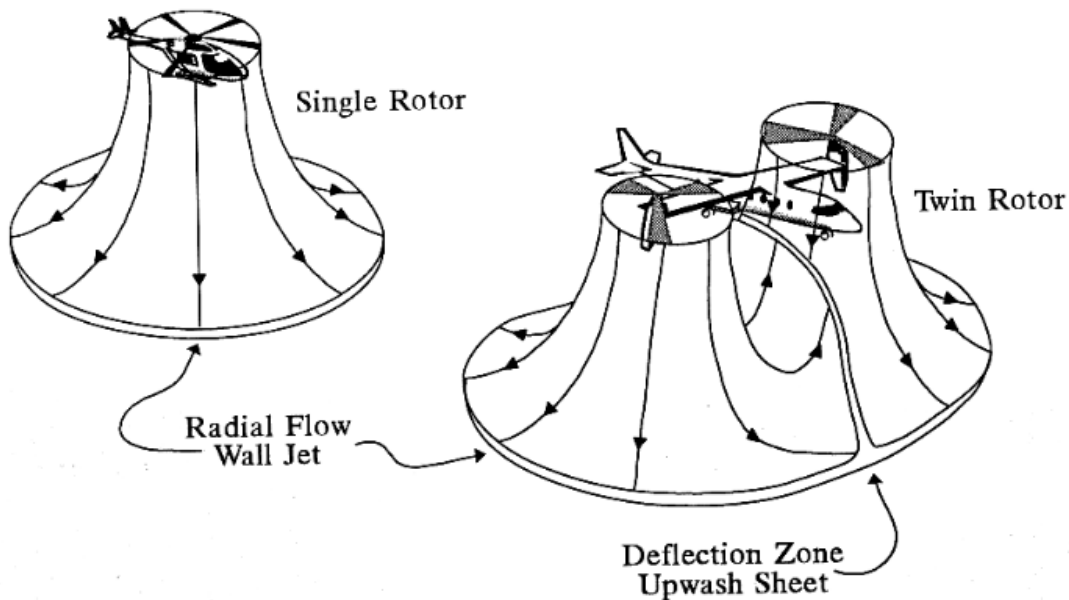


Figure K-1 Rotorwash Flow Fields of Single- and Twin-Rotor Configurations Operating in Close Proximity to Ground

The H-60 flight test data (Reference K-1) is considered to be of fair quality. Ambient winds ranging between 0- and +6- kts during flight testing decreased the overall quality of the data collected according to the authors of the report. Test data contain flight conditions for aircraft weights of 18,000 lb and 20,000 lb at wheel heights Above Ground Level (AGL) of 10, 30, 50, and 150 ft. In each case, velocity profile test data were measured at 0.5-, 1.0-, 1.5-, 2.0-, 3.0-, 5.0-, and 7.0-foot heights above the ground.

The CH-53E flight test data (Reference K-2) is considered to be of excellent quality. Test data contain flight conditions for aircraft weights (tethered) of 45,000, 56,000, and 70,000 lb at wheel heights above ground (AGL) of 20, 60, and 100 ft. However, information on test conditions is limited. In each case, velocity profile test data were measured at 1.5-, 3.0-, 5.0-, 7.0-, 9.0- and 11.0-foot heights above the ground.

The XV-15 flight test data (Reference K-3) is considered to be of good quality; however, the quantity is marginal and information on test conditions is limited. Test data contain flight conditions for aircraft weights of 12,475 lb at wheel heights above ground (AGL) of 2.0, 25.0, and 50 ft. In each case, velocity profile test data were measured at 0.5-, 1.0-, 1.5-, 2.0-, 3.0-, 5.0-, and 7.0-foot heights above the ground.

The V-22 flight test data (References K-4 and K-5) is considered to be of excellent quality. Test data contain flight conditions for aircraft weights / wheel height above ground combinations of 22,000 lb (0 ft), 45,900 lb (20 ft), 44,500 lb (60 ft), and 43,800 (100 ft). In each case, velocity profile test data were measured at 1.0-, 2.0-, 3.0-, 4.0-, 5.0-, and 7.0-foot heights above the ground.

The CH-47 flight test data (Reference K-6) is considered to be of excellent quality. Test data contain flight conditions for aircraft weight/wheel height above ground combinations of 33,000 to 50,000 lb and 20 to 100 ft at both 0- and 180-deg azimuths (a total of 10 test conditions). In each case, velocity profile test data were measured at 1.0-, 2.0-, 3.0-, 4.0-, 5.0-, 7.0-, 9.0-, and 12.0-foot heights above the ground. Data documented in Reference K-6 also contains test data points represented as 98 percentile. These data points remove ill-behaved data for the peak velocity profile which may be introduced due to sensor noise or anomalies in the data. Data reduction using the 98 percentile approach also appears as a recommendation for future test approach in the main report [Section 7.6](#).

	H-60	CH-53E	XV-15	V-22	CH-47
Number of Rotors	1	1	2	2	2
Number of Blades/Rotor	4	7	3	3	3
Rotor Radius, ft	26.83	39.5	12.5	19.04	30.0
Distance From Gear to Rotor, ft	9.42	17	12.67	21.3	18.0
Separation Between Rotors, ft	0	0	32.2	46.6	39.2
Thrust/Weight	1.035	1.05	1.13	1.105	1.055

Table K-1
Rotorcraft data supporting correlation

Correlation of RoWFoot to previous flight test data appears in Figures K-2 to K-61. Results of this correlation are divided into radial and centerline velocity profiles. Within each figure, flight test data points show measurements for the mean and peak velocity along with the RoWFoot predicted mean and peak velocity profiles. The summary of figures with reference to aircraft Gross Weight (GW) and wheel height above ground level appears in Table K-2 for radial velocity profiles and Table K-3 for centerline velocity profiles.

At the time of publication, the test data for the UH-60, V-22, and CH-47 are not publicly releasable. Correlation figures for RoWFoot to flight test data for these aircraft are contained in a limited distribution annex to this report.

H-60**

- Figure K-2: GW = 18,500 & 20,500 lb, AGL = 10 ft
- Figure K-3: GW = 18,500 & 20,500 lb, AGL = 30 ft
- Figure K-4: GW = 18,500 & 20,500 lb, AGL = 50 ft
- Figure K-5: GW = 18,500 & 20,500 lb, AGL = 150 ft

CH-53E

- Figure K-6: GW = 45,000 lb, AGL = 20 ft
- Figure K-7: GW = 45,000 lb, AGL = 60 ft
- Figure K-8: GW = 45,000 lb, AGL = 100 ft
- Figure K-9: GW = 56,000 lb, AGL = 20 ft
- Figure K-10: GW = 56,000 lb, AGL = 60 ft
- Figure K-11: GW = 56,000 lb, AGL = 100 ft
- Figure K-12: GW = 70,000 lb, AGL = 20 ft
- Figure K-13: GW = 70,000 lb, AGL = 60 ft
- Figure K-14: GW = 70,000 lb, AGL = 100 ft

XV-15

- Figure K-15: GW = 12,500 lb, AGL = 25, 2 & 50 ft, Azimuth = 270 deg

V-22**

- Figure K-16: GW = 22,200 lb, AGL = 0 ft, Azimuth = 270 deg
- Figure K-17: GW = 45,935 lb, AGL = 20 ft, Azimuth = 270 deg
- Figure K-18: GW = 44,539 lb, AGL = 60 ft, Azimuth = 270 deg
- Figure K-19: GW = 43,814 lb, AGL = 100 ft, Azimuth = 270 deg
- Figure K-20: GW = 45,935 lb, AGL = 20 ft, Azimuth = 240 & 300 deg
- Figure K-21: GW = 45,935 lb, AGL = 20 ft, Azimuth = 45 & 135 deg
- Figure K-22: GW = 45,935 lb, AGL = 20 ft, Azimuth = 210 & 330 deg

CH-47**

- Figure K-23: GW = 33,300 lb, AGL = 20 ft, Azimuth = 180 deg
- Figure K-24: GW = 40,800 lb, AGL = 20 ft, Azimuth = 180 deg
- Figure K-25: GW = 49,800 lb, AGL = 20 ft, Azimuth = 180 deg
- Figure K-26: GW = 40,600 lb, AGL = 60 ft, Azimuth = 180 deg
- Figure K-27: GW = 40,700 lb, AGL = 100 ft, Azimuth = 180 deg
- Figure K-28: GW = 33,900 lb, AGL = 20 ft, Azimuth = 0 deg
- Figure K-29: GW = 41,900 lb, AGL = 20 ft, Azimuth = 0 deg
- Figure K-30: GW = 49,900 lb, AGL = 20 ft, Azimuth = 0 deg
- Figure K-31: GW = 41,400 lb, AGL = 60 ft, Azimuth = 0 deg
- Figure K-32: GW = 41,400 lb, AGL = 100 ft, Azimuth = 0 deg

Table K-2
Summary of RoWFoot Correlation to Radial Outwash Test Data

**RoWFoot correlation figures contain limited distribution data. The figures appear in a limited distribution annex to this report.

XV-15

Figure K-33: GW = 12,500 lb, AGL = 25, Azimuth = 0 deg
Figure K-34: GW = 12,500 lb, AGL = 25, Azimuth = 180 deg

V-22**

Figure K-35: GW = 33,800 lb,	AGL = 0 ft,	Azimuth = 0 deg,	Offset = 0 ft
Figure K-36: GW = 44,000 lb,	AGL = 20 ft,	Azimuth = 0 deg,	Offset =+20 ft
Figure K-37: GW = 43,600 lb,	AGL = 20 ft,	Azimuth = 0 deg,	Offset =+10 ft
Figure K-38: GW = 44,600 lb,	AGL = 20 ft,	Azimuth = 0 deg,	Offset = 0 ft
Figure K-39: GW = 46,500 lb,	AGL = 20 ft,	Azimuth = 0 deg,	Offset =-10 ft
Figure K-40: GW = 45,200 lb,	AGL = 20 ft,	Azimuth = 0 deg,	Offset =-20 ft
Figure K-41: GW = 44,600 lb,	AGL = 20 ft,	Azimuth = 180 deg,	Offset =+20 ft
Figure K-42: GW = 43,700 lb,	AGL = 20 ft,	Azimuth = 180 deg,	Offset =+10 ft
Figure K-43: GW = 45,200 lb,	AGL = 20 ft,	Azimuth = 180 deg,	Offset = 0 ft
Figure K-44: GW = 43,500 lb,	AGL = 20 ft,	Azimuth = 180 deg,	Offset =-10 ft
Figure K-45: GW = 46,000 lb,	AGL = 20 ft,	Azimuth = 180 deg,	Offset =-20 ft
Figure K-46: GW = 44,100 lb,	AGL = 60 ft,	Azimuth = 180 deg,	Offset = 0 ft
Figure K-47: GW = 43,800 lb,	AGL = 100 ft,	Azimuth = 180 deg,	Offset = 0 ft

CH-47**

Figure K-48: GW = 33,100 lb,	AGL = 20 ft,	Azimuth = 90 deg,	Offset = 0 ft
Figure K-49: GW = 42,000 lb,	AGL = 20 ft,	Azimuth = 90 deg,	Offset =-20 ft
Figure K-50: GW = 41,400 lb,	AGL = 20 ft,	Azimuth = 90 deg,	Offset = 0 ft
Figure K-51: GW = 41,400 lb,	AGL = 20 ft,	Azimuth = 90 deg,	Offset =+20 ft
Figure K-52: GW = 41,700 lb,	AGL = 60 ft,	Azimuth = 90 deg,	Offset = 0 ft
Figure K-53: GW = 40,200 lb,	AGL = 100 ft,	Azimuth = 90 deg,	Offset = 0 ft
Figure K-54: GW = 49,500 lb,	AGL = 20 ft,	Azimuth = 90 deg,	Offset = 0 ft
Figure K-55: GW = 33,700 lb,	AGL = 20 ft,	Azimuth = 270 deg,	Offset = 0 ft
Figure K-56: GW = 41,900 lb,	AGL = 20 ft,	Azimuth = 270 deg,	Offset =-20 ft
Figure K-57: GW = 40,400 lb,	AGL = 20 ft,	Azimuth = 270 deg,	Offset = 0 ft
Figure K-58: GW = 41,800 lb,	AGL = 20 ft,	Azimuth = 270 deg,	Offset =+20 ft
Figure K-59: GW = 41,000 lb,	AGL = 60 ft,	Azimuth = 270 deg,	Offset = 0 ft
Figure K-60: GW = 41,000 lb,	AGL = 100 ft,	Azimuth = 270 deg,	Offset = 0 ft
Figure K-61: GW = 49,800 lb,	AGL = 20 ft,	Azimuth = 270 deg,	Offset = 0 ft

Table K-3
Summary of RoWFoot Correlation to Centerline Outwash Test Data

**RoWFoot correlation figures contain limited distribution data. The figures appear in a limited distribution annex to this report.

In the judgment of the main report authors, RoWFoot has been able to achieve good modeling accuracy when correlated against available flight test data. A breakdown by aircraft appears in Table K-4. The data quality is highly dependent on presence or absence of ambient winds and the aircraft flight state over the time period of each data collection point. The data quality represents an overall judgment of the test conditions and measurements during the flight test time period.

<u>Radial Outwash</u>	<u>Correlation</u>	<u>Data Quality</u>
H-60	Fair	Fair
CH-53E	Very Good	Excellent
XV-15	Fair	Good
V-22	Very Good	Excellent
CH-47	Very Good	Excellent

<u>Centerline Outwash</u>	<u>Correlation</u>	<u>Data Quality</u>
XV-15	Fair	Good
V-22	Good	Excellent
CH-47	Very Good	Excellent

Table K-4
Accuracy of RoWFoot Correlation and Data Quality

Additional tabular data in [Appendix M](#) contains results of projections using the CHARM vortex model calibrated to V-22 (Reference K-4) to extend the range of available data for disk loading and height above ground. Extension of flight test data to this tabular output corresponds to equivalent V-22 flight conditions given in Table K-5. Unfortunately, review of the high-fidelity tool data contained in [Appendix M](#) for symmetry and engineering trends show discrepancies that do not allow extension of the flight test data in this manner. Further work is recommended to either update previous or conduct new high-fidelity based modeling using lessons learned and apply these results to the conceptual-level model. Figures K-62 to K-85 should be updated with results produced by a revised high-fidelity model. This is a recommended future rotorwash development effort.

Radial Outwash

- Figure K-62: GW = 33,140 lb, AGL = 10 ft, Azimuth = 270 deg
- Figure K-63: GW = 33,140 lb, AGL = 19 ft, Azimuth = 270 deg
- Figure K-63: GW = 33,140 lb, AGL = 38 ft, Azimuth = 270 deg
- Figure K-65: GW = 33,140 lb, AGL = 57 ft, Azimuth = 270 deg
- Figure K-66: GW = 33,140 lb, AGL = 76 ft, Azimuth = 270 deg
- Figure K-67: GW = 33,140 lb, AGL = 152 ft, Azimuth = 270 deg
- Figure K-68: GW = 52,600 lb, AGL = 10 ft, Azimuth = 270 deg
- Figure K-69: GW = 52,600 lb, AGL = 19 ft, Azimuth = 270 deg
- Figure K-70: GW = 52,600 lb, AGL = 38 ft, Azimuth = 270 deg
- Figure K-71: GW = 52,600 lb, AGL = 57 ft, Azimuth = 270 deg
- Figure K-72: GW = 52,600 lb, AGL = 76 ft, Azimuth = 270 deg
- Figure K-73: GW = 52,600 lb, AGL = 152 ft, Azimuth = 270 deg

Centerline Outwash

Figure K-74: GW = 33,140 lb,	AGL = 10 ft,	Azimuth = 0 deg,	Offset = 0 ft
Figure K-75: GW = 33,140 lb,	AGL = 19 ft,	Azimuth = 0 deg,	Offset = 0 ft
Figure K-76: GW = 33,140 lb,	AGL = 38 ft,	Azimuth = 0 deg,	Offset = 0 ft
Figure K-77: GW = 33,140 lb,	AGL = 57 ft,	Azimuth = 0 deg,	Offset = 0 ft
Figure K-78: GW = 33,140 lb,	AGL = 76 ft,	Azimuth = 0 deg,	Offset = 0 ft
Figure K-79: GW = 33,140 lb,	AGL = 152 ft,	Azimuth = 0 deg,	Offset = 0 ft
Figure K-80: GW = 52,600 lb,	AGL = 10 ft,	Azimuth = 0 deg,	Offset = 0 ft
Figure K-81: GW = 52,600 lb,	AGL = 19 ft,	Azimuth = 0 deg,	Offset = 0 ft
Figure K-82: GW = 52,600 lb,	AGL = 38 ft,	Azimuth = 0 deg,	Offset = 0 ft
Figure K-83: GW = 52,600 lb,	AGL = 57 ft,	Azimuth = 0 deg,	Offset = 0 ft
Figure K-84: GW = 52,600 lb,	AGL = 76 ft,	Azimuth = 0 deg,	Offset = 0 ft
Figure K-85: GW = 52,600 lb,	AGL = 152 ft,	Azimuth = 0 deg,	Offset = 0 ft

Table K-5
Summary of RoWFoot Correlation to CHARM Vortex Model Results

Correlation of the conceptual-based model to this expanded data set increased the confidence it accurately modeled conditions at higher disk loading and altitude than previously available in flight test data.

Acquisition of future flight test correlation data correlation data may employ an advanced LIDAR type sensor (laser anemometer). The present method of mounting anemometers at several heights on a pole and varying the distance of the pole from the rotorcraft is “antiquated” when considering modern sensor technology. This data acquisition technique acquires a very limited set of velocity data at only several heights above the ground surface. LIDAR technology has the capability to measure a continuous velocity profile from ground level to a specified height within seconds. Then the beam can be refocused at a different distance from the rotor and the process repeated. All of this can be accomplished from one remote location several hundred feet from the hovering rotorcraft. Rotorwash data [unpublished data from Sam Ferguson (EMA) and Robb Lake (NAVAIR)] were acquired during a V-22 trailing wake-vortex project as a proof-of-concept rotorwash experiment. No efforts were made to optimize the acquisition software or develop an automated data reduction process for rotorwash application from the wake-vortex measurement configuration. However, these rough proof-of-concept results were quite remarkable. The amount of continuous velocity profile data that could have been obtained with the LIDAR sensor within one V-22 flight would have exceeded the amount of data that could have been obtained using today’s “standard method of test” within several days or weeks of low-wind weather conditions. An example of these data is presented in Figure K-86 at distances from the center of the rotor of 92 and 133 feet. The V-22 was hovering at a wheel height of 20 feet and the data were acquired along the 90-degree azimuth (single rotor azimuth or non-interaction plane). Data from the V-22 rotorwash test (Reference K-4) that are at approximately the same distance from the rotor are also plotted on the graphs to show general correlation of the data (triangles and circles are the mean and peak velocity points respectively). No efforts were made during the test to attempt to match the exact same V-22 test conditions (i.e. gross weight and wind conditions). The

investigators are convinced that this proof-of-concept test met all the standards to justify further development of the LIDAR method for future use in measuring large rotorcraft velocity profile characteristics (i.e. CH-47, CH-53K, and V-22).

References

- K-1. Meyerhoff, C. L.; Lake, R.; and Peters, Lt. D., "H-60 Helicopter Rotor Downwash Wind Velocity Evaluation," Naval Air Warfare Center Report SY-3R-94, February 1994.
- K-2. Ferguson, S. W., "Rotorwash Analysis Handbook, Volume II – Appendixes," Federal Aviation Administration, Washington D.C., Technical Report DOT/FAA/RD-93/31,II, June 1994.
- K-3. Harris, D. J., and Simpson, R. D., "Technical Evaluation of the Rotor Downwash Flow Field of the XV-15 Tilt Rotor Research Aircraft," Naval Air Test Center Technical Report No. SY-14R-83, July 1983.
- K-4. Lake, R. E., and Clark, W. J., "V-22 Rotor Downwash Survey," NAWCADPAX-98-88-RTR, July 1998.
- K-5. Smith, R. D., "Heliport/Vertiport Design Deliberations, 1997-2000," DOT/FAA/ND-00/1, May 2001.
- K-6. Silva, M. J., "CH-47D Tandem Rotor Outwash Survey," NAWCADPAX/EDR-2010/120, August 2010.

Figure Appears in Distribution B Report Annex
H-60 Correlation: GW = 18,500 & 20,500 lb, AGL = 10 ft
Figure K-2

Figure Appears in Distribution B Report Annex
H-60 Correlation: GW = 18,500 & 20,500 lb, AGL = 30 ft
Figure K-3

Figure Appears in Distribution B Report Annex
H-60 Correlation: GW = 18,500 & 20,500 lb, AGL = 50 ft
Figure K-4

Figure Appears in Distribution B Report Annex
H-60 Correlation: GW = 18,500 & 20,500 lb, AGL = 150 ft
Figure K-5

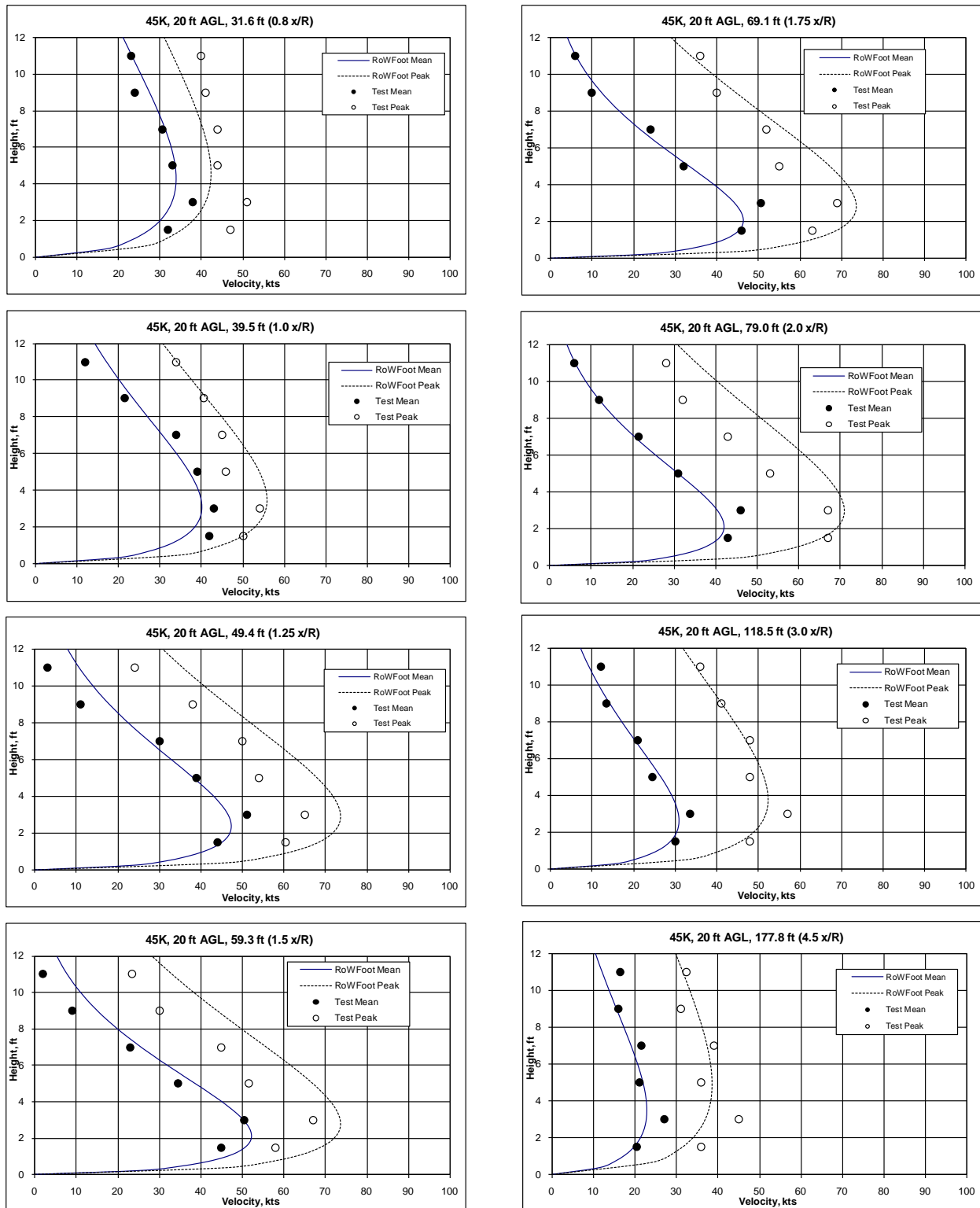


Figure K-6 CH-53E Correlation: GW = 45,000 lb, AGL = 20 ft

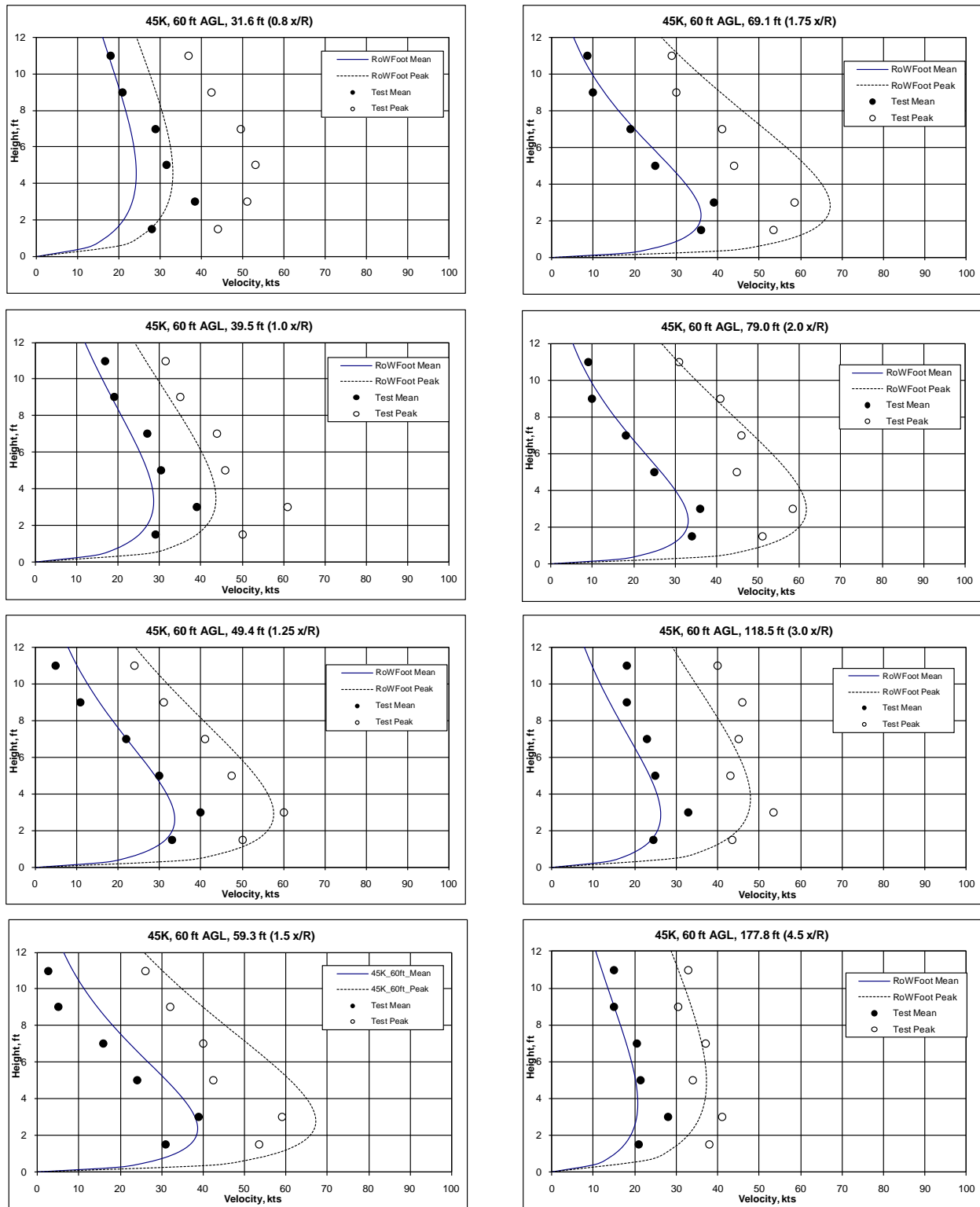


Figure K-7 CH-53E Correlation: GW = 45,000 lb, AGL = 60 ft

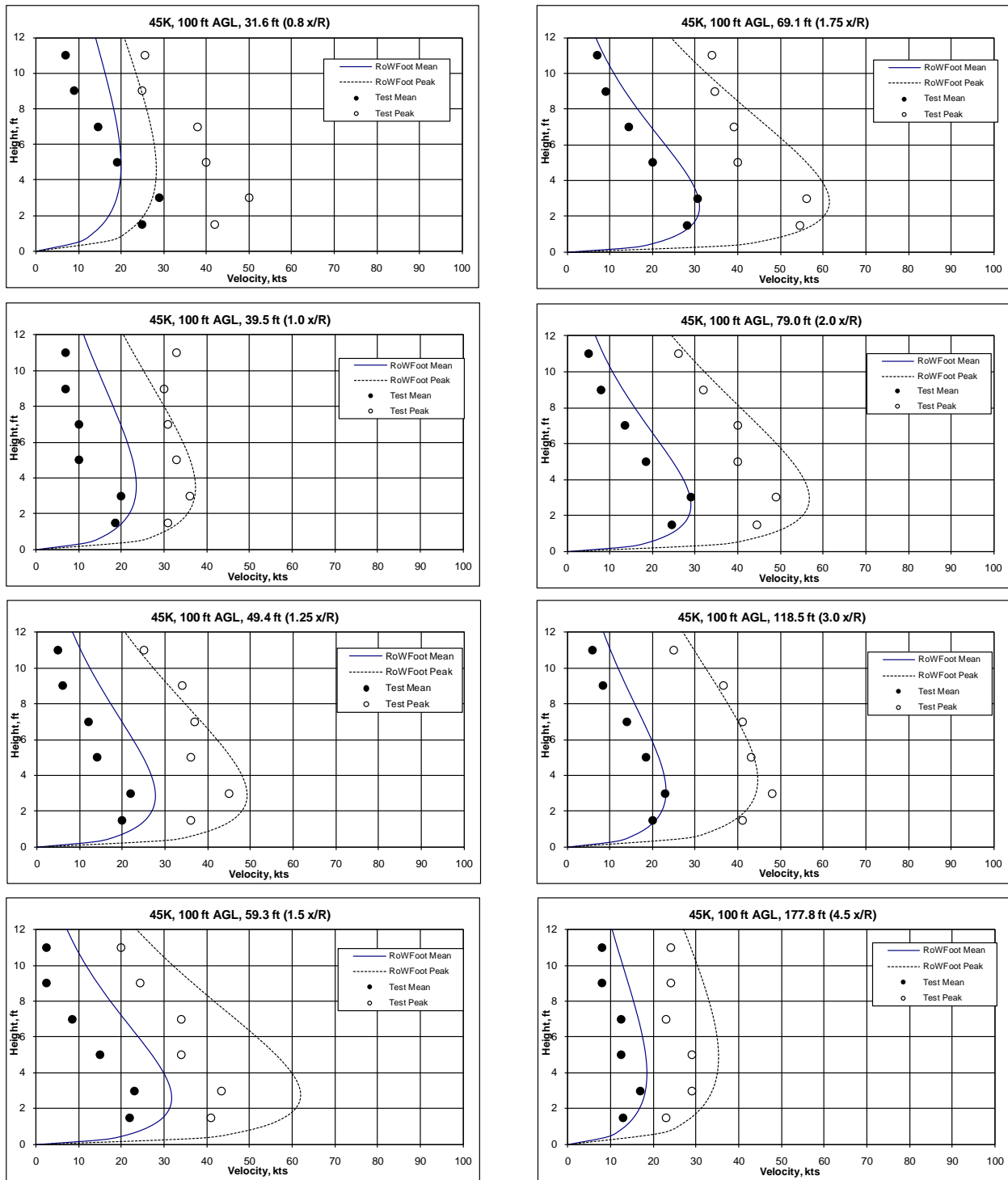


Figure K-8 CH-53E Correlation: GW = 45,000 lb, AGL = 100 ft

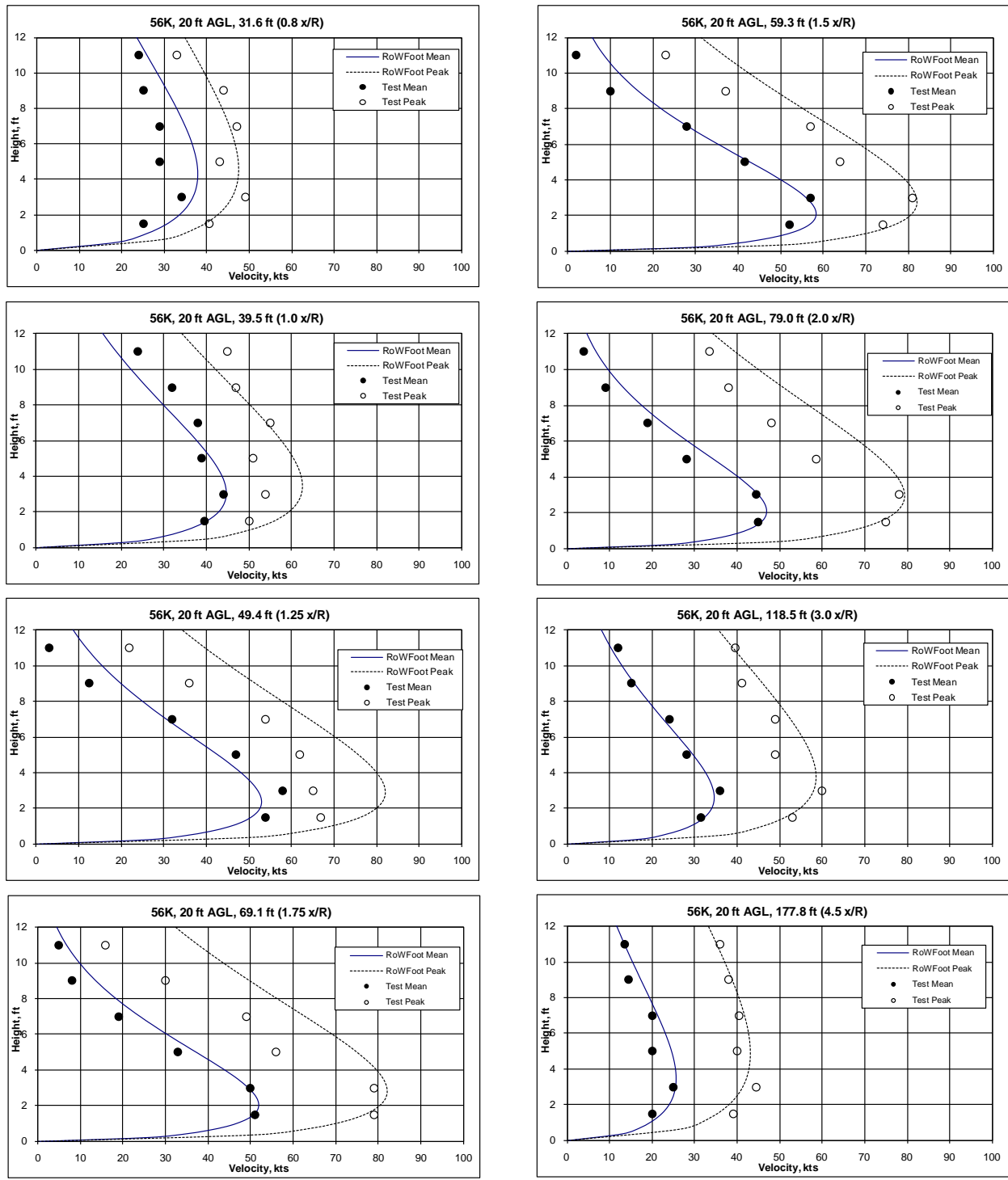


Figure K-9 CH-53E Correlation: GW = 56,000 lb, AGL = 20 ft

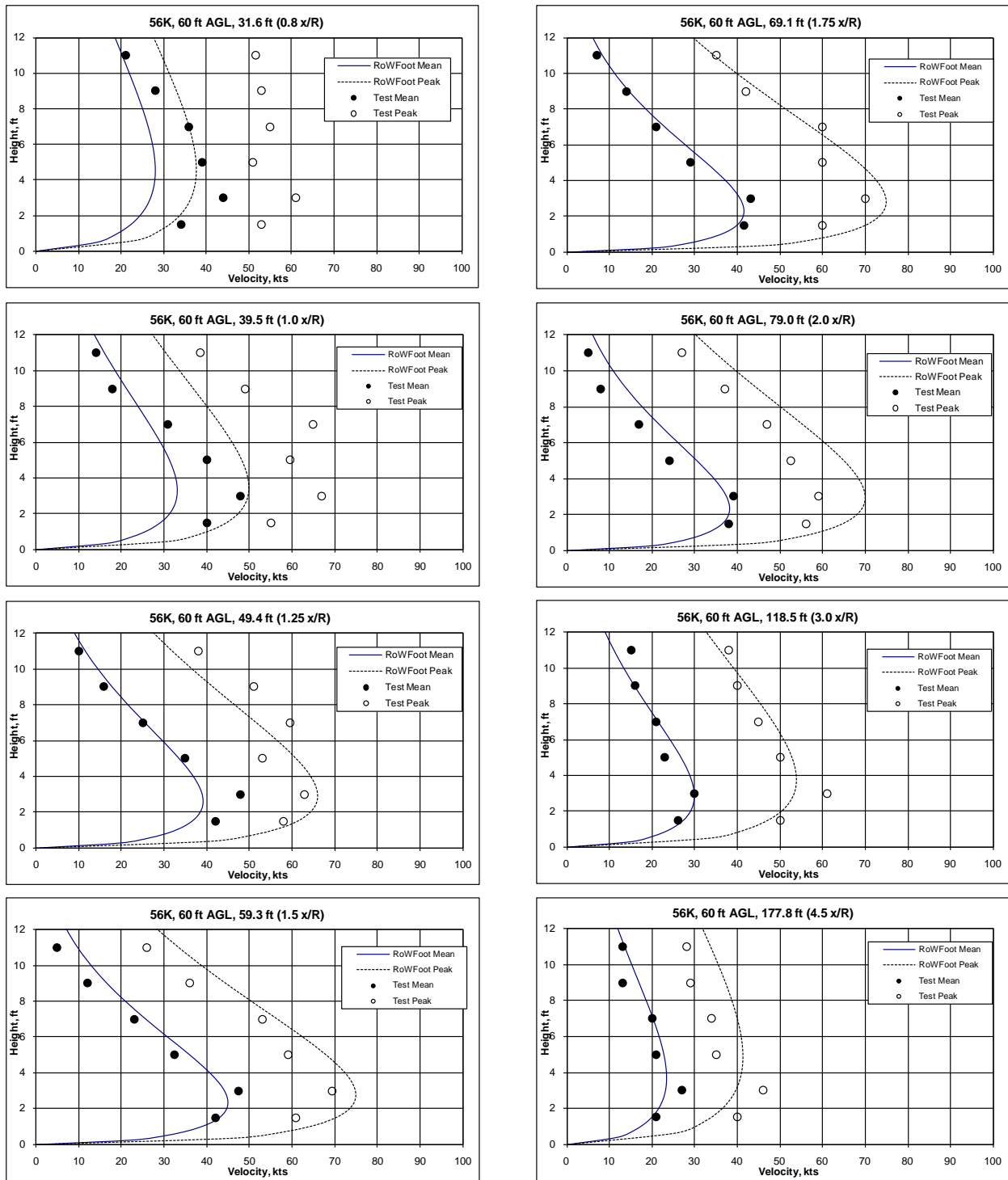


Figure K-10 CH-53E Correlation: GW = 56,000 lb, AGL = 60 ft

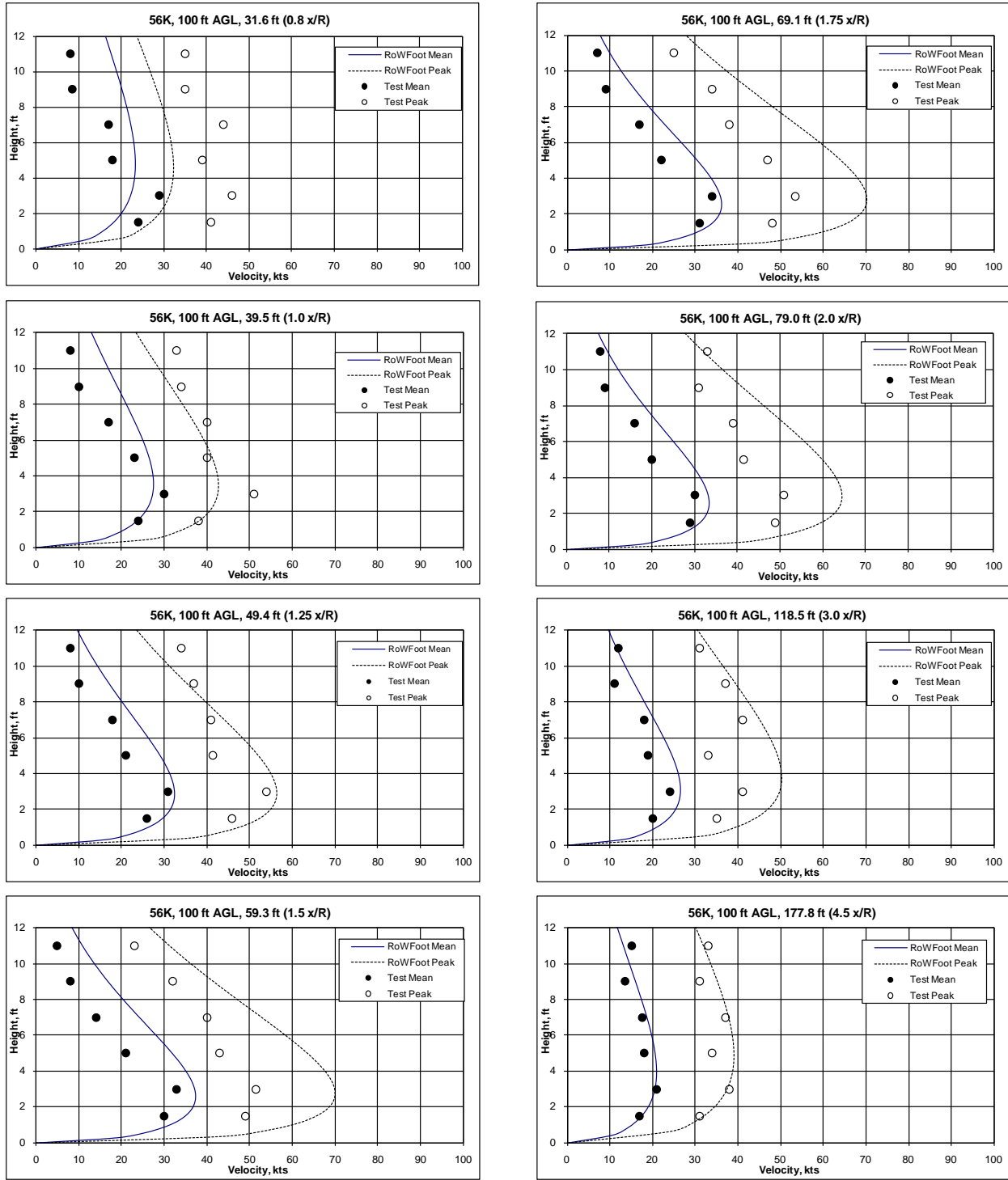


Figure K-11 CH-53E Correlation: GW = 56,000 lb, AGL = 100 ft

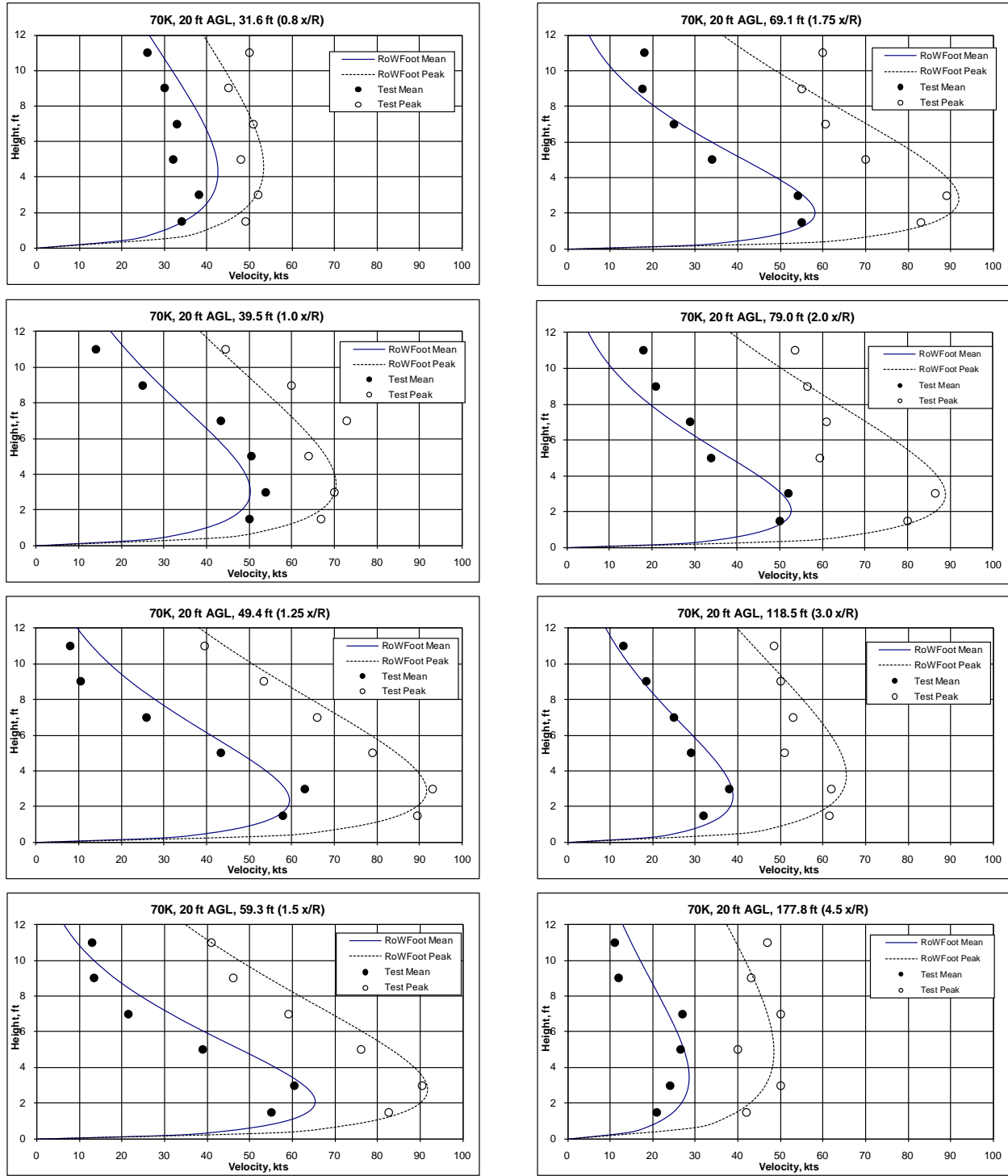


Figure K-12 CH-53E Correlation: GW = 70,000 lb, AGL = 20 ft

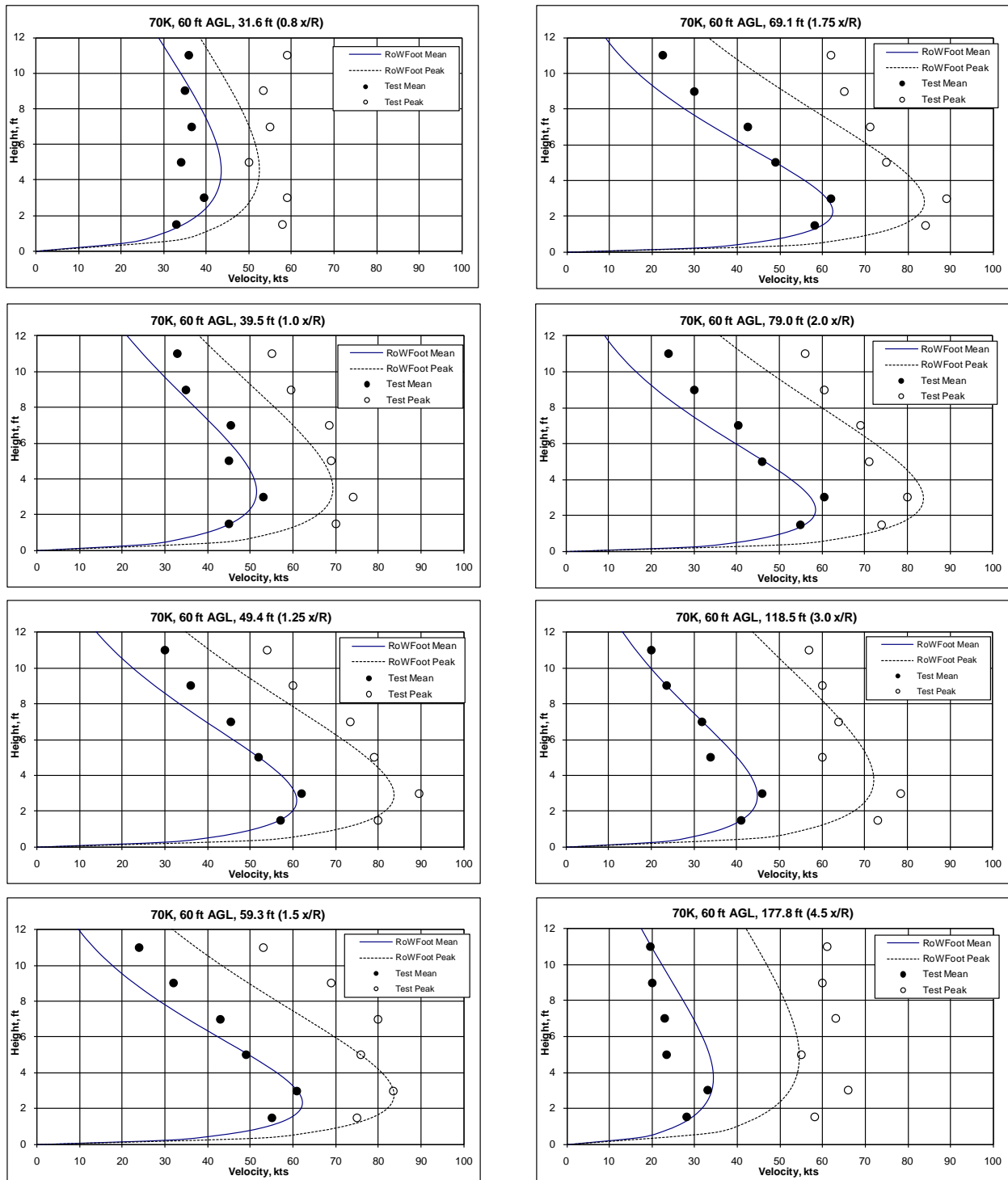


Figure K-13 CH-53E Correlation: GW = 70,000 lb, AGL = 60 ft

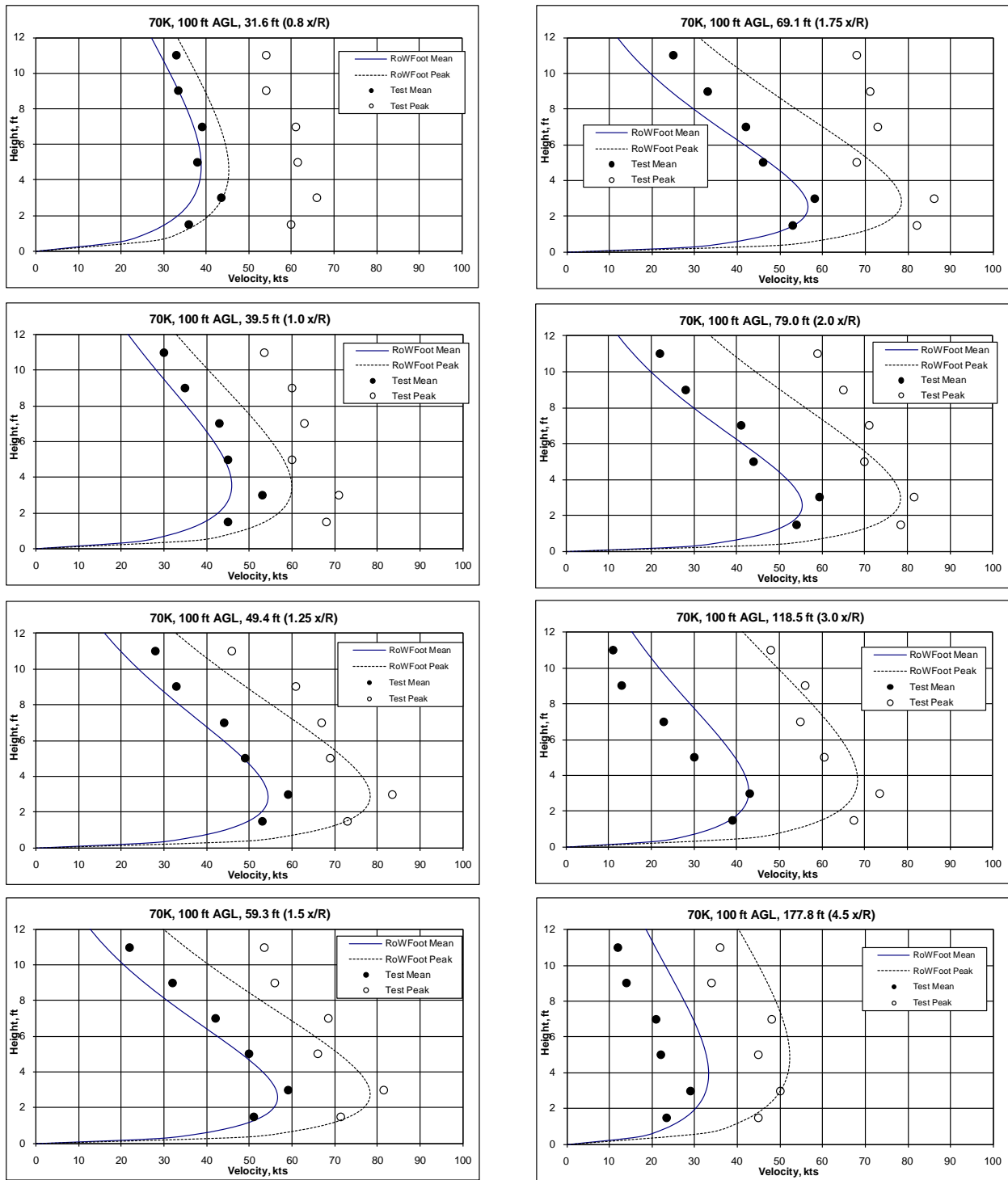


Figure K-14 CH-53E Correlation: GW = 70,000, AGL = 100 ft

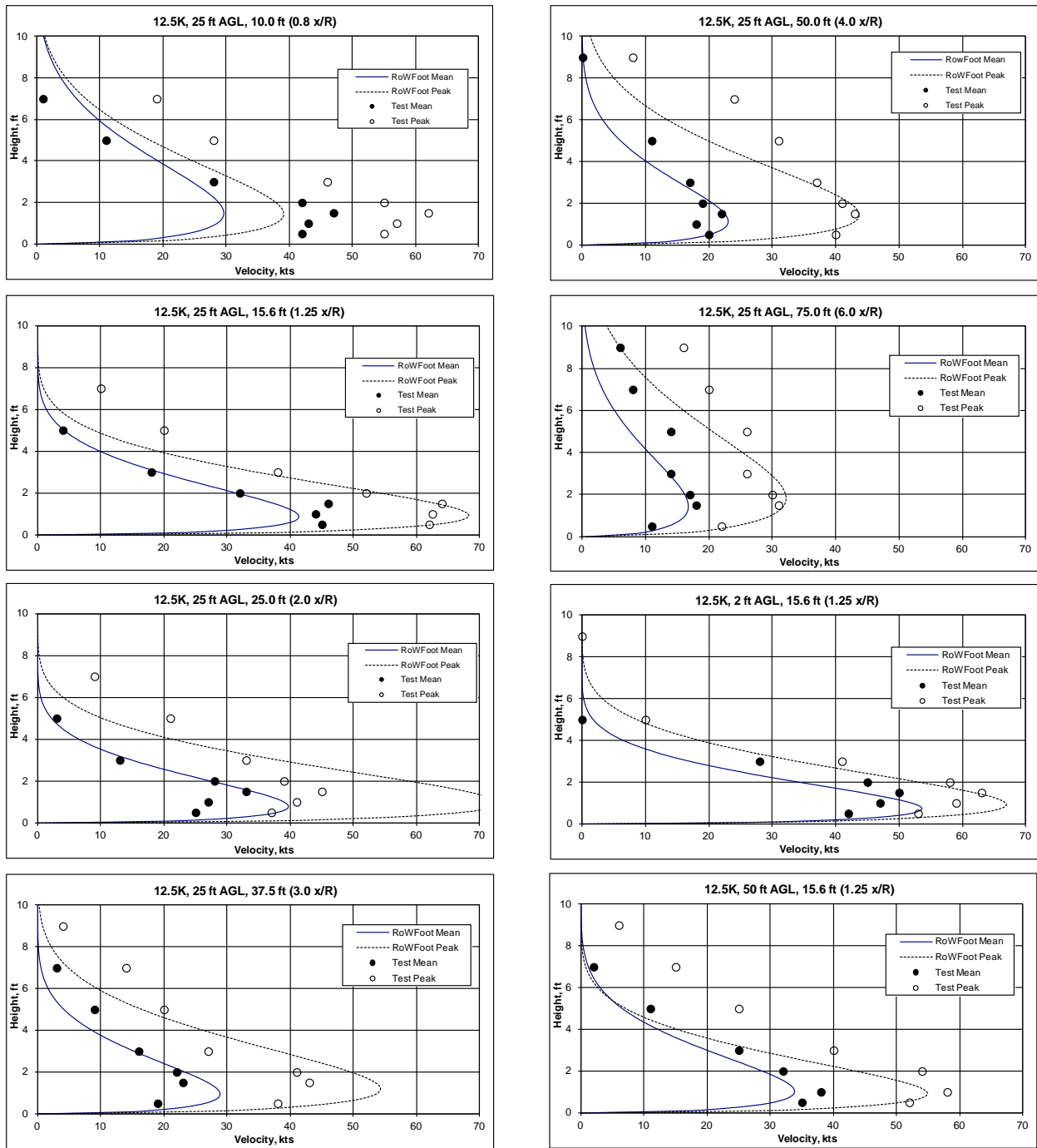


Figure K-15 XV-15 Correlation: GW = 12,500 lb, AGL = 25, 2 & 50 ft,
Azimuth = 270 deg

Figure Appears in Distribution B Report Annex
V-22 Correlation: GW = 22,200 lb, AGL = 0 ft, Azimuth = 270 deg
Figure K-16

Figure Appears in Distribution B Report Annex
V-22 Correlation: GW = 45,900 lb, AGL = 20 ft, Azimuth = 270 deg
Figure K-17

Figure Appears in Distribution B Report Annex
V-22 Correlation: GW = 44,539 lb, AGL = 60 ft, Azimuth = 270 deg
Figure K-18

Figure Appears in Distribution B Report Annex
V-22 Correlation: GW = 43,814 lb, AGL = 100 ft, Azimuth = 270 deg
Figure K-19

Figure Appears in Distribution B Report Annex
V-22 Correlation GW = 45,935 lb, AGL = 20 ft, Azimuth = 240 & 300 deg
Figure K-20

Figure Appears in Distribution B Report Annex
V-22 Correlation GW = 45,935 lb, AGL = 20 ft, Azimuth = 45 & 135 deg
Figure K-21

Figure Appears in Distribution B Report Annex
V-22 Correlation GW = 45,935 lb, AGL = 20 ft, Azimuth = 210 & 330 deg
Figure K-22

Figure Appears in Distribution B Report Annex
CH-47 Correlation GW = 33,300 lb, AGL = 20 ft, Azimuth = 180 deg
Figure K-23

Figure Appears in Distribution B Report Annex
CH-47 Correlation GW = 40,800 lb, AGL = 20 ft, Azimuth = 180 deg
Figure K-24

Figure Appears in Distribution B Report Annex
CH-47 Correlation GW = 49,800 lb, AGL = 20 ft, Azimuth = 180 deg
Figure K-25

Figure Appears in Distribution B Report Annex
CH-47 Correlation GW = 40,600 lb, AGL = 60 ft, Azimuth = 180 deg
Figure K-26

Figure Appears in Distribution B Report Annex
CH-47 Correlation GW = 40,700 lb, AGL = 100 ft, Azimuth = 180 deg
Figure K-27

Figure Appears in Distribution B Report Annex
CH-47 Correlation GW = 33,900 lb, AGL = 20 ft, Azimuth = 0 deg
Figure K-28

Figure Appears in Distribution B Report Annex
CH-47 Correlation GW = 41,900 lb, AGL = 20 ft, Azimuth = 0 deg
Figure K-29

Figure Appears in Distribution B Report Annex
CH-47 Correlation GW = 49,900 lb, AGL = 20 ft, Azimuth = 0 deg
Figure K-30

Figure Appears in Distribution B Report Annex
CH-47 Correlation GW = 41,400 lb, AGL = 78 ft, Azimuth = 0 deg
Figure K-31

Figure Appears in Distribution B Report Annex
CH-47 Correlation GW = 41,400 lb, AGL = 100 ft, Azimuth = 0 deg
Figure K-32

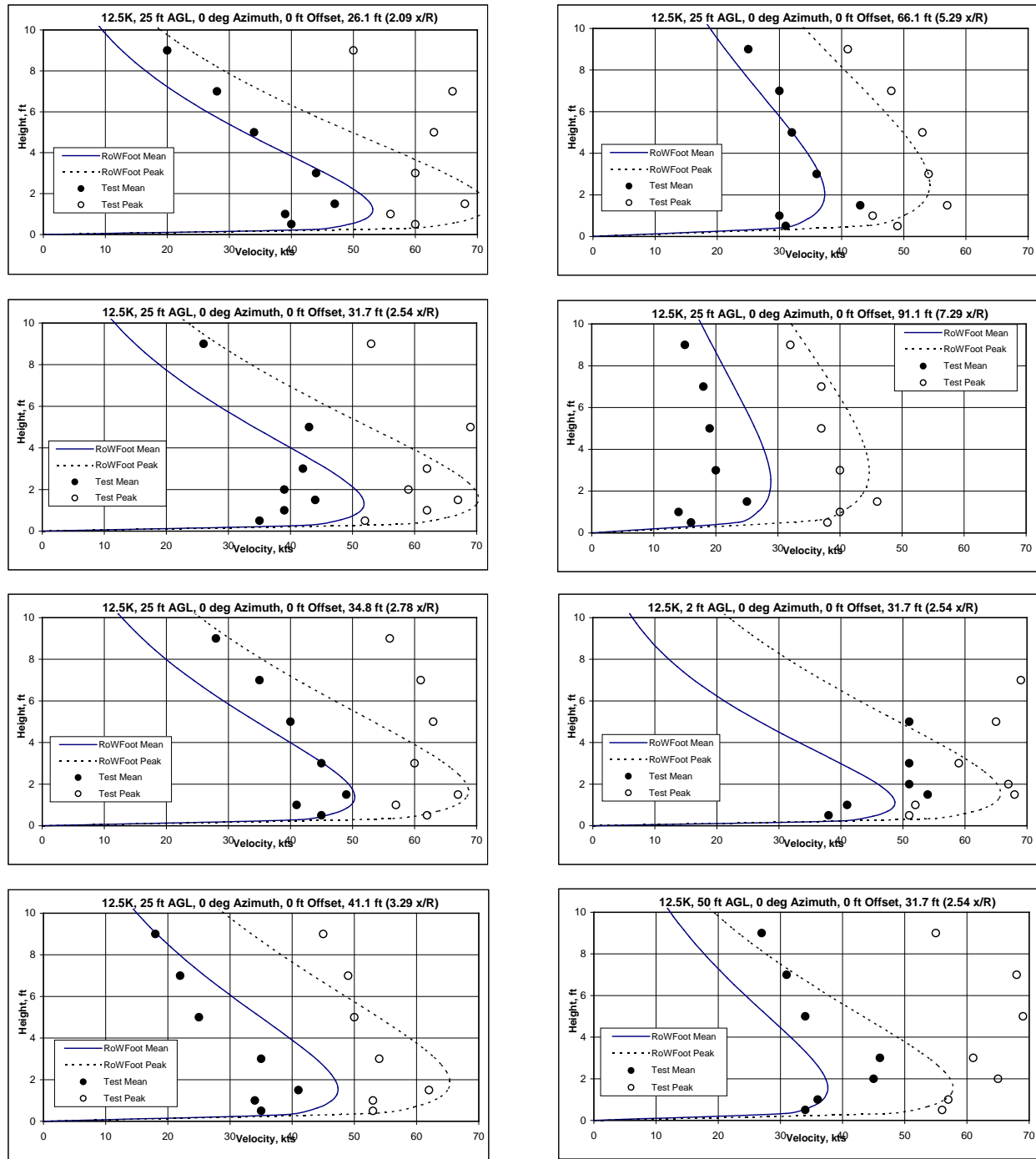


Figure K-33 XV-15 Correlation GW = 12,500 lb, AGL = 25 ft, Azimuth = 0 deg, Offset = 0 ft

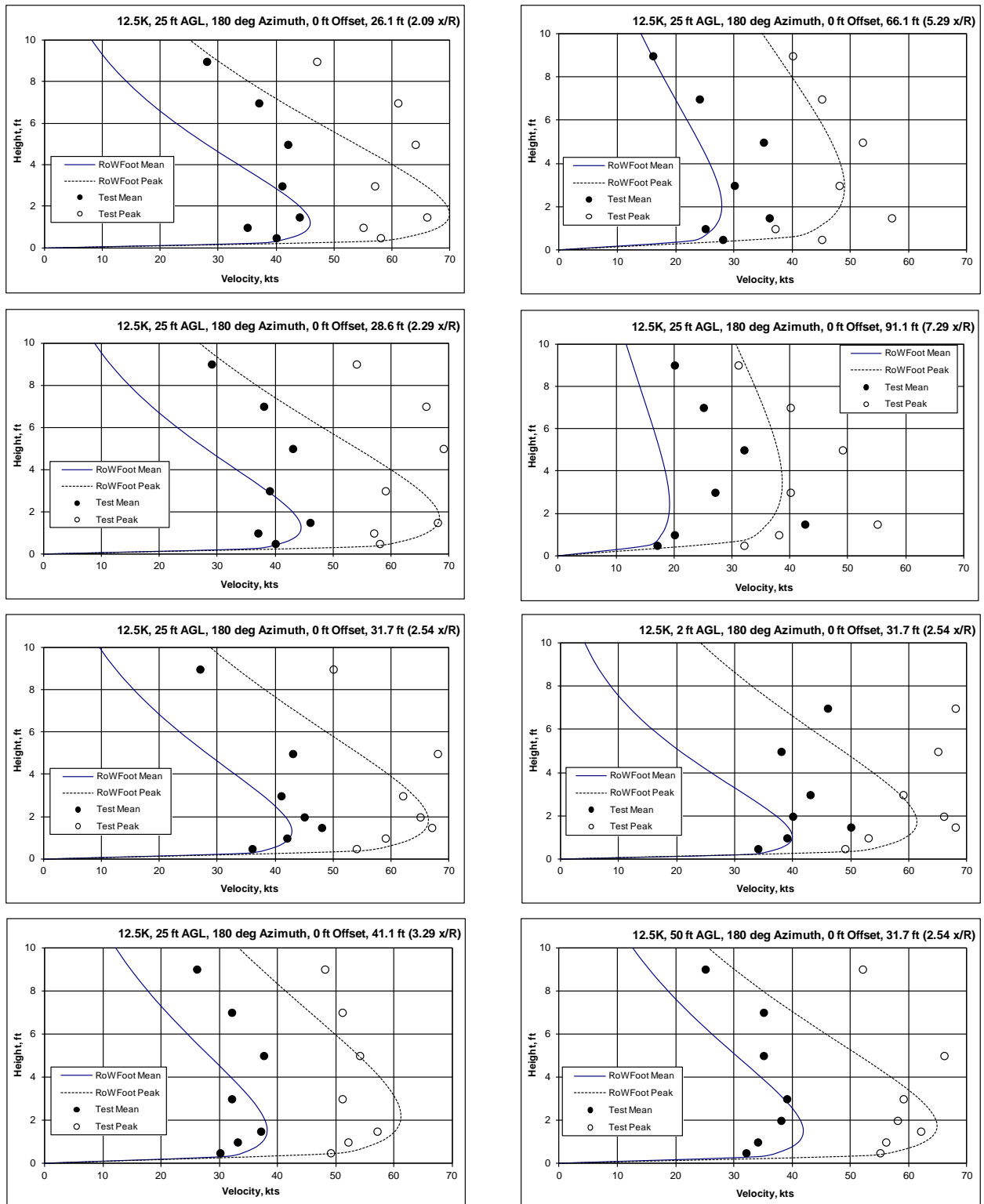


Figure K-34 XV-15 Correlation GW = 12,500 lb, AGL = 25 ft,
Azimuth = 180 deg, Offset = 0 ft

Figure Appears in Distribution B Report Annex
V-22 Correlation GW = 33,800 lb, AGL = 0 ft, Azimuth = 0 deg, Offset = 0 ft
Figure K-35

Figure Appears in Distribution B Report Annex
V-22 Correlation GW = 44,000 lb, AGL = 20 ft, Azimuth = 0 deg, Offset = +20 ft
Figure K-36

Figure Appears in Distribution B Report Annex
V-22 Correlation GW = 43,600 lb, AGL = 20 ft, Azimuth = 0 deg, Offset = +10 ft
Figure K-37

Figure Appears in Distribution B Report Annex
V-22 Correlation GW = 44,600 lb, AGL = 20 ft, Azimuth = 0 deg, Offset = 0 ft
Figure K-38

Figure Appears in Distribution B Report Annex
V-22 Correlation GW = 46,500 lb, AGL = 20 ft, Azimuth = 0 deg, Offset = -10 ft
Figure K-39

Figure Appears in Distribution B Report Annex
V-22 Correlation GW = 45,200 lb, AGL = 20 ft, Azimuth = 0 deg, Offset = -20 ft
Figure K-40

Figure Appears in Distribution B Report Annex
V-22 Correlation GW = 44,600 lb, AGL = 20 ft, Azimuth = 180 deg, Offset = +20 ft
Figure K-41

Figure Appears in Distribution B Report Annex
V-22 Correlation GW = 43,700 lb, AGL = 20 ft, Azimuth = 180 deg, Offset = +10 ft
Figure K-42

Figure Appears in Distribution B Report Annex
V-22 Correlation GW = 45,200 lb, AGL = 20 ft, Azimuth = 180 deg, Offset = 0 ft
Figure K-43

Figure Appears in Distribution B Report Annex
V-22 Correlation GW = 43,500 lb, AGL = 20 ft, Azimuth = 180 deg, Offset = -10 ft
Figure K-44

Figure Appears in Distribution B Report Annex
V-22 Correlation GW = 46,000 lb, AGL = 20 ft, Azimuth = 180 deg, Offset = -20 ft
Figure K-45

Figure Appears in Distribution B Report Annex
V-22 Correlation GW = 44,100 lb, AGL = 60 ft, Azimuth = 180 deg, Offset = 0 ft
Figure K-46

Figure Appears in Distribution B Report Annex
V-22 Correlation GW = 44,100 lb, AGL = 100 ft, Azimuth = 180 deg, Offset = 0 ft
Figure K-47

Figure Appears in Distribution B Report Annex
CH-47 Correlation GW = 33,100 lb, AGL = 20 ft, Azimuth = 90 deg, Offset = 0 ft
Figure K-48

Figure Appears in Distribution B Report Annex
CH-47 Correlation GW = 42,000 lb, AGL = 20 ft, Azimuth = 90 deg, Offset = -20 ft
Figure K-49

Figure Appears in Distribution B Report Annex
CH-47 Correlation GW = 41,400 lb, AGL = 20 ft, Azimuth = 90 deg, Offset = 0 ft
Figure K-50

Figure Appears in Distribution B Report Annex
CH-47 Correlation GW = 41,400 lb, AGL = 20 ft, Azimuth = 90 deg, Offset = +20 ft
Figure K-51

Figure Appears in Distribution B Report Annex
CH-47 Correlation GW = 41,700 lb, AGL = 60 ft, Azimuth = 90 deg, Offset = 0 ft
Figure K-52

Figure Appears in Distribution B Report Annex
CH-47 Correlation GW = 40,200 lb, AGL = 100 ft, Azimuth = 90 deg, Offset = 0 ft
Figure K-53

Figure Appears in Distribution B Report Annex
CH-47 Correlation GW = 49,500 lb, AGL = 20 ft, Azimuth = 90 deg, Offset = 0 ft
Figure K-54

Figure Appears in Distribution B Report Annex
CH-47 Correlation GW = 33,700 lb, AGL = 20 ft, Azimuth = 270 deg, Offset = 0 ft
Figure K-55

Figure Appears in Distribution B Report Annex
CH-47 Correlation GW = 41,900 lb, AGL = 20 ft, Azimuth = 270 deg, Offset = -20 ft
Figure K-56

Figure Appears in Distribution B Report Annex
CH-47 Correlation GW = 40,400 lb, AGL = 20 ft, Azimuth = 270 deg, Offset = 0 ft
Figure K-57

Figure Appears in Distribution B Report Annex
CH-47 Correlation GW = 41,800 lb, AGL = 20 ft, Azimuth = 270 deg, Offset = +20 ft
Figure K-58

Figure Appears in Distribution B Report Annex
CH-47 Correlation GW = 41,000 lb, AGL = 60 ft, Azimuth = 270 deg, Offset = 0 ft
Figure K-59

Figure Appears in Distribution B Report Annex
CH-47 Correlation GW = 41,000 lb, AGL = 100 ft, Azimuth = 270 deg, Offset = 0 ft
Figure K-60

Figure Appears in Distribution B Report Annex
CH-47 Correlation GW = 49,800 lb, AGL = 20 ft, Azimuth = 270 deg, Offset = 0 ft
Figure K-61

Update to High
Fidelity Model
Required To
Extend
Rotorwash
Database

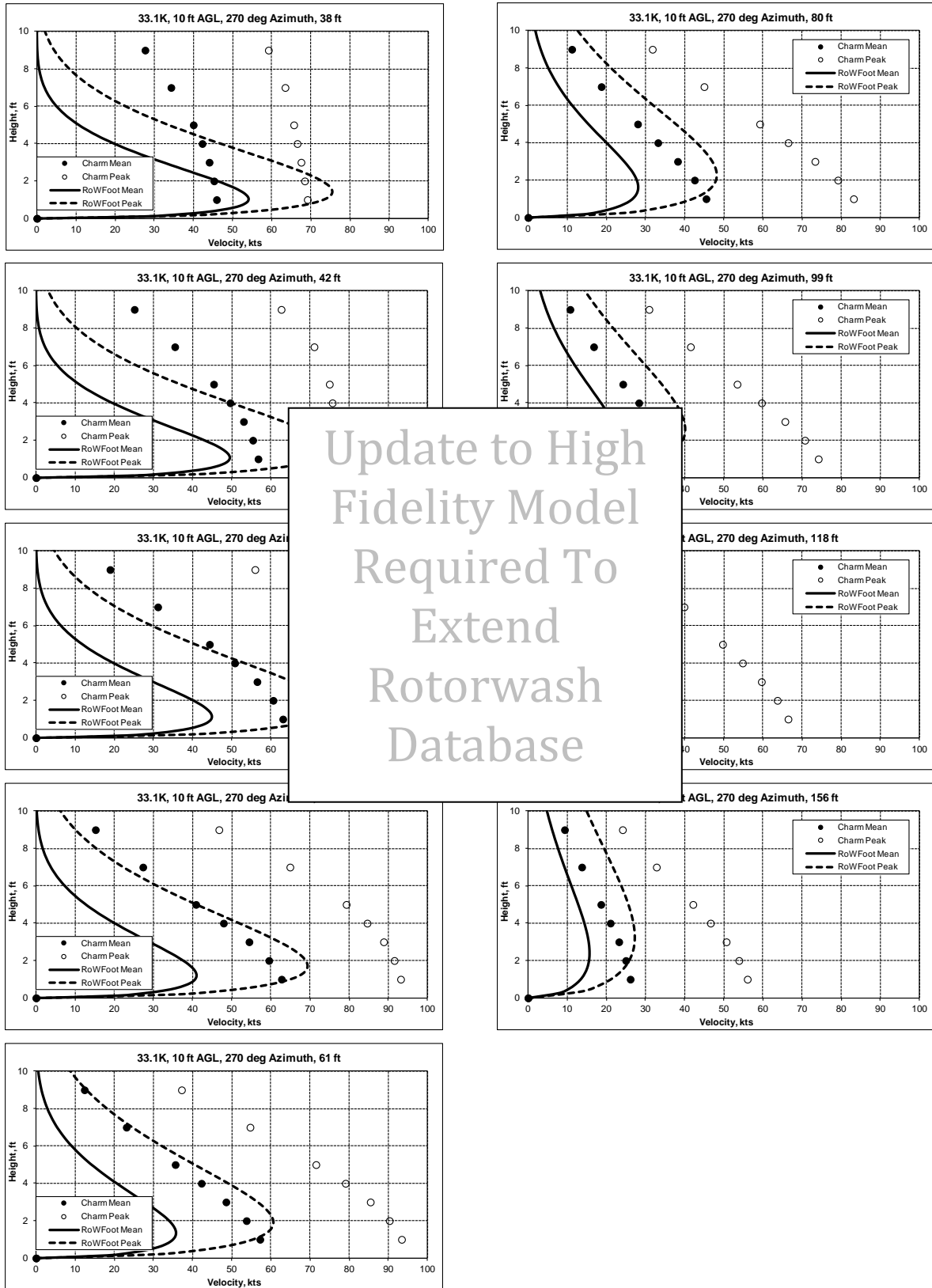


Figure K-62 V-22 Correlation GW = 33,140 lb, AGL = 10 ft,
Azimuth = 270 deg

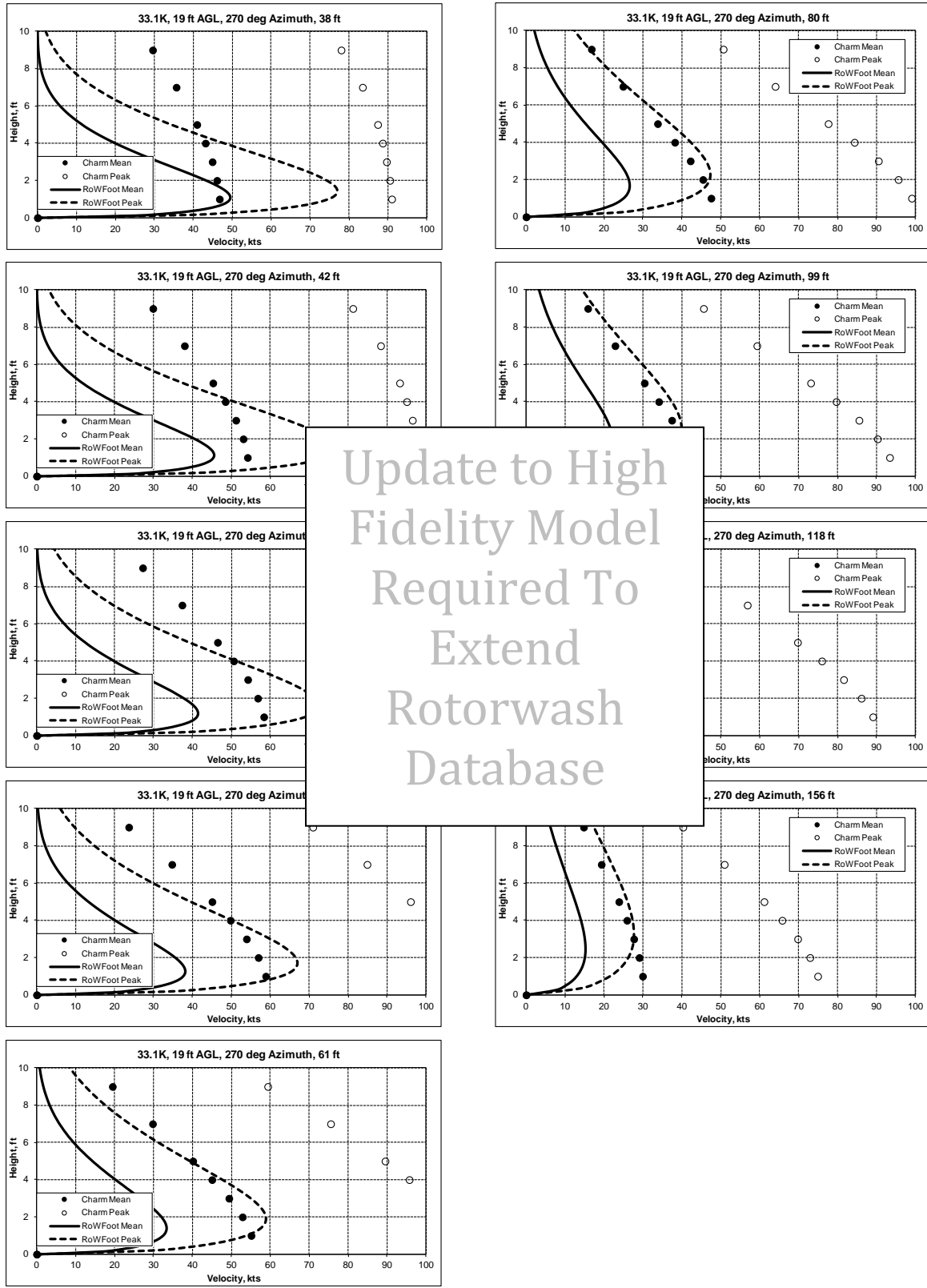


Figure K-63 V-22 Correlation GW = 33,140 lb, AGL = 19 ft,
Azimuth = 270 deg

Update to High Fidelity Model Required To Extend Rotorwash Database

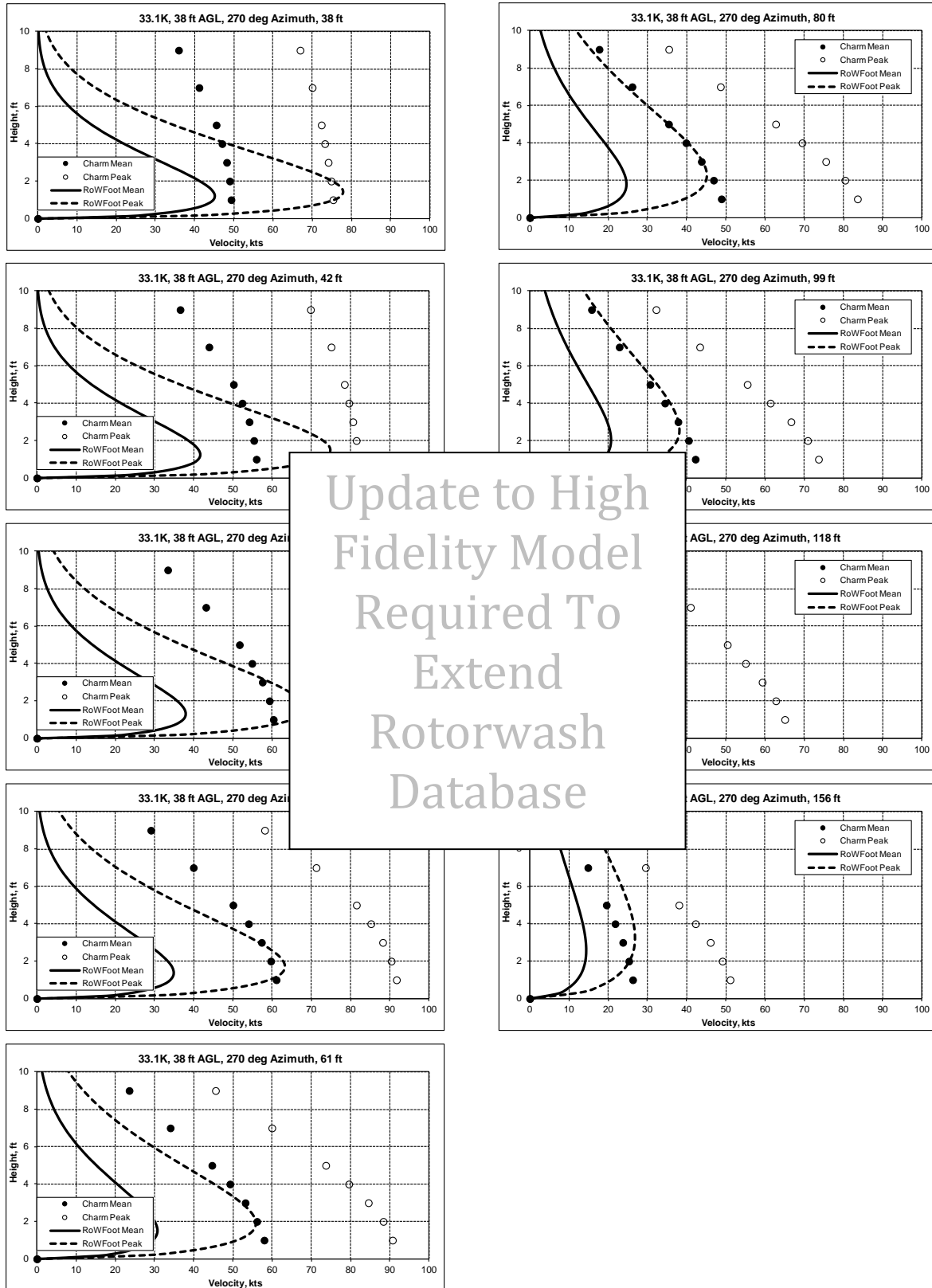


Figure K-64 V-22 Correlation GW = 33,140 lb, AGL = 38 ft, Azimuth = 270 deg

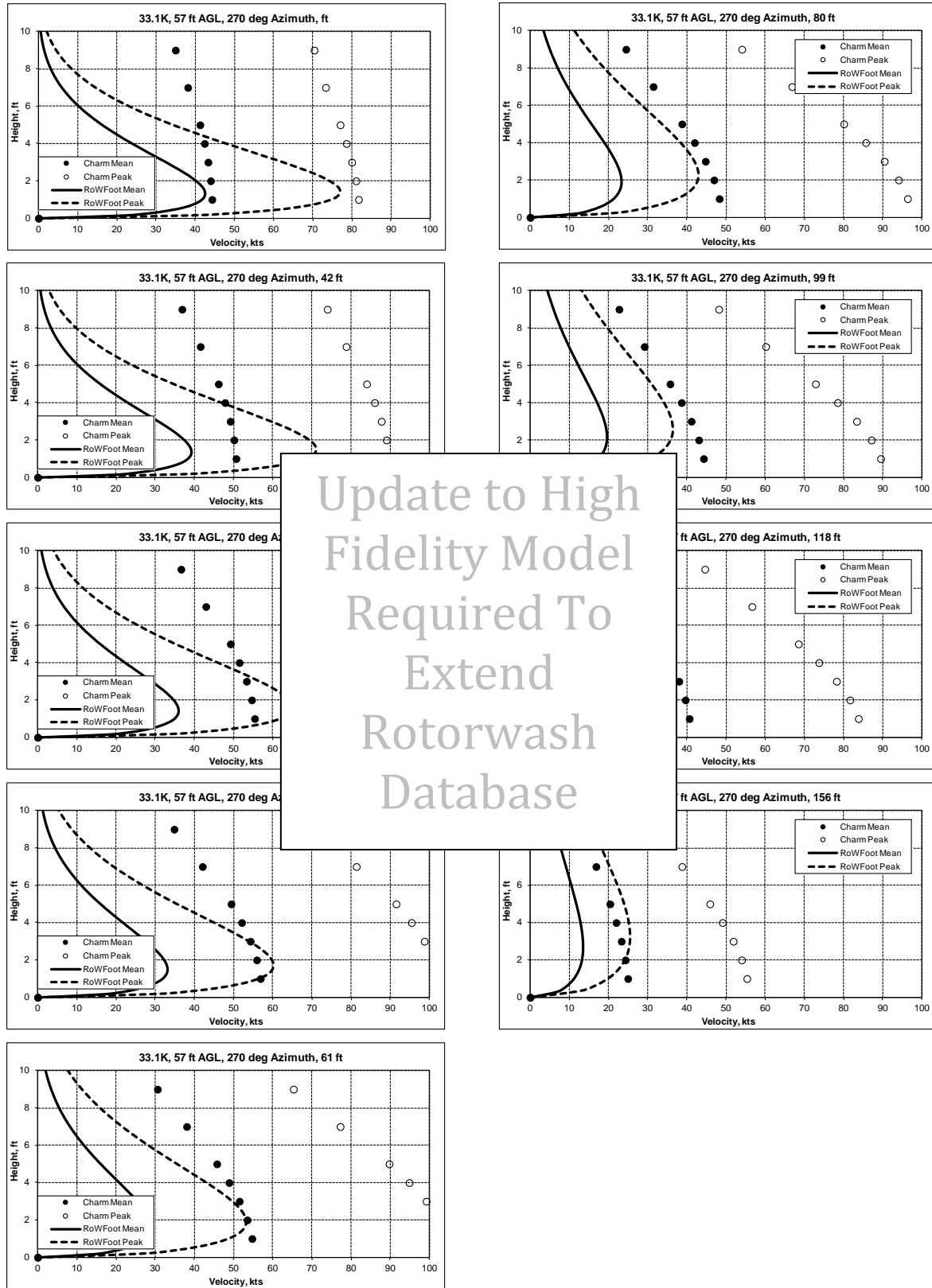


Figure K-65 V-22 Correlation GW = 33,140 lb, AGL = 57 ft, Azimuth = 270 deg

Update to High Fidelity Model Required To Extend Rotorwash Database

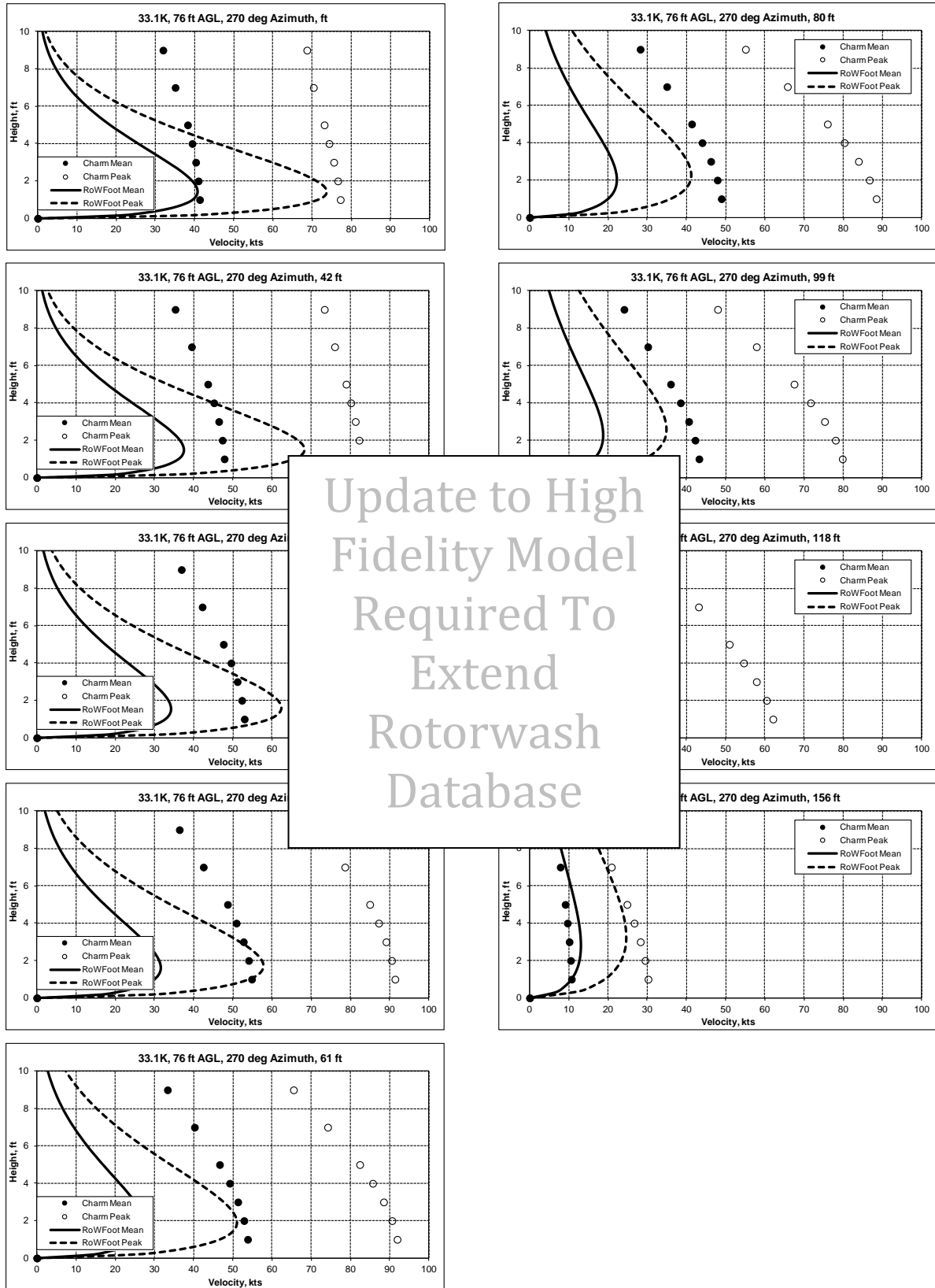


Figure K-66 V-22 Correlation GW = 33,140 lb, AGL = 76 ft, Azimuth = 270 deg

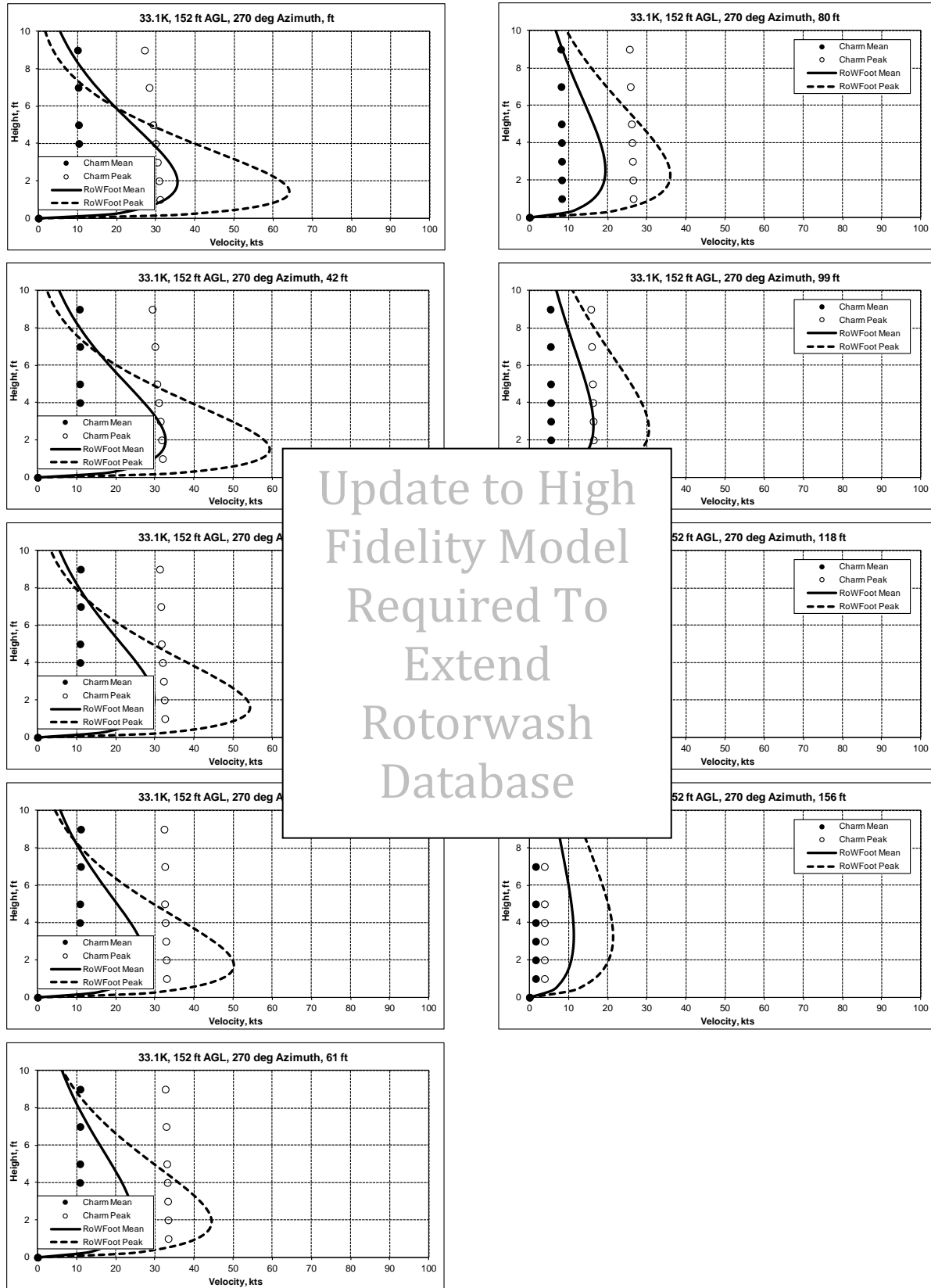


Figure K-67 V-22 Correlation GW = 33,140 lb, AGL = 152 ft,
Azimuth = 270 deg

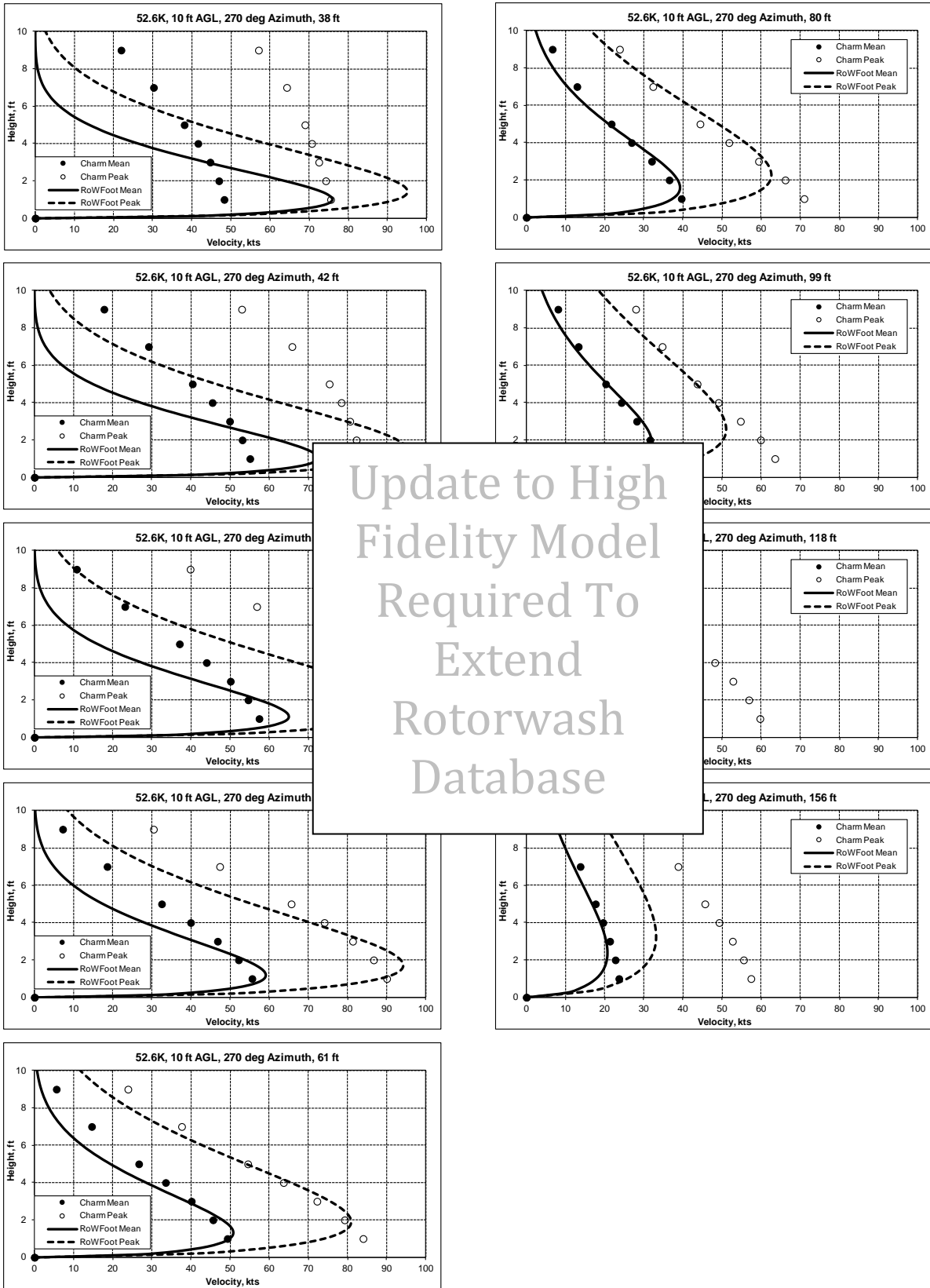


Figure K-68 V-22 Correlation GW = 52,600 lb, AGL = 10 ft,
Azimuth = 270 deg

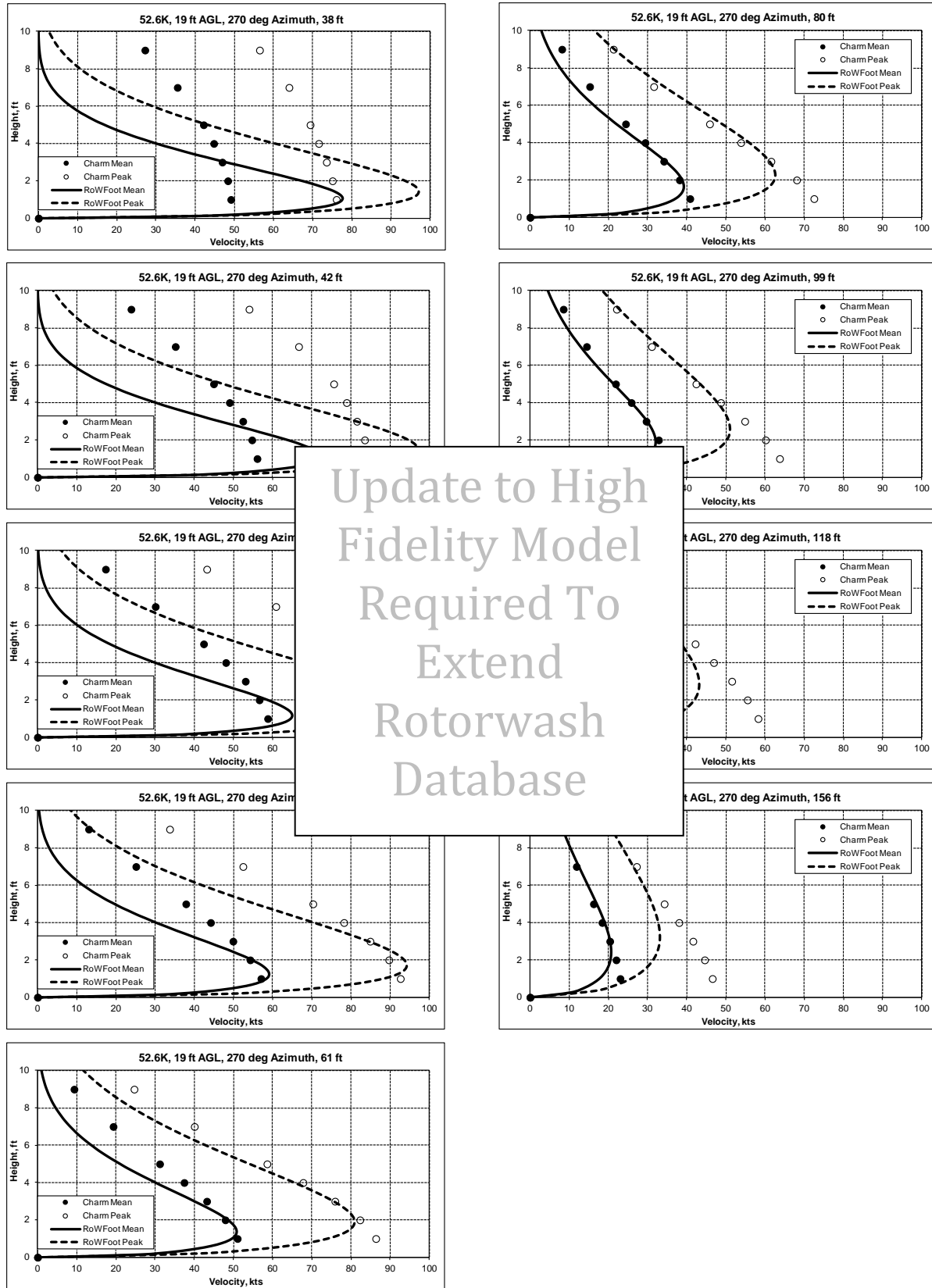


Figure K-69 V-22 Correlation GW = 52,600 lb, AGL = 19 ft,
Azimuth = 270 deg

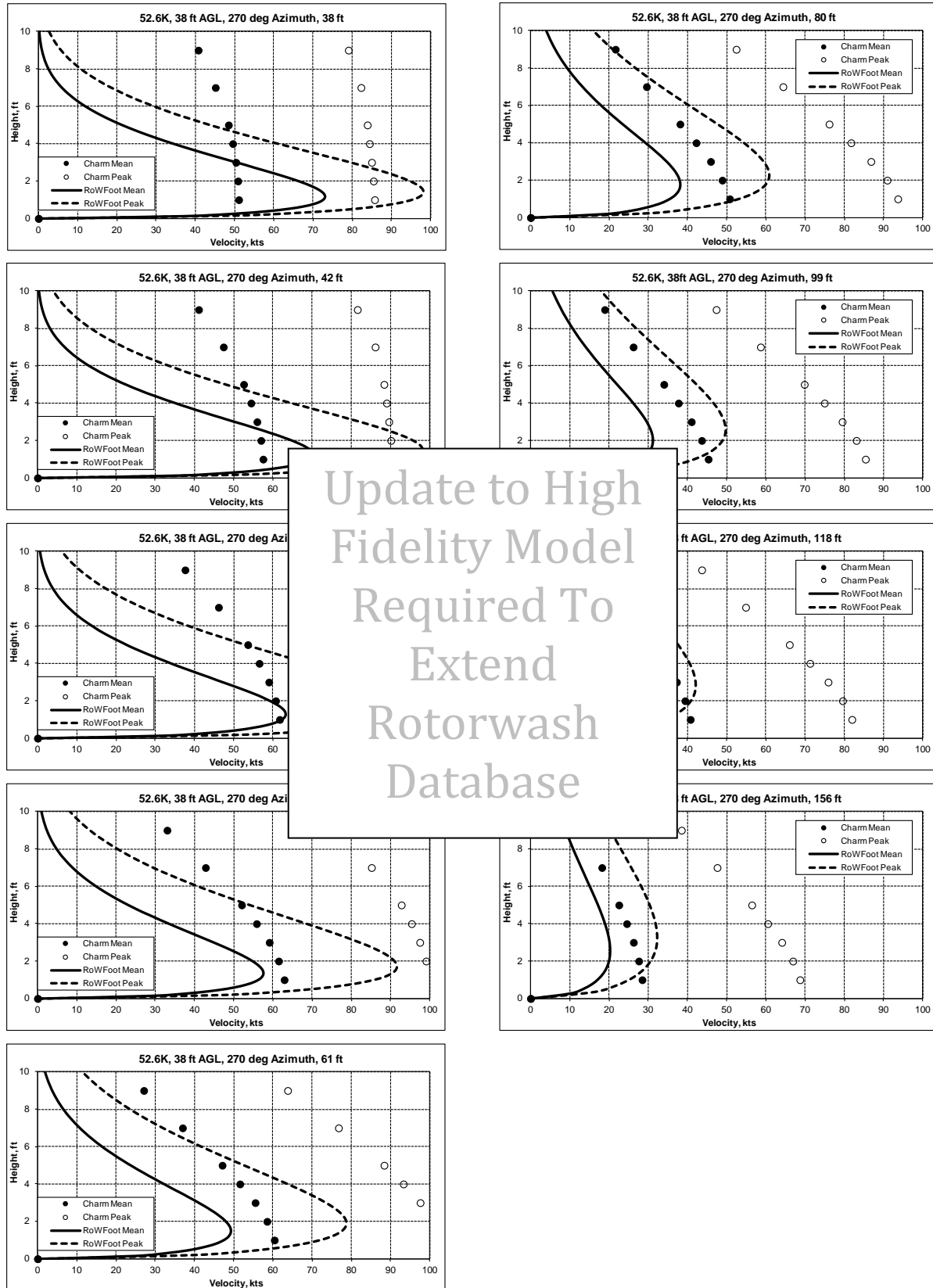


Figure K-70 V-22 Correlation GW = 52,600 lb, AGL = 38 ft,
Azimuth = 270 deg

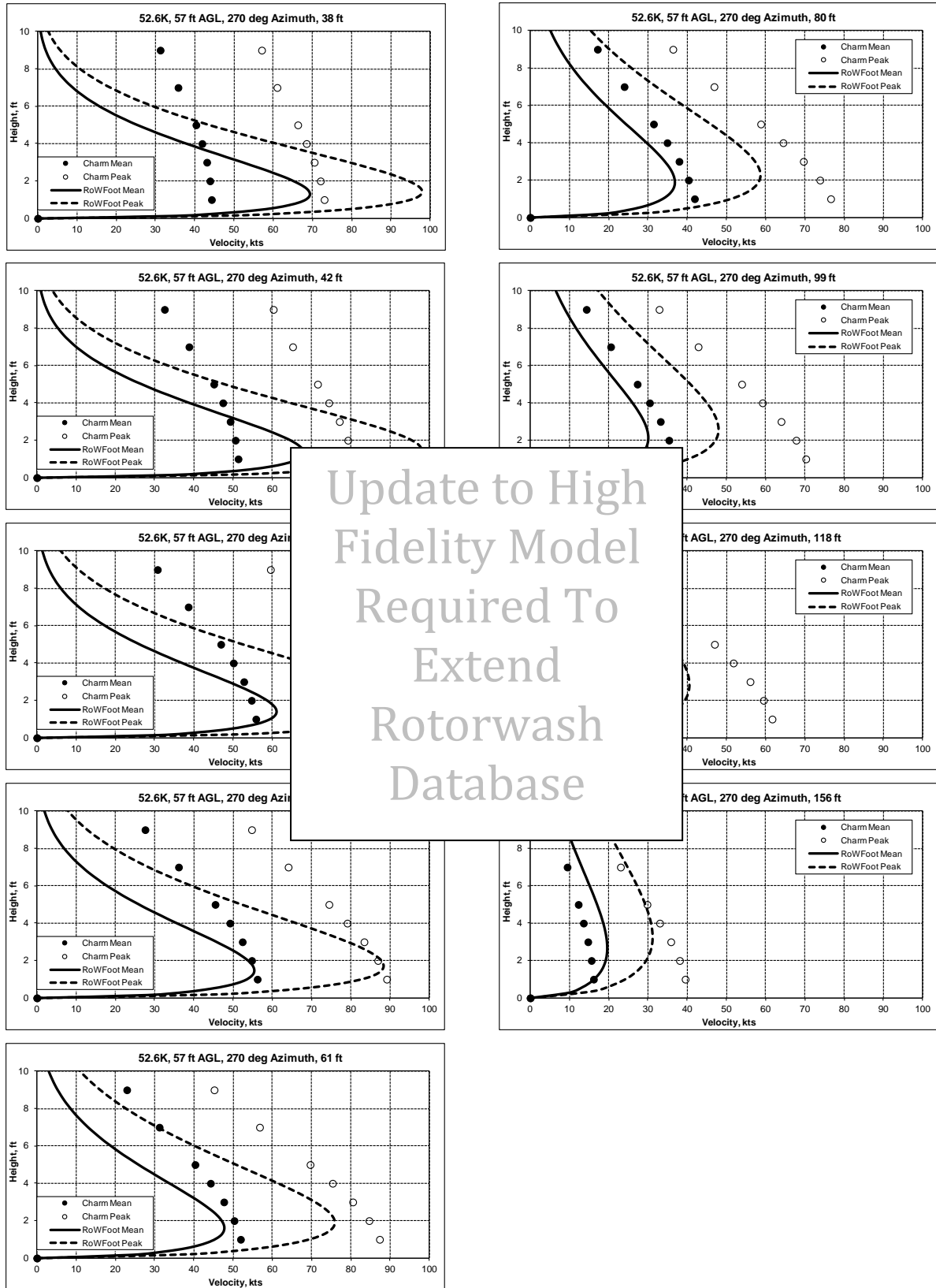


Figure K-71 V-22 Correlation GW = 52,600 lb, AGL = 57 ft,
Azimuth = 270 deg

Update to High Fidelity Model Required To Extend Rotorwash Database

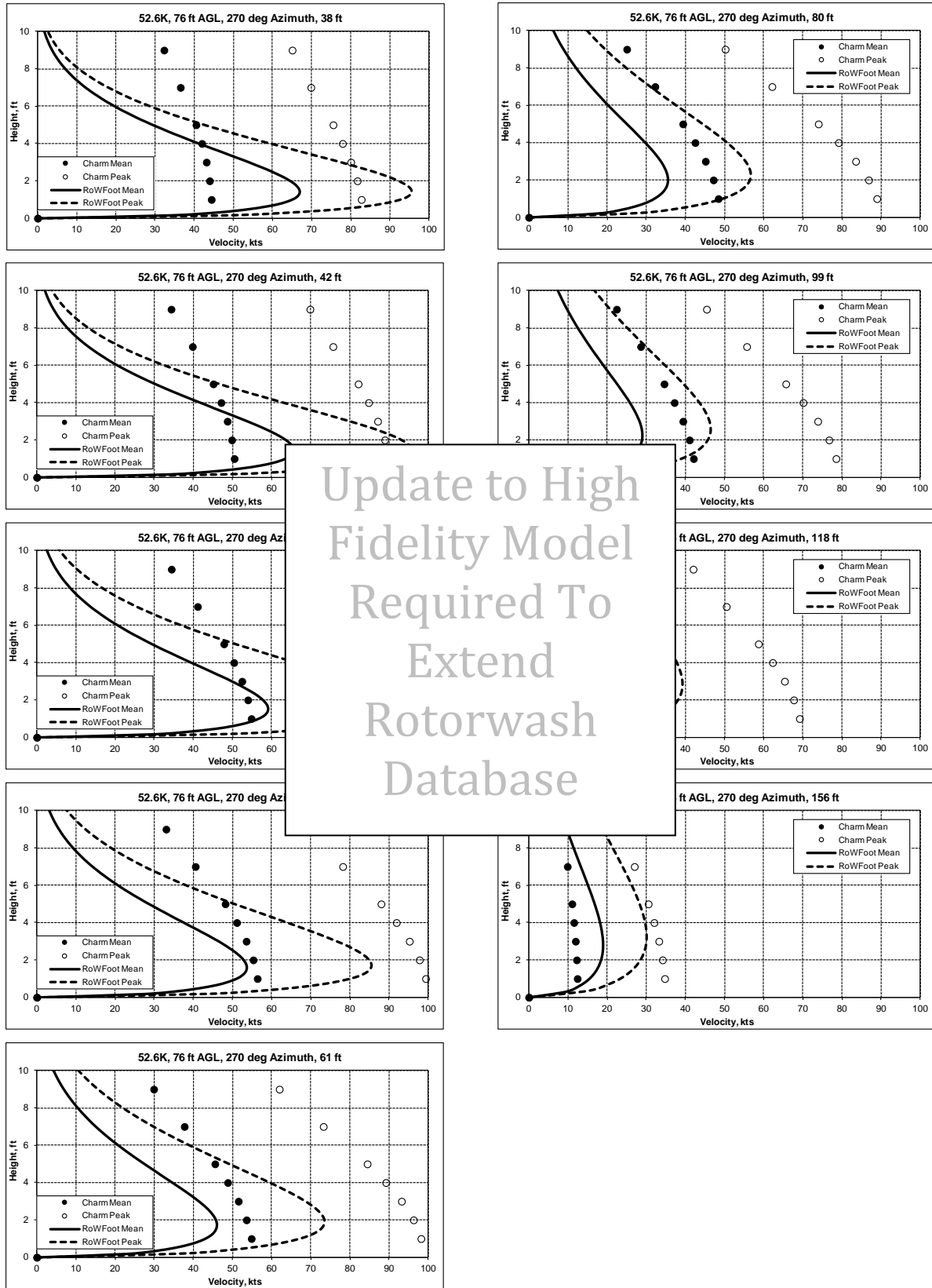


Figure K-72 V-22 Correlation GW = 52,600 lb, AGL = 76 ft, Azimuth = 270 deg

Update to High Fidelity Model Required To Extend Rotorwash Database

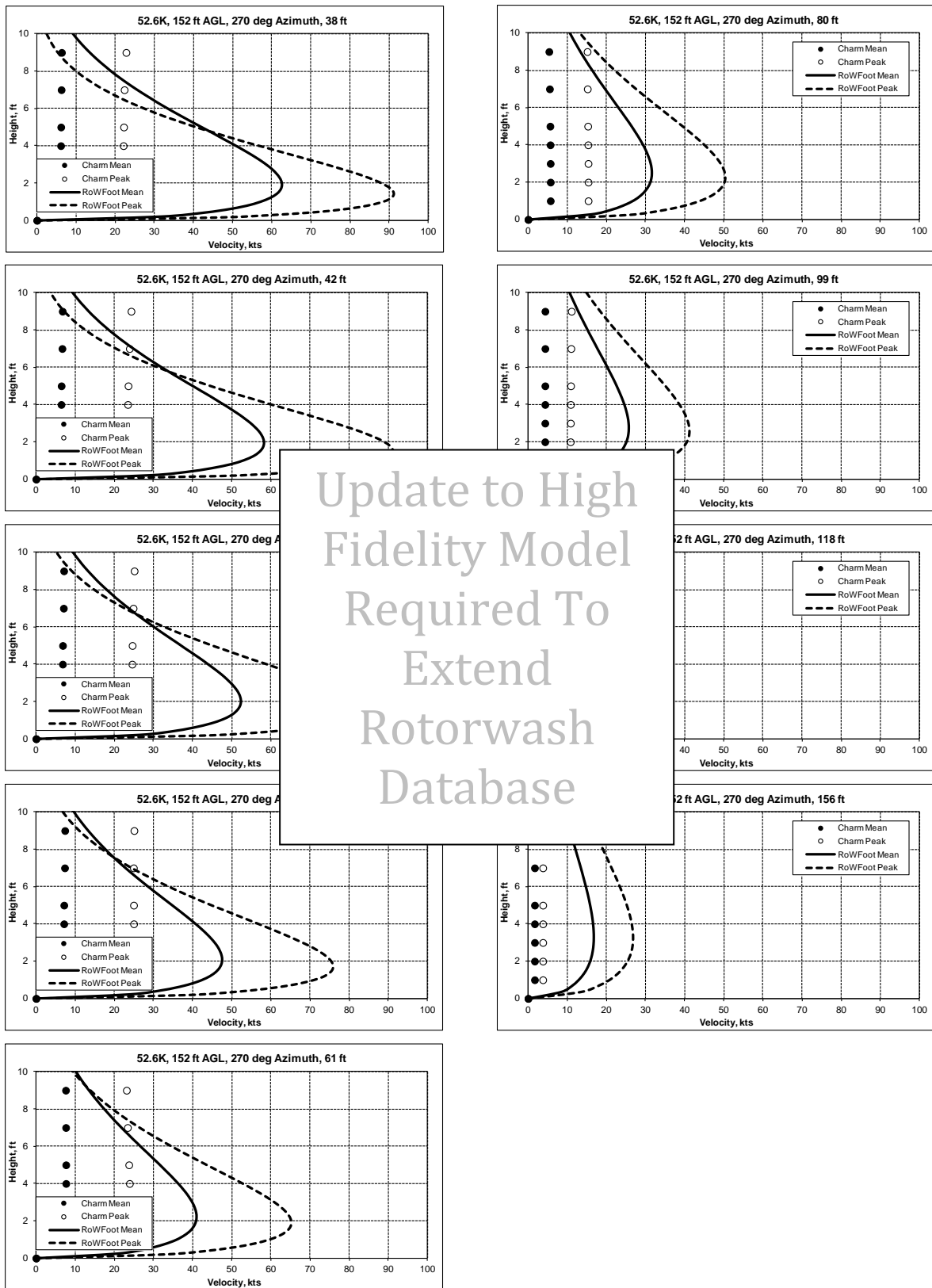


Figure K-73 V-22 Correlation GW = 52,600 lb, AGL = 152 ft, Azimuth = 270 deg

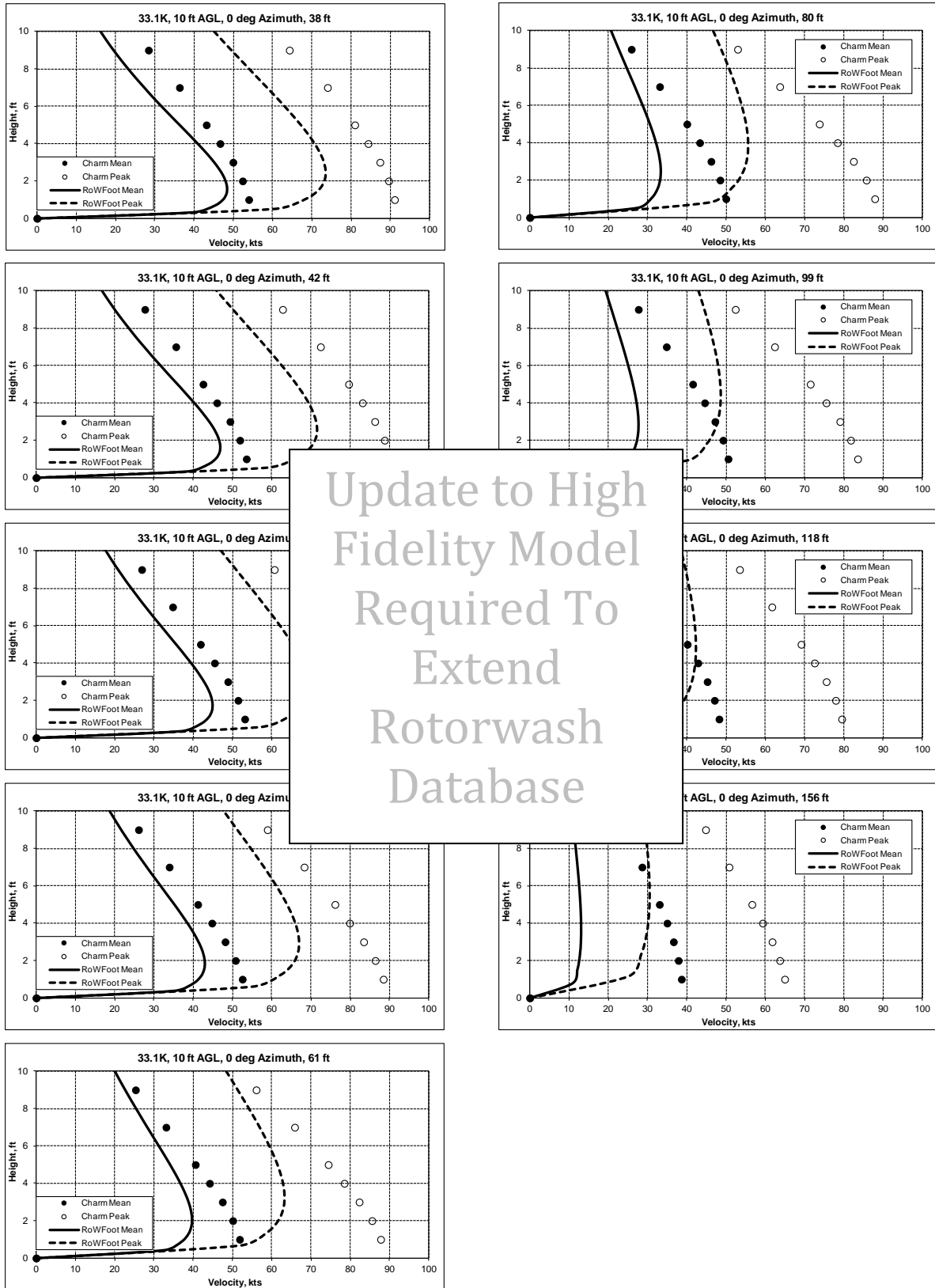


Figure K-74 V-22 Correlation GW = 33,140 lb, AGL = 10 ft, Azimuth = 0 deg, Offset = 0

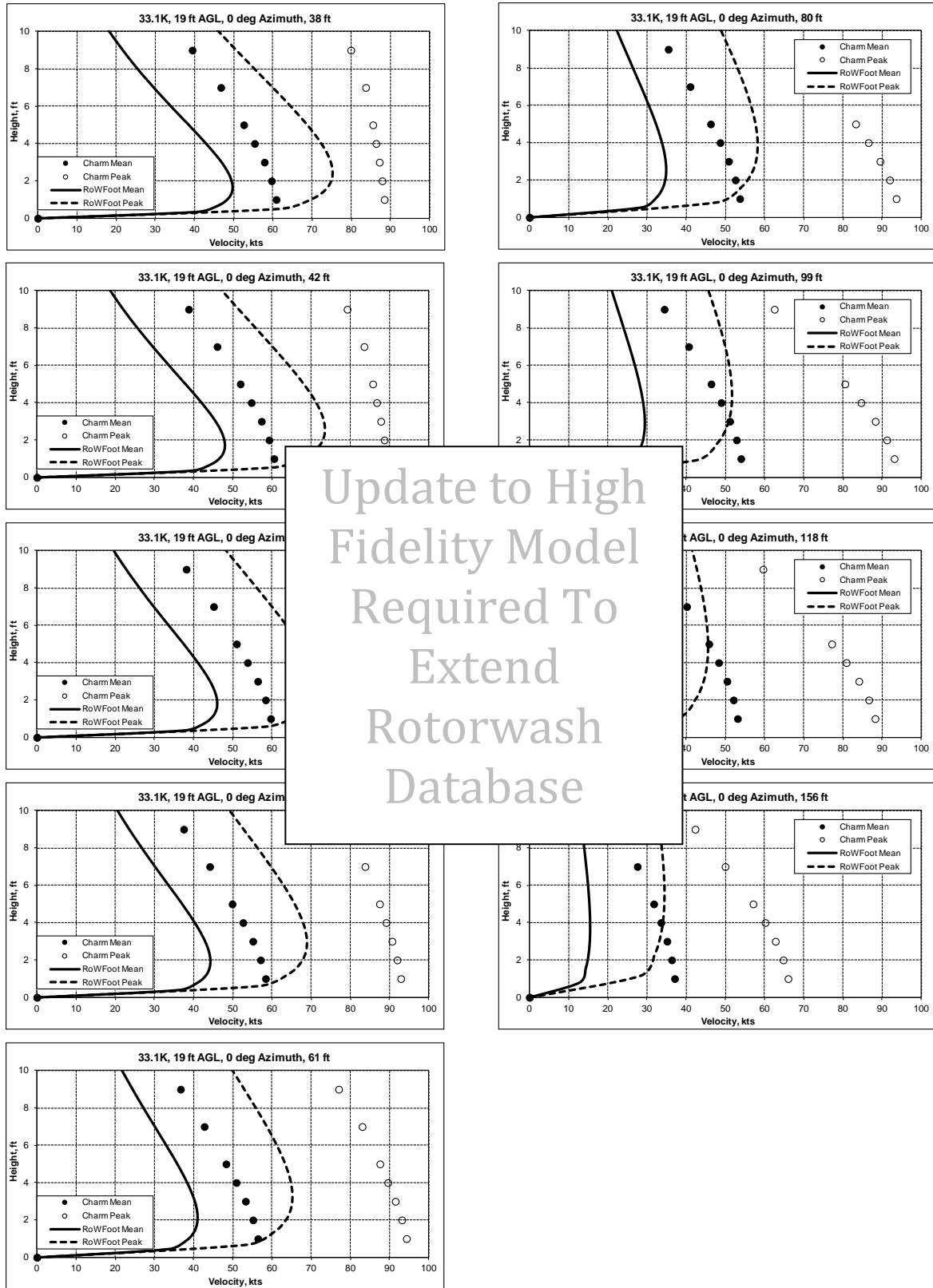


Figure K-75 V-22 Correlation GW = 33,140 lb, AGL = 19 ft,
Azimuth = 0 deg, Offset = 0

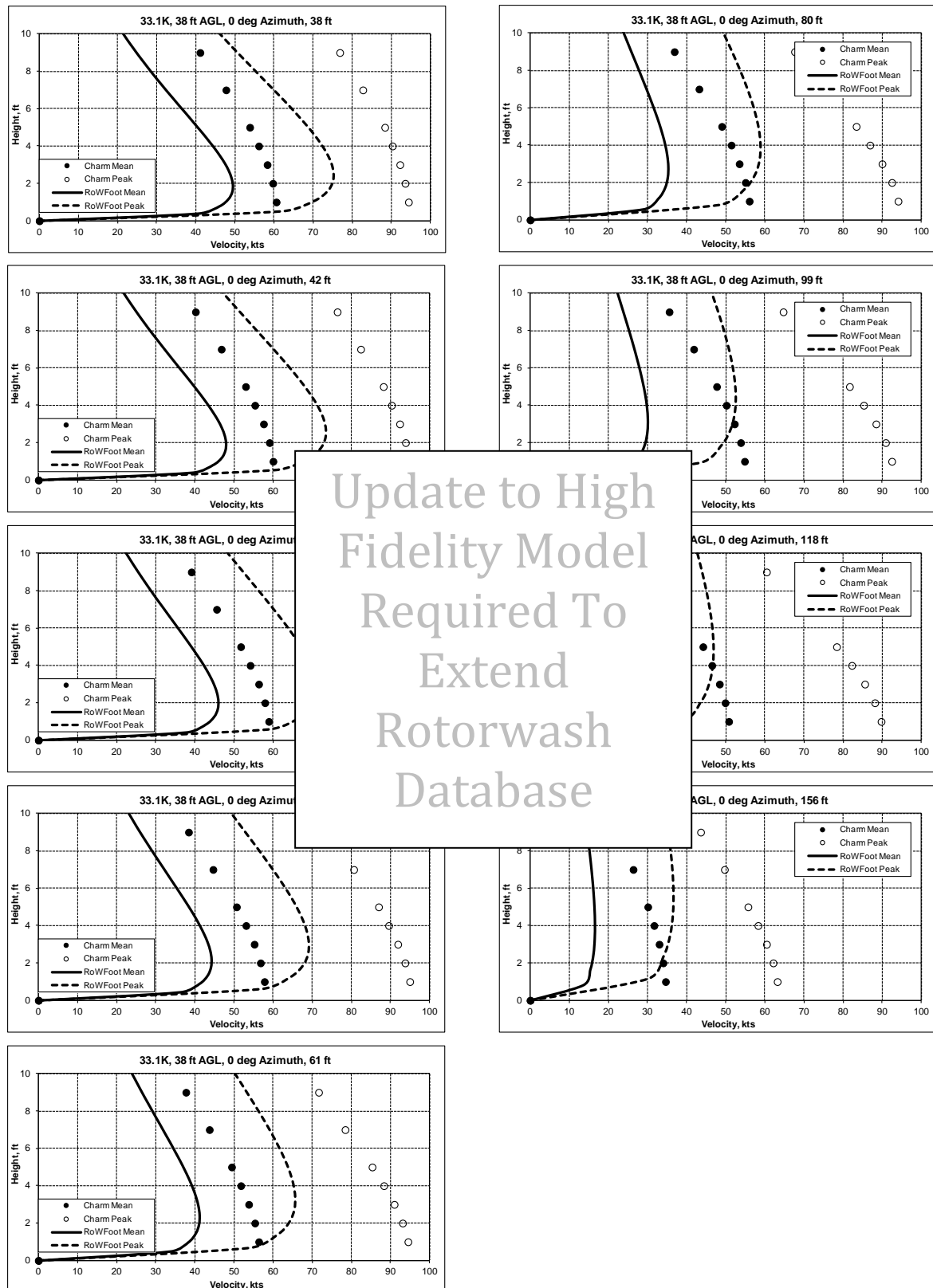


Figure K-76 V-22 Correlation GW = 33,140 lb, AGL = 38 ft,
Azimuth = 0 deg, Offset = 0

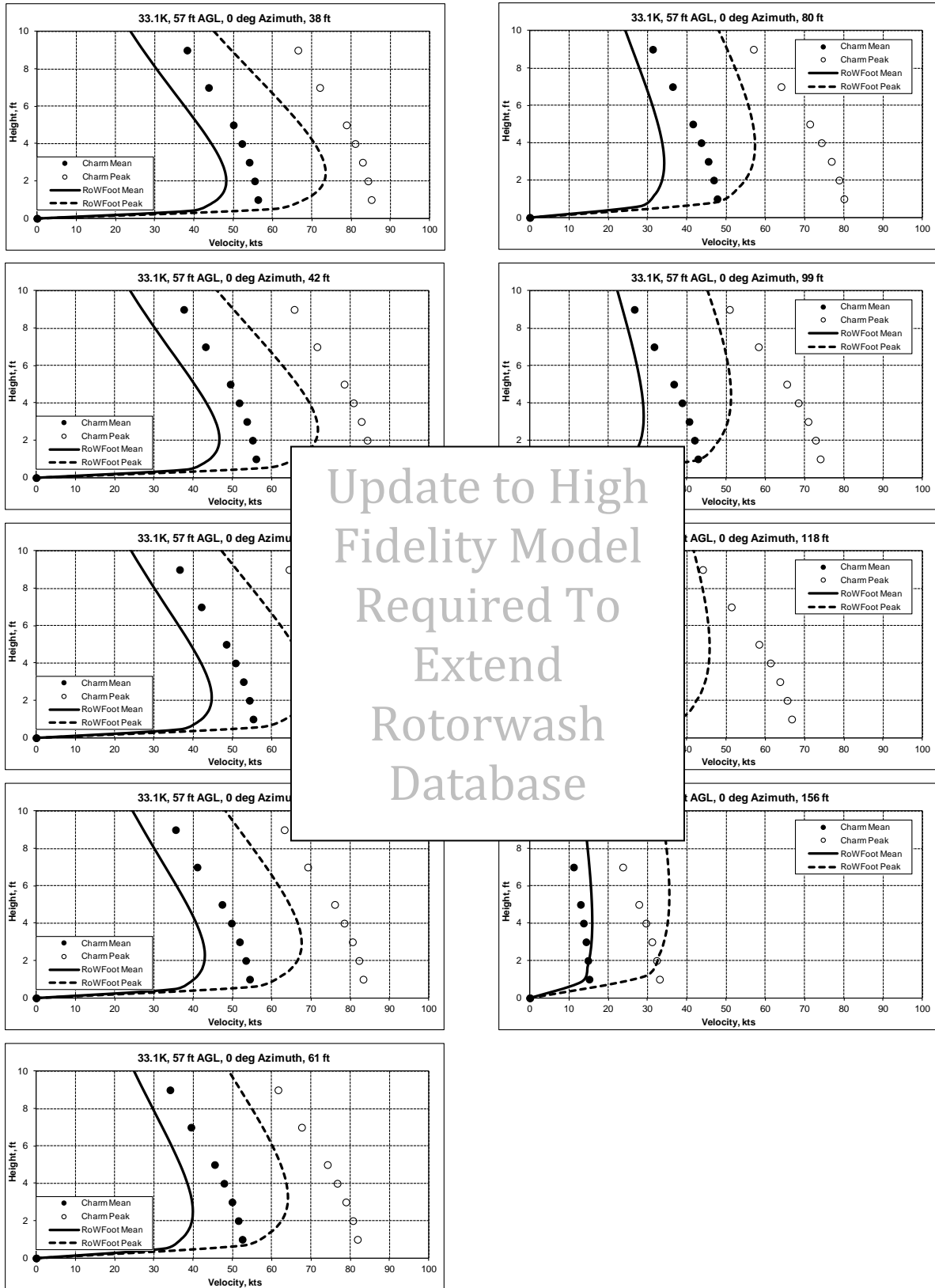


Figure K-77 V-22 Correlation GW = 33,140 lb, AGL = 57 ft, Azimuth = 0 deg, Offset = 0

Update to High Fidelity Model Required To Extend Rotorwash Database

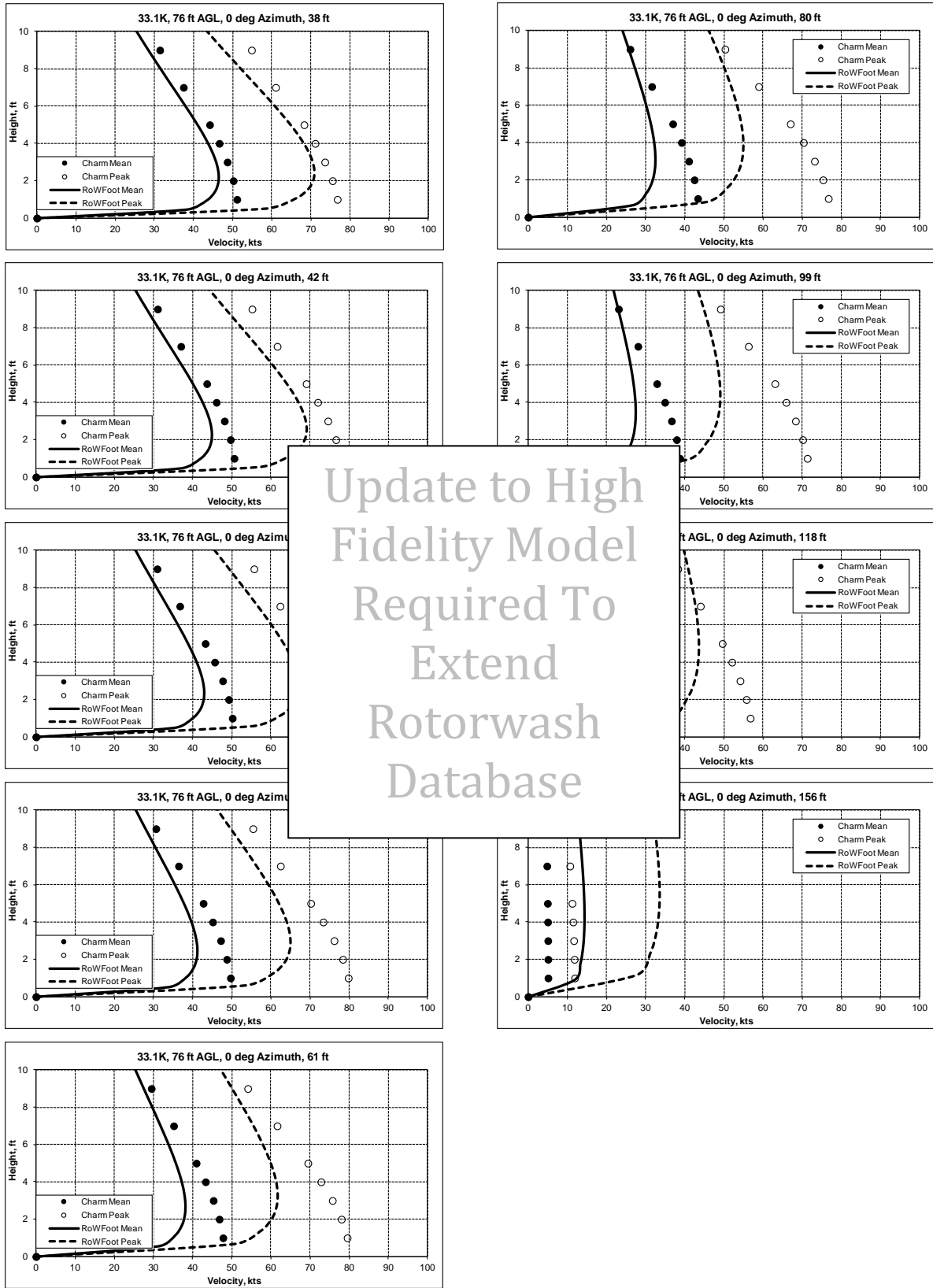


Figure K-78 V-22 Correlation GW = 33,140 lb, AGL = 76 ft, Azimuth = 0 deg, Offset = 0

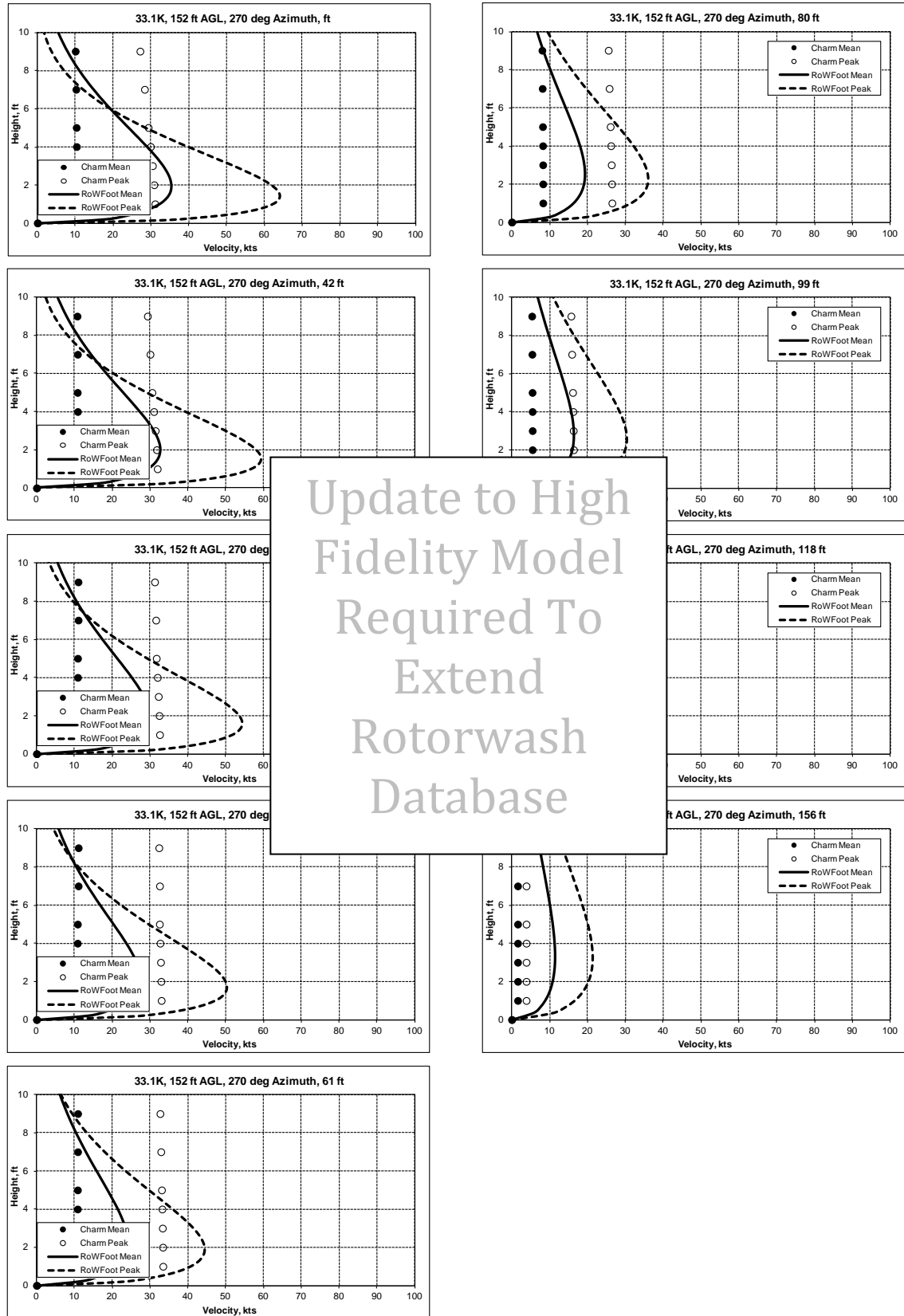


Figure K-79 V-22 Correlation GW = 33,140 lb, AGL = 152 ft,
Azimuth = 0 deg, Offset = 0

Update to High
Fidelity Model
Required To
Extend
Rotorwash
Database

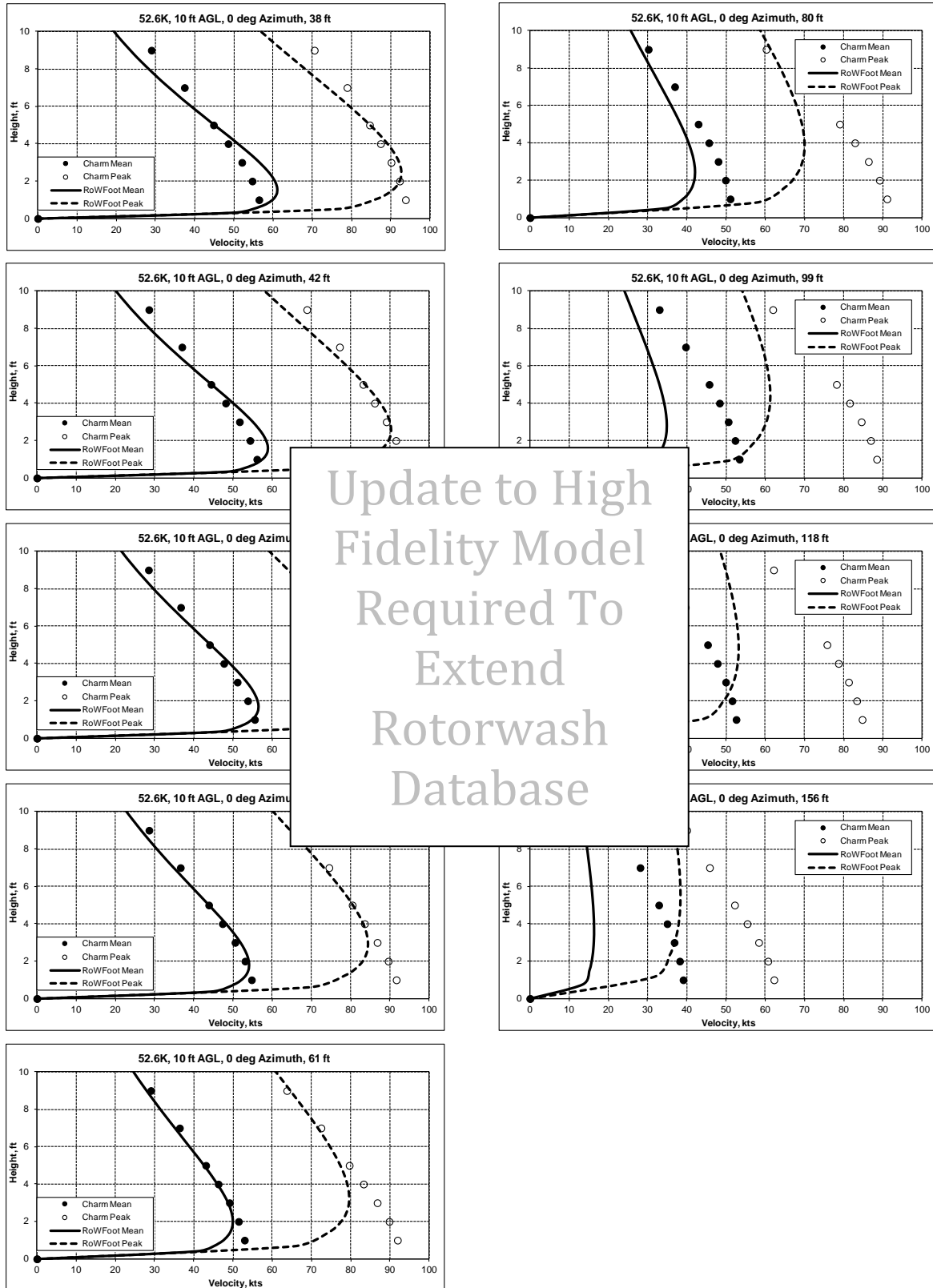
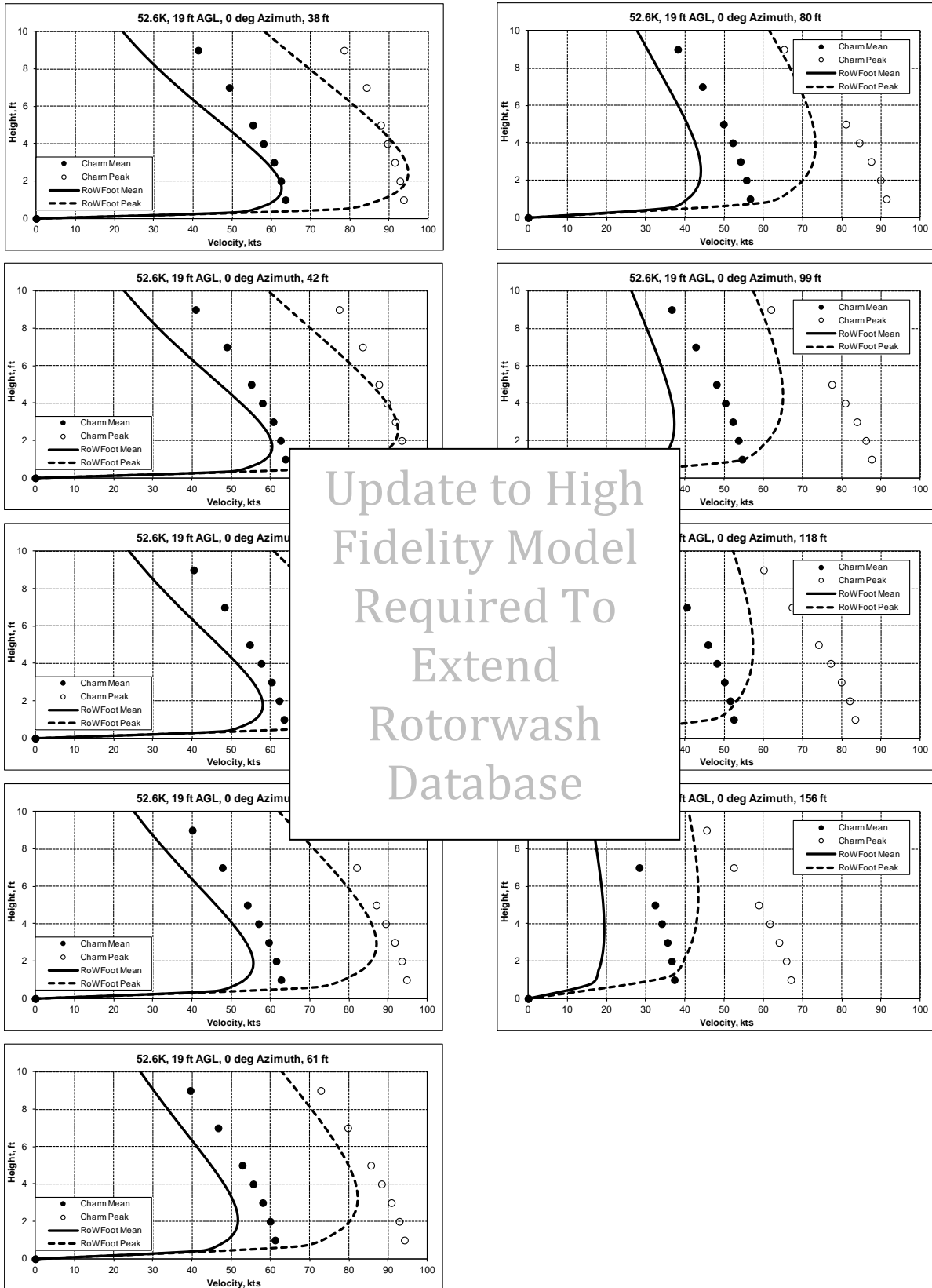


Figure K-80 V-22 Correlation GW = 52,600 lb, AGL = 10 ft,
Azimuth = 0 deg, Offset = 0



Update to High
Fidelity Model
Required To
Extend
Rotorwash
Database

Figure K-81 V-22 Correlation GW = 52,600 lb, AGL = 19 ft,
Azimuth = 0 deg, Offset = 0

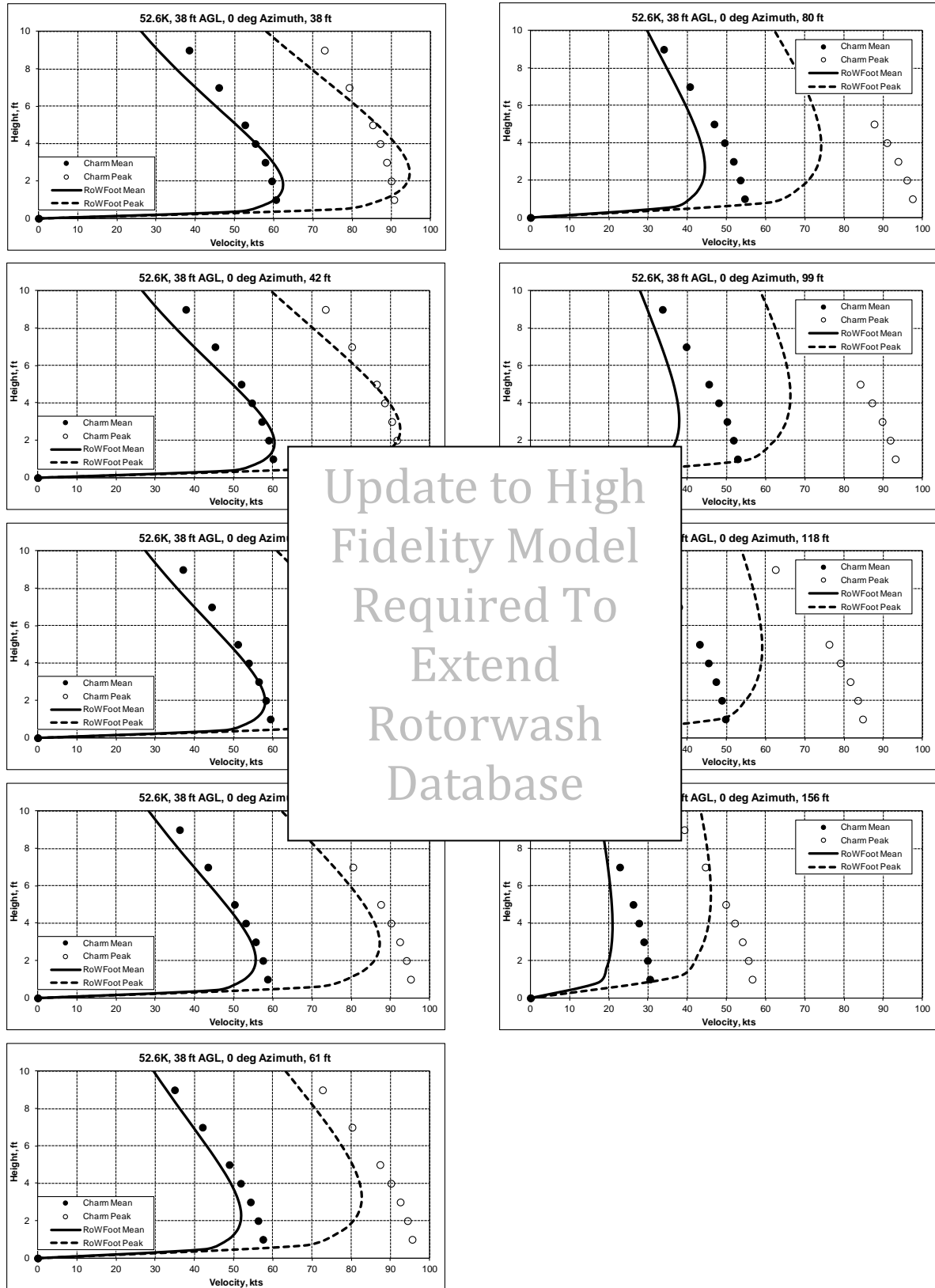


Figure K-82 V-22 Correlation GW = 52,600 lb, AGL = 38 ft, Azimuth = 0 deg, Offset = 0

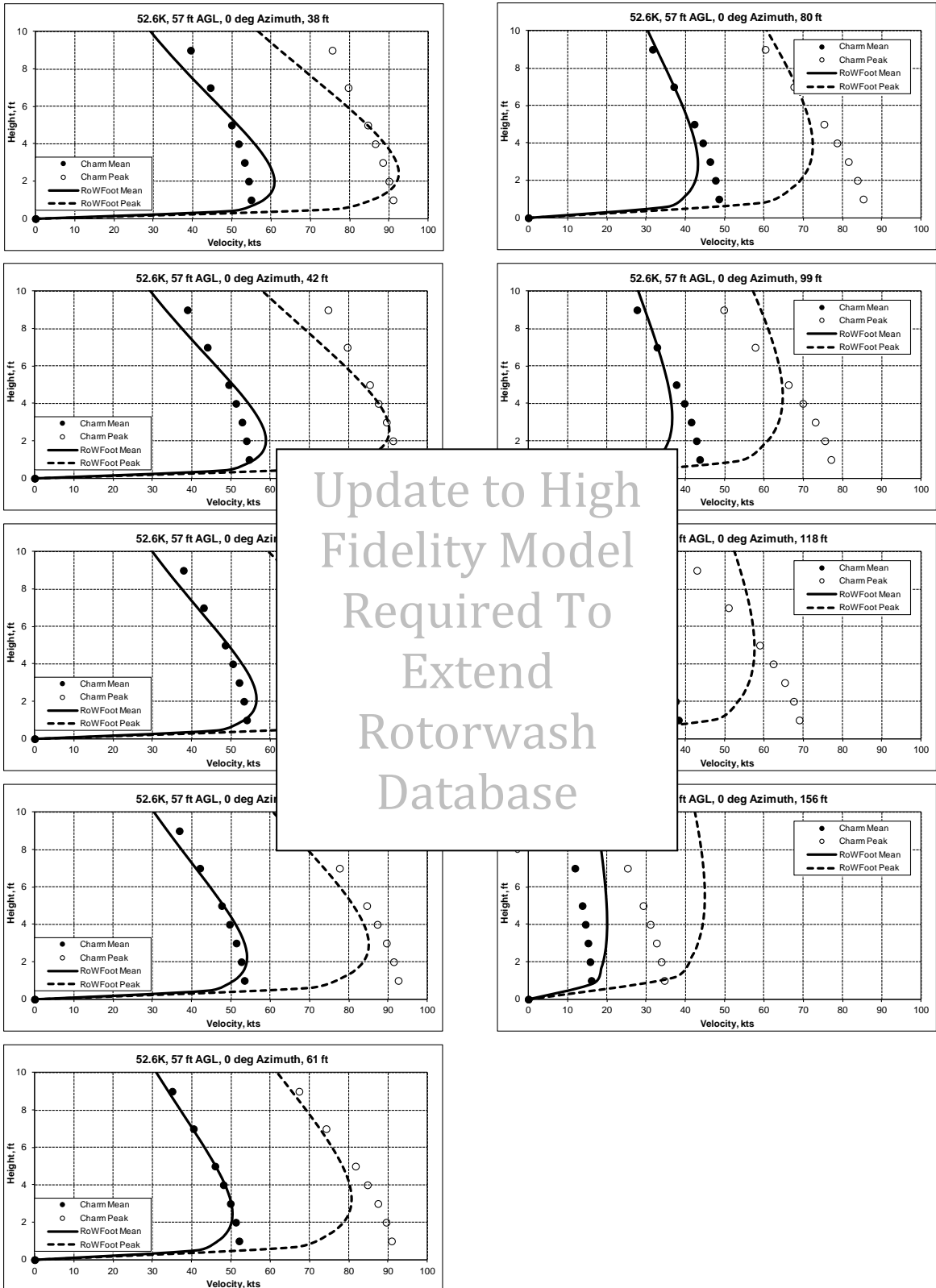


Figure K-83 V-22 Correlation GW = 52,600 lb, AGL = 57 ft, Azimuth = 0 deg, Offset = 0

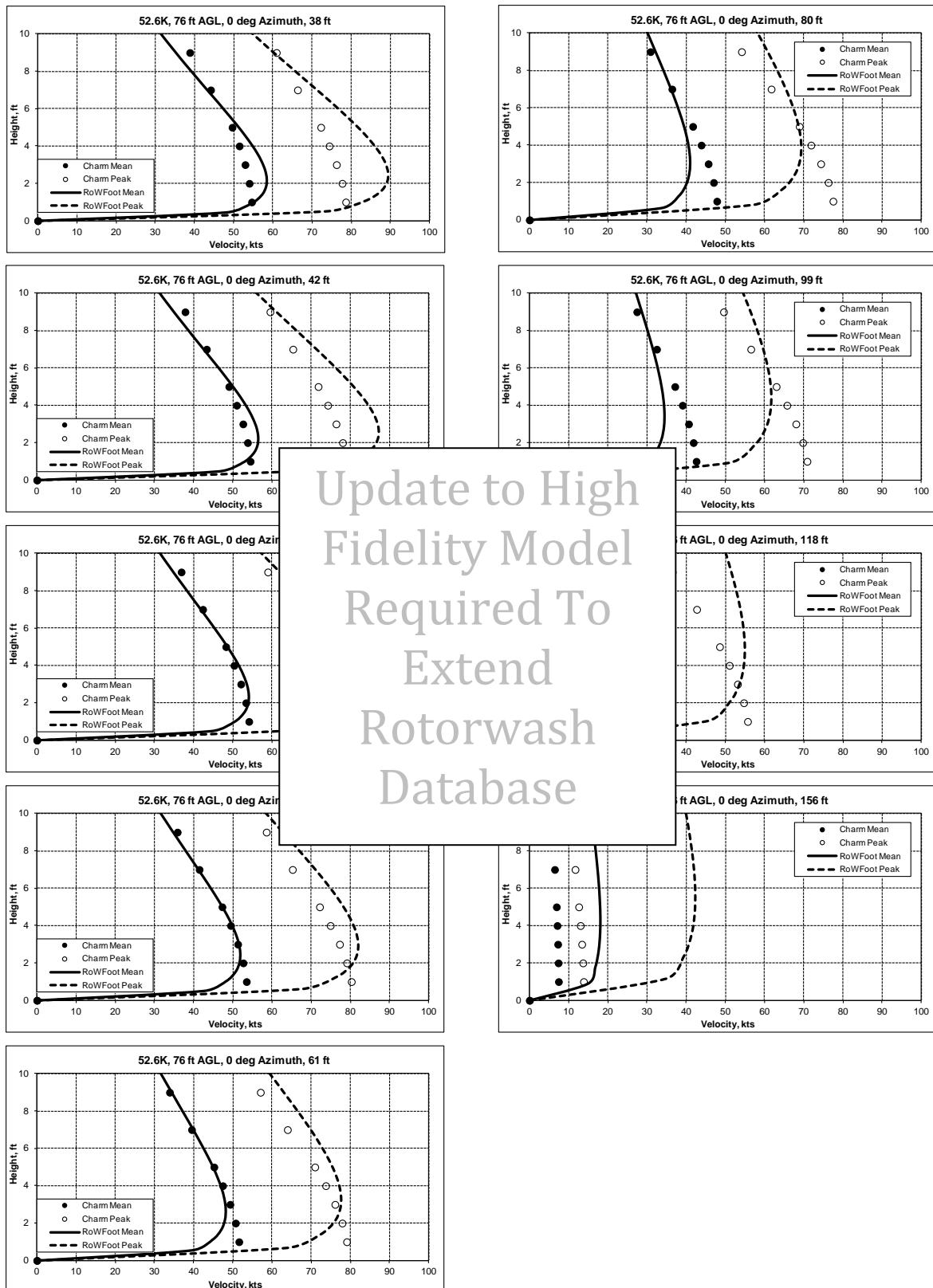


Figure K-84 V-22 Correlation GW = 52,600 lb, AGL = 76 ft,
Azimuth = 0 deg, Offset = 0

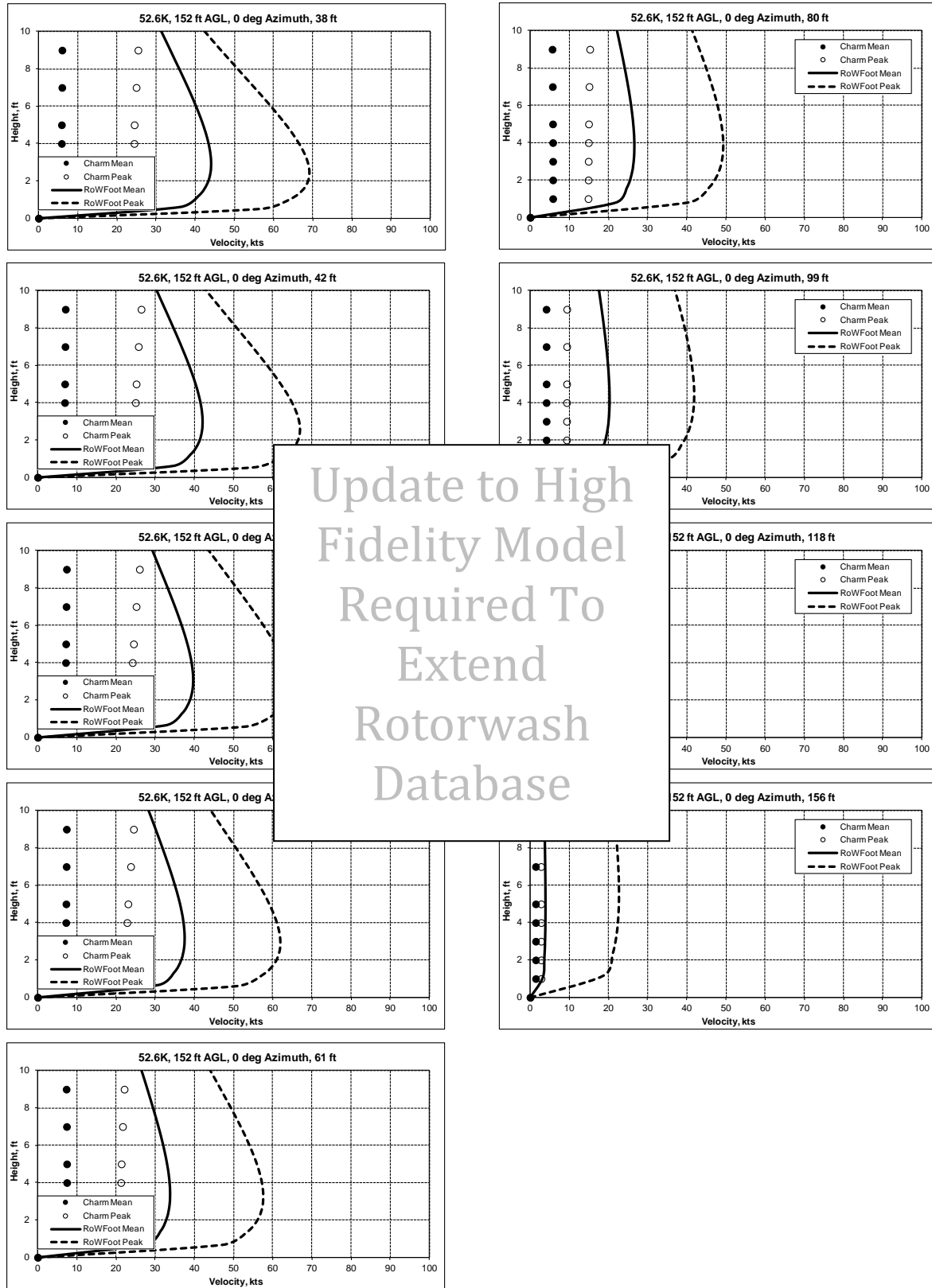


Figure K-85 V-22 Correlation GW = 52,600 lb, AGL = 152 ft, Azimuth = 0 deg, Offset = 0

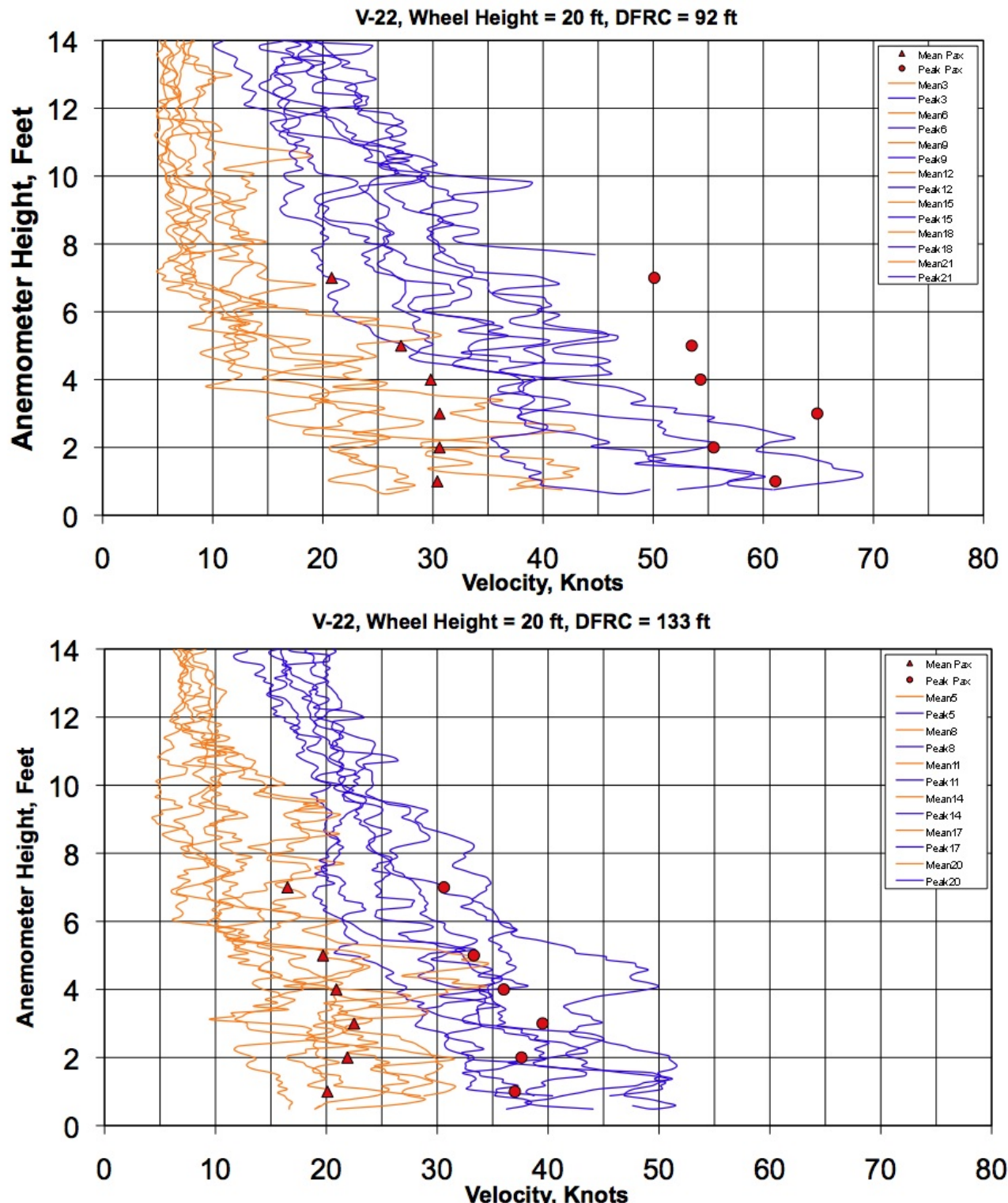


Figure K-86 V-22 Downwash Velocity Profiles during a 20-ft AGL Hover [unpublished data from Sam Ferguson (EMA) and Robb Lake (NAVAIR)]

Appendix L: Rotorwash High-Fidelity Modeling

Mike Cardamone, Mark Calvert, Marvin Moulton, and Mark Silva

Current high-quality flight test data are limited in range for the disk loading, hover height and location of velocity measurement locations. The intent was to extend this data set with a calibrated a high-fidelity (and computationally expensive) methodology to generate an expanded range of data outside of the flight test data set. This extended data set could then be utilized to correlate a conceptual level model with increased confidence when extrapolating outside of the range of measured flight test conditions. At present, however, the very complex and unsteady flow field of a rotorcraft in-ground effect has only recently begun yielding to CC-based treatment. In absence of adequate analytical tools, full-scale flow field surveys remain the most viable means of characterizing the outwash flow field. Results of calibration of the high-fidelity model to V-22 flight test data appear as graphs in [Appendix M](#). The extended data set for V-22 outwash velocity profiles appears as tables in [Appendix M](#). Although these results are not usable to provide confidence of conceptual level model extrapolation beyond the region bounded by flight test data, the results and methodology are retained to display lessons learned and facilitate further work in this effort.

The results presented in this appendix employed the Comprehensive Hierarchical Aeromechanics Rotorcraft Model (CHARM) version 3.0 software from Continuum Dynamics, Incorporated (Reference L-1) to extend the available range of tilt rotor outwash data. These data were used to verify conceptual level modeling at a wider range of aircraft disk loading and altitude than was available from flight test data. The CHARM results were also used to establish transition characteristics in the outwash going from the interaction plane to radial conditions. The specific analysis determined the outwash velocity profiles for given gross weights at various hover heights, azimuth locations, radial distances, and height above ground.

CHARM is a software tool typically used to determine rotor performance, aerodynamic loading, wake geometry, blade dynamics, blade deformation and body surface pressures for rotorcraft in hover, forward flight, axial flight, and maneuvering flight. It can model rotor craft with multiple rotors operating at different rotational speeds. CHARM calculates wake induced velocities using a full-span, Constant Vorticity Contour (CVC) free wake constructed from Basic Curved Vortex Elements. The free wake and surface panel calculations may be accelerated using the Hierarchical Fast Vortex (HFV) and Fast Panel methods. Near-real-time and real-time operations can be achieved with moderate fidelity using a Reduced Order Hierarchical Fast Vortex and Fast Panel methods. A vortex lattice method and 2-D airfoil tables are used to determine blade forces and moments. Hub loads and rotor blade deflection are calculated using linear finite element analysis. Smooth convergence of the rotor wake for low advance ratios in hover can be obtained through use of a Generalized Periodic Relaxation (GPR) algorithm. A more detailed description of the theoretical underpinnings of CHARM may be found in Reference L-2.

Though CHARM is typically used to calculate rotor performance and near-body rotor wake/fuselage interference (Reference L-3), the underlying algorithms have been used to model rotorcraft-induced brownout (Reference L-4).

The fuselage was not modeled as the inclusion of the fuselage significantly increased computation time (10-12 hours per case), and the resulting velocity profiles did not significantly differ (+/- 3 knots) from an analysis without a fuselage. The sample-point grid used for these calculations represented a vertical cylindrical grid with the longitudinal axis located at the midpoint between the two rotors. The bottom of the cylinder was placed at a height above ground of 1 foot and the top of the cylinder was placed at a height above ground of 12 feet.

All CHARM runs were run in a transient mode with 200 time-marching revolutions. CHARM's standard calculation procedure was used and a simple inflow model used for the initial wake induced velocity on the blade and wake geometry (References L-1 and L-5). The Hierarchical Fast Vortex Method (HFV) was used to increase accuracy, with a resulting increase in run time. The Fast Vortex Technology (FVT) was used for wake-on-wake calculations, wake-on blade calculations, and wake-on scan grid calculations. A free wake calculation was performed with wake on wake induced velocities included. All induced velocities were included for calculating wake geometry.

CHARM output velocities in three component form and nondimensional pressure coefficients for the sample point grid in ASCII text files. The output files were post-processed using a FORTRAN code. Data reduction within the FORTRAN code included coordinate transformations and statistical analysis to extract the minimum, mean, and maximum outwash velocities and forces.

References

- L-1. Wachspress, D.A.; Quackenbush, T.R.; and Boschitsch, A.H., "CHARM Version 3.0 User's Manual (Comprehensive Hierarchical Aeromechanics Rotorcraft Model)," CDI-TN-05-11, Continuum Dynamics, Inc., Ewing, NJ, March 2007.
- L-2. Wachspress, D.A.; Quackenbush, T.R.; and Boschitsch, A.H., "First-Principles Free-Vortex Wake Analysis for Helicopters and Tiltrotors," Proceedings of the American Helicopter Society's 59th Annual Forum, Phoenix, AZ, May 6-8, 2003.
- L-3. Wachspress, D.A.; Quackenbush, T.R.; and Boschitsch, A.H., "Rotorcraft Interactional Aerodynamics with Fast Vortex/Fast Panel Methods," Proceedings of the American Helicopter Society's 56th Annual Forum, Virginia Beach, VA, May 2-4, 2000.
- L-4. Wachspress, D.A.; Whitehouse, G.R.; Keller, J.D.; Yu, K.; Gilmore, P.; Dorsett, M.; and McClure, K., "A High Fidelity Brownout Model for Real-Time Flight Simulations and Trainers," Proceedings of the American Helicopter Society's 65th Annual Forum, Grapevine, TX, May 27-29, 2009.
- L-5. Quackenbush, T.R.; Boschitsch, A.H.; Wachspress, D.A.; and Chua, K., "Rotor Design Optimization Using a Free Wake Analysis," NASA-CR-177612, April 1993.

Appendix M: Rotorwash High-Fidelity Tool Correlation and Extension to Test Data

Mike Cardamone, Mark Calvert, Marvin Moulton, John Preston, and Mark Silva

This appendix contains the results of efforts to extend the rotorwash data set, as described in [Appendix L](#). Unfortunately, review of the results for symmetry and engineering trends show discrepancies that do not allow extension of the flight test data in this manner. Further work is suggested to update the previous or conduct new high-fidelity modeling using lessons learned and apply the results to the conceptual level model as previously described and originally intended.

Tables and figures within this appendix show the results of calibration of the high-fidelity CHARM vortex model described in [Appendix L](#) to V-22 flight test data (Reference M-1) and extension of the V-22 outwash data set using this calibrated model. For correlation to the configuration level modeling, the results in this appendix utilize aircraft symmetry along the aircraft centerline as well as fore and aft conditions. The high-fidelity model results contain both mean and peak outwash flow conditions. The peak outwash is calculated using the mean plus two times the velocity deviation. Input files associated with the [Appendix L](#) high-fidelity model, with resultant calibration and extension of the V-22 outwash data results, are documented as Figure M-1. The files depicted are the run characteristics and rotor wake input files. The blade geometry and 2-D airfoil section data input files contain propriety data and are not shown within this appendix.

V-22 flight test data (Reference M-1) was collected at distances from 19 to 156 ft from aircraft center both fore (0-degrees azimuth) and aft (180-degrees azimuth). Data were collected from negative to positive 20 ft of the aircraft centerline. Using symmetry, the data collection points for the 0/180 azimuth conditions are displayed as square data points in Figure M-1. Flight test data were also collected for a range of off centerline azimuth angles. Using symmetry, the data can be displayed with 30-, 45-, 60-, and 90-degree azimuth locations relative to the aircraft centerline at distances from 38 to 156 ft. This representation is shown as diamond data points within Figure M-2.

In each case, velocity profile test data were measured at 1-, 2-, 3-, 4-, 5-, and 7-foot heights above the ground. Most the flight test data was taken at a 20 ft landing gear height Above Ground Level (AGL) with a limited amount of data at 60 and 100 ft AGL. Table M-1 shows the full range of flight test data collected. Both mean and peak velocity conditions were captured and reported in Reference M-1.

For the conceptual level model correlation to the flight test data and high-fidelity model extension of the data, the 30-, 45-, 60-, and 90-degree azimuth data points must be expressed in terms of rotor center as opposed to aircraft center. Figure M-3 shows the data points for 30- to 90-degree azimuth angles in Figure M-2 with respect to rotor center.

```

V22_HIGE_transient.inp: V-22 Hover In-Ground Effect, Transient Soln
NROTOR
 2
PATHNAME
/home/cardamonemj/V-22/Cases/NOFUSELAGE/20ft_HIGE
INPUT FILENAMES Rotor 1
1rw.inp
bg.inp
bd.inp
air.inp
none
INPUT FILENAMES Rotor 2
2rw.inp
bg.inp
bd.inp
air.inp
none
SSPD      RHO ! SL/STD
1116.45   0.0023769
IGROUND HEIGHT ! BLAYER ! image method (HAGL specified in rw.inp)
 1       0.0    0.5
INFLOW    ! solution performed in shaft axes
 0
ADV      ALPHAS
 0.0     0.0
NPSI    NREV    CONVG1    CONVG2    CONVG3    MREV ! transient soln.
 24      5       0.0001   -1.      -1.      200
MELLOT  IPILOT
 1       0
IRST    IFREE  IGRP ! std. calculation procedure
 0       0       0
IWOUT   NRS   (ROUT(I),I=1,NRS)
 4       8       0.3    0.4    0.5    0.6    0.7    0.8    0.9    0.95
NPRINT  IBLPLT  (IFLPLT(I),I=1,4)
 0       0       3       3       3       3
IDEBUG
 0
ISCAN ! Generate Velocity Scan Grid Output
 1
ISTRSS (Stress calculation flag)
 0
IFV    IQUIK1
 2       1
IFVFW  IFVBL  IFVSU  IFVSC  IFVLS
 1       1       1       1
ISURF
 0
ISHIP
 0
IRECON NOISE
 0       0
NLS
 0

```

Run Characteristics Input File

```

V22_HIGE_R2rw_icoll0.inp: V-22 Left Rotor/Wake Input File for HIGE
NBLADE OMEGA ! 412 RPM, 103.8% Nr
 3   43.145
IROTAT XROTOR(3) XTILT(3) ITILT 1 CCW, Z=-(20.825+HAGL), 90 NAC
 -1   0. -23.288 -39.300  0.0  0.0  0.0
ICOLL COLLAD CT ! fixed coll; T=GW/(1-DL/T)=45000/(1-0.0931)=49620 lb
 0   53.89   0.013570
ITRIM A1W  B1W  AIS  B1S ! fixed cyclic
 0   0.0   0.0   0.0   0.0
NOWAKE ICNVCT NWAKES NPWAKE IFPAR MBCVE
 0       0       1       2       1       0
KSCHMKE KPC
 0       0
NCUT  AOVLAP ISKEW IUNS
 1   -1   1   0
NZONE (NVORT(I), I=1,NZONE) BUFFER KGMCHG
 3   24   6   2   2.   0
ICORE AKINEM A1 PCOREM CRMON ! vortex diffusion for outwash
 1   0.0   0.01   0.0   0.0
(NPTFW(I), I=1,NZONE) ! NREVS=2,2,12 for NPSI=24
 48   48   288
CORLIM Zone 1 Min core radii
24*0.01
CORLIM Zone 1 Max core radii
24*1.0
CORLIM Zone 2 Min core radii
6*0.01
CORLIM Zone 2 Max core radii
6*1.0
CORLIM Zone 3 Min core radii
2*0.1
CORLIM Zone 3 Max core radii
2*0.1
CUTLIM Zone 1 Min cutoff distance
24*0.01
CUTLIM Zone 1 Max cutoff distance
24*1.0
CUTLIM Zone 2 Min cutoff distance
6*0.01
CUTLIM Zone 2 Max cutoff distance
6*1.0
CUTLIM Zone 3 Min cutoff distance
2*0.1
CUTLIM Zone 3 Max cutoff distance
2*0.1
IDYNN
 1
SRAD  SHGT
 0.0   0.0
NHHII (Higher harmonic cyclic pitch input flag)
 0

```

Left Rotor/ Wake Input File

```

V22_HIGE_Rlw_icoll0.inp: V-22 Right Rotor/Wake Input File for HIGE
NBLADE OMEGA ! 412 RPM, 103.8% Nr
 3   43.145
IROTAT XROTOR(3) XTILT(3) ITILT 1 CCW, Z=-(20.825+HAGL), 90 NAC
 1   0. 23.288 -39.300  0.0  0.0  0.0
ICOLL COLLAD CT ! fixed coll; T=GW/(1-DL/T)=45000/(1-0.0931)=49620 lb
 0   53.89   0.013570
ITRIM A1W  B1W  AIS  B1S ! fixed cyclic
 0   0.0   0.0   0.0   0.0
NOWAKE ICNVCT NWAKES NPWAKE IFPAR MBCVE
 0       0       1       2       1       0
KSCHMKE KPC
 0       0
NCUT  AOVLAP ISKEW IUNS
 1   -1   1   0
NZONE (NVORT(I), I=1,NZONE) BUFFER KGMCHG
 3   24   6   2   2.   0
ICORE AKINEM A1 PCOREM CRMON ! vortex diffusion for outwash
 1   0.0   0.01   0.0   0.0
(NPTFW(I), I=1,NZONE) ! NREVS=2,2,12 for NPSI=24
 48   48   288
CORLIM Zone 1 Min core radii
24*0.01
CORLIM Zone 1 Max core radii
24*1.0
CORLIM Zone 2 Min core radii
6*0.01
CORLIM Zone 2 Max core radii
6*1.0
CORLIM Zone 3 Min core radii
2*0.1
CORLIM Zone 3 Max core radii
2*0.1
CUTLIM Zone 1 Min cutoff distance
24*0.01
CUTLIM Zone 1 Max cutoff distance
24*1.0
CUTLIM Zone 2 Min cutoff distance
6*0.01
CUTLIM Zone 2 Max cutoff distance
6*1.0
CUTLIM Zone 3 Min cutoff distance
2*0.1
CUTLIM Zone 3 Max cutoff distance
2*0.1
IDYNN
 1
SRAD  SHGT
 0.0   0.0
NHHII (Higher harmonic cyclic pitch input flag)
 0

```

Right Rotor/ Wake Input File

Figure M-1 CHARM Vortex Model Input Files

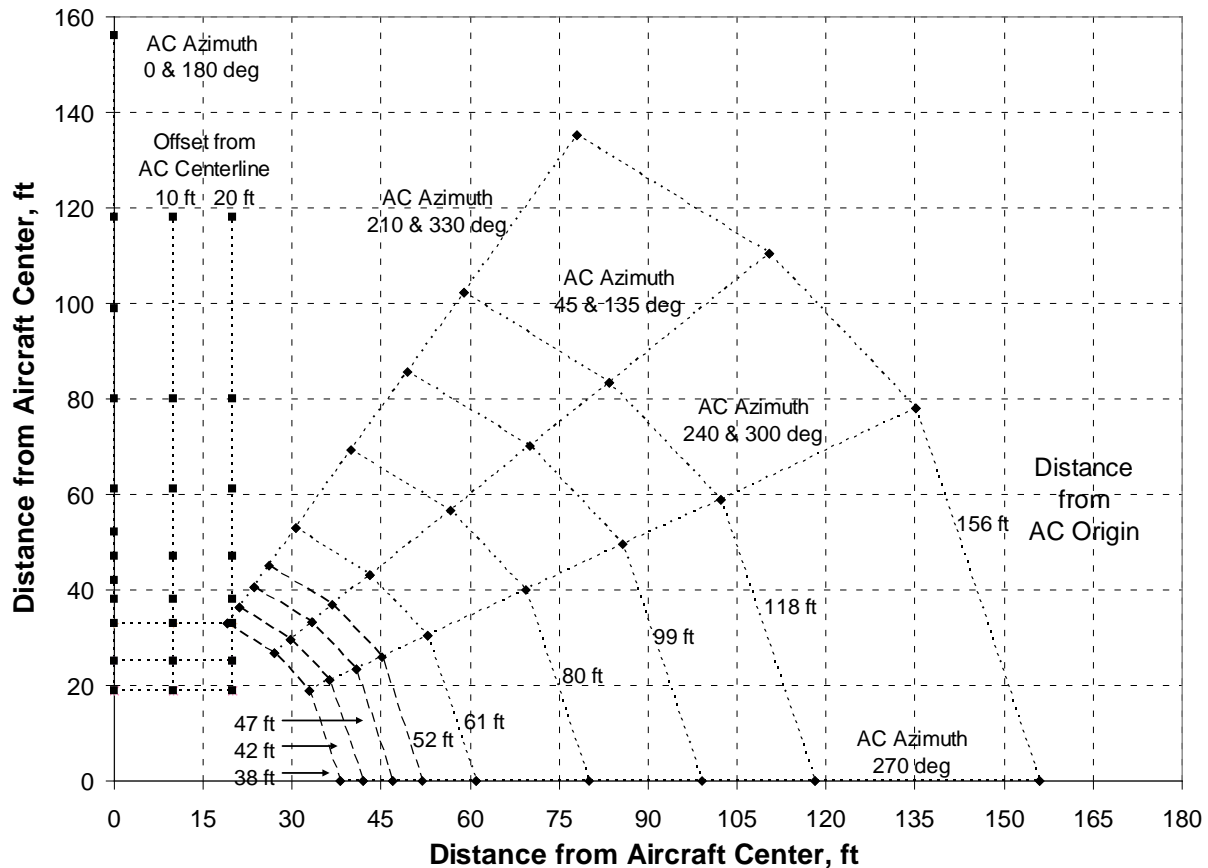


Figure M-2 V-22 Flight Test Data Locations (Symmetry)

Centerline	Offset, ft	Distance from Rotor Center, ft								
Height Above Ground Level (AGL), ft Azimuth, deg	20	19	25	33	38	47	61	80	118	
	180	10	19	25	33	38	47	61	80	118
	0	19	25	33	38	42	47	52	61	80
	-10	19	25	33	38	47	61	80	99	118
Wheel Height Above Ground Level, ft Azimuth, deg	20	19	25	33	38	47	61	80	118	
	10	19	25	33	38	47	61	80	118	156
	0	19	25	33	38	42	47	52	61	80
	-10	19	25	33	38	47	61	80	99	118
Azimuth = 0 deg, AGL, ft	60	0	19	25	33	38	47	61	80	118
	100	0	19	25	33	38	47	61	80	118
Radial	Azimuth, Deg	Distance from Rotor Center, ft								
Wheel Height Above Ground Level, ft	210	38	42	47	52	61	80	99	118	
	240	38	42	47	52	61	80	99	118	
	270	38	42	47	52	61	80	99	118	156
	300	38	42	47	52	61	80	99	118	
	330	38	42	47	52	61	80	99	118	
	45	38	42	47	52	61	80	99	118	
	135	38	42	47	52	61	80	99	118	
Wheel Height Above Ground Level, ft	60	270	38	42	47	52	61	80	99	118
Wheel Height Above Ground Level, ft	100	270	38	42	47	52	61	80	99	118

Table M-1 V-22 Flight Test Data Points, wrt Aircraft Center

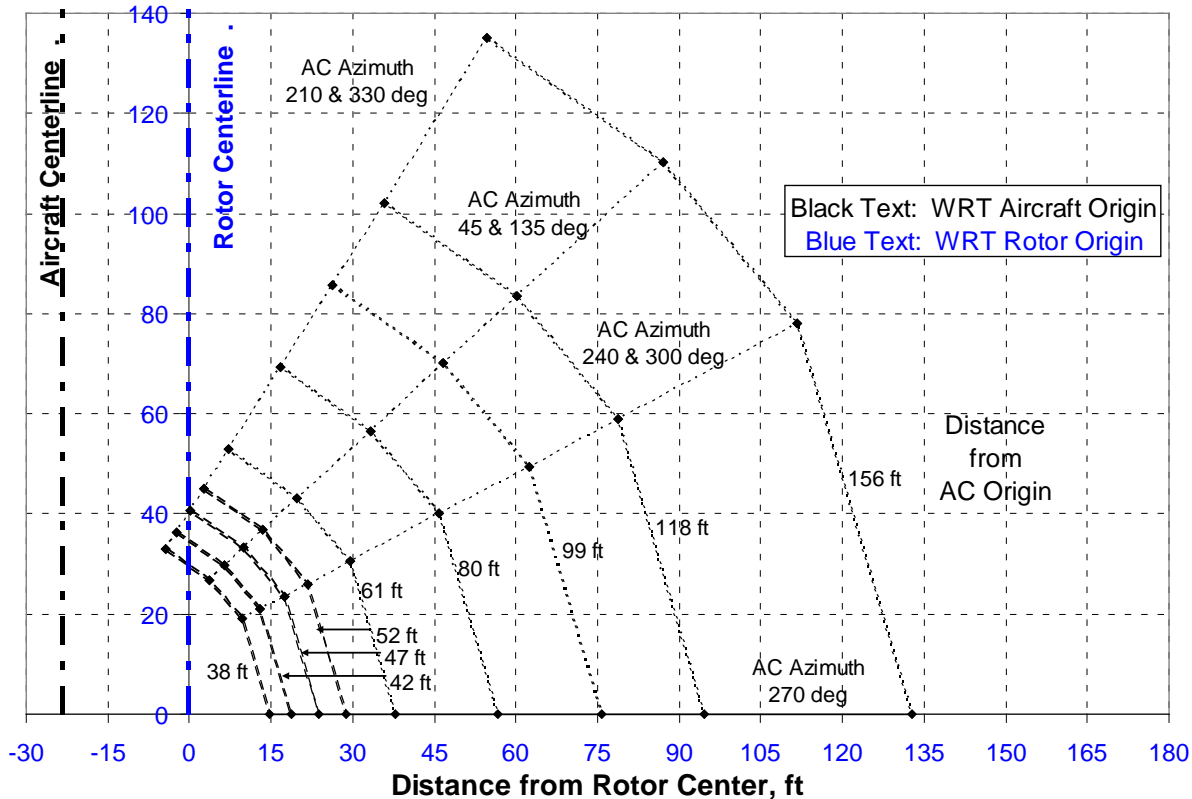


Figure M-3 V-22 Flight Test Data Locations wrt Rotor (Symmetry)

For a tilt rotor in zero ambient wind conditions, outwash data should be the same for equivalent port and starboard azimuth locations. Within the high-fidelity model, the results should be symmetric for azimuths of equal angle from the aircraft centerline. Rotor rotational direction and fuselage shape will have some effect on fore and aft symmetry, but these conditions should not affect the azimuth angle pairs in the port and starboard sides.

A review of Tables M-2 to M-13 shows inconsistencies with respect to symmetry between the 90- and 270-degree and 45- and 315-degree pairs. For within some of the tables the agreement is good. Others contain a close agreement for the mean velocity and large difference in magnitude for the equivalent peak velocity profile. An example of non-symmetry in the results is in Tables M-3A and M-3B. Within this table, the 270-deg azimuth consistently shows higher velocities than for the 90-deg azimuth. These differences are magnified within the peak velocity profile data.

Discrepancies within the symmetry indicate an underlying issue within the modeling, perhaps a convergence issue. Thus, the previous high-fidelity model results should be used with caution and not treated as an absolute.

Correlation of the CHARM vortex model in [Appendix L](#) to V-22 test data from Reference M-1 appears in Figures M-4 to M-14. These figures correspond to flight conditions of:

**Figure M-4:	GW = 45,935 lb,	AGL = 20 ft,	Azimuth = 270 deg	
**Figure M-5:	GW = 44,539 lb,	AGL = 60 ft,	Azimuth = 270 deg	
**Figure M-6:	GW = 43,814 lb,	AGL = 100 ft,	Azimuth = 270 deg	
**Figure M-7:	GW = 45,935 lb,	AGL = 20 ft,	Azimuth = 240 & 300 deg	
**Figure M-8:	GW = 45,935 lb,	AGL = 20 ft,	Azimuth = 45 & 135 deg	
**Figure M-9:	GW = 45,935 lb,	AGL = 20 ft,	Azimuth = 210 & 330 deg	
**Figure M-10:	GW = 45,935 lb,	AGL = 20 ft,	Azimuth = 0 & 180 deg,	Offset = 0 ft
**Figure M-11:	GW = 45,935 lb,	AGL = 20 ft,	Azimuth = 0 & 180 deg,	Offset = ± 10 ft
**Figure M-12:	GW = 45,935 lb,	AGL = 20 ft,	Azimuth = 0 & 180 deg,	Offset = ± 20 ft
**Figure M-13:	GW = 44,539 lb,	AGL = 60 ft,	Azimuth = 180 deg,	Offset = 0 ft
**Figure M-14:	GW = 43,814 lb,	AGL = 100 ft,	Azimuth = 180 deg,	Offset = 0 ft

**CHARM correlation figures contain limited distribution data. The figures appear in a limited distribution annex to this report.

At the time of publication, the test data for the V-22 are not publicly releasable. Correlation figures for CHARM to flight test data for this aircraft are contained in a limited distribution annex to this report.

The CHARM vortex model uses an artificially inserted zero magnitude at zero height in the velocity profile. Since the high-fidelity model does not contain the growth of the boundary layer due to complexity, the predicted shape of the velocity profile retains the sharp point at the 1-foot height for the peak magnitude.

For radial outwash in Figures M-4 and M-7 to M-9, in general the CHARM vortex model correlation was best for data cases at where the radial outwash forms a wall jet and before the boundary layer grows significantly. This corresponds to cases of 62 to 118 feet from the aircraft center. Inside of this region, the flow is transitioning from vertical (downwash) to horizontal (outwash) and the height of the peak velocity may be higher than 1-foot above the ground. Outside of this region, the test data show the velocity profile becoming more blunted and height of the maximum velocity magnitude rising vertically.

The centerline outwash in Figures M-10 to M-12 follows a similar trend to the radial outwash with the cases of best correlation being from 19 to 99 feet from aircraft center. In general, the correlation is also better for the interaction axis as opposed to where the case is offset, as in Figures M-11 and M-12.

Figures M-4 to M-6 (radial outwash) and Figures M-12 to M-14 (centerline outwash) show the model correlation to test data at 20, 60 and 100 feet aircraft height above ground. An increase in aircraft height above ground will change the location of where the wall jet occurs as well as increase the height of the boundary layer in the lower region of the velocity profile.

After calibration to flight test data, the high-fidelity model was used to extend the V-22 data set available for conceptual-based model correlation. The extended data set included conditions at approximately \pm 50% of the aircraft weight for flight test in Reference M-1 and at heights above ground non-dimensionalized by rotor radius of approximately 0.5, 1.0, 2.0, 3.0, 4.0, and 8.0. These conditions include azimuth angles of 0, 45, 90, 135, 180, 210, 240, 270, 300, and 330 degrees. These results are contained in Tables M-2 to M-13.

Table M-2A&B:	GW = 33,140 lb,	AGL = 10 ft
Table M-3A&B:	GW = 33,140 lb,	AGL = 19 ft
Table M-4A&B:	GW = 33,140 lb,	AGL = 38 ft
Table M-5A&B:	GW = 33,140 lb,	AGL = 57 ft
Table M-6A&B:	GW = 33,140 lb,	AGL = 76 ft
Table M-7A&B:	GW = 33,140 lb,	AGL = 152 ft
Table M-8A&B:	GW = 52,600 lb,	AGL = 10 ft
Table M-9A&B:	GW = 52,600 lb,	AGL = 19 ft
Table M-10A&B:	GW = 52,600 lb,	AGL = 38 ft
Table M-11A&B:	GW = 52,600 lb,	AGL = 57 ft
Table M-12A&B:	GW = 52,600 lb,	AGL = 76 ft
Table M-13A&B:	GW = 52,600 lb,	AGL = 152 ft

Review of Tables M-2 to M-13, in respect to Figures M-4 to M-14, show suspect trends in the data generated. From momentum theory, the maximum velocity in the rotorwash is two times the induced velocity, which is related to the square root of the aircraft gross weight. As the aircraft gross weight increases, the magnitude of the outwash should increase proportionally. As noted previously, the high-fidelity model was calibrated to the available flight test data that are for a very limited range of aircraft weight. Table M-14 compares the maximum magnitude within velocity profiles from the CHARM vortex model results at 61 feet from the aircraft center. Comparisons are made between data in previously presented tables and figures for cases of different weights with similar height above ground. As seen in Table M-14, the CHARM vortex modeling results do not follow a consistent or expected trend with gross weight for changes in the magnitude of the velocity profile maximum.

Data trends for aircraft height above ground are also suspect in the high-fidelity model results. Tables M-15 and M-16 show the maximum outwash velocity for increasing values of height above ground at a constant gross weight. At low heights, the velocity profile maximum will be influenced by ground effect. At heights at or above one rotor diameter (\sim 38 ft) the maximum velocity in the mean and peak profile is expected to gradually change in a consistent direction due to decay in the downwash and increasing height of the velocity profile of the outwash. The tables show somewhat constant maximum velocity up to 76-foot height with a steep slope at larger heights. The predicted values at 152-ft AGL appear low based on engineering judgment and should be verified with test data when possible.

In summary, discrepancies with the CHARM vortex model results symmetry, gross weight to maximum velocity trend, and height above ground to maximum outwash velocity exist. These trends indicate that the high-fidelity modeling results contained in this appendix are

of limited utility in extension of the rotorwash flight test database. In lieu of obtaining flight test data to extend the rotorwash database or an update to the existing high-fidelity modeling, engineering judgment should be used for how much emphasis to place on the validity of the high-fidelity modeling results contained within this appendix.

References

- M-1. Lake, R. E., and Clark, W. J., "V-22 Rotor Downwash Survey," NAWCADPAX-98-88-RTR, July 1998.

Figure Appears in Distribution B Report Annex
V-22 Correlation: GW = 45,935 lb, AGL = 20 ft, Azimuth = 270 deg
Figure M-4

Figure Appears in Distribution B Report Annex
V-22 Correlation: GW = 44,539 lb, AGL = 60 ft, Azimuth = 270 deg
Figure M-5

Figure Appears in Distribution B Report Annex
V-22 Correlation: GW = 43,814 lb, AGL = 100 ft, Azimuth = 270 deg
Figure M-6

Figure Appears in Distribution B Report Annex
V-22 Correlation: GW = 45,935 lb, AGL = 20 ft, Azimuth = 240 & 300 deg
Figure M-7

Figure Appears in Distribution B Report Annex
V-22 Correlation: GW = 45,935 lb, AGL = 20 ft, Azimuth = 45 & 135 deg
Figure M-8

Figure Appears in Distribution B Report Annex
V-22 Correlation: GW = 45,935 lb, AGL = 20 ft, Azimuth = 210 & 330 deg
Figure M-9

Figure Appears in Distribution B Report Annex
V-22 Correlation: GW = 45,935 lb, AGL = 20 ft, Azimuth = 0 & 180 deg, Offset = 0 ft
Figure M-10

Figure Appears in Distribution B Report Annex
V-22 Correlation: GW = 45,935 lb, AGL = 20 ft, Azimuth = 0 & 180 deg, Offset = \pm 10 ft
Figure M-11

Figure Appears in Distribution B Report Annex
V-22 Correlation: GW = 45,935 lb, AGL = 20 ft, Azimuth = 0 & 180 deg, Offset = \pm 20 ft
Figure M-12

Figure Appears in Distribution B Report Annex
V-22 Correlation: GW = 44,539 lb, AGL = 60 ft, Azimuth = 180 deg, Offset = 0 ft
Figure M-13

Figure Appears in Distribution B Report Annex
V-22 Correlation: GW = 43,814 lb, AGL = 100 ft, Azimuth = 180 deg, Offset = 0 ft
Figure M-14

GW, lb	33140	AGL, ft	10													
Azimuth, deg	0	38	42	47	52	61	80	99	118	156						
		Mean Peak kts kts														
0	0.0 0.0	0.0 0.0	0.0 0.0	0.0 0.0	0.0 0.0	0.0 0.0	0.0 0.0	0.0 0.0	0.0 0.0	0.0 0.0	0.0 0.0	0.0 0.0	0.0 0.0	0.0 0.0	0.0 0.0	
1	53.9 91.0	53.5 90.4	53.1 89.3	52.5 88.4	51.8 87.7	49.9 87.8	50.5 83.5	48.2 79.4	47.0 77.9	38.6 64.9						
2	52.3 89.5	51.9 88.7	51.4 87.4	50.7 86.3	50.1 85.5	48.4 85.7	49.2 81.7	47.0 79.0	45.2 75.5	37.8 63.6						
3	49.9 87.3	49.4 86.2	48.8 84.7	48.1 83.4	47.4 82.3	46.1 82.4	47.1 79.0	45.2 75.5	36.6 61.7							
4	46.6 84.3	46.0 83.1	45.4 81.3	44.8 79.8	44.2 78.4	43.3 78.3	44.5 75.5	42.8 72.5	34.9 59.3							
5	43.1 80.9	42.5 79.6	41.8 77.7	41.2 76.1	40.5 74.4	40.0 73.7	41.5 71.4	40.1 69.1	33.0 56.6							
7	36.3 74.0	35.6 72.4	34.8 70.2	33.9 68.2	33.1 65.8	33.1 63.6	34.8 62.3	34.1 61.6	28.6 50.7							
9	28.4 64.3	27.7 62.8	26.9 60.6	26.1 58.9	25.3 56.0	25.9 52.9	27.7 52.3	27.8 53.4	23.8 44.8							
12	19.7 53.3	18.8 51.6	18.1 49.7	17.5 47.8	16.6 43.5	17.4 39.8	18.8 39.9	19.7 41.8	17.2 36.7							
Azimuth, deg	45	38	42	47	52	61	80	99	118	156						
Dist wrt AC, ft		Mean Peak kts kts														
Height																
0	0.0 0.0	0.0 0.0	0.0 0.0	0.0 0.0	0.0 0.0	0.0 0.0	0.0 0.0	0.0 0.0	0.0 0.0	0.0 0.0	0.0 0.0	0.0 0.0	0.0 0.0	0.0 0.0	0.0 0.0	
1	54.6 88.1	56.5 89.7	56.8 90.5	55.5 91.0	51.4 88.9	49.1 86.1	40.2 80.2	36.0 83.7	33.9 78.5	27.2 59.8						
2	52.9 87.1	54.5 88.3	54.5 88.8	53.1 89.9	49.4 85.9	45.6 82.5	37.3 76.1	33.8 79.5	32.2 74.9	25.8 57.3						
3	50.4 85.8	51.4 86.5	51.0 86.4	49.4 85.9	45.6 82.5	37.3 76.1	33.8 79.5	32.2 74.9	25.8 57.3							
4	46.9 83.8	47.4 83.9	46.6 83.2	45.0 82.1	41.3 78.1	33.8 71.3	31.1 74.4	30.0 70.6	24.0 54.4							
5	43.0 81.5	43.1 80.8	41.9 79.5	40.3 77.9	36.7 73.2	30.0 66.1	28.2 69.0	27.5 66.1	21.9 51.1							
7	35.2 75.1	34.5 73.2	33.1 71.0	31.4 68.7	27.8 63.1	22.3 55.5	22.0 58.2	22.2 57.2	17.5 44.5							
9	26.8 65.7	25.9 63.2	24.5 60.1	22.9 57.6	19.5 52.5	15.2 44.8	16.2 48.0	17.1 48.8	13.2 38.0							
12	17.5 52.3	16.9 49.6	15.6 46.1	14.1 43.5	11.1 39.3	7.6 32.6	9.5 36.0	11.1 38.4	8.0 31.2							
Azimuth, deg	90	38	42	47	52	61	80	99	118	156						
Dist wrt AC, ft		Mean Peak kts kts														
Height																
0	0.0 0.0	0.0 0.0	0.0 0.0	0.0 0.0	0.0 0.0	0.0 0.0	0.0 0.0	0.0 0.0	0.0 0.0	0.0 0.0	0.0 0.0	0.0 0.0	0.0 0.0	0.0 0.0	0.0 0.0	
1	53.7 86.2	62.8 91.7	68.5 97.0	68.0 99.2	61.6 95.0	50.3 84.5	43.2 75.2	38.1 68.0	32.8 63.3							
2	53.3 85.6	62.0 90.9	66.8 96.1	65.6 97.7	58.6 92.7	47.5 81.2	40.9 72.1	36.2 65.2	31.5 61.6							
3	52.5 84.8	60.5 90.0	63.8 94.9	61.6 95.7	54.0 89.4	43.3 76.5	37.4 67.6	33.4 61.2	29.6 59.0							
4	51.3 83.9	58.1 89.2	59.4 93.5	56.0 93.0	48.3 85.5	38.2 71.2	33.3 62.7	30.1 56.7	27.1 56.0							
5	49.7 82.8	55.0 88.3	53.9 92.0	49.6 90.0	42.0 81.1	32.8 66.1	29.0 57.8	26.5 52.2	24.3 52.7							
7	44.8 79.9	46.4 86.1	41.2 86.9	36.1 81.9	29.8 71.5	23.0 57.6	21.0 49.1	19.9 44.3	18.7 46.2							
9	38.2 75.2	35.8 80.4	28.3 77.0	23.4 70.0	18.9 59.9	15.4 50.5	14.4 40.9	14.2 37.4	13.7 39.7							
12	27.4 65.2	21.7 66.3	14.3 57.9	10.8 50.7	9.2 46.3	8.9 42.8	8.0 31.6	8.5 30.1	8.0 31.2							
Azimuth, deg	135	38	42	47	52	61	80	99	118	156						
Dist wrt AC, ft		Mean Peak kts kts														
Height																
0	0.0 0.0	0.0 0.0	0.0 0.0	0.0 0.0	0.0 0.0	0.0 0.0	0.0 0.0	0.0 0.0	0.0 0.0	0.0 0.0	0.0 0.0	0.0 0.0	0.0 0.0	0.0 0.0	0.0 0.0	
1	54.4 83.3	54.8 83.5	53.5 82.9	51.2 82.0	46.9 79.3	41.5 72.3	35.4 66.3	32.7 60.0	25.7 50.4							
2	52.6 81.7	52.6 81.6	51.0 80.2	48.7 78.8	44.4 75.5	39.2 68.4	33.6 63.0	31.2 57.3	23.1 48.6							
3	49.5 79.6	49.1 79.1	47.3 76.5	44.8 74.3	40.6 70.1	35.8 62.8	31.0 58.0	29.0 53.2	22.7 45.8							
4	45.3 77.1	44.5 76.0	42.4 72.2	40.0 68.9	36.1 63.9	31.6 56.3	27.7 52.2	26.2 48.3	22.2 42.4							
5	40.5 74.3	39.4 72.5	37.1 67.7	34.8 63.4	31.2 57.6	27.1 49.6	24.1 46.2	23.2 43.1	20.7 38.7							
7	30.7 66.7	29.2 63.8	26.9 57.8	24.8 52.2	21.9 45.8	18.5 37.6	17.2 35.3	17.1 33.6	18.1 31.2							
9	20.5 55.4	19.0 52.0	17.0 46.3	15.3 41.0	13.5 35.1	11.2 28.1	11.2 26.6	11.7 26.3	14.2 24.7							
12	9.8 40.1	9.0 37.8	7.7 34.1	6.8 30.3	5.7 25.0	4.3 19.3	5.2 18.5	5.9 19.2	35.4 17.6							
Azimuth, deg	180	38	42	47	52	61	80	99	118	156						
Dist wrt AC, ft		Mean Peak kts kts														
Height																
0	0.0 0.0	0.0 0.0	0.0 0.0	0.0 0.0	0.0 0.0	0.0 0.0	0.0 0.0	0.0 0.0	0.0 0.0	0.0 0.0	0.0 0.0	0.0 0.0	0.0 0.0	0.0 0.0	0.0 0.0	
1	58.1 93.9	57.4 92.5	56.2 91.0	55.0 90.2	53.3 89.9	52.7 84.9	51.5 84.5	48.3 85.2	35.3 67.0							
2	56.3 92.0	55.5 90.5	54.4 88.8	53.3 87.9	51.8 87.4	51.3 82.7	50.1 82.4	47.2 83.3	34.6 65.7							
3	53.4 89.1	52.6 87.5	51.6 85.6	50.5 84.4	49.4 83.7	49.1 79.4	48.1 79.3	45.4 80.3	33.3 63.5							
4	49.5 85.4	48.7 83.6	47.9 81.5	47.0 80.2	46.3 79.3	46.4 75.5	45.4 75.6	43.1 76.6	31.7 60.7							
5	45.2 81.0	44.5 79.2	43.8 77.1	43.2 75.8	42.8 74.6	43.3 71.2	42.4 71.6	40.4 72.2	29.8 57.3							
7	36.9 71.8	36.2 70.1	35.6 68.1	35.2 66.5	35.3 65.1	36.5 62.4	36.0 63.2	34.4 62.6	25.4 49.6							
9	27.6 60.2	27.1 58.7	26.6 57.1	26.5 55.8	27.3 55.1	29.4 53.0	29.2 54.5	28.2 52.5	20.6 41.2							
12	17.6 45.9	17.0 44.3	16.7 43.0	16.8 42.1	17.8 42.0	20.3 40.4	20.6 42.3	19.7 38.7	14.0 29.9							
Azimuth, deg	210	38	42	47	52	61	80	99	118	156						
Dist wrt AC, ft		Mean Peak kts kts														
Height																
0	0.0 0.0	0.0 0.0	0.0 0.0	0.0 0.0	0.0 0.0	0.0 0.0	0.0 0.0	0.0 0.0	0.0 0.0	0.0 0.0	0.0 0.0	0.0 0.0	0.0 0.0	0.0 0.0	0.0 0.0	
1	50.8 88.2	50.8 88.6	50.1 88.2	49.0 87.0	46.1 84.8	40.6 81.4	38.3 73.8	34.7 68.0	24.8 53.5							
2	48.6 86.4	48.5 86.4	47.8 85.5	46.7 84.1	44.1 81.6	38.9 77.8	36.6 70.5	33.3 65.4	24.0 51.8							
3	45.2 83.7	45.0 83.0	44.3 81.8	43.3 80.1	41.0 77.2	36.4 72.6	34.2 65.7	31.3 61.4	22.7 49.3							
4	40.8 80.1	40.5 79.0	39.9 77.3	39.1 75.5	37.3 72.2	33.2 66.4	31.1 59.7	28.7 56.5	21.0 46.0							
5	36.1 75.9	35.8 74.4	35.3 72.8	34.8 71.1	33.5 67.4	29.9 60.1	27.7 53.4	25.8 51.1	19.1 42.4							
7	27.5 67.9	27.5 66.3														

Azimuth, deg		225									10									118		156	
Height	Dist wrt AC, ft	38		42		47		52		61		80		99		118		156					
		Mean	Peak	Mean	Peak	Mean	Peak	Mean	Peak														
		kts	kts	kts	kts	kts	kts	kts															
0	0.0	0.0	0.0	0.0	0.0	0.0	0.0	0.0	0.0	0.0	0.0	0.0	0.0	0.0	0.0	0.0	0.0	0.0	0.0	0.0	0.0		
1	50.3	83.1	50.9	83.9	49.7	82.7	47.4	80.6	43.6	77.5	37.5	70.5	33.9	62.2	31.8	60.1	21.2	47.3					
2	48.1	81.3	48.4	81.5	46.9	80.0	44.7	77.5	40.9	73.7	35.3	66.6	32.0	58.9	30.2	57.5	20.3	45.4					
3	44.6	78.3	44.4	77.8	42.8	75.9	40.5	72.9	36.9	68.2	32.1	61.0	29.2	54.1	27.9	53.6	18.9	42.5					
4	39.7	73.7	39.1	72.7	37.4	70.6	35.4	67.3	32.3	61.9	28.2	54.3	25.7	48.4	25.1	48.7	17.3	38.8					
5	34.3	68.3	33.5	66.8	31.8	64.6	30.2	61.1	27.5	55.4	24.1	47.7	22.1	42.5	22.0	43.5	15.4	34.8					
7	23.8	56.3	22.9	54.5	21.8	52.4	20.7	48.8	18.8	43.6	16.5	36.3	15.2	31.8	15.8	33.1	11.5	26.4					
9	14.0	43.9	13.4	42.6	13.0	40.5	12.5	37.2	11.7	33.6	10.3	28.2	9.4	23.6	10.4	23.8	8.0	18.9					
12	5.8	32.0	5.7	30.7	5.8	28.5	5.9	26.2	5.6	23.0	4.7	19.6	4.0	15.3	4.6	14.1	4.1	11.0					
Azimuth, deg		240									38									118		156	
Height	Dist wrt AC, ft	38		42		47		52		61		80		99		118		156					
		Mean	Peak	Mean	Peak	Mean	Peak	Mean	Peak														
		kts	kts	kts	kts	kts	kts	kts															
0	0.0	0.0	0.0	0.0	0.0	0.0	0.0	0.0	0.0	0.0	0.0	0.0	0.0	0.0	0.0	0.0	0.0	0.0	0.0	0.0	0.0		
1	49.0	76.0	52.1	81.0	52.3	84.3	50.7	84.2	46.3	79.8	37.4	66.1	32.3	57.1	30.0	52.2	22.6	43.3					
2	47.4	75.1	49.8	79.3	49.4	81.6	47.4	80.7	43.1	75.6	34.7	61.7	30.3	53.3	28.3	49.1	21.6	41.1					
3	44.7	73.5	46.0	76.6	44.8	77.5	42.5	75.6	38.3	69.3	30.9	55.6	27.2	47.9	25.8	44.5	19.9	37.9					
4	40.6	71.2	40.7	72.9	38.8	72.2	36.4	69.4	32.7	62.1	26.4	48.7	23.6	41.8	22.7	39.2	17.9	34.0					
5	35.8	68.3	34.8	68.5	32.4	66.2	30.2	62.6	27.1	54.7	21.9	42.2	19.9	35.9	19.5	33.8	15.7	29.8					
7	25.5	60.7	23.4	58.5	20.9	54.2	19.2	49.5	17.1	41.9	14.0	31.4	13.1	25.9	13.4	23.8	11.3	21.8					
9	15.7	51.1	13.4	47.9	11.4	42.8	10.3	38.3	9.4	32.2	8.0	23.3	7.7	18.6	8.2	16.2	7.5	15.5					
12	6.9	38.7	5.3	35.0	4.3	30.7	3.8	27.7	3.3	22.2	2.7	14.5	2.8	11.7	3.1	9.8	3.3	9.4					
Azimuth, deg		270									38									118		156	
Height	Dist wrt AC, ft	38		42		47		52		61		80		99		118		156					
		Mean	Peak	Mean	Peak	Mean	Peak	Mean	Peak														
		kts	kts	kts	kts	kts	kts	kts															
0	0.0	0.0	0.0	0.0	0.0	0.0	0.0	0.0	0.0	0.0	0.0	0.0	0.0	0.0	0.0	0.0	0.0	0.0	0.0	0.0	0.0		
1	45.9	69.1	56.7	77.7	63.0	87.3	62.7	93.1	57.2	93.4	45.5	83.1	37.8	74.1	34.2	66.4	26.1	56.0					
2	45.2	68.4	55.4	77.1	60.6	86.6	59.5	91.5	53.7	90.2	42.5	79.1	35.6	70.7	32.4	63.7	24.9	53.8					
3	44.0	67.5	53.0	76.4	56.5	85.6	54.4	88.8	48.5	85.4	38.2	73.3	32.2	65.6	29.7	59.6	23.2	50.6					
4	42.2	66.5	49.6	75.7	50.8	83.5	47.9	84.6	42.2	79.0	33.2	66.4	28.3	59.6	26.4	54.8	21.0	46.6					
5	40.0	65.6	45.4	74.9	44.3	80.6	40.8	79.2	35.6	71.5	28.0	59.2	24.2	53.4	23.0	49.7	18.6	42.1					
7	34.3	63.4	35.4	71.0	31.1	70.8	27.3	64.9	23.1	54.7	18.7	44.9	16.8	41.5	16.4	39.8	13.7	32.8					
9	27.6	59.1	25.1	62.6	18.9	55.9	15.2	46.7	12.4	37.2	11.2	31.7	10.7	30.9	10.9	31.0	9.3	24.1					
12	18.9	50.1	13.7	46.8	7.3	34.3	4.4	24.1	3.3	18.5	4.2	18.0	5.0	19.0	5.4	20.6	4.4	13.9	4.4	13.9	13.9		
Azimuth, deg		300									38									118		156	
Height	Dist wrt AC, ft	38		42		47		52		61		80		99		118		156					
		Mean	Peak	Mean	Peak	Mean	Peak	Mean	Peak														
		kts	kts	kts	kts	kts	kts	kts															
0	0.0	0.0	0.0	0.0	0.0	0.0	0.0	0.0	0.0	0.0	0.0	0.0	0.0	0.0	0.0	0.0	0.0	0.0	0.0	0.0	0.0		
1	50.3	73.9	55.9	78.9	58.6	83.3	58.2	85.8	54.2	86.4	45.4	76.6	40.3	70.1	35.5	64.5	29.5	55.1					
2	49.5	73.1	54.3	77.9	56.1	81.7	55.1	83.4	50.9	82.9	42.8	73.0	38.3	66.8	33.8	61.6	28.3	52.8					
3	47.9	72.1	51.5	76.5	51.9	79.3	50.2	79.8	46.0	77.7	39.0	67.8	35.2	62.2	31.4	57.4	26.4	49.4					
4	45.4	71.0	47.3	74.7	46.2	75.8	44.0	74.9	40.2	71.5	34.4	61.7	31.5	56.7	28.3	52.4	24.0	45.3					
5	42.3	69.8	42.3	72.3	39.8	71.4	37.3	69.2	34.0	64.9	29.6	55.4	27.5	51.0	25.0	47.2	21.4	40.8					
7	34.3	66.5	31.2	65.4	27.3	60.7	24.9	56.8	22.7	51.7	20.5	43.3	19.7	40.4	18.5	37.7	16.0	31.9					
9	24.9	59.9	20.0	54.9	16.0	48.2	14.3	43.8	13.4	39.1	12.9	32.4	13.0	31.1	12.8	29.7	11.2	24.0					
12	13.9	47.8	9.5	40.7	6.7	33.5	5.8	28.9	5.5	26.3	5.9	20.6	6.3	20.2	6.8	20.4	5.7	15.2					
Azimuth, deg		315									38									118		156	
Height	Dist wrt AC, ft	38		42		47		52		61		80		99		118		156					
		Mean	Peak	Mean	Peak	Mean	Peak	Mean	Peak														
		kts	kts	kts	kts	kts	kts	kts															
0	0.0	0.0	0.0	0.0	0.0	0.0	0.0	0.0	0.0	0.0	0.0	0.0	0.0	0.0	0.0	0.0	0.0	0.0	0.0	0.0	0.0		
1	52.5	78.1	54.3	81.8	54.4	84.2	53.2	84.6	50.0	82.8	44.1	71.5	39.7	63.4	36.8	59.8	30.3	48.4					
2	51.0	77.3	52.4	80.4	52.1	81.7	50.7	81.2	47.4	78.8	41.8	67.9	37.8	60.4	35.2</td								

GW, lb

33140

AGL, ft

19

Azimuth, deg

0

	38	42	47	52	61	80	99	118	156
	Mean Peak kts kts								
0	0.0 0.0	0.0 0.0	0.0 0.0	0.0 0.0	0.0 0.0	0.0 0.0	0.0 0.0	0.0 0.0	0.0 0.0
1	60.8 88.4	60.5 89.3	59.6 91.1	58.3 92.9	56.4 94.3	53.7 93.6	53.9 93.1	53.1 88.2	37.0 66.0
2	59.6 87.9	59.2 88.6	58.3 90.3	57.1 91.9	55.1 93.1	52.5 91.9	52.8 91.2	52.0 86.6	36.3 64.7
3	57.8 87.2	57.3 87.7	56.4 89.2	55.1 90.6	53.2 91.4	50.8 89.4	51.1 88.2	50.4 84.1	35.1 62.7
4	55.3 86.3	54.7 86.7	53.8 87.9	52.6 89.1	50.9 89.5	48.6 86.5	48.9 84.6	48.3 80.8	33.5 60.1
5	52.6 85.5	51.9 85.7	50.9 86.6	49.8 87.4	48.3 87.5	46.2 83.2	46.3 80.5	45.8 77.1	31.7 57.1
7	46.7 83.7	46.0 83.5	45.1 83.7	44.1 83.7	42.7 83.0	41.0 76.5	40.6 71.7	40.1 68.8	27.5 49.9
9	39.4 79.9	38.7 79.2	38.1 78.7	37.5 78.2	36.7 77.0	35.4 69.2	34.4 62.5	33.9 59.6	23.1 42.3
12	31.3 74.8	30.5 73.2	30.1 71.7	29.7 70.3	29.2 68.2	28.4 60.3	26.1 51.3	25.3 46.9	16.8 31.7

Azimuth, deg

45

	38	42	47	52	61	80	99	118	156
	Mean Peak kts kts								
0	0.0 0.0	0.0 0.0	0.0 0.0	0.0 0.0	0.0 0.0	0.0 0.0	0.0 0.0	0.0 0.0	0.0 0.0
1	53.4 85.5	54.3 89.2	53.2 90.7	50.6 90.1	46.1 85.6	38.6 73.3	35.2 65.7	33.5 59.8	23.5 51.4
2	51.6 84.2	52.2 87.4	50.8 88.1	48.2 86.9	43.7 81.6	36.5 69.3	33.5 62.4	32.0 57.2	22.6 49.1
3	48.7 82.1	48.7 84.3	47.0 84.1	44.4 82.0	40.0 75.7	33.3 63.5	30.9 57.5	29.7 53.3	21.2 45.6
4	44.5 78.7	44.0 80.0	42.2 78.8	39.6 76.1	35.5 68.6	29.5 56.6	27.7 51.7	27.0 48.7	19.4 41.3
5	39.7 74.7	38.7 75.1	36.7 73.0	34.3 69.5	30.6 61.1	25.3 49.5	24.1 45.6	23.9 44.0	17.3 36.5
7	29.5 65.1	27.8 63.8	26.0 60.6	24.1 55.7	21.1 46.6	17.3 36.8	17.2 34.0	17.8 34.9	13.1 27.3
9	19.4 54.7	17.5 51.9	15.8 47.2	14.5 41.7	12.6 33.8	10.6 27.0	11.1 24.9	12.2 27.1	9.2 20.0
12	9.9 42.8	8.2 38.3	6.7 31.9	5.7 26.6	4.5 21.3	4.1 17.7	5.0 16.5	6.1 18.3	4.8 13.7

Azimuth, deg

90

	38	42	47	52	61	80	99	118	156
	Mean Peak kts kts								
0	0.0 0.0	0.0 0.0	0.0 0.0	0.0 0.0	0.0 0.0	0.0 0.0	0.0 0.0	0.0 0.0	0.0 0.0
1	48.3 67.4	56.8 76.3	60.2 82.3	58.2 83.8	51.4 81.9	40.6 76.8	35.9 66.1	32.6 58.7	21.8 44.7
2	47.5 66.5	55.3 75.1	57.7 80.4	55.0 80.9	48.1 78.0	38.0 72.7	33.8 62.7	30.8 55.6	20.8 42.6
3	46.0 65.2	52.7 73.3	53.5 77.4	50.1 76.4	43.1 72.1	34.2 66.5	30.6 57.7	28.1 51.0	19.1 39.4
4	43.9 63.6	49.0 71.1	47.9 73.4	43.8 70.4	37.2 65.0	29.6 59.1	26.8 51.7	24.8 45.4	17.1 35.4
5	41.2 62.1	44.4 68.5	41.4 68.2	37.0 63.5	30.9 57.2	24.8 51.5	22.7 45.3	21.3 39.4	14.8 30.9
7	34.4 58.1	33.6 60.7	28.1 55.1	23.7 48.1	19.5 42.0	15.9 37.2	15.1 33.0	14.4 27.7	10.4 22.0
9	26.4 52.1	22.4 49.7	15.8 39.6	12.2 32.7	10.1 28.6	8.8 26.0	8.8 22.7	8.8 18.3	6.6 14.4
12	16.1 42.2	10.2 34.1	4.6 21.5	2.8 16.8	2.4 16.2	2.3 15.4	2.7 12.4	3.2 10.0	2.6 7.4

Azimuth, deg

135

	38	42	47	52	61	80	99	118	156
	Mean Peak kts kts								
0	0.0 0.0	0.0 0.0	0.0 0.0	0.0 0.0	0.0 0.0	0.0 0.0	0.0 0.0	0.0 0.0	0.0 0.0
1	47.3 73.2	47.7 76.2	46.8 77.9	45.6 77.2	43.8 72.6	40.2 67.5	36.5 64.9	33.6 59.8	18.7 40.8
2	45.2 71.2	45.4 73.7	44.4 74.8	43.1 73.8	41.4 69.3	38.2 64.8	34.8 62.6	32.2 58.0	17.2 39.2
3	41.9 68.2	41.8 69.9	40.7 70.2	39.4 68.8	37.7 64.5	35.1 60.8	32.3 59.3	30.0 55.3	16.8 36.8
4	37.4 64.4	37.1 65.2	36.0 64.5	34.8 63.0	33.3 59.2	31.5 56.3	29.2 55.4	27.4 52.1	16.3 33.8
5	32.6 60.2	32.1 60.2	31.0 58.9	29.9 57.0	28.7 53.9	27.7 51.8	25.9 51.3	24.5 48.9	15.0 30.5
7	23.0 51.2	22.5 50.2	21.7 48.3	21.0 46.5	20.5 44.6	20.7 43.6	19.5 43.4	18.8 42.5	13.2 24.0
9	13.9 41.9	13.5 40.1	13.4 38.4	13.3 37.3	13.6 36.2	14.7 36.1	14.0 35.7	13.8 36.4	11.3 18.6
12	5.8 31.9	5.8 29.5	6.3 28.1	6.8 27.8	7.3 26.5	8.6 27.4	8.2 26.4	8.1 28.1	32.2 13.4

Azimuth, deg

180

	38	42	47	52	61	80	99	118	156
	Mean Peak kts kts								
0	0.0 0.0	0.0 0.0	0.0 0.0	0.0 0.0	0.0 0.0	0.0 0.0	0.0 0.0	0.0 0.0	0.0 0.0
1	54.8 88.6	54.5 88.5	53.8 88.2	52.9 87.3	50.9 84.9	47.1 80.7	45.6 78.9	42.1 78.1	27.1 58.8
2	53.0 87.2	52.7 87.0	52.0 86.5	51.1 85.4	49.2 82.9	45.7 78.7	44.4 76.9	41.0 76.4	26.5 57.4
3	50.2 85.0	49.9 84.6	49.2 83.9	48.4 82.5	46.6 79.9	43.6 75.7	42.4 73.7	39.3 73.6	25.4 55.2
4	46.4 82.0	46.2 81.2	45.7 80.4	45.0 78.9	43.5 76.3	41.0 72.0	40.0 69.7	37.1 70.2	24.0 52.3
5	42.4 78.6	42.2 77.7	41.8 76.6	41.2 75.0	39.9 72.2	38.0 67.9	37.1 65.3	34.6 66.1	22.4 49.0
7	34.4 71.1	34.2 69.6	33.8 68.0	33.4 66.4	32.6 63.6	31.6 59.4	30.8 56.1	28.8 57.4	18.8 41.7
9	25.7 60.6	25.6 58.7	25.3 57.0	25.2 55.8	25.2 54.3	25.1 51.3	24.4 47.9	23.0 48.6	15.0 34.3
12	16.9 47.1	16.6 45.3	16.4 43.7	16.2 42.8	16.5 42.6	16.9 40.5	16.1 38.4	15.2 37.6	10.0 25.2

Azimuth, deg

210

	38	42	47	52	61	80	99	118	156
	Mean Peak kts kts								
0	0.0 0.0	0.0 0.0	0.0 0.0	0.0 0.0	0.0 0.0	0.0 0.0	0.0 0.0	0.0 0.0	0.0 0.0
1	56.0 88.3	55.3 89.9	53.7 91.2	51.6 91.8	48.4 92.9	45.6 92.3	45.1 89.8	43.0 86.3	29.4 64.2
2	54.3 86.3	53.5 87.7	51.9 88.8	49.9 89.3	46.8 90.4	44.4 90.2	44.1 88.1	42.1 84.6	28.7 62.5
3	51.6 83.4	50.6 84.6	49.1 85.3	47.2 85.6	44.4 86.8	42.6 86.9	42.6 85.6	40.6 81.9	27.5 59.9
4	47.8 79.7	46.8 80.7	45.4 81.2	43.8 81.3	41.4 82.5	40.3 83.0	40.6 82.5	38.8 78.5	26.0 56.5
5	43.7 76.1	42.7 76.9	41.5 77.0	40.1 76.8	38.2 78.0	37.7 78.7	38.4 79.0	36.6 74.8	24.1 52.6
7	35.4 69.6	34.6 69.7	33.6 69.1	32.6 68.5	31.5 69.2	32.3 70.0	33.4 71.6	31.6 66.9	20.0 43.7
9	26.4 61.9	25.8 61.8	25.3 60.9	24.8 60.0	24.9 60.2	26.6 60.9	27.9 63.0	26.2 58.7	15.6 3

Azimuth, deg		AGL, ft																	
		38		42		47		52		61		80		99		118		156	
Height	Dist wrt AC, ft	Mean kts	Peak kts																
0	0.0	0.0	0.0	0.0	0.0	0.0	0.0	0.0	0.0	0.0	0.0	0.0	0.0	0.0	0.0	0.0	0.0	0.0	0.0
1	51.8	92.5	51.5	95.5	50.0	96.9	47.7	96.9	45.0	94.3	43.8	88.2	39.0	84.8	35.2	79.4	27.2	66.8	
2	50.2	90.7	49.7	93.1	48.0	94.2	45.9	94.0	43.4	91.4	42.5	85.8	38.0	82.7	34.2	77.5	26.4	65.3	
3	47.5	87.8	46.7	89.6	45.1	90.2	43.0	89.7	40.9	87.1	40.5	82.4	36.4	79.6	32.6	74.6	25.3	62.9	
4	43.8	83.9	42.7	84.9	41.1	85.1	39.4	84.6	37.8	82.2	38.0	78.4	34.5	75.8	30.7	71.0	23.8	60.0	
5	39.5	79.7	38.4	80.2	36.9	80.0	35.6	79.3	34.4	77.2	35.2	74.4	32.3	71.7	28.5	67.0	22.0	56.7	
7	30.6	70.6	29.7	70.5	28.7	70.0	28.0	69.3	27.7	68.0	29.6	66.7	27.7	63.4	23.8	58.7	18.3	49.8	
9	21.3	60.3	20.8	59.8	20.3	59.0	20.1	58.4	21.0	59.1	23.8	58.9	22.7	55.2	19.1	50.3	14.6	42.7	
12	12.6	49.1	12.4	47.9	12.3	46.7	12.4	46.1	14.1	48.1	17.1	49.3	16.4	45.2	13.3	40.5	9.9	33.4	
Azimuth, deg		19																	
		38		42		47		52		61		80		99		118		156	
Height	Dist wrt AC, ft	Mean kts	Peak kts																
0	0.0	0.0	0.0	0.0	0.0	0.0	0.0	0.0	0.0	0.0	0.0	0.0	0.0	0.0	0.0	0.0	0.0	0.0	0.0
1	47.9	94.2	49.9	99.1	50.2	102.5	49.5	103.3	48.4	97.8	42.1	86.8	34.4	73.9	28.9	68.0	24.2	57.9	
2	46.6	92.8	48.3	97.4	48.3	100.3	47.6	100.6	46.6	94.8	40.6	84.1	33.1	71.4	27.9	65.7	23.5	56.0	
3	44.4	90.7	45.6	94.8	45.2	97.0	44.6	96.5	43.8	90.4	38.3	80.2	31.2	67.9	26.3	62.4	22.3	53.1	
4	41.4	88.0	41.9	91.3	41.3	92.8	40.7	91.5	40.2	85.4	35.5	75.6	28.9	63.7	24.4	58.3	20.7	49.4	
5	37.9	85.2	37.9	87.7	37.0	88.2	36.5	86.2	36.3	80.4	32.3	70.7	26.3	59.4	22.3	54.1	19.0	45.2	
7	30.3	78.9	29.6	80.1	28.8	79.0	28.5	76.5	28.5	71.1	25.9	61.2	21.1	51.3	17.9	46.1	15.3	36.9	
9	22.1	70.7	21.1	70.7	20.3	68.9	20.2	66.5	20.7	61.7	19.7	51.7	16.2	44.3	13.7	38.7	11.7	29.9	
12	13.7	60.8	12.8	60.3	12.3	58.4	12.3	56.2	12.6	51.2	12.9	41.9	10.8	36.9	8.8	30.3	7.2	22.5	
Azimuth, deg		270																	
		38		42		47		52		61		80		99		118		156	
Height	Dist wrt AC, ft	Mean kts	Peak kts																
0	0.0	0.0	0.0	0.0	0.0	0.0	0.0	0.0	0.0	0.0	0.0	0.0	0.0	0.0	0.0	0.0	0.0	0.0	0.0
1	46.7	90.9	54.1	98.2	58.3	105.8	58.8	109.8	55.1	108.0	47.5	99.0	41.9	93.3	37.9	89.0	29.9	74.9	
2	46.1	90.5	53.0	97.6	56.8	104.6	56.9	107.8	52.8	105.3	45.4	95.6	40.1	90.2	36.4	86.1	29.0	72.9	
3	44.9	89.6	51.1	96.5	54.2	102.7	53.9	104.7	49.4	101.0	42.2	90.5	37.4	85.5	34.1	81.5	27.7	69.7	
4	43.1	88.6	48.4	95.0	50.6	100.0	49.7	100.7	45.0	95.7	38.2	84.3	34.1	79.6	31.1	75.9	25.9	65.7	
5	40.9	87.3	45.3	93.2	46.4	97.0	45.0	96.0	40.1	89.5	33.8	77.6	30.4	73.1	27.9	69.7	23.8	61.1	
7	35.6	83.4	38.0	88.3	37.3	89.4	34.7	84.8	29.8	75.5	24.9	64.0	22.8	59.3	21.1	56.8	19.3	50.9	
9	29.6	78.0	29.8	81.2	27.2	78.6	23.6	70.9	19.4	59.3	16.8	50.6	15.8	45.6	14.9	44.4	14.8	40.3	
12	21.9	69.4	20.0	69.8	15.4	62.1	11.7	52.3	8.7	39.9	8.6	35.4	8.4	30.3	7.9	29.3	8.9	26.4	
Azimuth, deg		300																	
		38		42		47		52		61		80		99		118		156	
Height	Dist wrt AC, ft	Mean kts	Peak kts																
0	0.0	0.0	0.0	0.0	0.0	0.0	0.0	0.0	0.0	0.0	0.0	0.0	0.0	0.0	0.0	0.0	0.0	0.0	0.0
1	50.1	92.8	54.7	96.7	56.7	98.4	55.7	98.5	51.4	93.4	43.3	85.1	38.7	78.8	34.6	73.1	28.1	62.1	
2	49.4	91.8	53.5	95.4	54.9	96.6	53.7	96.1	49.2	90.3	41.4	82.2	37.0	75.8	33.2	70.3	27.2	60.3	
3	48.1	90.1	51.4	93.3	52.1	93.9	50.4	92.4	45.9	85.8	38.5	78.0	34.4	71.6	31.0	66.0	25.7	57.5	
4	46.0	87.8	48.3	90.3	48.0	90.3	46.1	87.8	41.6	80.5	35.0	73.2	31.3	66.6	28.3	61.0	23.9	53.9	
5	43.5	85.2	44.6	87.2	43.5	86.4	41.2	82.8	36.9	74.9	31.1	68.4	27.9	61.5	25.4	55.6	21.9	49.9	
7	36.9	79.3	36.1	80.2	33.8	77.6	31.0	72.3	27.1	64.4	23.4	59.4	21.2	51.7	19.4	45.1	17.4	41.2	
9	28.6	71.5	26.2	70.7	23.3	66.3	20.5	60.4	17.8	54.2	16.4	50.2	15.2	42.0	14.0	35.7	12.9	32.8	
12	18.2	59.5	15.1	56.0	13.5	44.0	12.3	41.1	11.6	39.7	9.3	37.9	8.8	30.1	8.2	24.8	7.5	22.8	
Azimuth, deg		315																	
		38		42		47		52		61		80		99		118		156	
Height	Dist wrt AC, ft	Mean kts	Peak kts																
0	0.0	0.0	0.0	0.0	0.0	0.0	0.0	0.0	0.0	0.0	0.0	0.0	0.0	0.0	0.0	0.0	0.0	0.0	0.0
1	54.3	88.3	54.5	89.6	54.1	90.4	53.3	91.5	51.3	92.5	47.5	88.9	43.0	81.8	39.9	72.2	32.1	65.1	
2	53.2	86.8	53.2	87.9	52.6	88.4	51.7	89.4	49.8	89.9	46.2	86.6	41.8	79.8	38.8	70.4	31.3	63.4	
3	51.4	84.4	51.2	85.2	50.3	85.4	49.2	86.1	47.3	86.1	44.1	83.1	39.9	76.7	37.1	67.7	30.1	60.7	
4	48.8	81.5	48.2	81.7	47.2	81.7	46.1	82.0	44.3	81.6	41.5	78.8	37.5	72.9	34.9	64.4	28.4	57.2	
5	45.9	78.5	45.1	78.3	43.8	77.9	42.6	77.8	40.9	76.9	38.5	74.2	34.8	68.5	32.5	60.9	26.5	53.3	
7	40.0	73.0	38.7	72.3	36.9	71.2	35.4	69.9	33.8	67.9	32.1	65.2	29.0	59.5	27.2	53.7	22.2	45.0	
9	32.6	66.4	31.1	65.8	29.0	64.0	27.6	61.8	26.3	59.3	25.5	56.6	22.9	50.0	21.8	46.2	17.8	37.0	
12	24.5	60.0	22.9	59.0	21.1	56.4	19.8	53.4	18.6	50.0	18.0	47.0	16.0	39.6	15.1	36.6	12.0	26.8	

Table M-3B Extension of V-22 Data Set, GW = 33,140 lb,
AGL = 19 ft

GW, lb	33140	AGL, ft	38												
Azimuth, deg	0	38	42	47	52	61	80	99	118	156					
Height		Mean Peak kts kts													
0	0.0	0.0 0.0	0.0 0.0	0.0 0.0	0.0 0.0	0.0 0.0	0.0 0.0	0.0 0.0	0.0 0.0	0.0 0.0	0.0 0.0	0.0 0.0	0.0 0.0	0.0 0.0	
1	60.6	94.4	60.0 94.8	58.9 94.9	57.8 94.9	56.3 94.4	56.0 94.0	54.8 92.4	50.8 89.7	34.6 63.2					
2	59.7	93.5	59.0 93.8	57.9 93.8	56.8 93.7	55.3 93.1	55.0 92.4	53.8 90.8	49.8 88.1	34.0 62.1					
3	58.3	92.2	57.5 92.3	56.3 92.2	55.2 91.9	53.7 90.9	53.4 89.9	52.2 88.4	48.4 85.5	33.0 60.4					
4	56.1	90.2	55.3 90.3	54.1 90.0	53.0 89.5	51.7 88.3	51.4 86.8	50.1 85.2	46.5 82.2	31.7 58.2					
5	53.8	88.3	52.9 88.2	51.7 87.7	50.6 86.9	49.4 85.3	49.0 83.3	47.7 81.6	44.2 78.3	30.1 55.7					
7	47.7	82.7	46.7 82.4	45.5 81.7	44.6 80.6	43.7 78.4	43.2 75.3	41.8 73.1	38.7 69.3	26.3 49.7					
9	41.1	76.8	40.1 76.4	39.1 75.4	38.4 74.1	37.7 71.6	36.8 67.6	35.5 64.7	32.8 60.4	22.3 43.6					
12	32.7	67.4	31.9 66.9	31.0 65.8	30.5 64.5	29.6 61.8	28.0 56.3	26.9 52.7	24.6 48.2	16.4 35.0					
Azimuth, deg	45	38	42	47	52	61	80	99	118	156					
Height	Dist wrt AC, ft	Mean Peak kts kts													
0	0.0	0.0 0.0	0.0 0.0	0.0 0.0	0.0 0.0	0.0 0.0	0.0 0.0	0.0 0.0	0.0 0.0	0.0 0.0	0.0 0.0	0.0 0.0	0.0 0.0	0.0 0.0	
1	53.3	81.6	54.1 84.6	53.2 86.3	51.3 86.4	47.0 83.7	39.3 73.3	35.8 67.2	33.9 62.3	23.9 46.8					
2	52.0	80.7	52.5 83.2	51.5 84.2	49.5 83.8	45.1 80.4	37.7 70.0	34.4 64.2	32.7 59.8	23.1 45.2					
3	49.8	79.3	50.0 81.0	48.8 81.1	46.6 79.9	42.2 75.6	35.1 65.1	32.0 59.7	30.7 56.0	21.8 42.7					
4	46.9	77.3	46.6 78.0	45.1 77.0	42.9 75.2	38.7 69.8	31.9 59.1	29.2 54.2	28.2 51.2	20.2 39.5					
5	43.4	74.9	42.7 74.8	41.1 72.9	38.9 70.1	34.7 63.7	28.4 52.6	25.9 48.1	25.3 45.9	18.2 35.9					
7	35.0	68.4	33.7 67.1	31.9 63.7	29.9 59.6	26.3 51.7	21.1 39.8	19.3 36.1	19.3 35.4	14.1 28.3					
9	26.5	60.2	24.9 57.8	23.2 53.4	21.6 48.6	18.7 40.3	14.5 29.0	13.2 26.1	13.6 26.3	10.0 21.4					
12	16.5	47.0	15.0 43.6	13.7 38.7	12.5 34.0	10.6 27.3	7.4 19.0	6.5 16.0	6.9 16.3	5.1 13.9					
Azimuth, deg	90	38	42	47	52	61	80	99	118	156					
Height	Dist wrt AC, ft	Mean Peak kts kts													
0	0.0	0.0 0.0	0.0 0.0	0.0 0.0	0.0 0.0	0.0 0.0	0.0 0.0	0.0 0.0	0.0 0.0	0.0 0.0	0.0 0.0	0.0 0.0	0.0 0.0	0.0 0.0	
1	53.0	79.8	59.6 85.8	62.7 90.3	62.0 92.7	57.5 92.4	47.8 81.4	40.8 71.1	36.3 64.2	27.2 54.1					
2	52.4	79.0	58.6 85.0	61.3 89.3	60.3 91.3	55.3 90.0	45.7 78.4	39.0 68.2	34.8 61.6	26.2 52.2					
3	51.2	77.7	56.9 83.6	59.0 87.6	57.3 88.9	51.9 86.3	42.5 73.7	36.3 63.6	32.4 57.5	24.6 49.3					
4	49.4	76.0	54.5 81.9	55.6 85.3	53.4 85.6	47.6 81.5	38.5 68.0	32.9 58.0	29.5 52.6	22.5 45.5					
5	47.3	74.2	51.5 79.9	51.6 82.5	48.7 81.7	42.6 76.0	34.1 61.7	29.2 51.8	26.1 47.3	20.2 41.2					
7	41.4	69.6	43.5 74.0	41.6 74.3	37.7 71.4	31.8 63.7	25.0 48.4	21.5 39.6	19.2 37.0	15.3 32.2					
9	34.6	63.7	34.6 65.8	31.0 63.1	26.8 58.6	22.0 51.1	16.9 35.7	14.7 29.0	13.1 27.8	10.7 23.8					
12	24.2	54.1	21.8 52.1	17.5 45.7	14.3 41.2	11.5 35.7	8.3 21.9	7.4 17.8	6.4 16.9	5.3 13.9					
Azimuth, deg	135	38	42	47	52	61	80	99	118	156					
Height	Dist wrt AC, ft	Mean Peak kts kts													
0	0.0	0.0 0.0	0.0 0.0	0.0 0.0	0.0 0.0	0.0 0.0	0.0 0.0	0.0 0.0	0.0 0.0	0.0 0.0	0.0 0.0	0.0 0.0	0.0 0.0	0.0 0.0	
1	46.9	76.3	47.6 78.5	47.6 79.8	46.5 79.4	43.5 76.9	38.1 67.5	33.7 62.6	31.8 56.9	19.7 37.7					
2	45.5	75.2	46.1 77.0	45.9 77.9	44.8 77.2	41.7 74.3	36.4 64.8	32.3 59.9	30.6 54.6	22.2 36.2					
3	43.3	73.5	43.7 74.7	43.3 75.0	42.0 73.9	38.9 70.4	33.7 60.6	30.2 55.9	28.7 51.2	22.1 33.9					
4	40.4	71.2	40.3 71.5	39.7 71.1	38.4 69.6	35.3 65.5	30.4 55.4	27.5 51.0	26.3 47.0	21.8 31.1					
5	37.1	68.6	36.7 68.2	35.8 66.9	34.4 64.8	31.4 60.0	26.8 49.6	24.5 45.7	23.6 42.5	20.5 28.0					
7	29.4	61.5	28.4 59.8	27.1 57.1	25.6 54.0	22.9 48.1	19.2 37.8	18.3 35.3	18.0 33.5	18.7 21.9					
9	21.8	52.5	20.4 49.5	18.8 46.1	17.3 42.6	15.2 36.4	12.7 27.6	12.6 26.4	12.7 25.7	15.4 16.9					
12	13.1	39.4	11.4 35.5	9.8 32.0	8.5 29.0	7.1 23.9	6.1 17.5	6.3 16.9	6.7 17.0	35.8 11.8					
Azimuth, deg	180	38	42	47	52	61	80	99	118	156					
Height	Dist wrt AC, ft	Mean Peak kts kts													
0	0.0	0.0 0.0	0.0 0.0	0.0 0.0	0.0 0.0	0.0 0.0	0.0 0.0	0.0 0.0	0.0 0.0	0.0 0.0	0.0 0.0	0.0 0.0	0.0 0.0	0.0 0.0	
1	57.2	90.9	57.1 90.8	57.0 90.5	56.5 89.9	55.5 88.2	52.5 85.7	49.1 81.5	45.0 74.2	21.5 42.1					
2	56.2	89.8	56.0 89.6	55.9 89.2	55.4 88.5	54.4 86.7	51.5 84.1	48.1 80.0	44.0 72.7	21.0 41.1					
3	54.4	88.0	54.3 87.7	54.2 87.1	53.7 86.3	52.7 84.2	49.8 81.5	46.4 77.6	42.4 70.3	20.3 39.5					
4	52.0	85.5	51.9 85.1	51.8 84.4	51.4 83.4	50.4 81.1	47.6 78.3	44.3 74.6	40.3 67.4	19.3 37.5					
5	49.4	82.7	49.3 82.2	49.2 81.1	48.8 80.0	47.8 77.5	45.1 74.6	41.9 71.1	37.8 64.0	18.2 35.1					
7	42.8	74.9	42.8 74.2	42.7 73.1	42.3 71.6	41.3 69.1	39.0 66.5	36.1 63.5	32.2 56.5	15.6 30.1					
9	35.8	66.7	35.8 65.9	35.8 64.8	35.4 63.2	34.6 60.9	32.6 58.6	30.1 55.7	26.4 49.1	13.0 25.2					
12	26.8	54.8	26.9 53.8	27.0 52.8	26.7 51.8	25.8 50.1	24.1 47.8	21.8 45.1	18.6 39.2	9.5 19.1					
Azimuth, deg	210	38	42	47	52	61	80	99	118	156					
Height	Dist wrt AC, ft	Mean Peak kts kts													
0	0.0	0.0 0.0	0.0 0.0	0.0 0.0	0.0 0.0	0.0 0.0	0.0 0.0	0.0 0.0	0.0 0.0	0.0 0.0	0.0 0.0	0.0 0.0	0.0 0.0	0.0 0.0	
1	48.8	78.3	48.8 78.1	47.9 78.2	46.6 78.9	44.6 77.7	42.1 72.9	41.3 73.2	38.2 64.5	19.1 39.9					
2	47.6	76.9	47.5 76.5	46.4 76.4	45.1 76.9	43.3 75.6	40.8 71.1	40.1 71.4	37.1 62.9	18.6 38.8					
3	45.6	74.8	45.2 74.1	44.1 73.7	42.8 73.9	41.1 72.4	38.8 68.4	38.2 68.7	35.3 60.4	17.8 37.0					
4	42.9	72.0	42.2 71.0	41.0 70.3	39.8 70.0	38.4 68.3	36.3 65.0	35.8 65.2	33.0 57.4	16.6 34.8					
5	39.8	69.1	38.9 67.6	37.5 66.5	36.4 65.8	35.2 63.7	33.3 61.1	32.9 61.3	30.4 54.0	15.3 32.2					
7	32.3	61.8	31.0 59.7	29.6 57.7	28.7 56.0	28.1 53.8	26.8 52.5	26.6 52.4	24.6 46.5	12.4 26.6					
9	24.8	54.7	23.5 51.7	22.1 48.8	21.5 46.7	21.4 44.7	20.6 44.2	20.5 43.1	18.9 38.9	9.4 21.2					
12	16.6	45.2	15.5 41.5	14.4 38.0	14.0 35.7	14.0 34.4	13.3 33.4	12.8 30.5	11.6 28.0	5.6 14.5					

Table M-4A Extension of V-22 Data Set, GW = 33,140 lb,
AGL = 38 ft

Azimuth, deg	225	AGL, ft		38	42		47		52		61		80		99		118		156		
Dist wrt AC, ft		Mean	Peak		Mean	Peak		Mean	Peak		Mean	Peak		Mean	Peak		Mean	Peak		Mean	Peak
Height		kts	kts		kts	kts		kts	kts		kts	kts		kts	kts		kts	kts		kts	kts
0		0.0	0.0		0.0	0.0		0.0	0.0		0.0	0.0		0.0	0.0		0.0	0.0		0.0	0.0
1		46.1	76.3		46.5	79.0		45.7	81.0		44.3	81.0		42.6	79.3		40.0	71.3		36.9	62.9
2		44.9	74.9		45.1	77.2		44.1	78.9		42.7	78.5		40.9	76.5		38.5	68.9		35.4	60.4
3		43.0	72.6		42.8	74.5		41.6	75.6		40.1	74.7		38.2	72.2		36.1	65.3		33.0	56.6
4		40.3	69.6		39.7	70.7		38.3	71.2		36.7	69.8		34.9	66.8		33.0	60.7		30.1	52.1
5		37.2	66.3		36.2	66.7		34.5	66.2		32.8	64.1		31.1	60.7		29.7	55.6		27.8	48.8
7		29.6	58.5		27.9	56.7		25.9	54.4		24.3	51.4		22.9	47.5		22.5	44.8		20.2	37.7
9		21.5	49.4		19.5	45.6		17.6	41.9		16.4	38.8		15.5	35.5		16.1	35.0		14.4	29.9
12		12.0	37.3		10.3	32.6		9.2	28.3		8.6	25.3		8.1	23.0		8.9	23.9		8.1	21.5
																				7.2	18.5
																				4.7	12.1

Azimuth, deg	240	38		42		47		52		61		80		99		118		156	
Dist wrt AC, ft		Mean kts	Peak kts																
Height																			
0	0.0	0.0	0.0	0.0	0.0	0.0	0.0	0.0	0.0	0.0	0.0	0.0	0.0	0.0	0.0	0.0	0.0	0.0	0.0
1	48.0	77.5	50.8	81.3	51.5	83.7	50.7	83.4	48.1	79.9	42.5	69.7	38.5	63.9	34.6	58.2	24.8	47.6	
2	47.1	76.5	49.6	80.0	50.0	81.8	48.9	81.1	46.0	77.0	40.6	66.8	36.8	61.2	33.3	55.7	23.9	46.1	
3	45.6	74.9	47.5	77.8	47.4	78.9	46.1	77.5	42.9	72.4	37.7	62.3	34.3	57.1	31.2	52.0	22.5	43.5	
4	43.4	72.8	44.7	75.0	43.9	74.9	42.2	72.7	38.8	66.7	34.1	56.7	31.0	52.1	28.6	47.4	20.7	40.5	
5	40.8	70.5	41.3	71.7	39.9	70.5	37.9	67.3	34.3	60.3	30.0	50.5	27.5	46.7	25.6	42.5	18.7	37.0	
7	34.0	64.7	33.0	63.6	30.5	59.8	28.0	54.8	24.5	46.5	21.6	37.8	20.3	36.3	19.5	33.3	14.3	29.7	
9	26.2	56.9	24.1	53.5	21.2	47.7	18.8	42.2	15.9	34.1	14.4	27.4	14.0	27.8	14.0	26.1	10.3	22.9	
12	15.7	44.2	13.3	38.6	10.9	32.2	9.4	27.5	7.5	21.1	7.1	17.5	7.3	18.7	7.7	18.6	5.4	14.7	

Azimuth, deg	270	38		42		47		52		61		80		99		118		156	
Dist wrt AC, ft		Mean kts	Peak kts																
Height																			
0	0.0	0.0	0.0	0.0	0.0	0.0	0.0	0.0	0.0	0.0	0.0	0.0	0.0	0.0	0.0	0.0	0.0	0.0	0.0
1	49.3	75.3	55.9	82.0	60.3	88.4	61.0	91.7	57.9	90.7	48.8	83.6	42.2	73.6	37.4	65.0	26.2	51.1	
2	48.9	74.8	55.3	81.4	59.3	87.6	59.6	90.3	56.1	88.3	46.9	80.4	40.5	70.8	35.9	62.7	25.3	49.1	
3	48.2	74.1	54.1	80.6	57.5	86.3	57.3	88.2	53.1	84.5	43.8	75.5	37.8	66.6	33.7	59.3	23.7	46.0	
4	47.0	73.2	52.3	79.5	54.8	84.5	54.0	85.1	49.2	79.5	39.8	69.4	34.4	61.3	30.9	55.0	21.8	42.2	
5	45.5	72.3	50.1	78.4	51.6	82.4	50.0	81.5	44.6	73.7	35.4	62.7	30.7	55.5	27.8	50.4	19.5	38.0	
7	41.1	70.0	43.9	75.0	43.1	76.0	39.9	71.2	34.0	59.9	26.1	48.6	22.8	43.3	21.2	41.0	14.8	29.5	
9	35.9	66.9	36.5	69.8	33.4	66.5	29.1	58.1	23.5	45.5	17.7	35.4	15.7	32.2	15.0	32.1	10.4	22.0	
12	27.3	59.8	25.3	58.4	20.1	49.2	15.7	38.1	11.7	27.6	8.9	21.2	8.1	19.9	7.9	20.6	5.4	13.7	

Azimuth, deg	300	38		42		47		52		61		80		99		118		156	
Dist wrt AC, ft		Mean	Peak																
Height		kts																	
0		0.0	0.0	0.0	0.0	0.0	0.0	0.0	0.0	0.0	0.0	0.0	0.0	0.0	0.0	0.0	0.0	0.0	0.0
1		51.8	79.0	56.0	83.3	58.1	86.6	57.7	87.8	53.9	84.6	46.7	78.6	41.8	71.5	37.6	66.5	24.5	50.6
2		51.1	77.8	55.1	81.8	56.8	84.8	56.1	85.7	52.0	81.8	44.9	75.8	40.3	69.2	36.4	64.5	23.6	48.9
3		49.9	76.1	53.4	79.6	54.5	82.1	53.5	82.3	49.1	77.6	42.2	71.6	38.0	65.8	34.5	61.4	22.3	46.1
4		48.1	73.9	50.9	77.0	51.4	78.7	50.0	77.9	45.3	72.2	38.7	66.5	35.1	61.6	32.0	57.6	20.5	42.6
5		46.0	71.9	48.0	74.3	47.7	74.9	45.9	72.9	41.0	66.1	34.8	60.8	31.9	57.0	29.1	53.3	18.6	38.8
7		40.1	67.6	40.3	68.1	38.6	65.8	36.1	61.0	31.3	53.1	26.6	49.0	25.0	47.7	23.0	44.4	14.4	30.7
9		33.2	63.0	31.6	61.1	28.8	55.5	26.0	48.7	22.2	40.8	19.0	38.0	18.5	39.0	17.0	36.0	10.5	23.3
12		23.3	54.7	20.0	48.8	16.5	39.9	14.2	32.9	12.0	26.7	10.6	25.3	10.8	28.2	9.8	25.6	5.8	14.6

Azimuth, deg	315		38		42		47		52		61		80		99		118		156	
Dist wrt AC, ft	Mean	Peak																		
Height	kts																			
0	0.0	0.0	0.0	0.0	0.0	0.0	0.0	0.0	0.0	0.0	0.0	0.0	0.0	0.0	0.0	0.0	0.0	0.0	0.0	0.0
1	51.3	77.4	52.9	81.8	53.2	85.4	52.2	86.5	49.3	86.0	42.1	77.9	37.0	71.4	34.0	66.8	20.3	49.1	19.6	47.2
2	50.5	76.5	51.8	80.6	51.9	83.8	50.6	84.7	47.6	83.6	40.5	75.2	35.7	69.3	32.9	64.8	19.6	47.2		
3	49.1	75.1	50.0	78.8	49.8	81.5	48.2	82.0	45.0	80.0	38.0	71.3	33.7	66.1	31.2	61.8	18.5	44.4		
4	47.0	73.4	47.5	76.6	46.9	78.6	45.1	78.5	41.7	75.4	35.0	66.5	31.2	62.1	29.0	58.1	17.0	40.8		
5	44.6	71.9	44.6	74.4	43.6	75.5	41.6	74.6	38.0	70.2	31.6	61.3	28.4	57.6	26.5	53.8	15.4	36.8		
7	38.2	67.8	37.4	68.8	35.7	67.8	33.4	65.0	29.9	58.5	24.7	50.7	22.3	48.1	20.9	44.8	11.9	28.6		
9	31.3	63.1	29.6	62.2	27.5	59.0	25.2	54.3	22.3	47.0	18.2	40.6	16.6	38.7	15.5	36.3	8.6	21.4		
12	21.9	54.6	19.7	51.0	17.5	45.3	15.5	39.4	13.5	32.8	11.0	28.6	9.6	26.8	8.8	25.2	4.8	13.4		

Azimuth, deg	330		38		42		47		52		61		80		99		118		156	
Dist wrt AC, ft	Mean	Peak																		
Height	kts																			
0	0.0	0.0	0.0	0.0	0.0	0.0	0.0	0.0	0.0	0.0	0.0	0.0	0.0	0.0	0.0	0.0	0.0	0.0	0.0	0.0
1	51.6	80.4	51.3	82.2	50.5	84.5	49.5	86.5	47.6	87.6	43.8	78.6	40.8	70.0	36.8	66.7	21.9	49.2		
2	50.7	79.4	50.2	81.0	49.3	83.0	48.2	84.7	46.3	85.6	42.5	76.7	39.7	68.2	35.7	65.1	21.3	47.9		
3	49.2	77.9	48.5	79.1	47.4	80.5	46.1	81.9	44.1	82.6	40.6	73.7	37.9	65.6	34.0	62.5	20.3	45.8		
4	46.9	75.9	46.0	76.5	44.7	77.4	43.4	78.4	41.5	78.9	38.1	70.1	35.6	62.4	31.9	59.3	19.1	43.1		
5	44.4	73.8	43.3	73.9	41.8	74.1	40.4	74.6	38.4	74.6	35.2	66.0	32.9	58.9	29.4	55.7	17.7	39.9		
7	38.0	67.8	36.4	67.0	34.7	66.1	33.1	65.5	31.2	64.5	28.9	57.2	27.0	51.4	23.9	47.8	14.5	33.0		
9	30.8	60.7	28.9	59.2	27.2	57.6	25.7	55.8	24.0	53.7	22.7	48.0	21.1	44.0	18.4	40.2	11.2	26.0		
12	21.6	48.8	19.7	46.9	18.3	44.6	17.0	42.1	15.7	39.4	15.1	36.0	13.8	34.5	11.6	30.4	6.8	17.2		

Table M-4B Extension of V-22 Data Set, GW = 33,140 lb,
AGL = 38 ft

GW, lb

33140

AGL, ft

57

Azimuth, deg

0

	38	42	47	52	61	80	99	118	156
	Mean Peak kts kts								
0	0.0 0.0	0.0 0.0	0.0 0.0	0.0 0.0	0.0 0.0	0.0 0.0	0.0 0.0	0.0 0.0	0.0 0.0
1	56.2 85.1	56.0 85.2	55.2 84.3	54.4 83.2	52.5 81.8	47.7 80.0	42.8 73.9	36.5 66.7	15.1 33.0
2	55.4 84.3	55.1 84.3	54.3 83.3	53.4 82.2	51.5 80.6	46.8 78.7	41.9 72.8	35.7 65.5	14.8 32.3
3	54.0 82.9	53.6 82.8	52.8 81.7	51.8 80.5	49.9 78.9	45.4 76.8	40.6 70.9	34.5 63.7	14.3 31.1
4	52.2 81.0	51.7 80.8	50.7 79.6	49.7 78.4	47.8 76.6	43.6 74.3	38.8 68.4	32.9 61.2	13.7 29.6
5	50.0 78.8	49.4 78.4	48.4 77.3	47.3 76.0	45.4 74.2	41.5 71.3	36.7 65.4	31.1 58.4	12.9 27.8
7	43.7 72.0	43.1 71.5	42.1 70.3	41.0 69.2	39.4 67.6	36.4 64.0	31.6 58.2	26.6 51.3	11.2 23.7
9	38.2 66.4	37.6 65.7	36.5 64.4	35.5 63.2	34.1 61.6	31.3 56.9	26.6 50.8	21.9 44.0	9.4 19.7
12	30.5 58.7	30.0 57.4	29.0 55.2	28.0 53.2	26.9 51.5	24.0 46.6	19.6 40.1	15.4 33.6	6.9 14.5

Azimuth, deg

45

Dist wrt AC, ft	38	42	47	52	61	80	99	118	156
Height	Mean Peak kts kts								
0	0.0 0.0	0.0 0.0	0.0 0.0	0.0 0.0	0.0 0.0	0.0 0.0	0.0 0.0	0.0 0.0	0.0 0.0
1	50.6 76.1	53.2 79.7	54.2 82.1	53.4 83.6	49.8 83.4	40.3 72.9	34.3 65.4	28.5 61.9	13.2 32.6
2	49.8 75.4	52.2 78.7	52.9 80.9	52.0 82.2	48.3 81.5	38.9 70.8	33.2 63.2	27.7 60.0	12.8 31.6
3	48.5 74.2	50.5 77.2	50.8 79.0	49.7 78.8	45.8 78.5	36.8 67.5	31.5 59.8	26.3 57.0	12.2 30.1
4	46.6 72.7	48.1 75.1	48.0 76.5	46.6 76.7	42.6 74.6	34.0 63.4	29.2 55.7	24.6 53.3	11.4 28.2
5	44.2 71.0	45.2 72.7	44.7 73.5	43.1 73.0	38.9 69.9	30.9 58.7	26.6 51.0	22.6 49.1	10.5 26.0
7	37.7 65.7	37.5 66.0	36.2 65.0	34.3 62.9	30.4 58.2	24.1 48.5	20.9 41.3	18.1 40.3	8.5 21.4
9	31.2 61.0	30.2 59.6	28.2 56.5	26.0 52.3	22.4 46.5	17.8 39.3	15.4 32.2	13.7 32.0	6.6 17.1
12	21.9 52.5	20.1 49.1	17.7 43.5	15.4 37.5	12.5 30.8	10.4 28.2	8.5 20.9	7.9 21.2	4.2 11.8

Azimuth, deg

90

Dist wrt AC, ft	38	42	47	52	61	80	99	118	156
Height	Mean Peak kts kts								
0	0.0 0.0	0.0 0.0	0.0 0.0	0.0 0.0	0.0 0.0	0.0 0.0	0.0 0.0	0.0 0.0	0.0 0.0
1	42.1 74.2	48.6 80.3	53.2 85.2	54.3 87.5	51.7 84.6	44.3 76.0	38.9 72.1	33.3 66.7	20.1 48.2
2	41.6 73.5	47.9 79.2	52.2 83.7	53.1 85.6	50.1 82.4	42.7 73.5	37.5 69.5	32.2 64.3	19.5 46.6
3	40.8 72.2	46.7 77.6	50.5 81.3	50.9 82.6	47.6 78.9	40.1 69.5	35.4 65.7	30.4 60.7	18.5 44.0
4	39.7 70.5	45.0 75.3	48.1 78.2	48.0 78.8	44.3 74.6	36.8 64.5	32.6 60.8	28.1 56.0	17.2 40.8
5	38.2 68.6	42.9 72.8	45.2 74.8	44.6 74.6	40.5 69.6	33.1 58.8	29.5 55.3	25.5 50.8	15.7 37.0
7	34.1 63.4	37.1 66.2	37.6 66.4	35.9 64.6	31.7 57.9	25.1 46.5	22.7 43.9	19.9 40.0	12.3 28.9
9	30.1 58.6	31.5 60.1	30.3 58.9	27.9 55.3	23.6 46.5	17.8 35.5	16.4 33.8	14.5 30.4	8.9 21.2
12	23.8 51.5	23.1 51.2	20.3 47.5	17.4 41.6	13.3 30.9	9.4 22.7	8.7 21.8	8.0 19.4	4.7 12.5

Azimuth, deg

135

Dist wrt AC, ft	38	42	47	52	61	80	99	118	156
Height	Mean Peak kts kts								
0	0.0 0.0	0.0 0.0	0.0 0.0	0.0 0.0	0.0 0.0	0.0 0.0	0.0 0.0	0.0 0.0	0.0 0.0
1	45.7 74.7	46.5 76.8	46.3 78.0	45.2 78.2	42.8 75.6	38.1 68.8	33.2 63.9	27.2 59.3	10.7 39.7
2	44.8 73.7	45.4 75.5	45.0 76.5	43.9 76.3	41.5 73.5	36.9 66.8	32.2 62.2	26.4 57.7	18.9 38.6
3	43.4 72.3	43.6 73.6	42.9 74.0	41.7 73.3	39.5 70.2	35.1 63.7	30.5 59.7	25.2 55.2	18.9 36.9
4	41.4 70.6	41.3 71.3	40.3 71.0	39.0 69.7	36.8 66.1	32.7 59.9	28.5 56.5	23.7 52.1	18.8 34.7
5	39.1 68.8	38.6 68.8	37.3 67.7	35.8 65.6	33.7 61.6	30.0 55.6	26.1 53.1	21.8 48.6	17.9 32.1
7	33.0 63.8	31.7 62.0	29.9 59.1	28.4 55.8	26.5 51.1	23.7 46.5	21.0 45.7	17.8 41.1	17.3 26.3
9	27.3 58.7	25.5 55.4	23.5 51.1	21.9 46.9	20.0 42.0	17.8 38.4	16.1 38.5	13.7 34.2	15.7 20.6
12	19.1 49.0	17.2 44.6	15.3 39.3	13.6 34.8	11.9 30.7	10.2 28.2	9.9 28.0	8.3 25.4	30.3 13.4

Azimuth, deg

180

Dist wrt AC, ft	38	42	47	52	61	80	99	118	156
Height	Mean Peak kts kts								
0	0.0 0.0	0.0 0.0	0.0 0.0	0.0 0.0	0.0 0.0	0.0 0.0	0.0 0.0	0.0 0.0	0.0 0.0
1	57.0 88.8	56.5 88.6	55.8 87.9	55.0 86.8	53.2 84.9	49.2 80.7	44.0 73.5	35.4 65.1	11.0 25.8
2	56.0 87.5	55.5 87.3	54.8 86.5	54.0 85.4	52.1 83.4	48.2 79.0	43.0 72.1	34.7 64.0	10.9 25.6
3	54.4 85.5	53.9 85.1	53.2 84.2	52.4 83.1	50.5 81.0	46.6 76.4	41.5 69.9	33.6 62.2	10.7 25.2
4	52.3 82.8	51.8 82.2	51.1 81.2	50.2 80.0	48.3 77.9	44.5 73.0	39.6 67.1	32.1 59.9	10.5 24.6
5	49.8 79.7	49.2 78.9	48.5 77.7	47.7 76.4	45.8 74.2	42.0 69.2	37.2 63.7	30.3 57.2	10.2 23.9
7	42.7 70.9	42.2 69.7	41.6 68.3	40.8 67.1	39.5 65.3	36.3 60.8	31.9 56.1	26.1 51.1	9.5 22.2
9	36.3 62.8	35.8 61.4	35.2 60.0	34.6 58.9	33.3 57.2	30.5 53.3	26.5 48.4	21.7 44.7	8.6 20.1
12	27.1 50.5	26.8 49.3	26.3 48.4	25.7 47.7	24.6 46.4	22.6 43.8	19.0 37.6	15.6 35.2	7.2 16.8

Azimuth, deg

210

Dist wrt AC, ft	38	42	47	52	61	80	99	118	156
Height	Mean Peak kts kts								
0	0.0 0.0	0.0 0.0	0.0 0.0	0.0 0.0	0.0 0.0	0.0 0.0	0.0 0.0	0.0 0.0	0.0 0.0
1	51.2 85.6	51.1 85.8	50.4 86.0	49.6 85.7	48.5 85.0	45.3 79.4	41.4 73.1	33.0 63.8	11.0 30.5
2	50.2 84.1	50.0 84.2	49.3 84.3	48.6 84.0	47.4 83.4	44.2 77.9	40.4 71.6	32.2 62.3	10.8 29.5
3	48.4 81.6	48.2 81.7	47.5 81.7	46.8 81.4	45.7 81.0	42.6 75.6	38.9 69.3	31.1 60.1	10.4 28.0
4	46.1 78.4	45.8 78.5	45.2 78.4	44.6 78.2	43.5 77.9	40.6 72.9	37.0 66.3	29.6 57.3	9.9 26.0
5	43.4 74.9	43.1 74.9	42.5 74.7	41.9 74.6	41.0 74.6	38.2 69.9	34.8 63.1	27.8 54.1	9.3 23.8
7	36.3 66.2	36.0 66.3	35.6 66.3	35.2 66.6	34.9 67.1	32.8 63.6	29.7 55.9	23.8 47.1	8.0 19.1
9	30.1 59.2	29.8							

Azimuth, deg		225		AGL, ft		57		38		42		47		52		61		80		99		118		156		
Height	Dist wrt AC, ft	Mean	Peak	Mean	Peak	Mean	Peak	Mean	Peak	Mean	Peak	Mean	Peak	Mean	Peak	Mean	Peak	Mean	Peak	Mean	Peak	Mean	Peak	Mean	Peak	
0	0.0	0.0	0.0	0.0	0.0	0.0	0.0	0.0	0.0	0.0	0.0	0.0	0.0	0.0	0.0	0.0	0.0	0.0	0.0	0.0	0.0	0.0	0.0	0.0	0.0	
1	47.4	86.0	47.9	87.0	47.0	86.7	45.4	85.4	43.4	82.8	42.0	77.6	39.1	75.7	32.3	67.3	14.5	35.5								
2	46.5	84.7	46.9	85.6	45.9	85.3	44.3	83.9	42.2	81.3	40.9	76.0	38.1	74.0	31.6	65.5	14.2	34.5								
3	44.9	82.6	45.3	83.5	44.2	82.2	42.6	81.8	40.4	78.9	39.2	73.6	36.6	71.3	30.4	62.8	13.6	32.8								
4	42.9	79.9	43.0	80.7	41.9	80.4	40.3	79.0	38.1	76.0	36.9	70.7	34.6	68.0	28.9	59.3	12.9	30.7								
5	40.4	76.8	40.5	77.6	39.3	77.2	37.7	76.0	35.4	72.9	34.4	67.6	32.3	64.2	27.0	55.3	12.1	28.3								
7	34.2	69.3	33.9	69.9	32.7	69.7	31.2	68.7	29.2	66.1	28.5	61.1	26.8	55.7	22.6	46.5	10.2	23.1								
9	28.6	62.8	28.2	63.1	26.9	62.9	25.5	62.2	23.6	59.8	22.8	54.7	21.1	47.4	18.0	38.0	8.2	18.2								
12	21.2	54.2	20.7	53.9	19.5	53.2	18.4	52.3	16.6	49.9	15.4	45.2	13.5	36.3	11.3	27.3	5.6	12.5								
Azimuth, deg		240		38		42		47		52		61		80		99		118		156						
Height	Dist wrt AC, ft	Mean	Peak	Mean	Peak	Mean	Peak	Mean	Peak	Mean	Peak	Mean	Peak	Mean	Peak	Mean	Peak	Mean	Peak	Mean	Peak	Mean	Peak			
0	0.0	0.0	0.0	0.0	0.0	0.0	0.0	0.0	0.0	0.0	0.0	0.0	0.0	0.0	0.0	0.0	0.0	0.0	0.0	0.0	0.0	0.0	0.0	0.0	0.0	
1	45.8	83.1	47.6	85.8	47.6	87.1	46.5	86.5	44.8	82.6	42.0	72.9	38.7	72.4	34.0	67.2	19.0	44.8								
2	45.2	82.4	46.8	85.0	46.6	85.8	45.3	84.9	43.5	80.9	40.8	71.2	37.8	70.9	33.2	65.7	18.6	43.6								
3	44.0	81.3	45.4	83.6	44.9	83.9	43.4	82.5	41.4	78.1	38.8	68.5	36.3	68.5	31.9	63.4	17.9	41.7								
4	42.5	79.9	43.4	81.8	42.6	81.5	40.8	79.5	38.7	74.7	36.3	65.1	34.3	65.5	30.2	60.4	17.0	39.3								
5	40.5	78.2	41.2	79.7	39.9	78.7	37.9	76.2	35.7	70.9	33.4	61.3	31.9	62.2	28.1	56.9	15.9	36.4								
7	35.4	73.4	35.1	73.8	33.1	71.8	30.7	68.4	28.6	61.9	26.9	52.8	23.5	49.3	23.4	49.3	13.4	29.9								
9	30.5	68.6	29.4	67.9	26.9	64.9	24.3	60.8	22.1	53.2	20.6	44.3	18.6	41.6	10.7	23.3										
12	23.4	60.0	21.5	57.2	18.7	53.3	16.3	48.8	13.8	41.2	12.4	33.1	13.2	33.9	11.8	30.1	6.8	14.8								
Azimuth, deg		270		38		42		47		52		61		80		99		118		156						
Height	Dist wrt AC, ft	Mean	Peak	Mean	Peak	Mean	Peak	Mean	Peak	Mean	Peak	Mean	Peak	Mean	Peak	Mean	Peak	Mean	Peak	Mean	Peak	Mean	Peak			
0	0.0	0.0	0.0	0.0	0.0	0.0	0.0	0.0	0.0	0.0	0.0	0.0	0.0	0.0	0.0	0.0	0.0	0.0	0.0	0.0	0.0	0.0	0.0	0.0	0.0	
1	44.3	81.7	50.6	89.7	55.4	97.6	56.8	102.7	54.7	104.5	48.3	96.3	44.3	89.4	40.6	83.8	24.9	55.3								
2	43.9	81.0	50.1	89.0	54.6	96.5	55.9	101.2	53.5	102.4	46.9	94.0	43.0	87.1	39.6	81.6	24.3	54.0								
3	43.3	79.9	49.1	87.7	53.3	94.6	54.3	98.7	51.5	99.2	44.7	90.4	41.1	83.3	38.0	78.2	23.3	51.8								
4	42.3	78.6	47.8	86.0	51.5	92.2	52.1	95.4	48.8	94.8	41.9	85.6	38.6	78.5	35.8	73.7	21.9	49.1								
5	41.2	77.0	46.1	84.0	49.2	89.2	49.4	91.5	45.7	89.7	38.7	80.0	35.7	72.8	33.3	68.5	20.4	45.9								
7	38.1	73.3	41.5	78.7	42.9	81.6	42.0	81.3	38.0	77.2	31.4	66.8	29.1	60.1	27.5	56.6	16.8	38.7								
9	34.9	70.4	36.8	73.9	36.6	74.1	34.8	71.6	30.6	65.3	24.4	54.0	22.7	48.1	21.3	44.6	13.1	31.4								
12	29.3	65.6	29.0	66.1	26.6	62.6	24.0	57.6	20.2	49.0	15.5	37.5	14.2	33.3	13.0	29.1	8.2	21.2								
Azimuth, deg		300		38		42		47		52		61		80		99		118		156						
Height	Dist wrt AC, ft	Mean	Peak	Mean	Peak	Mean	Peak	Mean	Peak	Mean	Peak	Mean	Peak	Mean	Peak	Mean	Peak	Mean	Peak	Mean	Peak	Mean	Peak			
0	0.0	0.0	0.0	0.0	0.0	0.0	0.0	0.0	0.0	0.0	0.0	0.0	0.0	0.0	0.0	0.0	0.0	0.0	0.0	0.0	0.0	0.0	0.0	0.0	0.0	
1	45.4	86.7	48.7	92.2	50.6	96.4	50.4	98.0	48.3	96.6	42.1	83.6	34.7	75.2	31.4	67.4	17.6	41.3								
2	44.9	85.5	48.0	90.8	49.6	94.8	49.3	96.2	47.0	94.7	40.8	81.5	33.7	72.9	30.5	65.6	17.1	39.9								
3	44.0	83.5	46.8	88.6	48.0	92.2	47.3	93.3	44.8	91.6	38.6	78.1	32.0	69.2	29.1	62.6	16.3	37.8								
4	42.7	81.1	45.1	85.7	45.8	88.9	44.8	89.6	41.9	87.7	35.9	73.8	29.9	64.6	27.3	58.8	15.2	35.1								
5	41.1	78.4	43.1	82.7	43.1	85.1	41.7	85.4	38.7	83.2	32.8	69.0	27.5	59.4	25.2	54.5	14.0	32.0								
7	36.8	72.5	37.5	75.8	36.1	76.3	34.0	75.0	31.0	72.1	25.9	58.5	22.2	48.4	20.4	44.9	11.3	25.5								
9	32.7	68.4	32.0	70.0	29.5	68.4	27.0	65.6	24.3	61.6	19.6	49.1	17.0	38.6	15.7	35.8	8.7	19.8								
12	26.3	62.9	24.0	61.1	20.7	56.6	18.4	52.0	15.9	46.7	12.0	36.7	10.5	27.0	9.5	24.7	5.5	13.6								
Azimuth, deg		315		38		42		47		52		61		80		99		118		156						
Height	Dist wrt AC, ft	Mean	Peak	Mean	Peak	Mean	Peak	Mean	Peak	Mean	Peak	Mean	Peak	Mean	Peak	Mean	Peak	Mean	Peak	Mean	Peak	Mean	Peak			
0	0.0	0.0	0.0	0.0	0.0	0.0	0.0	0.0	0.0	0.0	0.0	0.0	0.0	0.0	0.0	0.0	0.0	0.0	0.0	0.0	0.0	0.0	0.0	0.0	0.0	
1	49.4	87.2	50.5	91.3	50.2	93.2	49.2	93.5	47.2	92.2	42.9	86.2	37.4	78.0	31.4	65.8	16.0	37.4								
2	48.7	85.8	49.7	89.8	49.2	91.5	48.1	91.7	46.0	90.4	41.7	84.2	36.4	76.2	30.6	64.3	15.6	36.4								
3	47.6	83.6	48.3	87.3	47.6	88.9	46.3	88.9	44.1	87.6	39.8	81.1	34.9	73.3	29.4	61.9	15.0	34.9								
4	46.0	80.8	46.3	84.2	45.3	85.5	43.9	85.4	41.6	84.0	37.4	77.2	33.0	69.7	27.9	58.8	14.3	32.9								
5	44.1	77.6	44.1	80.7	42.7	81.7	41.2	81.4	38.8	79																

GW, lb

33140

AGL, ft

76

Azimuth, deg

0

	38	42	47	52	61	80	99	118	156
	Mean Peak kts kts								
0	0.0 0.0	0.0 0.0	0.0 0.0	0.0 0.0	0.0 0.0	0.0 0.0	0.0 0.0	0.0 0.0	0.0 0.0
1	51.1 76.7	50.6 77.9	50.1 78.9	49.7 79.7	47.7 79.5	43.3 76.6	38.7 71.3	29.0 56.7	5.1 11.9
2	50.2 75.5	49.7 76.6	49.2 77.6	48.7 78.3	46.8 78.0	42.4 75.3	37.9 70.1	28.4 55.7	5.1 11.8
3	48.6 73.5	48.1 74.5	47.7 75.5	47.2 76.1	45.3 75.7	41.0 73.1	36.6 68.3	27.4 54.1	5.0 11.6
4	46.6 71.0	46.1 71.9	45.6 72.9	45.1 73.3	43.3 72.8	39.1 70.3	34.9 65.9	26.1 52.0	5.0 11.4
5	44.1 68.2	43.6 69.0	43.2 69.8	42.7 70.2	40.9 69.4	36.9 66.9	32.9 63.0	24.5 49.6	4.9 11.2
7	37.4 61.0	37.0 61.6	36.7 62.3	36.4 62.4	35.1 61.6	31.6 58.9	28.0 56.2	20.9 44.0	4.8 10.7
9	31.4 54.8	31.0 55.2	30.9 55.7	30.6 55.4	29.4 54.1	26.0 50.3	23.1 49.1	17.2 38.2	4.6 10.0
12	22.1 45.4	22.0 45.2	22.0 44.9	21.8 44.4	20.7 42.3	17.7 37.0	15.7 37.5	11.8 29.4	4.2 8.9

Azimuth, deg

45

	38	42	47	52	61	80	99	118	156
	Mean Peak kts kts								
0	0.0 0.0	0.0 0.0	0.0 0.0	0.0 0.0	0.0 0.0	0.0 0.0	0.0 0.0	0.0 0.0	0.0 0.0
1	47.4 78.1	48.9 80.6	49.9 82.4	49.9 83.8	49.0 84.8	43.3 77.0	35.9 67.9	27.7 59.2	8.3 22.9
2	46.7 77.1	48.2 79.4	49.1 81.0	48.9 82.3	48.0 82.9	42.2 75.1	35.0 66.1	27.0 57.6	8.2 22.4
3	45.5 75.5	46.9 77.5	47.6 78.9	47.4 79.8	46.3 79.9	40.5 72.3	33.6 63.3	25.9 55.2	8.0 21.7
4	43.9 73.4	45.1 75.1	45.7 76.2	45.3 76.7	44.1 76.1	38.3 68.7	31.8 59.9	24.4 52.0	7.8 20.7
5	41.9 71.0	42.9 72.4	43.4 73.2	42.8 73.3	41.4 72.0	35.7 64.7	29.6 56.0	22.6 48.4	7.4 19.6
7	36.5 65.0	37.1 65.8	37.3 66.1	36.5 65.5	35.0 62.8	29.9 55.7	24.8 47.8	18.7 40.3	6.7 16.9
9	31.4 59.9	31.7 60.4	31.6 60.5	30.5 59.1	28.9 54.9	24.1 47.1	20.0 40.2	14.8 32.5	5.8 14.2
12	23.4 51.7	23.3 51.9	22.7 51.3	21.8 49.4	20.1 43.8	16.3 35.2	13.4 30.1	9.4 22.3	4.5 10.6

Azimuth, deg

90

	38	42	47	52	61	80	99	118	156
	Mean Peak kts kts								
0	0.0 0.0	0.0 0.0	0.0 0.0	0.0 0.0	0.0 0.0	0.0 0.0	0.0 0.0	0.0 0.0	0.0 0.0
1	46.1 75.1	51.6 82.0	55.5 87.9	56.4 91.2	53.6 91.8	45.7 83.7	38.4 73.4	31.8 66.3	11.9 30.6
2	45.7 74.2	51.1 80.9	54.8 86.6	55.5 89.7	52.4 90.0	44.4 81.6	37.4 71.4	30.9 64.5	11.6 29.8
3	45.0 72.7	50.1 79.0	53.5 84.4	53.8 87.2	50.5 86.9	42.4 78.2	35.7 68.3	29.6 61.6	11.1 28.4
4	43.9 70.8	48.8 76.7	51.6 81.6	51.6 83.9	47.9 83.0	39.8 73.9	33.5 64.3	27.7 57.9	10.5 26.7
5	42.6 68.8	47.0 74.1	49.3 78.3	48.9 80.0	44.7 78.3	36.8 68.9	31.0 59.7	25.6 53.7	9.7 24.7
7	38.9 64.5	42.2 68.2	43.1 70.4	41.8 70.6	37.1 67.1	30.1 57.9	25.4 49.6	21.0 44.7	8.1 20.4
9	35.0 61.1	37.0 62.9	36.5 62.6	34.4 60.9	29.4 55.9	23.4 47.2	19.8 40.0	16.2 36.2	6.5 16.4
12	27.8 56.1	28.0 55.0	26.0 51.2	22.9 46.6	18.5 40.3	14.4 32.9	12.1 27.7	9.7 25.4	4.5 11.6

Azimuth, deg

135

	38	42	47	52	61	80	99	118	156
	Mean Peak kts kts								
0	0.0 0.0	0.0 0.0	0.0 0.0	0.0 0.0	0.0 0.0	0.0 0.0	0.0 0.0	0.0 0.0	0.0 0.0
1	50.0 84.1	51.2 87.0	51.7 89.3	50.7 90.0	48.4 90.3	43.8 85.6	39.7 74.6	28.7 56.9	8.0 24.7
2	49.4 83.1	50.4 85.8	50.8 88.0	49.7 88.5	47.4 88.8	43.0 84.2	38.9 73.2	28.1 55.7	23.2 24.1
3	48.3 81.6	49.2 84.0	49.3 85.9	48.1 86.2	45.8 86.4	41.7 82.0	37.7 71.1	27.2 53.9	22.3 23.2
4	46.7 79.7	47.4 81.7	47.4 83.2	46.0 83.3	43.8 83.4	40.0 79.2	36.1 68.4	25.9 51.5	21.3 22.0
5	44.9 77.6	45.4 79.2	45.1 80.4	43.6 80.1	41.4 80.1	38.0 76.0	34.2 65.2	24.3 48.8	18.4 20.6
7	39.9 72.8	39.9 73.6	39.2 73.8	37.4 72.8	35.6 72.3	33.3 68.8	29.6 58.3	20.7 42.4	15.9 17.5
9	35.2 69.5	34.7 69.5	33.6 68.8	31.7 66.9	30.0 65.4	28.4 61.8	24.8 51.4	16.8 35.9	11.9 14.3
12	27.4 63.8	26.6 62.7	25.0 60.2	23.1 57.2	21.6 54.2	20.8 51.1	17.5 41.3	11.2 26.3	3.2 10.1

Azimuth, deg

180

	38	42	47	52	61	80	99	118	156
	Mean Peak kts kts								
0	0.0 0.0	0.0 0.0	0.0 0.0	0.0 0.0	0.0 0.0	0.0 0.0	0.0 0.0	0.0 0.0	0.0 0.0
1	58.1 88.3	58.3 88.9	58.4 89.8	58.2 90.4	56.9 89.9	53.0 85.3	44.2 72.6	30.4 53.4	7.6 15.7
2	57.4 87.6	57.6 88.0	57.6 88.8	57.3 89.4	56.0 88.8	52.2 84.3	43.5 71.6	30.0 52.6	7.5 15.5
3	56.1 86.3	56.3 86.6	56.3 87.3	56.0 87.7	54.7 87.2	51.0 82.7	42.4 70.1	29.2 51.2	7.4 15.3
4	54.5 84.6	54.6 84.8	54.6 85.3	54.2 85.6	52.9 85.0	49.3 80.6	40.9 68.0	28.2 49.6	7.3 14.9
5	52.5 82.5	52.6 82.6	52.6 83.0	52.1 83.1	50.9 82.5	47.3 78.2	39.1 65.7	27.0 47.6	7.1 14.4
7	47.0 76.7	47.0 76.6	47.0 76.7	46.7 76.7	45.8 76.3	42.4 72.3	34.8 60.2	24.2 43.2	6.7 13.3
9	42.1 71.0	42.1 70.9	42.1 70.8	41.7 70.7	40.7 70.2	37.2 66.0	30.2 54.5	21.1 38.6	6.3 12.0
12	34.0 60.4	34.0 60.3	34.0 60.3	33.6 60.2	32.7 60.0	29.0 55.6	23.2 45.2	16.3 31.0	5.5 10.1

Azimuth, deg

210

	38	42	47	52	61	80	99	118	156
	Mean Peak kts kts								
0	0.0 0.0	0.0 0.0	0.0 0.0	0.0 0.0	0.0 0.0	0.0 0.0	0.0 0.0	0.0 0.0	0.0 0.0
1	49.5 85.7	50.3 86.2	49.4 85.1	47.9 83.3	44.3 78.6	37.4 70.5	31.5 62.7	21.4 47.0	5.3 14.7
2	48.9 84.7	49.6 85.0	48.6 83.9	47.1 82.1	43.4 77.2	36.5 69.0	30.7 61.2	20.9 45.7	5.2 14.3
3	47.9 83.0	48.4 83.2	47.3 81.9	45.8 80.1	42.0 75.0	35.1 66.7	29.5 58.9	20.1 43.8	5.1 13.7
4	46.5 80.9	46.8 80.9	45.6 79.5	44.1 77.6	40.2 72.3	33.3 63.7	27.9 56.0	19.0 41.3	4.9 12.9
5	44.8 78.5	44.8 78.2	43.6 76.9	42.0 74.9	38.0 69.4	31.2 60.3	26.0 52.6	17.8 38.4	4.7 12.0
7	40.0 72.7	39.8 72.3	38.3 70.7	36.6 68.5	33.1 63.0	26.4 52.7	21.7 45.0	15.0 32.1	4.3 10.0
9	35.9 67.8	35.3 67.2	33.7 65.4	32.0 63.1	28.3 56.8	21.7 44.9	17.2 37.2	12.1 25.9	3.8 8.3

Azimuth, deg	225	AGL, ft	76	38	42	47	52	61	80	99	118	156
Height		Mean Peak kts kts		Mean Peak kts kts								
0	0.0	0.0	0.0	0.0	0.0	0.0	0.0	0.0	0.0	0.0	0.0	0.0
1	43.9	78.7	44.5	78.7	44.1	79.2	42.2	76.9	39.5	72.7	34.8	64.2
2	43.2	77.4	43.7	77.3	43.1	77.5	41.2	75.1	38.5	70.8	33.7	62.2
3	42.2	75.4	42.3	75.0	41.6	74.9	39.6	72.3	36.9	67.9	31.9	59.2
4	40.7	72.7	40.5	72.1	39.5	71.6	37.5	68.7	34.7	64.2	29.7	55.5
5	38.9	69.6	38.4	68.9	37.1	68.0	35.1	64.9	32.3	60.1	27.2	51.2
7	34.0	62.9	32.8	61.7	31.3	59.9	29.1	56.4	26.4	50.8	21.6	42.1
9	29.5	57.7	27.8	55.9	26.0	53.2	23.8	49.1	21.2	42.6	16.3	33.9
12	22.7	51.5	20.8	48.7	18.5	44.0	16.3	39.0	13.7	31.7	9.4	23.6
Azimuth, deg	240	AGL, ft	76	38	42	47	52	61	80	99	118	156
Height		Mean Peak kts kts		Mean Peak kts kts								
0	0.0	0.0	0.0	0.0	0.0	0.0	0.0	0.0	0.0	0.0	0.0	0.0
1	41.6	77.6	44.7	81.7	46.3	84.7	46.8	85.4	45.5	82.7	41.2	72.1
2	41.0	76.6	43.9	80.5	45.4	83.3	45.8	83.7	44.5	80.8	40.1	70.1
3	40.0	75.0	42.6	78.6	43.9	81.0	44.2	81.0	42.7	77.9	38.3	67.0
4	38.6	72.9	40.8	76.2	41.8	78.1	42.0	77.7	40.5	74.2	36.0	63.1
5	36.8	70.6	38.6	73.5	39.4	74.9	39.4	73.9	37.8	70.0	33.4	58.7
7	32.2	65.5	33.1	67.3	33.3	67.3	32.9	65.3	31.4	60.4	27.3	49.4
9	27.7	61.0	27.8	61.4	27.4	59.8	26.8	56.5	25.0	50.9	21.2	40.7
12	20.5	53.9	19.6	51.8	18.7	47.2	17.5	42.3	16.0	37.0	13.0	29.1
Azimuth, deg	270	AGL, ft	76	38	42	47	52	61	80	99	118	156
Height		Mean Peak kts kts		Mean Peak kts kts								
0	0.0	0.0	0.0	0.0	0.0	0.0	0.0	0.0	0.0	0.0	0.0	0.0
1	41.3	77.2	47.8	82.8	52.9	88.2	54.8	91.3	53.8	91.9	48.9	88.4
2	41.0	76.5	47.3	82.2	52.3	87.5	54.0	90.5	52.8	90.6	47.9	86.6
3	40.3	75.5	46.4	81.2	51.1	86.4	52.7	89.1	51.3	88.4	46.2	83.9
4	39.4	74.3	45.2	80.1	49.5	85.1	50.9	87.2	49.2	85.6	44.0	80.2
5	38.2	73.1	43.6	78.9	47.6	83.5	48.6	84.9	46.6	82.3	41.3	75.9
7	35.1	70.3	39.5	76.0	42.2	79.0	42.5	78.6	40.2	74.2	35.0	65.7
9	31.9	68.6	35.3	73.3	36.9	74.3	36.4	71.9	33.3	65.5	28.2	55.1
12	26.5	65.1	28.2	67.3	28.1	65.2	26.4	60.6	22.7	51.9	18.2	39.6
Azimuth, deg	300	AGL, ft	76	38	42	47	52	61	80	99	118	156
Height		Mean Peak kts kts		Mean Peak kts kts								
0	0.0	0.0	0.0	0.0	0.0	0.0	0.0	0.0	0.0	0.0	0.0	0.0
1	42.7	78.1	46.2	81.0	48.0	83.1	47.4	83.4	44.8	81.5	39.9	77.7
2	42.3	77.1	45.6	79.9	47.2	81.9	46.5	82.0	43.7	79.9	38.9	76.0
3	41.5	75.7	44.5	78.3	45.8	80.0	44.8	79.9	42.0	77.3	37.3	73.5
4	40.4	73.9	43.0	76.3	43.9	77.7	42.7	77.1	39.7	73.9	35.2	70.2
5	39.0	72.0	41.2	74.1	41.6	75.0	40.1	73.9	37.0	70.1	32.8	66.4
7	35.1	67.5	36.3	69.1	35.6	68.6	33.7	66.0	30.5	61.0	27.1	57.7
9	31.4	64.3	31.5	64.7	30.0	62.7	27.7	58.8	24.4	52.8	17.8	44.8
12	24.9	59.4	23.8	57.9	21.4	54.0	18.8	49.0	15.9	42.2	13.5	37.9
Azimuth, deg	315	AGL, ft	76	38	42	47	52	61	80	99	118	156
Height		Mean Peak kts kts		Mean Peak kts kts								
0	0.0	0.0	0.0	0.0	0.0	0.0	0.0	0.0	0.0	0.0	0.0	0.0
1	48.5	83.5	50.4	87.0	51.1	89.6	50.0	89.4	47.0	86.8	41.5	74.4
2	48.0	82.6	49.7	86.1	50.3	88.6	49.1	88.2	46.1	85.4	40.6	82.2
3	47.1	81.2	48.6	84.6	49.0	86.9	47.5	86.3	44.5	83.1	39.1	79.3
4	45.8	79.4	47.1	82.7	47.1	84.7	45.5	83.8	42.3	80.2	37.1	75.5
5	44.1	77.5	45.1	80.5	44.9	82.1	43.0	80.7	39.8	76.7	34.7	71.1
7	39.3	73.2	39.7	75.1	38.8	75.3	36.4	72.6	33.3	67.7	29.2	61.3
9	34.6	69.4	34.3	70.0	32.7	68.1	30.1	64.3	27.0	59.2	23.5	52.1
12	26.8	62.8	25.7	61.0	23.2	56.2	20.9	51.7	18.1	47.1	15.5	40.6
Azimuth, deg	330	AGL, ft	76	38	42	47	52	61	80	99	118	156
Height		Mean Peak kts kts		Mean Peak kts kts								
0	0.0	0.0	0.0	0.0	0.0	0.0	0.0	0.0	0.0	0.0	0.0	0.0
1	50.2	79.6	51.3	81.6	51.6	83.2	51.0	83.3	49.5	82.7	45.7	80.8
2	49.5	78.6	50.6	80.5	50.8	82.0	50.2	82.1	48.6	81.4	44.8	79.3
3	48.4	77.2	49.3	78.8	49.5	80.2	48.9	80.1	47.1	79.2	43.3	77.0
4	46.8	75.4	47.6	76.8	47.7	77.9	47.0	77.7	45.1	76.5	41.4	74.0
5	44.9	73.5	45.5	74.6	45.6	75.3	44.8	74.9	42.7	73.2	39.0	70.4
7	39.5	68.9	39.9	69.2	39.5	69.0	38.6	67.8	36.7	65.5	33.3	62.0
9	34.5	65.6	34.4	65.1	33.9	63.8	32.9	61.6	30.5	57.7	27.2	53.2
12	26.1	59.2	25.8	57.7	24.7	54.9	23.6	51.5	21.2	45.6	18.1	40.1

Table M-6B Extension of V-22 Data Set, GW = 33140 lb,
AGL = 76 ft

GW, lb

33140

AGL, ft

152

Azimuth, deg

0

	38	42	47	52	61	80	99	118	156
	Mean Peak kts kts								
0	0.0 0.0	0.0 0.0	0.0 0.0	0.0 0.0	0.0 0.0	0.0 0.0	0.0 0.0	0.0 0.0	0.0 0.0
1	12.2 36.1	12.8 34.6	12.4 31.9	11.6 29.5	10.1 25.0	6.4 14.4	4.2 9.5	3.0 6.4	1.5 3.4
2	12.2 36.0	12.8 34.5	12.3 31.9	11.6 29.5	10.2 25.0	6.4 14.4	4.2 9.5	3.0 6.4	1.5 3.4
3	12.1 35.8	12.7 34.4	12.3 31.8	11.6 29.5	10.2 24.9	6.4 14.4	4.2 9.5	3.0 6.4	1.5 3.4
4	12.1 35.5	12.7 34.2	12.3 31.7	11.5 29.5	10.2 24.9	6.4 14.4	4.2 9.5	3.0 6.4	1.5 3.4
5	12.1 35.3	12.6 34.1	12.3 31.7	11.5 29.5	10.2 24.9	6.4 14.4	4.2 9.5	3.0 6.4	1.5 3.4
7	12.0 34.9	12.6 34.0	12.2 31.9	11.5 29.9	10.3 24.9	6.4 14.3	4.2 9.5	2.9 6.5	1.4 3.4
9	12.0 35.0	12.6 34.5	12.3 32.8	11.6 30.8	10.4 25.4	6.3 14.3	4.2 9.5	2.9 6.4	1.4 3.4
12	12.1 36.0	12.7 35.9	12.5 34.7	12.0 32.8	10.6 26.7	6.2 14.3	4.2 9.5	2.9 6.4	1.4 3.4

Azimuth, deg

45

	38	42	47	52	61	80	99	118	156
	Mean Peak kts kts								
0	0.0 0.0	0.0 0.0	0.0 0.0	0.0 0.0	0.0 0.0	0.0 0.0	0.0 0.0	0.0 0.0	0.0 0.0
1	12.3 39.4	13.5 40.5	14.6 41.5	15.2 41.7	15.2 39.5	11.5 29.2	6.7 16.7	3.6 8.3	1.7 3.6
2	12.4 39.4	13.5 40.5	14.6 41.5	15.3 41.7	15.2 39.3	11.4 29.0	6.6 16.6	3.6 8.3	1.7 3.6
3	12.5 39.4	13.6 40.5	14.7 41.4	15.3 41.6	15.1 39.1	11.3 28.7	6.6 16.5	3.6 8.3	1.7 3.6
4	12.6 39.5	13.8 40.5	14.8 41.4	15.3 41.5	15.1 38.8	11.2 28.2	6.6 16.3	3.6 8.3	1.7 3.6
5	12.8 39.6	13.9 40.6	14.9 41.4	15.4 41.3	15.0 38.5	11.0 27.7	6.5 16.1	3.6 8.3	1.7 3.6
7	13.0 39.5	14.1 40.3	15.0 41.0	15.3 40.6	14.7 37.5	10.6 26.6	6.4 15.6	3.5 8.2	1.6 3.5
9	13.3 39.5	14.2 40.2	15.0 40.5	15.2 39.8	14.3 36.4	10.2 25.7	6.2 15.0	3.5 8.2	1.6 3.5
12	13.4 39.1	14.0 39.2	14.5 38.9	14.6 37.9	13.5 34.7	9.7 24.6	5.8 14.3	3.4 8.1	1.6 3.5

Azimuth, deg

90

	38	42	47	52	61	80	99	118	156
	Mean Peak kts kts								
0	0.0 0.0	0.0 0.0	0.0 0.0	0.0 0.0	0.0 0.0	0.0 0.0	0.0 0.0	0.0 0.0	0.0 0.0
1	6.8 25.2	7.7 26.6	8.3 29.4	9.1 32.7	10.4 34.6	8.7 25.7	5.7 15.7	3.6 9.3	1.8 4.3
2	6.9 25.2	7.8 26.6	8.4 29.4	9.1 32.7	10.4 34.4	8.7 25.7	5.7 15.7	3.7 9.3	1.8 4.3
3	7.0 25.3	7.9 26.6	8.5 29.4	9.2 32.6	10.4 34.0	8.7 25.5	5.7 15.7	3.7 9.3	1.8 4.3
4	7.1 25.4	8.0 26.8	8.6 29.4	9.2 32.5	10.4 33.6	8.6 25.4	5.7 15.7	3.7 9.3	1.8 4.3
5	7.3 25.6	8.2 26.9	8.7 29.5	9.3 32.4	10.3 33.1	8.6 25.1	5.7 15.6	3.7 9.3	1.8 4.3
7	7.8 26.4	8.6 27.8	9.1 30.0	9.5 32.3	10.2 32.1	8.4 24.4	5.7 15.5	3.7 9.3	1.8 4.3
9	8.3 27.9	9.1 29.3	9.5 31.2	9.8 32.9	10.2 31.4	8.1 23.6	5.6 15.3	3.6 9.2	1.8 4.3
12	9.2 31.0	9.9 32.4	10.1 33.6	10.2 34.1	10.2 30.9	7.6 22.3	5.5 15.0	3.6 9.2	1.8 4.3

Azimuth, deg

135

	38	42	47	52	61	80	99	118	156
	Mean Peak kts kts								
0	0.0 0.0	0.0 0.0	0.0 0.0	0.0 0.0	0.0 0.0	0.0 0.0	0.0 0.0	0.0 0.0	0.0 0.0
1	8.4 26.8	8.1 25.8	7.7 24.7	7.4 23.7	6.2 20.7	4.3 14.3	3.3 9.8	2.3 6.5	1.4 3.5
2	8.3 26.8	8.1 25.8	7.7 24.7	7.4 23.7	6.2 20.7	4.3 14.3	3.3 9.8	2.3 6.5	4.8 3.5
3	8.3 26.7	8.1 25.8	7.7 24.7	7.4 23.6	6.2 20.6	4.3 14.2	3.3 9.9	2.3 6.5	4.8 3.5
4	8.3 26.7	8.1 25.7	7.7 24.6	7.4 23.6	6.2 20.5	4.3 14.1	3.3 9.9	2.3 6.5	4.9 3.5
5	8.3 26.6	8.1 25.6	7.6 24.5	7.4 23.5	6.1 20.3	4.3 14.0	3.3 9.9	2.3 6.5	5.3 3.5
7	8.1 26.2	7.9 25.3	7.5 24.2	7.2 23.1	6.0 20.0	4.3 13.8	3.4 9.9	2.3 6.5	5.6 3.5
9	8.0 26.1	7.8 25.2	7.4 24.0	7.1 22.9	5.9 19.7	4.2 13.6	3.4 9.9	2.3 6.5	5.9 3.5
12	7.8 25.6	7.6 24.9	7.2 23.7	6.9 22.6	5.6 19.1	4.2 13.5	3.4 10.0	2.3 6.5	6.2 3.4

Azimuth, deg

180

	38	42	47	52	61	80	99	118	156
	Mean Peak kts kts								
0	0.0 0.0	0.0 0.0	0.0 0.0	0.0 0.0	0.0 0.0	0.0 0.0	0.0 0.0	0.0 0.0	0.0 0.0
1	7.9 27.8	7.5 26.8	7.1 25.1	6.8 23.4	5.5 18.7	3.3 10.7	2.5 7.5	1.8 5.0	0.9 2.7
2	7.9 27.9	7.5 26.9	7.1 25.2	6.8 23.5	5.5 18.8	3.3 10.7	2.5 7.5	1.8 5.0	0.9 2.7
3	7.9 27.9	7.5 27.0	7.1 25.3	6.8 23.6	5.5 18.9	3.3 10.7	2.5 7.5	1.8 5.0	0.9 2.7
4	7.9 28.1	7.6 27.2	7.1 25.5	6.9 23.8	5.5 19.0	3.3 10.7	2.5 7.5	1.8 5.0	0.9 2.7
5	7.9 28.2	7.6 27.4	7.2 25.8	6.9 24.0	5.6 19.1	3.3 10.7	2.5 7.5	1.8 5.0	0.9 2.7
7	8.0 28.8	7.5 28.0	7.1 26.3	6.8 24.6	5.6 19.4	3.3 10.7	2.5 7.5	1.8 5.0	0.9 2.7
9	8.0 29.6	7.6 28.7	7.1 27.1	6.8 25.2	5.6 19.7	3.3 10.6	2.5 7.5	1.8 5.0	0.9 2.7
12	8.0 30.6	7.6 29.7	7.1 27.7	6.8 25.5	5.5 19.7	3.2 10.4	2.5 7.5	1.7 5.0	0.9 2.6

Azimuth, deg

210

	38	42	47	52	61	80	99	118	156
	Mean Peak kts kts								
0	0.0 0.0	0.0 0.0	0.0 0.0	0.0 0.0	0.0 0.0	0.0 0.0	0.0 0.0	0.0 0.0	0.0 0.0
1	7.1 25.5	7.3 25.3	7.1 24.5	7.1 23.5	6.4 19.8	4.0 11.8	2.7 7.4	1.9 5.0	0.9 2.4
2	7.2 25.5	7.3 25.3	7.1 24.5	7.1 23.4	6.3 19.8	4.0 11.7	2.7 7.4	1.9 5.0	0.9 2.4
3	7.2 25.5	7.3 25.3	7.1 24.4	7.1 23.3	6.3 19.7	4.0 11.7	2.7 7.4	1.9 5.0	0.9 2.4
4	7.3 25.5	7.4 25.2	7.1 24.2	7.1 23.1	6.3 19.6	4.0 11.7	2.7 7.4	1.9 5.0	0.9 2.4
5	7.3 25.5	7.4 25.2	7.1 24.1	7.1 22.9	6.2 19.5	4.0 11.6	2.7 7.4	1.9 5.0	0.9 2.4
7	7.3 25.2	7.4 24.8	7.0 23.6	6.9 22.5	6.1 19.2	3.9 11.5	2.7 7.4	1.9 5.0	0.9 2.4
9	7.4 25.0	7.4 24.5	7.0 23.2	6.8 22.2	6.0 18.9	3.9 11.4	2.6 7.3	1.8 5.0	0.9 2.4
12	7.3 24.5	7.3 23.9	6.8 22.5	6.5 21.5	5.6 18.4	3.7 11.2	2.6 7.2	1.8 5.0	0.9 2.4

Table M-7A Extension of V-22 Data Set, GW = 33,140 lb,

AGL = 152 ft

Azimuth, deg	225	AGL, ft				152	AGL, ft				152	AGL, ft				156			
Dist wrt AC, ft		38		42		47		52		61		80		99		118			
Height		Mean kts	Peak kts																
0	0.0	0.0	0.0	0.0	0.0	0.0	0.0	0.0	0.0	0.0	0.0	0.0	0.0	0.0	0.0	0.0	0.0	0.0	0.0
1	8.6	27.8	8.9	28.0	9.0	27.6	8.9	25.9	7.6	21.6	5.1	15.7	3.3	9.3	2.0	5.4	1.1	2.8	
2	8.6	27.8	8.9	27.9	9.0	27.5	8.9	25.8	7.6	21.5	5.1	15.6	3.3	9.3	2.0	5.4	1.1	2.8	
3	8.6	27.8	8.9	27.8	8.9	27.3	8.8	25.6	7.5	21.4	5.1	15.3	3.2	9.2	2.0	5.4	1.1	2.8	
4	8.6	27.7	8.9	27.7	8.9	27.1	8.8	25.4	7.4	21.2	5.0	15.0	3.2	9.1	2.0	5.4	1.1	2.8	
5	8.6	27.6	8.8	27.5	8.8	26.8	8.7	25.1	7.3	21.0	5.0	14.7	3.2	9.0	2.0	5.4	1.1	2.8	
7	8.5	27.1	8.7	27.0	8.7	26.4	8.5	24.7	7.1	20.6	4.8	14.0	3.1	8.8	2.0	5.4	1.1	2.8	
9	8.3	26.6	8.5	26.5	8.5	25.9	8.3	24.3	6.8	20.3	4.6	13.3	3.1	8.6	2.0	5.4	1.1	2.8	
12	7.8	25.5	8.1	25.7	8.0	25.4	7.8	24.0	6.4	20.1	4.3	12.6	3.0	8.3	2.0	5.4	1.1	2.7	

Azimuth, deg		240		38		42		47		52		61		80		99		118		156	
Dist wrt AC, ft	Height	Mean kts	Peak kts																		
0	0	0.0	0.0	0.0	0.0	0.0	0.0	0.0	0.0	0.0	0.0	0.0	0.0	0.0	0.0	0.0	0.0	0.0	0.0	0.0	0.0
1	9.3	28.5		9.5	28.1	9.8	27.9	9.6	26.1	8.4	24.2	6.1	20.7	4.3	14.4	2.7	7.8	1.2	3.2		
2	9.3	28.3		9.5	27.9	9.8	27.7	9.6	26.0	8.4	24.1	6.1	20.6	4.3	14.3	2.7	7.8	1.2	3.2		
3	9.2	28.0		9.4	27.6	9.7	27.4	9.5	25.8	8.4	24.1	6.1	20.5	4.3	14.1	2.7	7.8	1.2	3.2		
4	9.1	27.7		9.3	27.2	9.6	27.0	9.4	25.6	8.3	24.0	6.0	20.3	4.2	13.9	2.7	7.8	1.2	3.2		
5	9.0	27.2		9.2	26.8	9.4	26.6	9.2	25.3	8.2	23.9	6.0	20.1	4.2	13.7	2.7	7.8	1.2	3.2		
7	8.8	25.9		8.9	25.7	9.1	25.7	9.0	24.8	8.0	23.7	5.9	19.5	4.1	13.2	2.7	7.8	1.2	3.2		
9	8.4	24.7		8.6	24.7	8.7	25.0	8.6	24.4	7.7	23.4	5.8	18.8	4.0	12.7	2.7	7.7	1.2	3.2		
12	7.8	22.9		8.0	23.2	8.1	24.0	8.0	23.8	7.2	22.7	5.5	17.8	3.9	12.3	2.7	7.7	1.2	3.2		

Azimuth, deg	270	38		42		47		52		61		80		99		118		156		
Dist wrt AC, ft		Mean	Peak																	
Height		kts																		
0	0.0	0.0	0.0	0.0	0.0	0.0	0.0	0.0	0.0	0.0	0.0	0.0	0.0	0.0	0.0	0.0	0.0	0.0	0.0	
1	10.4	31.1	10.9	31.9	10.8	32.5	10.7	33.0	10.7	33.4	8.2	26.5	5.5	16.4	3.3	9.3	1.6	3.8		
2	10.4	30.8	10.9	31.7	10.9	32.4	10.7	32.9	10.8	33.3	8.2	26.4	5.5	16.3	3.3	9.3	1.6	3.8		
3	10.4	30.4	10.9	31.4	10.9	32.2	10.8	32.8	10.8	33.3	8.2	26.3	5.4	16.3	3.3	9.3	1.6	3.8		
4	10.3	29.9	10.8	31.0	10.9	31.9	10.8	32.6	10.8	33.2	8.2	26.2	5.4	16.2	3.3	9.3	1.6	3.8		
5	10.3	29.3	10.8	30.5	10.9	31.7	10.8	32.5	10.8	33.0	8.2	26.1	5.4	16.1	3.3	9.3	1.6	3.8		
7	10.2	28.3	10.8	30.0	11.0	31.5	11.0	32.5	10.9	32.9	8.1	25.8	5.4	15.9	3.3	9.2	1.6	3.8		
9	10.0	27.1	10.7	29.3	11.0	31.2	11.0	32.3	10.9	32.6	8.0	25.5	5.3	15.7	3.3	9.2	1.6	3.8		
12	9.7	26.0	10.5	28.9	10.8	31.0	10.9	32.1	10.8	32.2	7.9	25.2	5.3	15.5	3.3	9.1	1.6	3.8		

Azimuth, deg	300	38		42		47		52		61		80		99		118		156	
Dist wrt AC, ft		Mean	Peak																
Height		kts																	
0		0.0	0.0	0.0	0.0	0.0	0.0	0.0	0.0	0.0	0.0	0.0	0.0	0.0	0.0	0.0	0.0	0.0	0.0
1		13.3	35.7	13.4	37.1	13.4	38.3	13.1	38.5	12.2	36.2	8.1	24.0	4.8	13.5	3.1	8.1	1.5	3.6
2		13.2	35.6	13.4	37.0	13.4	38.2	13.1	38.4	12.2	36.1	8.1	23.9	4.8	13.5	3.1	8.1	1.5	3.6
3		13.2	35.4	13.4	36.9	13.3	38.1	13.1	38.2	12.2	35.8	8.0	23.8	4.8	13.5	3.1	8.1	1.5	3.6
4		13.1	35.1	13.3	36.7	13.3	37.9	13.0	38.0	12.2	35.5	8.0	23.6	4.8	13.4	3.1	8.1	1.5	3.6
5		12.9	34.8	13.1	36.5	13.2	37.7	13.0	37.7	12.1	35.2	8.0	23.4	4.8	13.4	3.1	8.1	1.5	3.6
7		12.5	34.3	12.8	36.1	13.0	37.2	12.9	37.1	12.0	34.4	7.8	22.8	4.8	13.2	3.1	8.1	1.5	3.6
9		12.1	33.7	12.4	35.4	12.7	36.4	12.7	36.3	11.8	33.7	7.7	22.3	4.7	13.1	3.0	8.1	1.4	3.5
12		11.3	32.7	11.6	33.9	12.1	34.8	12.2	34.9	11.6	32.8	7.5	21.4	4.6	12.8	3.0	8.0	1.4	3.5

Azimuth, deg		315		38		42		47		52		61		80		99		118		156	
Dist wrt AC, ft	Height	Mean	Peak																		
		kts																			
0		0.0	0.0	0.0	0.0	0.0	0.0	0.0	0.0	0.0	0.0	0.0	0.0	0.0	0.0	0.0	0.0	0.0	0.0	0.0	0.0
1		14.4	37.0	13.9	37.3	13.0	36.6	12.3	35.5	10.6	30.9	7.1	20.2	4.5	11.6	2.8	6.7	1.5	3.4		
2		14.3	36.8	13.9	37.1	13.0	36.5	12.2	35.3	10.6	30.7	7.1	20.1	4.5	11.6	2.8	6.7	1.5	3.4		
3		14.1	36.5	13.7	36.8	12.9	36.2	12.2	35.0	10.5	30.3	7.1	19.9	4.5	11.6	2.8	6.7	1.5	3.4		
4		13.9	36.1	13.5	36.5	12.7	35.8	12.1	34.5	10.4	29.8	7.1	19.8	4.5	11.5	2.8	6.7	1.5	3.4		
5		13.7	35.7	13.3	36.1	12.6	35.3	11.9	34.0	10.3	29.2	7.0	19.5	4.5	11.5	2.8	6.7	1.5	3.4		
7		13.0	34.7	12.7	35.2	12.1	34.2	11.5	32.5	10.0	27.7	6.9	19.1	4.4	11.4	2.8	6.7	1.5	3.4		
9		12.3	33.8	12.0	34.0	11.5	32.7	11.0	30.8	9.5	26.2	6.7	18.7	4.4	11.2	2.8	6.7	1.4	3.4		
12		10.9	32.2	10.7	31.9	10.3	30.2	10.0	28.3	8.9	24.5	6.5	18.5	4.3	11.0	2.7	6.7	1.4	3.4		

Azimuth, deg		330		38		42		47		52		61		80		99		118		156	
Dist wrt AC, ft	Height	Mean kts	Peak kts																		
0		0.0	0.0	0.0	0.0	0.0	0.0	0.0	0.0	0.0	0.0	0.0	0.0	0.0	0.0	0.0	0.0	0.0	0.0	0.0	0.0
1		13.3	37.4	13.0	37.1	12.4	35.9	11.5	33.9	9.8	29.4	6.6	18.2	4.5	10.8	2.9	7.0	1.4	3.3		
2		13.3	37.1	12.9	36.9	12.3	35.7	11.5	33.8	9.8	29.3	6.6	18.2	4.5	10.8	3.0	7.0	1.4	3.3		
3		13.1	36.7	12.8	36.5	12.3	35.4	11.4	33.5	9.9	29.1	6.6	18.1	4.5	10.8	3.0	7.0	1.4	3.3		
4		12.9	36.1	12.6	36.0	12.2	35.1	11.4	33.2	9.9	28.9	6.6	18.0	4.5	10.8	3.0	7.0	1.4	3.3		
5		12.7	35.5	12.4	35.4	12.0	34.6	11.3	32.9	9.9	28.6	6.6	17.9	4.5	10.8	3.0	7.0	1.4	3.3		
7		12.2	34.2	12.0	34.4	11.6	33.6	11.1	31.9	9.8	27.7	6.7	17.6	4.5	10.7	3.0	7.0	1.4	3.3		
9		11.6	33.0	11.5	33.3	11.2	32.5	10.8	30.8	9.7	26.7	6.7	17.2	4.5	10.7	2.9	7.0	1.4	3.3		
12		10.6	31.3	10.6	31.5	10.6	30.5	10.2	28.8	9.3	24.9	6.6	16.7	4.5	10.7	2.9	7.0	1.4	3.3		

Table M-7B Extension of V-22 Data Set, GW = 33,140 lb,
AGL = 152 ft

GW, lb	52600	AGL, ft	10	Azimuth, deg 0												
				38	42	47	52	61	80	99	118	156				
Height	Mean Peak kts kts															
0	0.0 0.0	0.0 0.0	0.0 0.0	0.0 0.0	0.0 0.0	0.0 0.0	0.0 0.0	0.0 0.0	0.0 0.0	0.0 0.0	0.0 0.0	0.0 0.0	0.0 0.0	0.0 0.0	0.0 0.0	
1	56.4 93.7	56.1 93.2	55.5 92.1	54.7 91.6	52.9 91.9	51.1 91.0	53.4 88.4	52.6 84.7	39.1 62.2							
2	54.7 92.2	54.3 91.5	53.7 90.2	53.0 89.6	51.4 89.8	49.9 89.1	52.3 86.9	51.5 83.3	38.2 60.7							
3	52.0 90.1	51.6 89.1	51.1 87.6	50.5 86.7	49.1 86.7	48.0 86.3	50.6 84.5	49.9 81.2	36.8 58.3							
4	48.5 87.4	48.1 86.1	47.6 84.5	47.3 83.5	46.2 83.2	45.6 82.8	48.3 81.5	47.8 78.6	35.0 55.4							
5	44.8 84.6	44.4 83.1	44.0 81.4	43.8 80.4	43.0 79.6	42.9 79.0	45.7 78.1	45.3 75.7	32.8 52.2							
7	37.4 78.8	37.0 77.1	36.7 75.5	36.6 74.4	36.4 72.4	36.9 70.4	39.7 70.7	39.6 69.3	28.1 45.8							
9	29.0 70.5	28.5 68.8	28.4 67.5	28.6 66.5	29.0 63.7	30.2 60.2	33.0 61.9	33.3 62.1	23.1 40.0							
12	20.3 60.3	19.8 58.9	19.5 57.4	19.6 56.1	20.4 52.2	21.5 46.3	23.8 49.6	24.7 51.7	16.5 32.6							
Height	Mean Peak kts kts															
Azimuth, deg 45	38	42	47	52	61	80	99	118	156							
Height	Mean Peak kts kts															
0	0.0 0.0	0.0 0.0	0.0 0.0	0.0 0.0	0.0 0.0	0.0 0.0	0.0 0.0	0.0 0.0	0.0 0.0	0.0 0.0	0.0 0.0	0.0 0.0	0.0 0.0	0.0 0.0	0.0 0.0	
1	53.2 94.7	56.2 96.7	57.7 96.9	57.5 96.0	55.0 92.6	47.3 82.7	43.8 77.4	39.9 75.0	33.0 60.9							
2	51.8 93.8	54.4 95.5	55.7 95.4	55.3 94.0	52.9 90.1	45.5 80.0	42.1 74.9	38.4 72.4	31.9 59.2							
3	49.4 92.5	51.6 93.8	52.4 93.1	52.0 91.1	49.7 86.8	42.8 76.1	39.6 71.3	36.1 68.5	30.1 56.5							
4	46.2 90.4	47.7 91.1	48.2 89.8	47.7 87.5	45.8 82.9	39.5 71.8	36.5 67.2	33.2 63.6	27.9 53.1							
5	42.4 88.3	43.3 88.3	43.5 86.5	43.0 83.7	41.5 79.0	35.8 67.5	33.1 62.9	30.0 58.2	25.5 49.5							
7	34.2 82.1	34.1 80.8	34.0 78.6	33.6 75.5	32.8 71.2	28.7 59.9	26.3 54.8	23.4 47.3	20.3 42.0							
9	25.1 71.5	24.4 68.8	24.2 66.8	24.2 64.5	24.3 61.6	22.2 52.6	19.9 46.5	17.2 36.8	15.5 35.1							
12	15.0 55.3	13.9 51.4	14.0 50.3	14.6 49.3	15.4 47.2	15.5 43.6	12.9 35.8	10.5 25.4	9.6 26.3							
Height	Mean Peak kts kts															
Azimuth, deg 90	38	42	47	52	61	80	99	118	156							
Height	Mean Peak kts kts															
0	0.0 0.0	0.0 0.0	0.0 0.0	0.0 0.0	0.0 0.0	0.0 0.0	0.0 0.0	0.0 0.0	0.0 0.0	0.0 0.0	0.0 0.0	0.0 0.0	0.0 0.0	0.0 0.0	0.0 0.0	
1	47.4 83.6	56.8 92.7	63.1 100.4	64.3 103.2	60.8 102.1	50.9 92.7	44.5 84.6	39.5 77.9	32.8 65.3							
2	47.0 83.0	56.1 91.8	61.6 99.2	62.1 101.6	58.2 99.7	48.3 89.5	42.3 81.8	37.8 75.7	31.4 63.4							
3	46.3 82.1	54.8 90.6	59.1 97.4	58.5 99.2	54.1 96.1	44.5 84.9	39.1 77.7	35.1 72.3	29.3 60.5							
4	45.4 81.3	52.9 89.4	55.5 95.3	53.8 96.1	49.0 91.6	40.0 79.6	35.2 73.0	31.8 68.2	26.7 57.1							
5	44.1 80.4	50.4 88.1	51.1 93.0	48.5 92.5	43.4 86.5	35.1 74.1	31.0 68.1	28.3 63.9	23.8 53.5							
7	40.5 77.9	43.9 85.0	41.2 87.4	37.4 83.7	32.1 74.3	25.7 62.8	23.0 58.5	21.4 54.8	18.1 46.6							
9	35.8 73.9	36.0 79.9	31.0 78.9	26.4 71.2	21.1 58.7	17.2 50.8	16.0 48.7	15.2 45.5	13.1 40.3							
12	28.3 66.2	25.4 69.1	18.8 61.9	13.8 49.5	10.1 38.7	8.9 36.4	8.9 35.0	8.6 32.0	7.6 32.2							
Height	Mean Peak kts kts															
Azimuth, deg 135	38	42	47	52	61	80	99	118	156							
Height	Mean Peak kts kts															
0	0.0 0.0	0.0 0.0	0.0 0.0	0.0 0.0	0.0 0.0	0.0 0.0	0.0 0.0	0.0 0.0	0.0 0.0	0.0 0.0	0.0 0.0	0.0 0.0	0.0 0.0	0.0 0.0	0.0 0.0	
1	52.8 90.9	53.5 92.1	53.3 91.8	52.3 90.1	50.0 85.4	43.3 76.8	38.8 65.6	35.0 61.8	26.1 47.4							
2	51.1 89.6	51.7 90.2	51.3 89.2	50.2 87.4	47.8 82.6	41.6 74.3	37.2 63.0	33.7 59.5	21.1 45.3							
3	48.5 87.7	48.8 87.4	48.3 85.7	47.0 83.6	44.6 78.8	38.9 71.0	34.8 59.4	31.7 56.0	20.8 42.1							
4	45.0 85.2	45.1 84.1	44.4 81.7	43.0 79.4	40.8 74.7	35.8 67.2	31.9 55.2	29.3 51.9	20.4 38.4							
5	41.1 82.5	41.0 80.8	40.1 77.7	38.8 75.3	36.8 70.7	32.4 63.3	28.8 51.0	26.5 47.6	19.4 34.4							
7	33.1 76.3	32.7 73.8	31.7 70.0	30.7 67.2	29.3 63.0	25.8 55.4	22.7 43.1	21.0 39.3	17.6 27.2							
9	24.9 67.4	24.2 64.7	23.5 61.0	23.1 58.3	22.6 54.4	19.5 46.7	17.1 35.7	15.9 32.2	16.1 21.6							
12	16.6 54.6	15.8 52.0	15.7 48.9	16.0 46.7	16.0 43.1	12.4 34.5	11.0 26.7	10.0 23.6	32.8 21.6							
Height	Mean Peak kts kts															
Azimuth, deg 180	38	42	47	52	61	80	99	118	156							
Height	Mean Peak kts kts															
0	0.0 0.0	0.0 0.0	0.0 0.0	0.0 0.0	0.0 0.0	0.0 0.0	0.0 0.0	0.0 0.0	0.0 0.0	0.0 0.0	0.0 0.0	0.0 0.0	0.0 0.0	0.0 0.0	0.0 0.0	
1	56.4 90.8	56.2 92.5	55.2 93.4	54.1 93.4	52.0 90.8	48.0 84.2	45.8 79.4	42.9 74.7	31.3 62.2							
2	54.5 89.4	54.2 90.8	53.3 91.4	52.3 91.3	50.4 88.6	46.6 81.8	44.7 77.4	41.9 72.9	30.5 60.7							
3	51.5 87.2	51.2 88.3	50.5 88.6	49.6 88.3	47.9 85.4	44.6 78.3	43.0 74.6	40.3 70.2	29.3 58.4							
4	47.5 84.5	47.2 85.1	46.7 85.0	46.2 84.7	44.9 81.7	42.0 74.2	40.8 71.0	38.3 66.8	27.7 55.4							
5	43.1 81.3	42.9 81.7	42.6 81.2	42.4 80.8	41.5 77.9	39.1 69.9	38.3 67.3	36.0 63.1	25.9 51.9							
7	34.6 74.9	34.4 74.5	34.3 73.5	34.5 72.9	34.3 70.3	33.0 61.8	32.8 59.7	30.8 55.2	21.8 44.1							
9	25.7 65.5	25.5 64.9	25.7 64.1	26.1 63.8	26.7 62.0	26.9 53.9	26.9 52.1	25.3 47.1	17.6 35.9							
12	16.6 53.0	15.2 51.1	14.9 48.8	14.8 46.7	14.6 43.9	16.0 36.3	19.2 42.0	17.9 36.6	12.0 25.1							
Height	Mean Peak kts kts															
Azimuth, deg 210	38	42	47	52	61	80	99	118	156							
Height	Mean Peak kts kts															
0	0.0 0.0	0.0 0.0	0.0 0.0	0.0 0.0	0.0 0.0	0.0 0.0	0.0 0.0	0.0 0.0	0.0 0.0	0.0 0.0	0.0 0.0	0.0 0.0	0.0 0.0	0.0 0.0	0.0 0.0	
1	54.7 85.9	53.6 85.7	51.4 84.0	49.1 81.2	45.2 77.9	39.9 79.1	37.9 75.0</									

Azimuth, deg		225								10								118										
Height	Dist wrt AC, ft	38		42		47		52		61		80		99		118		156										
		Mean	Peak																									
0	0.0	0.0	0.0	0.0	0.0	0.0	0.0	0.0	0.0	0.0	0.0	0.0	0.0	0.0	0.0	0.0	0.0	0.0	0.0	0.0	0.0	0.0	0.0	0.0	0.0			
1	52.7	80.4	52.8	81.1	51.3	80.1	49.1	78.6	44.0	75.5	37.3	70.9	35.8	67.6	34.1	63.6	21.4	47.0										
2	50.4	78.7	50.1	78.7	48.4	77.0	46.1	74.9	41.0	71.2	34.9	66.8	34.0	64.7	32.7	61.4	20.6	45.0										
3	46.6	76.0	45.9	74.9	43.8	72.4	41.5	69.7	36.4	65.0	31.3	61.0	31.2	60.5	30.5	58.0	19.4	42.0										
4	41.3	72.4	40.0	70.2	37.9	66.7	35.7	63.5	31.1	58.0	27.1	54.4	28.0	55.7	27.9	54.1	17.8	38.3										
5	35.3	68.1	33.6	65.1	31.5	60.7	29.6	57.1	25.5	50.9	22.7	47.8	24.5	50.8	25.0	49.9	16.0	34.3										
7	23.2	58.0	21.3	54.2	19.6	49.2	18.2	45.0	15.6	38.4	14.9	35.8	17.8	41.4	19.1	41.7	12.2	26.4										
9	11.7	46.3	10.2	42.8	8.9	37.8	8.4	33.8	7.9	28.5	8.7	25.9	12.0	32.3	13.7	33.9	8.7	19.7										
12	2.4	34.3	1.6	31.3	0.9	27.0	1.0	23.7	1.9	19.6	3.0	15.5	5.8	20.7	7.4	23.4	4.6	12.7										
Azimuth, deg		240								38								42										
Height	Dist wrt AC, ft	Mean		Peak																								
0	0.0	0.0	0.0	0.0	0.0	0.0	0.0	0.0	0.0	0.0	0.0	0.0	0.0	0.0	0.0	0.0	0.0	0.0	0.0	0.0	0.0	0.0	0.0	0.0	0.0			
1	52.2	76.6	54.4	79.9	53.3	81.8	50.7	80.6	45.1	78.4	37.0	68.8	32.9	61.6	29.1	59.6	20.7	47.1										
2	50.2	75.1	51.6	78.1	50.1	79.2	47.2	77.1	41.6	73.6	34.3	64.2	30.8	58.1	27.5	56.4	19.7	45.0										
3	46.8	73.0	47.2	75.4	45.0	75.2	41.8	71.7	36.4	66.5	30.2	57.5	27.7	52.9	25.1	51.7	18.3	42.0										
4	41.9	70.3	41.1	71.5	38.2	69.6	35.1	64.9	30.3	58.0	25.4	49.8	24.0	47.0	22.1	46.1	16.5	38.2										
5	36.2	67.1	34.2	66.6	31.1	62.8	28.1	57.0	24.0	49.0	20.6	42.1	20.2	41.0	19.0	40.4	14.5	34.1										
7	23.8	58.2	20.7	54.2	17.6	47.8	15.3	40.9	12.9	32.7	12.2	28.9	13.3	30.8	13.1	30.3	10.4	26.0										
9	11.9	46.5	8.5	40.1	6.0	32.2	4.8	26.1	4.6	20.4	5.8	19.6	7.9	23.2	8.2	22.8	6.8	19.0										
12	1.4	32.2	-0.9	25.0	-2.2	17.5	-2.2	13.3	-1.3	11.1	0.8	11.8	2.9	15.3	3.4	20.4	2.9	11.3										
Azimuth, deg		270								38								42										
Height	Dist wrt AC, ft	Mean		Peak																								
0	0.0	0.0	0.0	0.0	0.0	0.0	0.0	0.0	0.0	0.0	0.0	0.0	0.0	0.0	0.0	0.0	0.0	0.0	0.0	0.0	0.0	0.0	0.0	0.0	0.0			
1	48.2	75.5	55.0	83.3	57.4	90.1	55.6	90.0	49.3	84.0	39.6	70.9	33.9	63.5	29.3	59.7	23.6	57.4										
2	46.9	74.2	53.1	82.2	54.6	87.9	52.1	86.6	45.6	79.2	36.5	66.1	31.6	59.8	27.7	56.8	22.7	55.5										
3	44.7	72.4	49.9	80.6	50.1	84.3	46.8	81.3	40.1	72.2	32.0	59.3	28.2	54.7	25.2	52.8	21.3	52.7										
4	41.6	70.6	45.4	78.4	44.0	79.2	39.9	74.0	33.5	63.6	26.9	51.7	24.3	49.1	22.3	48.1	19.6	49.2										
5	38.1	68.9	40.4	75.3	37.1	72.7	32.5	65.6	26.7	54.5	21.7	44.4	20.3	43.6	19.3	43.4	17.6	45.6										
7	30.2	64.2	29.2	65.8	23.1	56.8	18.6	47.3	14.6	37.6	12.9	32.3	13.3	34.7	13.6	34.9	13.8	38.8										
9	21.9	57.0	17.8	53.0	10.8	39.8	7.2	30.4	5.6	23.9	6.6	23.8	8.1	27.9	9.1	28.0	10.3	33.0										
12	12.0	44.5	6.4	35.8	1.1	23.0	-0.5	15.8	-0.5	12.5	0.3	12.0	2.3	13.4	2.6	12.2	3.7	12.9	4.2	13.4								
Azimuth, deg		300								38								42										
Height	Dist wrt AC, ft	Mean		Peak																								
0	0.0	0.0	0.0	0.0	0.0	0.0	0.0	0.0	0.0	0.0	0.0	0.0	0.0	0.0	0.0	0.0	0.0	0.0	0.0	0.0	0.0	0.0	0.0	0.0	0.0			
1	51.8	78.8	54.1	84.0	53.7	86.1	51.5	84.5	46.8	80.9	38.1	70.3	34.1	61.5	31.6	57.2	21.2	46.1										
2	49.9	77.7	51.5	82.3	50.6	83.3	48.1	80.7	43.5	76.0	35.5	65.8	31.9	57.9	29.9	54.3	20.3	44.1										
3	46.6	76.2	47.3	79.7	45.6	78.9	42.9	74.8	38.6	68.8	31.7	59.4	28.7	52.6	25.2	52.8	21.3	52.7										
4	42.0	74.0	41.5	75.8	39.1	72.7	36.5	67.3	32.7	60.2	27.2	52.1	24.9	46.6	24.2	45.1	19.6	49.2										
5	36.7	71.1	35.1	70.6	32.2	65.4	29.6	58.8	26.6	51.1	22.5	44.7	20.9	40.4	20.8	39.9	15.4	33.7										
7	25.3	61.7	22.3	56.9	19.1	48.9	17.1	41.6	15.5	34.1	14.3	31.9	13.6	29.2	14.4	30.1	11.6	26.2										
9	14.1	48.4	10.5	40.6	7.9	32.2	6.8	25.9	6.7	21.0	7.8	22.1	7.9	20.3	9.0	21.8	8.1	20.1										
12	2.1	28.4	1.1	24.5	0.5	20.2	0.8	17.0	1.6	15.3	3.3	15.0	3.7	12.5	4.1	12.7	3.6	9.7										
Azimuth, deg		330								38								42										
Height	Dist wrt AC, ft	Mean		Peak																								
0	0.0	0.0	0.0	0.0	0.0	0.0	0.0	0.0	0.0	0.0	0.0	0.0	0.0	0.0	0.0	0.0	0.0	0.0	0.0	0.0	0.0	0.0	0.0	0.0	0.0			
1	52.2	88.2	51.8	89.3	50.5	88.5	48.5	87.1	45.3	83.7	41.7	74.4	37.8	72.0	33.6	66.4	23.5	55.8										
2	50.1	85.7	49.4	86.2	47.9	85.2	45.9	83.6	43.0	79.9	39.7	71.1	36.3	69.6	32.3	64.4	22.8	54										

GW, lb

52600

AGL, ft

19

Azimuth, deg

0

	38	42	47	52	61	80	99	118	156
	Mean Peak kts kts								
0	0.0 0.0	0.0 0.0	0.0 0.0	0.0 0.0	0.0 0.0	0.0 0.0	0.0 0.0	0.0 0.0	0.0 0.0
1	63.6 93.7	63.7 94.6	63.4 94.9	62.7 94.7	61.1 94.1	56.6 91.3	54.5 87.6	52.4 83.4	37.3 67.0
2	62.4 92.8	62.5 93.4	62.2 93.6	61.4 93.4	59.9 92.8	55.6 89.8	53.6 86.1	51.5 82.0	36.6 65.8
3	60.6 91.4	60.7 91.8	60.3 91.9	59.5 91.6	58.0 90.8	54.1 87.5	52.2 83.8	50.0 79.8	35.5 64.0
4	58.0 89.6	57.9 89.7	57.6 89.6	56.9 89.3	55.6 88.3	52.2 84.4	50.3 80.9	48.1 77.1	34.1 61.6
5	55.3 87.9	55.1 87.6	54.7 87.4	54.1 87.0	52.8 85.6	49.8 81.0	48.0 77.4	45.8 74.0	32.3 58.8
7	49.2 84.2	48.8 83.4	48.3 82.9	47.7 81.9	46.6 79.7	44.4 73.4	42.7 69.9	40.5 67.3	28.3 52.4
9	41.3 78.5	40.9 77.5	40.4 76.9	40.0 75.8	39.5 72.8	38.1 65.2	36.6 61.9	34.3 60.0	23.8 45.5
12	32.1 72.5	31.7 71.2	31.3 70.2	31.0 68.7	30.6 64.0	29.9 55.7	28.2 52.3	25.6 50.3	17.4 36.3

Azimuth, deg

45

Dist wrt AC, ft Height	38	42	47	52	61	80	99	118	156
	Mean Peak kts kts								
0	0.0 0.0	0.0 0.0	0.0 0.0	0.0 0.0	0.0 0.0	0.0 0.0	0.0 0.0	0.0 0.0	0.0 0.0
1	56.7 94.8	58.6 97.7	59.1 98.7	58.5 98.2	56.2 96.9	51.9 92.5	48.0 87.7	45.5 85.1	36.9 68.4
2	55.4 93.2	57.0 96.0	57.2 96.8	56.4 96.1	54.2 94.5	50.2 90.1	46.6 85.5	44.2 82.8	36.0 66.8
3	53.3 90.9	54.4 93.6	54.2 94.0	53.3 93.0	51.2 90.8	47.6 86.5	44.3 82.1	42.3 79.3	34.5 64.5
4	50.2 88.0	50.8 90.3	50.2 90.4	49.3 89.1	47.6 86.3	44.2 82.1	41.4 77.9	39.8 75.0	32.7 61.6
5	46.8 84.9	46.9 86.7	46.0 86.4	45.0 84.8	43.4 81.2	40.4 77.1	38.1 73.2	37.0 70.3	30.5 58.2
7	39.3 78.3	38.6 78.9	37.4 77.5	36.3 75.1	34.9 70.2	32.3 66.3	30.9 63.0	30.8 60.6	25.7 50.9
9	30.6 69.2	29.5 68.3	28.3 66.0	27.3 63.1	26.2 58.1	24.2 54.9	23.6 52.2	24.4 51.1	20.8 43.2
12	20.8 57.3	19.8 55.3	18.8 52.2	18.1 49.0	16.8 43.2	15.1 40.4	14.9 37.6	16.0 37.8	14.1 32.5

Azimuth, deg

90

Dist wrt AC, ft Height	38	42	47	52	61	80	99	118	156
	Mean Peak kts kts								
0	0.0 0.0	0.0 0.0	0.0 0.0	0.0 0.0	0.0 0.0	0.0 0.0	0.0 0.0	0.0 0.0	0.0 0.0
1	48.7 82.8	55.9 93.4	60.3 101.6	60.5 103.0	55.7 97.4	44.3 83.8	37.6 79.4	34.0 74.2	27.0 57.2
2	48.0 82.1	54.8 92.5	58.8 100.2	58.4 101.0	53.2 94.3	41.9 80.1	35.7 76.0	32.5 71.3	26.0 55.2
3	46.8 81.2	53.1 91.2	56.2 98.0	55.1 97.9	49.3 89.6	38.2 74.7	32.9 71.0	30.3 67.0	24.4 52.2
4	45.1 80.1	50.6 89.5	52.6 94.9	50.5 93.6	44.3 84.0	33.7 68.3	29.5 65.0	27.6 61.8	22.4 48.6
5	43.1 79.0	47.7 87.4	48.3 91.2	45.3 88.5	38.9 77.6	28.9 61.8	25.7 58.7	24.6 56.4	20.2 44.7
7	38.2 75.9	40.7 81.7	38.4 81.1	33.9 75.6	27.7 63.9	19.6 49.6	18.5 46.6	18.8 46.1	15.6 36.9
9	32.2 70.5	32.0 72.5	27.0 67.2	22.0 59.1	17.1 48.8	11.7 39.6	12.2 36.3	13.7 37.8	11.5 30.3
12	23.8 61.1	20.6 58.0	14.0 46.6	9.4 37.2	6.3 31.5	4.2 30.5	5.8 25.4	8.2 28.8	6.8 22.6

Azimuth, deg

135

Dist wrt AC, ft Height	38	42	47	52	61	80	99	118	156
	Mean Peak kts kts								
0	0.0 0.0	0.0 0.0	0.0 0.0	0.0 0.0	0.0 0.0	0.0 0.0	0.0 0.0	0.0 0.0	0.0 0.0
1	49.1 80.8	50.2 83.9	50.2 87.0	49.2 88.6	46.5 88.6	41.9 80.0	41.3 77.4	41.2 75.5	32.7 57.4
2	47.3 78.9	48.1 81.7	48.1 84.5	47.1 85.8	44.6 85.5	40.4 77.3	39.9 75.1	39.9 73.6	25.3 55.9
3	44.3 76.2	45.0 78.7	45.0 80.9	44.0 81.8	41.7 81.0	38.1 73.4	37.8 71.7	38.0 70.8	24.9 53.6
4	40.4 73.2	40.9 75.1	40.8 76.6	40.1 77.0	38.3 75.8	35.2 68.7	35.1 67.7	35.5 67.3	24.3 50.7
5	36.4 70.3	36.6 71.8	36.6 72.6	36.1 72.2	34.6 70.6	32.1 63.9	32.1 63.4	32.6 63.4	22.7 47.6
7	28.3 64.9	28.5 65.3	28.5 64.3	28.3 62.9	27.2 60.8	25.9 55.2	26.0 55.3	26.6 55.4	19.9 41.3
9	20.4 58.6	20.4 57.5	20.6 55.4	20.7 53.4	20.4 51.3	20.1 47.6	20.4 48.1	20.8 47.6	16.2 35.2
12	12.7 49.7	12.8 47.4	13.0 44.4	13.2 42.1	13.1 40.0	14.0 39.3	14.0 40.1	13.6 38.0	37.9 26.7

Azimuth, deg

180

Dist wrt AC, ft Height	38	42	47	52	61	80	99	118	156
	Mean Peak kts kts								
0	0.0 0.0	0.0 0.0	0.0 0.0	0.0 0.0	0.0 0.0	0.0 0.0	0.0 0.0	0.0 0.0	0.0 0.0
1	61.8 95.2	60.8 94.0	59.4 92.7	57.8 91.2	55.3 89.4	51.5 83.0	49.0 78.5	47.0 76.3	32.7 63.3
2	60.4 94.0	59.4 92.6	58.0 91.1	56.4 89.4	54.0 87.3	50.2 80.9	47.8 76.5	45.9 74.5	31.9 61.7
3	58.2 92.2	57.2 90.5	55.8 88.7	54.2 86.6	51.9 84.2	48.1 77.6	45.9 73.4	44.1 71.6	30.6 59.2
4	55.1 89.7	54.1 87.6	52.8 85.4	51.3 83.1	49.2 80.2	45.5 73.5	43.5 69.7	41.9 68.0	29.0 55.9
5	51.8 86.9	50.8 84.6	49.5 81.9	48.1 79.3	46.1 75.9	42.5 68.9	40.7 65.6	39.2 64.0	27.0 52.0
7	44.7 80.5	43.7 77.5	42.4 74.3	41.1 71.1	39.2 66.4	35.8 59.3	34.4 56.8	33.1 55.3	22.5 43.6
9	36.1 71.9	35.1 68.7	34.1 65.2	33.0 61.7	31.3 56.3	28.6 49.6	27.7 47.8	26.6 46.6	17.8 35.0
12	26.3 60.1	25.4 57.3	24.5 53.7	23.3 49.9	21.6 44.0	19.6 38.3	18.8 35.9	17.5 34.6	11.3 23.6

Azimuth, deg

210

Dist wrt AC, ft Height	38	42	47	52	61	80	99	118	156
	Mean Peak kts kts								
0	0.0 0.0	0.0 0.0	0.0 0.0	0.0 0.0	0.0 0.0	0.0 0.0	0.0 0.0	0.0 0.0	0.0 0.0
1	50.0 82.3	48.9 82.6	47.2 81.7	45.6 79.3	42.9 74.1	39.5 68.7	37.5 65.0	36.3 62.8	24.5 47.9
2	48.1 80.4	46.8 80.3	45.0 78.9	43.4 76.3	40.9 71.2	37.8 66.2	36.1 62.9	35.1 60.9	23.8 46.4
3	45.0 77.5	43.6 76.7	41.7 74.8	40.1 71.9	37.7 66.9	35.3 62.4	33.8 59.7	33.1 57.9	22.5 44.2
4	40.8 73.3	39.2 71.7	37.4 69.3	35.9 66.5	33.9 61.8	32.1 57.8	31.0 55.7	30.6 54.1	21.0 41.4
5	36.3 68.9	34.6 66.7	32.9 63.9	31.5 60.9	29.7 56.2	28.7 52.9	27.8 51.3	27.8 49.9	19.1 38.3
7	27.1 58.9	25.6 56.2	24.1 53.4	23.0 50.4	21.5 45.5	21.6 43.1	21.3 41.8</		

Azimuth, deg		225		19		38		42		47		52		61		80		99		118		156	
Height	Dist wrt AC, ft	Mean	Peak																				
0	0.0	0.0	0.0	0.0	0.0	0.0	0.0	0.0	0.0	0.0	0.0	0.0	0.0	0.0	0.0	0.0	0.0	0.0	0.0	0.0	0.0	0.0	
1	48.3	77.9	48.6	80.3	47.6	81.2	46.0	80.5	43.2	77.9	39.3	69.8	35.1	62.3	33.3	59.2	25.0	47.6					
2	46.1	75.8	46.2	77.6	45.1	78.2	43.5	77.3	40.8	74.4	37.1	66.6	33.3	59.4	31.8	56.5	24.1	46.0					
3	42.7	72.5	42.4	73.4	41.2	73.6	39.6	72.5	37.1	69.4	33.8	62.1	30.6	55.0	29.5	52.6	22.6	43.6					
4	37.8	67.5	37.3	67.8	36.2	67.7	34.9	66.7	32.6	63.5	29.8	56.8	27.4	50.0	26.6	47.8	20.7	40.4					
5	32.7	62.1	32.0	61.8	30.9	61.5	29.8	60.5	27.9	57.4	25.6	51.4	23.9	44.9	23.5	42.9	18.5	36.9					
7	22.3	50.4	21.7	49.4	21.1	49.0	20.4	48.1	19.0	45.5	17.7	40.8	17.2	35.6	17.2	33.9	14.0	29.4					
9	12.1	38.5	11.8	37.4	11.8	37.1	11.7	36.5	11.4	34.6	11.0	31.0	11.4	27.8	11.6	26.2	9.6	22.1					
12	3.6	27.9	3.7	27.2	4.1	26.8	4.3	25.8	4.6	23.4	4.7	20.4	5.7	20.6	5.8	18.5	4.5	13.0					
Azimuth, deg		240		38		42		47		52		61		80		99		118		156			
Height	Dist wrt AC, ft	Mean	Peak																				
0	0.0	0.0	0.0	0.0	0.0	0.0	0.0	0.0	0.0	0.0	0.0	0.0	0.0	0.0	0.0	0.0	0.0	0.0	0.0	0.0	0.0	0.0	
1	49.0	78.2	51.3	83.9	51.3	87.0	49.7	86.8	46.0	82.7	38.0	67.8	31.5	53.3	29.4	47.8	21.7	43.0					
2	47.3	77.0	49.2	82.0	48.8	84.4	46.9	83.7	43.2	78.9	35.6	64.0	29.6	49.9	27.8	45.1	20.7	41.2					
3	44.6	75.0	45.8	78.9	44.8	80.3	42.7	78.8	39.0	73.3	31.9	58.6	26.8	45.0	25.3	41.0	19.2	38.3					
4	40.7	72.1	41.0	74.8	39.5	74.8	37.4	72.6	33.8	66.6	27.6	52.5	23.3	39.3	22.4	36.2	17.4	34.8					
5	36.2	68.5	35.8	69.8	34.0	68.6	31.9	66.0	28.4	59.8	23.1	46.4	19.7	33.6	19.2	31.3	15.3	30.9					
7	26.4	59.5	25.1	58.3	23.2	55.7	21.4	53.1	18.4	47.3	15.0	35.9	13.1	23.9	13.1	22.5	11.1	23.3					
9	16.3	48.5	14.6	45.8	13.1	43.1	12.0	41.1	10.2	36.4	8.6	27.3	7.7	17.3	8.0	15.9	7.3	16.5					
12	6.3	35.3	5.1	31.7	4.6	29.8	4.3	29.0	3.6	25.1	2.9	17.7	2.8	11.7	3.0	9.7	3.0	9.3					
Azimuth, deg		270		38		42		47		52		61		80		99		118		156			
Height	Dist wrt AC, ft	Mean	Peak																				
0	0.0	0.0	0.0	0.0	0.0	0.0	0.0	0.0	0.0	0.0	0.0	0.0	0.0	0.0	0.0	0.0	0.0	0.0	0.0	0.0	0.0	0.0	
1	49.1	76.0	56.0	84.8	58.7	91.6	57.0	92.6	51.0	86.3	40.8	72.5	34.9	63.7	31.7	58.2	23.0	46.5					
2	48.3	75.0	54.7	83.5	56.6	89.6	54.2	89.6	47.9	82.3	38.1	68.0	32.8	60.1	30.0	55.5	22.0	44.5					
3	46.9	73.5	52.4	81.5	53.0	86.2	49.9	84.9	43.2	75.9	34.1	61.5	29.6	54.8	27.5	51.5	20.4	41.6					
4	44.7	71.5	49.0	78.8	48.0	81.4	44.2	78.2	37.4	67.7	29.4	53.8	25.8	48.7	24.4	46.9	18.4	38.0					
5	42.1	69.3	44.9	75.6	42.4	75.5	37.8	70.3	31.2	58.6	24.4	45.8	21.8	42.4	21.2	42.1	16.2	34.3					
7	35.5	64.0	35.2	66.6	30.1	60.8	25.1	52.4	19.3	40.0	15.2	31.6	14.4	31.0	14.9	33.4	11.8	27.2					
9	27.2	56.4	23.9	54.0	17.3	43.2	13.0	33.7	9.3	24.6	8.1	21.3	8.5	22.1	9.6	25.7	8.0	21.2					
12	16.4	45.3	10.9	36.6	5.4	23.7	2.9	16.6	1.6	13.6	2.0	12.8	3.0	13.1	4.2	16.3	3.8	13.8					
Azimuth, deg		300		38		42		47		52		61		80		99		118		156			
Height	Dist wrt AC, ft	Mean	Peak																				
0	0.0	0.0	0.0	0.0	0.0	0.0	0.0	0.0	0.0	0.0	0.0	0.0	0.0	0.0	0.0	0.0	0.0	0.0	0.0	0.0	0.0	0.0	
1	52.3	80.1	55.4	86.6	55.6	90.3	54.0	90.1	49.5	83.9	40.4	71.2	35.4	66.5	32.6	62.1	22.1	47.9					
2	51.0	79.2	53.5	85.0	53.2	87.8	51.3	86.7	46.7	79.8	37.9	67.0	33.5	63.5	31.0	59.6	21.2	46.0					
3	48.7	77.8	50.4	82.5	49.4	83.7	47.1	81.3	42.4	73.6	34.1	60.9	30.6	59.2	28.6	56.0	19.8	43.1					
4	45.4	75.8	46.0	78.8	44.2	77.9	41.7	74.2	37.1	66.1	29.6	53.8	27.2	54.1	25.6	51.7	18.0	39.6					
5	41.5	73.1	41.1	74.1	38.5	71.1	35.7	66.3	31.3	57.9	24.8	46.7	23.6	49.0	22.5	47.3	16.0	35.8					
7	32.3	65.1	30.1	61.9	26.7	55.6	23.9	49.8	20.1	42.1	15.9	34.1	16.6	39.7	16.4	38.9	11.9	28.1					
9	21.8	53.5	18.5	46.8	15.2	39.5	12.9	34.4	10.5	28.6	8.9	24.4	10.7	31.4	11.1	31.0	8.1	21.2					
12	6.8	31.2	5.3	25.9	4.0	21.6	3.2	19.7	2.8	17.7	3.5	17.0	5.4	19.4	6.5	23.6	5.2	18.6					
Azimuth, deg		315		38		42		47		52		61		80		99		118		156			
Height	Dist wrt AC, ft	Mean	Peak																				
0	0.0	0.0	0.0	0.0	0.0	0.0	0.0	0.0	0.0	0.0	0.0	0.0	0.0	0.0	0.0	0.0	0.0	0.0	0.0	0.0	0.0	0.0	
1	51.8	82.5	52.5	86.3	51.5	88.0	50.0	87.5	46.3	83.3	40.1	74.8	35.5	70.5	32.8	65.3	23.7	52.2					
2	50.0	80.8	50.3	83.8	49.0	84.8	47.3	83.9	43.6	79.4	37.9	71.4	33.8	67.7	31.4	62.9	22.8	50.5					
3	47.0	78.0	46.7	79.9	45.0	79.8	43.2	78.3	39.6	73.6	34.6	66.3	31.3	63.5	29.3	59.2	21.4	47.8					
4	42.7	74.2	41.8	74.8	39.8	73.5	38.0	71.4	34.7	66.6	30.6	60.2	28.1	58.5	26.7	54.8	19.7	44.4					
5	37.8	69.8	36.4	69.0	34.2	66.5	32.4	63.7	29.4	59.1	26.3	53.7	24.7	53.1	23.8	50.0	17.7	40.8					
7	27.4	59.4	25.4	56.2	23.2	51.7	21.4	48.0	19.1	44.0	17.8	40.8	18.0	42.0	18.0	40.8	13.6	33.4					
9	16.9	46.9	14.8	41.9	12.8	36.5	11.4	33.2	10.3	30.4	10.5	29.2	11.9	31.5	12.6	32.7	9.7	26.7					
12	6.8	31.2	5.3	25.9	4.0	21.6	3.2	19.7	2.8	17.7	3.5	17.0	5.4	19.4	6.5	23.6	5.2	18.6					

Table M-9B Extension of V-22 Data Set, GW = 52,600 lb,
AGL = 19 ft

GW, lb	52600	AGL, ft	38													
Azimuth, deg	0	38	42	47	52	61	80	99	118	156						
Height		Mean Peak kts kts														
0	0.0	0.0	0.0	0.0	0.0	0.0	0.0	0.0	0.0	0.0	0.0	0.0	0.0	0.0	0.0	
1	60.5	90.6	60.0	92.4	59.3	94.2	58.6	95.1	57.4	95.5	54.6	97.4	52.8	93.0	49.7	84.7
2	59.5	89.9	58.9	91.6	58.2	93.2	57.4	94.0	56.2	94.3	53.5	96.0	51.8	91.7	48.8	83.5
3	57.8	88.8	57.1	90.3	56.4	91.8	55.6	92.3	54.3	92.5	51.8	93.7	50.1	89.7	47.3	81.5
4	55.3	87.1	54.6	88.5	53.8	89.7	53.0	90.1	51.8	90.1	49.5	90.9	48.0	87.1	45.4	79.0
5	52.6	85.2	51.9	86.4	51.0	87.3	50.2	87.5	48.8	87.3	46.8	87.6	45.5	84.1	43.1	76.2
7	46.0	79.2	45.2	80.1	44.4	80.5	43.4	80.4	42.0	80.2	40.6	80.2	39.7	77.1	37.8	69.5
9	38.4	72.9	37.8	73.4	37.0	73.4	36.2	73.1	34.9	72.6	34.0	72.4	33.7	70.0	32.1	62.5
12	29.1	64.2	28.6	64.3	28.0	63.7	27.3	62.9	25.9	61.8	25.4	61.7	25.8	59.9	24.2	52.3
Azimuth, deg	45	38	42	47	52	61	80	99	118	156						
Height	Dist wrt AC, ft	Mean Peak kts kts														
0	0.0	0.0	0.0	0.0	0.0	0.0	0.0	0.0	0.0	0.0	0.0	0.0	0.0	0.0	0.0	0.0
1	52.9	73.5	54.2	75.5	53.7	76.1	51.9	76.6	48.4	77.0	42.3	71.3	38.1	69.6	34.7	65.0
2	51.5	72.0	52.5	73.6	51.7	73.8	49.8	74.0	46.2	73.9	40.3	68.4	36.5	67.0	33.3	62.7
3	49.3	69.6	49.8	70.8	48.5	70.4	46.4	70.0	42.9	69.1	37.3	63.9	34.0	63.0	31.3	59.2
4	46.1	66.6	46.0	67.3	44.3	66.0	42.1	64.9	38.6	63.3	33.5	58.4	31.0	57.9	28.6	54.8
5	42.4	63.3	41.7	63.3	39.6	61.2	37.3	59.3	33.9	56.9	29.3	52.5	27.5	52.2	25.6	49.8
7	33.4	55.1	31.8	53.7	29.2	50.0	27.0	47.0	24.2	43.7	20.9	40.4	20.3	40.3	19.3	39.3
9	23.9	45.2	21.8	42.1	19.2	37.6	17.3	34.6	15.5	31.5	13.6	29.6	13.7	29.3	13.4	29.4
12	12.8	30.9	10.7	26.4	8.9	22.6	7.8	20.7	6.9	18.9	6.1	18.3	6.4	17.3	6.6	18.0
Azimuth, deg	90	38	42	47	52	61	80	99	118	156						
Height	Dist wrt AC, ft	Mean Peak kts kts														
0	0.0	0.0	0.0	0.0	0.0	0.0	0.0	0.0	0.0	0.0	0.0	0.0	0.0	0.0	0.0	0.0
1	50.4	69.5	57.1	76.9	60.4	82.3	59.6	83.3	54.7	80.2	44.8	71.1	39.4	66.0	35.5	59.5
2	49.8	68.7	56.1	76.0	58.8	80.9	57.6	81.2	52.3	77.2	42.6	67.7	37.5	62.8	33.9	56.7
3	48.7	67.4	54.4	74.5	56.2	78.5	54.3	77.8	48.7	72.6	39.3	62.3	34.6	57.9	31.5	52.5
4	47.0	65.8	51.9	72.4	52.5	75.3	49.9	73.5	44.0	67.0	35.2	55.8	31.1	52.0	28.5	47.3
5	44.9	64.1	48.7	70.0	48.1	71.6	44.7	68.5	38.7	60.9	30.6	48.6	27.2	45.6	25.2	41.7
7	39.0	60.0	40.4	63.8	37.2	62.1	32.9	56.9	27.5	48.0	21.4	34.7	19.4	33.4	18.3	31.0
9	32.1	55.1	31.0	55.8	25.9	50.3	21.5	43.6	17.3	34.7	13.5	23.8	12.6	23.3	12.2	22.2
12	21.5	46.5	18.0	42.7	12.7	33.8	9.5	26.5	7.2	20.1	5.9	14.8	5.6	13.4	5.7	13.7
Azimuth, deg	135	38	42	47	52	61	80	99	118	156						
Height	Dist wrt AC, ft	Mean Peak kts kts														
0	0.0	0.0	0.0	0.0	0.0	0.0	0.0	0.0	0.0	0.0	0.0	0.0	0.0	0.0	0.0	0.0
1	46.5	71.5	46.6	72.7	45.7	73.5	44.0	74.6	41.4	75.8	37.6	70.4	34.0	63.8	31.7	59.9
2	44.9	69.4	44.7	70.3	43.7	70.8	42.0	71.6	39.5	72.3	35.8	66.9	32.5	60.8	30.4	57.3
3	42.3	66.1	41.8	66.6	40.6	66.7	38.8	67.1	36.4	67.1	33.1	61.8	30.1	56.4	28.3	53.4
4	38.7	61.8	37.9	61.7	36.5	61.3	34.8	61.3	32.6	60.5	29.8	55.5	27.1	50.9	25.7	48.7
5	34.6	57.0	33.6	56.3	32.1	55.4	30.3	54.9	28.4	53.4	26.2	48.7	23.9	45.0	22.8	43.5
7	25.3	45.9	23.9	44.1	22.4	42.4	20.9	41.0	19.7	38.8	18.8	35.8	17.3	33.7	16.8	33.2
9	16.4	35.0	14.9	32.4	13.7	30.2	12.6	28.6	12.1	26.6	12.4	25.9	11.6	24.5	11.5	24.7
12	6.9	22.3	5.9	19.6	5.3	17.8	4.9	16.7	4.9	15.9	5.8	16.7	5.6	15.6	5.5	15.8
Azimuth, deg	180	38	42	47	52	61	80	99	118	156						
Height	Dist wrt AC, ft	Mean Peak kts kts														
0	0.0	0.0	0.0	0.0	0.0	0.0	0.0	0.0	0.0	0.0	0.0	0.0	0.0	0.0	0.0	0.0
1	57.7	90.1	57.5	90.0	56.9	89.1	56.5	87.9	55.9	87.1	54.1	84.8	51.4	80.2	46.0	74.0
2	56.5	88.8	56.2	88.7	55.7	87.7	55.2	86.5	54.7	85.7	52.9	83.3	50.3	78.8	45.0	72.7
3	54.5	86.8	54.2	86.6	53.7	85.5	53.2	84.3	52.7	83.6	51.2	81.0	48.6	76.5	43.5	70.7
4	51.8	84.2	51.5	83.7	51.0	82.7	50.6	81.6	50.2	80.9	48.9	78.2	46.4	73.7	41.5	68.1
5	48.8	81.3	48.5	80.6	47.9	79.6	47.6	78.6	47.3	78.0	46.2	75.0	43.8	70.5	39.2	65.2
7	41.5	73.7	41.1	72.9	40.7	72.0	40.6	71.4	40.7	71.5	40.0	68.1	37.8	63.5	33.8	58.4
9	33.8	66.0	33.6	65.1	33.3	64.4	33.4	64.1	33.8	64.5	33.5	61.1	31.5	56.1	28.0	51.1
12	24.7	55.5	24.5	54.5	24.7	53.8	24.7	53.7	25.0	54.0	24.4	50.4	22.7	45.0	20.0	40.6
Azimuth, deg	210	38	42	47	52	61	80	99	118	156						
Height	Dist wrt AC, ft	Mean Peak kts kts														
0	0.0	0.0	0.0	0.0	0.0	0.0	0.0	0.0	0.0	0.0	0.0	0.0	0.0	0.0	0.0	0.0
1	54.7	84.4	54.3	86.5	53.2	88.5	51.8	89.3	48.8	87.7	44.4	78.2	43.0	72.9	38.0	67.9
2	53.7	83.3	53.2	85.1	52.0	86.7	50.7	87.3	47.7	85.4	43.3	75.9	41.8	70.8	36.9	65.8
3	52.1	81.7	51.5	83.0	50.2	84.0	48.8	84.3	45.8	81.9	41.5	72.3	40.1	67.6	35.1	62.7
4	49.7	79.4	49.0	80.2	47.7	80.5	46.3	80.4	43.4	77.4	39.2	67.7	37.8	63.4	32.9	58.6
5	47.2	77.1	46.3	77.3	44.9	76.8	43.5	76.2	40.6	72.4	36.5	62.6	35.1	58.8	30.3	54.1
7	40.7	70.8	39.6	70.0	38.2	68.5	36.7	66.8	34.0	61.5	30.5	51.4	29.1	48.9	24.6	44.6
9	33.5	63.2	32.4	61.7	30.9	59.8	29.6	57.7	27.3	51.6	24.4	41.6	22.9	39.9	19.0	35.6
12	24.3	52.3	23.4	50.6	22.1	49.0	21.1	46.8	19.4	40.9	16.8	30.6	14.9	29.2	11.7	25.1

Table M-10A Extension of V-22 Data Set, GW = 52,600 lb,
AGL = 38 ft

Azimuth, deg	225	AGL, ft		38	42		47		52		61		80		99		118		156	
Dist wrt AC, ft		Mean	Peak	Mean	Peak	Mean	Peak	Mean	Peak	Mean	Peak	Mean	Peak	Mean	Peak	Mean	Peak	Mean	Peak	
Height		kts	kts	kts	kts	kts	kts	kts	kts	kts	kts	kts	kts	kts	kts	kts	kts	kts	kts	
0		0.0	0.0	0.0	0.0	0.0	0.0	0.0	0.0	0.0	0.0	0.0	0.0	0.0	0.0	0.0	0.0	0.0	0.0	
1		51.0	86.4	51.2	89.5	49.9	89.9	48.1	89.1	45.0	88.0	41.6	78.3	37.9	73.1	34.6	65.5	21.9	52.9	
2		50.1	85.3	50.1	87.9	48.7	87.9	46.8	86.9	43.7	85.3	40.3	75.9	36.8	70.7	33.5	63.4	21.3	51.4	
3		48.5	83.7	48.3	85.5	46.7	84.9	44.7	83.4	41.6	81.3	38.4	72.2	34.9	67.2	31.7	60.3	20.3	49.1	
4		46.2	81.5	45.8	82.5	44.0	81.1	41.9	79.1	38.9	76.3	35.9	67.7	32.6	62.8	29.4	56.4	19.1	46.2	
5		43.7	79.4	43.0	79.6	41.1	77.3	38.9	74.6	35.8	70.7	33.0	62.6	29.9	57.9	26.9	52.0	17.6	42.7	
7		37.3	74.3	36.3	73.2	34.2	69.4	32.0	65.2	28.9	58.8	26.7	52.0	24.0	47.7	21.3	42.8	14.3	35.3	
9		30.2	66.6	29.0	64.9	27.0	60.5	25.0	55.9	22.2	47.6	20.4	41.7	18.3	38.1	15.8	34.0	10.9	27.8	
12		20.8	55.1	19.6	53.1	18.2	49.1	16.9	44.6	14.4	35.1	12.6	29.1	11.4	26.5	9.2	22.9	6.5	18.4	

Azimuth, deg	240	38		42		47		52		61		80		99		118		156	
Dist wrt AC, ft		Mean	Peak																
Height		kts																	
0		0.0	0.0	0.0	0.0	0.0	0.0	0.0	0.0	0.0	0.0	0.0	0.0	0.0	0.0	0.0	0.0	0.0	0.0
1		50.6	88.0	52.7	90.9	53.4	92.0	52.6	91.4	50.7	89.4	45.4	84.7	41.6	76.2	37.8	69.7	24.8	52.5
2		50.0	87.3	51.8	89.7	52.2	90.5	51.1	89.5	48.9	87.0	43.8	81.9	40.1	73.8	36.5	67.7	24.1	51.1
3		48.8	86.3	50.2	88.1	50.1	88.1	48.7	86.4	46.2	83.3	41.2	77.7	37.8	70.0	34.6	64.5	23.0	48.9
4		47.0	85.0	48.0	86.0	47.3	85.0	45.6	82.5	42.7	78.7	38.0	72.4	35.0	65.3	32.1	60.6	21.5	46.1
5		44.9	83.9	45.3	84.0	44.1	81.8	41.9	78.3	38.8	73.5	34.5	66.5	31.8	60.1	29.3	56.1	19.8	43.0
7		39.2	80.7	38.5	78.9	36.3	74.4	33.6	69.1	30.2	62.2	26.9	53.8	25.0	49.0	23.4	46.4	16.1	36.3
9		32.4	74.7	30.8	71.5	28.1	65.4	25.3	59.3	22.0	50.8	19.8	41.5	18.7	38.3	17.6	37.0	12.5	30.0
12		22.5	63.7	20.6	60.1	18.1	53.9	15.8	47.3	13.0	37.2	11.5	26.9	11.2	25.7	10.5	25.1	7.7	21.6

Azimuth, deg	270	38		42		47		52		61		80		99		118		156	
Dist wrt AC, ft		Mean	Peak	Mean	Peak	Mean	Peak	Mean	Peak	Mean	Peak	Mean	Peak	Mean	Peak	Mean	Peak	Mean	Peak
Height		kts	kts	kts	kts	kts	kts	kts	kts	kts	kts	kts							
0		0.0	0.0	0.0	0.0	0.0	0.0	0.0	0.0	0.0	0.0	0.0	0.0	0.0	0.0	0.0	0.0	0.0	0.0
1		51.1	85.7	57.5	90.4	61.7	95.7	62.9	100.0	60.4	103.1	50.7	93.6	45.3	85.4	40.7	81.9	28.4	68.7
2		50.8	85.4	56.9	90.0	60.7	95.2	61.4	99.0	58.5	100.9	48.8	90.9	43.6	83.0	39.4	79.5	27.6	66.8
3		50.3	84.9	55.9	89.5	59.0	94.5	59.1	97.4	55.5	97.5	45.9	86.8	41.0	79.4	37.2	75.8	26.2	64.0
4		49.5	84.4	54.4	89.0	56.5	93.5	55.8	95.3	51.6	93.2	42.2	81.7	37.7	74.9	34.4	71.2	24.5	66.8
5		48.4	83.8	52.5	88.3	53.6	92.2	52.0	92.7	47.1	88.3	38.1	76.1	34.0	69.8	31.2	66.0	22.5	56.4
7		45.1	82.2	47.4	86.1	46.1	87.7	42.8	85.1	36.9	76.7	29.6	64.3	26.2	58.6	24.3	54.8	18.2	47.6
9		40.7	79.0	41.1	81.5	37.6	79.8	33.0	74.3	27.1	63.7	21.6	52.4	18.9	47.3	17.5	43.6	13.8	38.5
12		32.6	71.2	30.8	71.2	25.5	64.6	20.8	56.5	15.9	45.8	12.8	37.8	10.6	33.3	9.6	29.4	8.4	26.4

Azimuth, deg	300		38		42		47		52		61		80		99		118		156	
Dist wrt AC, ft	Mean	Peak																		
Height	kts																			
0	0.0	0.0	0.0	0.0	0.0	0.0	0.0	0.0	0.0	0.0	0.0	0.0	0.0	0.0	0.0	0.0	0.0	0.0	0.0	0.0
1	53.5	94.2	57.2	97.6	59.3	98.4	59.3	97.0	57.2	92.8	50.2	83.8	43.1	76.1	38.1	68.4	25.5	55.2		
2	53.0	93.4	56.5	96.4	58.2	96.8	58.0	95.3	55.6	90.4	48.5	81.1	41.7	73.7	36.8	66.3	24.7	53.3		
3	52.1	92.0	55.2	94.6	56.4	94.5	55.9	92.6	53.2	86.9	46.0	77.0	39.5	70.1	34.9	63.0	23.3	50.4		
4	50.7	90.3	53.2	92.2	53.9	91.6	53.0	89.2	50.0	82.6	42.7	72.2	36.8	65.8	32.4	59.0	21.7	46.7		
5	49.1	88.3	50.9	89.7	51.0	88.3	49.6	85.3	46.3	78.0	39.0	67.3	33.7	61.1	29.6	54.5	19.8	42.5		
7	44.4	83.3	45.0	83.3	43.7	80.2	41.5	75.9	37.8	67.8	31.2	57.6	27.1	51.8	23.7	45.4	15.7	33.9		
9	38.8	76.9	38.1	75.4	35.6	70.2	32.8	65.0	29.2	57.2	23.8	48.9	20.6	42.8	17.9	36.8	11.9	26.0		
12	30.1	65.9	28.2	62.3	24.9	55.1	22.0	49.5	19.0	43.8	15.3	38.1	12.9	31.5	11.1	26.7	7.3	17.1		

Azimuth, deg		315		38		42		47		52		61		80		99		118		156	
Distr wt AC, ft	Height	Mean	Peak	Mean	Peak	Mean	Peak	Mean	Peak	Mean	Peak	Mean	Peak	Mean	Peak	Mean	Peak	Mean	Peak	Mean	Peak
		kts	kts	kts	kts	kts	kts	kts	kts	kts	kts	kts	kts	kts	kts	kts	kts	kts	kts	kts	kts
0		0.0	0.0	0.0	0.0	0.0	0.0	0.0	0.0	0.0	0.0	0.0	0.0	0.0	0.0	0.0	0.0	0.0	0.0	0.0	0.0
1		53.0	100.9	54.4	103.6	54.8	103.7	54.4	102.3	52.9	98.8	48.4	87.8	42.8	79.1	37.0	70.7	26.2	58.2		
2		52.3	99.5	53.4	102.0	53.7	101.9	53.2	100.4	51.7	96.6	47.2	85.2	41.6	76.8	35.9	68.6	25.4	56.6		
3		50.9	97.3	51.9	99.5	51.9	99.2	51.3	97.5	49.7	93.3	45.2	81.3	39.8	73.1	34.2	65.5	24.2	54.1		
4		49.0	94.2	49.7	96.2	49.5	95.6	48.8	93.8	47.1	89.3	42.7	76.6	37.4	68.6	32.0	61.5	22.7	50.8		
5		46.7	90.8	47.2	92.5	46.8	91.7	45.9	89.8	44.1	84.8	39.8	71.6	34.7	63.8	29.6	57.1	20.9	47.2		
7		41.1	82.6	41.1	83.5	40.3	82.1	39.2	80.2	37.3	75.0	33.6	62.1	29.0	54.1	24.3	47.8	17.0	39.3		
9		34.9	73.1	34.5	73.2	33.3	71.4	32.2	69.9	30.4	65.8	27.4	54.5	23.4	46.0	19.2	39.3	13.1	31.6		
12		26.4	59.3	25.8	58.1	24.6	56.3	23.6	55.5	22.1	54.1	20.2	46.7	16.7	37.5	13.1	30.6	8.2	21.8		

Azimuth, deg	330		38		42		47		52		61		80		99		118		156	
Dist wrt AC, ft	Mean	Peak																		
Height	kts																			
0	0.0	0.0	0.0	0.0	0.0	0.0	0.0	0.0	0.0	0.0	0.0	0.0	0.0	0.0	0.0	0.0	0.0	0.0	0.0	0.0
1	54.9	97.1	54.4	98.8	53.4	98.6	52.7	97.5	51.2	94.8	48.3	87.2	44.1	80.4	40.4	71.2	28.7	57.1	28.0	54.4
2	53.8	95.3	53.2	96.9	52.2	96.5	51.4	95.4	50.1	92.7	47.2	85.1	43.1	78.6	39.4	69.7	28.0	54.4		
3	52.0	92.5	51.3	93.9	50.3	93.4	49.5	92.3	48.2	89.5	45.5	81.9	41.6	75.9	37.9	67.4	26.8	52.2		
4	49.4	88.8	48.6	89.7	47.6	89.1	47.0	88.2	45.9	85.6	43.3	78.1	39.7	72.6	35.9	64.6	25.3	49.4		
5	46.7	84.7	45.9	85.3	44.9	84.6	44.3	83.8	43.3	81.3	40.7	74.0	37.5	69.0	33.7	61.5	23.5	46.1		
7	40.2	75.1	39.3	75.0	38.4	74.2	37.9	73.6	37.3	71.5	35.1	65.6	32.6	61.7	28.7	54.6	19.5	39.1		
9	33.2	65.2	32.6	64.9	31.9	64.1	31.5	63.6	31.3	62.4	29.5	58.1	27.3	54.5	23.7	47.5	15.6	32.3		
12	24.8	53.1	24.7	53.3	24.4	52.8	24.1	52.4	24.0	52.4	22.5	48.8	20.5	44.8	17.2	37.7	10.4	23.6		

Table M-10B Extension of V-22 Data Set, GW = 52,000 lb,
AGL = 38 ft

GW, lb	52600	AGL, ft	57	Azimuth, deg 0													
				38	42	47	52	61	80	99	118	156					
		Mean Peak kts kts															
0	0.0	0.0 0.0	0.0 0.0	0.0 0.0	0.0 0.0	0.0 0.0	0.0 0.0	0.0 0.0	0.0 0.0	0.0 0.0	0.0 0.0	0.0 0.0	0.0 0.0	0.0 0.0	0.0 0.0		
1	54.9	91.0	54.6 92.3	54.0 92.9	53.4 92.6	52.0 90.9	48.5 85.2	43.6 77.0	38.2 69.0	16.0 34.6	37.5 67.5	15.7 33.8	36.3 65.3	15.2 32.6	32.8 58.9	13.7 29.2	
2	54.3	90.0	53.9 91.2	53.3 91.8	52.6 91.4	51.2 89.5	47.6 83.8	42.8 75.5	39.7 69.9	34.7 62.3	14.5 31.0	37.6 66.2	32.8 58.9	13.7 29.2	28.4 50.9	11.9 25.2	
3	53.2	88.4	52.8 89.5	52.1 90.1	51.3 89.6	49.8 87.4	46.2 81.5	41.5 73.0	36.3 65.3	34.7 62.3	14.5 31.0	37.6 66.2	32.8 58.9	13.7 29.2	23.7 42.9	9.9 21.4	
4	51.7	86.5	51.2 87.5	50.4 87.9	49.6 87.2	48.0 84.7	44.4 78.6	39.7 69.9	34.7 62.3	14.5 31.0	37.6 66.2	32.8 58.9	13.7 29.2	23.7 42.9	9.9 21.4	16.9 32.1	
5	49.9	84.6	49.4 85.3	48.5 85.5	47.6 84.5	45.9 81.7	42.2 75.3	37.6 66.2	32.8 58.9	13.7 29.2	23.7 42.9	9.9 21.4	16.9 32.1	7.3 16.6			
7	44.5	79.6	44.0 79.6	43.0 78.9	42.1 77.6	40.4 74.2	37.0 67.6	32.7 57.7	28.4 50.9	11.9 25.2	23.7 42.9	9.9 21.4	16.9 32.1	7.3 16.6			
9	39.5	75.5	38.9 74.7	37.9 73.1	36.8 71.1	35.0 67.3	31.6 60.3	27.7 49.7	23.7 42.9	9.9 21.4	16.9 32.1	7.3 16.6					
12	32.0	68.5	31.3 67.2	30.3 64.7	29.3 61.8	27.3 57.2	23.9 50.5	20.4 40.4	16.9 32.1	7.3 16.6							
Azimuth, deg	45																
Dist wrt AC, ft		38	42	47	52	61	80	99	118	156							
Height		Mean Peak kts kts															
0	0.0	0.0 0.0	0.0 0.0	0.0 0.0	0.0 0.0	0.0 0.0	0.0 0.0	0.0 0.0	0.0 0.0	0.0 0.0	0.0 0.0	0.0 0.0	0.0 0.0	0.0 0.0	0.0 0.0	0.0 0.0	
1	48.0	82.8	49.6 85.3	49.6 86.7	48.6 86.8	46.0 85.1	40.3 74.2	36.8 62.5	32.7 57.4	13.2 34.4	31.7 55.5	12.9 33.4	30.1 52.7	12.4 31.9	28.6 58.9	11.8 29.9	
2	47.2	81.7	48.6 83.9	48.4 85.0	47.4 84.9	44.7 82.9	39.1 71.8	35.6 60.4	31.7 55.5	12.9 33.4	30.1 52.7	12.4 31.9	28.6 58.9	11.8 29.9	25.7 45.2	11.0 27.7	
3	45.9	79.8	47.0 81.6	46.6 82.4	45.5 81.9	42.8 79.5	37.2 68.1	33.7 57.1	30.1 52.7	12.4 31.9	28.6 58.9	11.8 29.9	25.7 45.2	11.0 27.7	22.6 39.5	20.4 36.9	9.3 23.0
4	44.1	77.5	44.9 78.8	44.3 79.0	43.1 78.1	40.3 75.1	34.7 63.3	31.3 53.1	28.1 49.1	11.8 29.9	25.7 45.2	11.0 27.7	22.6 39.5	20.4 36.9	15.2 29.4	7.6 18.6	
5	41.9	74.9	42.4 75.6	41.6 75.2	40.2 73.8	37.4 70.1	31.9 58.0	28.6 48.6	25.7 45.2	11.0 27.7	22.6 39.5	20.4 36.9	15.2 29.4	7.6 18.6	5.2 13.3		
7	36.3	68.3	36.0 68.0	34.7 66.4	33.3 64.0	30.4 58.3	25.6 47.0	22.6 39.5	20.4 36.9	9.3 23.0	22.6 39.5	20.4 36.9	15.2 29.4	7.6 18.6			
9	30.9	63.0	30.1 61.8	28.4 59.0	26.9 55.4	23.9 47.2	19.5 37.6	16.9 31.7	15.2 29.4	7.6 18.6	22.6 39.5	20.4 36.9	15.2 29.4	7.6 18.6			
12	23.3	55.8	21.9 53.7	20.0 49.1	18.3 43.7	15.3 33.3	12.0 27.1	9.8 22.8	8.7 20.6	5.2 13.3	22.6 39.5	20.4 36.9	15.2 29.4	7.6 18.6			
Azimuth, deg	90																
Dist wrt AC, ft		38	42	47	52	61	80	99	118	156							
Height		Mean Peak kts kts															
0	0.0	0.0 0.0	0.0 0.0	0.0 0.0	0.0 0.0	0.0 0.0	0.0 0.0	0.0 0.0	0.0 0.0	0.0 0.0	0.0 0.0	0.0 0.0	0.0 0.0	0.0 0.0	0.0 0.0	0.0 0.0	
1	44.9	78.7	49.1 85.8	51.1 89.9	50.8 90.4	47.2 87.9	40.4 82.6	36.8 73.8	31.5 64.3	12.1 35.6	30.4 62.2	11.7 34.7	28.6 58.9	11.2 33.1	23.7 49.9	9.7 28.8	
2	44.1	77.5	48.0 84.3	49.8 88.2	49.2 88.4	45.5 85.5	38.8 79.7	35.4 71.2	30.4 62.2	11.7 34.7	32.2 55.5	12.9 33.4	30.1 52.7	12.4 31.9	28.6 58.9	11.8 29.9	
3	42.7	75.5	46.2 82.0	47.6 85.4	46.8 85.3	42.9 81.7	36.4 75.3	33.2 67.2	28.6 58.9	11.2 33.1	30.1 52.7	12.4 31.9	28.6 58.9	11.8 29.9	25.7 45.2	11.0 27.7	
4	40.8	73.3	43.8 79.2	44.6 82.1	43.5 81.4	39.5 76.9	33.3 69.6	30.5 62.2	26.4 54.7	10.5 31.1	28.6 58.9	11.8 29.9	25.7 45.2	11.0 27.7	22.6 39.5	20.4 36.9	9.3 23.0
5	38.5	70.9	40.9 76.3	41.2 78.5	39.7 77.0	35.5 71.4	29.8 63.1	27.3 56.4	23.7 49.9	9.7 28.8	28.6 58.9	11.8 29.9	25.7 45.2	11.0 27.7	22.6 39.5	20.4 36.9	
7	32.9	66.4	34.1 70.2	33.1 70.2	30.7 66.6	26.6 59.1	22.2 49.4	20.6 44.0	17.9 39.5	7.9 23.6	22.6 39.5	20.4 36.9	15.2 29.4	12.4 26.6	10.5 24.0		
9	31.3	67.5	30.5 67.1	29.2 65.9	27.5 63.7	24.3 58.0	20.2 47.0	18.1 44.1	15.2 37.3	15.9 21.7	22.6 39.5	20.4 36.9	15.2 29.4	12.4 26.6	10.5 24.0		
12	23.2	61.5	21.9 59.6	20.3 57.5	18.7 54.7	15.8 48.5	12.2 35.2	11.6 34.7	9.4 27.6	3.6 15.4	22.6 39.5	20.4 36.9	15.2 29.4	12.4 26.6	10.5 24.0		
Azimuth, deg	135																
Dist wrt AC, ft		38	42	47	52	61	80	99	118	156							
Height		Mean Peak kts kts															
0	0.0	0.0 0.0	0.0 0.0	0.0 0.0	0.0 0.0	0.0 0.0	0.0 0.0	0.0 0.0	0.0 0.0	0.0 0.0	0.0 0.0	0.0 0.0	0.0 0.0	0.0 0.0	0.0 0.0	0.0 0.0	
1	49.9	84.2	51.7 86.9	52.4 89.2	51.5 89.1	48.2 86.7	42.2 77.1	36.4 70.4	30.0 62.3	12.3 38.3	35.3 68.8	29.1 60.8	21.1 37.4	18.0 35.9	15.7 33.1	12.9 33.4	
2	49.1	83.0	50.7 85.6	51.1 87.6	50.2 87.3	46.9 84.7	40.9 75.1	35.3 68.8	30.1 62.3	12.3 38.3	32.2 55.5	26.0 55.5	20.4 34.0	18.0 31.8	15.7 33.1	12.9 33.4	
3	47.6	81.3	49.0 83.6	49.2 85.1	48.0 84.6	44.7 81.7	38.8 72.2	33.5 66.2	27.8 58.4	20.8 35.9	32.2 55.5	26.0 55.5	20.4 34.0	18.0 31.8	15.7 33.1	12.9 33.4	
4	45.6	79.2	46.6 81.1	46.6 82.2	45.3 81.3	41.8 78.0	36.2 68.5	31.4 62.9	26.0 55.5	18.0 31.8	32.2 55.5	26.0 55.5	20.4 34.0	18.0 31.8	15.7 33.1	12.9 33.4	
5	43.3	76.9	43.9 78.5	43.5 79.0	42.1 78.1	38.6 74.0	33.2 64.5	28.8 59.3	24.0 52.1	18.0 31.8	32.2 55.5	26.0 55.5	20.4 34.0	18.0 31.8	15.7 33.1	12.9 33.4	
7	37.1	71.7	37.0 72.4	36.0 71.9	34.4 70.2	31.1 65.4	26.6 55.8	23.4 51.5	19.6 44.6	17.7 26.7	32.2 55.5	26.0 55.5	20.4 34.0	18.0 31.8	15.7 33.1	12.9 33.4	
9	41.3	72.7	41.2 72.4	41.0 71.8	41.0 70.7	41.0 68.8	39.7 68.1	36.2 64.6	30.1 55.3	12.1 23.9	32.2 55.5	26.0 55.5	20.4 34.0	18.0 31.8	15.7 33.1	12.9 33.4	
12	33.5	61.4	33.3 60.8	33.1 59.9	33.2 59.2	33.5 58.6	32.9 59.5	29.2 54.8	23.9 46.6	10.0 0.0	32.2 55.5	26.0 55.5	20.4 34.0	18.0 31.8	15.7 33.1	12.9 33.4	
Azimuth, deg	210																
Dist wrt AC, ft		38	42	47	52	61	80	99	118	156							
Height		Mean Peak kts kts															
0	0.0	0.0 0.0	0.0 0.0	0.0 0.0	0.0 0.0	0.0 0.0	0.0 0.0	0.0 0.0	0.0 0.0	0.0 0.0	0.0 0.0	0.0 0.0	0.0 0.0	0.0 0.0	0.0 0.0	0.0 0.0	
1	49.9	91.8	49.8 94.1	49.2 95.9	48.2 97.2	46.4 97.0	42.2 93.0	38.5 83.4	32.1 68.4	11.1 30.6	38.5 83.4	32.1 68.4	11.1 30.6	38.5 83.4	32.1 68.4	11.1 30.6	
2	49.1	91.0	48.9 93.2	48.2 94.9	47.2 96.1	45.3 95.7	41.2 91.4	37.6 81.7	31.3 66.6	10.9 29.7	38.5 83.4	32.1 68.4	11.1 30.6	38.5 83.4	32.1 68.4	11.1 30.6	
3	47.6	89.8	47.4 91.8	46.6 93.4	45.6 94.4	43.6 93.6	39.6 89.0	36.2 79.0	30.1 63.8	10.5 28.4	38.5 83.4	32.1 68.4	11.1 30.6	38.5 83.4	32.1 68.4	11.1 30.6	
4	45.7	88.2	45.3 90.0	44.5 91.4	43.5 92.1	41.4 91.0	37.6 85.8	34.5 75.5	28.5 60.3	10.0 26.8	38.5 83.4	32.1 68.4	11.1 30.6	38.5 83.4	32.1 68.4		

Azimuth, deg		225		AGL, ft		57		38		42		47		52		61		80		99		118		156		
Height	Dist wrt AC, ft	Mean	Peak	Mean	Peak	Mean	Peak	Mean	Peak	Mean	Peak	Mean	Peak	Mean	Peak	Mean	Peak	Mean	Peak	Mean	Peak	Mean	Peak	Mean	Peak	
0	0.0	0.0	0.0	0.0	0.0	0.0	0.0	0.0	0.0	0.0	0.0	0.0	0.0	0.0	0.0	0.0	0.0	0.0	0.0	0.0	0.0	0.0	0.0	0.0	0.0	
1	46.1	86.2	46.8	89.1	46.4	91.8	45.3	91.7	43.6	89.0	41.3	81.1	37.4	71.1	30.3	60.1	10.1	30.0								
2	45.2	85.1	45.8	87.8	45.3	90.1	44.0	89.6	42.3	86.7	40.0	78.8	36.3	69.3	29.5	58.4	9.9	29.3								
3	43.8	83.4	44.2	85.6	43.4	87.3	42.0	86.4	40.2	83.0	38.0	75.4	34.5	66.5	28.2	55.8	9.5	28.1								
4	41.8	81.2	41.9	82.8	40.9	83.7	39.4	82.2	37.4	78.4	35.5	71.0	32.2	62.9	26.4	52.6	9.1	26.5								
5	39.5	78.7	39.3	79.6	38.1	79.6	36.3	77.4	34.2	73.1	32.5	66.1	29.5	58.9	24.4	49.0	8.6	24.7								
7	33.2	72.0	32.5	71.3	30.8	69.2	29.0	65.8	27.0	61.0	25.9	55.3	23.8	50.2	19.9	41.2	7.4	20.6								
9	27.3	65.8	26.0	63.3	24.1	59.5	22.2	54.9	20.4	49.7	19.3	45.0	18.1	41.5	15.2	33.7	6.2	16.6								
12	18.9	55.3	17.3	51.2	15.4	45.4	13.7	39.9	12.1	35.3	11.0	31.7	10.6	29.0	8.9	23.6	4.4	11.8								
Azimuth, deg		240		38		42		47		52		61		80		99		118		156						
Height	Dist wrt AC, ft	Mean	Peak	Mean	Peak	Mean	Peak	Mean	Peak	Mean	Peak	Mean	Peak	Mean	Peak	Mean	Peak	Mean	Peak	Mean	Peak	Mean	Peak			
0	0.0	0.0	0.0	0.0	0.0	0.0	0.0	0.0	0.0	0.0	0.0	0.0	0.0	0.0	0.0	0.0	0.0	0.0	0.0	0.0	0.0	0.0	0.0	0.0	0.0	
1	43.5	79.4	46.2	83.6	47.4	86.2	47.4	86.6	45.9	82.9	42.4	73.1	37.3	63.5	32.3	56.0	13.5	32.5								
2	42.7	78.1	45.1	81.9	46.1	84.2	46.0	84.3	44.5	80.3	41.0	70.6	36.1	61.3	31.2	54.2	13.1	31.6								
3	41.3	75.9	43.4	79.3	44.1	81.1	43.8	80.6	42.2	76.2	38.8	66.6	34.1	57.8	29.5	51.4	12.6	30.1								
4	39.3	73.0	41.0	75.8	41.3	77.0	40.9	75.9	39.2	70.9	35.9	61.6	31.6	53.4	27.3	47.8	11.8	28.1								
5	37.0	70.1	38.2	72.1	38.2	72.2	37.5	70.3	35.8	64.7	32.6	55.9	28.6	48.5	24.7	43.7	11.0	25.8								
7	30.8	63.0	31.0	63.0	30.2	60.7	29.3	57.0	27.7	50.4	25.1	43.4	22.2	38.3	19.0	34.9	9.0	20.6								
9	24.8	56.8	24.1	54.3	22.8	49.2	21.8	43.8	20.2	37.2	17.9	32.5	16.1	29.3	13.7	26.6	7.1	15.6								
12	16.3	47.6	14.8	42.1	13.2	34.0	12.1	28.0	11.0	23.0	9.1	20.1	8.6	18.8	7.1	16.3	4.5	9.9								
Azimuth, deg		270		38		42		47		52		61		80		99		118		156						
Height	Dist wrt AC, ft	Mean	Peak	Mean	Peak	Mean	Peak	Mean	Peak	Mean	Peak	Mean	Peak	Mean	Peak	Mean	Peak	Mean	Peak	Mean	Peak	Mean	Peak			
0	0.0	0.0	0.0	0.0	0.0	0.0	0.0	0.0	0.0	0.0	0.0	0.0	0.0	0.0	0.0	0.0	0.0	0.0	0.0	0.0	0.0	0.0	0.0	0.0	0.0	
1	44.3	73.0	51.3	80.6	55.8	86.8	56.2	89.1	51.9	87.3	41.9	76.5	36.7	70.2	31.9	61.6	16.1	39.5								
2	43.9	72.0	50.6	79.2	54.7	84.9	54.7	86.9	50.3	84.6	40.3	73.8	35.3	67.7	30.7	59.4	15.6	38.1								
3	43.1	70.4	49.3	77.1	52.7	81.9	52.3	83.3	47.6	80.5	37.9	69.6	33.2	63.9	28.8	56.0	14.7	35.8								
4	41.9	68.4	47.4	74.4	50.1	78.4	49.2	79.1	44.2	75.3	34.9	64.4	30.4	59.2	26.4	51.7	13.6	33.0								
5	40.3	66.2	45.1	71.5	46.9	74.6	45.4	74.4	40.3	69.6	31.4	58.7	27.3	53.9	23.7	46.9	12.3	29.8								
7	35.8	61.0	38.8	65.2	38.6	66.4	36.1	64.0	31.2	56.7	23.9	46.8	20.5	42.8	17.9	37.0	9.4	23.0								
9	31.2	57.0	32.5	60.2	30.7	59.5	27.6	54.7	22.9	45.2	17.1	36.4	14.3	32.8	12.5	28.3	6.7	16.9								
12	23.9	51.9	23.2	52.8	20.0	47.9	16.6	40.2	12.7	30.0	9.1	23.6	7.0	20.9	6.0	18.1	3.5	10.2								
Azimuth, deg		300		38		42		47		52		61		80		99		118		156						
Height	Dist wrt AC, ft	Mean	Peak	Mean	Peak	Mean	Peak	Mean	Peak	Mean	Peak	Mean	Peak	Mean	Peak	Mean	Peak	Mean	Peak	Mean	Peak	Mean	Peak			
0	0.0	0.0	0.0	0.0	0.0	0.0	0.0	0.0	0.0	0.0	0.0	0.0	0.0	0.0	0.0	0.0	0.0	0.0	0.0	0.0	0.0	0.0	0.0	0.0	0.0	
1	47.1	77.1	52.2	82.8	55.3	87.9	55.3	90.8	52.4	88.8	46.5	78.7	42.8	73.6	37.9	65.9	17.2	36.3								
2	46.6	76.3	51.4	81.8	54.1	86.7	53.9	89.1	50.9	86.6	44.9	76.1	41.3	71.1	36.6	63.9	16.6	35.1								
3	45.7	74.9	50.1	80.3	52.2	84.7	51.6	86.3	48.3	83.0	42.4	72.2	38.9	67.3	34.6	60.8	15.7	33.2								
4	44.4	73.2	48.1	78.3	49.6	82.1	48.6	82.7	45.0	79.3	39.2	67.3	35.9	62.5	32.0	56.9	14.5	30.8								
5	42.7	71.3	45.7	76.1	46.4	78.8	44.9	78.3	41.1	72.9	35.5	61.7	32.5	57.1	29.0	52.4	13.2	28.1								
7	37.5	66.2	38.9	69.6	37.9	69.6	35.7	66.9	32.1	60.3	27.3	49.5	25.0	45.4	22.5	42.7	10.4	22.4								
9	32.4	61.5	32.1	62.5	29.7	60.0	27.1	56.1	23.9	49.0	19.8	38.5	17.9	34.7	16.2	33.3	7.7	17.0								
12	24.0	52.8	20.8	44.2	18.4	38.5	16.7	35.1	14.3	31.4	11.7	26.1	10.9	25.8	9.7	24.3	5.4	11.2								
Azimuth, deg		330		38		42		47		52		61		80		99		118		156						
Height	Dist wrt AC, ft	Mean	Peak	Mean	Peak	Mean	Peak	Mean	Peak	Mean	Peak	Mean	Peak	Mean	Peak	Mean	Peak	Mean	Peak	Mean	Peak	Mean	Peak			
0	0.0	0.0	0.0	0.0	0.0	0.0	0.0	0.0	0.0	0.0	0.0	0.0	0.0	0.0	0.0	0.0	0.0	0.0	0.0	0.0	0.0	0.0	0.0	0.0	0.0	
1	49.2	87.2	50.1	88.8	50.0	89.0	49.1	87.2	47.9	82.4	44.5	74.9	41.0	68.8	37.0	64.1	17.0	34.9								
2	48.5	86.1	49.2	87.4	48.9	87.3	47.9	85.2	46.6	80.2	43.3	73.0	39.9	67.2	36.1	62.7	16.7	34.3								
3	47.2	84.3	47.6	85.1	47.2	84.5	46.1	82.1	44.6	76.9	41.4	70.0	38.3	64.8	34.6	60.5	16.1	33.2								
4	45.4	81.8	45.5	82.1	44.8	80.8	43.6	78.0	42.1	72.5	39.0	66.2	36.2	61.6	32.7	57.7	15.4	31.8								
5	43.2	78.9	42.9	78.6	42.1	76.6	40.8																			

GW, lb	52600	AGL, ft	76	38	42	47	52	61	80	99	118	156	
Azimuth, deg	0			Mean Peak kts kts									
Height	0	0.0	0.0	0.0	0.0	0.0	0.0	0.0	0.0	0.0	0.0	0.0	0.0
	1	54.6	78.6	54.4	79.1	54.1	80.0	53.5	80.2	51.5	79.0	47.8	77.4
	2	54.0	77.7	53.7	78.0	53.3	78.9	52.6	79.1	50.7	77.9	47.0	76.2
	3	52.9	76.2	52.6	76.3	52.0	77.1	51.3	77.2	49.3	76.0	45.6	74.3
	4	51.4	74.4	51.0	74.2	50.3	74.8	49.4	74.9	47.4	73.7	43.8	71.8
	5	49.6	72.2	49.0	71.8	48.2	72.1	47.2	72.1	45.2	70.9	41.7	68.8
	7	44.1	66.3	43.3	65.3	42.3	65.2	41.4	65.2	39.5	63.9	36.4	61.7
	9	38.8	60.9	37.8	59.5	36.8	58.9	35.8	58.5	33.9	57.0	30.8	54.1
	12	29.7	51.0	28.8	49.5	27.9	48.5	27.0	47.8	25.2	46.4	22.5	42.5
Azimuth, deg	45			38	42	47	52	61	80	99	118	156	
Dist wrt AC, ft				Mean Peak kts kts									
Height	0	0.0	0.0	0.0	0.0	0.0	0.0	0.0	0.0	0.0	0.0	0.0	0.0
	1	50.7	79.5	53.5	82.8	55.0	84.5	54.8	84.7	52.3	84.5	45.8	82.0
	2	50.2	78.7	52.9	81.8	54.2	83.4	53.9	83.4	51.3	82.9	44.8	80.1
	3	49.4	77.4	51.8	80.3	52.9	81.7	52.4	81.5	49.7	80.5	43.2	77.2
	4	48.2	75.8	50.2	78.4	51.1	79.5	50.4	79.0	47.6	77.5	41.1	73.5
	5	46.7	73.9	48.4	76.2	48.9	76.9	48.0	76.2	45.1	74.1	38.6	69.2
	7	42.2	69.1	43.1	70.7	43.0	70.6	41.7	69.3	38.7	66.1	32.7	59.6
	9	37.8	64.9	37.9	65.6	37.1	64.3	35.5	62.3	32.3	58.4	26.7	50.5
	12	30.1	58.1	29.3	57.0	27.5	53.8	25.7	51.2	22.8	46.6	18.4	38.5
Azimuth, deg	90			38	42	47	52	61	80	99	118	156	
Dist wrt AC, ft				Mean Peak kts kts									
Height	0	0.0	0.0	0.0	0.0	0.0	0.0	0.0	0.0	0.0	0.0	0.0	0.0
	1	41.2	67.0	47.1	73.0	52.0	79.1	54.2	83.1	53.5	85.1	46.7	83.3
	2	40.8	66.3	46.5	72.2	51.1	78.2	53.1	81.9	52.1	83.4	45.3	81.1
	3	40.1	65.3	45.5	71.0	49.6	76.7	51.2	80.0	49.9	80.7	43.2	77.6
	4	39.1	64.1	44.0	69.7	47.6	74.9	48.8	77.5	47.1	77.2	40.5	73.2
	5	37.9	63.1	42.2	68.3	45.2	73.0	45.9	74.9	43.7	73.4	37.3	68.2
	7	34.6	61.1	37.7	65.4	39.1	68.4	38.7	68.4	36.1	64.7	30.1	57.3
	9	31.3	60.1	33.2	63.2	33.2	64.1	31.7	62.0	28.6	56.1	23.1	46.7
	12	25.7	57.7	26.0	58.4	24.3	55.6	21.6	50.5	18.3	42.6	13.8	32.1
Azimuth, deg	135			38	42	47	52	61	80	99	118	156	
Dist wrt AC, ft				Mean Peak kts kts									
Height	0	0.0	0.0	0.0	0.0	0.0	0.0	0.0	0.0	0.0	0.0	0.0	0.0
	1	43.9	70.4	44.7	73.6	44.9	76.5	44.1	78.4	42.3	79.2	37.3	75.1
	2	43.1	69.5	43.9	72.6	44.0	75.3	43.2	77.1	41.4	77.7	36.3	73.2
	3	41.9	68.3	42.6	71.1	42.6	73.5	41.8	75.0	40.0	75.3	34.7	70.0
	4	40.3	66.8	40.8	69.3	40.8	71.2	39.9	72.4	38.0	72.1	32.7	66.0
	5	38.4	65.2	38.7	67.4	38.6	68.7	37.7	69.4	35.8	68.5	30.3	61.4
	7	33.4	61.6	33.3	62.5	33.0	62.4	32.1	61.9	30.3	59.5	24.9	51.0
	9	28.6	58.2	28.1	57.8	27.7	56.3	26.7	54.6	24.9	50.6	19.7	41.2
	12	21.3	51.4	20.5	49.3	19.8	46.0	18.8	43.1	17.0	37.8	12.5	28.8
Azimuth, deg	180			38	42	47	52	61	80	99	118	156	
Dist wrt AC, ft				Mean Peak kts kts									
Height	0	0.0	0.0	0.0	0.0	0.0	0.0	0.0	0.0	0.0	0.0	0.0	0.0
	1	55.8	81.8	55.8	82.1	55.4	82.0	54.5	81.5	51.6	80.1	45.7	75.4
	2	55.1	80.7	55.1	80.8	54.6	80.7	53.7	80.1	50.8	78.8	44.9	74.1
	3	53.8	78.8	53.8	78.9	53.3	78.6	52.4	78.0	49.5	76.6	43.6	72.2
	4	52.1	76.3	52.1	76.3	51.6	76.0	50.6	75.3	47.7	73.9	41.9	69.7
	5	50.0	73.5	50.0	73.4	49.5	73.0	48.5	72.2	45.6	70.7	39.9	66.8
	7	44.0	66.1	44.0	65.8	43.6	65.4	42.8	64.5	40.2	63.3	34.9	60.0
	9	38.5	59.8	38.5	59.4	38.1	58.8	37.3	57.9	35.0	56.7	29.7	54.3
	12	29.6	49.4	29.7	49.0	29.3	48.3	28.5	47.6	26.8	46.8	21.9	42.8
Azimuth, deg	210			38	42	47	52	61	80	99	118	156	
Dist wrt AC, ft				Mean Peak kts kts									
Height	0	0.0	0.0	0.0	0.0	0.0	0.0	0.0	0.0	0.0	0.0	0.0	0.0
	1	53.6	85.2	53.4	84.5	52.5	83.7	51.0	82.4	48.1	81.7	41.8	79.1
	2	53.0	84.4	52.7	83.5	51.8	82.8	50.2	81.5	47.2	80.6	41.0	77.9
	3	51.9	83.0	51.6	82.0	50.6	81.3	49.0	80.1	45.8	78.8	39.7	75.9
	4	50.5	81.2	50.1	80.1	49.0	79.5	47.3	78.3	44.0	76.7	38.1	73.4
	5	48.8	79.1	48.2	78.0	47.1	77.5	45.3	76.3	41.9	74.3	36.1	70.5
	7	43.9	74.0	43.2	73.3	41.8	72.4	40.0	71.2	36.9	68.7	31.5	63.4
	9	39.5	69.7	38.7	68.9	37.2	68.5	35.4	67.1	32.0	63.4	26.8	55.9
	12	32.3	62.2	31.4	61.6	29.8	61.0	28.0	59.3	24.6	54.5	19.7	44.3

Table M-12A Extension of V-22 Data Set, GW = 52,600 lb,
AGL = 76 ft

Azimuth, deg		225		AGL, ft		76		38		42		47		52		61		80		99		118		156			
Height	Dist wrt AC, ft	Mean	Peak	Mean	Peak	Mean	Peak	Mean	Peak	Mean	Peak	Mean	Peak	Mean	Peak	Mean	Peak	Mean	Peak	Mean	Peak	Mean	Peak	Mean	Peak		
0	0.0	0.0	0.0	0.0	0.0	0.0	0.0	0.0	0.0	0.0	0.0	0.0	0.0	0.0	0.0	0.0	0.0	0.0	0.0	0.0	0.0	0.0	0.0	0.0	0.0		
1	49.6	85.6	50.4	87.9	50.4	90.6	49.9	92.4	48.6	93.7	41.6	84.4	35.3	73.2	26.5	59.6	6.2	19.2									
2	49.1	84.8	49.9	87.1	49.8	89.7	49.1	91.4	47.7	92.6	40.8	83.1	34.6	71.7	26.0	58.3	6.1	18.8									
3	48.2	83.5	48.8	85.8	48.6	88.4	47.9	89.9	46.3	90.9	39.5	81.0	33.5	69.3	25.0	56.3	5.9	18.1									
4	46.9	82.0	47.4	84.2	47.1	86.7	46.3	88.0	44.4	88.7	37.7	78.4	31.9	66.3	23.8	53.6	5.7	17.2									
5	45.4	80.3	45.7	82.5	45.3	84.9	44.3	85.9	42.2	86.1	35.7	75.2	30.1	62.9	22.4	50.6	5.5	16.2									
7	40.8	75.9	40.8	78.1	40.1	79.8	38.9	80.2	36.7	79.3	30.9	68.0	25.9	55.2	19.0	43.5	4.9	14.1									
9	36.7	72.1	36.4	74.0	35.5	75.1	34.1	74.9	31.6	73.2	26.1	60.8	21.6	48.1	15.5	36.5	4.4	12.2									
12	29.8	64.5	29.3	65.6	27.9	65.5	26.7	64.8	24.4	62.4	19.2	49.5	15.3	38.3	10.5	26.3	3.5	9.7									
Azimuth, deg		240		38		42		47		52		61		80		99		118		156							
Height	Dist wrt AC, ft	Mean	Peak	Mean	Peak	Mean	Peak	Mean	Peak	Mean	Peak	Mean	Peak	Mean	Peak	Mean	Peak	Mean	Peak	Mean	Peak	Mean	Peak				
0	0.0	0.0	0.0	0.0	0.0	0.0	0.0	0.0	0.0	0.0	0.0	0.0	0.0	0.0	0.0	0.0	0.0	0.0	0.0	0.0	0.0	0.0	0.0	0.0	0.0		
1	47.2	84.2	50.2	90.0	51.9	95.4	52.0	98.4	50.6	99.0	44.6	91.1	38.8	76.6	31.4	67.9	10.2	31.0									
2	46.7	83.3	49.5	88.9	51.1	94.1	51.0	97.0	49.5	97.4	43.6	89.5	37.9	75.2	30.8	66.7	10.0	30.5									
3	45.8	81.9	48.3	87.3	49.6	92.1	49.4	94.7	47.7	95.0	41.9	87.0	36.5	73.1	29.8	64.7	9.8	29.7									
4	44.5	80.2	46.7	85.2	47.7	89.6	47.3	91.8	45.4	91.9	39.8	83.8	34.7	70.3	28.4	62.1	9.5	28.7									
5	42.8	78.3	44.7	82.9	45.4	86.7	44.9	88.4	42.8	88.3	37.4	80.0	32.6	67.0	26.8	59.0	9.1	27.5									
7	38.2	73.8	39.3	77.4	39.5	79.7	38.6	80.3	36.6	80.0	31.8	71.3	27.7	59.5	23.0	52.0	8.3	24.8									
9	33.6	69.9	34.1	72.0	33.9	72.9	32.8	72.5	30.7	71.4	26.3	62.3	22.6	51.7	19.0	44.6	7.3	21.7									
12	26.2	63.1	26.1	63.0	25.4	61.8	24.3	59.8	22.6	57.8	18.5	49.0	15.4	40.1	12.9	33.4	5.8	17.1									
Azimuth, deg		270		38		42		47		52		61		80		99		118		156							
Height	Dist wrt AC, ft	Mean	Peak	Mean	Peak	Mean	Peak	Mean	Peak	Mean	Peak	Mean	Peak	Mean	Peak	Mean	Peak	Mean	Peak	Mean	Peak	Mean	Peak				
0	0.0	0.0	0.0	0.0	0.0	0.0	0.0	0.0	0.0	0.0	0.0	0.0	0.0	0.0	0.0	0.0	0.0	0.0	0.0	0.0	0.0	0.0	0.0	0.0	0.0		
1	44.4	82.7	50.4	90.0	54.8	96.3	56.3	99.3	54.8	98.1	48.4	88.9	42.1	78.5	35.0	69.1	12.4	34.7									
2	43.9	81.6	49.8	88.9	53.9	95.0	55.3	97.7	53.5	96.2	47.1	86.8	41.0	76.7	34.2	67.7	12.2	34.1									
3	43.1	80.0	48.7	87.1	52.4	92.9	53.5	95.2	51.5	93.2	45.1	83.5	39.4	73.8	33.0	65.3	11.9	33.2									
4	41.9	77.9	47.1	84.7	50.3	90.2	51.1	91.8	48.8	89.2	42.5	79.1	37.2	70.1	31.4	62.2	11.5	32.0									
5	40.5	75.5	45.1	82.1	47.8	87.0	48.1	87.9	45.5	84.4	39.3	74.0	34.5	65.6	29.5	58.6	11.0	30.5									
7	36.5	69.8	39.8	75.6	41.1	79.0	40.5	78.1	37.7	73.2	32.2	62.1	28.6	55.6	25.0	50.4	9.8	27.0									
9	32.3	65.0	34.3	69.8	34.4	71.0	33.0	68.3	29.9	61.9	25.0	50.2	22.4	45.4	20.1	42.0	8.5	22.9									
12	25.4	58.2	25.7	60.5	24.3	58.2	22.8	54.0	20.5	50.5	17.0	42.4	14.2	33.9	13.4	31.8	11.1	27.0	4.6	11.9							
Azimuth, deg		315		38		42		47		52		61		80		99		118		156							
Height	Dist wrt AC, ft	Mean	Peak	Mean	Peak	Mean	Peak	Mean	Peak	Mean	Peak	Mean	Peak	Mean	Peak	Mean	Peak	Mean	Peak	Mean	Peak	Mean	Peak				
0	0.0	0.0	0.0	0.0	0.0	0.0	0.0	0.0	0.0	0.0	0.0	0.0	0.0	0.0	0.0	0.0	0.0	0.0	0.0	0.0	0.0	0.0	0.0	0.0	0.0		
1	43.3	78.4	47.9	84.5	51.5	90.3	52.4	92.2	50.8	90.9	44.4	85.1	38.4	78.9	30.9	67.6	10.5	32.6									
2	42.9	77.7	47.3	83.6	50.8	89.2	51.5	90.8	49.6	89.5	43.3	83.4	37.4	77.0	30.2	66.0	10.2	31.7									
3	42.1	76.6	46.3	82.2	49.4	87.4	49.8	88.7	47.8	87.1	41.5	80.6	35.9	74.0	29.0	63.3	9.9	30.3									
4	41.1	75.2	44.8	80.4	47.5	85.1	47.7	86.0	45.4	84.0	39.2	77.0	34.0	70.2	27.4	59.9	9.5	28.6									
5	39.7	73.5	43.0	78.4	45.3	82.4	45.0	82.8	42.4	80.3	36.5	72.7	31.7	65.8	25.6	55.9	8.9	26.5									
7	35.9	68.8	38.2	72.9	39.2	75.7	38.2	75.0	35.3	71.1	30.1	62.6	26.4	55.9	21.3	47.1	7.7	22.0									
9	32.2	64.7	33.4	67.9	33.3	69.1	31.5	67.1	28.1	61.7	23.6	52.0	21.0	46.1	17.0	38.3	6.4	17.4									
12	26.2	56.3	25.1	56.1	22.8	54.0	20.5	50.5	17.0	42.4	14.2	33.9	13.4	31.8	11.8	28.7	5.0	13.0									
Azimuth, deg		330		38		42		47		52		61		80		99		118		156							
Height	Dist wrt AC, ft	Mean	Peak	Mean	Peak	Mean	Peak	Mean	Peak	Mean	Peak	Mean	Peak	Mean	Peak	Mean	Peak	Mean	Peak	Mean	Peak	Mean	Peak				
0	0.0	0.0	0.0	0.0	0.0	0.0	0.0	0.0	0.0	0.0	0.0	0.0	0.0	0.0	0.0	0.0	0.0	0.0	0.0	0.0	0.0	0.0	0.0	0.0	0.0		
1	48.3	89.3	49.8	92.1	50.2	93.1	49.8	92.5	48.0	88.1	43.6	83.9	38.1	76.2	28.5	61.8	8.9	25.3									
2	47.7	88.4	49.1	91.0	49.4	91.8	48.9	91.2	47.1	86.6	42.7	82.3	37.3	74.9	27.9	60.6	8.8	24.8									
3	46.8	86.8	47.9	89.3	48.0	89.8	47.6	89.0	45.6	84.4	41.3	79.9	36.1	72.8	26.9	58.8	8.5	23.9									
4	45.4	84.8	46.3	87.0	46.3	87.3	45.7	86.3	43.6	81.7	39.5	76.9	34.6	70.0	25.7	56.4	8.3	22.8									
5	43.8	82.5	44.4	84.4	44.1	84.																					

GW, lb

52600

AGL, ft

152

Azimuth, deg

0

	38.0		42.0		47.0		52.0		61.0		80.0		99.0		118.0		156.0	
	Mean kts	Peak kts																
0	0.0	0.0	0.0	0.0	0.0	0.0	0.0	0.0	0.0	0.0	0.0	0.0	0.0	0.0	0.0	0.0	0.0	0.0
1	5.9	24.4	6.8	24.7	7.0	23.7	7.1	22.3	7.4	21.0	5.8	14.8	4.1	9.3	2.8	6.0	1.4	2.8
2	5.9	24.4	6.8	24.7	7.1	23.8	7.1	22.4	7.4	21.1	5.8	14.8	4.1	9.3	2.8	6.0	1.4	2.8
3	5.9	24.4	6.9	24.8	7.1	24.0	7.2	22.6	7.4	21.1	5.8	14.9	4.1	9.3	2.8	6.0	1.4	2.8
4	5.9	24.4	6.9	25.0	7.1	24.2	7.2	22.8	7.4	21.2	5.8	14.9	4.1	9.3	2.8	6.0	1.4	2.8
5	5.9	24.4	6.9	25.1	7.2	24.5	7.2	23.0	7.4	21.3	5.8	14.9	4.1	9.3	2.8	6.0	1.4	2.8
7	6.0	24.9	7.0	25.7	7.3	25.1	7.3	23.7	7.4	21.7	5.7	15.0	4.1	9.4	2.8	5.9	1.4	2.8
9	6.0	25.4	7.1	26.4	7.4	26.0	7.3	24.5	7.3	22.1	5.6	15.2	4.1	9.4	2.8	5.9	1.4	2.7
12	6.1	26.3	7.2	27.5	7.5	27.1	7.4	25.4	7.1	22.7	5.5	15.6	4.1	9.4	2.8	5.9	1.4	2.7

Azimuth, deg

45

	38		42		47		52		61		80		99		118		156	
	Mean kts	Peak kts																
0	0.0	0.0	0.0	0.0	0.0	0.0	0.0	0.0	0.0	0.0	0.0	0.0	0.0	0.0	0.0	0.0	0.0	0.0
1	4.7	27.5	5.6	29.0	6.9	30.7	8.0	31.3	9.6	30.0	8.7	23.1	6.3	17.1	4.0	10.6	1.9	4.4
2	4.7	27.3	5.6	28.8	6.9	30.5	8.0	31.1	9.5	29.9	8.7	23.2	6.3	17.1	4.0	10.6	1.9	4.4
3	4.6	27.0	5.5	28.5	6.9	30.2	8.0	30.9	9.5	29.8	8.7	23.2	6.3	17.2	4.0	10.6	1.9	4.4
4	4.5	26.5	5.5	28.0	6.8	29.8	7.9	30.6	9.5	29.7	8.7	23.3	6.3	17.2	4.0	10.6	1.9	4.4
5	4.4	26.1	5.4	27.6	6.7	29.4	7.8	30.3	9.4	29.5	8.7	23.3	6.3	17.3	4.0	10.6	1.9	4.4
7	4.2	25.0	5.2	26.6	6.6	28.6	7.8	29.7	9.2	29.2	8.6	23.6	6.4	17.5	4.0	10.6	1.9	4.4
9	3.9	24.3	5.0	26.0	6.5	28.1	7.6	29.4	8.9	29.0	8.5	24.0	6.4	17.7	4.0	10.6	1.9	4.4
12	3.6	23.8	4.7	25.6	6.2	27.9	7.3	29.3	8.4	29.4	8.3	25.0	6.4	18.0	4.0	10.6	1.9	4.4

Azimuth, deg

90

	38		42		47		52		61		80		99		118		156	
	Mean kts	Peak kts																
0	0.0	0.0	0.0	0.0	0.0	0.0	0.0	0.0	0.0	0.0	0.0	0.0	0.0	0.0	0.0	0.0	0.0	0.0
1	4.3	30.0	5.5	30.4	6.1	30.1	6.4	29.2	7.6	27.4	8.2	25.7	6.4	17.2	4.0	9.6	1.9	4.0
2	4.3	29.8	5.4	30.2	6.1	29.9	6.4	29.0	7.6	27.4	8.2	25.7	6.4	17.2	4.0	9.6	1.9	4.0
3	4.2	29.4	5.3	29.9	6.0	29.6	6.3	28.7	7.6	27.4	8.3	25.8	6.4	17.2	4.0	9.6	1.9	4.0
4	4.1	29.0	5.2	29.4	5.9	29.1	6.3	28.3	7.6	27.4	8.3	25.8	6.4	17.2	4.0	9.6	1.9	4.0
5	3.9	28.5	5.1	28.9	5.8	28.6	6.1	27.9	7.6	27.4	8.3	25.8	6.4	17.2	4.0	9.6	1.9	4.0
7	3.5	27.3	4.7	27.5	5.5	27.3	5.9	26.9	7.5	27.6	8.3	26.0	6.4	17.2	4.0	9.5	1.9	4.0
9	3.2	26.5	4.4	26.6	5.2	26.4	5.8	26.4	7.5	28.2	8.4	26.4	6.4	17.2	3.9	9.4	1.9	4.0
12	2.8	25.7	4.1	25.7	5.0	25.8	5.7	26.5	7.5	29.7	8.5	27.4	6.3	17.0	3.9	9.3	1.9	3.9

Azimuth, deg

135

	38		42		47		52		61		80		99		118		156	
	Mean kts	Peak kts																
0	0.0	0.0	0.0	0.0	0.0	0.0	0.0	0.0	0.0	0.0	0.0	0.0	0.0	0.0	0.0	0.0	0.0	0.0
1	7.7	22.9	7.4	21.9	6.8	20.2	6.5	18.7	5.6	15.5	4.5	11.7	3.3	8.2	2.3	5.3	1.2	2.6
2	7.7	22.9	7.4	21.9	6.8	20.2	6.5	18.7	5.6	15.5	4.5	11.7	3.3	8.2	2.3	5.3	-2.3	2.6
3	7.6	22.8	7.3	21.9	6.8	20.2	6.5	18.7	5.6	15.5	4.5	11.7	3.3	8.2	2.3	5.3	-2.4	2.6
4	7.6	22.8	7.3	21.9	6.8	20.1	6.5	18.7	5.6	15.5	4.5	11.7	3.3	8.2	2.3	5.3	-2.5	2.6
5	7.6	22.8	7.3	21.9	6.8	20.1	6.4	18.6	5.5	15.5	4.5	11.7	3.3	8.2	2.3	5.3	-2.7	2.6
7	7.5	23.1	7.2	22.1	6.7	20.2	6.4	18.8	5.5	15.5	4.5	11.8	3.3	8.3	2.3	5.3	-2.9	2.6
9	7.3	23.3	7.0	22.1	6.6	20.1	6.3	18.7	5.4	15.5	4.6	11.9	3.3	8.3	2.3	5.3	-3.2	2.6
12	7.0	23.4	6.7	22.0	6.3	19.9	6.0	18.7	5.4	15.7	4.6	12.2	3.3	8.3	2.2	5.3	-0.6	2.6

Azimuth, deg

180

	38		42		47		52		61		80		99		118		156	
	Mean kts	Peak kts																
0	0.0	0.0	0.0	0.0	0.0	0.0	0.0	0.0	0.0	0.0	0.0	0.0	0.0	0.0	0.0	0.0	0.0	0.0
1	6.8	23.1	6.3	21.0	5.8	19.4	5.6	18.3	4.7	14.7	3.0	8.4	2.2	6.0	1.5	3.9	0.7	2.0
2	6.9	23.1	6.3	21.0	5.8	19.4	5.6	18.3	4.									

Azimuth, deg		225								152							
Dist wrt AC, ft	Height	38		42		47		52		61		80		99		118	
		Mean kts	Peak kts														
	0	0.0	0.0	0.0	0.0	0.0	0.0	0.0	0.0	0.0	0.0	0.0	0.0	0.0	0.0	0.0	0.0
	1	5.7	21.1	5.7	20.9	5.8	20.2	6.1	20.0	5.6	18.3	4.3	13.2	3.0	8.4	1.8	4.8
	2	5.7	21.1	5.7	20.9	5.8	20.2	6.1	20.0	5.6	18.4	4.3	13.2	3.0	8.4	1.8	4.8
	3	5.7	21.1	5.7	20.8	5.7	20.1	6.0	20.0	5.6	18.3	4.3	13.1	3.0	8.4	1.8	4.8
	4	5.7	21.0	5.7	20.8	5.7	20.1	6.0	19.9	5.5	18.3	4.3	13.0	3.0	8.3	1.8	4.8
	5	5.7	21.0	5.7	20.7	5.6	20.1	5.9	19.9	5.5	18.3	4.2	12.9	3.0	8.3	1.8	4.8
	7	5.7	21.0	5.7	20.7	5.6	20.1	5.9	20.0	5.3	18.2	4.1	12.7	2.9	8.2	1.8	4.8
	9	5.6	21.3	5.6	21.0	5.4	20.3	5.6	20.2	5.1	18.1	4.0	12.4	2.9	8.1	1.8	4.8
	12	5.4	21.9	5.3	21.6	5.1	20.9	5.2	20.5	4.7	18.1	3.8	12.2	2.8	8.0	1.8	4.8
Azimuth, deg		240								156							
Dist wrt AC, ft	Height	38		42		47		52		61		80		99		118	
		Mean kts	Peak kts														
	0	0.0	0.0	0.0	0.0	0.0	0.0	0.0	0.0	0.0	0.0	0.0	0.0	0.0	0.0	0.0	0.0
	1	6.1	21.7	6.1	21.8	6.1	21.8	6.2	21.6	5.6	19.2	4.5	14.3	3.5	10.0	2.4	6.0
	2	6.1	21.7	6.1	21.8	6.1	21.8	6.2	21.6	5.5	19.2	4.5	14.3	3.6	10.0	2.4	6.0
	3	6.1	21.7	6.1	21.8	6.0	21.7	6.1	21.5	5.5	19.2	4.5	14.3	3.6	10.1	2.4	6.0
	4	6.1	21.6	6.0	21.7	6.0	21.6	6.1	21.5	5.5	19.1	4.5	14.3	3.6	10.1	2.4	6.0
	5	6.0	21.6	6.0	21.6	5.9	21.6	6.0	21.5	5.4	19.1	4.5	14.3	3.6	10.1	2.4	6.0
	7	5.9	21.7	5.8	21.7	5.7	21.5	5.8	21.4	5.3	19.0	4.5	14.4	3.6	10.2	2.4	6.0
	9	5.7	22.0	5.6	22.0	5.5	21.7	5.6	21.5	5.1	19.0	4.5	14.6	3.6	10.3	2.4	6.0
	12	5.1	22.8	5.0	22.8	5.0	22.4	5.2	21.9	4.9	19.1	4.5	14.9	3.6	10.3	2.4	5.9
Azimuth, deg		270								156							
Dist wrt AC, ft	Height	38		42		47		52		61		80		99		118	
		Mean kts	Peak kts														
	0	0.0	0.0	0.0	0.0	0.0	0.0	0.0	0.0	0.0	0.0	0.0	0.0	0.0	0.0	0.0	0.0
	1	6.0	21.9	6.3	23.2	6.7	24.4	7.1	25.0	7.6	24.2	5.7	15.4	4.3	10.8	3.1	7.4
	2	6.0	22.0	6.3	23.2	6.7	24.4	7.1	25.0	7.6	24.1	5.7	15.4	4.3	10.8	3.2	7.4
	3	6.0	22.0	6.4	23.3	6.7	24.5	7.1	25.0	7.6	24.0	5.7	15.3	4.3	10.8	3.2	7.5
	4	6.1	22.1	6.4	23.4	6.8	24.5	7.1	24.9	7.6	23.9	5.6	15.3	4.3	10.8	3.2	7.5
	5	6.1	22.2	6.4	23.5	6.8	24.6	7.1	24.9	7.6	23.7	5.6	15.3	4.3	10.9	3.2	7.5
	7	6.2	22.3	6.6	23.9	7.0	24.8	7.3	24.9	7.6	23.4	5.5	15.1	4.3	11.0	3.2	7.6
	9	6.3	22.8	6.7	24.3	7.1	25.1	7.4	25.0	7.6	23.1	5.3	15.1	4.3	11.1	3.2	7.6
	12	6.4	23.6	6.8	25.0	7.1	25.6	7.4	25.4	7.5	23.1	5.1	15.3	4.3	11.3	3.2	7.7
Azimuth, deg		300								156							
Dist wrt AC, ft	Height	38		42		47		52		61		80		99		118	
		Mean kts	Peak kts														
	0	0.0	0.0	0.0	0.0	0.0	0.0	0.0	0.0	0.0	0.0	0.0	0.0	0.0	0.0	0.0	0.0
	1	4.2	20.9	4.4	22.8	4.7	24.8	5.4	25.8	6.9	24.8	6.4	14.6	5.0	10.9	3.4	7.8
	2	4.2	20.9	4.4	22.8	4.8	24.7	5.4	25.6	6.9	24.7	6.4	14.6	5.0	11.0	3.4	7.8
	3	4.2	20.9	4.5	22.7	4.8	24.5	5.4	25.4	6.9	24.5	6.4	14.5	5.0	11.0	3.4	7.8
	4	4.3	20.8	4.5	22.6	4.8	24.3	5.4	25.1	6.9	24.2	6.4	14.4	5.0	11.1	3.4	7.8
	5	4.3	20.8	4.6	22.5	4.8	24.0	5.4	24.7	6.8	23.8	6.4	14.3	5.0	11.1	3.4	7.9
	7	4.5	20.7	4.7	22.1	5.0	23.1	5.4	23.6	6.6	23.0	6.4	14.0	5.0	11.3	3.4	7.9
	9	4.6	20.8	4.9	21.9	5.1	22.7	5.4	22.9	6.5	22.3	6.3	13.9	5.0	11.4	3.5	8.0
	12	4.8	21.0	5.0	21.7	5.2	22.1	5.5	22.2	6.3	21.4	6.3	14.3	5.1	11.8	3.5	8.1
Azimuth, deg		315								156							
Dist wrt AC, ft	Height	38		42		47		52		61		80		99		118	
		Mean kts	Peak kts														
	0	0.0	0.0	0.0	0.0	0.0	0.0	0.0	0.0	0.0	0.0	0.0	0.0	0.0	0.0	0.0	0.0
	1	4.5	23.3	4.3	23.8	4.5	24.1	5.1	23.4	6.6	21.4	6.3	14.7	4.3	9.3	2.8	6.3
	2	4.5	23.2	4.3	23.7	4.5	23.9	5.1	23.3	6.6	21.3	6.3	14.6	4.3	9.3	2.9	6.3
	3	4.5	23.1	4.3	23.5	4.5	23.7	5.0	23.0	6.6	21.2	6.3	14.6	4.3	9.4	2.9	6.3
	4	4.5	22.9	4.3	23.3	4.5	23.4	5.0	22.7	6.6	20.9	6.3	14.5	4.3	9.4	2.9	6.3
	5	4.5	22.7	4.3	23.0	4.5	23.0	5.0	22.3	6.5	20.6	6.3	14.4	4.3	9.4	2.9	6.3
	7	4.5	22.5	4.4	22.6	4.5	22.4	5.0	21.7	6.4	19.9	6.2	14.1	4.3	9.4	2.9	6.3
	9	4.5	22.3	4.4	22.1	4.6	21.7	5.0	20.9	6.3	19.3	6.1	13.7	4.3	9.4	2.8	6.4
	12	4.6	22.1	4.6	21.6	4.9	20.8	5.2	19.9	6.2	18.5	5.9	13.3	4.2	9.5	2.8	6.4
Azimuth, deg		330								156							
Dist wrt AC, ft	Height	38		42		47		52		61		80		99		118	
		Mean kts	Peak kts														
	0	0.0	0.0	0.0	0.0	0.0	0.0	0.0	0.0	0.0	0.0	0.0	0.0	0.0	0.0	0.0	0.0
	1	4.7	23.7	4.6	23.5	5.1	23.1	5.6	21.6	6.8	19.1	6.0	14.3	3.9	8.6	2.7	5.9
	2	4.7	23.6	4.6	23.5	5.1	23.1	5.6	21.6	6.8	19.1	6.0	14.3	3.9	8.6	2.7	5.9
	3	4.7	23.6	4.6	23.3	5.1	22.9	5.6	21.4	6.8	19.0	6.0	14.3	3.9	8.6	2.7	5.9
	4	4.6	23.5	4.6	23.2	5.1	22.7	5.6	21.2	6.8	18.8	6.0	14.3	3.9	8.6	2.7	5.9

Reference	AGL, ft	Azimuth, deg	GW, lb	Velocity Profile Max, kts	
				Mean	Peak
Table M-3A	19	180	33,140	51	85
**Figure M-10	20	180	45,935	47	83
Table M-9A	19	180	52,600	55	89
Table M-3B	19	270	33,140	55	108
**Figure M-4	20	270	45,935	65	100+
Table M-9B	19	270	52,600	51	86
Table M-5A	57	180	33,140	53	85
**Figure M-13	60	180	45,935	52	93
Table M-11A	57	180	52,600	58	92
Table M-5B	57	270	33,140	55	105
**Figure M-5	60	270	45,935	57	95
Table M-11B	57	270	52,600	52	87

Table M-14 Outwash Velocity vs. Gross Weight at 61 feet
From Aircraft Center

**CHARM correlation figures contain limited distribution data. The figures appear in a limited distribution annex to this report.

Reference	AGL, ft	Azimuth, deg	GW, lb	Velocity Profile Max, kts	
				Mean	Peak
Table M-2A	10	180	33,140	53	90
Table M-3A	19	180	33,140	51	85
Table M-4A	38	180	33,140	56	88
Table M-5A	57	180	33,140	53	85
Table M-6A	76	180	33,140	57	90
Table M-7A	152	180	33,140	6	20
**Figure M-10	20	180	45,935	50	80
**Figure M-13	60	180	44,539	52	92
**Figure M-14	100	180	43,814	34	61
Table M-8A	10	180	52,600	52	91
Table M-9A	19	180	52,600	55	89
Table M-10A	38	180	52,600	56	87
Table M-11A	57	180	52,600	58	92
Table M-12A	76	180	52,600	52	80
Table M-13A	152	180	52,600	5	15

Table M-15 Outwash Velocity vs. AGL at 61 feet From Aircraft Center,
180 degree Azimuth

**CHARM correlation figures contain limited distribution data. The figures appear in a limited distribution annex to this report.

Reference	AGL, ft	Azimuth, deg	GW, lb	Velocity Profile Max, kts	
				Mean	Peak
Table M-2B	10	270	33,140	57	93
Table M-3B	19	270	33,140	55	108
Table M-4B	38	270	33,140	58	91
Table M-5B	57	270	33,140	55	105
Table M-6B	76	270	33,140	54	92
Table M-7B	152	270	33,140	11	24
**Figure M-4	20	270	45,935	65	100+
**Figure M-5	60	270	44,539	56	93
**Figure M-6	100	270	43,814	45	93
Table M-8B	10	270	52,600	49	84
Table M-9B	19	270	52,600	51	86
Table M-10B	38	270	52,600	60	103
Table M-11B	57	270	52,600	52	87
Table M-12B	76	270	52,600	55	98
Table M-13B	152	270	52,600	8	24

Table M-16 Outwash Velocity vs. AGL at 61 feet From Aircraft Center,
270 degree Azimuth

**CHARM correlation figures contain limited distribution data. The figures appear in a limited distribution annex to this report.

Appendix N: Shipboard Effects on Rotorwash

Sam Ferguson

The rotorwash flight test database documented in [Appendix K](#) of this report has slowly been developed over the past 30 years. This achievement has been accomplished at great monetary expense. One of the primary impediments to acquisition of high-quality data has been the interference of winds above those acceptable for hover performance quality data (generally accepted to be 3 knots or less by most engineers). Therefore, since testing is expensive, testing on windy days has been avoided whenever possible. The focused effort to acquire rotorwash data at this condition has been justified for several reasons. The first reason is that in most scenarios this condition presents the worst-case condition around the full 360-degree azimuth. A second reason is that this condition is the best for baseline mathematical model development purposes. However, while this condition may be good for analyses like preliminary design tradeoff studies, the daily operational conditions for most rotorcraft usually involve wind.

An excellent example of the need for rotorwash data in wind conditions results from the limitations involved with operating large rotorcraft on board ships. Personnel near or underneath rotorcraft (i.e. sling load operations) during launch/recovery have a very limited area to work and ships launch/recover aircraft into the wind. Also, the effect of a rotor being partially over the deck edge (i.e. the V-22) has significant effects on the development of the rotorwash flow field below the aircraft when compared to operation over land. As further discussion is presented in this appendix, these conditions will be referred to as Wind-Over-Deck (WOD) and Deck Edge (DE) effects, respectively.

Effect of Wind-Over-Deck

The logical question to ask at this point is, "What data does the rotorwash flight test database contain for wind effects?" Unfortunately, the answer to this question is complicated. While land-based data are contained within the database for winds in the range of 0 to < 10 knots, acquisition of these data was not intended and only taken as an alternative to "no data" due to program scheduling and aircraft availability issues. The majority of these data are for random wind azimuths not coincident with the azimuth of the rotorwash sensors. As far as is known, no test organization has ever intentionally acquired land-based data for "undesirable" wind conditions AND then repeated the data collection for zero wind conditions for the primary purpose of documenting wind effects.

Rotorwash data have been acquired for the V-22 on both land (Reference N-1) and ship (Reference N-2). However, the shipboard data were acquired at only 0- and 20-knot WOD conditions at LHA 2, spot 4 (50% of left rotor over-the-deck near the island, Figure N-1). No data were acquired at intermediate WOD speeds or with both rotors over the deck. The 20-knot condition is most appropriate for application to normal V-22 shipboard operations, but it leaves a huge gap in test conditions for mathematical modeling purposes. The reason that this gap is "huge and critical" is that between 0 and 20 knots, the rotorwash flow field begins the transition from a vertical column of air to a ground vortex

(when in ground effect) and a poorly defined trailing wake structure (noted by pilots as transition speed). It is extremely important to note that the presence of the ground vortex at 20 knots, WOD is confirmed by the test report. More will be discussed later about the data in Reference N-2.

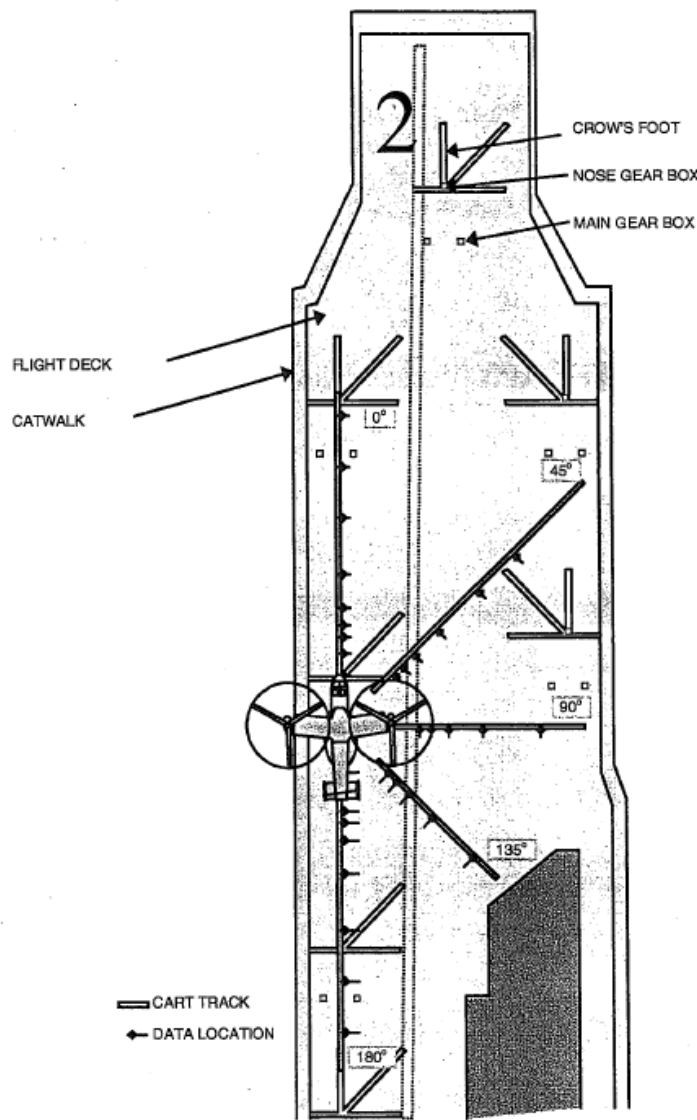


Figure N-1 V-22 Shipboard Downwash Test Arrangement (Reference N-2)

The development of a simple wind effects mathematical model for a conceptual level tool like the one being focused on in this report has been proposed and evaluated in Reference N-3. This specific model is broken into two components. The first component applies to the wind velocity range from 0 to 10 knots. The second component calculates the presence of the ground vortex (Figure N-2) at winds greater than 10 knots (if the vortex is predicted to exist) as a function of rotor advance ratio and height above ground. Available flight and model test data acquired through 1994 are reviewed and discussed in detail in this reference. The proposed simple and conservative wind model is as follows:

$$k_{wind} = -0.5 \left(\frac{h_{rotor}}{R} \right) + 2.5$$

This model is applied per the following steps:

1. The factor k_{wind} is calculated as a function of rotor height above ground.
2. This factor is multiplied by the wind speed (as limited to a maximum wind speed value of 10 knots).
3. The resulting velocity is then uniformly added to the predicted “no wind” mean and peak velocity profile velocities at all heights above ground on the downwind side of the rotorcraft. On the upwind side, the resulting velocity is then uniformly subtracted from the predicted “no wind” mean and peak velocity profile velocities at all heights above ground.

This very simple and conservative wind model was deemed empirically acceptable in the Reference N-3 study only for the upwind and downwind azimuths. No attempt was made to adjust the model for use 360 degrees around the rotorcraft to obtain a “footprint.” Also, the model does not account for rotor plane effects, i.e. as the wind increases the tip path plane must flap to maintain a trimmed position over a fixed spot on the ground. This trim effect should have a small tendency to further decrease upwind profile velocities and increase downwind profile velocities.

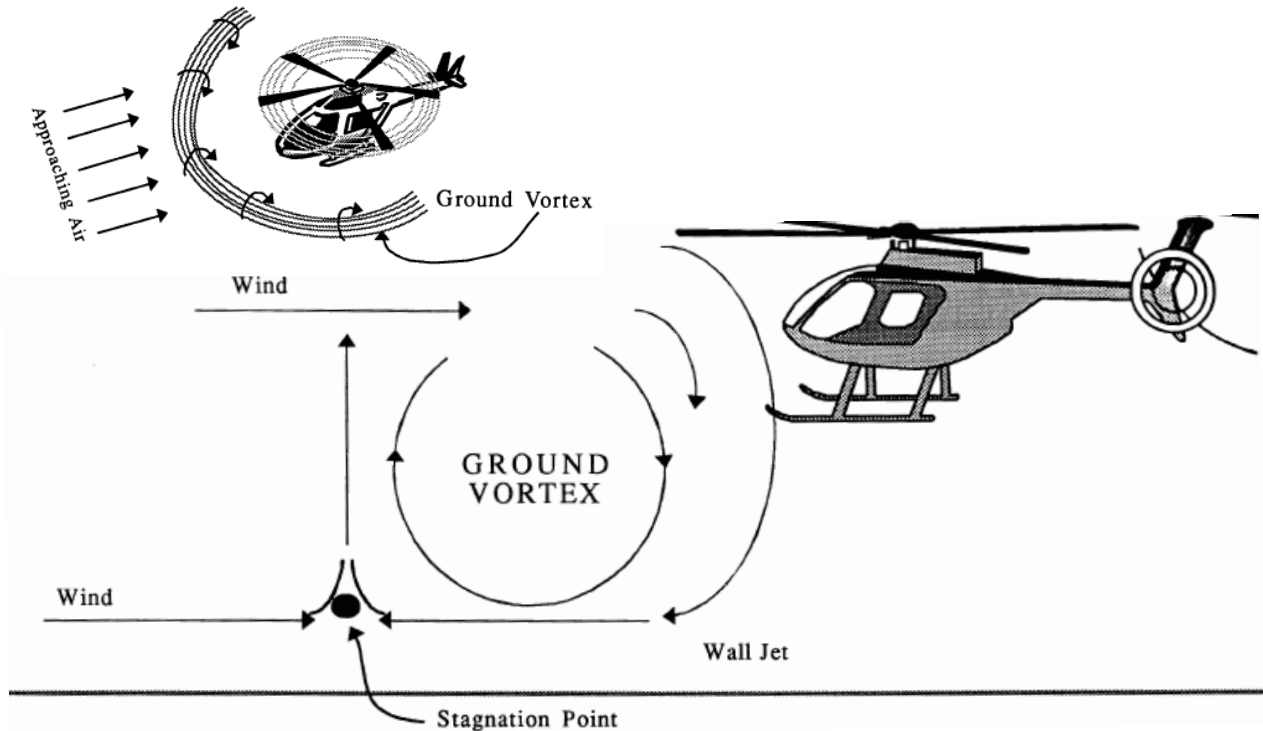


Figure N-2 Ground Vortex Structural Characteristics (Reference N-3)

At wind speeds in excess of 10 knots, the same wind model is used up to the speed of the predicted formation of the ground vortex. At this wind speed and greater speeds, simple vortex theory calculations are made to estimate velocity profiles. This theory is documented in Section 2.2 of Reference N-3. This mathematical model is almost exclusively based on scale model data obtained from the Princeton Long Track facility. Very little well documented flight test data were ever identified.

The V-22 data contained in Reference N-2 provide a limited view of what can be expected for a typical tilt rotor WOD launch condition. The peak upwind profile velocities were substantially less at 0- and 20-knot WOD conditions when compared to the 0-knot condition on land. The peak downwind profile velocities averaged 10-knots more at the 20-knot WOD condition when compared to both the land and shipboard 0-knot conditions.

While these V-22 data are quite useful, the acknowledgment in the report of the existence of an upwind ground vortex confuses and limits modeling capabilities without further empirical data. The addition of DE effects (and the ship superstructure) further complicates the issue from a mathematical modeling perspective. On the downwind side, the 10-knot variation for a 20-knot WOD speed is clearly not predicted by the < 10-knot empirical wind model previously presented. Since only two WOD data points exist, the transition cannot be reliably predicted. Therefore, WOD conditions of two or three intermediate conditions need to be measured to develop a transition between the two components of the wind model. Also, questions have to be answered as to what WOD speed the ground vortex forms to correlate the Reference N-3 model.

Effect of Deck-Edge

The effect of a rotor being partially over a ship deck edge has significant influence on the development of the rotorwash flow field below the aircraft when compared to operation over land. In Figure N-1, the location of the V-22 on the LHA 2, spot 4 shows ~50% of the port rotor over-the-deck. A significant portion of the port side rotorwash mass flow will be "dumped" overboard and not appear on the flight deck.

Data in Reference N-2 were acquired for only the 0- and 20-knot WOD condition. At this point the available data set is insufficient to confirm a mathematical relationship between deck edge rotor overhang and any resultant changes to the rotorwash. Limited radial data were taken and the combined flow interaction region essentially never formed due to the mass of air dumped over the port side.

The model approach described in the previous section does not account for deck edge effects. In general, the report notes that the shipboard V-22 velocity profiles appeared to look like the single rotor helicopter velocity profiles on land. This observation is not surprising since much of the left rotor mass flow is not present on the ship deck, and the outwash will be dominated by the rotorwash generated by the right rotor.

Additional deck position data are also critical since the deck is wide enough for two V-22 rotors to both be over the deck during a 20-foot hover. A tandem rotorcraft located at the

edge of the deck would present an additional configuration difference since the interaction plane would form across the deck.

Summary

As far as is known, no attempts have been made to develop shipboard focused WOD or DE models for a conceptual level tool. To summarize the identified conceptual level modeling options, the following statements listed can be made:

1. A simple empirically based mathematical model has already been investigated and proposed for use at wind speeds < 10 knots. This model, or a simple derivative, requires further investigation for potential improvement based on post 1994 flight test data. It also requires further development for 360-deg azimuth use to calculate a rotorwash footprint.
2. A simple experimentally based ground-vortex mathematical model exists to predict rotorwash profiles directly upwind of a rotorcraft at wind speeds above 10 knots. Further work needs to be conducted to apply this model to a 360-deg ground or shipboard environment.
3. No conceptual level models have been developed for WOD or DE use at this time. Guidance exists for the development of a limited capability model for the LHA 2, spot 4 location with 50% of a left rotor over-the-deck edge near the island. However, empirical data for correlation of the model for WOD speeds between 0 and 20 knots does not exist. Also, data do not exist for other deck locations aboard ship, especially with both rotors over the deck. Further work needs to be conducted to develop models for these effects.

It is important to note that due to the documented unknowns, the release of any version of these models in the conceptual level model described in [Appendix I](#) could not be justified as appropriate at this time. Recommendations that are an outcome of the above summary statements are included in [Section 7](#) of this report.

References

- N-1. Lake, R. E., and Clark, W. J., "V-22 Rotor Downwash Survey," NAWCADPAX-98-88-RTR, July 1998.
- N-2. Lake, R. E., "Shipboard V-22 Rotor Downwash Survey," NAWCADPAX-99-87-RTR, September 1999.
- N-3. Ferguson, S. W., "Rotorwash Analysis Handbook, Volume I – Development and Analysis," Federal Aviation Administration, Washington D.C., Technical Report DOT/FAA/RD-93/31,I, June 1994.

Appendix O: Conceptual-Based Model Comparisons and Trends

John Preston and Sam Ferguson

This appendix documents outwash differences between rotorcraft configurations and the engineering trends of each configuration using the conceptual rotorwash model (RoWFoot) presented in Appendices [I](#) and [K](#). The rotorcraft configurations include a single main rotor helicopter, tandem helicopter, and tilt rotor. At the same thrust per rotor, the mean radial velocity profile is similar for the helicopter, tandem, and tilt rotor. The helicopter and tandem peak radial velocity profiles are similar while the tilt rotor's is smaller in magnitude. For centerline outwash, the tandem has a higher velocity magnitude than the tilt rotor. Rotorwash differences between configurations are supported by flight test data. Explanation of the differences arises from the distribution of the air mass flow within the rotorwash.

Calculated drag force on personnel is determined using the peak velocity profile and a representative silhouette (PAXman). The peak velocity profile is a collection of maximum velocity points measured over a finite time interval. These maximum velocity points do not occur at the same time, and the calculated drag force for is larger than reality by an unknown amount. Previous laboratory testing measured the capability of ground personnel to resist steady horizontal forces. Based on a limited amount of test data for ground personnel in the unsteady flow under a hovering helicopter, a ratio of actual to calculated force of 0.8 was derived. No equivalent test data are known to exist for the tandem or tilt rotor. Due to similar radial outwash, the tandem uses the same value as the helicopter. Since the magnitude of the tilt rotor's peak velocity profile is smaller than the equivalent helicopter and tandem, it uses a ratio of 1.0.

For each configuration, trends are shown for changes in rotor radius, thrust per rotor, and height above ground. Engineering graphs are presented for velocity profile and force on PAXman. These graphs can be used to explore the effect of design and operational changes on the outwash environment. The comparisons between configurations are based on identical rotor size and thrust, NOT equivalent mission designs.

Introduction

An initial review of results of the conceptual rotorwash model may be counterintuitive. A common analytical architecture was used with configuration specific empirical tuning of coefficients and exponents. This process resulted in differences with the model as determined by test data. Of course, these differences are limited by the quality and amount of test data available. The recent availability of tandem rotor flight test data was a major factor in allowing this approach.

Known previous prediction methodologies did not treat the rotorcraft configurations independently. This limitation resulted in the prediction of the outwash velocity profile

magnitude and shape without consideration being made for the impact of spacing between multiple rotors.

The “PAXman” model has been used for many years to calculate force on ground personnel. The underlying model is retained and has an addition to apply a correction in translation from peak velocity profile to actual conditions. As previously discussed, the measured points peak velocity profile did not occur simultaneously but is a collection of the maximum magnitude of wind velocity measured over a time interval at each sensor height during flight test.

Conceptual Level Model

Within the rotorwash flight test data sets, there were differences in the flight test conditions and the test setup. Relative differences between the data sets would propagate into the conceptual model (RoWFoot), which is empirically derived from the available test data. Extrapolation beyond the range of flight test may also introduce deviation from actual rotorwash conditions. When available, additional test data should be used to refine the modeling.

Flight test conditions vary due to the flight state of the aircraft and ambient wind conditions. The flight state of the aircraft will vary based on how precisely the rotorcraft was hovered at a defined altitude and ground position. Ambient winds varied during the test and influenced both the rotorwash flow field and the ability to maintain a precision hover. The ambient wind speed may be different at the location of the rotorcraft when compared with the location of the anemometer. Wind gusts during data acquisition will also affect the accuracy of the data.

The test setup for the CH-53E (Reference O-1) included a tethered cable to maintain a precision hover. Simulated changes in weight were accomplished by increasing tension on the cable. The V-22 (Reference O-2) and CH-47D (Reference O-3) test data were for untethered hover. During the CH-53E test, an ion beam sensor was used to measure wind speed while during the V-22 and CH-47D tests an acoustic sensor was used.

Most of the previous differences in test procedures should result in small differences to the measured outwash velocities. The ambient wind speed has the largest potential to affect results when comparing the flight test data. This is a real-life condition which the test engineer has limited control over.

Differences Between Rotorcraft Configurations

The RoWFoot predicts rotorwash conditions for three rotorcraft configurations including the single main rotor helicopter, tandem, and tilt rotor. Physical differences between these configurations will produce changes in the rotorwash. For the tandem and tilt rotor, the rotorwash mixes under the aircraft and changes where the mass flow exits region under the aircraft. This affects the magnitude and shape of the outwash velocity profile.

Therefore, at identical thrust per rotor, rotor radius, and equivalent flight condition, the velocity profiles are different for the helicopter, tandem, and tilt rotor.

Table O-1 gives the characteristics of the rotorcraft configurations used to illustrate rotorwash differences in RoWFoot. Note that the thrust per rotor is the same at value at 75,000 pounds with a rotor radius of 40 feet. All cases used to show the differences between rotorcraft configurations were executed at 20 feet Above Ground Level (AGL). After presentation of these results in the next section, the authors offer an explanation of the perceived physics underlying the differences.

	Helicopter	Tandem	Tiltrotor
# Rotors	1	2	2
Radius, ft	40.0	40.0	40.0
Rotor Separation, ft	0.0	52.3	102.3
Gear to Rotor, ft	25.00	25.00	25.00
Area / Rotor, sqft	5,027	5,027	5,027
Gross Weight, lb	71,429	142,180	137,615
Disk Loading (T), psf	14.92	14.92	14.92
T/W	1.050	1.055	1.090
Thrust / Rotor, lb	75,000	75,000	75,000

Table O-1 Description of Rotorcraft Characteristics

Differences in Rotorwash Between Configurations

The number and separation of the aircraft rotors appears to be the primary cause of differences in the magnitude and shape of the outwash velocity profile. Multiple rotors produce flow field interactions that are manifested in the outwash mass flow distribution and magnitude. Figure O-1 graphically represents the tilt rotor having an upwash sheet. Under the aircraft, this is commonly referred to as a fountain effect. The following paragraphs describe differences observed in test data and the RoWFoot model correlation in [Appendix K](#). After a description of the differences, the authors comment on the perceived underlying physics.

The outwash for the single main rotor helicopter is nearly uniform with a small distortion from the tail rotor. In RoWFoot, there is no distinction in modeling the radial and centerline outwash. Actual aircraft, such as the CH-53 and H-60 (References O-1 and O-4), have secondary or tertiary effects due to the tail rotor thrust direction, main rotor swirl, and fuselage blockage.

For the tandem, downwash from the two rotors mixes in the transition region under aircraft and is conjectured to combine to form a single area of stagnation. A single rotor dominates the radial outwash with a possibility of increased mass flow due to the opposite rotor. Directly under the rotor overlap region, the tandem produces a higher downwash velocity which later appears in its centerline outwash. The mass flow in the centerline

region contains flow from both rotors and will be larger than the mass flow in the radial case. A second-order effect is the main rotor swirl and fuselage blocking. Since the rotors on a tandem rotate in opposite directions, the outwash will be slightly stronger on the port side of the CH-47D, as seen in the [Appendix I](#) correlation to test data (Reference O-3).

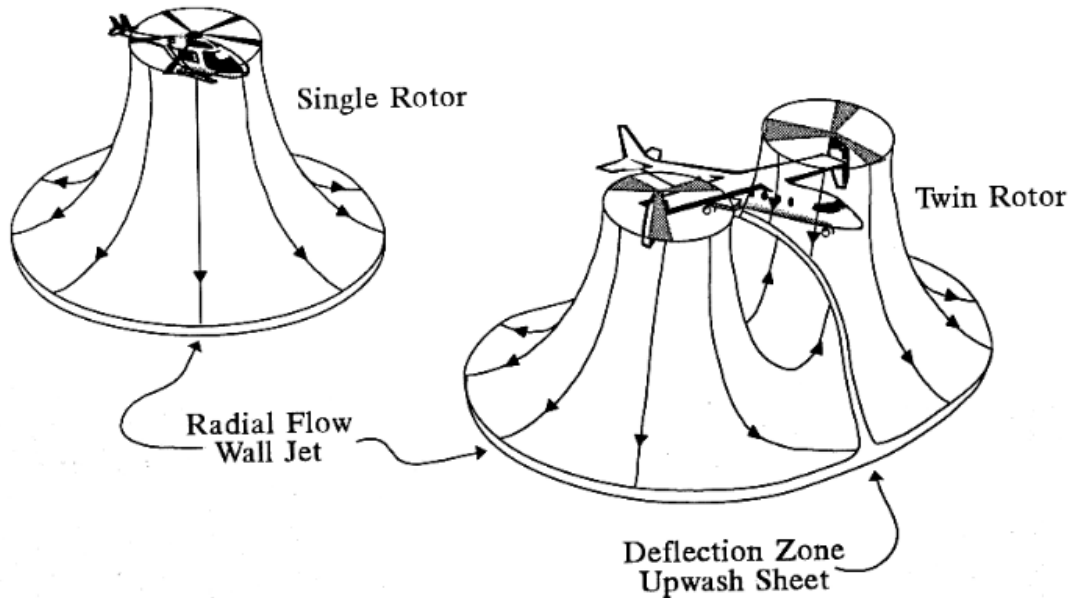


Figure 0-1 Rotorwash Flow Fields of Single- and Twin-Rotor Configurations Operating in Close Proximity to Ground

The tilt rotor has separated rotors which causes a different flow environment under the aircraft compared to the tandem. Since there is no overlap of the rotors, the magnitude of the downwash will be similar to the helicopter and not contain the tandem's higher velocity magnitude in its overlap region. Mass flow in the tilt rotor's centerline region is greater than its radial outwash. Its mass flow distribution will also be different to the tandem due to the fountain effect under the tilt rotor caused by the separated rotors. This effect may be magnified in the V-22 flight test data due to each of the rotors being outwardly canted by 2 degrees. The fountain effect will push more of the mass flow upwards in the centerline outwash region as compared to the helicopter. In the tilt rotor, the rotors are separated by a wider distance as compared to the tandem. This increase in separation distance gives a wider a larger exit area for the centerline flow for the tilt rotor relative to the tandem. The combined fountain effect and larger centerline area results in different centerline velocity profiles compared to the tandem. A second-order effect is the main rotor swirl and fuselage blocking. This affect will also tend to shift the aerodynamic center of a stagnation point forward to the aircraft nose (an operational example is that a ground relay crew person will stand in this dead air spot). From this secondary or tertiary effect, the outwash will be slightly stronger along the aft centerline of the V-22, as seen in the [Appendix K](#) correlation to test data (Reference O-2).

Velocity Profile Comparison

Figure O-2 presents the radial velocity profiles for the helicopter, tandem, and tilt rotor aircraft described in Table O-1. Each of the velocity profiles in this figure are at one rotor diameter or 80 feet from the rotor center. Both mean and peak velocity profiles are displayed. In Figure O-2, the tandem helicopter legend notation showing the extrapolated modeling conditions is explained with Tables O-2 and O-3 in a later part of this appendix.

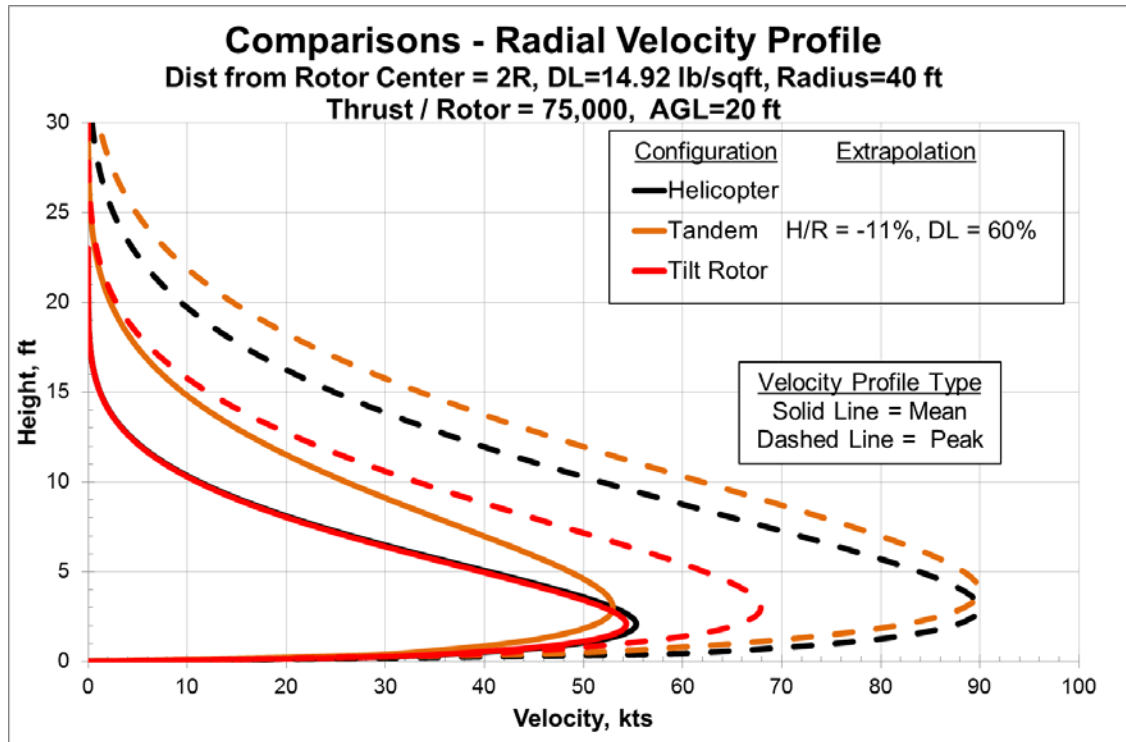


Figure O-2 Velocity Profile Comparisons, Radial Outwash

The solid lines in Figure O-2 are the RoWFoot mean velocity profiles. The helicopter, tandem, and tilt rotor aircraft all exhibit similar profiles with nearly equivalent magnitudes. Results for the tilt rotor and helicopter closely align and the tandem appears to be fuller with increased mass flow higher above the ground.

The dashed lines in Figure O-2 are the RoWFoot peak velocity profiles. The tandem and helicopter results are similar. The predicted tilt rotor peak velocity distribution is significantly less than the other two configurations. This result of the reduced tilt rotor delta magnitude from the mean to peak velocity profile is supported by the test data, as seen in [Appendix K](#). For the tilt rotor, this indicates a lower magnitude of velocity changes or “gusts” in the outwash as compared to the helicopter and tandem.

Figure O-3 presents the centerline velocity profiles for the helicopter, tandem, and tilt rotor aircraft described in Table O-1. Each of the velocity profiles in this figure is at one rotor diameter or 80 feet from the aircraft center (measured from the line connecting the center of the rotor hubs). Both mean and peak velocity profiles are displayed. In Figure O-3, the

tandem helicopter legend notation showing the extrapolated modeling conditions is explained with Tables O-2 and O-3 in a later part of this appendix.

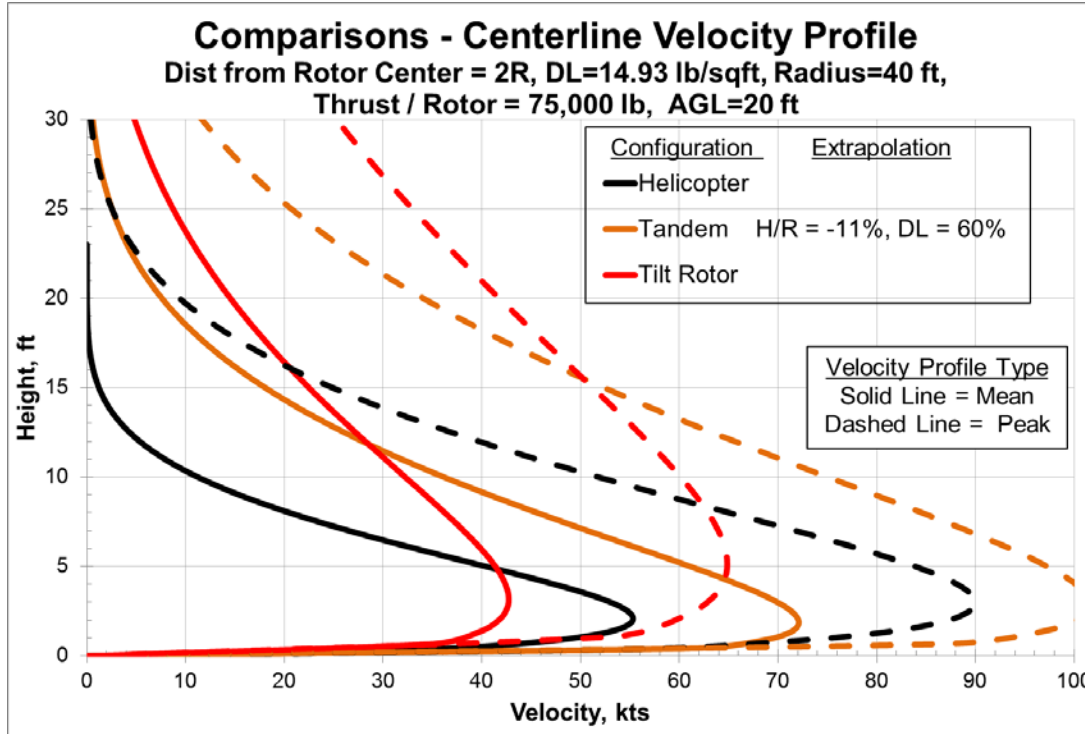


Figure O-3 Velocity Profile Comparisons, Centerline Outwash

The solid lines in Figure O-3 are the RoWFoot mean velocity profiles. The helicopter, tandem, and tilt rotor aircraft all exhibit different profiles and magnitudes. The helicopter radial outwash is identical to its centerline. Compared to the helicopter, the tandem has an increased velocity magnitude. Earlier in this appendix, this observation was attributed to the increased downwash velocity from the overlap region between the two rotors. The tandem also has a higher mass flow which agrees with the assertion with the combined flow from the rotors will cause a fuller velocity profile. Compared to the helicopter, the tilt rotor has a lower magnitude but fuller velocity profile. Previously, this characteristic was theorized to possibly occur from the fountain effect under the aircraft causing the mass flow to exit the aircraft at greater height from the ground plane. Once again, the tilt rotor results are in agreement with the available test data.

The dashed lines in Figure O-3 are the RoWFoot peak velocity profiles. Compared to the helicopter, the tandem has an increased velocity magnitude and mass flow. This is in agreement with the ~10-knot delta exhibited in the mean velocity profile with a similar reasoning for the cause. The magnitude of the tilt rotor velocity profile is in agreement with the peak radial velocity in Figure O-2. The curve shape for the tilt rotor indicates a mass flow distribution higher in the centerline outwash flow field.

As discussed in the previous section, the tilt rotor has a wider rotor separation than the tandem in Table O-1. If the combined mass flow for two rotors is constrained to the region

between the rotor shafts, then the mass flow for the tandem will be constrained to a smaller exit area than the tilt rotor. The tilt rotor's distribution of mass flow due to the larger exit area and fountain effect and the tandem's increased velocity magnitude due to rotor overlap may provide the explanation for the differences in their centerline velocity distribution. Confirmation of the hypothesized explanation of effect of rotor separation by experiment is highly recommended. The authors recommend testing the effect of separation and overlap on rotorwash of equal thrust rotors. The current conceptual level modeling is based on rotor separation from the V-22, XV-15, and CH-47 (References O-2, O-5, and O-3, respectively).

As evidenced by Figures O-2 and O-3, the type of rotorcraft configuration may have a significant bearing on the rotorwash. Distribution of the mass flow and the magnitude of the outwash are the primary factors in determination of the drag force imparted on personnel or objects in the rotorwash environment. Care should be taken when attempting to tailor rotorwash to reduce the outwash impact since this may increase other operational concerns such as brownout.

Outwash Personnel Stability Limit Ratio

In Reference O-6, test subjects were able to function at higher calculated drag forces than their corresponding measured stability limit. The use of the peak velocity profile to predict the force on personnel resulted in higher drag magnitudes than would be realistically encountered. To account for this difference, the personnel stability ratio is introduced. This ratio is the wind drag force divided by the calculated peak drag force. At an individual's maximum capability, the wind drag force should equal their measured ability to resist a horizontal load.

Test results for individuals to resist horizontal loads appear in [Appendix C](#). This personnel force capability represents the measured ability of personnel to perform in an outwash environment. In Reference O-6, test subjects that were tested for maximum effort capability were also exposed to maximum effort conditions under a hovering CH-53E. Test results measuring the force limit of forward movement while maintaining stability was 87 lbs for Subject #3 and 115 lbs for Subject #4. These tests were conducted under static conditions. A non-steady force that would be encountered in outwash will tend to lower the stability limit from the measured results.

The calculated drag force for these two test subjects used a projected shape based on Subjects 2, 3, and 4, an assumed drag coefficient, and the peak velocity profile measured during flight test. The projected shape is referred to as "PAXman" and is described on Table 7, p 159 of Rotorwash Analysis Handbook Volume I (Reference O-6). The assumed drag coefficient is 1.0 for calculation purposes. Reference O-7 contained peak velocity profiles for distances from the aircraft rotor center at 0.2-, 0.4-, 0.8-, 1.0-, 1.25-, 1.5-, 1.75-, 2.0-, 3.0-, 4.5-, and 6.0-rotor radii (39.5 ft). Measurements were taken at 1.0-, 1.5-, 3.0-, 5.0-, 7.0-, 9.0-, and 11.0-ft heights. At each height, the peak velocity was recorded as the transducer maximum measurement for over a period of 18 seconds. Since measurements at each height were treated individually, the peak velocity profile can be

misleading since the highest magnitude may not occur simultaneously at all points. This will lead to an over prediction of the dynamic pressure and higher forces than actually encountered.

Ideally, a test subjects measured stability limit would equal their calculated performance limit based on drag force. As noted above, the non-steady nature of outwash and peak velocity measurement method will cause conflicting directions in the errors. A simple way to combine the two errors is to take the test subject's demonstrated performance in the outwash and determine the calculated drag force based on the peak velocity profile and ratio to their measured stability limit. The validity of this relation is very weak due to the very limited data that can be applied.

Pages 165-168 of Reference 0-6 states, "... the forward movement of subject 3 was completely restrained near the position marked 80 feet (from the center of the test site) during the 37-foot hover at 56,000 pounds." From Figure 74, on page 160, at 20 ft hover (37-ft rotor height) and a distance of 80 feet from rotor center, the peak force is ~105 lbs. The measured stability limit for Subject 3 is 87 lbs. Using these values for Subject 3, the resultant personnel stability ratio would be $87 \text{ lb} / 105 \text{ lb} = 0.83$.

Page 168 of reference 0-6 states "Subject 4 also participated in a qualitative survey during the 70,000 pound gross weight evaluation. While he was able to completely penetrate the flow field at all three hover heights, did did experience great difficulty when moving in the peak force region, and postural stability could not be controlled." From Figure 75, on page 161, the highest peak force encountered would be at ~60-ft from rotor center during a 20-ft hover and correspond to ~140 lbs. The measured stability limit for Subject 4 is 115 lb. Using these values for Subject 4, the resultant personnel stability ratio would be $115 \text{ lb} / 140 \text{ lb} = 0.82$.

From the two proceeding paragraphs, Subjects 3 and 4 would have personnel stability ratios of 0.83 and 0.82. Averaging these two values give 0.825. Since only two data points were available for derivation, the number of significant figures in the averaged value tends to give a false sense of accuracy to the number. For this reason, 0.8 is used in calculations for peak force on personnel in rotorwash operational footprints. Further research is required to validate this ratio for a wider range of test subject, test conditions, aircraft, and flight conditions. At best, this is a rough approximation and should be used with caution.

No equivalent test data exist for the tandem and tilt rotor to derive an equivalent personnel stability ratio. For this reason, velocity profile similarity is used for these configurations as compared to the helicopter.

In Figure O-2, the tandem mean and peak radial velocity profile is similar to the helicopter for rotors of equal thrust. In the Figure O-3 centerline case, the delta in maximum velocity magnitude of the mean and peak is consistent with the helicopter. For this reason, the tandem is also assigned a value of 0.8 in calculations for peak force on personnel in rotorwash operational footprints.

In Figure O-2, the tilt rotor mean radial velocity profile is similar to the helicopter for rotors of equal thrust. The peak velocity profile is less in magnitude as compared to the helicopter peak velocity profile. In the Figure O-3 centerline case, the delta in maximum velocity magnitude of the mean and peak is significantly less than the helicopter. For this reason, the tilt rotor is assigned a value of 1.0 in calculations for peak force on personnel in rotorwash operational footprints.

Force on PAXman Comparison

The calculated drag force on personnel uses the peak velocity profile, personnel limit stability ratio, and a representative silhouette (PAXman). Figure O-4 applies the Figure O-2 and O-3 velocity profiles on PAXman within RoWFoot. Drag force is calculated with a drag coefficient of 1.0. The helicopter, tandem, and tilt rotor are described in Table O-1. Radial conditions are represented as solid lines and have the origin at the rotor center (tandem at 0-degree azimuth, tilt rotor at 90-degrees azimuth). Centerline conditions are represented as dashed lines and have the origin on the aircraft centerline located between the rotors (tandem at 90 degrees and tilt rotor at 0 degrees). Distances along the X-axis extend to 7 rotor radii.

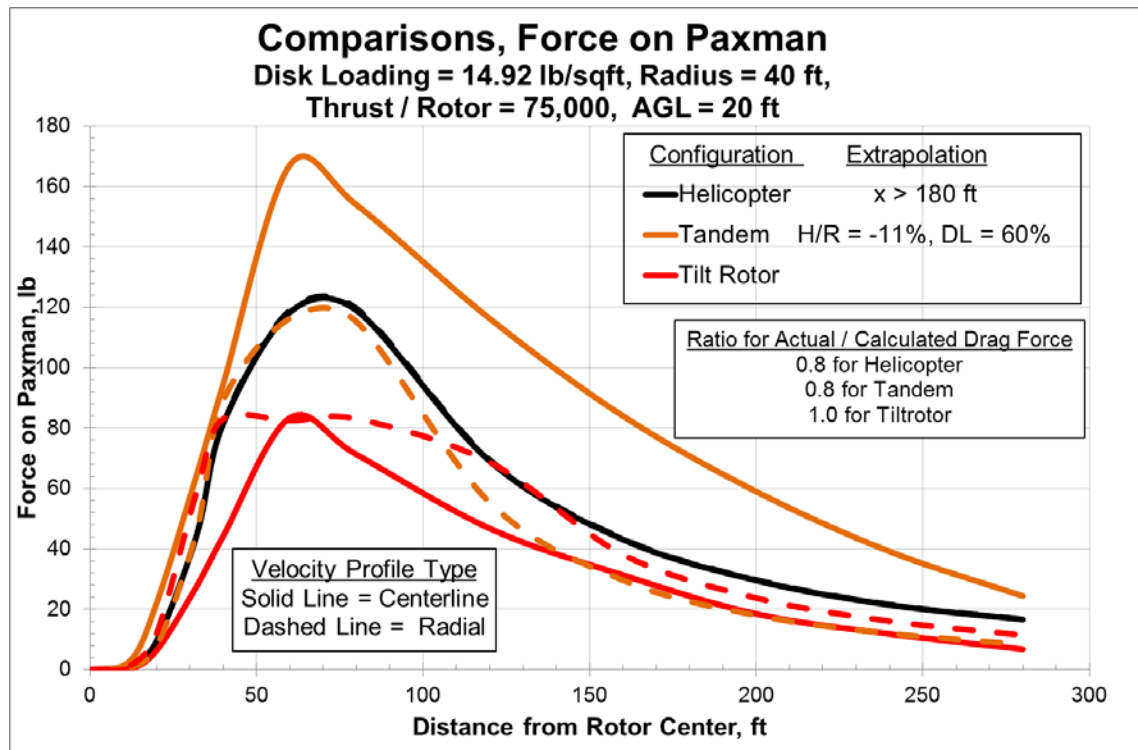


Figure O-4 Drag Force on Ground Personnel

The helicopter has identical radial and centerline velocity profiles. Thus, the radial and centerline force on PAXman calculated force will be the same.

The tandem radial force results compare closely to the helicopter. This is expected since the velocity profiles were similar in Figure O-2. During comparisons to the velocity profiles in Figure O-2, note that wind velocity occurring above the height of the PAXman model (~6 feet) will not appear in the resultant drag calculations. The tandem centerline drag force is significantly higher than the helicopter. This is due to the higher magnitude of velocity in Figure O-3 occurring below the 6' level. Previously, this was theorized to originate from the overlap region of the tandem rotor producing higher velocity conditions in the downwash.

Tilt rotor radial and centerline forces on personnel are lower than the helicopter due to the lower velocity profiles seen in Figures O-2 and O-3. As previously discussed, the helicopter and tandem use an outwash personnel stability limit ratio of 0.8, while the tilt rotor value is 1.0. An interesting feature in Figure O-4 is the comparison of tilt rotor radial and centerline force on personnel graphs. The dashed (radial case) exceeds the solid (centerline) case for most of the case. This is explained by the distribution of the mass flow in Figures O-2 and O-4. At heights in the velocity profile above ~6 feet, the PAXman model is not affected. In other words, the tilt rotor centerline case distributes the mass flow over a greater height and thus allows much of the higher energy air to pass over the head of ground personnel. This rotor scaling effect causes interesting trends with force on the PAXman model as seen in the following sections.

Scaling Trends—Velocity Profile

Variation in key rotorwash factors will affect the size and magnitude of the resultant velocity profile flow fields. This variation can occur by changes to the design or operation of the rotorcraft. The following figures present scaling trends for changes in thrust per rotor, rotor radius, and height Above Ground Level (AGL). These trends are shown for variations of the helicopter, tandem, and tilt rotor previously given in Table O-1. Baseline input data from Figures O-2 and O-3 are repeated in Figures O-5 to O-13 at one diameter from rotor center to enable reference back to the cross configuration comparisons. Table O-2 gives the input data for scaling trends presented in Figures O-5 to O-13. The light green shading indicates the baseline input set. In Table O-2, the first set of rows shows input for Thrust/Rotor from 25,000 to 125,000 lb. The second set of rows shows input for variation of rotor radius from 10 to 50 feet at a constant disk loading. The last set of rows shows variation of hover height above ground with no change to the aircraft weight or size.

	Thrust / Rotor = 25,000			Thrust / Rotor = 50,000			Thrust / Rotor = 75,000			Thrust / Rotor = 100,000			Thrust / Rotor = 125,000		
	Heli	TD	TR	Heli	TD	TR	Heli	TD	TR	Heli	TD	TR	Heli	TD	TR
No Rotors	1	2	2	1	2	2	1	2	2	1	2	2	1	2	2
Radius, ft	40.0	40.0	40.0	40.0	40.0	40.0	40.0	40.0	40.0	40.0	40.0	40.0	40.0	40.0	40.0
Rotor Separation	0.0	52.3	102.3	0.0	52.3	102.3	0.0	52.3	102.3	0.0	52.3	102.3	0.0	52.3	102.3
Gear to Rotor	25.00	25.00	25.00	25.00	25.00	25.00	25.00	25.00	25.00	25.00	25.00	25.00	25.00	25.00	25.00
Area / Rotor, sqft	5,027	5,027	5,027	5,027	5,027	5,027	5,027	5,027	5,027	5,027	5,027	5,027	5,027	5,027	5,027
Gross Weight, lb	23,810	47,393	45,872	47,619	94,787	91,743	71,429	142,180	137,615	95,238	189,573	183,486	119,048	236,967	229,358
Disk Loading (T), psf	4.97	4.97	4.97	9.95	9.95	9.95	14.92	14.92	14.92	18.89	18.89	18.89	24.87	24.87	24.87
T/W	1.050	1.055	1.090	1.050	1.055	1.090	1.050	1.055	1.090	1.050	1.055	1.090	1.050	1.055	1.090
Thrust / Rotor	25,000	25,000	25,000	50,000	50,000	50,000	75,000	75,000	75,000	100,000	100,000	100,000	125,000	125,000	125,000
	R = 10			R = 20			R = 30			R = 40			R = 50		
	Heli	TD	TR	Heli	TD	TR	Heli	TD	TR	Heli	TD	TR	Heli	TD	TR
No Rotors	1	2	2	1	2	2	1	2	2	1	2	2	1	2	2
Radius, ft	10.0	10.0	10.0	20.0	20.0	20.0	30.0	30.0	30.0	40.0	40.0	40.0	50.0	50.0	50.0
Rotor Separation	0.0	13.1	25.6	0.0	26.1	51.1	0.0	39.2	76.7	0.0	52.3	102.3	0.0	65.3	127.8
Gear to Rotor	25.00	25.00	25.00	25.00	25.00	25.00	25.00	25.00	25.00	25.00	25.00	25.00	25.00	25.00	25.00
Area / Rotor, sqft	314	314	314	1,257	1,257	1,257	2,827	2,827	2,827	5,027	5,027	5,027	7,854	7,854	7,854
Gross Weight, lb	4,464	8,886	8,601	17,857	35,545	34,404	40,179	79,976	77,408	71,429	142,180	137,615	111,607	222,156	215,023
Disk Loading (T), psf	14.92	14.92	14.92	14.92	14.92	14.92	14.92	14.92	14.92	14.92	14.92	14.92	14.92	14.92	14.92
T/W	1.050	1.055	1.090	1.050	1.055	1.090	1.050	1.055	1.090	1.050	1.055	1.090	1.050	1.055	1.090
Thrust / Rotor	4,688	4,688	4,688	18,750	18,750	18,750	42,188	42,188	42,188	75,000	75,000	75,000	117,188	117,188	117,188
	AGL = 10			AGL = 20			AGL = 80			AGL = 120			AGL = 160		
	Heli	TD	TR	Heli	TD	TR	Heli	TD	TR	Heli	TD	TR	Heli	TD	TR
No Rotors	1	2	2	1	2	2	1	2	2	1	2	2	1	2	2
Radius, ft	1	2	2	20.0	20.0	20.0	40.0	40.0	40.0	40.0	40.0	40.0	40.0	40.0	40.0
Rotor Separation	40.0	40.0	40.0	40.0	40.0	40.0	40.0	40.0	40.0	40.0	40.0	40.0	40.0	40.0	40.0
Gear to Rotor	0.0	52.3	102.3	0.0	52.3	102.3	0.0	52.3	102.3	0.0	52.3	102.3	0.0	52.3	102.3
Area / Rotor, sqft	25.00	25.00	25.00	25.00	25.00	25.00	25.00	25.00	25.00	25.00	25.00	25.00	25.00	25.00	25.00
Gross Weight, lb	5,027	5,027	5,027	5,027	5,027	5,027	5,027	5,027	5,027	5,027	5,027	5,027	5,027	5,027	5,027
Disk Loading (T), psf	71,429	142,180	137,615	71,429	142,180	137,615	71,429	142,180	137,615	71,429	142,180	137,615	71,429	142,180	137,615
T/W	14.92	14.92	14.92	14.92	14.92	14.92	14.92	14.92	14.92	14.92	14.92	14.92	14.92	14.92	14.92
Thrust / Rotor	1.050	1.055	1.090	1.050	1.055	1.090	1.050	1.055	1.090	1.050	1.055	1.090	1.050	1.055	1.090
	75,000	75,000	75,000	75,000	75,000	75,000	75,000	75,000	75,000	75,000	75,000	75,000	75,000	75,000	75,000

Table O-2 Scaling Trends Input Data Set

As previously documented in [Appendix J](#), RoWFoot uses an empirically tuned conceptual level analysis model. When extrapolation occurs outside of basic parameters beyond the test data boundaries, the confidence in the predictive model is decreased. Table O-3 presents basic parameters of rotor separation and rotor height previously provided in Table O-2 in nondimensional quantities. The main rotor(s) radius is used to non-dimensionalize these distances. The table also includes the disk loading as a basic parameter for indication of model extrapolation. Colored areas in Table O-3 show conditions where the parameter values are outside of the test data range, as given in [Appendix J](#), and indicate modeling extrapolation for the associated condition.

	Thrust / Rotor = 25,000			Thrust / Rotor = 50,000			Thrust / Rotor = 75,000			Thrust / Rotor = 100,000			Thrust / Rotor = 125,000		
	Heli	TD	TR	Heli	TD	TR	Heli	TD	TR	Heli	TD	TR	Heli	TD	TR
Rotor Separation, ND	0.00	1.31	2.56	0.00	1.31	2.56	0.00	1.31	2.56	0.00	1.31	2.56	0.00	1.31	2.56
Rotor Height, ND	1.13	1.13	1.13	1.13	1.13	1.13	1.13	1.13	1.13	1.13	1.13	1.13	1.13	1.13	1.13
Disk Loading (T), psf	4.97	4.97	4.97	9.95	9.95	9.95	14.92	14.92	14.92	19.89	19.89	19.89	24.87	24.87	24.87
	R = 10			R = 20			R = 30			R = 40			R = 50		
	Heli	TD	TR	Heli	TD	TR	Heli	TD	TR	Heli	TD	TR	Heli	TD	TR
Rotor Separation, ND	0.00	1.31	2.56	0.00	1.31	2.56	0.00	1.31	2.56	0.00	1.31	2.56	0.00	1.31	2.56
Rotor Height, ND	4.50	4.50	4.50	2.25	2.25	2.25	1.50	1.50	1.50	1.13	1.13	1.13	0.90	0.90	0.90
Disk Loading (T), psf	14.92	14.92	14.92	14.92	14.92	14.92	14.92	14.92	14.92	14.92	14.92	14.92	14.92	14.92	14.92
	AGL = 10			AGL = 20			AGL = 80			AGL = 120			AGL = 160		
	Heli	TD	TR	Heli	TD	TR	Heli	TD	TR	Heli	TD	TR	Heli	TD	TR
Rotor Separation, ND	0.00	1.31	2.56	0.00	1.31	2.56	0.00	1.31	2.56	0.00	1.31	2.56	0.00	1.31	2.56
Rotor Height, ND	0.88	0.88	0.88	1.13	1.13	1.13	2.63	2.63	2.63	3.63	3.63	3.63	4.63	4.63	4.63
Disk Loading (T), psf	14.92	14.92	14.92	14.92	14.92	14.92	14.92	14.92	14.92	14.92	14.92	14.92	14.92	14.92	14.92

Table O-3 Modeling Extrapolation for the Scaling Trends Input Data Set

As the magnitude of extrapolation increases, the confidence in the predictive results decreases. Table O-4 takes the values shown in Table O-3 and provides a measurement of

the amount of extrapolation beyond the non-dimensional bounds for the conceptual level model. The amount of extrapolation is measured using the percentage the parameter in Table 0-3 is below the lower bound or above the upper bound of the non-dimensional test data range in [Appendix J](#). A negative value indicates the parameter is below the lower range of test data. A positive value indicates the value of the parameter is above the high range of test data. The value of this extrapolation in % appears in the legends of Figures O-2 through O-22, where appropriate.

	Thrust / Rotor = 25,000			Thrust / Rotor = 50,000			Thrust / Rotor = 75,000			Thrust / Rotor = 100,000			Thrust / Rotor = 125,000		
	Heli	TD	TR	Heli	TD	TR	Heli	TD	TR	Heli	TD	TR	Heli	TD	TR
Rotor Separation, ND	0%	0%	0%	0%	0%	0%	0%	0%	0%	0%	0%	0%	0%	0%	0%
Rotor Height, ND	0%	-11%	0%	0%	-11%	0%	0%	-11%	0%	0%	-11%	0%	0%	-11%	0%
Disk Loading (T), psf	-40%	-19%	-53%	0%	7%	-7%	0%	60%	0%	33%	113%	0%	66%	167%	24%
	R = 10			R = 20			R = 30			R = 40			R = 50		
Rotor Separation, ND	0%	0%	0%	0%	0%	0%	0%	0%	0%	0%	0%	0%	0%	0%	0%
Rotor Height, ND	0%	14%	0%	0%	0%	0%	0%	0%	0%	0%	-11%	0%	0%	-29%	-20%
Disk Loading (T), psf	0%	60%	0%	0%	60%	0%	0%	60%	0%	0%	60%	0%	0%	60%	0%
	AGL = 10			AGL = 20			AGL = 80			AGL = 120			AGL = 160		
Rotor Separation, ND	0%	0%	0%	0%	0%	0%	0%	0%	0%	0%	0%	0%	0%	0%	0%
Rotor Height, ND	0%	-31%	-22%	0%	-11%	0%	0%	0%	0%	0%	0%	0%	0%	18%	0%
Disk Loading (T), psf	0%	60%	0%	0%	60%	0%	0%	60%	0%	0%	60%	0%	0%	60%	0%

Table O-4 Magnitude of Modeling Extrapolation for the Scaling Trends Input Data Set

In using the chosen color scheme, the value of 50% is arbitrarily chosen as the transition point from “yellow” to “red” and is not based on research or any engineering judgment of the severity of the decrease in modeling confidence. In Table O-4, the colors indicate:

Green	No Extrapolation of Parameter
Yellow	< 50% Extrapolation of Parameter
Red	≥ 50% Extrapolation of Parameter

Documentation of the RoWFoot model validity with respect to distance from the rotor center appears in [Appendix J](#). For each of the three rotorcraft configurations (single main rotor helicopter, tandem helicopter, and tilt rotor), the non-dimensional lower bound of the modeling validity is 0.80 for all cases except for the tilt rotor’s interaction plane condition which was 1.00. In the cases for Figures O-4 and Figures O-14 through O-22, the condition is showing a rapid decrease in velocity from the lower model validity bound to the theoretical stagnation point directly under the rotor. For this reason, the lower bound of modeling validity with respect to distance from the rotor center does not appear in the figures of this appendix.

As summarized in [Appendix J](#), modeling cases that exceed the upper bound for the distance from the rotor center are expected to have a slowly decreasing confidence with extrapolation in the modeling for the radial outwash and a decreasing confidence in the modeling for the centerline outwash. For a 40-foot radius rotor, this upper bound distance would occur at 180 (4.5R), 310 (7.75R), and 280 (7R) feet from the rotor center for the single main rotor helicopter, tandem helicopter, and tilt rotor, respectively. The maximum distance displayed by curves in Figures O-4 and Figures O-14 through O-22 is 280 feet (7R).

Helicopter scaling trends are presented in Figures O-5 to O-7. For the helicopter, radial, and centerline cases are the same as modeled in RoWFoot. Each of the velocity profiles displayed is at one diameter from the rotor center.

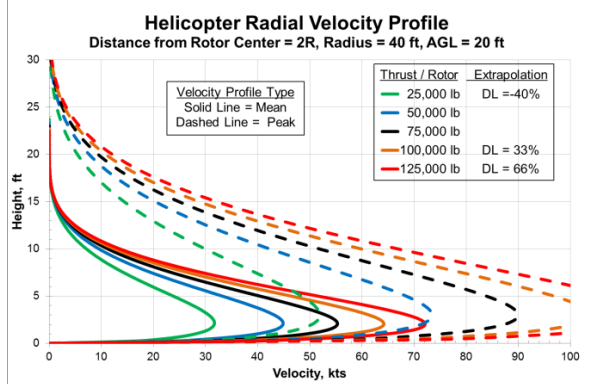


Figure O-5 Helicopter: Effect of Rotor Thrust on Velocity Profile

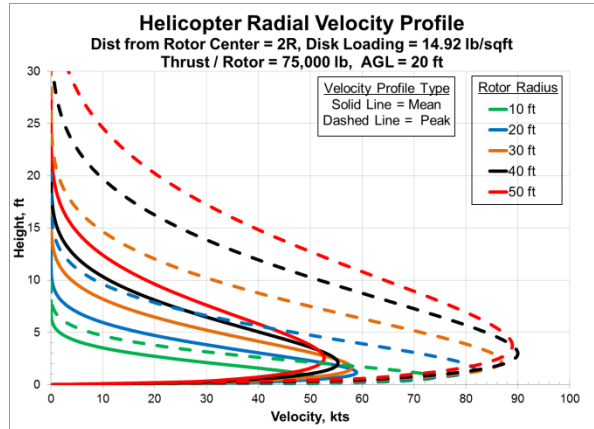


Figure O-6 Helicopter: Effect of Rotor Radius on Velocity Profile

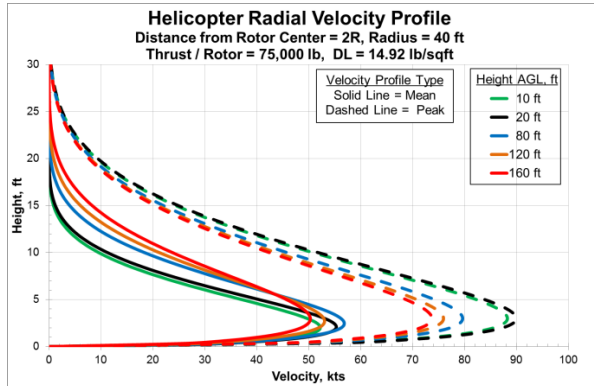


Figure O-7 Helicopter: Effect of Height Above Ground on Velocity Profile

In Figure O-5, the increase in thrust per rotor corresponds to an increase in the magnitude of the maximum velocity in the velocity profile. Figure O-7 shows the effect that variation in altitude has on the magnitude and shape of the profile. This is due to ground effect at low altitude and decay of the downwash with high altitude. In Figure O-6, the velocity profile height varies according to the rotor radius and the magnitude results from the ground effect or downwash decay (ratio of rotor altitude to diameter).

Tandem scaling trends are presented in Figures O-8 to O-10. The graphs on the left are for radial outwash, and the ones on the right are for centerline outwash. Each of the velocity profiles displayed is at one diameter from the rotor center.

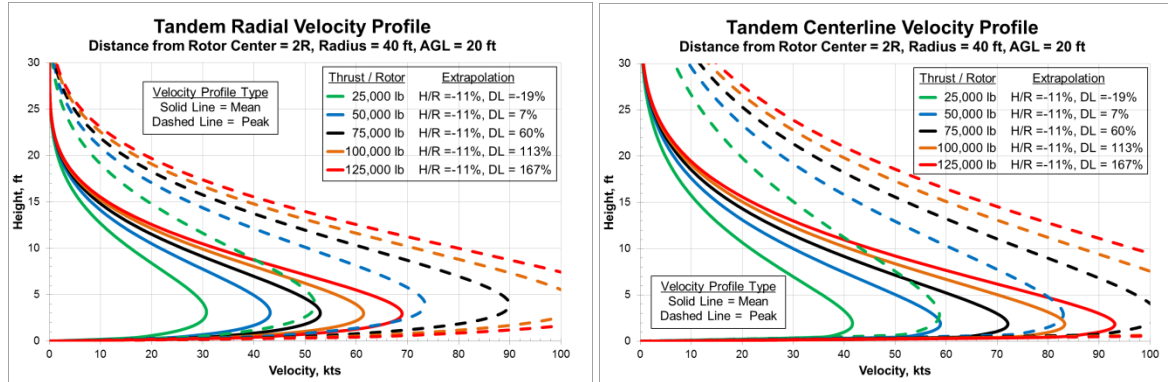


Figure O-8 Tandem: Effect of Rotor Thrust on Velocity Profile

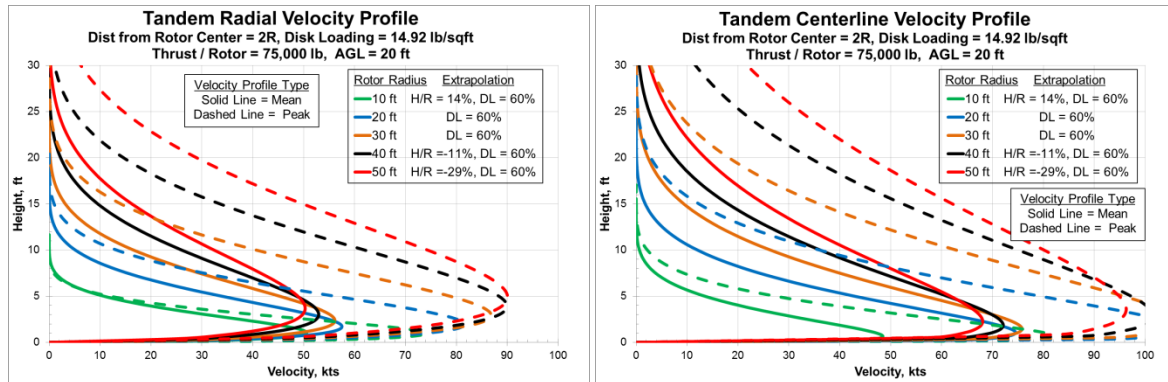


Figure O-9 Tandem: Effect of Rotor Radius on Velocity Profile

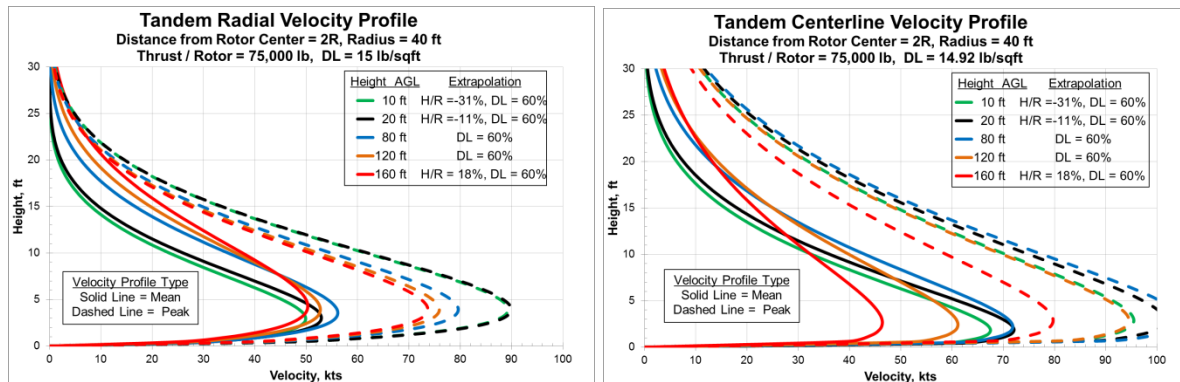


Figure O-10 Tandem: Effect of Height Above Ground on Velocity Profile

In Figure O-8, the increase in thrust per rotor corresponds to an increase in the magnitude of the maximum velocity in the velocity profile. Figure O-10 shows the effect that variation in altitude has on the magnitude and shape of the profile. This is due to ground effect at low altitude and decay of the downwash with altitude. In Figure O-9, the velocity profile height varies according to the rotor radius and the magnitude results from the ground effect or downwash decay (ratio of rotor altitude to diameter).

Tilt rotor scaling trends are presented in Figures O-11 to O-13. The graphs on the left are for radial outwash, and the ones on the right are for centerline outwash. Each of the velocity profiles displayed is at one diameter from the rotor center.

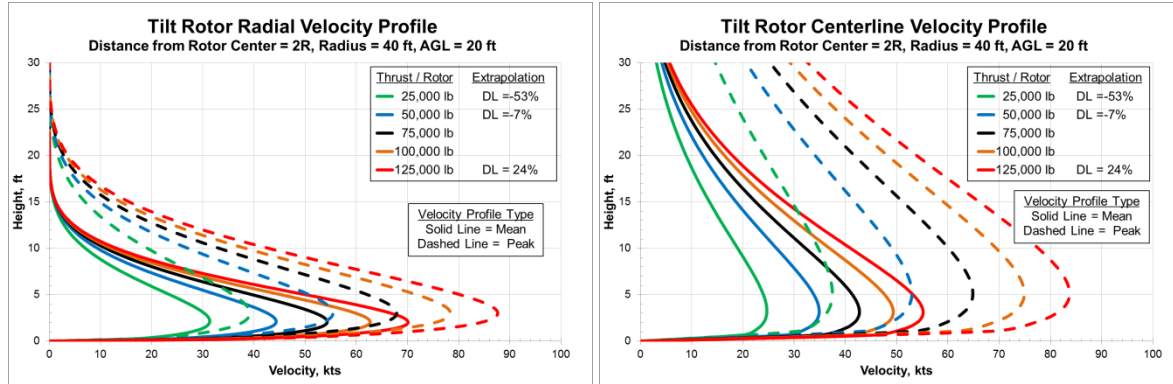


Figure O-11 Tilt Rotor: Effect of Rotor Thrust on Velocity Profile

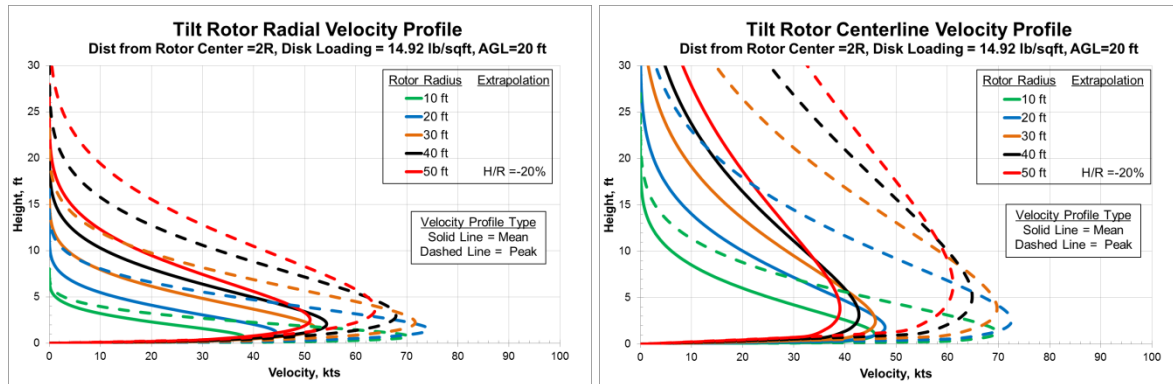


Figure O-12 Tilt Rotor: Effect of Rotor Radius on Velocity Profile

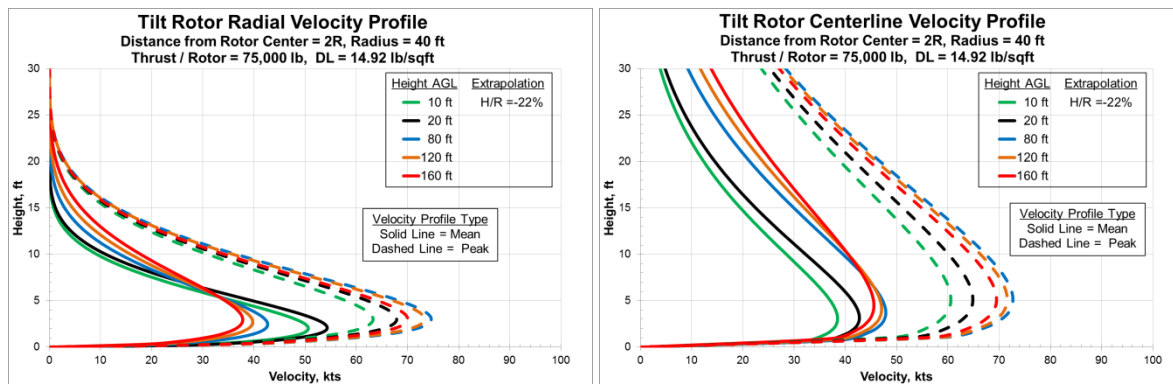


Figure O-13 Tilt Rotor: Effect of Height Above Ground on Velocity Profile

In Figure O-11, the increase in thrust per rotor corresponds to an increase in the magnitude of the maximum velocity in the velocity profile. Figure O-13 shows the effect that variation in altitude has on the magnitude and shape of the profile. This is due to ground effect at low altitude and decay of the downwash with altitude. In Figure O-12, the velocity profile height varies according to the rotor radius and the magnitude results from the ground effect or downwash decay (ratio of rotor altitude to diameter).

Scaling Trends – Force on Personnel

The calculated drag force on personnel uses the peak velocity profile, personnel limit stability ratio, and a representative silhouette (PAXman). Figures 0-14 to 0-22 apply the velocity profiles from Figures 0-5 to 0-13 to the PAXman model with the previously determined personnel stability ratio of 0.8 for helicopter and tandem and 1.0 for the tilt rotor. Radial conditions are represented as solid lines and have the origin at the rotor center (tandem at 0-degree azimuth, tilt rotor at 90-degrees azimuth). Centerline conditions are represented as dashed lines and have the origin on the aircraft centerline located between the rotors (tandem at 90 degrees and tilt rotor at 0 degrees). Distances along the X-axis extend to 7 rotor radii. Baseline input data from Figure 0-4 are repeated in Figures 0-14 to 0-22 from the origin to 7 rotor radii distance range to enable reference back to the cross configuration comparisons.

When comparing Figures 0-14 to 0-22 with the corresponding velocity profiles given in Figures 0-5 to 0-13, only the velocity profile below 6 feet height is of interest. The distribution width of the PAXman shape is greatest in the torso region, so the peak velocity profile having the highest magnitude in this region will typically produce the highest drag force. Changes in rotor size will change the height of the velocity profile. At first glance, some of the trends for larger rotors may seem counter intuitive until the connection is made from the height of the PAXman model and the vertical location in the velocity profile of the highest velocity outwash.

Helicopter scaling trends are presented in Figures O-14 to O-16. For the helicopter, radial and centerline cases are the same as modeled in RoWFoot. The personnel drag force variation displayed is for 0 to 7 rotor radii from the rotor center.

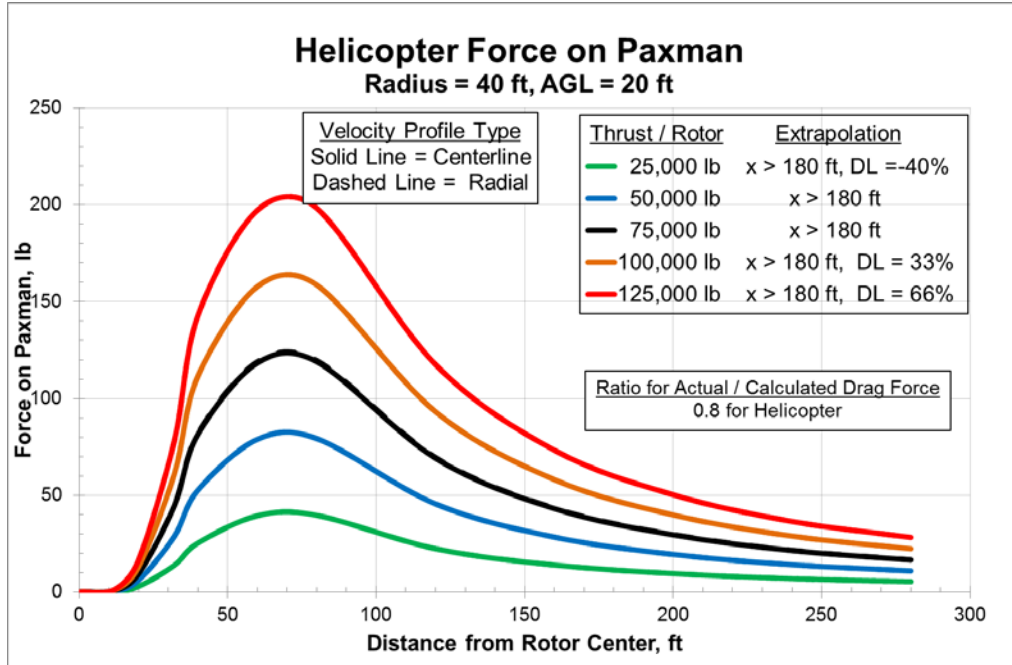


Figure O-14 Helicopter: Effect of Rotor Thrust on PAXman Drag

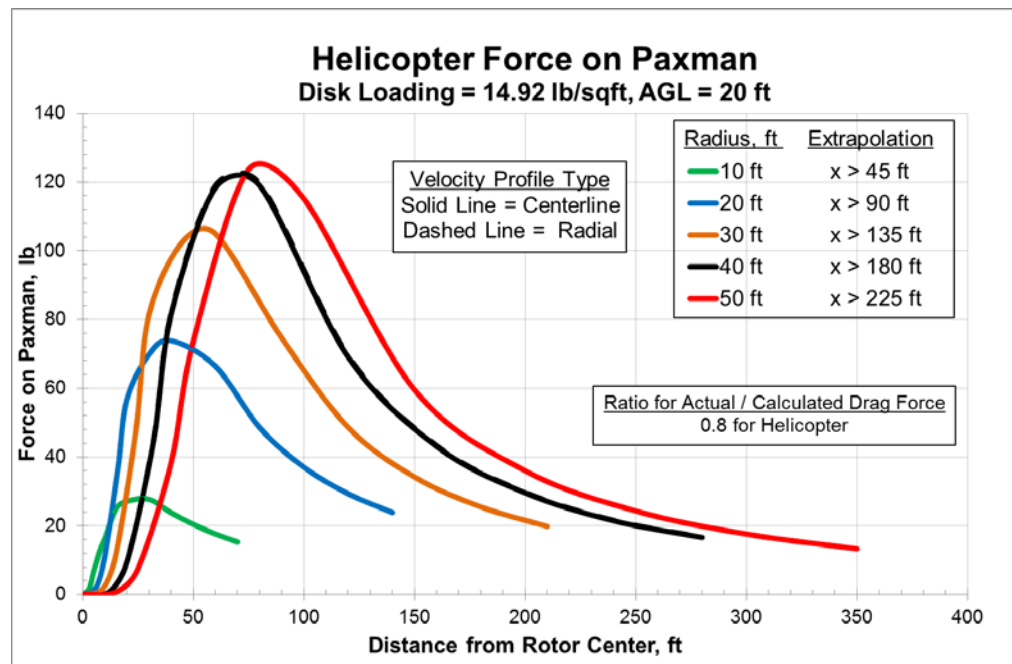


Figure O-15 Helicopter: Effect of Rotor Radius on PAXman Drag

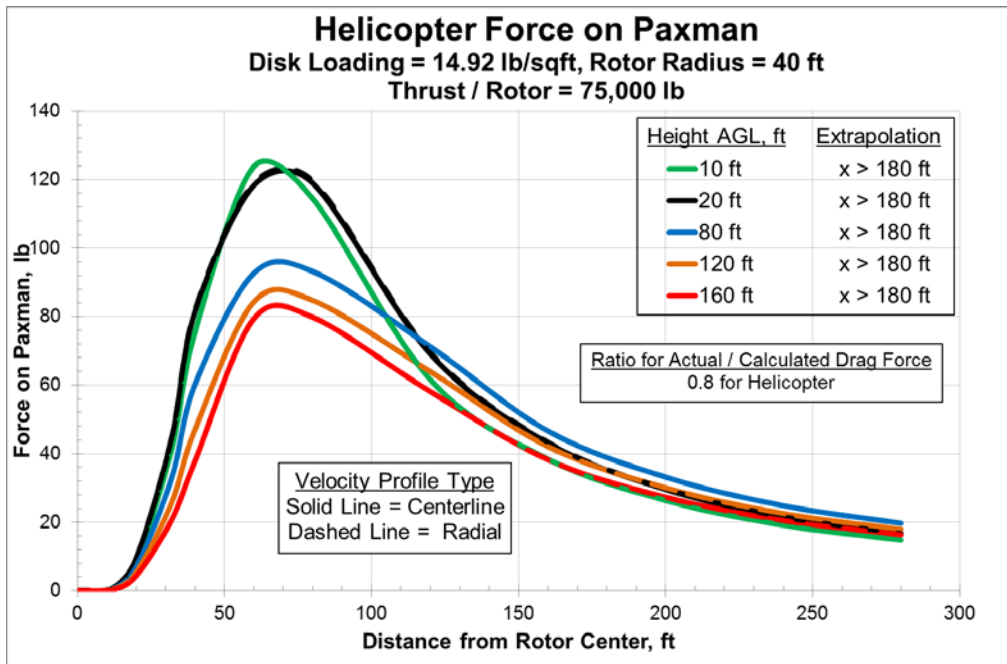


Figure O-16 Helicopter: Effect of Height Above Ground on PAXman Drag

In Figure O-14, as the thrust per rotor increases, the corresponding increase to the velocity profile in Figure O-5 yields an increase to the drag on the PAXman model. Figure O-15 shows the variation of the rotor radius at constant disk loading to the drag on PAXman. Of note here is that the maximum velocity region of the corresponding velocity profile (Figure O-6) does not exceed the torso region of the PAXman model. The AGL trend in Figure O-16 is caused by the decay of the downwash decreasing the magnitude of the outwash velocity profile, as seen in Figure O-7.

Tandem scaling trends are presented in Figures 0-17 to 0-19. In each graph, the solid lines represent centerline outwash (90- and 270-degrees azimuth angles) and the dashed lines represent radial outwash (0- and 180-degree azimuth angles). The personnel drag force variation displayed is for 0 to 7 rotor radii from the rotor center.

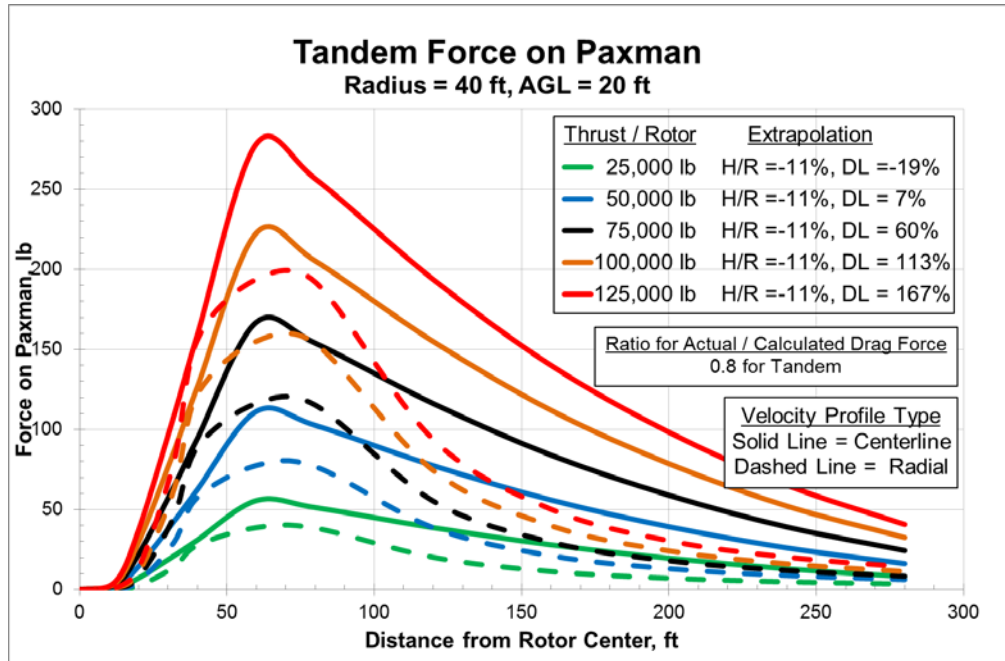


Figure 0-17 Tandem: Effect of Rotor Thrust on PAXman Drag

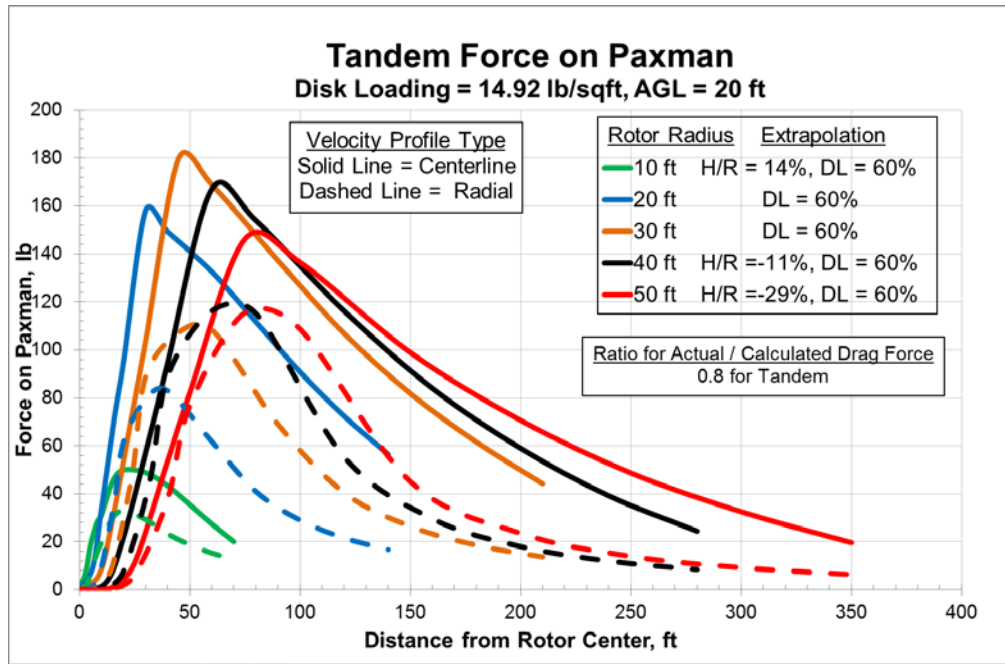


Figure 0-18 Tandem: Effect of Rotor Radius on PAXman Drag

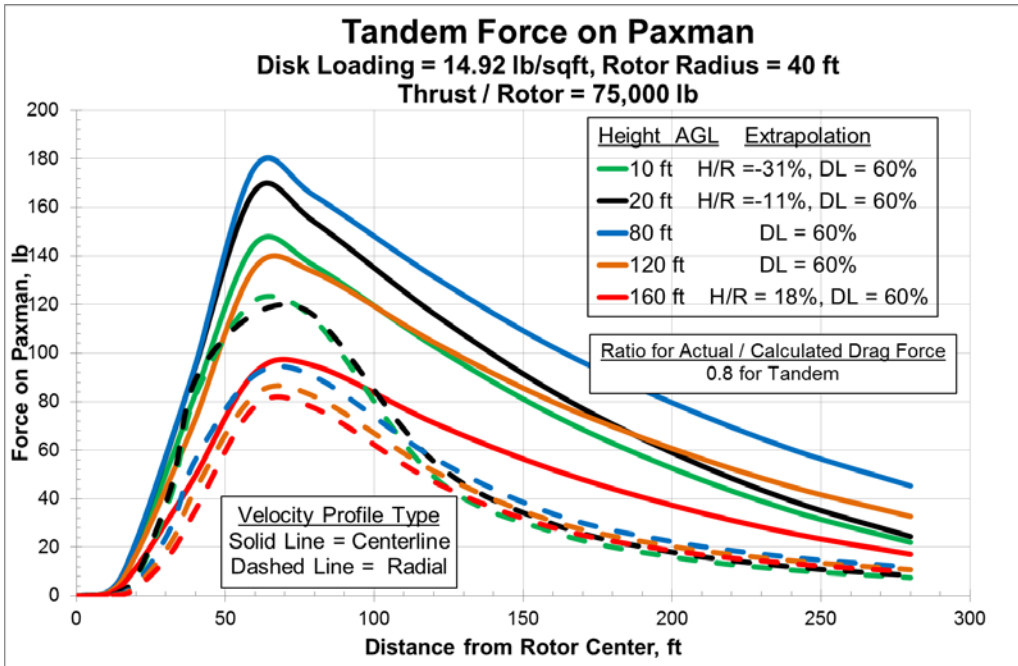


Figure O-19 Tandem: Effect of Height Above Ground on PAXman Drag

In Figure O-17, as the thrust per rotor increases, the corresponding increase to the velocity profile in Figure O-8 yields an increase to the drag on the PAXman model. Figure O-18 shows the variation of the rotor radius at constant disk loading to the drag on PAXman. As the maximum velocity of the corresponding velocity profile (Figure O-9) rises above the PAXman torso area region for the larger rotor radii, there is a reduction in the resultant drag in Figure O-18. The AGL trend in Figure O-19 is caused by the decay of the downwash decreasing the magnitude of the outwash velocity profile, as seen in Figure O-10.

Tilt rotor scaling trends are presented in Figures O-20 to O-22. In each graph, the solid lines represent centerline outwash (0- and 180-degrees azimuth angles) and the dashed lines represent radial outwash (90- and 270-degree azimuth angles). The personnel drag force variation displayed is for 0 to 7 rotor radii from the rotor center.

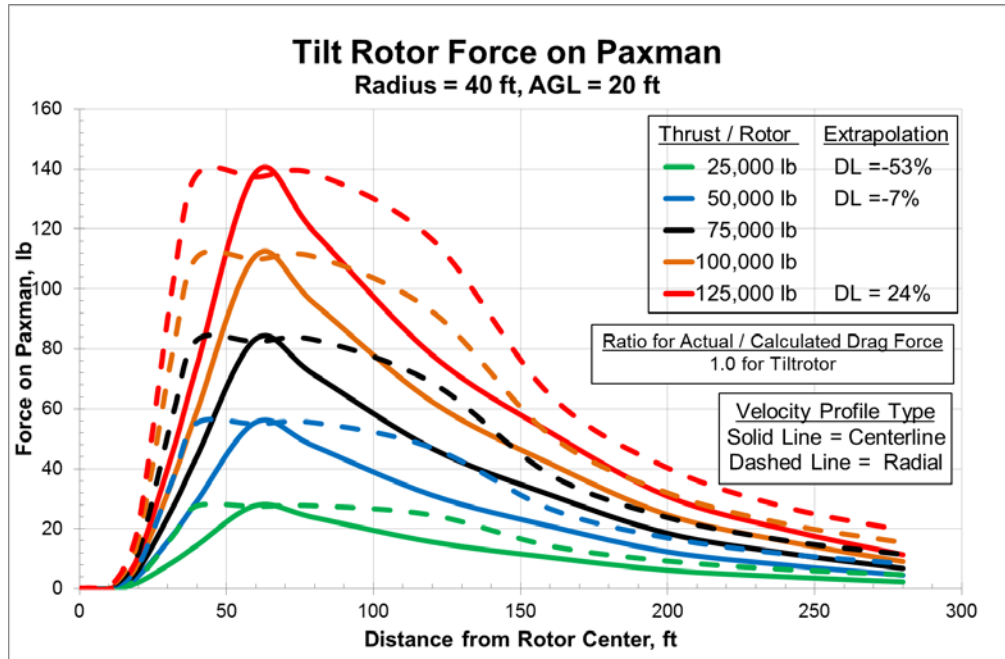


Figure O-20 Tilt Rotor: Effect of Rotor Thrust on PAXman Drag

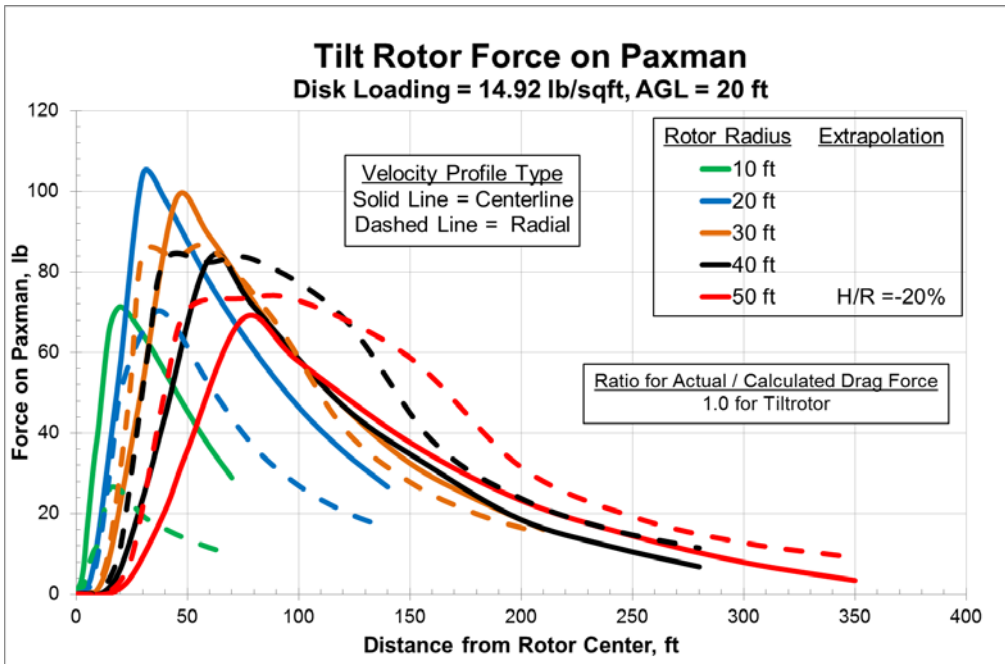


Figure O-21 Tilt Rotor: Effect of Rotor Radius on PAXman Drag

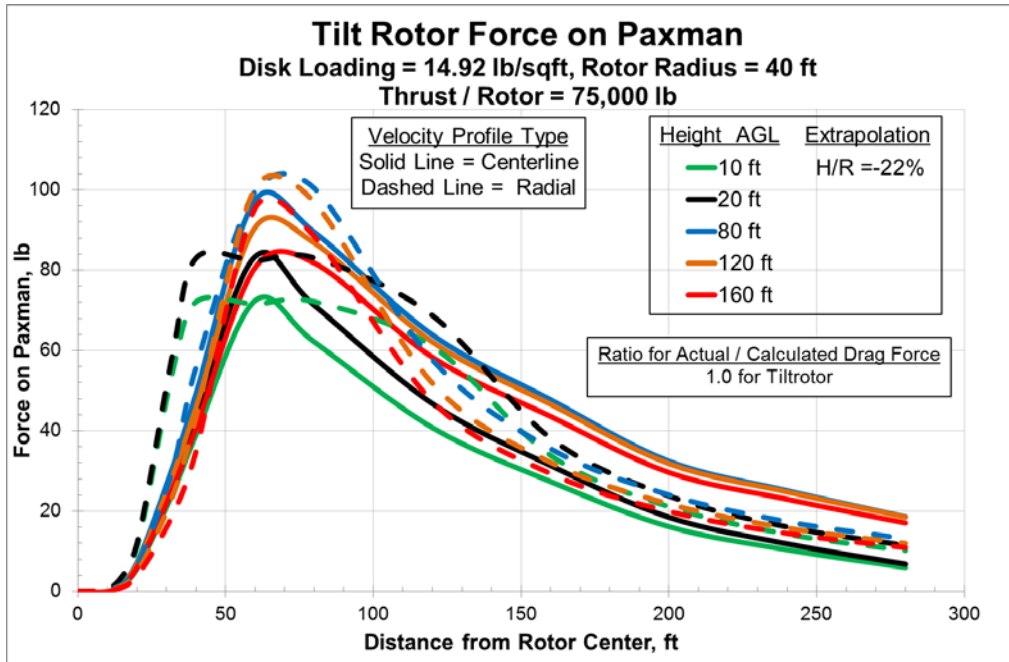


Figure O-22 Tilt Rotor: Effect of Height Above Ground on PAXman Drag

In Figure O-20, as the thrust per rotor increases, the corresponding increase to the velocity profile in Figure O-11 yields an increase to the drag on the PAXman model. Figure O-21 shows the variation of the rotor radius at constant disk loading to the drag on PAXman. As the maximum velocity of the corresponding velocity profile (Figure O-12) rises above the PAXman torso area region for the larger rotor radii, there is a reduction in the resultant drag in Figure O-21. The AGL trend in Figure O-22 is caused by the decay of the downwash decreasing the magnitude of the outwash velocity profile, as seen in Figure O-13.

Summary

The conceptual rotorwash model RoWFoot is capable of generating outwash velocity profiles for single main rotor helicopters, tandem helicopters, and tilt rotors. Using the peak velocity profile, a representative silhouette (PAXman) is used to determine the maximum drag force produced on ground personal. Drag forces from the PAXman model are then corrected with a personnel stability ratio to approximate realistic forces encountered by ground personnel.

At equivalent rotor conditions, outwash wind velocity profiles are dependent on the type of rotorcraft configuration. The separation distance of multiple rotors changes the magnitude and distribution of the mass flow. At the same thrust per rotor, the mean radial velocity profile is similar for the helicopter, tandem, and tilt rotor. The helicopter and tandem peak radial velocity profiles are similar, while the tilt rotor's are smaller in magnitude. For centerline outwash, the tandem velocity magnitude is higher than the tilt rotor. These differences are supported by flight test data. Explanation of the differences arises from the distribution of the air mass flow within the rotorwash.

As the thrust per rotor increases, the outwash wind velocity and force on PAXman also increases. As the rotor radius increases, height of the outwash velocity profile also increases. At a constant disk loading, as the height of the outwash maximum velocity air increases above the PAXman's torso region, the resulting drag decreases. Height of the rotor above ground level can decrease the outwash velocity due to ground effect at low altitude or decay in the downwash at high altitude.

Additional testing is strongly encouraged to explore the effect of rotor spacing on the centerline outwash velocity profile distribution. Testing is also needed to confirm the personnel stability ratio for actual to calculated peak force on PAXman, especially for the tandem and tilt rotor configurations.

References

- O-1. Harris, D. J., and Simpson, R. D., "CH-53E Helicopter Downwash Evaluation. Final Report," Naval Air Test Center Technical Report No. SY-89R-78, August 1, 1978.
- O-2. Lake, R. E., and Clark, W. J., "V-22 Rotor Downwash Survey," NAWCADPAX-98-88-RTTR, July 1998.
- O-3. Silva, M. J., "CH-47D Tandem Rotor Outwash Survey," NAWCADPAX/EDR-2010/120, August 2010.
- O-4. Meyerhoff, C. L.; Lake, R.; and Peters, Lt. D., "H-60 Helicopter Rotor Downwash Wind Velocity Evaluation," Naval Air Warfare Center Report SY-3R-94, February 1994.

O-5. Harris, D. J., and Simpson, R. D., "Technical Evaluation of the Rotor Downwash Flow Field of the XV-15 Tilt Rotor Research Aircraft," Naval Air Test Center Technical Report No. SY-14R-83, July 1983.

O-6. Ferguson, S. W., "Rotorwash Analysis Handbook, Volume I – Development and Analysis," Federal Aviation Administration, Washington D.C., Technical Report DOT/FAA/RD-93/31,I, June 1994.

O-7. Ferguson, S. W., "Rotorwash Analysis Handbook, Volume II – Appendixes, Federal Aviation Administration, Washington D.C., Technical Report DOT/FAA/RD-93/31,II, June 1994.

Appendix P: Rotorwash Footprint Generation Process

Kenneth Smith, U.S. Navy

This appendix documents the process used to create the graphical representation for the predicted impact a hovering rotorcraft will have on the ground environment. It post-processes results of the configuration level analysis and incorporates hazard limits to produce plots of the predicted impact or “rotorwash footprint.”

Rotorwash configuration level analysis calculates output for two flow regions: radial flow, where the rotorwash is dominated by a single rotor and centerline flow, where the rotorwash is generated and influenced by two or more rotors (applicable to tilt rotors, tandem helicopters, etc.). Between these flow regions, a “transition” flow region connects outwash characteristics found within the radial flow and centerline flow regions. Within the transition region, outwash velocity profiles are calculated using a 2-D linear interpolation between the centerline and radial flow regions which have different profile heights and magnitudes. These differences necessitated the 2-D interpolation.

For a tilt rotor, the different flow regions are shown in Figure P-1, where the “Interpolated Flow” area is exaggerated to show the relationship. Even though the angle used to define the interpolated flow region is still being studied, the angle the interpolated flow line makes with the centerline flow (and centerline of the aircraft) was 5 degrees for the plots generated in this report.

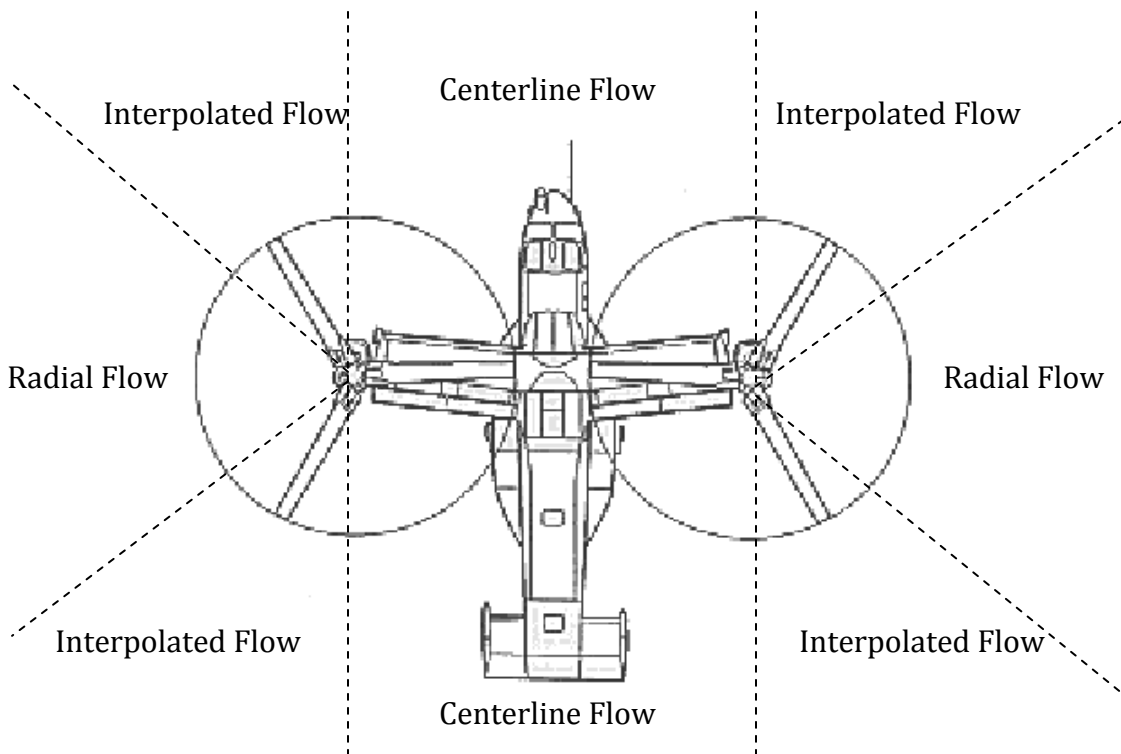


Figure P-1 Depiction of Centerline, Radial, and Interpolated Flow Regions for a Tilt Rotor
(Interpolated Flow Region Exaggerated)

The underlying assumption in Figure P-1 is configuration level modeling applies for the entire area between the two rotors, essentially creating a “flat front” to the centerline outwash profile. This has weak correlation with the “spike” shape seen test data and is a recommended area for future model development. The “flat front” approximation provides a conservative approach until the configuration level modeling is refined to capture the complex interaction in the centerline flow region which generates the “spike” shape seen in test data.

Configuration level modeling (RoWFoot) outputs two files: “Profiles.csv” and “Max_v_Profiles.csv.” Post-processing of this comma separated files (csv) occurs using a MATLAB code to generate the contour plot display of the rotorwash footprint. Three sets of data are output into Max_v_Profiles.csv: Centerline Flow force and velocity, Radial Flow force and velocity, and Interpolated Flow force and velocity. All of these have distances associated with them, which are measured from the rotor hub center. A screenshot of the Max_v_Profiles.csv output is shown in Figure P-2. Note that under “Azimuth,” the “0” and “5” degree rows are calculated within RoWFoot. The “2.5” degree row is the Interpolated Flow transition region. Also note that the output shown in Figure P-2 is for one of the analysis conditions depicted in [Section 5.0](#).

1													
LZ Ops	Int Payload R = 39.5	AGL = 20									2/13/2012	24:40.0	
Plot Title:	EFFECTS Max Velocity Profile-	GW: 141605. lbs	ALG: 20.0 ft	Air Density: 0.00238 slug/ft^3	T/W: 1.090	Force Calculation: PEAK							
X Axis:	Velocity (kts)												
Y Axis:	Angle (deg)												
Distance from Rotor to Center:	50.5												
Radius:	39.5												
Dist (ft):	0	11.85	19.75	31.6	39.5	59.25	79	118.5	158	197.5	237	276.5	
Azimuth	Max Velocities (mph):												
	0 x/R	0.30 x/R	0.50 x/R	0.80 x/R	1.00 x/R	1.50 x/R	2.00 x/R	3.00 x/R	4.00 x/R	5.00 x/R	6.00 x/R	7.00 x/R	
0	0	25.11	36.83	52.39	61.93	81.92	76.97	65.93	55.97	46.74	38.06	29.82	
2.5	0	22.32	37.03	59.84	69.85	79.62	77.2	68.42	54.9	45.13	37.34	30.76	
5	0	20.43	38.69	69.62	80.48	80.48	80.48	73.61	56.01	45.31	38.1	32.91	
Object Shape:	PAXMAN												
	0 x/R	0.30 x/R	0.50 x/R	0.80 x/R	1.00 x/R	1.50 x/R	2.00 x/R	3.00 x/R	4.00 x/R	5.00 x/R	6.00 x/R	7.00 x/R Peak	
Dist (ft):	0	11.85	19.75	31.6	39.5	59.25	79	118.5	158	197.5	237	276.5	
Azimuth	0 Force (lbs)	0	0.38	6.79	29.55	47.2	88.8	76.41	50.58	33.87	19.93	12.99	7.59
	Moment (0	1.04	23.31	101.11	159.25	295.87	255.2	170.66	115.83	67.28	44.64	26.37
2.5	Force (lbs)	0	0.72	8.41	37.94	59.48	84.76	77.81	55.8	33.1	20.98	13.19	8.32
	Moment (0	2.1	29.56	130.98	202.77	283.84	261.77	190.68	113.79	72.47	45.63	28.68
5	Force (lbs)	0	1.46	12.74	62.64	88.23	87.33	88.08	73.14	40.61	25.37	17.17	12.24
	Moment (0	5.25	45.29	213.82	292.26	279.6	285.2	244.72	138.53	87.54	59.64	42.6

Figure P-2 Example of Max_v_Profiles.csv Output for Notional Large Tilt Rotor

In MATLAB, the velocity profiles and peak forces (not shown in Figure P-2) are read from Max_v_Profiles.csv to allow the drawing of the peak velocity and force contour plots. The distances and the corresponding velocities from the rotor hub center and physical separation of the rotors are used to generate matrices representing the top-view of the peak velocity and force profiles on the PAXman Model described in [Appendix C](#). The output only has the three different velocity vs. distance data: centerline, transition, and radial.

From those three data sets, the entire area around the aircraft is mapped, based on the rotor hub locations.

The matrices are generated within MATLAB with the assumption the rotorwash profiles are symmetrical around the aircraft centerline. In other words, the rotorwash characteristics for the starboard side are generated and a mirror of the matrices created is used for the other side. An example of the matrix generated for the peak forces “Forces_total” is shown in Figure P-3. Note that the total matrix size was 20 x 60, where the first 18 columns were the fore centerline, column 19 was the transition region, Columns 20-39 were the radial flow, Columns 40 was the transition region, and Columns 41-59 were the aft centerline data points. The column numbers are shown in red, the shaded blue region is the mirrored part of the matrix, and the different flow regions are labeled. Note that where the blue shaded region meets the white region is the distances closest to the aircraft. Note, also, that many of the columns are hidden in Figure P-3 as there were 60 total columns.

FORE CENTERLINE					TRANSITION	RADIAL				TRANSITION	AFT CENTERLINE			
0	1	2	17	18	19	20	21	38	39	40	41	42	58	59
25.4	25.4	25.4	25.4	25.4	21.0	19.9	19.9	19.9	19.9	21.0	25.4	25.4	25.4	25.4
40.6	40.6	40.6	40.6	40.6	33.1	33.9	33.9	33.9	33.9	33.1	40.6	40.6	40.6	40.6
73.1	73.1	73.1	73.1	73.1	55.8	50.6	50.6	50.6	50.6	55.8	73.1	73.1	73.1	73.1
88.1	88.1	88.1	88.1	88.1	77.8	76.4	76.4	76.4	76.4	77.8	88.1	88.1	88.1	88.1
87.3	87.3	87.3	87.3	87.3	84.8	88.8	88.8	88.8	88.8	84.8	87.3	87.3	87.3	87.3
88.2	88.2	88.2	88.2	88.2	59.5	47.2	47.2	47.2	47.2	59.5	88.2	88.2	88.2	88.2
62.6	62.6	62.6	62.6	62.6	37.9	29.6	29.6	29.6	29.6	37.9	62.6	62.6	62.6	62.6
12.7	12.7	12.7	12.7	12.7	8.4	6.8	6.8	6.8	6.8	8.4	12.7	12.7	12.7	12.7
1.5	1.5	1.5	1.5	1.5	0.7	0.4	0.4	0.4	0.4	0.7	1.5	1.5	1.5	1.5
0.0	0.0	0.0	0.0	0.0	0.0	0.0	0.0	0.0	0.0	0.0	0.0	0.0	0.0	0.0
0.0	0.0	0.0	0.0	0.0	0.0	0.0	0.0	0.0	0.0	0.0	0.0	0.0	0.0	0.0
1.5	1.5	1.5	1.5	1.5	0.7	0.4	0.4	0.4	0.4	0.7	1.5	1.5	1.5	1.5
12.7	12.7	12.7	12.7	12.7	8.4	6.8	6.8	6.8	6.8	8.4	12.7	12.7	12.7	12.7
62.6	62.6	62.6	62.6	62.6	37.9	29.6	29.6	29.6	29.6	37.9	62.6	62.6	62.6	62.6
88.2	88.2	88.2	88.2	88.2	59.5	47.2	47.2	47.2	47.2	59.5	88.2	88.2	88.2	88.2
87.3	87.3	87.3	87.3	87.3	84.8	88.8	88.8	88.8	88.8	84.8	87.3	87.3	87.3	87.3
88.1	88.1	88.1	88.1	88.1	77.8	76.4	76.4	76.4	76.4	77.8	88.1	88.1	88.1	88.1
73.1	73.1	73.1	73.1	73.1	55.8	50.6	50.6	50.6	50.6	55.8	73.1	73.1	73.1	73.1
40.6	40.6	40.6	40.6	40.6	33.1	33.9	33.9	33.9	33.9	33.1	40.6	40.6	40.6	40.6
25.4	25.4	25.4	25.4	25.4	21.0	19.9	19.9	19.9	19.9	21.0	25.4	25.4	25.4	25.4

Figure P-3 Example of Forces_total Matrix for Notional Large Tilt Rotor

After the X- and Y- coordinates, max velocities, and total forces are set up as shown above in Figure P-3, the figures shown in [Section 5.0](#) of the main report body may be generated. The following command is used in MATLAB to generate the figure displaying the max velocities around the aircraft:

```
figure(1)

contour(X_total,Y_total,Max_Velo);

title('Peak Velocity in Ground Plane')

xlabel('Aircraft y-axis (ft)')

ylabel('Aircraft x-axis (ft)')
```

where x_{total} , y_{total} , and Max_Velo are the matrixes indicating each X- and Y-coordinate and each velocity associated with the X- and Y-coordinates. Note that the centerline flow areas in front of and behind the aircraft are flat indicating the same velocities exist in the entire region in front of the aircraft between the two rotors. As previously noted, there is recommendation for future efforts to refine modeling in areas off the aircraft centerline axis to improve correlation in other parts of this region.

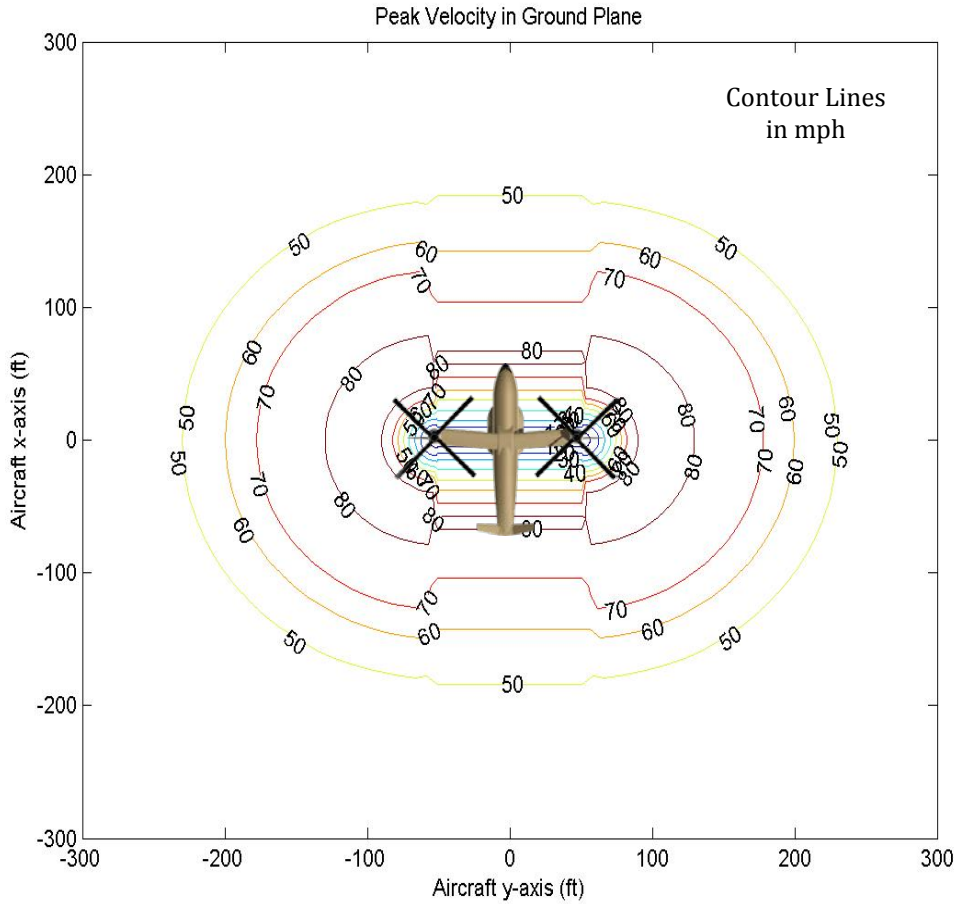


Figure P-4 Example of the Peak Velocity Plot for a Notional Large Tilt Rotor

The force plot is generated with the following code:

```
figure(2)

contour(X_total,Y_total,Forces_total,'ShowText','on','Level
Step',80,...'LevelList',[80 87 115]);

title('Peak Force on PAXMAN')

xlabel('Aircraft y-axis (ft)')
```

```
ylabel('Aircraft x-axis (ft)')
```

where `Forces_total` is the matrix of the forces on PAXman. The '`LevelList`' command indicates which force lines should be drawn. In this case, the 87- and 115-lb peak forces (reference Table 3.1 of main report) correspond to the different hazard zones for rotorwash forces. Figure P-5 shows the force plot with the 80-, 87-, and 115-lb peak forces drawn.

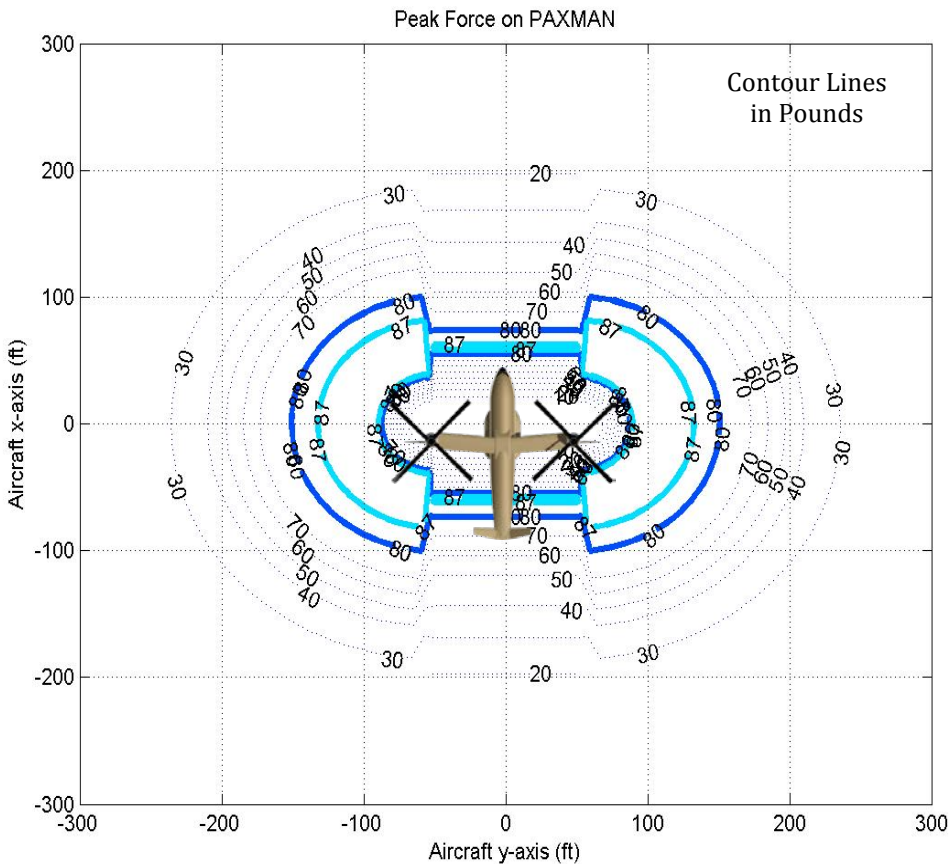


Figure P-5 Example of Peak Force on PAXman Plot for a Notional Large Tilt Rotor

The three-dimensional plot of the forces on PAXman is generated with the following code:

```
figure(3)  
surf(X_total,Y_total,Forces_total)  
title('Force Distribution in Ground Plane')  
xlabel('Aircraft y-axis (ft)')  
ylabel('Aircraft x-axis (ft)')  
zlabel('Peak Force (lb)')
```

The three-dimensional plot of the forces on PAXman is shown in Figure P-6.

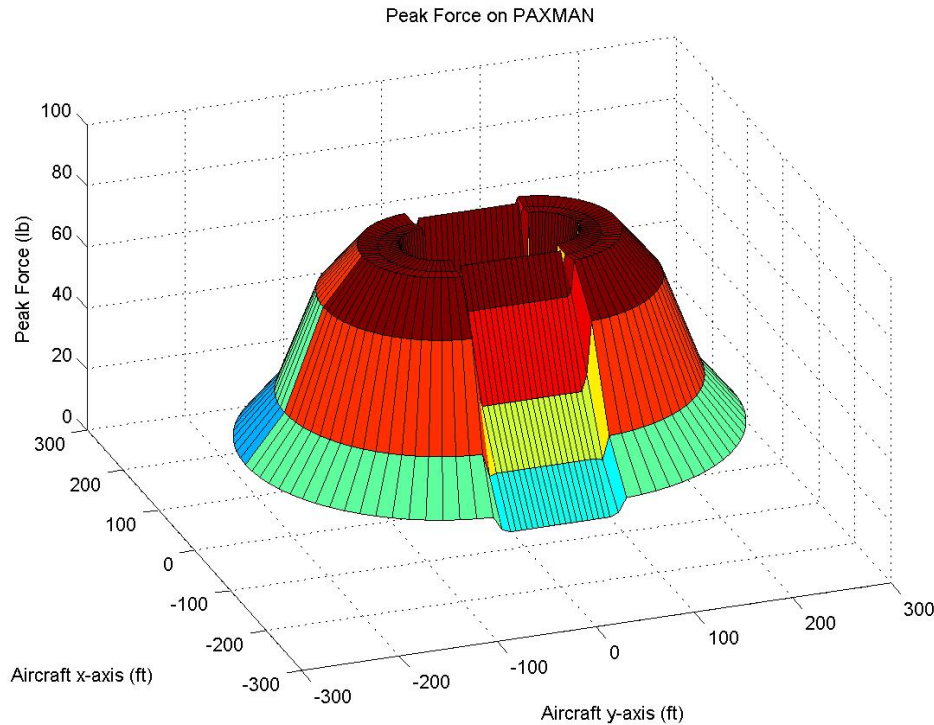


Figure P-6 Example of the Peak Force on PAXman 3-D Plot Generated in MATLAB for Notional Large Tilt Rotor

Note that the “step down” in the middle of Figure P-6 is due to the nature of the calculations. The flow in these areas has not been fully characterized and the rotorwash flow in this area is likely very turbulent due to recirculation and wake/ground interactions.

Finally, the different force contours from various azimuths from the aircraft hubs can be generated as well. These contours are useful for defining the different distances that personnel should be from the aircraft based on relative position to the hovering vehicle. Figure P-7 shows both the 0-deg azimuth (off the aircraft nose, in line with the aircraft centerline) and the 45-deg azimuth (the angle is measured from the aircraft centerline, with the line going through the center of the hub). The code used to generate the figures shown is as follows:

```
figure(4)

subplot(2,1,1); plot(Distances(:,1),Forces(1:10,1), 'b.-')
grid on

xlabel('Distance from Hub Center along 0 deg AZ (ft)')
ylabel('Estimated Peak Force on standard man in centerline
flow (lb)')
```

```

subplot(2,1,2); plot(Distances(1:10,1),Forces(1:10,20),'b.-')
grid on
xlabel('Distance from Hub Center along 45 deg AZ (ft)')
ylabel('Estimated Peak Force on standard man in radial flow (lb)')

```

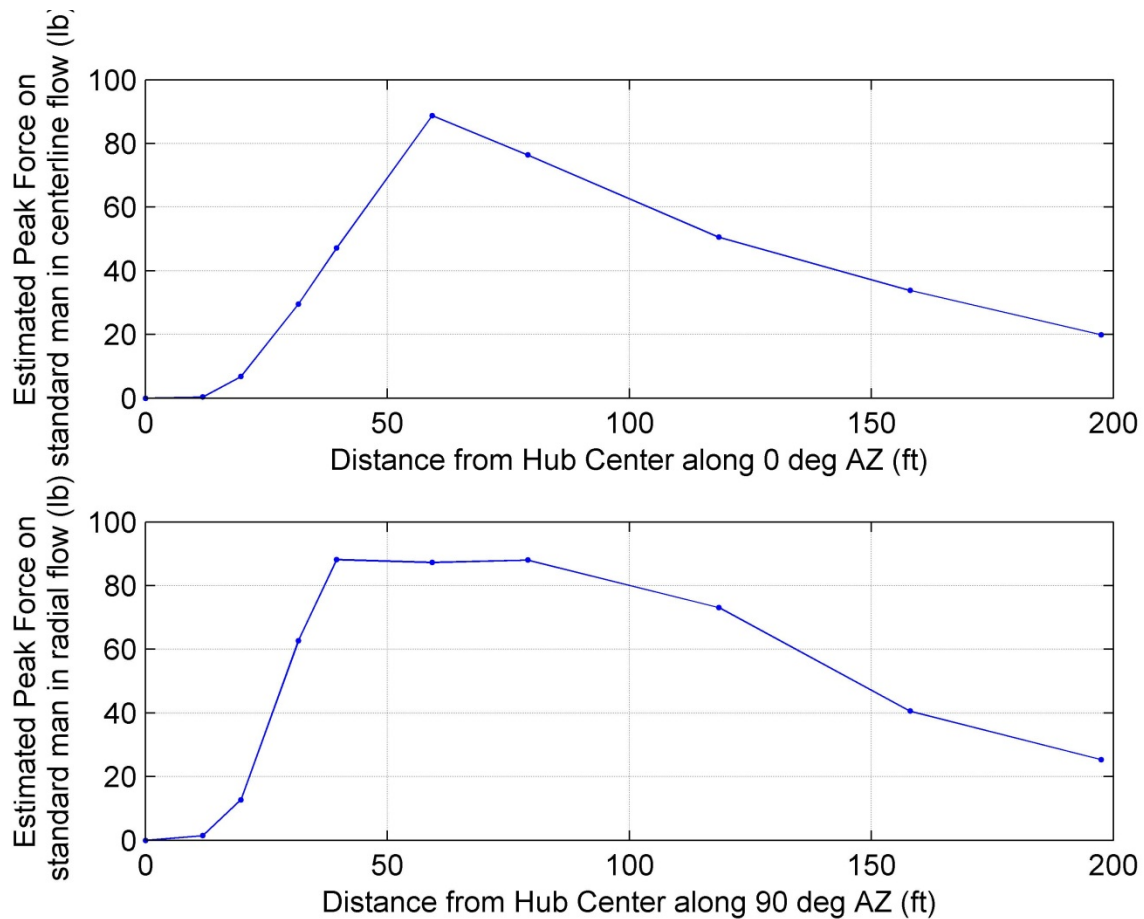


Figure P-7 Example of Peak Force on PAXman vs. Distance for 0-deg azimuth and 90-deg Azimuth From Hub Center for Notional Large Tilt Rotor

Appendix Q: Rotorwash Hazard Analysis Reference List

Sam Ferguson and John Preston

DOWNWASH/OUTWASH FLOW FIELD DATA

FULL-SCALE ROTORCRAFT

1. Anon., "A Comparison of Downwash and Outflow From a Tilt-Wing Aircraft and a Helicopter," Canadair Report RAG-084-107, February 1971.
2. Anon., "Comparative Downwash and Simulated Forest Rescue Tests of the HH-3E, HH-53B and the XC-142A Aircraft," Aeronautical Systems Division X68-15759, December 1967.
3. Anon., "Heavy Lift Helicopter (HLH) Concept Formulation Study (U), Inclosure 7 to Annex B to Appendix II – Downwash and Disc Loading," United States Army Combat Developments Command, Aviation Agency, Action Control Number 2958, June 1972.
4. Anon., "S.E.R. XV-5A Flight Test Summary," Ryan Aeronautical Co. and General Electric Co., November 1966.
5. Anon., "Spray Generation Test VZ8P-A, Final Report," Report 59-X-31, Piasecki Aircraft Corporation, June 30, 1963.
6. Ball, LCDR J. C., "XV-15 Shipboard Evaluation," NATC, AHS 39th Annual Forum Proceedings, #84-46359, May 1983.
7. Ball, LCDR J. C., and Bowes, R. H., "USN/USMC Assessment of the XV-15 Tilt Rotor Research Aircraft, Second Interim Report," NATC RW-29R-83, September 1983.
8. Ball, LCDR J. C., and DuFresne, D. A., "Shipboard Evaluation of the XV-15 Tilt Rotor Research Aircraft," Naval Air Test Center Technical Report No. RW-54R-82, April 18, 1983.
9. Carter, Capt. T. W.; Traskos, R. L.; Porter, S. L.; and Rausch, C. F., "Navy Technical Evaluation of the CL-84-1 Tilt-Wing V/STOL Aircraft in the Sea Control Ship Environment," NATC FT-33R-75, March 1975.
10. Dyke, R. W., "An Investigation of the Over the Water Aspects of VTOL Airplanes at High Disk Loading," Curtiss-Wright Corporation, VTOL Systems Group, Report No. 012-26, December 1963.
11. Fradenburgh, E. A., "Flow Field Measurements for a Hovering Rotor Near the Ground," Fifth Annual Western Forum of the American Helicopter Society, Los Angeles, California, September 1958.
12. Ferguson, S. W., "Tiltrotor Maneuvering and Ground-Taxi Rotorwash Characteristics," EMA Report 98-1-1, EMA, October 1998. [see reference #36 for public distribution of test data contained within report]

13. Hancock, R. N., "External Noise and Downwash Measurements on the Vought XC-142A," LTV Aerospace Corporation, Presented at the Joint Symposium on Environmental Effects on VTOL Designs Preprint No. SW-70-8 (# 71-15409), November 1970.
14. Harris, D. J., and Simpson, R. D., "Technical Evaluation of the Rotor Downwash Flow Field of the XV-15 Tilt Rotor Research Aircraft," Naval Air Test Center Technical Report No. SY-14R-83, July 1983.
15. Harris, D. J., and Simpson, R. D., "CH-53E Helicopter Downwash Evaluation. Final Report," Naval Air Test Center Technical Report No. SY-89R-78, August 1, 1978.
16. Harris, D. J., and Simpson, R. D., "CL-84 Tilt-Wing Vertical and Short Takeoff and Landing Downwash Evaluation. Final Report," Naval Air Test Center Technical Report No. SY-52R-76, April 9, 1976.
17. Harris, D. J., and Simpson, R. D., "Downwash Evaluation Under the U.S. Army Heavy Lift Helicopter Rotor. Final Report," Naval Air Test Center Technical Report No. SY-17R-76, March 16, 1976.
18. Hewitt, J. J., "Downwash Measurement – A Standardized Test," Master's Thesis in Aerospace Engineering, University of Glasgow, May 2008.
19. Jenkins, B. Z., and Marks, A. S., "Rotor Downwash Velocities About the UH-1M Helicopter - Flight Test Measurements and Theoretical Calculations," Army Missile Research Development and Engineering Laboratory, Redstone Arsenal, Alabama, January 1975.
20. Kuhn, R. E., "An Investigation to Determine Conditions Under Which Downwash from VTOL Aircraft Will Start Surface Erosion from Various Types of Terrain," NASA TN D-56, September 1959.
21. Lake, R. E., and Clark, W. J., "V-22 Rotor Downwash Survey," NAWCADPAX-98-88-RTR, July 1998.
22. Lake, R. E., "Shipboard V-22 Rotor Downwash Survey," NAWCADPAX-99-87-RTR, September 1999.
23. Larsen, MAJ E., "Qualitative Comparison of Three VSTOL Aircraft (XC-142A; XV-5A; CL-84); Final Report," NATC FT-66R-67, October 1967.
24. Leese, G. W., and Knight, J. T. Jr., "Helicopter Downwash Data," Miscellaneous Paper S-74-17, U.S. Army Engineer Waterways Experiment Station, Vicksburg, Mississippi, June 1974.
25. Leese, G. W., "UH-1H Downwash Velocity Measurements," Army Engineer Waterways Experiment Station, Vicksburg, Mississippi, August 1972.
26. Lucero, F. N., and Jones, LtC. G. E., "XC-142A Operational Suitability Tests," Air Force Flight Test Center, FTC-TR-67-28, December 1968.
27. Marsh, K. R., "Research on VTOL Water Hover Effects, Including the Effects of Wind and Waves," LTV Aerospace Corporation, Report No. 2-55400/8R-6140, April 1968.

28. Meyerhoff, C. L., and Gordge, D., "Navy Developmental Test (DT-IIA) of the V-22 Aircraft - Contributory Rotor Downwash Report," Naval Air Test Center Technical Report ACS-CR-90-04, SY71A, Summer 1990.
29. Meyerhoff, C. L.; Lake, R.; and Peters, Lt. D., "H-60 Helicopter Rotor Downwash Wind Velocity Evaluation," Naval Air Warfare Center Report SY-3R-94, February 1994.
30. Meyerhoff, C. L., "MV-22 Qualitative Rotor Downwash Evaluation, Final Report," Aircrew Systems Department RW-15R-91, March 1991.
31. Michaelsen, O. E., "A Comparison of Outflows From a Helicopter, Tilt Wing, and Jet Lift Hovering Aircraft," AIAA 8th Annual Meeting and Technical Display, Washington, D.C., AIAA Paper No. 71-992, October 25, 1971.
32. Morse, Andy, "VTOL Downwash Impingement Study, Velocity Survey," U.S. Army Transportation Research Command Technical Report No. 60-58, August 1960.
33. O'Bryan, T. C., "An Experimental Study of the Effect of Downwash From a Twin Propeller VTOL Aircraft on Several Types of Ground Surfaces," NASA TN D-1239, May 1962.
34. O'Bryan, T. C., "An Investigation of the Effect of Downwash from a VTOL Aircraft and a Helicopter in the Ground Environment," NASA TN D-977, October 1961.
35. Patton, W. G., and Simpson, R. D., "Investigation of SH-3/HH-3 Helicopter Downwash Environment," Naval Air Test Center Report ST-197R-71, September 24, 1971.
36. Silva, M. J., "CH-47D Tandem Rotor Outwash Survey," NAWCADPAX/EDR-2010/120, August 2010.
37. Silva, M. J., and Riser, R., "CH-47D Tandem Rotor Outwash Survey," Proceedings of the American Helicopter Society's 67th Annual Forum, Virginia Beach, VA, May 3-5, 2011.
38. Smith, R. D., "Heliport/Vertiport Design Deliberations, 1997-2000," DOT/FAA/ND-00/1, May 2001.
39. Weiss, R. M.; Morrow, J. G.; Gallagher, D.; DiMeo, M.; and Erlichman, S., "Analysis of Heliport Environmental Data: Indianapolis Downtown Heliport, Wall Street Heliport, Volume I Summary," Federal Aviation Administration, Technical Center, Atlantic City, NJ, Technical Report DOT/FAA/CT-TN87/54-I, October 1988.
40. Weiss, R. M.; Morrow, J. G.; Gallagher, D.; DiMeo, M.; and Erlichman, S., "Analysis of Heliport Environmental Data: Indianapolis Downtown Heliport, Wall Street Heliport, Volume II Wall Street Heliport Data Plots," Federal Aviation Administration, Technical Center, Atlantic City, NJ, Technical Report DOT/FAA/CT-TN87/54-II, May 1989.
41. Weiss, R. M.; Morrow, J. G.; Gallagher, D.; DiMeo, M.; and Erlichman, S., "Analysis of Heliport Environmental Data: Indianapolis Downtown Heliport, Wall Street Heliport, Volume III Indianapolis Downtown Heliport Data Plots," Federal Aviation Administration, Technical Center, Atlantic City, NJ, Technical Report DOT/FAA/CT-TN87/54-III, October 1989.

42. Weiss, R. M., "Analysis of Heliport Environmental Data; Intracoastal City," Federal Aviation Administration, Technical Center, Atlantic City, NJ, Technical Report DOT/FAA/CT-TN89/43, July 1990.

MODEL-SCALE ROTORCRAFT

1. Anon., "VTOL Downwash Impingement Study Velocity Survey," Hiller Aircraft Corporation, Hiller Report No. 60-15, August 1960.
2. Newsom, W. A., and Tosti, L. P., "Slipstream Flow Around Several Tilt-Wing VTOL Aircraft Models Operating Near Ground," NASA TN D-1382.
3. Peterka, J. A., "Wind Tunnel Tests: Dallas Convention Center Expansion," Cermak Peterka Peterson, Inc., Fort Collins, CO, CPP Project 90-0666, June 1991.
4. Skujins, O., "An Experimental Investigation of Rotor Forces and Flow Field in the Vicinity of a Step Ground Plane," West Virginia University, Department of Aerospace Engineering, July 1970.

JET CONFIGURATIONS

1. Anon., "Harrier FOD Avoidance H.S.A.'s Guide to Clean Living in Jet V/STOL," HSK 39, Hawker Siddeley Aviation Limited, August 1971
2. Lake, R.; McCarthy, K.; Nantz, R.; and Gonzalez, H., "AV-8B -408 External Environment Outwash Flow Speed and Temperature Survey," NAWCADPAX/RTR-2000/114, August 2000.

SENSOR MEASUREMENTS AND LIMITATIONS

1. Fisher, L. R., "Wind-Tunnel Oscillation Tests of the Bendix-Friez Aerovane Anemometer," NACA RM SL53G30a, August 1953.
2. Landgrebe, A. J., and Johnson, B. V., "Measurement of Model Helicopter Rotor Flow Velocities With a Laser Doppler Velocimeter," Journal of the American Helicopter Society, July 1974.
3. Meyerhoff, C. L.; Lake, R. E.; and Gordge, D. N., "Rotorwash Wind Sensor Evaluation," DOT/FAA/RD-93/10, August 1993.
4. Stanton, R. O., "Suitability of a Drag Sphere Anemometer for Measurement of VTOL Aircraft Downwash, US Army Aviation Materiel Laboratories," USAAVLabs Technical Note 4 / N78-78216, June 1970.

ROTORWASH FLOW FIELD PREDICTION METHODOLOGIES

MOMENTUM ANALYSIS METHODS

1. Ferguson, S. W., and Kocurek, J. D., "Rotorwash Flow Fields: Flight Test Measurement, Prediction Methodologies, and Operational Issues," Paper Presented at the American Helicopter Society Vertical Lift Aircraft Design Conference, San Francisco, CA, January 17-19, 1990.
2. Ferguson, S. W., and Kocurek, J. D., "Analysis and Recommendation of Separation Requirements for Rotorcraft Operation at Heliports and Airports," Systems Technology, Inc., STI Report TR-1224-1, September 1986.
3. Ferguson, S. W., and Kocurek, J. D., "Rotorwash Computer Model - User's Guide," Federal Aviation Administration, Washington D.C., Technical Report DOT/FAA/RD-90/25, November 1991.
4. Ferguson, S. W., "Rotorwash Analysis Handbook, Volume I – Development and Analysis," Federal Aviation Administration, Washington D.C., Technical Report DOT/FAA/RD-93/31,I, June 1994.
5. Ferguson, S. W., "Rotorwash Analysis Handbook, Volume II – Appendixes," Federal Aviation Administration, Washington D.C., Technical Report DOT/FAA/RD-93/31,II, June 1994.
6. George, M.; Kisielowski, E.; and Douglas, D. S., "Investigation of the Downwash Environment Generated by V/STOL Aircraft Operating in Ground Effect," USAAVLABS Technical Report 68-52, July 1968.
7. George, M.; Tang, J.; Mills, S.; and Douglas, D., "Downwash Environment for the Boeing Model 160 V/STOL Aircraft," Dynasciences Corporation Report DCR-268, January 1968.
8. George, M. M., "Downwash Impingement Design Criteria for VTOL Aircraft," TRECOM Technical Report 64-48, U.S. Army Transportation Research Command, Fort Eustis, VA, August 1964.
9. Glauert, M. B., "The Wall Jet," Journal of Fluid Mechanics, Vol. 1, Part 6, December 1956, pp. 625-643.
10. Hill, W. G.; Jenkins, R. G.; Kalemaris, S. G.; and Siclari, M. J., "Study of VTOL In-Ground-Effect Flow Field Including Temperature Effect," NASA CR-166258, April 1982.
11. Hohler, D. J., "An Analytical Method of Determining General Downwash Flow Field Parameters for V/STOL Aircraft," AFAPL-TR-66-90, November 1966.
12. Hrycak, P.; Lee, D. T.; Gauntner, J. W.; and Livingood, J. N. B., "Experimental Flow Characteristics of a Single Turbulent Jet Impinging on a Flat Plate," NASA TN D-5690, March 1970.
13. Launder, B. E., and Rodi, W., "The Turbulent Wall Jet - Measurements and Modeling," University of Manchester and Universitat Karlsruhe, Ann. Rev. Fluid Mech. 1983.
14. Launder, B. E., and Rodi, W., "The Turbulent Wall Jet," University of Manchester and Universitat Karlsruhe, Prog. Aerospace Sci., Vol. 19, pp.81-128, 1983.

15. Liu, J.; McVeigh, M. A.; and Rajagopalan, Dr. G., "Single- and Dual-Rotor Flowfield and Outwash Predictions," American Helicopter Society Tilt Rotor/Runway Independent Aircraft Technology and Applications Specialists' Meeting, Arlington, Texas, March 2001.
16. Ludwig, G. R., and Brady, W. G., "Theoretical and Experimental Studies of Impinging Uniform and Nonuniform Jets," TRECOM Technical Report 64-42, U. S. Army Transportation Research Command, Fort Eustis, VA, August 1964.
17. Migdal, D.; Hill, W. G. Jr.; Jenkins, R. C.; and Siclari, M. J., "VTOL in Ground Effect Flows for Closely Spaced Jets," NASA CR 152321, December 1979.
18. Miller, P., and Wilson, M., "Wall Jets Created by Single and Twin High Pressure Jet Impingement," Aeronautical Journal, pp. 87-100, March 1993.
19. Preston, J. R., "VTOL Downwash/Outwash Operational Effects Model," Paper Presented at the 50th Annual Forum of the American Helicopter Society, Washington D.C., May 11-13, 1994.
20. Unitt, Lt. P. J., "A Comprehensive Review of V/STOL Downwash Impingement With Emphasis on Wind Induced Recirculation," Thesis for Air Force Institute of Technology, Report GAM/AE/69-9, March 1969.
21. Velkoff, Dr. H. R., "A Comparative Study of Downwash-Outflow Effects of Various VTOL Configurations as a Factor in the Design Selection Process," Paper Presented at the 18th European Rotorcraft Forum, Avignon, France, September 15-18, 1992.
22. Velkoff, Dr. H. R., "A Comparative Study of Downwash-Outflow Effects of Various VTOL Configurations as a Factor in the Design Selection Process," Advanced Systems Research and Analysis Office, U. S. Army Aviation and Troop Command, NASA Ames Research Center, January 1993.
23. Wareing, J. T., "Consideration of V/STOL Downwash and the Ground Environment," LTV Aerospace Corp. Society of Automotive Engineers - Air Transportation Meeting 680282 / A68-31310, April 1968.
24. Watts, A., "V/STOL Downwash Impingement Study - Velocity Estimate," Canadair Aerodynamic Memorandum MAA-284-001, January 1969, Revised April 1971.
25. Wernicke, R. K., "Prediction of Tilt Rotor Outwash," AIAA Paper No. 81-0013, AIAA 19th Aerospace Sciences Meeting, January 12-15, 1981.

CONSTANT VORTICITY CONTOUR (CVC) METHODS

1. Wachspress, D.A.; Quackenbush, T.R.; and Boschitsch, A.H., "CHARM Version 3.0 User's Manual (Comprehensive Hierarchical Aeromechanics Rotorcraft Model)," CDI-TN-05-11, Continuum Dynamics, Inc., Ewing, NJ, March 2007.
2. Wachspress, D.A.; Quackenbush T.R.; and Boschitsch, A.H., "First-Principles Free-Vortex Wake Analysis for Helicopters and Tiltrotors," Proceedings of the American Helicopter Society's 59th Annual Forum, Phoenix, AZ, May 6-8, 2003.

3. Wachspress, D.A.; Quackenbush, T.R.; and Boschitsch, A.H., "Rotorcraft Interactional Aerodynamics with Fast Vortex/Fast Panel Methods," Proceedings of the American Helicopter Society's 56th Annual Forum, Virginia Beach, VA, May 2-4, 2000.
4. Wachspress, D.A.; Whitehouse, G.R.; Keller, J.D.; Yu, K.; Gilmore, P.; Dorsett, M.; and McClure, K., "A High Fidelity Brownout Model for Real-Time Flight Simulations and Trainers," Proceedings of the American Helicopter Society's 65th Annual Forum, Grapevine, TX, May 27-29, 2009.
5. Quackenbush, T.R.; Boschitsch, A.H.; Wachspress, D.A.; and Chua, K., "Rotor Design Optimization Using a Free Wake Analysis," NASA-CR-177612, April 1993.

CFD METHODS

1. Lestari, A.; Niazi, S.; and Rajagopalan, R. G., "Preliminary Numerical Analysis of a Quad Tiltrotor Flowfield and Performance," American Helicopter Society Tilt Rotor/Runway Independent Aircraft Technology and Applications Specialists' Meeting, Arlington, Texas, March 2001.
2. Liu, J.; McVeigh, M. A.; and Rajagopalan, Dr. G., "Single- and Dual-Rotor Flowfield and Outwash Predictions," American Helicopter Society Tilt Rotor/Runway Independent Aircraft Technology and Applications Specialists' Meeting, Arlington, Texas, March 2001.
3. Vorwald, J. G.; Tai, T. C.; and Walker, M. A., "Analytical Predictions of Flow Field Characteristics for a Hovering V-22 Including the Potential for V-22 Outflow to Overturn a Parked, Unsecured Helicopter," CARDIVNSWC-TR-94/011, June 1994.

ROTORWASH HAZARD ANALYSIS

COMPREHENSIVE HAZARD ANALYSIS

1. Anon., "Environmental Effects on VTOL Designs," Proceedings of the Joint Symposium, University of Texas and American Helicopter Society, Arlington, Texas, Nov. 1970.
2. Anon., "Symposium on Ground Effect Phenomena," Princeton University and U.S. Army TRECOM, Oct. 1959.
3. Anon., "VTOL Aircraft Downwash Impingement Symposium - A Compilation of the Papers Presented," US Army Transportation Research Command, TREC TR 61-1, December 1960.
4. Ferguson, S. W., "Analysis of Rotorwash Effects in Helicopter Mishaps," Federal Aviation Administration, Washington D.C., Technical Report DOT/FAA/RD-90/17, May 1991.
5. Ferguson, S. W., and Kocurek, J. D., "Rotorwash Flow Fields: Flight Test Measurement, Prediction Methodologies, and Operational Issues," Paper Presented at the American Helicopter Society Vertical Lift Aircraft Design Conference, San Francisco, CA, January 17-19, 1990.
6. Ferguson, S. W., and Kocurek , J. D., "Analysis and Recommendation of Separation Requirements for Rotorcraft Operation at Heliports and Airports," Systems Technology, Inc., STI Report TR-1224-1, September 1986.

7. Ferguson, S. W., and Kocurek, J. D., "Rotorwash Computer Model - User's Guide," Federal Aviation Administration, Washington D.C., Technical Report DOT/FAA/RD-90/25, November 1991.
8. Ferguson, S. W., "Rotorwash Analysis Handbook, Volume I – Development and Analysis," Federal Aviation Administration, Washington D.C., Technical Report DOT/FAA/RD-93/31,I, June 1994.
9. Ferguson, S. W., "Rotorwash Analysis Handbook, Volume II – Appendixes," Federal Aviation Administration, Washington D.C., Technical Report DOT/FAA/RD-93/31,II, June 1994.
10. George, M.; Kisielowski, E.; and Douglas, D. S., "Investigation of the Downwash Environment Generated by V/STOL Aircraft Operating in Ground Effect," USAAVLABS Technical Report 68-52, July 1968.
11. George, M.; Tang, J.; Mills, S.; and Douglas, D., "Downwash Environment for the Boeing Model 160 V/STOL Aircraft," Dynasciences Corporation Report DCR-268, January 1968.
12. George, M. M., "Downwash Impingement Design Criteria for VTOL Aircraft," TRECOM Technical Report 64-48, U.S. Army Transportation Research Command, Fort Eustis, VA, August 1964.
13. Kuhn, R. E., and Eshleman, J., "Ground Effects on V/STOL and STOL Aircraft -- A Survey," NASA Ames, AIAA/AHS/ASEE Aircraft Design Systems and Operations Meeting, TN 86-10962, October 1985.
14. Leese, G. W., "Helicopter Downwash Blast Effects Study," U.S. Army Engineer Waterways Experiment Station TR-3-664, Vicksburg, Mississippi, October 1964.
15. Liu, H., and Nateghi, F., "Wind Damage to Airport: Lessons Learned," Journal of Aerospace Engineering, Vol. 1, April 1988, pp 105-116.
16. Mitchell, K., "Proceedings of the 1985 NASA Ames Research Center's Ground Effects Workshop," NASA Ames Research Center, N87-24410 to N87-24422, August, 1985.
17. Preston, J. R., "VTOL Downwash/Outwash Operational Effects Model," Paper Presented at the 50th Annual Forum of the American Helicopter Society, Washington D.C., May 11-13, 1994.
18. Velkoff, Dr. H. R., "A Comparative Study of Downwash-Outflow Effects of Various VTOL Configurations as a Factor in the Design Selection Process," Paper Presented at the 18th European Rotorcraft Forum, Avignon, France, September 15-18, 1992.
19. Velkoff, Dr. H. R., "A Comparative Study of Downwash-Outflow Effects of Various VTOL Configurations as a Factor in the Design Selection Process," Advanced Systems Research and Analysis Office, U. S. Army Aviation and Troop Command, NASA Ames Research Center, January 1993.

PERSONNEL HAZARDS

1. Ahuja, R.; Dalui, S. K.; and Gupta, V. K., "Unpleasant Pedestrian Wind Condition Around Buildings," Journal of Civil Engineering (Building and Housing), Vol. 7, 2006, pp 147-154.
2. Anon, "Design Guide for Wind," Wellington City District Plan (New Zealand), July 2000.

3. Anon., Anthropometry of U.S. Military Personnel, Military Handbook DOD-HDBK-743, October 3, 1980.
4. Bellamy, R. F. (MD), and Zajtchuk, R. (MD), "Textbook of Military Medicine," Section on Conventional Warfare Ballistic, Blast, and Burn Injuries, Chapter 4 - The Physics and Biophysics of Wound Ballistics," Borden Institute (Office of the Surgeon General, Department of the Army), pp 111. 1990.
5. Duma, S. M.; Ng, T. P.; Kennedy, E. A.; Stitzel, J. D.; Herring, I. P.; and Kuhn, F., "Determination of Significant Parameters for Eye Injury Risk from Projectiles," *The Journal of Trauma Injury, Infection, and Critical Care*, October 2005.
6. Evans, M. B. (MD), "Gunshot Wound Ballistics," Baylor College of Medicine, February 2004.
7. Gordon, C. C.; Churchill, T.; Clauser, C. E.; Bradtmiller, B.; McConville, J. T.; Tebbetts, I.; and Walker, R. A., "1988 Anthropometric Survey of U.S. Army Personnel: Methods and Summary Statistics," Technical Report Natick/TR-89/044, September 1989.
8. Hoerner, Dr. S. F., Fluid Dynamic Drag, Published by Author, 1958.
9. Hueske, E., "Practical Analysis and Reconstruction of Shooting Incidents," CRC Press, November 2005.
10. Hunt, J. C. R.; Poulton, E. C.; and Mumford, J. C., "The Effects of Wind on People: New Criteria Based on Wind Tunnel Experiments," *Building and Environment*, Vol. 11, 1976.
11. Hunt, J. C. R., and Poulton, E. C., "Some Effects of Wind on People," Symposium on External Flows, pp. K1-9, Dept. of Aeronautical Engineering, University of Bristol, July 1972.
12. Jordan, S. C.; Johnson, T.; Sterling, M.; and Baker, C. J., "Evaluating and Modeling the Response of an Individual to a Sudden Change in Wind Speed," *Building and Environment*, Vol. 43, 2008.
13. Jordan, S. C., "An Investigation of the Slipstreams and Wakes of Trains and the Associated Effects on Trackside People and Objects," PH. D. Dissertation in Civil Engineering, University of Birmingham, January 2008.
14. Kennedy, E.; Manoogian, S.; and Duma, S., "Development of Parametric Eye Injury Criteria," USAARL Contract Report No. CR-2008-05, July 2008.
15. Klapper, J., "Downwash Effects and the Feasibility of High Disc Loading Marine Assault VSTOL Aircraft," Naval Air Systems Command, Advanced Design Section Letter Report No. 77-11-1 (AIR-530132A), November 1977.
16. Loving, D. L., "Aerodynamic Measurements Made During Navy Investigation of Human Tolerance to Wind Blasts," NACA RM L7C25, November 1948.
17. Murakami, S.; Uehara, K.; and Deguchi, K., "Wind Tunnel Modeling Applied to Pedestrian Comfort," 5th International Conference on Wind Engineering, Ft. Collins, CO, Paper No. III-6, 1979.

18. Murakami, S., and Deguchi, K., "New Criteria for Wind Effects on Pedestrians," *Journal of Wind Engineering and Industrial Aerodynamics*, Vol. 7, 1981.
19. Ratcliff, M.A., and Peterka, J.A., "Comparison of Pedestrian Wind Acceptability Criteria," *Journal of Wind Engineering and Industrial Aerodynamics*, Vol. 36, 1990.
20. Schane, LTC W. P., "Adverse Effects of Downwash Upon Man," U. S. Army Aeromedical Research Laboratory, Presented at the Joint Symposium on Environmental Effects on VTOL Designs, Preprint No. SW-70-10 (# 71-15411) November 1970.
21. Schane, W. P., "Effects of Downwash Upon Man," U.S. Army Aeromedical Research Unit Report No. 68-3, November 1967.
22. Schmitt, T. J., "Wind-Tunnel Investigation of Air Loads on Human Beings," David Taylor Model Basin Aerodynamics Laboratory Report 892, January 1954.
23. Wright, N. L., and Plaga, J. A., "Assessment of Human Performance in a Simulated Rotorcraft Downwash Environment," AFRL-HE-WP-TR-2007-0064, May 2007.
24. Yu, J. T. S., "Wind Effects on Pedestrians," RED Consultants Limited, Hong Kong, 2005.

ENTRAINED PARTICLE, FLYING DEBRIS, AND PARTICULATE CLOUDS HAZARDS

1. Anon., "Jet-lift Erosion," Rolls-Royce, FLIGHT International, pages 355-356, March 8, 1962.
2. Anon., "Review and Assessment of VTOL Downwash Effects Near the Ground," unpublished draft report, January 1968.
3. Anon., "Snow Stabilization Techniques for Helicopter Landings," Franklin Institute Research Laboratories, Technical Report No. LWL-CR-05C71 / N72-28271, September 1971.
4. Anon., "VTOL Downwash Impingement Study - Summary Report," Hiller Aircraft Corp., TCRC TR 61-37, August 1961.
5. Anon., "VTOL Soil Erosion Problems," The AEROPLANE and ASTRONAUTICS, page 254, March 8, 1962.
6. Baker, C. J., "The Debris Flight Equations," *Journal of Wind Engineering and Industrial Aerodynamics*, Vol. 95, 2007, pp. 329-353.
7. Dyke, R. W., "An Investigation of the Over the Water Aspects of VTOL Airplanes at High Disk Loading," Curtiss-Wright Corporation, VTOL Systems Group, Report No. 012-26, December 1963.
8. Ebersol, J. F., "Obscuration by Helicopter-Produced Snow Clouds," *Optical Engineering*, Vol. 22, No. 1, January/February 1983.
9. Govindarajan, B.; Leishman, J. G.; and Gumerov, N. A., "Evaluation of Particle Clustering Algorithms in the Prediction of Brownout Dust Clouds," Proceedings of the American Helicopter Society's 67th Annual Forum, Virginia Beach, VA, May 3-5, 2011.

10. Grotz, C. A., "Simulated VTOL Exhaust Impingement on Ground Surfaces," The Boeing Company, Society of Automotive Engineers - Engineering and Manufacturing Meeting, Oct. 1961.
11. Haehnel, R. B.; Cushman-Roisin, B.; and Dade, W. B., "Cratering by a Subsonic Jet Impinging on a Bed of Loose Particles," American Society of Civil Engineers, Proceedings of the Tenth Conference on Engineering, Construction, and Operations in Challenging Environment, March 2006.
12. Holmes, J. D.; Baker, C. J.; and Tamura, Y., "Tachikawa Number: A Proposal," Journal of Wind Engineering and Industrial Aerodynamics, Vol. 94, 2006, pp. 41-47.
13. Holmes, J. D., "Trajectories of Spheres in Strong Winds with Application to Windborne Debris," Journal of Wind Engineering and Industrial Aerodynamics, Vol. 92, 2004, pp. 9-22.
14. Holmes, J. D.; Letchford, C. W.; and Lin, N., "Investigations of Plate-Type Windborne Debris – Part II: Computed Trajectories," Journal of Wind Engineering and Industrial Aerodynamics, Vol. 94, 2006, pp. 21-39.
15. Johnson, B.; Leishman, J. G.; and Sydney, A., "Investigation of Sediment Entrainment in Brownout Using High-Speed Particle Image Velocimetry," Proceedings of the American Helicopter Society's 65th Annual Forum, Grapevine, TX, May 27-29, 2009.
16. Keller, J. D.; Whitehouse, G. R.; Wachspress, D. A.; Teske, M. E.; and Quackenbush, T. R., "A Physics-Based Model of Rotorcraft Brownout for Flight Simulation Applications," Presented at the 62nd Forum of the American Helicopter Society, May 2006.
17. Kind, R. J., and Wardlaw, R. L., "Design of Rooftops Against Gravel Blow-off," NRC No. 15544, National Aeronautical Establishment, National Research Council of Canada, Ottawa, Canada, 1976.
18. Kind, R. J., and Wardlaw, R. L., "The Development of a Procedure for the Design of Rooftops Against Gravel Blow-Off and Scour in High Winds," Symposium on Roofing Technology, Paper No. 16, 1977, pp. 112-123.
19. Kok, J. F., and Renno, N. O., "A Comprehensive Numerical Model of Wind Blown Sand," University of Michigan, 2009.
20. Kordi, B., and Kopp, G. A., "Evaluation of the Quasi-Steady Theory Applied to Windborne Flat Plates in Uniform Flow," Journal of Engineering Mechanics, ASCE, Vol. 135, July 2009, pp. 657-668.
21. Kuhn, R. E., "An Investigation to Determine Conditions Under Which Downwash from VTOL Aircraft Will Start Surface Erosion from Various Types of Terrain," NASA TN D-56, September 1959.
22. Kuhn, R. E., "Height of Spray Produced By Vertical Takeoff and Landing (VTOL) Aircraft," David W. Taylor Naval Ship Research and Development Center Report DTNSRDC/ASED-79/04, April 1979.

23. Kuhn, R. E.; Margason, R. J.; and Curtis, P., "Jet-Induced Effects, The Aerodynamics of Jet- and Fan-Powered V/STOL Aircraft in Hover and Transition," Volume 217, Progress in Astronautics and Aeronautics, AIAA, 2006.
24. Lin, N., "Simulation of Windborne Debris Trajectories," Master's Thesis in Civil Engineering, Texas Tech University, August 2005.
25. Lin, N.; Letchford, C. W.; and Holmes, J. D., "Investigations of Plate-Type Windborne Debris – Part I: Experiments in Wind Tunnel and Full Scale," Journal of Wind Engineering and Industrial Aerodynamics, Vol. 94, 2006, pp. 51-76.
26. Lin, N.; Holmes, J. D.; and Letchford, C. W., "Trajectories of Wind-Borne Debris in Horizontal Winds and Applications to Impact Testing," Journal of Structural Engineering, ASCE, Vol. 133, February 2007, pp. 274-282.
27. Marsh, K. R., "Research on VTOL Water Hover Effects, Including the Effects of Wind and Waves," LTV Aerospace Corporation, Report No. 2-55400/8R-6140, April 1968.
28. Masters, F., and Gurley, K., "Performance of Embedded Gravel Roof Systems in Extreme Wind Loading," Department of Civil and Coastal Engineering, University of Florida, March 18, 2008.
29. Morse, A., and Newhouse, H., "VTOL Downwash Impingement Study Surface Erosion Tests," U.S. Army Transportation Research Command, TREC TR 60-67, Ft. Eustis, VA, October 1960.
30. Nordquist, W. S., and Dickson, D. H., "Helicopter Downwash Applied to Fog Clearing: A Status Summary," Atmospheric Sciences Laboratory, White Sands Missile Range, NM, Technical Report ECOM-5465, October 1972.
31. Nordquist, W. S., "Fog Clearing Using Helicopter Downdrafts: A Numerical Model," Atmospheric Sciences Laboratory, White Sands Missile Range, NM, Technical Report ECOM-5527, December 1973.
32. O'Bryan, T. C., "An Experimental Study of the Effect of Downwash From a Twin Propeller VTOL Aircraft on Several Types of Ground Surfaces," NASA TN D-1239, May 1962.
33. O'Bryan, T. C., "An Investigation of the Effect of Downwash from a VTOL Aircraft and a Helicopter in the Ground Environment," NASA TN D-977, October 1961.
34. Pamadi, B. N., "Downwash Impingement," Indian Institute of Technology, Bombay, India, AIAA Journal Vol. 18, No. 8 / X80-43136, November 1979.
35. Plank, V. G.; Spatola, A. A.; and Hicks, J. R., "Fog Modification By Use of Helicopters," Atmospheric Sciences Laboratory, White Sands Missile Range, NM, Technical Report ECOM-5339 (also Technical Report AFCRL-70-0593), October 1970.
36. Ray, G. D., "Ground Erosion Caused by V/STOL Aircraft," 6-2720-151, Boeing Memo, July 1964.
37. Richards, P. J.; Williams, N.; Laing, B.; McCarty, M.; and Pond, M., "Numerical Calculation of the Three-Dimensional Motion of Wind-Borne Debris," Journal of Wind Engineering and Industrial Aerodynamics, Vol. 96, 2008, pp. 2188-2202.

38. Rodgers, S. J., "Evaluation of the Dust Cloud Generated by Helicopter Rotor Blade Downwash," MSA Research Corp., 7th Annual National Conference on Environmental Effects on Aircraft and Propulsion Systems / A6810643, September 1967.
39. Rogers, S. J., "Evaluation of the Dust Cloud Generated by Helicopter Rotor Downwash," USAAVLABS TR-67-81, March 1968.
40. Rogers, S. J., "Evaluation of the Dust Cloud Generated by Helicopter Rotor Downwash," Proceedings of 7th Annual Conference on Environmental Effects on Aircraft and Propulsion Systems, Sponsored by Institute of Environmental Sciences and the U.S. Naval Air Propulsion Test Center, Mt. Prospect, IL, September 25-27, 1967.
41. Simiu, E., and Cordes, M. R., "Tornado-Borne Missile Speed Probabilities," Journal of Structural Engineering, ASCE, Vol. 109, January 1983, pp. 154-168.
- 42 Syal, M., and Leishman, J. G., "Comparisons of Predicted Brownout Dust Clouds with Photogrammetry Measurements," Proceedings of the American Helicopter Society's 67th Annual Forum, Virginia Beach, VA, May 3-5, 2011.
43. Sydney, A.; Baharani, A.; and Leishman, J. G., "Understanding Brownout Using Near-Wall Dual-Phase Flow Measurements," Proceedings of the American Helicopter Society's 67th Annual Forum, Virginia Beach, VA, May 3-5, 2011.
44. Tan, P. M.; Hale, R. W.; and Ordway, D. E., "Experimental Study of Pilot Visibility From a VTOL Air / Sea Craft Near the Ocean Surface," Therm Advanced Research, Inc., TAR-TR 6704 / N68-12243, July 1967.
45. Tanner, P. E., "Photogrammetric Characterization of a Brownout Cloud," Proceedings of the American Helicopter Society's 67th Annual Forum, Virginia Beach, VA, May 3-5, 2011.
46. Tatom, J. W.; Hinson, B. L.; and Harris, A. E., "VTOL Transport Dust Cloud / Pilot Visibility Model Study," Lockheed-Georgia Company 67-ENV-14.
47. Velkoff, H., and Sheppard, A., "The Utilization of Helicopter Rotor Technology in the Prevention of Frost in Orange Groves," Eleventh European Rotorcraft Forum Paper No. 35, September 1985.
48. Vidal, R. J., "Aerodynamic Process in the Downwash Impingement Problem," Cornell Aeronautical Laboratory, Inc., IAS 30th Annual Meeting, IAS Paper No. 62-36, January 1962.
49. Wachspress, D. A.; Whitehouse, G. R.; Keller, J. D.; Yu, K.; Gilmore, P.; Dorsett, M.; and McClure, K., "A High-Fidelity Brownout Model for Real-Time Flight Simulations and Trainers," Proceedings of the American Helicopter Society's 65th Annual Forum, Grapevine, TX, May 27-29, 2009.
50. Wang, K., "Flying Debris Behavior," Master's Thesis in Civil Engineering, Texas Tech University, May 2004.
51. Wang, K. Y., and Letchford, C. W., "Flying Debris Behavior," Proceedings of the Eleventh International Conference on Wind Engineering, Lubbock, Texas, June 2-5, 2003, pp. 1663-1678.

52. White, R. P., Jr. and Vidal, R. J., "Study of the VTOL Downwash Impingement Problem," US Army Transportation Research Command, TREC 60-70, Cornell Aeronautical Lab. Inc., November 1960.
53. Wills, J. A. B.; Lee, B. E.; and Wyatt, T. A., "A Model of Wind-Borne Debris Damage," Journal of Wind Engineering and Industrial Aerodynamics, Vol. 90, 2002, pp. 555-565.

DAMAGE TO MATERIALS BY ENTRAINED PARTICLES AND FLYING DEBRIS

1. Abraham, V. J., "Missile Impact Resistance of Window Glass Construction," Master's Thesis in Civil Engineering, Texas Tech University, May 1995.
2. Anon, "Wind-Borne Debris, Impact Resistance of Residential Glazing," NAHB Research Center, January 2002.
3. Anon, "A Summary Report on Debris Impact Testing at Texas Tech University," Wind Science and Engineering Research Center, June 2003.
4. Anon, "Advanced Vehicles Concepts, Technical Transfer Dispatch #6, ULSAB-AVC Body Structure Materials," ULSAB-AVC Consortium, May 2001. (refer to "<http://www.autosteel.org/Content/NavigationMenu2/Automotive/TechnicalInformation/default.htm>")
5. Anon, "Ultralight Steel Auto Closures – Engineering Report," Porsche Engineering Services, April 2000. (refer to "<http://www.autosteel.org/Content/NavigationMenu2/Automotive/TechnicalInformation/default.htm>")
6. Beason, W. L.; Meyers, G. E.; and James, R. W., "Hurricane Related Window Glass Damage in Houston," Journal of Structural Engineering, Vol. 110, December 1984, pp. 2843-2857.
7. Beason, W. L., "Breakage Characteristics of 1/4 Inch Tempered Glass Subjected to Small Missile Impact," Final Report to Institute for Disaster Research, Texas Tech University, October 1975.
8. Bole, S., "Investigation of the Mechanics of Windborne Missile Impact on Window Glass," Master's Thesis in Civil Engineering, Texas Tech University, December 1999.
9. Burley, C. E.; Niemeier, B. A.; and Koch, G. P., "Dynamic Denting of Autobody Panels," Society of Automotive Engineers, SAE Paper 760165, February 1976.
10. Burley, C. E., and Niemeier, B. A., "Denting Properties of Aluminum Autobody Components," Society of Automotive Engineers, SAE Paper 770199, February 1977.
11. Dear, J. P.; Lee, H.; and Brown, S. A., "Impact Damage Processes in Composite Sheet and Sandwich Honeycomb Materials," International Journal of Impact Engineering, Vol. 32, 2005, pp. 130-154.
12. Dharani, L. R.; Ji, F.; Behr, R. A.; Minor, J. E.; and Kremer, P. A., "Breakage Prediction of Laminated Glass Using the "Sacrificial Ply" Design Concept," Journal of Architectural Engineering, Vol. 10, December 2004, pp. 126-135.

13. DiCello, J. A., and George, R. A., "Design Criteria For The Dent Resistance Of Auto Body Panels," SAE International, Paper 740081, 1974.
14. Grant, P. V.; Cantwell, W. J.; McKenzie, H.; and Corkhill, P., "The Damage Threshold of Laminated Glass Structures," International Journal of Impact Engineering, Vol. 21, 1998, pp. 737-746.
15. Hodgins, B., "The Numerical Prediction of the Dent Resistance of Medium Scale Aluminum Structural Panel Assemblies," M.S. Dissertation in Mechanical Engineering, University of Waterloo (Canada), 2001.
16. Ji, F. S.; Dharani, L. R.; and Behr, R. A., "Damage Probability in Laminated Glass Subjected to Low Velocity Small Missile Impacts," Journal of Materials Science, Vol. 33, 1998, pp. 4775-4782.
17. Kaiser, N. D.; Behr, R. A.; Minor, J. E.; Dharani, L. R.; Ji, F.; and Kremer, P. A., "Impact Resistance of Laminated Glass Using "Sacrificial Ply" Design Concept," Journal of Architectural Engineering, Vol. 6, March 2000, pp. 24-34.
18. McCormick, M. A.; Fekete, J. R.; Meuleman, D. J.; and Shi, M. F., "Effect of Steel Strengthening Mechanisms on Dent Resistance of Automotive Body Panels," SAE International, Paper 980960, 1998.
19. Minor, J. E., "Performance of Roofing Systems in Wind Storms," NRCA/NBS Proceedings of the Symposium on Roofing Technology, Paper 17, September 1977.
20. Minor, J. E., "Windborne Debris and the Building Envelope," Journal of Wind Engineering and Industrial Aerodynamics, Vol. 53, 1994, pp. 207-227.
21. Minor, J. E.; Beason, W. L.; and Harris, P. L., "Designing for Windborne Missiles in Urban Areas," Journal of Structural Division, Vol. 104, November 1978, pp. 1749-1780.
22. Minor, J. E., "Lessons Learned from Failures of the Building Envelope in Windstorms," Journal of Architectural Engineering, Vol. 11, March 2005, pp. 10-13.
23. Niemeier, B. A., and Burley, C. E., "Hailstone Response of Body Panels – Real and Simulated," Society of Automotive Engineers, SAE Paper 780398, February 1978.
24. Pantelides, C. P.; Horst, A. D.; and Minor, J. E., "Postbreakage Behavior of Heat Strengthened Laminated Glass Under Wind Effects," Journal of Structural Engineering, Vol. 119, February 1993, pp. 454-467.
25. Persson, J.; Breder, K.; and Rowcliffe, D. J., "Loading Rate Effects During Indentation and Impact on Glass with Small Spheres," Journal of Materials Science, Vol. 28, 1993, pp. 6484-6489.
26. Sadagopan, S., and Urban, D., "Formability Characterization of a New Generation of High Strength Steels," American Iron and Steel Institute, Report TRP 0012, March 2003. (refer to "<http://www.autosteel.org/Content/NavigationMenu2/Automotive/TechnicalInformation/default.htm>")
27. Saxe, T. J.; Behr, R. A.; Minor, J. E.; Kremer, P. A.; and Dharani, L. R., "Effects of Missile Size and Glass Type on Impact Resistance of "Sacrificial Ply" Laminated Glass," Journal of Architectural Engineering, Vol. 8, March 2002, pp. 24-39.

28. Shih, H. C., and Horvath, C. D., "Effects of Material Bending and Hardening on Dynamic Dent Resistance," SAE International, Paper 2005-01-0832, 2005.
29. Shi, M. F.; Meuleman, D. J.; Alaniz, C. L.; and Zurdosky, S. J., "An Evaluation of the Dynamic Dent Resistance of Automotive Steels," SAE International, Paper 910287, 1991.
30. Shi, M. F.; Brindza, J. A.; Michel, P. F.; Bucklin, P.; Belanger, J. P.; and Prencipe, J. M., "Static and Dynamic Dent Resistance Performance of Automotive Steel Body Panels," SAE International, Paper 970158, 1997.
31. Souter, R. K., and Emerson, J. B., "Summary of Available Hail Literature and the Effect of Hail on Aircraft in Flight," NACA TN 2734, September 1952.
32. Thomas, D.; Hodgins, B.; Worswick, M.; Finn, M. J.; and Gong, K., "Static and Dynamic Denting of Paint Baked AA6111 Panels: Comparison of Finite Element Predictions and Experiments," SAE International, Paper 2001-01-3047, 2001.
33. Thomas, D., "The Numerical Prediction of Panel Dent Resistance Incorporating Panel Forming Strains," M.S. Dissertation in Mechanical Engineering, University of Waterloo (Canada), 2001.
34. Thomson, R. G., and Hayduk, R. J., "An Analytical Evaluation of the Denting of Airplane Surfaces by Hail," NASA TN D-5363, August 1969.
35. Wang, Y., and Mallick, P. K., "Dynamic Denting Study of Aluminum Alloys," SAE International, Paper 2004-01-0183, 2004.
36. Yukutake, E.; Kaneko, J.; Sugamata, M.; and Kubota, M., "Dent Resistance of AZ31 Magnesium Alloy Sheets," Journal of Japan Institute of Light Metals, Vol. 56, No. 5, pp. 277-282, 2006.
37. Yutori, Y.; Nomura, S.; Kokubo, I.; and Ishigaki, H. "Studies On The Static Dent Resistance," Proceedings of the 11th IDDRG, Memoires Scientifiques Revue Metallurgie, Volume 77(4), pp. 561-569, April 1980.

STRUCTURE AND EQUIPMENT HAZARDS

1. Anon, "Minimum Design Loads for Buildings and Other Structures," American Society of Civil Engineers (ASCE) Press, ASCE Standard ASCE/SEI 7-05, Copyright 2006.
2. Anon, "Standard Test Method for Wind-Resistance of Asphalt Shingles (Fan-Induced Method)," ASTM Standard D3161-09, January 2009.
3. Anon, "Standard Test Method for Wind Resistance of Asphalt Shingles (Uplift Force/Uplift Resistance Method)," ASTM Standard D7158-08d, September 2008.
4. Bi, A., "Probabilistic Assessment of Wind Loads on a Full Scale Low Rise Building," M.S. Dissertation in Civil Engineering, Texas Tech University, May 2006.
5. Hu, X., "Wind Loading Effects and Equivalent Static Wind Loading on Low-Rise Buildings," PH. D. Dissertation in Civil Engineering, Texas Tech University, May 2006.

6. Hurley, G. E.; Pitman, C. W.; and Trick, L. L., "HH-46A/CV-64 Rotor Engage/Disengage Test," Naval Air Test Center Report No. RW-55R-84, October 30, 1984.
7. Kola, S., "Comparison of Wind Load Standards," M.S. Dissertation in Civil Engineering, Texas Tech University, December 1995.
8. Letchford, C. W., "Wind Loads on Rectangular Signboards and Hoardings," Journal of Wind Engineering and Industrial Aerodynamics, Vol. 89, 2001, pp. 135-151.
9. Lin, J. X.; Montpellier, P. R.; Tillman, C. W.; and Riker, W. I., "Aerodynamic Devices for Mitigation of Wind Damage Risk," 4th International Conference on Advances in Wind and Structures (AWAS '08), Jeju, Korea, May 2008.
10. Mehta, K. C., and Delahay, J. M., "Guide to the Use of the Wind Load Provisions of ASCE 7-02," American Society of Civil Engineers (ASCE) Press, 2004.
11. Peterka, J. A., "Wind Tunnel Tests: Dallas Convention Center Expansion," Cermak Peterka Peterson, Inc., Fort Collins, CO, CPP Project 90-0666, June 1991.
12. Peterka, J. A.; Cermak, J. E.; Cochran, L. S.; Cochran, B. C.; Hosoya, N.; Derickson, R. G.; Harper, C. ; Jones, J.; and Metz, B., "Wind Uplift Model for Asphalt Shingles," Journal of Architectural Engineering, Vol. 3, No. 4, December 1997.
13. Shikha Jain, B. E., "Wind Effects on a Full-Scale Frame," M.S. Dissertation in Civil Engineering, Texas Tech University, December 2002.
14. Smith, D. A.; Chappell, K.; Mehta, K. C.; and Letchford, C. W., "Windstorm Mitigation Initiative, Report on C-130 Testing," Wind Science and Engineering, Texas Tech University, January 2002.
15. Thorndon, CW3 D. C., "Rotorwash Damage," Missouri Army National Guard, Report of Army Aircraft Accidents Vol 22 No. 7 / Flightfax, April 1994.
16. Traasdahl, E. C., and Ruffa, S. A., "CH-46E/LHA Engage/Disengage Dynamic Interface Test," Naval Air Test Center Report No. RW-58R-84, January 30, 1985.
17. Wolfe, R., "Wind Resistance of Light-Frame Structures," Proceedings of the Third Wood Building/Architecture Technical Seminar, Korean Forest Research Institute and American Forest and Paper Association, Seoul, Korea, November 1996.
18. Wu, F., "Full-Scale Study of Conical Vortices and Their Effects Near Roof Corners," PH. D. Dissertation in Civil Engineering, Texas Tech University, 2000.
19. Zhao, Z., "Wind Flow Characteristics and Their Effects on Low-Rise Buildings," PH. D. Dissertation in Civil Engineering, Texas Tech University, December 1997.
20. Zhou, N., "Wind Loads Simulation Methodologies and Application to the Full Scale Data," PH. D. Dissertation in Civil Engineering, Texas Tech University, December 2005.
21. Zhu, H., "C-130 Testings on Low-Rise Buildings," PH. D. Dissertation in Civil Engineering, Texas Tech University, May 2006.

HELIPORT/VERTIPORT DESIGN

1. Anon., "Heliport Design," U. S. Department of Transportation, Federal Aviation Administration, Washington D.C., Advisory Circular 150/5390-2, January 4, 1988.
2. Armstrong, J. P., "Evaluation and Control of Dust and Foreign Object Damage (FOD) at the VTOL Forward Operating Site," Army Engineer Waterways Experiment Station, Vicksburg, Mississippi.
3. Bennett, R., "Heliport Design for San Bernardino County Relocation Medical Center, Colton, CA," Prepared by Heliport Consultants, Westlake Village, CA, 1991.
4. Dzamba, L. D.; Hawley, R. J.; and Adams, R. J., "Analysis of Helicopter Mishaps at Heliports, Airports, and Unimproved Sites," Federal Aviation Administration, Washington D.C., Technical Report DOT/FAA/RD-90/8, December 1990.
5. Farell, C., and Sitheeq, M. M., "Aerodynamic Considerations for Rooftop Helideck Design," American Society of Civil Engineers, Proceedings of the Fifth Conference on Engineering, Construction, and Operations in Space, pp. 1245-1251, June 1996.
6. Ferguson, S. W., "Rotorwash Analysis Handbook, Volume I – Development and Analysis," Federal Aviation Administration, Washington D.C., Technical Report DOT/FAA/RD-93/31,I, June 1994.
7. Ferguson, S. W., "Evaluation of Rotorwash Characteristics for Tiltrotor and Tiltwing Aircraft in Hovering Flight," Federal Aviation Administration, Washington D.C., Technical Report DOT/FAA/RD-90/16, December 1990.
8. Ferguson, S. W., "Evaluation of Rotorwash Characteristics for the Bell/Boeing V-22, Bell 214ST, and Sikorsky S-76B," Prepared for JPJ Architects, Inc. and the City of Dallas Aviation Department, EMA Technical Report TR-91-1-1, February 1991.
9. Leese, G. W., and Carr, J. W., "Materials Evaluation for Aircraft Blast and Helicopter Downwash Protection," Army Engineer Waterways Experiment Station, Vicksburg, Mississippi, June 1975.
10. Lin, J. X.; Montpellier, P. R.; Tillman, C. W.; and Riker, W. I., "Aerodynamic Devices for Mitigation of Wind Damage Risk," 4th International Conference on Advances in Wind and Structures (AWAS '08), Jeju, Korea, May 2008.
11. Liu, H., and Nateghi, F., "Wind Damage to Airport: Lessons Learned," Journal of Aerospace Engineering, Vol. 1, April 1988, pp. 105-116.
12. McKinley, J. B., "Evaluating Wind Flow Around Buildings on Heliport Placement," DOT/FAA/PM-84/25, October 1984.
13. Negrette, A., "The Unseen Hazard of Rotor Downwash," Rotor & Wing International, Vol. 26, No. 2, February 1992.
14. Nordquist, W. S., and Dickson, D. H., "Helicopter Downwash Applied to Fog Clearing: A Status Summary," Atmospheric Sciences Laboratory, White Sands Missle Range, NM, Technical Report ECOM-5465, October 1972.

15. Peterka, J. A., "Wind Tunnel Tests: Dallas Convention Center Expansion," Cermak Peterka Peterson, Inc., Fort Collins, CO, CPP Project 90-0666, June 1991.
16. Schane, Col. W. P., "Downwash - The Dangers and Defense," Vertiflite, May/June 1972.
17. Schwartz, C. W.; Witczak, M. W.; and Leahy, R. B., "Structural Design Guidelines for Heliports," DOT/FAA/PM-84/23, October 1984.
18. Surry, D., and Stone, G. K., "A Study of the Effects of the Proposed Rockefeller University Faculty Housing Project on Nearby Helicopter Operations and the Adjacent Building," Boundary Layer Wind Tunnel Laboratory, The University of Western Ontario, London, Ontario, Canada, Report BLWT-SS12-1983, May 1983.
19. Smith, R. D., "Safe Heliports Through Design and Planning, A Summary of FAA Research and Development," Federal Aviation Administration, Washington D.C., Technical Report DOT/FAA/RD-93/17, February 1994.
20. Smith, R. D., "Heliport/Vertiport Design Deliberations, 1997-2000," DOT/FAA/ND-00/1, May 2001.
21. Tomita, H., "Effect of Jet-Engine Exhaust on Blast Fences," U. S. Naval Civil Engineering Laboratory, Port Hueneme, CA, Technical Note N-593, May 16, 1964.
22. Tomita, H., "Effects of Jet-Engine Exhaust on Virginia Diabase Concrete Pavement," U. S. Naval Civil Engineering Laboratory, Port Hueneme, CA, Technical Report 089, November 14, 1960.
23. Vorwald, J. G.; Tai, T. C.; and Walker, M. A., "Analytical Predictions of Flow Field Characteristics for a Hovering V-22 Including the Potential for V-22 Outflow to Overturn a Parked, Unsecured Helicopter," CARDIVNSWC-TR-94/011, June 1994.
24. Wu, F., "Full-Scale Study of Conical Vortices and Their Effects Near Roof Corners," PH. D. Dissertation in Civil Engineering, Texas Tech University, 2000.

GROUND VORTEX EFFECTS

1. Bolanovich, M., and Marks, M. D., "Experimental Downwash Velocity, Static Pressure, and Temperature Distributions in Ground Effect for a 75-Foot Jet Driven Rotor," McDonnell Aircraft Corporation, Dec. 1958.
2. Cimbala, J. M.; Billet, M. L.; Gaublomme, D. P.; and Oefelein, J. C., "Experiments on the Unsteadiness Associated With a Ground Vortex," Journal of Aircraft, Vol. 28, No. 4, April 1991, pp. 261-267.
3. Cimbala, J. M.; Stinebring, D. R.; Treaster, A. L.; Billet, M. L.; and Walters, M. M., "Experimental Investigation of a Jet Impinging on a Ground Plane in the Presence of a Cross Flow," Journal of Aircraft, Vol. 25, No. 10, October 1988, pp. 923-931.
4. Curtiss, H. C., Jr.; Putman, W. F.; and Hanker, E. J., Jr., "Rotor Aerodynamics in Ground Effect at Low Advance Ratios," Department of Mechanical and Aerospace Engineering, Princeton University Report No. 1571-MAE, July 27, 1982.

5. Curtiss, H. C., Jr.; Sun M.; and Hanker, E. J., Jr., "Dynamic Phenomena in Ground Effect," AHS Paper No. A-83-39-76-0000, Presented at the 39th Forum of the American Helicopter Society, May 9-11, 1983.
6. Curtiss, H. C., Jr.; Sun, M.; Putman, W. F.; and Hunker, E. J., Jr., "Rotor Aerodynamics in Ground Effect at Low Advance Ratios," Journal of the American Helicopter Society, Vol. 29, No. 1, January 1984, p. 48.
7. Curtiss, H. C., Jr.; Erdman, W.; and Sun, M., "Ground Effect Aerodynamics," Presented at the International Conference on Rotorcraft Basic Research, Research Triangle Park, NC, February 19-21, 1985.
8. Dudley, M. R.; and Eshleman, J. E., "Full-Scale Ground Effects of Twin Impinging Jets Beneath a Subsonic Tactical V/STOL Aircraft," NASA Ames Research Center, AIAA-86-2704, October 1986.
9. DuWaldt, F. A., "Wakes of Lifting Propellers (Rotors) in Ground Effect," Cornell Aeronautical Laboratory No. BB-1665-5-3, November 1966.
10. Fradenburgh, E. A., "Flow Field Measurements for a Hovering Rotor Near the Ground," Sikorsky Aircraft Library, Sikorsky Aircraft Division, September 1958.
11. Greenberg, M. D., and Kaskel, A. L., "Inviscid Flow Field Induced by a Rotor in Ground Effect," Therm Advanced Research, Inc., NASA CR-1027, May 1968.
12. Hunker, E. J., Jr., and Smith, R. P., "Parameters Affecting Helicopter Interactional Aerodynamics in Ground Effect," Journal of the American Helicopter Society, Vol. 30, No. 1, January 1985.
13. Holcombe, G. C., "Effect of Ground Proximity on Download," 8-7444-1-178, Vertol Interoffice Memorandum, April 1971.
14. Lavi, R., "Parametric Investigation of VTOL Ground Proximity Effects," AIAA Paper No. 67-440, Northrop Corporation, July 1967.
15. Newman, E. M., "A New Approach to the Calculation of the Effect of the Ground on the Performance of Rotary Wing Aircraft," Professional Development Center, Special Project Report Number 71-02 / N72-23036, November 1971.
16. O'Malley, J. A., "Flow Phenomena Experienced With VTOL Aircraft in Ground Proximity," Bell Aircraft.
17. Putman, W. F., "An Experimental Investigation of Ground Effect on a Four-Propeller Tilt-Wing V/STOL Model," Department of Aerospace and Mechanical Sciences Report 892, USAAVLABS Technical Report 68-45 / N68-36289, July 1968.
18. Rossow, V. J., "Effect of Ground and Ceiling Planes on Shape of Energized Wakes," NASA Ames Research Center, AIAA Journal of Aircraft, Vol. 31, No. 5; Engineering Notes, pages 1227 - 1231, December 1993.
19. Schade, R. O., "Ground Interference Effects," NASA Langley, TN D-727, April 1961.

20. Schwantes, E., "Survey of the Ground Effect of V/STOL Aircrafts With Jet Propulsion - Report of Literature," NASA, TT F-12,573, October 1969.
21. Sheridan, P. F., and Wiesner, W., "Aerodynamics of Helicopter Flight Near the Ground," Boeing Vertol Company, 33rd Annual National AHS Forum, Preprint No. 77.33-04, May 1977.
22. Siclari, M. J.; Hill, W.G. Jr.; Jenkins, R. C.; and Migdal, D., "VTOL In-Ground Effect Flows for Closely Spaced Jets," Grumman Aerospace Corp., AIAA-80-1880, August 1980.
23. Sun, M., "A Study of Helicopter Rotor Aerodynamics in Ground Effect," Ph.D. Thesis, Princeton Mechanical and Aerodynamics Engineering Department, June 1983.

TRAILING WAKE VORTEX EFFECTS AND HAZARDS

1. Anon., "Helicopter Wake Turbulence," Approach, November 1984.
2. Anon., "Proceedings of the Conference on the Effects of Helicopter Downwash on Free Projectiles," US Army Aviation Systems Command, N79-12067, November 1975.
3. Burnham, D. C., and Teager, S. A., "Preliminary Measurements of Helicopter Wake-Vortex Velocity Profiles," DOT-TSC-FA527-PM-85-7, March 1985.
4. Connor, A. B., and O'Bryan, T. C., "A Brief Evaluation of Helicopter Wake as a Potential Operational Hazard to Aircraft," NASA TN D-1227, March 1962.
5. Curtiss, Dr. H. C., and Zhou, C., "The Response of Helicopters to Fixed Wing Aircraft Wake Encounters," Proceedings of the Aircraft Wake Vortices Conference – Volume 1 of 2, Washington D.C., October 29-31, 1991, DOT/FAA/SD-92/1.1, June 1992.
6. Dunham, R. E.; Holbrook, G. T.; Mantay, W. R.; Campbell, R. L.; and VanGunst, R. W., "Flight Test Experience of a Helicopter Encountering an Airplane Trailing Vortex," Presented at the 32nd Forum of the American Helicopter Society, Preprint 1063, May 1976.
7. Ferguson, S. W., "Rotorwash Analysis Handbook, Volume I – Development and Analysis," Federal Aviation Administration, Washington D.C., Technical Report DOT/FAA/RD-93/31,I, June 1994.
8. Ferguson, S. W., and Dreier, M. E., "Empirical Wake Turbulence Model of Tiltrotor Aircraft," SAE International, Paper 2005-01-3182, 2005.
9. Johnson, W. A., and Myers, T. T., "A Model for Human Pilot Behavior During Wake Vortex Encounter Upsets," FAA-RD-76-8, April 1976.
10. Johnson, W. A., and Teper, G. L., "Analysis of Vortex Wake Encounter Upsets," NASA CR-127491, August 1974.
11. Mantay, W. R.; Holbrook, G. T.; Campbell, R. L.; and Tomaine, R. L., "Helicopter Response to an Airplane's Trailing Vortex," Journal of Aircraft, Vol. 14, No. 4, April 1977, pp. 357-363.

12. Romander, E.; Betzina, M.; Silva, M.; Wadcock, A.; and Yamauchi, G., "Investigating Tiltrotor Formation Flight Via 1/48-Scale Wind Tunnel Experiment," Presented at the 62nd Forum of the American Helicopter Society, May 2006.
13. Sammonds, R. L., and Stinnett, G. W. Jr., "Hazard Criteria for Wake Vortex Encounters," NASA TM X-62,473, August 1975.
14. Schillings, J. J.; Ferguson, S. W.; Brand, A. G.; Mullins, B. R.; and Libby, J., "Wake Vortex Measurements of the XV-15 Tiltrotor Using a Mobile Ground-Based LIDAR System," Presented at the 57nd Forum of the American Helicopter Society, May 2001.
15. Teager, S. A.; Biehl, K. J.; Garodz, L. J.; Tymczyszyn, J. J.; and Burnham, D. C., "Flight Test Investigation of Rotorcraft Wake Vortices in Forward Flight," Federal Aviation Administration, Technical Center, Atlantic City, NJ, Technical Report DOT/FAA/CT-94/117, February 1996.
16. Tymczyszyn, J. J.; Biehl, K. J.; and Teager, S. A., "Flight Test Investigation of the Wake Vortices Generated By Helicopters," Proceedings of the Aircraft Wake Vortices Conference – Volume 1 of 2, Washington D.C., October 29-31, 1991, DOT/FAA/SD-92/1.1, June 1992.

OTHER HAZARD ANALYSIS REFERENCES

1. Baldwin, J. L., "Climatic Atlas of the United States," Prepared by the Environmental Sciences Services Administration, U.S. Department of Commerce, June 1968.
2. Turner, R. E., and Hill, C. K., "Terrestrial Environment (Climatic) Criteria Guidelines for Use in Aerospace Vehicle Development," NASA Technical Memorandum 82473, June 1982.

LOW SPEED INTERACTIONAL AERODYNAMICS (GENERAL REFERENCES)

1. Balch, D. T., "Experimental Study of Main Rotor/Tail Rotor/Airframe Interaction in Hover," 39th Annual Forum of the American Helicopter Society, St. Louis, Missouri, May 1983.
2. Cimbala, J. M.; Billet, M. L.; Gaublomme, D. P.; and Oefelein, J. C., "Experiments on the Unsteadiness Associated With a Ground Vortex," Journal of Aircraft, Vol. 28, No. 4, April 1991, pp. 261-267.
3. Cimbala, J. M.; Stinebring, D. R.; Treaster, A. L.; Billet, M. L.; and Walters, M. M., "Experimental Investigation of a Jet Impinging on a Ground Plane in the Presence of a Cross Flow," Journal of Aircraft, Vol. 25, No. 10, October 1988, pp. 923-931.
4. Curtiss, H. C., Jr.; Putman, W. F.; and Hanker, E. J., Jr., "Rotor Aerodynamics in Ground Effect at Low Advance Ratios," Department of Mechanical and Aerospace Engineering, Princeton University Report No. 1571-MAE, July 27, 1982.
5. Curtiss, H. C., Jr.; Sun, M.; and Hanker, E. J. Jr., "Dynamic Phenomena in Ground Effect," AHS Paper No. A-83-39-76-0000, Presented at the 39th Forum of the American Helicopter Society, May 9-11, 1983.

6. Curtiss, H. C., Jr.; Sun, M.; Putman, W. F.; and Hanker, E. J., Jr., "Rotor Aerodynamics in Ground Effect at Low Advance Ratios," *Journal of the American Helicopter Society*, Vol. 29, No. 1, January 1984, p. 48.
7. Curtiss, H. C., Jr.; Erdman, W.; and Sun, M., "Ground Effect Aerodynamics," Presented at the International Conference on Rotorcraft Basic Research, Research Triangle Park, NC, February 19-21, 1985.
8. DuWaldt, F. A., "Wakes of Lifting Propellers (Rotors) in Ground Effect," Cornell Aeronautical Laboratory No. BB-1665-5-3, November 1966.
9. Eppel, J. C.; Riddle, D. W.; and Stevens, V. C., "Flight Measured Downwash of QSRA," 26 Aircraft Symposium, Sendai, Japan, A89-51303, October 1988.
10. Hanker, E. J., Jr.; and Smith, R. P., "Parameters Affecting Helicopter Interactional Aerodynamics in Ground Effect," *Journal of the American Helicopter Society*, Vol. 30, No. 1, January 1985.
11. Marks, A. S., "Theoretical Downwash Velocities About the AH-1G Helicopter at Hover and 140 Knots," Army Missile Research, Development and Engineering Laboratory, AD-A008 339 / N75-24693, December 1974.
12. Sheridan, P. F.; Hanker, E. J.; and Blake, B. B., "Investigation of Operational and Design Factors Resulting From Main Rotor and Tail Rotor Interactions," USAAVRADCOM-TR-82-D-40, January 1984.
13. Sheridan, P. F., "Interactional Aerodynamics of the Single Rotor Helicopter Configuration. Volume 1: Final Report," USARTL-TR-78-23A, September 1978.
14. Silva, M. J.; Wadcock, A. J.; Yamauchi, G. K.; and Long, K. R., "Wind Tunnel Investigation of the Aerodynamic Interactions Between Helicopters and Tiltrotors in a Shipboard Environment," American Helicopter Society 4th Decennial Specialist's Conference on Aeromechanics, San Francisco, CA, January 21-23, 2004.
15. Sun, M., "A Study of Helicopter Rotor Aerodynamics in Ground Effect," Ph.D. Thesis, Princeton Mechanical and Aerodynamics Engineering Department, June 1983.
16. Weisner, W., and Kohler, G., "Tail Rotor Performance in Presence of Main Rotor, Ground, and Winds," Presented at the 29th Annual National Forum of the American Helicopter Society, May 1973.

JET EFFECTS (GENERAL REFERENCES)

1. Anon., "Full-Scale Tests of Grumman Design 698-411 Tilt-Nacelle V/STOL Model at the NASA-Ames Research Center," Grumman Report PDR 698-33, December 1981.
2. Anon., "Theoretical and Experimental Studies of Impinging Uniform and Nonuniform Jets," Cornell Aeronautical Laboratory, Inc., TRECOM TR 64-42, August 1964.
3. Brady, W. G., and Ludwig, G., "Theoretical and Experimental Studies of Impinging Uniform Jets," Cornell Aeronautical Laboratory, Inc., IAS Paper No. 63-29, January 1963.

4. Chaplin, H. R., "Theory of the Annular Nozzle in Proximity to the Ground," David Taylor Lab Aero Report 923, July 1957.
5. Childs, R. E., and Dixon, D., "Unsteady Three-Dimensional Simulations of a VTOL Upwash Fountain," Paper Presented at AIAA 24th Aerospace Sciences Meeting, January 6-9, 1986.
6. Cimbala, J. M.; Stinebring, D. R.; Treaster, A. L.; Billet, M. L.; and Walters, M. M., "Experimental Investigation of a Jet Impinging on a Ground Plane in the Presence of a Cross Flow," AIAA Powered Lift Conference 1987, 87-2326, Dec. 1987.
7. Cox, M. and Abbott, W. A., "Studies of the Flow Fields Created by Single Vertical Jets Directed Downwards Upon a Horizontal Surface," Ministry of Technology, U.D.C. No. 532.525:533.691.18, C.P. No. 912 (London: Her Majesty's Stationery Office), October 1964.
8. Donaldson, C. D., and Snedeker, R. S., "A Study of Free Jet Impingement. Part 1. Mean Properties of Free and Impinging Jets," Journal of Fluid Mechanics, Vol. 45, Part 2, 1971, pp. 281- 319.
9. Dudley, M; Falarski, M.; Pisano, A.; and Hill, W., "Ground Effect Hover Characteristics of a Large-Scale Twin Tilt-Nacelle V/STOL Model," NASA Ames Research Center, Naval Air Systems Command, and Grumman Aircraft Corp., AIAA-81-2609, December 1981.
10. Higgins, C. C., and Wainwright, T. W., "Dynamic Pressure and Thrust Characteristics of Cold Jets Discharging from Several Exhaust Nozzles Designed for VTOL Downwash Suppression," The Boeing Company, NASA TN D-2263, April 1964.
11. Hill, W. G.; Jenkins, R. G.; Kalemaris, S. G.; and Siclari, M. J., "Study of VTOL In-Ground-Effect Flow Field Including Temperature Effect," NASA CR-166258, April 1982.
12. Hill, W. G., Jr., and Jenkins, R. C., "Effect of Nozzle Spacing on Ground Interference Forces for a Two-Jet V/STOL Aircraft," Journal of Aircraft, Vol. 17, No. 9, September 1980, pp. 684-689.
13. Hill, W. G., Jr., and Jenkins, R. C., "Experimental Investigation of Multiple Jet Impingement Flows Applicable to VTOL Aircraft in Ground Effect," Grumman Research Department Memorandum RM-605, November 1975.
14. Hill, W. G., Jr., and Jenkins, R. C., "Ground Impingement of a Fan Jet Exhaust Plume," Grumman Research Memorandum RM - 653, May 1978.
15. Hrycak, P.; Lee, D. T.; Gauntner, J. W.; and Livingood, J. N. B., "Experimental Flow Characteristics of a Single Turbulent Jet Impinging on a Flat Plate," NASA TN D-5690, March 1970.
16. Jenkins, R. C., and Hill, W. G., Jr., "Investigation of VTOL Upwash Flows Formed by Two Impinging Jets," Grumman Research Department RE-548, November 1977.
17. Kohlman, D. L., Introduction to V/STOL Airplanes, Iowa State University Press, 1981.
18. Knott, P. G., "The Ground Environment Created by High Specific Thrust Vertical Land Aircraft," AIAA Powered Lift Conference 1987, 87-2309, Dec. 1987.

19. Kuhn, R. E., "An Analysis of the Pressures, Forces and Moments Induced by the Ground Vortex Generated by a Single Impinging Jet," NASA CR 4765, February 1997.
20. Kuhn, R. E., "The Effects of Crossflow on the Pressures and Lift Induced by the Fountain Generated Between Two Impinging Jets," NASA CR 206955, February 1998.
21. Lean, D., "A Discussion of Some Jet - Lift V/STOL Aircraft Characteristics and their Likely Effect on Operational Applications," Ministry of Technology, C.P. No. 1082, 1970.
22. Malin, M. R., "Prediction of Radially Spreading Turbulent Jets," CHAM Limited, AIAA Journal, Vol. 26, No. 6, November 1987.
23. Migdal, D.; Hill, W. G., Jr.; Jenkins, R. C.; and Siclari, M. J., "VTOL in Ground Effect Flows for Closely Spaced Jets," NASA CR 152321, December 1979.
24. Miller, P., and Wilson, M., "Wall Jets Created by Single and Twin High Pressure Jet Impingement," Aeronautical Journal, pp. 87-100, March 1993.
25. Murdin, P. M., "Flow Surveys of a Jet Impinging Normally Onto a Plane Surface," Royal Aircraft Establishment, TR 68024, January 1968.
26. Myers, G. E.; Schauer, J. J.; and Eustis, R. H., "Plane Turbulent Wall Jet Flow Development and Friction Factor," Universities of Washington and Stanford, Journal of Basic Engineering / Transactions of the ASME, March 1963.
27. Peck, R. E., "Aerodynamics of a Round Jet in a Counterflowing Wind," Journal of Aircraft, Vol. 18, No. 1, January 1981, pp. 61-62.
28. Platzer, M. F., and Margason, R. J., "Prediction Methods for Jet V/STOL Propulsion Aerodynamics," Journal of Aircraft, Vol. 15, No. 2, February 1978, pp. 69-77.
29. Rolls, L. S., "Operational Experience With Gas - Driver Remote Lift / Cruise Fans in V/STOL Applications," NASA Ames, July 1975.
30. Ryan, E. R., and Cosgrove, W. J., "Empirically Determined Wind and Scale Effects on Hot Gas Recirculation Characteristics of Jet V/STOL Aircraft," Bell Aerosystems Company, NASA CR-1445, October 1969.
31. Siclari, M. J.; Hill W. G., Jr.; Jenkins, R. C.; and Migdal, D., "VTOL In-Ground Effect Flows for Closely Spaced Jets," AIAA Paper No. 80-1880, AIAA Aircraft Systems Meeting, August 4-6, 1980.
32. Siclari, M. J.; Hill, W. G., Jr.; and Jenkins, R. C., "Stagnation Line and Upwash Formation of Two Impinging Jets," AIAA Journal, Vol. 19, No. 10, October 1981, pp. 1286-1293.
33. Siclari, M. J.; Migdal, D.; and Palcza, J. L., "Development of Theoretical Models for Jet-Induced Effects on V/STOL Aircraft," Journal of Aircraft, Vol. 13, No. 12, December 1976, pp. 936- 944.
34. Spratt, R. W., "Ground Environment Characterization of STOVL Fighter Propulsion Systems," Universal Technology Corporation, AD-A225 372, August 1990.

35. Steptoe, W. J., "Estimated STOVL Strike Fighter Danger Area," Center for Naval Analyses, CRM 91-171, January 1992.
36. Williams, D. E., "Reduction of V/STOL Downwash Effects by Jet Exhaust Flow Control," Naval Air Systems Command, TN-1410, December 1975.
37. Wohllebe, F. A., and Siclari, M. J., "Fountain and Upwash Flowfields of Multijet Arrangements," Journal of Aircraft, Vol. 15, No. 8, August 1978, pp. 468-473.

OTHER REFERENCES

1. Heyson, H. H., "Some Wake Related Operation Limitations of Rotorcraft," NASA TM-81920, December 1980.
2. Heyson, H. H., "Theoretical Study of the Effect of Ground Proximity on the Induced Efficiency of Helicopter Rotors," NASA TM X-71951, May 3, 1977.
3. Kerns, T., "JVX Downwash Effects Analysis (Rescue Operations Trade Study)," Bell - Boeing Report No. 901-919-004, February 1984.
4. White, F., and Blake, B. B., "Improved Method of Predicting Helicopter Control Response and Gust Sensitivity," Presented at the 35th Annual National Forum of the American Helicopter Society, Washington, D.C., May 1979.

Appendix R: Comments on References Providing New Information or Insight to the Rotorwash Hazard Analysis Problem

Sam Ferguson

DOWNWASH/OUTWASH FLOW FIELD DATA

FULL-SCALE ROTORCRAFT

1. Lake, R. E., and Clark, W. J., "V-22 Rotor Downwash Survey," NAWCADPAX-98-88-RTR, July 1998.

This reference is the formal data report for the 1998 NAVAIR V-22 Rotorwash Downwash Survey on the V-22 EMD aircraft. An extensive matrix of data was acquired as a function of distance and azimuth angle from the center of the V-22, gross weight, and wheel height above ground. This test is clearly the most comprehensive rotorwash test for tilt rotor aircraft conducted to date. Analytical predictions using several methodologies have compared well with these flight test results. Therefore, the quality of these test data are considered excellent.

2. Lake, R. E., "Shipboard V-22 Rotor Downwash Survey," NAWCADPAX-99-87-RTR, September 1999.

This reference is the second NAVAIR V-22 Rotorwash Downwash Survey report on the V-22 EMD aircraft. It was conducted on the U.S.S. Saipan (LHA-2) during 0- and 20-knot Wind-Over-Deck (WOD) conditions. The test aircraft hovered at 20 ft above the deck at a target gross weight of 45,000 pounds. Velocity measurements were taken at positions between 25 and 118 ft from the center of the aircraft at several azimuths. The downwash velocity field was analyzed for flow field dynamics, direction, mean/peak velocity, forces on personnel, and limitations on personnel. These results are compared with results from land-based CH-53E downwash data. These data should be excellent for correlation purposes with analytical methodologies.

3. Hewitt, J. J., "Downwash Measurement – A Standardized Test," Master Thesis in Aerospace Engineering, University of Glasgow, May 2008.

The purpose of this master's thesis is to document a proposed methodology (including details for using the test equipment) for conducting rotorwash testing at AgustaWestland. This work was completed as part of an internship in Yeovil in 2007 and 2008. The rotorwash flight test data that are presented in the report are from a variety of single main rotor helicopter models (EH101, Apache Mk 1, Schweizer 269C, AW109, and Lynx Mk 9). The data were acquired with a Gill Wind Master ultrasonic anemometer. Data are consistently measured for a specific test plan for each of the helicopter models. However, since this was a student project, winds had to be accepted "as is" for each test. Therefore, almost all the data involve hover with a headwind. The sensor array in each case was positioned directly ahead (or upwind) of the helicopter. This test configuration, while producing good data for correlation of a model with an ambient wind, does not represent the limiting condition for maximum rotorwash velocity along the ground.

4. Silva, M. J., "CH-47D Tandem Rotor Outwash Survey," NAWCADPAX/EDR-2010/120, August 2010.

This reference is the formal data report for the 2011 NAVAIR CH-47 Rotorwash Downwash Survey on an Army CH-47D aircraft. An extensive matrix of data was acquired as a function of

distance and azimuth angle from the center of the CH-47, gross weight, and wheel height above ground. This test is clearly the most comprehensive and highest quality rotorwash test for tandem rotor aircraft conducted to date. Analytical predictions using several methodologies have compared well with these flight test results. Therefore, the quality of these test data are considered excellent.

5. Silva, M. J., and Riser, R., "CH-47D Tandem Rotor Outwash Survey," Proceedings of the American Helicopter Society's 67th Annual Forum, Virginia Beach, VA, May 3-5, 2011.

This reference summarizes test results from the NAVAIR CH-47 flight test. It is a public release document and does an excellent job summarizing the test setup and equipment, execution, data reduction and results from the CH-47 outwash survey. The figures contained in this report are invaluable for explaining how the test data are depicted and the linkage to the operational environment surrounding the aircraft. The report contains the CH-47 rotorwash operational footprint using test data for aircraft hovering at 20-ft height above ground at a 41,000-lb gross weight. It documents how the operational footprint was generated using flight test data outwash velocity profile, the PAXman model representation and ground personnel stability limits. It also contains the much of the flight test data in multiple graphical formats.

6. Smith, R. D., "Heliport/Vertiport Design Deliberations, 1997-2000," DOT/FAA/ND-00/1, May 2001.

This reference documents FAA sponsored civil heliport/vertiport design work conducted during the 1997 to 2000 time period. Two sections of this report document important information for developing a methodology to define rotorwash footprints. The first is titled, "CTR Rotorwash – Hazard Threshold for Civilian Passengers" (pp. 145-158). This section documents the discussion of overturning force requirements for personnel in a civilian vertiport environment. Supporting data for these requirements are detailed. The second section is titled, "Civil Tiltrotor – Maneuvering and Ground Taxi Rotorwash" (pp. 81-143). The flight test data documented in this section are from a FAA sponsored follow-on test of V-22 rotorwash characteristics. These data were acquired using the same test equipment and personnel that conducted the original V-22 Rotorwash Downwash Survey (NAWCADPAX-98-88-RTR). Data acquired during this follow-on test focused on static ground operations at several thrust levels below takeoff thrust as well as dynamic ground taxi and air taxi conditions. The data were measured at the same distances from the center of the V-22 and the same azimuths. These data are meant to complement the hover data documented in the original NAVAIR report and enhance the database for civilian tilt rotor applications.

JET CONFIGURATIONS

1. Lake, R.; McCarthy, K.; Nantz, R.; and Gonzalez, H., "AV-8B -408 External Environment Outwash Flow Speed and Temperature Survey," NAWCADPAX/RTR-2000/114, August 2000.

This report provides excellent documentation of the AV-8B outwash flow field and temperature characteristics along the ground. Its applicability is limited for rotorcraft in that the effective disk loading is much higher than rotorcraft. However, the report provides excellent supporting data for modeling the high disk loading endpoint of the rotorwash problem as well as data on temperature effects.

SENSOR MEASUREMENTS AND LIMITATIONS

1. Fisher, L. R., "Wind-Tunnel Oscillation Tests of the Bendix-Friez Aerovane Anemometer," NACA RM SL53G30a, August 1953.

This reference begins, "It has long been recognized that certain types of anemometers, when exposed to an airstream which is fluctuating in velocity, will register a mean air velocity which is higher than the velocity it would register in a steady airstream." The people that conducted rotorwash testing in the 1950s and 1960s should have wisely taken this circa 1953 comment into consideration. Since the 1980s, it has been understood that early rotorwash experimental data taken with mechanical anemometers had "problems" when used for methodology correlation purposes. This led to the wind tunnel test of a cup and vane anemometer in 1993 (a type used by the FAA) to define its performance capabilities (or limitations) in rotorwash applications (see next reference). This 1953 sensor dynamic characteristics test should be useful in helping better quantify why References 30, 31, and 41 through 45 listed in Table 1 of the Rotorwash Analysis Handbook were considered of such limited usefulness. It is even possible, with some additional work, that the data from this report could be used to develop and apply an approximate correction factor to the data contained in the previously listed references.

2. Meyerhoff, C. L.; Lake, R. E.; and Gordge, D. N., "Rotorwash Wind Sensor Evaluation," DOT/FAA/RD-93/10, August 1993.

This reference documents the wind tunnel test of the static and dynamic characteristics of a cup-type anemometer (mechanical type). This anemometer was utilized by the FAA Technical Center for the acquisition of rotorwash data in References 6 through 9 as listed in Table 1 of the Rotorwash Analysis Handbook. Prior use of rotorwash data from these references indicated that there appeared to be a shift in the measured velocity data from predicted analytical results when used for correlation purposes. This wind tunnel test confirmed that the frequency response of the cup anemometer resulted in a bias toward a higher than actual velocity when the flow was of an oscillatory type. This high side velocity bias is due to the different drag coefficients on the opposite sides of the anemometer cup which result in asymmetric acceleration/deceleration characteristics in oscillatory flow conditions. As a result, this type of mechanical anemometer is not desirable for use in measuring highly oscillatory rotorwash flow.

ROTORWASH FLOW FIELD PREDICTION METHODOLOGIES

MOMENTUM ANALYSIS METHODS

1. Liu, J.; McVeigh, M. A.; and Rajagopalan, Dr. G., "Single- and Dual-Rotor Flowfield and Outwash Predictions," American Helicopter Society Tilt Rotor/Runway Independent Aircraft Technology and Applications Specialists' Meeting, Arlington, Texas, March 2001.

This reference documents modifications to momentum-based outwash flow field analyses (Hogan, ROTWASH, EFFECTS) based on CH-53E, XV-15, and V-22 flight test data and CFD analysis (ROT3DC). These modifications were made to the HOGAN analysis, and the results show improved correlation of the velocity profile results and allow prediction of profiles at all azimuths around the aircraft (instead of just the 0-, 90-, 180-, and 270-deg azimuths for dual-rotor configurations). Commentary on the flight test data correlation and the CFD analysis results provides additional insight to asymmetry conditions that exist for the dual-rotor configuration. These asymmetry affects are predicted (by ROT3DC) for the outwash results as a

function of distance from the center of the aircraft, particularly along the interaction plane close to the aircraft.

2. Hrycak, P.; Lee, D. T.; Gauntner, J. W.; and Livingood, J. N. B., "Experimental Flow Characteristics of a Single Turbulent Jet Impinging on a Flat Plate," NASA TN D-5690, March 1970.

An experimental study of the flow characteristics of a circular air jet impinging on a smooth flat plate is investigated. Jets issuing from circular nozzles of 0.125, 0.250, and 0.375 inches (0.317, 0.635, and 0.952 cm) in diameter were considered. Nozzle Reynolds numbers ranged from 600 to 100,000. The normal distance between the nozzle exit and the plate was varied from 2 to 30 nozzle diameters. Some of the flow characteristics studied were potential core length, velocity, and pressure distributions, spread of the jet, and velocity decay along the jet axis. A theoretical derivation based on a method previously used for a two-dimensional nozzle and an empirical equation for the maximum velocity decay for a radial wall jet are presented for the circular nozzle. Good agreement between theory and experiment was achieved. An empirical relation for the spread of the wall jet is also included.

CFD METHODS

1. Liu, J.; McVeigh, M. A.; and Rajagopalan, Dr. G., "Single- and Dual-Rotor Flowfield and Outwash Predictions," American Helicopter Society Tilt Rotor/Runway Independent Aircraft Technology and Applications Specialists' Meeting, Arlington, Texas, March 2001.

See comments in previous section for this reference.

2. Lestari, A.; Niazi, S.; and Rajagopalan, R. G., "Preliminary Numerical Analysis of a Quad Tiltrotor Flowfield and Performance," American Helicopter Society Tilt Rotor/Runway Independent Aircraft Technology and Applications Specialists' Meeting, Arlington, Texas, March 2001.

This reference describes the use of the ROT3DC analysis tool and its application to prediction of the flow field around a quad tilt rotor configuration. The resolution of detail in the figures does not provide a detailed insight into outwash flow fields around the aircraft. However, the same model is used for the Lui paper described in the previous section for outwash flow field analysis.

3. Vorwald, J. G.; Tai, T. C.; and Walker, M. A., "Analytical Predictions of Flow Field Characteristics for a Hovering V-22 Including the Potential for V-22 Outflow to Overturn a Parked, Unsecured Helicopter," CARDIVNSWC-TR-94/011, June 1994.

The downwash from a hovering V-22 was studied to better understand the high-velocity flow field and its interaction with shipboard operations. This analytical investigation was also performed to determine if the outwash is strong enough to overturn a nearby helicopter. The potential of the outflow overturning a second helicopter was analyzed by dividing the problem into five sections: rotor downwash, steady flow field, unsteady flow component, aerodynamic force on the second vehicle, and tipping criteria. Two hover heights, 14 ft and 25 ft, were evaluated. CAMRAD/JA was used to predict the non-uniform rotor downwash and CFL3D was used to predict the steady state flow field. These predictions are in good agreement with measured data (however, these data were early V-22 DT-IIA outwash data of lower quality). Two locations in the flow field were considered for tip over evaluation: 105 ft in front and 105 ft behind the V-22. The predicted velocities are higher 105 ft in front of the V-22; therefore, the tip over evaluation was performed 105 ft. An empirical relationship for the unsteady flow in the

outflow jet was developed from flight test data. The aerodynamic forces on the unsecured second vehicle were calculated by applying two-dimensional strip theory to a vertical distribution of the flat plate drag area. The second vehicle overturns when the aerodynamic moment exceeds the static inertial moment. In the tip over evaluation, the outflow wind vector is aligned with the second vehicle's fuselage centerline; tip over due to side wind was not evaluated. A preliminary evaluation of the potential for tip over in uniform flow was performed on 14 helicopters. The six vehicles with the greatest potential were then evaluated in the predicted, non-uniform outflow. Based on the non-uniform flow evaluation, none of the Navy helicopters will tip over. The TH-57B/C and SH-2F helicopters have the greatest risk of tipping over. The sensitivity to ambient wind and unsteady flow was evaluated. Unsteady flow significantly increases the potential for overturning. The predicted steady flow field was reviewed to identify significant flow characteristics for future validation.

ROTORWASH HAZARD ANALYSIS

PERSONNEL HAZARDS

1. Wright, N. L., and Plaga, J. A., "Assessment of Human Performance in a Simulated Rotorcraft Downwash Environment," AFRL-HE-WP-TR-2007-0064, May 2007.

This reference documents Air Force research into human performance for air rescue operations, such as litter transport, in a rotor downwash flow field. The criteria were developed in support of the Personnel Recovery Vehicle (PRV) procurement (for replacement of the MH-53 and HH-60). Test subjects (18 men and women) in the experiment were dressed as para-rescuemen (PJs) with all appropriate gear. A series of 24 tasks were assigned to the test subjects to accomplish while being blasted by high-velocity air. A weakness of the test was that the air was a steady flow, not oscillatory like real rotorcraft, and a typical helicopter profile variation in velocity above the ground was not simulated (mentioned by authors). The result of the study was a recommendation that 65 knots be the limit allowed for PJs to approach a hovering rotorcraft. The results are certainly insightful, but the limitations of the experimental setup restrict application of the results to some extent.

2. Loving, D. L., "Aerodynamic Measurements Made During Navy Investigation of Human Tolerance to Wind Blasts," NACA RM L7C25, November 1948.

This reference documents early research into the tolerance potential of the unprotected human face when suddenly blasted with wind. The test scenario reproduces the initial seconds of exposure following the ejection from an aircraft. Information on aerodynamic loads imposed on the human head is documented. While the information is good background, it will have very limited applicability to this project since the test subject is fixed in position and exposure time is extremely short (to avoid injury). The test subjects were not required to conduct any tasks and the aerodynamic velocities involved are above those already known to be limits for the rotorwash scenarios of interest.

3. Murakami, S., and Deguchi, K., "New Criteria for Wind Effects on Pedestrians," Journal of Wind Engineering and Industrial Aerodynamics, Vol. 7, 1981.

This excellent reference documents three experiments (one wind tunnel and two outdoors) of pedestrians as affected by winds of a range of airspeeds. The test subjects are not protected military personnel but people of all size, weight, sex, and age combinations. Extensive

documentation is provided, including wind tunnel drag measurements of both men and women from several positions relative to the wind. The primary result of the research is development of criteria for evaluating wind effects on pedestrians where u = the instantaneous wind speed averaged over 3 seconds.

$U < 5 \text{ m/s}$	no effect
$5 < U < 10 \text{ m/s}$	some effect
$10 < U < 15 \text{ m/s}$	serious effect
$15 < U \text{ m/s}$	very serious effect

These results are also compared with prior experiments. It should be noted that the force balance wind tunnel data (experiment 1) only involved young men/women from 4.9 to 5.9 ft tall and 85 to 140 lbs. This is the lower range for using these data with applied force criteria (conservative criteria).

4. Murakami, S.; Uehara, K.; and Deguchi, K., "Wind Tunnel Modeling Applied to Pedestrian Comfort," 5th International Conference on Wind Engineering, Ft. Collins, CO, Paper No. III-6, 1979.

This reference is essentially an earlier publication of most of the same data discussed in the previous reference by Murakami. Some of the data, figures, and photos are slightly different in presentation format and units from the previous reference. It is worth conducting a review of both documents to obtain the most complete understanding of the described experiments.

5. Ratcliff, M. A.; and Peterka, J. A., "Comparison of Pedestrian Wind Acceptability Criteria," Journal of Wind Engineering and Industrial Aerodynamics, Vol. 36, 1990.

This reference reviews and compares pedestrian wind acceptability criteria from 1975 through the late 1980s. Isyumov and Davenport (1975) indicate a mean wind speed of $> 34 \text{ mph}$ is "dangerous." Lawson and Penwarden (1975) state a mean wind speed above 13.85 m/s (31 mph) or a peak $> 23.7 \text{ m/s}$ (53 mph) is "unacceptable." Melbourne (1978) states a peak $> 23.0 \text{ m/s}$ (51.4 mph) is "unacceptable." Hunt indicates acceptability (with conditions) for wind speeds $< 20\text{-}30 \text{ m/s}$ ($44.7\text{-}67.1 \text{ mph}$) for steady wind, $< 20 \text{ m/s}$ (44.7 mph) for non-uniform or gusty wind (gusty defined by equation, not instantaneous or peak wind speed).

6. Hunt, J. C. R.; Poulton, E. C.; and Mumford, J. C., "The Effects of Wind on People: New Criteria Based on Wind Tunnel Experiments," Building and Environment, Vol. 11, 1976.

This excellent reference documents a series of wind tunnel experiments for unprotected civilian personnel as affected by winds in a wide range of settings. Unfortunately, most of the data are below the threshold for rotorcraft applications. The test subjects are generally people of all size, weight, sex, and age combinations. Extensive documentation is provided, including wind tunnel force measurements. Novel use of mechanisms is demonstrated to measure personnel force (as exerted by feet) and generate gust conditions for test purposes. The results are also compared with prior experiments. One of the several interesting results is the development of criteria for defining safety of walking. This condition is as follows:

Steady uniform wind, $u < 20\text{-}30 \text{ m/s}$
 Non-uniform winds (except for elderly), $u < 13\text{-}20 \text{ m/s}$
 Gusty winds, $u^* < 20 \text{ m/s}$ (where u^* is not the instantaneous peak, see reference for definition)

Results for elderly people (> 50 years old) indicate that gusty winds above 8.5 m/s clearly have a quantifiable effect on stability (13 to 15 m/s is normally considered the threshold for this effect). It should be noted that the majority of the test subjects appear to be people on the lower range of weight and height distributions as compared to today's general population (and especially with respect to the military population).

7. Jordan, S. C.; Johnson, T.; Sterling, M.; and Baker, C. J., "Evaluating and Modeling the Response of an Individual to a Sudden Change in Wind Speed," *Building and Environment*, Vol. 43, 2008.

This reference documents a series of wind tunnel experiments and analytical calculations undertaken to evaluate the response of an individual to a sudden change in wind speed. The wind tunnel testing subjected 31 people (male/female = 19/12, age 18-50 years, average mass male/female = 118/160 lbs) to step changes in wind speed of up to 20 m/s as applied in approximately 0.2 seconds. These test subjects were unprotected civilian personnel. Loss of balance (to a gust) was demonstrated to be a function of orientation to the wind and test subject weight. Loss of balance does not mean a fall occurs but that the body must compensate by moving the legs so as not to fall. Being pushed backwards in a pivot over the heel is less stable than a forward pivot on the toes; sideways is the least stable yet it is compensated for by a lower drag coefficient. The developed analytical model for predicting unbalance is shown to correlate relatively well with the test data. This model is developed to simulate a starting wind speed condition with a gust of varying frequency. Also, a reference list is provided of reported limiting values of acceleration for human stability. The 50th percentile child is shown to be particularly sensitive to sudden changes in wind velocity by the analytical model. Some general results are:

- 1) 50% of test subjects are displaced by a sudden 11-12 m/s (24.6 mph) gust.
- 2) 100% of test subjects are displaced by 15 m/s gust (33.6 mph) or approximately a sudden delta of 13.5 lb (female) and 19.3 lb (male) overturning force.

This work was conducted as a Ph.D. dissertation; see next reference for additional details.

8. Jordan, S. C., "An Investigation of the Slipstreams and Wakes of Trains and the Associated Effects on Trackside People and Objects," Ph.D. Dissertation in Civil Engineering, University of Birmingham, January 2008.

This is the PH. D. dissertation for the above listed reference by Jordan, Johnson, Sterling, and Baker. The highlights of the paper are covered in more detail in the thesis.

9. Ahuja, R.; Dalui, S. K.; and Gupta, V. K., "Unpleasant Pedestrian Wind Condition Around Buildings," *Journal of Civil Engineering (Building and Housing)*, Vol. 7, 2006, pp. 147-154.

This paper provides a general summary of data for pedestrian wind conditions and comfort. It also includes a good table of wind condition information from another reference (Simiu, E. and R.H. Scanlan, *Wind Effects on Structures - An Introduction to Wind Engineering*, John Wiley & Sons, New York, 1978) that is very informative.

10. Anon, "Design Guide for Wind," *Wellington City District Plan (New Zealand)*, July 2000.

This document is oriented toward providing design guidelines for the city building code. The document states "Although there is an obviously subjective element to a person's "comfort", and

there are slight divergences of opinion amongst researchers, there is a remarkably close agreement on the general effects of winds upon people. These effects may be summarized as:

- 10 m/sec - generally the limit for comfort when standing or sitting for lengthy periods in open space
- 15 m/sec - generally the limit of acceptability for comfort whilst walking
- 18 m/sec - threshold of danger level
- 23 m/sec - completely unsuitable for walking."

Additionally, the document provides sketches on how to mitigate undesirable wind conditions within cities.

11. Yu, J. T. S., "Wind Effects on Pedestrians," RED Consultants Limited, Hong Kong, 2005.

This document is oriented toward providing design guidelines for building in a city. General guidelines for pedestrian comfort are defined in a table credited to A.D. Penwarden (1975). These and additional criteria are used as proposed guidelines. The results of a case study of wind problem areas within Hong Kong are provided. This case study utilized a wind tunnel investigation of problem areas for proposing solutions to the identified problems.

12. Hunt, J. C. R., and Poulton, E. C., "Some Effects of Wind on People," Symposium on External Flows, pp. K1-9, Dept. of Aeronautical Engineering, University of Bristol, July 1972.

This reference is partly the justification for a series of planned wind experiments involving average people to determine acceptable mean/gust wind speeds for architectural purposes (unsure if they were conducted). The reference has a unique perspective on how both limit mean/gust speeds should be determined. The commentary refers to criteria involving oxygen expenditure, body dynamics, various time constants involved in taking steps on difference surfaces, wind gust speed and directional variations, and other factors. A justification for 14.4 to 17 m/s of steady wind is proposed and made. The proposed gust limits are less quantitatively defined, but the discussion on how to obtain data to set the limits is interesting. Overall, the reference is a quite interesting academic commentary on the question of what is an acceptable wind condition for average people. Also, references are provided on wind tunnel tests on humans from as early as 1928. Appendix B of the document outlines the proposed testing.

13. Schmitt, T. J., "Wind-Tunnel Investigation of Air Loads on Human Beings," David Taylor Model Basin Aerodynamics Laboratory Report 892, January 1954.

An investigation was conducted in the Taylor Model Basin 8x10 foot subsonic, atmospheric Wind Tunnel 2 to determine the drag coefficient of man. Tests were made at several yaw angles with 16 subjects of various sizes in five body positions: standing, sitting, supine, and two squat positions. Data were obtained for the subjects in both the clothed and nude conditions. A parameter was formulated from the available physical characteristics of the subjects tested and all coefficients were based on this. Drag coefficients were obtained which should be reliable in predicting drag forces on men of average stature under a variety of conditions. Lift, side force, and moments were also obtained which indicate relative trends of motion for each position.

14. Hueske, E., "Practical Analysis and Reconstruction of Shooting Incidents," CRC Press, November 2005.

This document is a general reference for crime scene analysis. It provides guideline information that states that the minimum velocity for projectile penetration of human skin (dependent on projectile shape and mass) is between 200 and 300 ft/sec (136 mph/61.0 m/s, and 205 mph/91.4 m/s).

15. Evans, M. B. (MD), "Gunshot Wound Ballistics," Baylor College of Medicine, February 2004.

This document is a general reference for gunshot wound ballistics analysis. It provides guideline information that states that the minimum velocity for projectile penetration of human skin (dependent on projectile shape and mass) is between 125 and 230 ft/sec (85.2 mph/38.1 m/s and 157 mph/70.1 m/s).

16. Bellamy, R. F. (MD), and Zajtchuk, R. (MD), "Textbook of Military Medicine," Section on Conventional Warfare Ballistic, Blast, and Burn Injuries, Chapter 4 - The Physics and Biophysics of Wound Ballistics," Borden Institute (Office of the Surgeon General, Department of the Army), p. 111, 1990.

This reference is part of a multi-volume reference on military medicine (as title infers). It provides guideline information that states the minimum velocity for projectile penetration of human skin is 262 ft/sec (179 mph/80 m/s).

17. Kennedy, E.; Manoogian, S.; and Duma, S., "Development of Parametric Eye Injury Criteria," USAARL Contract Report No. CR-2008-05, July 2008.

This reference is an excellent source of medical information for the damage potential of small projectiles that strike the human eye. Detailed data are provided that define the probabilities for corneal abrasion, hyphema (bruising), lens dislocation, retinal detachment, and globe (eyeball) rupture. These data are quantified as probability curves as a function of normalized impact energy. For rotorwash applications, the numbers for corneal abrasion and hyphema (bruising) are considered limiting conditions since the eye damage will probably not result in permanent damage. Values for these conditions are: 1) 50% risk of corneal abrasion - 1,487 J/m², and 2) 50% risk of hyphema (bruising) - 12,756 J/m². (Additional references were being written for publishing at the time of the writing of this reference list.)

18. Duma, S. M.; Ng, T. P.; Kennedy, E. A.; Stitzel, J. D.; Herring, I. P.; and Kuhn, F., "Determination of Significant Parameters for Eye Injury Risk from Projectiles," The Journal of Trauma Injury, Infection, and Critical Care, October 2005.

This document provides older data values for the eye injury data documented in the reference cited as Kennedy, E., S. Manoogian, and S. Duma, "Development of Parametric Eye Injury Criteria," USAARL Contract Report No. CR-2008-05, July 2008. (Additional references were being written for publication at the time of the writing of this reference list.)

19. Gordon, C. C.; Churchill, T.; Clauser, C. E.; Bradtmiller, B.; McConville, J. T.; Tebbetts, I.; and Walker, R. A., "1988 Anthropometric Survey of U.S. Army Personnel: Methods and Summary Statistics," Technical Report Natick/TR-89/044, September 1989.

Results of the 1987-1988 anthropometric survey of Army personnel are presented in the form of summary statistics, percentile data, and frequency distributions. These anthropometric data are presented for a subset of personnel (1,774 men and 2,208 women) sampled to match the proportions of age categories and racial/ethnic groups found in the active duty Army of June

1988. Data documented in this report include 132 standard measurements made in the course of the survey, 60 derived dimensions calculated largely by adding and subtracting standard measurement data, and 48 head and face dimensions. Measurement descriptions, visual indices, and a glossary of terms are included to help identify and locate dimensions. Descriptions of the procedures and techniques used in this survey, explanations of the complex sampling plan, computer-editing procedures, strategies for minimizing observer error, comparisons of data with previous surveys, and tabular material in appendices (designed to help users understand various practical applications of the dimensional data) are also provided.

ENTRAINED PARTICLE, FLYING DEBRIS, AND PARTICULATE CLOUD HAZARDS

1. Kuhn, R. E.; Margason, R. J.; and Curtis, P., "Jet-Induced Effects, The Aerodynamics of Jet- and Fan-Powered V/STOL Aircraft in Hover and Transition," Volume 217, Progress in Astronautics and Aeronautics, AIAA, 2006.

This book primarily deals with the technology of high disk loading jet and fan V/STOL aircraft (i.e. AV-8 Harrier). However, Chapter 6 does contain some useful data on the effects of exhaust temperature on different types of surface, ground erosion, and spray formation (over water). There is a good list of references related to these subjects. For this project, the application of these data is limited due to the high disk loadings of the presented data.

2. Haehnel, R. B.; Cushman-Roisin, B.; and Dade, W. B., "Cratering by a Subsonic Jet Impinging on a Bed of Loose Particles," American Society of Civil Engineers, Proceedings of the Tenth Conference on Engineering, Construction, and Operations in Challenging Environment, March 2006.

This document reports on the dynamics of cratering as resulting from a turbulent jet (i.e. rotorcraft) during landing and takeoff operations. Materials representative of natural soils are used in the experiment. This study aids in defining the geometry associated with small particles being lifted into the air to become a hazard to the vehicle generating the particulate cloud as well and anything in close proximity. The characteristics of the resulting crater are defined.

3. Kok, J. F., and Renno, N. O., "A Comprehensive Numerical Model of Wind Blown Sand," University of Michigan, 2009.

This paper presents a highly detailed numerical model for the prediction of "saltation" or blowing sand. This model simulates the motion of saltating particles due to gravity, fluid drag, particle spin, fluid shear, and turbulence. The paper provides background information on the small particle erosion and cloud forming process for anyone interested in the details and vocabulary associated with this subject. The paper also contains a detailed reference list. Additional published documents were in work by these authors at the time this reference was reviewed.

4. Wills, J. A. B.; Lee, B. E.; and Wyatt, T. A., "A Model of Wind-Borne Debris Damage," Journal of Wind Engineering and Industrial Aerodynamics, Vol. 90, 2002, pp. 555-565.

This paper presents a model describing the damage that might be done to buildings by wind-borne debris in a sustained high-speed wind condition (i.e. typhoon or hurricane). However, this paper has important applications for rotorwash hazard analysis. A methodology is described for characterizing the initial wind velocities required to lift cube-, sheet-, and rod-like

debris into the wind stream. The methodology is generic and wind tunnel data are provided to validate the models. Also, a damage function concept is proposed that may one day have an application for broadening the types of debris that can be analyzed without doing individual tests on each of the types of debris. However, this concept will require further development. One important reason to review this paper is because much subsequent research in the literature utilizes concepts originally presented in this paper as the basis for further experimentation.

5. Wang, K., "Flying Debris Behavior," Master's Thesis in Civil Engineering, Texas Tech University, May 2004.

Wang expands on the concepts of Wills, Lee, and Wyatt that lighter density particles and sheets can be more dangerous than heavy particles and sheets. Quite simply, if a large wood sheet becomes airborne, it can accelerate to obtain significant momentum or energy before impact. A similar size metal sheet may not become airborne as easily and therefore might present less of an overall hazard. Wang also confirms results by conducting wind tunnel tests on sheet debris in the Texas Tech University wind tunnel. The goals of the research project were to 1) examine flight initiation wind speeds for sheet debris under different restraining forces and 2) examine sheet debris flight behavior after takeoff. Wang's results are quite interesting. Early in his experiments, when he tried to confirm the results of Wills, Lee, and Wyatt; he was not successful. After a review of data, he determined that the results could be the effect of the experimental setup (or friction coefficient). As a result, the mounting system was modified to provide a very slight gap (< 3 mm) between the sheet and the mounting surface in the center of the tunnel. Results from this second experimental mounting configuration almost exactly matched the results of Wills, Lee, and Wyatt. The important lesson to be learned for rotorwash applications is that slight adjustments in the friction coefficient of a projectile or debris can significantly affect the initial flight speeds that the projectile or debris becomes airborne. Two additional important results are quantified by Wang's experiments. The first result is that the average value of the fraction of wind speed (J) that a sheet object reaches during flight varies as a function of thickness or mass increase. It is interesting to note the result from Wills, Lee, and Wyatt does not fit on Wang's graph where it might be expected. Wang discusses possible reasons for this in his discussion. The more important result is that sheet objects can be expected to accelerate to between 0.5 and 0.8 times the wind speed that is propelling them before impact. The second result is that Wang's variation of restraining force had minimal, if any, effect on the average value of J before impact. The only significant affect was on the initial speed that the object became airborne.

6. Simiu, E., and Cordes, M. R., "Tornado-Borne Missile Speed Probabilities," Journal of Structural Engineering, ASCE, Vol. 109, January 1983, pp. 154-168.

This paper presents a statistical approach to the hazards that result from large flying missiles of several types. The target is nuclear power plant components. The missile speeds that are considered in the analysis are much higher speeds than could be reached with rotorwash as the propelling source (tornadoes would be the most likely source). However, the analysis approach may be useful for future rotorwash hazard analysis applications.

7. Kind, R. J., and Wardlaw, R. L., "The Development of a Procedure for the Design of Rooftops Against Gravel Blow-Off and Scour in High Winds," Symposium on Roofing Technology, Paper No. 16, 1977, pp. 112-123.

This paper presents a simple general procedure that is step-by-step for the design of rooftops against gravel blow-off and scour in high winds. It is the culmination of several wind tunnel tests and other reports. It provides guidance to the critical gust speeds for scour (initiation of gravel movement) as well as the gust speeds required to carry gravel completely off a roof.

8. Holmes, J. D., "Trajectories of Spheres in Strong Winds with Application to Windborne Debris," *Journal of Wind Engineering and Industrial Aerodynamics*, Vol. 92, 2004, pp. 9-22.

In this paper, the trajectories of spheres carried by strong winds are studied theoretically and numerically. The application is to wind-borne debris occurring in severe windstorms such as hurricanes. It is shown that the effect of vertical air resistance is significant and should be included to accurately predict both horizontal and vertical velocities and displacements. Turbulence appears to have little effect on average trajectories but produces significant variability in individual trajectories. No correlation with test data is provided.

9. Lin, N., "Simulation of Windborne Debris Trajectories," Master's Thesis in Civil Engineering, Texas Tech University, August 2005.

Lin's thesis investigates the aerodynamics of flying debris through simulating debris trajectories. Extensive wind-tunnel tests on compact-like, plate-like, and rod-like debris are carried out in the Texas Tech University wind tunnel. The simulation procedure is well documented. Full-scale experiments are conducted using a C-130 Hercules aircraft to generate high winds. Three categories of parameters affecting debris trajectories are investigated: wind field, debris properties, and debris initial support. It is determined that although many parameters influence debris trajectory in the vertical direction, the Tachikawa parameter K governs the horizontal trajectory of debris. Empirical aerodynamic functions for debris horizontal trajectory are established based on both experimental data and theoretical equations of debris motion. These functions can be used to predict debris horizontal speed (at a given flight distance) and flight distance (for a given flight time). The application of these functions in developing debris impact criteria is discussed.

10. Holmes, J. D.; Baker, C. J.; and Tamura, Y., "Tachikawa Number: A Proposal," *Journal of Wind Engineering and Industrial Aerodynamics*, Vol. 94, 2006, pp. 41-47.

This paper describes the studies of windborne debris by Masao Tachikawa and shows that a parameter defined by him, representing the ratio of aerodynamic to gravity forces, is the main non-dimensional parameter determining the trajectories of debris items of all types. A case for naming this parameter as the "Tachikawa Number" is made. A good reference list of all the debris work conducted by Professor Tachikawa is also provided at the end of the paper.

11. Richards, P. J.; Williams, N.; Laing, B.; McCarty, M.; and Pond, M., "Numerical Calculation of the Three-Dimensional Motion of Wind-Borne Debris," *Journal of Wind Engineering and Industrial Aerodynamics*, Vol. 96, 2008, pp. 2188-2202.

In this paper, wind tunnel tests are described for rectangular plates with side length ratios of 1, 2, and 4 and long rods with sectional side length ratios of 1, 2, and 3. A range of initial angles of attack and tilt angles were also tested. The results clearly show that the force coefficients depend on both of these angles. Further, it is shown that the center of pressure moves both towards and across the wind. A 6-Degrees-Of-Freedom (6-DOF) trajectory model is developed, which makes use of the measured forces and a model for the center of pressure position. This trajectory model also incorporates damping terms and hysteresis effects due to dynamic stall

and apparent camber. It is shown that the computed trajectories reasonably match those observed with model and full-scale plates and rods in free flight. It is shown that this motion includes significant lateral movement and that horizontal speed very close to, or even exceeding, the wind speeds are predicted.

12. Lin, N.; Letchford, C. W.; and Holmes, J. D., "Investigations of Plate-Type Windborne Debris – Part I: Experiments in Wind Tunnel and Full Scale," *Journal of Wind Engineering and Industrial Aerodynamics*, Vol. 94, 2006, pp. 51-76.

This paper investigates the aerodynamic characteristics of plate-type debris. It then defines a model for the trajectory of windborne debris for incorporation into wind hazard risk assessment methodologies. These data and models have direct application to rotorwash hazard analysis. Experiments to determine the flight characteristics of various types of debris are described as conducted in the Texas Tech University wind tunnel. The trajectory data are presented in dimensionless form. Empirical expressions for estimating the horizontal flight speed and distance can then be derived. Results from wind-tunnel experiments are also shown to be in reasonable agreement with those from full-scale debris tests. These results can be used to validate numerical calculations of trajectories of plate-type windborne debris. This is an excellent resource along with the thesis by Lin (listed as a separate reference). The next reference is the second part of the two part paper.

13. Holmes, J. D.; Letchford, C. W.; and Lin, N., "Investigations of Plate-Type Windborne Debris – Part II: Computed Trajectories," *Journal of Wind Engineering and Industrial Aerodynamics*, Vol. 94, 2006, pp. 21-39.

This reference is a continuation of the previously listed paper. Trajectories of plates, carried by strong winds, were studied experimentally through wind tunnel and full-scale tests. The application is for predicting windborne debris trajectories in severe windstorms such as hurricanes. However, these data are applicable to rotorwash hazard analysis applications. A numerical model of square plate trajectories is developed and results are compared with experimental data from Tachikawa and data are presented in the Part I paper. Generally, good to excellent agreement is found between the modeled and experimental data. Lift forces induced by the Magnus effect were found to be significant in determining the trajectories.

14. Lin, N.; Holmes, J. D.; and Letchford, C. W., "Trajectories of Wind-Borne Debris in Horizontal Winds and Applications to Impact Testing," *Journal of Structural Engineering*, ASCE, Vol. 133, February 2007, pp. 274-282.

This paper considers the trajectories of compact- and rod-type wind-borne debris in horizontal winds using a combination of experimental and numerical studies. It is an excellent continuation of the Lin thesis and the other referenced papers by the same authors. These types of debris are representative of the roof gravel and timber debris currently used for testing building facades and storm shutters. The presented results indicate that the ratio of horizontal debris speed to wind gust speed is primarily a function of the horizontal distance traveled by the debris as it accelerates toward the wind speed. Empirical expressions to approximate the horizontal speed of debris as a function of travel distance and time are developed and may be used to establish rational debris impact criteria. These results have rotorwash hazard analysis application.

15. Baker, C. J., "The Debris Flight Equations," *Journal of Wind Engineering and Industrial Aerodynamics*, Vol. 95, 2007, pp. 329-353.

This paper presents a mathematical analysis of the equations of debris flight. In particular, the two-dimensional motions of two types of debris are considered, compact- and plate-like debris. The equations of motion for flight are derived in a generalized dimensionless form that reveals the fundamental controlling parameters of the problem. Simplified forms of the equations are then derived for the debris types. Large time asymptotic solutions are then derived for velocities and energies. Numerical solutions of the equations of motion are presented for a range of the controlling dimensionless parameters that are typical of full-scale conditions. These results are compared, where possible, with experimental data. The effect of simulating atmospheric turbulence on the flight of both types of debris is also evaluated. It is shown that if the gust wind speed during the course of the debris flight is used as the normalizing velocity, the variations in trajectory, although noticeable, are not particularly large. A discussion of how this analysis could be used in the design process is presented. Overall, the paper presents an excellent alternative formulation and solution to the debris problem when compared with the excellent approaches presented by other authors (such as the Lin, Holmes, and Letchford approach that is described in other references).

16. Kordi, B., and Kopp, G. A., "Evaluation of the Quasi-Steady Theory Applied to Windborne Flat Plates in Uniform Flow," *Journal of Engineering Mechanics*, ASCE, Vol. 135, July 2009, pp. 657-668.

This paper analyzes debris models based on a quasi-steady theory for the flight of windborne plates. It is shown that the effects of rotational lift, drag, and pitching moment are important and are therefore included in the described model. This model was used with success to predict the behavior of thin, square plates in a uniform stream, based on comparisons with existing experimental data. In fact, some of the scatter in the existing experimental data was explained by the numerical results. It is also shown that the buoyancy parameter is the key parameter in determining initial flight speeds. Normalization of spatial coordinates using this parameter resulted in the successful collapsing of data into a non-dimensional format.

17. Masters, F., and Gurley, K., "Performance of Embedded Gravel Roof Systems in Extreme Wind Loading," Department of Civil and Coastal Engineering, University of Florida, March 18, 2008.

The objective of the report was to provide a response to the Florida Building Commission on a proposal to eliminate gravel and stone roofing systems from hurricane prone areas in Florida. The report establishes that a scientific basis does exist for gravel and stone roofing systems to significantly contribute to property damage in high winds. The report documents two practical solutions to the calculation of gravel/stone blow-off, airborne transport, and downstream impact effects. Example calculations are provided. These results are clearly applicable to use in rotorwash hazard analyses. A good reference list is provided as a basis for the conclusions presented in the report.

18. Keller, J. D.; Whitehouse, G. R.; Wachspress, D. A.; Teske, M. E.; and Quackenbush, T. R., "A Physics-Based Model of Rotorcraft Brownout for Flight Simulation Applications," Presented at the 62nd Forum of the American Helicopter Society, May 2006.

This paper describes the development of a physics-based aerodynamic analysis suitable for engineering simulation of rotorcraft brownout conditions. Central to the brownout analysis is a comprehensive free-wake and fast panel model to predict the rotorwash flow field in close proximity to the ground, which is used to drive debris particle entrainment/transport and visual obscuration models to predict the degraded visual environment. Once completed, this analysis

may be coupled with any flight simulation environment. Results are presented demonstrating the ability to predict the rotorwash field in near ground operations as well as qualitative visualization of the brownout encounter in a visual simulation environment.

19. Govindarajan, B.; Leishman, J. G; and Gumerov, N. A., "Evaluation of Particle Clustering Algorithms in the Prediction of Brownout Dust Clouds," Proceedings of the American Helicopter Society's 67th Annual Forum, Virginia Beach, VA, May 3-5, 2011.

This paper investigates methods of clustering particles to simplify the task of simulating rotorcraft brownout conditions. The critical issue in simulation is the processing of extremely large numbers of particles so as to obtain dust clouds of acceptable fidelity. Computing the motion of each and every individual sediment particle in a dust cloud (which can reach into tens of billions per cubic meter) is computationally prohibitive. The paper documents the development of computationally efficient algorithms that can be applied as a function of problem requirements. Depending on the requirements, these algorithms offer the potential to significantly reduce computational costs while retaining the overall accuracy of a predicted brownout dust cloud.

20. Johnson, B.; Leishman, J. G.; and Sydney, A., "Investigation of Sediment Entrainment in Brownout Using High-Speed Particle Image Velocimetry," Proceedings of the American Helicopter Society's 65th Annual Forum, Grapevine, TX, May 27-29, 2009.

The "brownout phenomenon," the dual-phase flow environment induced by a rotor hovering above a sediment bed, was studied using high-speed flow visualization and Particle Image Velocimetry (PIV). The high frame rate camera, combined with advanced particle recognition software, permitted a simultaneous investigation of the evolution of the rotor wake in ground effect in conjunction with the processes of sediment uplift. High-resolution PIV measurements in the surface boundary layer showed large excursions in the ground shear produced by the wake vortices, these excursions being correlated with localized, intermittent increases in sediment entrainment rates. Once entrained, significant quantities of sediment were trapped and vertically transported by the vortex-induced upwash field. Large sediment particles were often spun out of the flow, and these particles adopted a modified saltation trajectory. In particular, the surface and upwash velocities were shown to strengthen significantly during the viscous merging of adjacent wake vortices. This mechanism proved fundamental in defining the concentration of entrained sediment and the maximum height to which sediment could be transported. Particles reaching sufficient heights were observed to recirculate into the rotor wake and return back towards the ground to initiate further sediment ejection. While providing new insight into the time- and length-scales associated with sediment entrainment by a rotor wake, the observations also bring into question the validity of equilibrium particle flux models currently being used for brownout simulations.

21. Syal, M., and Leishman, J. G., "Comparisons of Predicted Brownout Dust Clouds with Photogrammetry Measurements," Proceedings of the American Helicopter Society's 67th Annual Forum, Virginia Beach, VA, May 3-5, 2011.

In this paper, results from a Lagrangian dust cloud simulation are compared to dust cloud photogrammetry measurements generated by a helicopter during taxi-pass and approach-to-touchdown maneuvers. An inviscid-viscous matching method is used to predict the flow field arising from a combination of the rotor flow and the viscous flow region adjacent to the ground. Although not all of the data required to conduct the simulations were measured (e.g., exact weight of the helicopter, wind conditions, and trim state), the comparisons to the measured

evolution of the overall shapes and characteristic dimensions of the dust clouds are found to be relatively good. The results document the sensitivity of the predicted dust clouds to the weight of the helicopter, the ambient winds, and the flight path of the helicopter. An analysis of the predicted dust clouds using different particle sizes showed that the clouds contained mostly small particles that were entrained into the flow by unsteady pressure uplift and bombardment ejection mechanisms.

22. Sydney, A.; Baharani, A.; and Leishman, J. G., "Understanding Brownout Using Near-Wall Dual-Phase Flow Measurements," Proceedings of the American Helicopter Society's 67th Annual Forum, Virginia Beach, VA, May 3-5, 2011.

The two-phase flow environment produced by 1- and 2-bladed laboratory-scale rotors operating in-ground effect over a mobile sediment bed was studied. Time-resolved flow visualization, particle image, and particle tracking velocimetry were used. The high imaging rate of these systems allowed the time-history of the rotor wake interactions with the bed to be documented, providing a better understanding of the transient mechanisms that lead to the uplift of sediment and the formation of dust clouds. Three size ranges of characterized glass microspheres were used to represent sediment particles. The near-wall measurements exposed at least six fundamental uplift and sediment transport mechanisms below the rotor: 1. Creep, 2. Modified saltation and saltation bombardment, 3. Unsteady pressure loading effects, 4. Vortex induced trapping, 5. Reingestion bombardment (local and global), and 6. Secondary suspension. The highest sediment entrainment levels occurred within the wake impingement zone, mainly from the action of the blade tip vortices on the bed. Once entrained, significant quantities of sediment were intermittently trapped in the vortex-induced upwash field. Secondary sediment suspension was more prevalent with the 2-bladed rotor because of the merging of adjacent blade tip vortices and higher upwash velocities. The reingestion of the suspended particles into the vortex flow was also observed, often causing bombardment ejection of sediment from the underlying bed.

23. Tanner, P. E., "Photogrammetric Characterization of a Brownout Cloud," Proceedings of the American Helicopter Society's 67th Annual Forum, Virginia Beach, VA, May 3-5, 2011.

Brownout is a dangerous problem for rotorcraft operating in arid and dusty environments, such as Iraq and Afghanistan. Although interest in brownout has increased in the past decade, the fundamental physics that govern the shape and size of the cloud are not yet well understood. Many computational studies, as well as a few scaled experimental studies, have been performed in an attempt to further this understanding and to simulate and predict the brownout cloud formation. However, the phenomenon significantly lacks experimental data, particularly at full-scale, that is needed to validate brownout simulations being performed. In an effort to increase the available validation data set, tests were performed at the U.S. Army Yuma Proving Ground using photogrammetry to obtain brownout cloud data of an EH-60L Black Hawk. This application of the photogrammetry technique was verified in an earlier study. Landing approach data were examined in greater detail and enabled velocity components of points in the cloud to be determined, as well as the dimensions of structures within the cloud. Particle testing was performed on a sediment sample from the landing zone to document soil characteristics.

24. Wachspress, D. A.; Whitehouse, G. R.; Keller, J. D.; Yu, K.; Gilmore, P.; Dorsett, M.; and McClure, K., "A High-Fidelity Brownout Model for Real-Time Flight Simulations and Trainers," Proceedings of the American Helicopter Society's 65th Annual Forum, Grapevine, TX, May 27-29, 2009.

Excessive dust and debris kicked up by rotorwash during takeoff and landing, or “brownout,” can eliminate visibility creating a safety hazard and severely damaging engine parts and rotor blades. Brownout has also accounted for a significant number of helicopter accidents in Iraq and Afghanistan. It is recognized that brownout related mishaps can be greatly reduced through training. However, brownout rendering in training simulators is typically simplistic, lacking the level of physical fidelity required to properly characterize the brownout cloud. This paper describes the development and implementation of a “physics-based” brownout model that captures the complex flow field generated by rotorcraft maneuvering in the vicinity of the ground as well as the physical process of debris entrainment, transport, and visual obscuration. This model can be operated for off-line brownout analysis at high-fidelity or in real time piloted simulations at lower fidelity. These models, their validation, and the integration of the real-time brownout module into a U.S. Army flight simulation are described.

DAMAGE TO MATERIALS BY ENTRAINED PARTICLES AND FLYING DEBRIS

1. Dear, J. P.; Lee, H.; and Brown, S. A., "Impact Damage Processes in Composite Sheet and Sandwich Honeycomb Materials," *International Journal of Impact Engineering*, Vol. 32, 2005, pp. 130-154.

This reference provides impact damage documentation for “modern to advanced composite panel materials” for air/marine/road/rail vehicles. The reference in itself is not unique. However, it provides excellent examples of the type of impact damage that could be expected from flying debris with an advanced rotorcraft and modern equipment in the field. Specimens of Sheet Moulding Compound (SMT), Glass Mat Thermoplastic (GMT), and honeycomb sandwich panels (different skin/core materials) were impact tested by 5 kg and 1.55 kg projectiles (drop test) at up to 4.4 m/s (9.8 mph), or from a height of 1 meter (and less for the honeycomb panels). Damage is documented in detail and varies depending on velocity of impact and the of type material. Data are representative of risk due to flying debris that can be produced by a rotorcraft since these mass/velocity combinations can be produced by a large rotorcraft.

2. Grant, P. V.; Cantwell, W. J.; McKenzie, H.; and Corkhill, P., "The Damage Threshold of Laminated Glass Structures," *International Journal of Impact Engineering*, Vol. 21, 1998, pp. 737-746.

The effect of varying the thickness of individual glass layers on the outer layer impact resistance of a range of laminated glass constructions (similar to that which might be used in vehicle or aircraft windshields) is examined in this excellent reference. Granite chippings (gravel), similar to those used in traditional road construction, are used as projectiles and are accelerated to velocities in excess of 20 m/s for impact testing. Tests are conducted at both normal and 45-degree angles to the surface of the outer glass laminate and the critical velocity for damage initiation is documented. The results of this low velocity experiment indicate that the thickness of the outer glass ply is the primary parameter in determining the critical velocity for damage initiation, whereas the inner thickness has a secondary influence on this threshold. Off-axis impact testing indicates that it is the normal component of the impact velocity that determines the damage threshold. A detailed optical inspection of the failed laminates highlights the changes in the fracture mode from flexure-induced star cracking to top surface cone cracking as the overall laminate thickness is increased.

3. Ji, F. S.; Dharani, L. R.; and Behr, R. A., "Damage Probability in Laminated Glass Subjected to Low Velocity Small Missile Impacts," *Journal of Materials Science*, Vol. 33, 1998, pp. 4775-4782.

The probability of impact site damage in the outer ply of laminated glass that is subjected to low

velocity small missile impact is investigated. Instead of just measuring the minimum velocity required to damage the outer layer, a series of controlled impact tests were conducted to establish the probability of damage P_d at various impact velocities. A compressed air cannon was used to propel a 2-gram steel ball of 7.94 mm diameter normal to the outer glass ply with a cannon-to-glass distance of 25 mm. This distance insured that the velocity loss between the cannon muzzle and the impact site was negligible.

Results from this experiment are presented for two laminated glass units. The first laminated glass unit is composed of two 4.81-mm glass layers sandwiching a PVB inter-layer of 1.52 mm. The second unit is composed of two 4.78-mm glass layers sandwiching a PVB inter-layer of 0.76 mm. Results indicate that the 50% and 100% lines of probability for damage of the thicker test specimen are at 6.75 and 13.5 m/s, respectively. The same probabilities of damage are 5.5 and 10.0 m/s for the thinner unit. It must be emphasized that these damage probabilities are for the outside layer of glass and do not suggest inner layer damage or failure of the laminated glass unit as a whole.

4. Persson, J.; Breder, K.; and Rowcliffe, D. J., "Loading Rate Effects During Indentation and Impact on Glass with Small Spheres," *Journal of Materials Science*, Vol. 28, 1993, pp. 6484-6489.

This document provides the interested reader a good background into the mechanics of glass failure due to projectile impact. It also discusses the effect of loading rate during impact and how this parameter affects the failure process.

5. Beason, W. L., "Breakage Characteristics of 1/4 Inch Tempered Glass Subjected to Small Missile Impact," Final Report to Institute for Disaster Research, Texas Tech University, October 1975.

Polished plate glass (annealed) and fully tempered (heat treated) $\frac{1}{4}$ -inch thick sheet glass is tested to failure by 0.7- and 5.55-gm steel ball missiles. Statistical results are presented for cases involving no pressure loading and a pressure loading of 200 psf acting inward on the glass. The Mean Minimum Breakage Velocity (MMBV) is determined statistically from the results of the experiment. Details for the glass failure modes are provided.

6. Kaiser, N. D.; Behr, R. A.; Minor, J. E.; Dharani, L. R.; Ji, F.; and Kremer, P. A., "Impact Resistance of Laminated Glass Using "Sacrificial Ply" Design Concept," *Journal of Architectural Engineering*, Vol. 6, March 2000, pp. 24-34.

Annealed (AN) laminated architectural glass specimens are tested for inner ply impact resistance for a steel ball size of 2 gm, PVB interlayer thickness, and inner/outer glass ply type/thickness. The outer layer is broken or "sacrificed" in the experiment to define the Mean Minimum Breakage Velocity (MMBV) that cracks the inner ply. All results are provided in a cumulative breakage probability format as a function of impact velocity. The documentation is excellent and thorough; however, applicability to rotorwash related applications is limited since the outer glass ply is "sacrificed" to stop the projectile.

7. Saxe, T. J.; Behr, R. A.; Minor, J. E.; Kremer, P. A.; and Dharani, L. R., "Effects of Missile Size and Glass Type on Impact Resistance of "Sacrificial Ply" Laminated Glass," *Journal of Architectural Engineering*, Vol. 8, March 2002, pp. 24-39.

Annealed (AN), heat-strengthened (HS), and fully tempered (FT) laminated architectural glass specimens are tested for inner ply impact resistance as a function of steel ball size (2-, 8.4-, and 28.2-gm sizes) and inner/outer glass ply type/thickness. The outer layer is broken or

“sacrificed” in the experiment to define the Mean Minimum Breakage Velocity (MMBV) for each steel ball size that cracks the inner ply. All results are provided in a cumulative breakage probability format as a function of impact velocity. This reference is an extension of the Kaiser reference (previously listed). The documentation is excellent and thorough; however, applicability to rotorwash related applications is limited since the outer glass ply is “sacrificed” to stop the projectile.

8. Dharani, L. R.; Ji, F.; Behr, R. A.; Minor, J. E.; and Kremer, P. A., "Breakage Prediction of Laminated Glass Using the ‘Sacrificial Ply’ Design Concept," *Journal of Architectural Engineering*, Vol. 10, December 2004, pp. 126-135.

This reference is an extension of the Saxe reference (listed previously) and explores analytical modeling of the Mean Minimum Breakage Velocity (MMBV) for laminated architectural glass. Additional test data are summarized for inner ply breakage. However, applicability to rotorwash related applications is limited since the outer glass ply is “sacrificed” to stop the projectile.

9. Pantelides, C. P.; Horst, A. D.; and Minor, J. E., "Postbreakage Behavior of Heat Strengthened Laminated Glass Under Wind Effects," *Journal of Structural Engineering*, Vol. 119, February 1993, pp. 454-467.

Heat-Strengthened (HS) laminated architectural glass specimens are tested for outer ply impact resistance to a steel ball size of 2.03 gm. The interlayer thickness/type are varied. Two glass plies of 5 mm (3/16 inch) each are used. Breakage criteria are defined as: 1) DT – the minimum missile impact velocity that produces a surface fracture that can be visually detected at arm's length in good light and 2) BT – the minimum missile impact velocity that causes a glass ply to fracture through its entire thickness. The average DT value for the glass specimens with a PVB interlayer is 26.2 fps (8.0 m/s) and the mean BT value is 51.4 fps (15.7 m/s), a factor of approximately 2. The documentation is thorough and very applicable for rotorwash related applications where heat-strengthened (HS) glass is of interest.

10. Minor, J. E., "Lessons Learned from Failures of the Building Envelope in Windstorms," *Journal of Architectural Engineering*, Vol. 11, March 2005, pp. 10-13.

This reference is a short summary by the author of lessons learned over 33 years with respect to building envelope damage by windstorms. It provides a good overview of the potential for airborne missiles to do serious damage to structure, especially glass. Data are referenced to the damage potential for 2-gm size roof gravel to break Annealed (AN), Heat-Strengthened (HS), and Fully Tempered (FT) glass.

11. Minor, J. E., "Performance of Roofing Systems in Wind Storms," NRCA/NBS Proceedings of the Symposium on Roofing Technology, Paper 17, September 1977.

The performance of roofing systems for buildings is discussed from both a pressure loading and windborne missile perspective. A table of the impact velocities that 0.61- and 5.55-gm steel balls will cause glass breakage is included for five type/sizes of glass. These impact velocities range from a low of 37.4 ft/sec to a high of 71.4 ft/sec.

12. Minor, J. E., "Windborne Debris and the Building Envelope," *Journal of Wind Engineering and Industrial Aerodynamics*, Vol. 53, 1994, pp. 207-227.

This reference is a short summary by the author of lessons learned over 23 years with respect to building envelope damage by windstorms. It provides a good overview of the potential for airborne missiles (both roof gravel and 2x4 timbers) to do serious damage to structure, especially glass. Data are referenced to the damage potential for 5-gm size roof gravel to break Annealed (AN), Heat-Strengthened (HS), and Fully Tempered (FT) glass. Also, an introduction of the damage potential of 9 and 15 lb 2x4 timber missiles is discussed. Of less interest with respect to rotorwash issues is discussion on pressure loadings and building code development.

13. Minor, J. E.; Beason, W. L.; and Harris, P. L., "Designing for Windborne Missiles in Urban Areas," Journal of Structural Division, Vol. 104, November 1978, pp. 1749-1780.

This paper offers design information for reducing the effects of wind damage in urban environments and is referenced widely in the literature. It is also one of the first papers to recommend standardized missiles for design purposes in building a database of impact resistant materials (i.e. 2x4 inch timber and 5-gm gravel). A table of airspeeds that 5-gm gravel will accelerate to as a function of wind speed is provided (later references provide additional data as well as modeling methods). A table of minimum breakage velocities for Annealed (AN), Heat-Strengthened (HS), and Fully Tempered (FT) glass is provided from several experiments. These data are used to construct a glass design chart associated with 5% probability of glass failure for the various types/thicknesses of tested glass.

14. Beason, W. L.; Meyers, G. E.; and James, R. W., "Hurricane Related Window Glass Damage in Houston," Journal of Structural Engineering, Vol. 110, December 1984, pp. 2843-2857.

Hurricane Alicia struck downtown Houston, TX on August 18, 1983. Researchers were allowed into downtown Houston the following day to help survey the damage and eventually develop a "lessons learned" report. This paper summarizes these results. Key lessons learned that are applicable to rotorwash analysis are: 1) high winds produce impact damage from windborne missiles and 2) roof gravel size stones (1/4 to 1/2 inches) can be lifted into the wind stream at lower than expected velocities (< 50 mph) and can break all common types and thicknesses of glass (3/4-inch thick tempered glass can be broken at a minimum velocity of 37.2 mph by average size roof gravel). Other types of loose building material, debris, and failed parts of secondary structures located on exteriors and roofs of structures (lights, signs, antennas) present equally dangerous hazards. These results are confirmed by other referenced studies listed in the paper.

15. Anon, "Wind-Borne Debris, Impact Resistance of Residential Glazing," NAHB Research Center, January 2002.

Residential glass (annealed) is tested for impact resistance to "large missile" 2x4 lumber and pieces of roofing shingle material. The annealed glass that is tested includes various aspect ratios (2x2 and 2x4 foot panels) of 3/32- and 5/32-inch thick glass. The impact speed to determine fragility was accomplished using two methods. One method involved use of a pendulum and the second utilized an air cannon. The 2x4 used in the test was a 3 foot long Southern Yellow Pine weighting 4.6 pounds. The shingle "missile" was a 0.46 pound piece of three-tab GAF composition roof shingle. Results from these tests are presented as functions of momentum ($P = mv$, lb-sec) and kinetic energy ($E = 0.5mv^2$, ft-lb). The results indicate a steep slope for the momentum that is required to break 100% of the test specimens for both thicknesses of glass. There was also little difference in fragility between the two thicknesses impacted by the 2x4 missile (during the tests, all the glass specimens shattered except one). With shingle missiles, the momentum required to break the glass was less, but there was more

variability required to break 100% of the test specimens. It was also reported that post-failure analysis indicated that the glass showed more signs of perforation. This indicates a different loading per unit surface area upon impact for the two types of missiles.

16. Bole, S., "Investigation of the Mechanics of Windborne Missile Impact on Window Glass," Master's Thesis in Civil Engineering, Texas Tech University, December 1999.

This thesis uses 2x4 missiles of various lengths (4.5, 9, and 18 pounds) to investigate the impact resistance of annealed and tempered monolithic (single pane) and laminated glass. It also investigates whether kinetic energy or momentum criteria better describe the impact resistance. Various types of impact are also investigated; these include direct central impact, near edge (or eccentric) impact, and oblique central and eccentric impact. The results were not directed toward the minimum energy or momentum required to break the glass specimens. Therefore, the usefulness of the data for rotorwash applications is limited. However, one of the key findings was that for a constant kinetic energy (350 ft-lb for each specimen), the behavior of the glass specimens to "three different missiles having different mass and momenta, but the same kinetic energy upon impact, produced vastly different results. Therefore, kinetic energy of an impacting missile by itself cannot serve to predict the response of the impacted system components." This conclusion would indicate that energy deposited per projected impact area or some other measure might be a better indicator of impact resistance.

17. Anon, "A Summary Report on Debris Impact Testing at Texas Tech University," Wind Science and Engineering Research Center, June 2003.

This document is a summary of damage resulting from numerous types of large missiles that have been launched at numerous types of building materials. The types of missiles include lumber, PVC pipes, electrical conduit, and clay bricks. Types of building material include wood and metal plate stud walls, masonry and concrete walls, brick walls, plywood panels, and doors. Summary results of impact speeds, energy, momentum, and damage are provided. Most of the velocities of the projectiles exceed what rotorwash-propelled missiles can probably attain; however, it is good background material.

18. Abraham, V. J., "Missile Impact Resistance of Window Glass Construction," Master's Thesis in Civil Engineering, Texas Tech University, May 1995.

This thesis used a large 2x4 missile (9 pounds) launched at 50 fps (34 mph) to investigate the impact resistance of ¼-inch tempered monolithic (or non-laminated) and laminated glass. The experiment also focused on checkout of the new Texas Tech facility for conducting impact testing as well as the feasibility of conducting testing in accordance with two new building standards, SSTD 11-93 and 12-94. Generally, the results are not applicable to rotorwash applications because missile penetration, not cracks in the glass was the failure criteria. As expected, the monolithic glass performed worse than the laminated glass. The thesis should be read for details. The thesis does a good job of explaining how this type of testing is conducted.

19. Burley, C. E.; Niemeier, B. A.; and Koch, G. P., "Dynamic Denting of Autobody Panels," Society of Automotive Engineers, SAE Paper 760165, February 1976.

This paper publishes dynamic dent data for aluminum sheet (2036-T4, 5182-0, and 5056-H111) and steel (1010-CQ) used in automobile panels. These data are presented in the form of the ratio of dent depth to sheet thickness as a function of impact velocity. From these data a dent threshold velocity is defined and is used with the slope to calculate the dent depth for a panel of

defined thickness. The minimum and maximum gauge of panels that were tested varied from 0.027 to 0.040 inches, respectively. The projectile used to make the dent with the use of an air cannon was a one-inch diameter aluminum ball. Several models are proposed to expand the usefulness of these data, but the derived coefficients are not presented in the paper.

20. Burley, C. E., and Niemeier, B. A., "Denting Properties of Aluminum Autobody Components," Society of Automotive Engineers, SAE Paper 770199, February 1977.

This paper publishes dynamic dent data for actual automotive roof, fender, and door units. Both aluminum and steel components are used in the tests. The minimum and maximum gauge of these components varied from 0.0317 (doors) to 0.040 (roof) inches, respectively. These data are presented in the format of dent depth versus impact velocity for each material and component type. The impact velocity range was 20 to 60 mph for most components and the projectile was a one-inch diameter aluminum ball.

21. Niemeier, B. A., and Burley, C. E., "Hailstone Response of Body Panels – Real and Simulated," Society of Automotive Engineers, SAE Paper 780398, February 1978.

This paper publishes dynamic dent data for the effects of real and simulated hail on four steel and four aluminum production automobile hoods (model year 1977). These data are presented in the form of dent depth versus impact velocity. A correlation between hail of 1.25 and 1.5 inches in diameter and a one-inch aluminum ball indentor is established for reference purposes. This correlation is based on laboratory and actual field data collected from a hailstorm that damaged a car with a hood identical to one of the laboratory-tested hoods. These data are excellent for rotorwash hazard analysis purposes.

22. Thomson, R. G., and Hayduk, R. J., "An Analytical Evaluation of the Denting of Airplane Surfaces by Hail," NASA TN D-5363, August 1969.

This report presents an analytical method to calculate dent depth and width for sheet metal. The method applies to dent depths up to the depth where the sheet becomes punctured. Results, while not correlated with test data, are presented for aluminum sheet (2024-T4). The analysis was developed for hailstone impact analyses on aircraft. The presented method needs to be reviewed in the context of test data (now available) to determine its usefulness for rotorwash applications.

23. Souter, R. K., and Emerson, J. B., "Summary of Available Hail Literature and the Effect of Hail on Aircraft in Flight," NACA TN 2734, September 1952.

This report presents a very exhaustive summary of hail literature through 1952 and its effect on aircraft. These references are from many countries and go back as far as 1784. The relative velocities used in the analyses for hail impacting aircraft components make the data of minimal use for rotorwash analysis purposes. However, a simple method to calculate dent depth is provided that might be useful if it is correlated with recent experimental data for shallow dents at lower velocities. The discussion of hail in general, from a 1952 perspective, provides quite interesting reading.

24. Hodgins, B., "The Numerical Prediction of the Dent Resistance of Medium Scale Aluminum Structural Panel Assemblies," M.S. Dissertation in Mechanical Engineering, University of Waterloo (Canada), 2001.

An examination of static and dynamic dent resistance of structural panel assemblies representing automotive hoods is described in this thesis. Fabricated aluminum (AA5754 and AA6111) panel assemblies incorporating typical components of real automotive parts are tested. The assemblies allowed for parametric assessment of numerous factors affecting dent resistance including: panel thickness, panel curvature, panel support configuration and dent site location. An extensive experimental program evaluated the panel components under both static and dynamic denting conditions. Numerical simulations of the dent testing were undertaken using finite element techniques.

25. Thomas, D., "The Numerical Prediction of Panel Dent Resistance Incorporating Panel Forming Strains," M.S. Dissertation in Mechanical Engineering, University of Waterloo (Canada), 2001.

This thesis presents a numerical finite element method for predicting both static and dynamic denting in automotive body panels. Experimental validation of dent predictions using this method is shown to predict trends in dent resistance quite well. This reference is appropriate for structural engineers wanting a detailed treatment of the subject. However, experimental data on the sensitivity of aluminum (AA5754 and AA6111) to static and dynamic denting are presented for sheet thicknesses varying from 0.81 to 1.05 mm in thickness. The paper by Thomas et al., that is provided as an additional reference discusses this and additional work.

26. Thomas, D.; Hodgins, B.; Worswick, M.; Finn, M. J.; and Gong, K., "Static and Dynamic Denting of Paint Baked AA6111 Panels: Comparison of Finite Element Predictions and Experiments," SAE International, Paper 2001-01-3047, 2001.

This paper presents comparisons of finite element model predictions of static and dynamic denting with experimental results. Panels were stamped from 0.81-, 0.93- and 1.00-mm AA6111-T4 and then paint-baked to produce representative automotive outer body panels. Each type of panel was statically and dynamically dented at three locations using a 25.4-mm steel ball. Static denting was accomplished with incremental loading of 22.24-N loads up to a maximum of 244.48 N. Dynamic denting was accomplished by dropping the steel ball from heights ranging from 200 to 1,200 mm. The finite element predicted results show good correlation with the experiments, but also highlight the sensitivity of the predictions to formulation of the finite element problem. The thesis by Thomas that is provided as an additional reference discusses this work.

27. Yukutake, E.; Kaneko, J.; Sugamata, M.; and Kubota, M., "Dent Resistance of AZ31 Magnesium Alloy Sheets," Journal of Japan Institute of Light Metals, Vol. 56, No. 5, pp. 277-282, 2006.

Dent resistance of AZ31 magnesium alloy sheets is examined under static and dynamic denting tests. These tests are carried out for AZ31-O and AZ31-H24 sheets using circular blanks. Dent depth is measured and compared with that of aluminum alloys, copper alloy, and cold-rolled steel sheets.

28. Shi, M. F.; Meuleman, D. J.; Alaniz, C. L.; and Zurdosky, S. J., "An Evaluation of the Dynamic Dent Resistance of Automotive Steels," SAE International, Paper 910287, 1991.

The effects of sheet thickness, yield strength, strain aging, and prestrain on the dynamic dent resistance of sheet steel is investigated using an instrumented drop-weight test. It was found that the dynamic dent resistance is less dependent on the sheet thickness and the yield strength of the material than the static dent resistance. An empirical relation of dynamic denting force and energy with sheet thickness and material yield strength is derived for a flat panel. Data

confirm that dynamic dent resistance is improved using high-strength steels, including bake hardenable and rephosphorized steels.

29. Shi, M. F.; Brindza, J. A.; Michel, P. F.; Bucklin, P.; Belanger, J. P.; and Prencipe, J. M., "Static and Dynamic Dent Resistance Performance of Automotive Steel Body Panels," SAE International, Paper 970158, 1997.

As sheet metal thickness is reduced, dent sensitivity of automobile body panels becomes of increasing concern. In this paper, both quasi-static and dynamic dent tests are evaluated. Fully assembled doors made from mild and medium strength bake and non-bake hardenable steels are examined. Quasi-static dent tests are conducted at a test speed of 0.1 m/min while dynamic dent tests are conducted at a speed of 26.8 m/min. Dynamic dent testing is of interest because it more closely approximates real life denting scenarios, such as auto assembly handling/shipping damage, and parking lot damage from car door and shopping cart impact. The dent resistance performance of three types of steel is examined and compared for both static and dynamic test conditions.

30. McCormick, M. A.; Fekete, J. R.; Meuleman, D. J.; and Shi, M. F., "Effect of Steel Strengthening Mechanisms on Dent Resistance of Automotive Body Panels," SAE International, Paper 980960, 1998.

The panel dent resistance is an important consideration when selecting a type of steel for automotive use. Yield strength, thickness of the formed part, and stiffness (related to curvature) of the panel each contribute to the overall denting behavior. This study examines the dent resistance of several grades of steel, the objective being to determine if a fundamental difference in denting behavior exists between bake and non-bake hardenable grades after normalizing with respect to yield strength and thickness in the panel. Several key parameters that may contribute to the denting process are examined, including effects of yield strength, strain aging, work hardening, and stiffness.

31. Wang, Y., and Mallick, P. K., "Dynamic Denting Study of Aluminum Alloys," SAE International, Paper 2004-01-0183, 2004.

This paper describes the results of dynamic denting experiments conducted on AA5754 and AA6061 aluminum alloys. Dynamic denting tests were performed using a drop weight impact machine. The drop height was varied from 38 to 914 mm to generate impact velocities ranging from 53.4 to 254 m/min. The dent depth created at different drop heights was related to the input impact energy and peak load observed in the tests. The effects of sheet thickness and yield strength were investigated.

32. Shih, H. C., and Horvath, C. D., "Effects of Material Bending and Hardening on Dynamic Dent Resistance," SAE International, Paper 2005-01-0832, 2005.

A previously published acceleration compensation methodology for dynamic dent testing is successfully applied to calculate dent loads and applied energy in dynamic dent testing. This procedure was validated utilizing a hydraulic controlled dynamic dent tester on a number of low carbon and bake hardenable steels. The four different steel grades used were: DQSK, BH210, BH280, and DP600. The impact of strain rate on material bending and hardening in high-speed dynamic dent resistance testing is studied. Previous work investigated these factors in static dent resistance. The procedure utilized in that research is further developed and adapted for high-speed testing and used as a basis for a new, single loading incremental dynamic dent test.

This new test is used to investigate the effects of material bending and hardening in high-speed dynamic dent resistance. Due to higher impact energy in the dynamic testing, the 0.1-mm visible dent depth commonly used as a static dent test criterion may need to be modified.

33. Anon, "Advanced Vehicles Concepts, Technical Transfer Dispatch #6, ULSAB-AVC Body Structure Materials," ULSAB-AVC Consortium, May 2001. (refer to "<http://www.autosteel.org/Content/NavigationMenu2/Automotive/TechnicalInformation/default.htm>").

This reference provides static and dynamic dent data for metals used in automobile manufacturing. Coefficients for the equations of simple dent prediction methodologies are also provided.

34. Anon, "Ultralight Steel Auto Closures – Engineering Report," Porsche Engineering Services, April 2000. (refer to "<http://www.autosteel.org/Content/NavigationMenu2/Automotive/TechnicalInformation/default.htm>").

This reference provides extensive dent data for steel alloys used in automobile manufacturing (see Section 10 of the report).

35. Sadagopan, S., and Urban, D., "Formability Characterization of a New Generation of High Strength Steels," American Iron and Steel Institute, Report TRP 0012, March 2003. (refer to "<http://www.autosteel.org/Content/NavigationMenu2/Automotive/TechnicalInformation/default.htm>").

This reference provides extensive dent data for steel alloys used in automobile manufacturing (see Section 8 of the report).

STRUCTURE AND EQUIPMENT HAZARDS

1. Anon, "Minimum Design Loads for Buildings and Other Structures," American Society of Civil Engineers (ASCE) Press, ASCE Standard ASCE/SEI 7-05, Copyright 2006.

ASCE Standard ASCE/SEI 7-05 provides minimum load requirements for the design of buildings and other structures that are subject to building code requirements. Chapter 6 – Wind Loads provides detailed requirements for wind loads using three accepted methods. These three methods are: Method 1 – Simplified Procedure as specified in Section 6.4, Method 2 – Analytical Procedure as specified in Section 6.5, and Method 3 – Wind Tunnel Procedure as specified in Section 6.6. While many of these procedural requirements are not applicable to issues involving rotorwash, the wind loads specified in sections 6.1.4.1 and 6.2.4.2 are applicable. These sections specify the absolute minimum allowed loads for any design situation. Section 6.1.4.1 applies to the Main Wind-Force Resisting System (MWFRS). The MWFRS is defined as “the assemblage of structural elements assigned to provide support and stability for the overall structure.” Section 6.1.4.2 applies to components and cladding, defined as “elements of the building envelope that do not qualify as part of the MWFRS.” In both of these sections, the minimum wind load “shall not be less than 10 lb/ft² (0.48 kN/m²) multiplied by the area of the building or structure projected onto a vertical plane normal to the assumed wind direction.” It should be noted that structures, as defined by sections in the standard, could be street signs, light poles, and other odd shaped fixed objects. Therefore, for rotorwash applications, it should be assumed that 10 lb/ft² (0.48 kN/m²) should be considered a key threshold condition that should not be exceeded in avoiding hazardous situations involving buildings and structures.

In a separate telephone discussion with Dr. J. A. Peterka, one of the people involved in helping to develop the series of ASCE wind standards over the years, he notes that this minimum load condition is not based solely on winds, but it is considered as a minimum from several different historical perspectives (i.e. people pressing on a surface, age of structure). The reason for this discussion resulted from the calculation of the dynamic pressure (not necessarily the load since load is equal to the pressure times an area) that results from using the minimum wind speeds required for use in Methods 1 and 2 (from Figure 6-1 Basic Wind Speed in the standard). The minimum wind speeds are 85 mph in the three west coast states (California, Oregon, Washington) and 90 mph on the interior of the rest of the United States (coastal regions have special requirements). These wind speeds are defined as 3-second gust wind speeds in miles per hour at 33 feet above ground (in the boundary layer the wind speed would be reduced). The strict calculation of dynamic pressure (q) using air velocity (V) in ft/sec ($q = 0.5 * \text{air density} * V^2$) for 90 mph (132 ft/sec) is 20.71 lb/ft². However, the formula used in the standard is based on units of mph as the input. Therefore, the "dynamic pressure" at 90 mph is 9.63 lb/ft² as multiplied by additional coefficients that exist in the equation that also correct for the "units problem." Values for these coefficients are obtained from tables in the standard. These dynamic pressures, as defined at 33 feet, are considerably higher than the 10 lb/ft² minimum. Therefore, the question arises as to how this standard of 10 lb/ft² (0.48 kN/m²) should be applied for rotorwash related hazards, i.e. to signs or small fixed structures that can be totally engulfed by rotorwash. The velocity associated with a dynamic pressure of 10 lb/ft² is 62.5 mph (or 91.2 ft/sec or 54.3 kts). It should also be noted that the design wind requirements for asphalt shingles began at 60 and 90 mph for the lowest grades and increase to 150 mph for the highest grade (Standards ASTM D3161 or ASTM D7158 or UL 2390/ASTM D6381). These standards, since stated in mph, are generally more stringent design standards than 10 lb/ft². Of course, these standards do not take into account the effects of weathering, age, and incorrect installation for an asphalt shingle roof. In summary, the application of the 10 lb/ft² (0.48 kN/m²) load standard for rotorwash applications will require additional engineering effort to specify the appropriate way to use the standard since rotorwash is better characterized through a dynamic pressure measurement and not an applied load for hazard analysis purposes.

2. Mehta, K. C., and Delahay, J. M., "Guide to the Use of the Wind Load Provisions of ASCE 7-02," American Society of Civil Engineers (ASCE) Press, 2004.

This reference supports the use of the ASCE/SEI 7-02 version of "Minimum Design Loads for Buildings and Other Structures" through example calculations for each major section. The document also presents background information on how the standards were developed and provides supporting references. An updated version of this "How To" user's guide does not exist for the latest ASCE/SEI 7-05 version of the standard.

3. Peterka, J. A.; Cermak, J. E.; Cochran, L. S.; Cochran, B. C.; Hosoya, N.; Derickson, R. G.; Harper, C.; Jones, J.; and Metz, B., "Wind Uplift Model for Asphalt Shingles," Journal of Architectural Engineering, Vol. 3, No. 4, December 1997.

The wind uplift model for asphalt shingles that is presented in this summary report was developed at the request of the Asphalt Roofing Manufacturers Association (ARMA) by an independent group of wind engineers. The model was developed and validated through a series of wind tunnel and full-scale tests. The uplift mechanism is fully defined in the model so that the model can be used for loads calculations during product development. An example of how to correctly use the model is presented in the report. An excellent history of the problem of making load calculations on a sloped roof is also presented.

Details about the standards for testing asphalt shingles are not discussed in the report. Therefore, for details on the design wind requirements for asphalt shingles, which began at 85/90 mph for the lowest grade and increase to 150 mph for the highest grade, the reader is referred to Standards ASTM D3161, ASTM D7158, and UL 2390/ASTM D6381.

4. Bi, A., "Probabilistic Assessment of Wind Loads on a Full Scale Low Rise Building," M.S. Dissertation in Civil Engineering, Texas Tech University, May 2006.

The full-scale design loads and pressures on a rectangular-shape-low-rise building (13 ft high, flat roof, and no architectural features on the roof) located in open terrain are reported. These data are discussed in the context of developing reliability methods into building codes as an improvement to the practice of using only peak wind velocity and pressure coefficients (proportional to wind speed) as the basis for design standards. For rotorwash purposes, the thesis documents good full-scale wind loading data on a simple generic structure. The thesis also provides good background information on the development of wind load standards, the details of factors affecting wind loads on low-rise buildings (including the wind load equation in ASCE 7-05), and additional references in this field of study. If rotorwash data are substituted for wind data, then insight can be obtained as to the hazard potential of large rotorcraft on generic structures.

5. Hu, X., "Wind Loading Effects and Equivalent Static Wind Loading on Low-Rise Buildings," PH. D. Dissertation in Civil Engineering, Texas Tech University, May 2006.

Wind-induced full-scale pressures acting on the low rise Wind Engineering Research Field Laboratory (WERFL) building of Texas Tech University are integrated over each surface to obtain three forces and moments at the base of the building along the three principal axes with its origin at the geometric center of the building. Mean and fluctuating pressure distributions around the WERFL building are investigated. The pressure distributions producing maximum fluctuations along-wind loading, across-wind loading, and the torsional moment are investigated. A method to investigate the load combination of these forces is proposed and comparisons with the methods of ASCE 7-05 are made.

6. Zhou, N., "Wind Loads Simulation Methodologies and Application to the Full Scale Data," PH. D. Dissertation in Civil Engineering, Texas Tech University, December 2005.

Several methodologies of varying complexity that simulate wind-induced loads of low-rise buildings are investigated. A description of the modeling approaches and analytical codes used in the investigation are provided along with references. Comparisons of the results of these methodologies are compared with full-scale data from the low-rise Wind Engineering Research Field Laboratory (WERFL) building at Texas Tech University.

7. Anon, "Standard Test Method for Wind Resistance of Asphalt Shingles (Uplift Force/Uplift Resistance Method)," ASTM Standard D7158-08d, September 2008.

This standardized test method defines a procedure for calculating the wind resistance of asphalt shingles when applied in accordance with manufacturer's instructions, and sealed under defined conditions. Shingle designs that depend on interlocking or product rigidity to resist the wind cannot be evaluated using this test method. This method calculates uplift force exerted on a shingle by wind for a specified velocity. The uplift force is compared to the mechanical uplift resistance of the shingle. A shingle is determined to be wind resistant at a specified basic wind speed (based on shingle class) when the measured uplift resistance exceeds the calculated uplift

force for that velocity (3-second gust, ASCE 7-02). Examples of the calculation procedure are provided in addition to references for both wind tunnel and full-scale testing.

8. Anon, "Standard Test Method for Wind-Resistance of Asphalt Shingles (Fan-Induced Method)," ASTM Standard D3161-09, January 2009.

This test method defines a procedure for evaluating the wind resistance of asphalt shingles that results from the shingle's rigidity or mechanical interlocking or any combination thereof (including with sealant). The shingles are applied to a test panel in accordance with the manufacturer's instructions and tested at a 2:12 (17%) slope, or at the lowest slope permitted by those instructions. The fan-induced test is conducted for two hours (or until failure) on the test specimen at a defined speed as based on the classification of the shingle being tested.

9. Wolfe, R., "Wind Resistance of Light-Frame Structures," Proceedings of the Third Wood Building/Architecture Technical Seminar, Korean Forest Research Institute and American Forest and Paper Association, Seoul, Korea, November 1996.

This paper does not provide any detailed wind speed or dynamic pressure threshold information that is not better obtained from other documents listed in this summary (i.e. Minimum Design Loads for Buildings and Other Structures, ASCE Standard ASCE/SEI 7-05). The paper does provide a good description of some of the failure modes of light-frame structures and emphasizes the importance of flying debris as a serious hazard that is produced by high winds.

10. Letchford, C. W., "Wind Loads on Rectangular Signboards and Hoardings," Journal of Wind Engineering and Industrial Aerodynamics, Vol. 89, 2001, pp. 135-151.

This paper documents drag or normal force coefficients for a range of rectangular signboards (or hoardings) with varying aspect ratios, clearance ratios (relative to the ground), and porosities for a range of wind directions relative to a signboard. These data are also compared with data from other literature sources. This paper is an excellent resource if loads calculations are required for signboards or walls along the surface of the ground.

11. Shikha Jain, B. E., "Wind Effects on a Full-Scale Frame," M.S. Dissertation in Civil Engineering, Texas Tech University, December 2002.

This thesis documents the wind aerodynamic and loading effects on the structure of a single story rectangular building. In this case, the building is the Texas Tech University Wind Engineering Research Field Laboratory (WERFL) structure. The results are compared with wind tunnel data for this same structure and calculations from design load specification ASCE 7-98. This reference provides a good graphical description of the general wind flow around a simple rectangular building as well as a methodology to calculate loads on the structure. The results and methodology are applicable to calculation of rotorwash loads on a similar structure.

12. Kola, S., "Comparison of Wind Load Standards," M.S. Dissertation in Civil Engineering, Texas Tech University, December 1995.

This thesis compares the wind loading standards of the United States, Great Britain (England), Australia, and Canada. Parameters that are evaluated include reference wind speed, annual probability, terrain factor, gust factor, and pressure coefficients. A case study is then evaluated to compare the standards through calculation of wind loading forces for both a low-rise (15 feet tall) and a high-rise structure (160 feet tall). Differences in the calculations are then evaluated.

The reference is limited in application to rotorwash, but the techniques provide insight into how rotorwash loads might be applied to structures.

13. Zhao, Z., "Wind Flow Characteristics and Their Effects on Low-Rise Buildings," Ph.D. Dissertation in Civil Engineering, Texas Tech University, December 1997.

Two fundamental flow phenomena, the separation bubble (SB) and conical vortex, over the roof (flat and rectangular) of the Texas Tech University Wind Engineering Research Field Laboratory (WERFL) structure are studied in terms of flow characteristics and pressure-generating mechanisms. The separation bubble, having a mean reattachment-point approximately 10 ft from the leading edge, is oblong and elongated in the horizontal direction. Pressure distribution on the roof surface is intimately related to the structure of the SB. Low pressures (high suctions) on the leading roof corner are always related to strong vortices. Major findings contribute to understanding the mechanisms of pressure generation and the roles of turbulence and other properties of the incident wind in loading effects on this low-rise building.

14. Zhu, H., "C-130 Testings on Low-Rise Buildings," Ph.D. Dissertation in Civil Engineering, Texas Tech University, May 2006.

Investigations of wind-induced building damage have shown that roof and roofing systems are the most vulnerable parts of the building envelope to failure. Roof damage typically initiates around the roof corners and edges where extremely high suctions occur due to flow separation. In an effort to improve the structural performance of buildings in strong wind events, the behavior of two instrumented low-rise buildings was studied at near ultimate wind loads. This controlled full-scale experiment utilized the propeller wake of a C-130 transport aircraft to generate the desired winds. The test structures represented two low-rise residential constructions, in particular, a manufactured home and a modular home. The flow characteristics, induced external and internal pressures, and selected structural responses were measured during each event. To support several aspects of the full scale research effort, two wind tunnel tests were also performed in the Texas Tech Wind Tunnel. Results from the test were compared with the recommended ASCE 7-02 design standard. From a rotorwash perspective, the C-130 flow field has similarities with a rotorwash flow field. Therefore, this document is useful in application of rotorwash flow field data to loading calculations for structures. The listed reference by D. A. Smith (2002) provides additional data from these experiments.

15. Smith, D. A.; Chappell, K.; Mehta, K. C.; and Letchford, C. W., "Windstorm Mitigation Initiative, Report on C-130 Testing," Wind Science and Engineering, Texas Tech University, January 2002.

This document presents the results of using a C-130 transport aircraft to generate near ultimate wind loads on an instrumented manufactured home. The C-130 generated flow characteristics, the induced external and internal pressures on the instrumented home, and selected structural responses of the home were measured during each test event. This report, in essence, documents the test and the collected data for future use. Further discussion of these data are provided in the referenced thesis by H. Zhu (2006).

HELIPORT/VERTIPORT DESIGN

1. Smith, R. D., "Heliport/Vertiport Design Deliberations, 1997-2000," DOT/FAA/ND-00/1, May 2001.

This reference documents FAA sponsored civil heliport/vertiport design work conducted during the 1997 to 2000 time period. Two sections of this report document important information for developing a methodology to define rotorwash footprints. The first is titled, "CTR Rotorwash – Hazard Threshold for Civilian Passengers" (pp. 145-158). This section documents the discussion of overturning force requirements for personnel in a civilian vertiport environment. Supporting data for these requirements are detailed. The second section is titled, "Civil Tiltrotor – Maneuvering and Ground Taxi Rotorwash" (pp. 81-143). The flight test data documented in this section are from a FAA sponsored follow-on test of V-22 rotorwash characteristics. These data were acquired using the same test equipment and personnel that conducted the original V-22 Rotorwash Downwash Survey (NAWCADPAX-98-88-RTR). Data acquired during this follow-on test focused on static ground operations at several thrust levels below takeoff thrust as well as dynamic ground taxi and air taxi conditions. The data were measured at the same distances from the center of the V-22 and the same azimuths. These data are meant to complement the hover data documented in the original NAVAIR report and enhance the database for civilian tilt rotor applications.

2. Farrell, C., and Sitheeq, M. M., "Aerodynamic Considerations for Rooftop Helideck Design," American Society of Civil Engineers, Proceedings of the Fifth Conference on Engineering, Construction, and Operations in Space, pp. 1245-1251, June 1996.

An analysis of wind conditions and the aerodynamic design for the rooftop helideck of the Fairview Medical Center (FMC), Minneapolis, is presented as based on a literature search and an examination of Federal Aviation Administration (FAA) and United Kingdom Civil Aviation Authority (CAA) guidelines. The literature search identifies similar studies that have been conducted. The following issues are examined: pilot comments; the advisability of a model study; the need for field measurements; and the configuration of the helideck, including its location on the rooftop, dimensions, and the size of the air gap under it.

3. Liu, H., and Nateghi, F., "Wind Damage to Airport: Lessons Learned," Journal of Aerospace Engineering, Vol. 1, April 1988, pp. 105-116.

On June 17, 1985, a severe storm struck the Regional Airport at Columbia, Missouri. This storm struck at midnight and passed directly through the National Weather Service Station that was equipped with sophisticated weather instruments. During the one-minute period of time containing the maximum gust of the storm, the average wind speed was 50 mph (22 m/s) and the several second gust peaked at 96 mph (83 kts, 43 m/s), a ratio of 1.92. The results were heavy damage to 24 lightweight aircraft parked outdoors, a hanger, most parked cars, and to other airport facilities. The analysis of this incident has significant applications to rotorwash incident avoidance.

Most of the aircraft that were damaged had a complete failure of their tie-down systems. Two modes of failure were involved: 1) failure of the rope and 2) failure of the connector ring on the aircraft. Samples of broken ropes, mostly nylon and polypropylene, were collected and laboratory tested. Of the tested ropes, none exceeded 40% of the load capability of a new rope of the same material. Subsequent trips to the airport over the next several months documented that the average tie-down procedures used were lax and often improper to restrain an aircraft.

A survey of vehicle damage in the terminal parking lot indicated that almost all of the vehicles on the north side had a damaged windshield or window(s) or both. Paint was damaged and dents were found in panels. Small gravel was strewn about and was the most obvious source of glass

and structural damage (gravel was also found inside vehicles). A survey of the airport layout revealed that the gravel came from a gravel road to the southwest of the parking lot. Along the line of the wind, the gravel had caused substantial damage, including the breaking of windows in the National Weather Service building. Vehicles and structures, such as the terminal building, that were not along the path of the wind from the road did not sustain damage. Additional damage documented at the airport was the result of more random events involving flying debris and structural failure, such as a hanger door.

4. Lin, J. X.; Montpellier, P. R.; Tillman, C. W.; and Riker, W. I., "Aerodynamic Devices for Mitigation of Wind Damage Risk," 4th International Conference on Advances in Wind and Structures (AWAS '08), Jeju, Korea, May 2008.

This report discusses roof edge design innovations for reducing wind loads as well as minimizing displacement of ballast gravel. The aerodynamic approach to reducing roof loadings is based on full scale research that defines the uplift potential of roof edge vortices. Pressure measurements show a reduction of up to 75% in the uplift pressures in the roof corner area (when compared with present design practices). The threshold velocities for roof scouring (displacement of ballast gravel by corner edge vortices) are shown to increase by as much as a factor of two compared to conventional roof designs. While rotorwash induced air loads would not be expected to have a large impact on heliport or vertiport design, the hazards related to scouring of roof gravel are a well-known roof heliport design issue. This paper provides better insight into this problem as well as design process mitigation strategies. A list of references is provided.

5. Wu, F., "Full-Scale Study of Conical Vortices and Their Effects Near Roof Corners," Ph.D. Dissertation in Civil Engineering, Texas Tech University, 2000.

Investigations of wind-induced building damage have shown that the roof and roofing systems are the most vulnerable parts of the building envelope to failure. Damage to the roof typically initiates around the roof corners and edges where extremely high suctions occur because of flow separation. It is known that the high suctions near the roof corners and edges are mainly induced by a separated flow phenomenon, conical vortices. Full-scale experiments were conducted at Wind Engineering Research Field Laboratory (WERFL) of Texas Tech University to understand the mechanism for generation of conical vortex flow and the associated high roof surface suctions. Through decomposition of the incident wind vector into three parts: the wind speed, horizontal wind angle-of-attack, and vertical wind angle-of-attack, it was found that each part plays a different role in influencing the conical vortices and corner pressures. For rotorwash applications, the suction pressures are not particularly critical. However, rotorwash generated conical vortices could be a potential mechanism that transports gravel and other forms of debris across a roof. This transport mechanism could then create hazards for other personnel as well as the rotorcraft generating the flow field. Understanding of this mechanism should lead to improved heliport design configurations.

TRAILING WAKE VORTEX EFFECTS AND HAZARDS

1. Teager, S. A.; Biehl, K. J.; Garodz, L. J.; Tymczyszyn, J. J.; and Burnham, D. C., "Flight Test Investigation of Rotorcraft Wake Vortices in Forward Flight," Federal Aviation Administration, Technical Center, Atlantic City, NJ, Technical Report DOT/FAA/CT-94/117, February 1996.

This report presents the results of helicopter flight tests and wake vortex measurements that were designed to provide data necessary for the assessment of hazards to following aircraft. The tests were conducted using four helicopter types (CH-53E, UH-60, S-76, and UH-1) with weights varying from 7,600 to 70,000 pounds. A laser velocimetry system was used to measure the strength of the wakes that were also probed by small fixed-wing aircraft. Wake strength and decay characteristics were determined from the measured data. Separation criteria resulting from the test are discussed.

2. Schillings, J. J.; Ferguson, S. W.; Brand, A. G.; Mullins, B. R.; and Libby, J., "Wake Vortex Measurements of the XV-15 Tiltrotor Using a Mobile Ground-Based LIDAR System," Presented at the 57nd Forum of the American Helicopter Society, May 2001.

This report presents the initial results of a research program to measure trailing wake vortices of tilt rotor aircraft. Wake measurements of the Bell XV-15 were made using the MIT Lincoln Laboratory LIDAR system. Measured data include time histories of vortex positions, circulation strengths, and wake velocities. Selected data from each of the XV-15's modes of flight are presented in the paper. In airplane mode, the trailing wake resembles the wake of a fixed-wing aircraft of equal weight. In helicopter mode, the wake consists of a pair of vortices separated by the distance between the advancing blade tips. In conversion mode, the separation distance of the vortices is approximately a linear function of nacelle angle. Initial circulation is calculated using an analytical method and compared to flight test results. This analytical method suggests that during helicopter and conversion mode flight the wing tip vortex combines with the vortex from the advancing blades, while the vorticity from the retreating blades has a weaker influence.

3. Ferguson, S. W., and Dreier, M. E., "Empirical Wake Turbulence Model of Tiltrotor Aircraft," SAE International, Paper 2005-01-3182, 2005.

This report describes the methods used to collect and reduce wake turbulence data behind two distinct types of tilt rotor aircraft using a Light Detection and Ranging (LIDAR) measurement system, which uses laser velocimetry to measure the velocity of dust particles in air that has been disturbed by the passage of an aircraft. The test aircraft flew at various combinations of weight, rotor speed, airspeed, and configuration. The MIT LL LIDAR system measured the wake vortices with minimal pretest preparation and a large quantity of high-quality data were obtained in only a few days of testing. The data verifies that tilt rotor and fixed-wing wake characteristics are very similar. Data reduction methods used a classical horseshoe vortex system as a template and employed a vortex that had a rotational core and an irrotational outer field. Intersecting polynomials that are linear in downstream distance and bi-linear in downstream distance and mast angle adequately modeled vortex strength. A bi-quadratic polynomial function of downstream distance and mast angle adequately modeled core size.

4. Romander, Betzina, E.; Silva, M.; Wadcock, A.; and Yamauchi, G., "Investigating Tiltrotor Formation Flight Via 1/48-Scale Wind Tunnel Experiment," Presented at the 62nd Forum of the American Helicopter Society, May 2006.

This report describes two small-scale wind tunnel tests conducted in the Army 7x10-foot wind tunnel at NASA Ames Research Center. These tests featured two 1/48-scale V-22 models that were operated in a variety of simulated flight conditions including climb, descent, and level flight at various airspeeds and spatial separations. Forces and moments experienced by the trail aircraft were used to deduce the influence of the lead aircraft on the trail aircraft. Particle Image Velocimetry (PIV) data were collected to relate these forces and moments to features in the lead aircraft wake. In general, the roll moment on the trail aircraft is shown to be a maximum when

the aircraft are laterally offset by a full wingspan and the trail aircraft is vertically positioned so as to be in the wake of the lead aircraft. Furthermore, the roll moment is maximum when operating near 50 knots full-scale flight speed. Because the interaction persists far downstream and the vertical position of the wake is dependent on descent angle and flight speed, lateral separation has been determined to be the best means of avoiding adverse interactions between aircraft.

LOW SPEED INTERACTIONAL AERODYNAMICS (GENERAL REFERENCES)

1. Silva, M. J.; Wadcock, A. J.; Yamauchi, G. K.; and Long, K. R., "Wind Tunnel Investigation of the Aerodynamic Interactions Between Helicopters and Tiltrotors in a Shipboard Environment," American Helicopter Society 4th Decennial Specialist's Conference on Aeromechanics, San Francisco, CA, January 21-23, 2004.

The design and execution of a small-scale wind tunnel investigation of V-22 shipboard interactional aerodynamic phenomena is described. The objective of the investigation was to quantify the aerodynamic disturbances driving the uncommanded roll response experienced by a ground turning V-22 on the deck of an amphibious ship during recovery operations of upwind rotorcraft. Testing was conducted in the U.S. Army 7x10 Wind Tunnel at NASA Ames Research Center. Model hardware included the fabrication of a 1/48-scale representation of an LHA class ship as well as 1/48-scale powered models of the on-deck V-22 and three upwind aircraft representing a CH-46, a CH-53, and a second V-22. Data acquired include Particle Image Velocimetry measurements of the flow field and force and moment measurements of the on-deck V-22 response. An overview of the test design and a discussion of the results are presented.

INITIAL DISTRIBUTION LIST

		<u>Copies</u>
Defense Systems Information Analysis Center SURVICE Engineering Company 4695 Millennium Drive Belcamp, MD 21017	Ms. Jessica Owens jessica.owens@dsiac.org	Electronic
Defense Technical Information Center 8725 John J. Kingman Rd., Suite 0944 Fort Belvoir, VA 22060-6218	Mr. Jack L. Rike jackie.l.rike.civ@dtic.mil	Electronic
AMSAM-L	Ms. Anne C. Lanteigne hay.k.lanteigne.civ@mail.mil	Electronic
	Mr. Michael K. Gray michael.k.gray7.civ@mail.mil	Electronic
RDMR		Electronic
RDMR-CSI		Electronic
ARMY		
John Berry	john.d.berry6.civ@mail.mil	
Mark Calvert	mark.e.calvert.civ@mail.mil	
Michael Cardamone	michael.j.cardamone.mil@mail.mil	
Ned Chase	ned.a.chase.civ@mail.mil	
Jay Fletcher	jay.w.fletcher.civ@mail.mil	
Joe Grobmyer	joseph.e.grobmyer.civ@mail.mil	
John Grobmeier	john.r.grobmeier.civ@mail.mil	
COL Keith Hirschman	keith.a.hirschman.mil@mail.mil	
Charles Ingalls	charles.c.ingalls.civ@mail.mil	
Ernest B. Keen	ernest.b.keen.civ@mail.mil	
Barry Lakinsmith	barry.r.lakinsmith.civ@mail.mil	
Tom Maier	thomas.h.maier.civ@mail.mil	
Kelly McGuire	kelly.b.mcguire3.civ@mail.mil	
Layne Merritt	layne.b.merritt.civ@mail.mil	
Alex Moodie	alex.m.moodie.civ@mail.mil	
Marty Moulton	marvin.a.moulton.civ@mail.mil	
John Preston	john.preston.civ@mail.mil	
Mike Scully	michael.p.scully4.vol@mail.mil	
Bruce Tenney	bruce.s.tenney.civ@mail.mil	
Oliver Wong	oliver.d.wong.civ@mail.mil	

NAVY

Natalie Van Osch
Kevin McCarthy
Judah Milgram
Mark Silva
Steven Troutman

natalie.vanosch@navy.mil
kevin.mccarthy@navy.mil
judah.milgram@navy.mil
mark.silva@navy.mil
stephen.troutman@navy.mil

AIR FORCE

Bill Blake
Alicia Hartong
Adam Ladd
Rob Mitchell
Ryan Plumley
Barth Shenk
Dave Wisniewski
Cale Zeune

William.Blake2@wpafb.af.mil
Alicia.hartong@us.af.mil
adam.ladd@us.af.mil
robert.mitchell.61@us.af.mil
ryan.plumley@us.af.mil
barth.shenk@us.af.mil
david.wisniewski@us.af.mil
cale.zeune@us.af.mil

NASA

Susan Gorton
Wayne Johnson
Bill Warmbrodt
Mike Watts
Gloria Yamauchi

susan.a.gorton@nasa.gov
wayne.johnson@nasa.gov
william.warmbrodt@nasa.gov
michael.e.watts@nasa.gov
gloria.k.yamauchi@nasa.gov

CONTRACTOR (and Author)

Sam Ferguson (EMA) emaswf@aol.com